

# **Cycles within cycles**

—

## **The significance of temperature cycling, microbial Fe cycling and low-grade metamorphic nutrient immobilization for the genesis of banded iron formations**

### **Dissertation**

der Mathematisch-Naturwissenschaftlichen Fakultät

der Eberhard Karls Universität Tübingen

zur Erlangung des Grades eines

Doktors der Naturwissenschaften

(Dr. rer. nat.)

vorgelegt von

M. Sc. Manuel Schad

aus Stuttgart

Tübingen

2020



# **Cycles within cycles**

—

## **The significance of temperature cycling, microbial Fe cycling and low-grade metamorphic nutrient immobilization for the genesis of banded iron formations**

### **Dissertation**

der Mathematisch-Naturwissenschaftlichen Fakultät

der Eberhard Karls Universität Tübingen

zur Erlangung des Grades eines

Doktors der Naturwissenschaften

(Dr. rer. nat.)

vorgelegt von

M. Sc. Manuel Schad

aus Stuttgart

Tübingen

2020

Gedruckt mit Genehmigung der Mathematisch-Naturwissenschaftlichen Fakultät der Eberhard Karls Universität Tübingen.

Tag der mündlichen Qualifikation:	10.02.2021
Stellvertretender Dekan:	Prof. Dr. József Fortágh
1. Berichterstatter:	Prof. Dr. Andreas Kappler
2. Berichterstatter:	Prof. Dr. James Nebelsick





---

## Table of content

<b>Summary</b> .....	11
<b>Zusammenfassung</b> .....	15
<b>Statement of personal contribution introduction</b> .....	19
<b>Introduction</b> .....	21
Abstract .....	23
Introduction .....	25
When and where did cyanobacteria evolve? .....	25
Consequences of oxygenic photosynthesis for the marine iron cycle .....	37
Influence of oxygenic photosynthesis on terrestrial iron cycling .....	49
Conclusion .....	52
<b>Questions and Goals</b> .....	69
<b>Statement of personal contribution chapter 1</b> .....	73
<b>Chapter 1</b> .....	75
Abstract .....	77
Introduction .....	79
Material and methods .....	82
Results and discussion .....	85
Conclusions .....	99
Supplemental information .....	107
<b>Statement of personal contribution chapter 2</b> .....	155
<b>Chapter 2</b> .....	157
Abstract .....	159
Introduction .....	161
Material and methods .....	165
Results .....	174
Discussion .....	189
Conclusions .....	205

## Table of content

---

Supplemental information .....	219
<b>Statement of personal contribution chapter 3 .....</b>	<b>225</b>
<b>Chapter 3.....</b>	<b>227</b>
Abstract.....	229
Introduction .....	231
Materials and methods.....	234
Results .....	242
Discussion.....	260
Conclusions .....	279
Supplemental information .....	295
<b>General conclusions and outlook .....</b>	<b>311</b>
<b>Acknowledgments.....</b>	<b>327</b>
<b>Curriculum Vitae .....</b>	<b>331</b>







## Summary

Banded Iron Formations (BIFs), Fe- and Si-rich marine chemical sedimentary deposits which formed during the Archean and Paleoproterozoic (between 3.8 to 1.85 Ga), are the product of complex interplay between a suite of different key processes: environmental factors such as nutrient availability and temperature, microbial activity, diagenesis, and low-grade metamorphism. Major deposits formed during the Neoproterozoic and Paleoproterozoic eras are frequently used for reconstructing the paleoenvironment and yet, critical aspects of their genesis are highly debated. Even fundamental questions such as the nature of the primary precipitate and the mechanisms underlying its formation remain poorly constrained.

One potential model for the deposition of Archean and early Paleoproterozoic BIFs suggests that they formed through the metabolic activity of anoxygenic photoautotrophic Fe(II)-oxidizing bacteria (photoferrotrophs). This microbial activity would have led to the formation of poorly soluble Fe(III) (oxyhydr)oxides, which co-precipitated to varying degrees with organic carbon ( $C_{org}$ ), thus forming primary BIF sediments. Photoferrotrophic bacteria as agents of BIF deposition is currently supported by the interpretation of BIF P/Fe ratios, which is based on the empirical partitioning coefficients for phosphate ( $PO_4^{3-}$ ) adsorption onto primary Fe(III) (oxyhydr)oxides, ultimately suggesting a  $PO_4^{3-}$ -poor ocean during the Archean and early Paleoproterozoic. However, it is unknown how stable the association between  $PO_4^{3-}$  and primary Fe(III) (oxyhydr)oxides would have been under metamorphic conditions relevant for thermally immature (sub-greenschist facies) BIFs. The stability of the  $PO_4^{3-}$ -Fe(III) mineral co-precipitate and potential metamorphic  $PO_4^{3-}$  remobilization could have important implications for the interpretation of P/Fe ratios in BIFs and the proposed mechanism for BIF deposition.

Additionally, it remains unresolved how variations in the activity of photoferrotrophs, in response to temperature fluctuations, and the transformation of primary biogenic Fe(III) minerals during microbial Fe cycling in an early ocean would have influenced the deposition of BIFs. A previous study suggested that temperature fluctuations may be responsible for the alternating

deposition of Fe- and Si-rich layers in BIFs, and thus have created their characteristic banding, by influencing the metabolic activity of photoferrotrophs. While such a proposition is sensible, it remains unclear what would ultimately cause the separation between Si and Fe, especially given the high adsorption affinity of Si to freshly formed Fe(III) (oxyhydr)oxides. Furthermore, it is poorly constrained how cell-Fe(III) mineral aggregates formed by photoferrotrophs would have been altered during sedimentation. One process whose significance for BIF genesis is well documented is dissimilatory Fe(III) reduction (DIR). DIR is a microbial metabolism where heterotrophic bacteria couple Fe(III) reduction to  $C_{org}$  oxidation, utilizing substrates such as cell-Fe(III) mineral aggregates, resulting in the formation of secondary minerals such as magnetite and siderite, both of which are found in BIFs today. While both photoferrotrophy and DIR are individually well understood in the context of BIF genesis, it is unknown how, and to what extent, both metabolic processes would have already interacted in the water column and how this potential microbial Fe cycle would have influenced the (trans)formation of secondary Fe minerals as well as the properties of the minerals formed.

In summary, the overall goal of this thesis was to identify factors and mechanisms influencing the initial deposition of BIFs and to determine how the interplay between different microbial metabolisms would have influenced the (mineralogical) (trans)formation of primary precipitates during BIF genesis. Specifically, this thesis aimed to (1) quantify the influence of low-grade metamorphism on the post-depositional remobilization of  $PO_4^{3-}$  from primary Fe(III) (oxyhydr)oxides. (2) Verify the validity of a temperature-cycling model for creating the characteristic banding in BIFs and identify the mechanism(s) ultimately responsible for the separation of Fe and Si. (3) Determine the influence of repeated microbial Fe cycling occurring under conditions relevant for the ancient ocean (high Fe and Si concentrations) on the resulting secondary mineralogy. Specifically, the formation and preservation of minerals such as magnetite and siderite during dynamic, alternating redox cycles.

In **chapter one** of this thesis we exposed  $PO_4^{3-}$ -loaded ferrihydrite synthesized in the presence of different Si concentrations (0 mM, 0.5 mM, and 1.6 mM) to low-grade metamorphic conditions (170°C, 1.2 kbar) for 14 days. Following 14 days of incubation we found that metamorphic mineral transformation was primarily driven by  $C_{org}$  reactivity: hematite was the main mineral product in the absence of  $C_{org}$  or when complex  $C_{org}$  was used as proxy for ancient biomass. By contrast, magnetite and vivianite were formed when highly reactive glucose was

used. Metamorphic  $\text{PO}_4^{3-}$  remobilization depended on the mineral transformation pathway and up to 10 mol.%  $\text{PO}_4^{3-}$  was remobilized when hematite was formed. However,  $\text{PO}_4^{3-}$  was effectively immobilized when magnetite and vivianite were present (<1.5 mol.% mobilization). Collectively our results suggest that, although  $\text{C}_{\text{org}}$  reactivity had a profound influence on the metamorphic mineral transformation pathway, the overall extent of metamorphic  $\text{PO}_4^{3-}$ -mobilization was minor. Therefore, BIFs likely record ancient seawater  $\text{PO}_4^{3-}$  concentrations with high fidelity (reliable within 10%), thus supporting an  $\text{PO}_4^{3-}$ -starved ancient ocean.

In the study conducted in **chapter two** we cultivated the marine photoferrotroph *Rhodovulum iodosum* under conditions relevant for the ancient ocean and exposed it to temperatures fluctuating between 26°C (warm periods) and 5°C (cold period). We could show that during warm periods *R. iodosum* was metabolically active, resulting in the precipitation of primary Fe(III) (oxyhydr)oxides. Conversely, its metabolic activity was reduced during cold periods, which instead triggered the abiotic precipitation of amorphous Si. This confirms that temperature fluctuations could have triggered the alternating deposition of Fe-rich and Si-rich layers in BIFs. Furthermore, the combined results of scanning electron microscopy (SEM) analyses, surface charge measurements and potentiometric titrations suggest that  $\text{C}_{\text{org}}$  co-precipitated with Fe(III) (oxyhydr)oxides was responsible for the separation of Fe and Si, either by occupying surface functional groups required for Si sorption or due to electrostatic repulsion due to negatively-charged carboxyl/phosphodiester groups.

Finally, in **chapter three** we co-cultivated the marine photoferrotroph *Chlorobium* sp. N1 with a marine Fe(III)-reducing enrichment culture under conditions relevant for the ancient ocean. Our results show that photoferrotrophs and Fe(III)-reducing bacteria formed a highly dynamic microbial Fe redox cycle. Combined wet geochemical and SEM results suggest that Si and  $\text{C}_{\text{org}}$  were co-precipitated with freshly formed Fe(III) (oxyhydr)oxides during Fe(II) oxidation and released back into solution upon reductive dissolution of the Fe(III) minerals during microbial Fe(III) reduction. High concentrations of Si favored the formation of short-range ordered Fe(III) minerals like ferrihydrite while a mixed Fe(II)-bearing mineral phase, consisting of siderite and/or a Fe(II)-silicate, formed during Fe(III) reduction. No magnetite formation was observed over three consecutive microbial Fe cycles. Overall, our results imply that microbial Fe cycling would have been an important process in the ancient ocean water column, leading to the co-deposition of a ferrihydrite-Si composite and Fe(II) minerals in the initial BIF sediments.

In summary, this PhD thesis better constrained the microbial processes that took place during the initial deposition of Neoproterozoic to early Paleoproterozoic-aged BIFs and provided further evidence of the crucial role microbes likely played during the initial formation of primary BIF sediments. Their metabolic activity (as modulated by the paleoenvironment) and the microbial Fe cycle created by the interplay between different Fe-metabolizing bacteria offer potential explanations for some of the characteristics of BIFs: (1) their banding, (2) the presence of minerals such as siderite and Fe(II)-silicates, and (3) the low amount of  $C_{org}$  preserved in BIFs. This PhD thesis highlights the complexity underlying the genesis of BIFs, which is best untangled by taking a multidisciplinary approach.

## Zusammenfassung

Gebänderte Eisenerze (Banded Iron Formations, BIFs), Fe- und Si-reiche marine chemische Sedimentablagerungen, die während des Archaikums und Paläoproterozoikums (zwischen 3,8 und 1,85 Ga) gebildet wurden, sind das Produkt des komplexen Zusammenspiels zwischen einer Reihe unterschiedlicher Schlüsselprozesse: Umweltfaktoren wie Nährstoffverfügbarkeit und Temperatur, mikrobieller Aktivität, Diagenese und niedriggradiger Metamorphose. Bedeutende Ablagerungen, die während des Nearchaikums und frühen Paläoproterozoikums gebildet wurden, werden häufig zur Rekonstruktion der Paläoumwelt verwendet, jedoch sind kritische Aspekte ihrer Entstehung höchst umstritten. Selbst grundlegende Fragen wie die Art des primären Präzipitats und die dessen Bildung zugrunde liegenden Mechanismen sind nach wie vor schlecht eingegrenzt.

Ein mögliches Modell für die Ablagerung von archaischen und frühproterozoischen BIFs legt nahe, dass sie durch die Stoffwechselaktivität von anoxygenen photoautotrophen Fe(II)-oxidierenden Bakterien (Photoferrotrophen) gebildet wurden. Diese mikrobielle Aktivität hätte zur Bildung von schlecht löslichen Fe(III) (Oxyhydr)Oxiden geführt, die in unterschiedlichem Maße zusammen mit organischen Kohlenstoff ( $C_{org}$ ) ausgefällt wurden und somit primäre BIF-Sedimente bildeten. Photoferrotrophe Bakterien als Ursache der BIF-Ablagerung werden gegenwärtig durch die Interpretation der P/Fe-Verhältnisse in BIFs gestützt, welche auf empirischen Verteilungskoeffizienten für die Adsorption von Phosphat ( $PO_4^{3-}$ ) an primären Fe(III) (Oxyhydr)Oxiden beruht, und letztlich auf einen  $PO_4^{3-}$ -armen Ozean während des Archaikums und frühen Paleoproterozoikums hindeutet. Es ist jedoch unbekannt, wie stabil die Verbindung zwischen  $PO_4^{3-}$  und primären Fe(III) (Oxyhydr)Oxiden unter für thermisch unreife (Sub-Grünschiefer-Fazies) BIFs relevanten metamorphen Bedingungen gewesen wäre. Die Stabilität des  $PO_4^{3-}$ -Fe(III)-Mineral-Co-Präzipitats und die potentielle metamorphe  $PO_4^{3-}$  Remobilisierung könnte wichtige Folgen für die Interpretation der P/Fe-Verhältnisse in BIFs und den vorgeschlagenen Mechanismus der BIF-Ablagerung haben.

Darüber hinaus bleibt ungeklärt, wie Schwankungen in der Aktivität von Photoferrotrophen als Reaktion auf Temperaturschwankungen und die Umwandlung von primären biogenen Fe(III)-Mineralen während des mikrobiellen Fe-Zyklus in einem frühen Ozean die Ablagerungen von BIFs beeinflusst hätten. Eine frühere Studie legt nahe, dass Temperaturschwankungen für die abwechselnde Ablagerung von Fe- und Si-reichen Schichten in BIFs verantwortlich sind und somit, durch Beeinflussung der Stoffwechselaktivität von photoferrotrophen Bakterien ihre charakteristische Bänderung erzeugt haben könnten. Obwohl solch ein Vorschlag vernünftig ist, bleibt unklar, was schlussendlich die Trennung zwischen Si und Fe verursachen würde, insbesondere angesichts der hohen Adsorptionsaffinität von Si zu frisch geformten Fe(III) (Oxyhydr)Oxiden. Außerdem ist kaum eingegrenzt, wie von Photoferrotrophen gebildete Zell-Fe(III)-Mineralaggregate während der Sedimentation modifiziert worden wären. Ein Prozess, dessen Bedeutung für die Entstehung von BIFs gut belegt ist, ist die dissimilatorische Fe(III)-Reduktion (DIR). DIR ist ein mikrobieller Metabolismus, bei dem heterotrophe Bakterien Fe(III)-Reduktion an  $C_{org}$ -Oxidation koppeln, indem sie sich Substrate wie Zell-Fe(III)-Mineralaggregate zu Nutze machen, was zur Bildung von sekundären Mineralen wie Magnetit und Siderit führt, die heutzutage beide in BIFs gefunden werden. Während sowohl Photoferrotrophie als auch DIR im Kontext der Entstehung von BIFs wohlverstanden sind, ist unbekannt, wie und in welchem Ausmaß beide Stoffwechselprozesse einander bereits in der Wassersäule beeinflusst haben könnten und wie dieser potentielle mikrobielle Fe-Zyklus die Bildung und Umwandlung von sekundären Fe-Mineralen sowie deren Eigenschaften beeinflusst hätte.

Zusammenfassend war das übergeordnete Ziel dieser Arbeit, die die anfängliche Ablagerung von BIFs beeinflussenden Faktoren und Mechanismen zu identifizieren und festzustellen, wie das Zusammenspiel verschiedener mikrobieller Metabolismen die Bildung und (mineralogische) Umwandlung von primären Präzipitaten während der Entstehung von BIFs beeinflusst hätte. Konkret zielte diese Arbeit darauf ab, (1) den Einfluss von niedriggradigem Metamorphismus auf die Remobilisierung von  $PO_4^{3-}$  aus primären Fe(III) (oxyhydr)Oxiden nach deren Ablagerung zu quantifizieren. (2) Die Stichhaltigkeit eines Temperaturfluktuationsmodells für die Bildung der charakteristischen Bänderung in BIFs zu überprüfen und den Mechanismus/ die Mechanismen zu identifizieren, die schlussendlich für die Separierung von Fe und Si verantwortlich sind. (3) Den Einfluss wiederholter mikrobieller Fe-Zyklen, die unter für den



vorzeitlichen Ozean relevanten Bedingungen auftreten (hohe Fe und Si Konzentrationen), auf die sekundäre Mineralogie zu bestimmen. Insbesondere die Bildung und den Erhalt von Mineralen wie Magnetit und Siderit während dynamischer, alternierender Redox-Zyklen.

In **Kapitel 1** dieser Arbeit haben wir  $\text{PO}_4^{3-}$ -beladenen Ferrihydrit, der in Gegenwart verschiedener Si-Konzentrationen synthetisiert wurde (0 mM, 0,5 mM und 1,6 mM), für 14 Tage niedriggradigen metamorphen Bedingungen (170°C, 1,2 kbar) ausgesetzt. Nach 14 Tagen Inkubation stellten wir fest, dass die metamorphe Mineralumwandlung hauptsächlich durch die Reaktivität des  $\text{C}_{\text{org}}$  bestimmt wurde: In Abwesenheit von  $\text{C}_{\text{org}}$  oder wenn komplexer  $\text{C}_{\text{org}}$  als Proxy für vorzeitliche Biomasse verwendet wurde, war Hämatit das Hauptmineralprodukt. Im Gegensatz hierzu wurden Magnetit und Vivianit geformt, wenn hochreaktive Glukose verwendet wurde. Metamorphe  $\text{PO}_4^{3-}$  Remobilisierung war abhängig vom Mineralumwandlungsweg und bis zu 10 mol.%  $\text{PO}_4^{3-}$  wurden remobilisiert, wenn Hämatit gebildet wurde.  $\text{PO}_4^{3-}$  wurde jedoch effektiv immobilisiert, wenn Magnetit und Vivianit vorhanden waren (<1.5 mol.% Mobilisierung). Zusammengenommen legen unsere Ergebnisse nahe, dass, obwohl die  $\text{C}_{\text{org}}$ -Reaktivität einen tiefgreifenden Einfluss auf den metamorphen Mineralumwandlungsweg hatte, das generelle Ausmaß der metamorphen  $\text{PO}_4^{3-}$ -Mobilisierung gering war. Daher dokumentieren BIFs vorzeitliche Meerwasser  $\text{PO}_4^{3-}$ -Konzentrationen wahrscheinlich mit hoher Genauigkeit (verlässlich innerhalb von 10%), was somit einen  $\text{PO}_4^{3-}$ -armen vorzeitlichen Ozean stützt.

In der in **Kapitel 2** durchgeführten Studie haben wir den marinen Photoferrotrophen *Rhodovulum iodosum* unter für den vorzeitlichen Ozean relevanten Bedingungen kultiviert und ihn schwankenden Temperaturen zwischen 26°C (Warmzeiten) und 5°C (Kälteperiode) ausgesetzt. Wir konnten zeigen, dass *R. iodosum* während Warmzeiten metabolisch aktiv war, was zur Ausfällung von primären Fe(III) (Oxyhydr)Oxiden führte. Umgekehrt war seine Stoffwechselaktivität während Kälteperioden verringert, die stattdessen die abiotische Ausfällung von amorphem Si auslösten. Dies bestätigt, dass Temperaturschwankungen die alternierende Ablagerung von Fe-reichen und Si-reichen Schichten in BIFs ausgelöst haben könnten. Außerdem legen die kombinierten Ergebnisse von Rasterelektronenmikroskopie (REM)-Analysen, Oberflächenladungsmessungen und potentiometrische Titrations nahe, dass  $\text{C}_{\text{org}}$ , der zusammen mit Fe(III) (Oxyhydr)Oxiden ausgefällt wurde, für die Trennung von Fe und Si verantwortlich war, entweder durch die Besetzung von funktionellen Oberflächengruppen, die für

die Si-Sorption notwendig sind oder aufgrund von elektrostatischer Abstoßung durch negativ geladene Carboxyl-/ Phosphodiester-Gruppen.

Abschließend haben wir in **Kapitel 3** den marinen Photoferrotrophen *Chlorobium* sp. N1 mit einer Fe(III)-reduzierenden Anreicherungskultur unter für den vorzeitlichen Ozean relevanten Bedingungen co-kultiviert. Unsere Ergebnisse zeigen, dass Photoferrotrophe und Fe(III)-reduzierende Bakterien einen hochdynamischen mikrobiellen Fe-Redoxzyklus bildeten. Kombiniert legen nass-geochemische und REM-Ergebnisse nahe, dass während der Fe(II)-Oxidation Si und C<sub>org</sub> zusammen mit frisch gebildeten Fe(III) (Oxyhydr)Oxiden ausgefällt und nach reduktiver Auflösung der Fe(III)-Minerale während mikrobieller Fe(III)-Reduktion wieder in Lösung gebracht wurden. Hohe Si-Konzentrationen begünstigten die Bildung von amorphen Fe(III)-Mineralen wie Ferrihydrit, wohingegen während der Fe(III)-Reduktion eine gemischte Fe(II)-haltige Mineralphase, bestehend aus Siderit und/oder einem Fe(II)-Silikat, gebildet wurde. Während drei aufeinanderfolgenden mikrobiellen Fe-Zyklen wurde keine Magnetit-Bildung beobachtet. Insgesamt deuten unsere Ergebnisse darauf hin, dass der mikrobielle Fe-Kreislauf ein wichtiger Prozess in der vorzeitlichen Meerwassersäule gewesen wäre, was zu der gleichzeitigen Ablagerung einer Ferrihydrit-Si-Verbindung und Fe(II)-Mineralen in den ursprünglichen BIF-Sedimenten geführt hätte.

Insgesamt konnte diese Doktorarbeit die mikrobiellen Prozesse, die während der anfänglichen Ablagerung der BIFs des Neoproterozoikums und frühen Paläoproterozoikums stattfanden, besser einschränken und lieferte weitere Beweise für die entscheidende Rolle, die Bakterien wahrscheinlich bei der anfänglichen Bildung von primären BIF-Sedimenten spielten. Ihre metabolische Aktivität (durch die Paläoumwelt moduliert) und der durch das Zusammenspiel verschiedener Fe-metabolisierender Bakterien entstandene Fe-Zyklus bieten mögliche Erklärungen für einige der Eigenschaften von BIFs: (1) ihre Bänderung, (2) das Vorhandensein von Mineralen wie Siderit und Fe(II)-Silikaten und (3) die geringe Menge an C<sub>org</sub>, die in BIFs erhalten ist. Diese Doktorarbeit hebt die Komplexität hervor, die der Entstehung von BIFs zugrunde liegt und die am besten durch einen multidisziplinären Ansatz entschlüsselt und dadurch verstanden werden kann.

## Statement of personal contribution

### Introduction

#### **How did the evolution of oxygenic photosynthesis influence the temporal and spatial development of the microbial iron cycle on ancient Earth?**

Manuel Schad, Kurt O. Konhauser, Patricia Sánchez-Baracaldo, Andreas Kappler, Casey Bryce

**Published in:** *Free Radical Biology and Medicine* **140** (2019) 154-166

The work described in this chapter was supported by grants from the German Research Foundation (DFG) to Prof. Andreas Kappler and Dr. Casey Bryce, grants from the Natural Science and Engineering Research Council (NSERC) to Prof. Kurt O. Konhauser and a Royal Society University Research Fellowship to Dr. Patricia Sánchez-Baracaldo.

The framework of this review was conceptualized by Prof. Andreas Kappler and Prof. Kurt O. Konhauser. The paper was written in equal parts by Dr. Casey Bryce, Dr. Patricia Sánchez-Baracaldo, Prof. Kurt O. Konhauser and myself. I was further responsible for the final editing and revisions following the peer-review process. Prof. Andreas Kappler provided feedback and corrections to the manuscript. The paper was reviewed by two anonymous reviewers.



## Introduction

### How did the evolution of oxygenic photosynthesis influence the temporal and spatial development of the microbial iron cycle on ancient Earth?

Manuel Schad<sup>a</sup>, Kurt O. Konhauser<sup>b</sup>, Patricia Sánchez-Baracaldo<sup>c</sup>, Andreas Kappler<sup>a</sup>, Casey Bryce<sup>a</sup>

<sup>a</sup> Geomicrobiology, Center for Applied Geosciences, University of Tübingen, 72076, Tübingen, Germany

<sup>b</sup> Department of Earth and Atmospheric Sciences, University of Alberta, Edmonton, AB T6G 2E3, Canada

<sup>c</sup> School of Geographical and Earth Sciences, University of Bristol, Bristol, BS8 1SS, UK

**Published in:** *Free Radical Biology and Medicine* **140** (2019) 154-166

Schad M., Konhauser K. O., Sánchez-Baracaldo P., Kappler, A. and Bryce, C. (2019). How did the evolution of oxygenic photosynthesis influence the temporal and spatial development of the microbial iron cycle on ancient Earth? *Free Radic. Biol. Med.*, **140**, 154-166.

<https://doi.org/10.1016/j.freeradbiomed.2019.07.014>.



**ABSTRACT**

Iron is the most abundant redox active metal on Earth and thus provides one of the most important records of the redox state of Earth's ancient atmosphere, oceans and landmasses over geological time. The most dramatic shifts in the Earth's iron cycle occurred during the oxidation of Earth's atmosphere. However, tracking the spatial and temporal development of the iron cycle is complicated by uncertainties about both the timing and location of the evolution of oxygenic photosynthesis, and by the myriad of microbial processes that act to cycle iron between redox states. In this review, we piece together the geological evidence to assess where and when oxygenic photosynthesis likely evolved, and attempt to evaluate the influence of this innovation on the microbial iron cycle.





## 1. INTRODUCTION

The question of how oxygenic photosynthesis impacted the Archean (4.0–2.5 Ga) iron cycle should have a rather straightforward answer because the reaction of reduced (ferrous) iron with oxygen is rapid at circumneutral pH. Accordingly, as oxygen became available with the evolution of oxygenic photosynthesis, oxidized (ferric) iron should have precipitated out of seawater as an Fe(III) (oxyhydr)oxide mineral phase. However, the question is complicated by uncertainties in terms of when and where cyanobacteria first evolved and how this influenced the evolution and activity of iron-metabolizing bacteria, i.e. microaerophilic, nitrate-reducing and phototrophic Fe(II)-oxidizers as well as Fe(III)-reducers. Dating the onset of oxygenic photosynthesis has become a point of significant contention because there is no consensus on the timing of the evolution of cyanobacteria; putative evidence permits a possible range from as early as 3.8 Ga to as late as 2.4 Ga. The question regarding where cyanobacteria evolved first is also becoming more contentious, with cyanobacterial evolution having been proposed both on land as benthic mats and in the oceans as plankton. Furthermore, both questions are not trivial for the development of iron-metabolizing bacteria as the evolution of early cyanobacteria and the resulting oxygenation of the Earth's atmosphere and oceans would have significantly altered the biogeochemical iron cycle. Below, we summarize the evidence regarding the timing and location of cyanobacterial evolution, and present a hypothesis that attempts to place our current understanding of iron cycling on the early Earth within the context of cyanobacterial evolution and expansion.

## 2. WHEN AND WHERE DID CYANOBACTERIA EVOLVE?

There are a variety of studies based on geological, geochemical and biological evidence attempting to constrain the timing of the evolution of oxygenic photosynthesis. As a result, there is a wide range of interpretations of the rock record and a lack of consensus on both when and where oxygenic photosynthesis evolved. In this section, we present a chronological review of the key geological and geochemical evidence used to infer either an early (Archean) or late (Palaeoproterozoic) timing for the emergence of cyanobacteria. Against this geological backdrop, we discuss the genetic evidence which points to either scenario. We then review current literature

which aims to determine the location of cyanobacterial evolution and the expansion of cyanobacteria in the Earth system.

## **2.1. Geological evidence for an Archean evolution for cyanobacteria**

Numerous studies have provided evidence that suggests cyanobacteria could be as ancient as the oldest sedimentary rocks on Earth. Rosing and Frei (2004) reported elevated uranium (U)/thorium (Th) ratios in pelagic shales from the 3.8–3.7 Gyr Isua supracrustal belt in southwest Greenland. Those authors interpreted the high U/Th ratio as reflecting the presence of oxidizing (O<sub>2</sub>-rich) fluids which facilitated the preferential transport of U to the site of sedimentation where it was ultimately scavenged by planktonic biomass. However, other workers have suggested that this U(VI) might not require O<sub>2</sub> (Kopp et al., 2005). The same rocks were also previously described as having up to 0.4 wt% reduced carbon with  $\delta^{13}\text{C}$  values as low as  $-25.6\text{‰}$  (Rosing, 1999) – evidence seemingly pointing to biological carbon fixation. However, the biogenicity of such isotopic signatures in similar geologic settings has been questioned and instead Fischer-Tropsch-type synthesis of organic compounds has been invoked to explain highly negative  $\delta^{13}\text{C}$  values (Brasier et al., 2002; Fedo and Whitehouse, 2002; McCollom and Seewald, 2006; Van Zuilen et al., 2002). Iron formations (IF), from another location at Isua, were subsequently shown to contain positively fractionated chromium (Cr) isotopes, relative to the crust, suggesting oxidative chemical weathering involving the presence of atmospheric O<sub>2</sub> as an intermediate (Frei et al., 2016). At the 3.8 Gyr Nuvvuagittuq belt in Quebec, Canada, putative “microfossils” were recently described from ferruginous cherts that were interpreted as marine hydrothermal precipitates (Dodd et al., 2017). The “microfossils” occur as micrometer-sized hematite tubes and filaments that are reminiscent of modern O<sub>2</sub>-dependent, microaerophilic Fe(II)-oxidizing bacteria found in Fe(II)-rich modern environments. Importantly, extant Fe(II)-oxidizing bacteria generally use O<sub>2</sub> as the electron acceptor, so by extension, if the “microfossils” are as advertised, then aerobic metabolisms must already have evolved by 3.8 Gyr.

More compelling is the geochemical evidence of oxygen oases at 3.3–3.0 Ga. Satkoski et al. (2015) measured U enrichment and positive  $\delta^{56}\text{Fe}$  values in shallow-water sediment compared to deep-water sediments in the 3.25 Ga Manzimnyama IF of the Fig Tree Group in South Africa. The authors suggested that a discrete redox boundary between deep and shallow waters existed at this time. They proposed that deepwater iron-rich IF samples were oxidized in water where O<sub>2</sub>

contents were lower than shallow-water iron-poor IF samples that were precipitated entirely above the redoxcline where O<sub>2</sub> contents were uniformly elevated. In marine shales from the 3.2 Gyr old Soanesville Group in northwestern Australia, nitrogen (N) isotope values of the kerogen within the shales were interpreted as being derived from biological nitrogen fixation, most probably using molybdenum (Mo)-based nitrogenase (Stüeken et al., 2015). Given that Mo is sourced from oxidative weathering of Mo-bearing sulfide minerals in crustal rocks, the use of a Mo-based enzyme suggests Mo availability (and by extension some oxidative weathering because Mo is more mobile under oxidizing conditions) already occurred at that time. Interestingly, the Gorge Creek Group that immediately overlies the Soanesville Group contains shales that are hundreds of meters thick, hundreds of kilometers in aerial extent, deficient in sulfur and iron, and with up to 10 wt% total organic carbon (TOC). Buick (2010) speculated that only oxygenic photosynthesis could have generated that much biomass as anoxygenic photosynthesis would have been limited in electron donors. Similarly, in the 3.22 Gyr Moodies Group in South Africa, the presence of microbial mats and associated sedimentary structures in siliciclastic tidal and alluvial deposits (Homann et al., 2015; Homann et al., 2018) suggests the presence of a phototrophic community, which has been interpreted to consist of early cyanobacteria based on the mat morphology and facies association. Furthermore, recent findings of terrestrial microbial mats draping fluvial conglomerates with N isotopes suggestive of denitrification (Homann et al., 2018) strengthens the argument that localised sources of oxygen were already present at that time. This is because the presence of significant amounts of nitrate cannot be explained by lightning-induced oxidation of N-compounds but requires the activity of aerobic ammonium-oxidizing microorganisms.

Based on the distribution of Cr isotopes and redox-sensitive metals in both a palaeoweathering horizon and shallow-water IF from the ca. 2.96 Gyr Mozaan Group in South Africa, Crowe et al. (2013) argued that there was already extensive mobilization of redox-sensitive elements from land to the oceans via oxidative weathering. Those authors also calculated a minimum estimate for atmospheric oxygen being  $3 \times 10^{-4}$  percent atmospheric levels (PAL): to place this value in context, previous estimates for the so-called Great Oxidation Event (GOE) at 2.32 Gyr placed atmospheric O<sub>2</sub> levels at only  $10^{-5}$  PAL (e.g., Bekker et al., 2004). That study, however, has been called into question on the grounds that the Cr isotope values were instead the product of modern oxidative weathering rather than Mesoarchean oxidative

weathering (Albut et al., 2018). Planavsky et al. (2014) also measured Mo isotopes from the same IF units in the Mozaan Group and reported large negative  $\delta^{98}\text{Mo}$  fractionations that are consistent with the sorption of Mo onto manganese (Mn) (oxyhydr)oxides that precipitated in the shallow water column. This is of significance since Mn(IV) (oxyhydr)oxide formation requires biologically-driven Mn(II) oxidation using  $\text{O}_2$  as the electron acceptor, hence the shallow marine environment already had significant dissolved oxygen accumulation (for an alternate mechanism invoking Mn-based phototrophy, see Johnson et al., 2013).

By 2.7 Ga, a wide range of geochemical analyses support the premise for widespread ocean oxygenation. Stüeken et al. (2012) suggested that an increase in the total sulfur and Mo supply to marginal marine sediments at that time was best explained by the biological oxidation of crustal sulphide minerals. In 2.7–2.6 Ga black shales, enrichment in Mo, rhenium (Re) and osmium (Os), as well as fractionation of Fe and Mo isotopes, all suggest that  $\text{O}_2$ -rich niches already existed at that time (Czaja et al., 2012; Kurzweil et al., 2016; Siebert et al., 2005; Thomazo et al., 2013; Wille et al., 2007). Also, continuously increasing  $\delta^{98}\text{Mo}$  values in the black shales, carbonates, and IF of the Marra Mamba and Wittenoom formations (2.6–2.5 Ga) in the Hamersley Basin have been tied to the sorption of light Mo isotopes onto Mn(IV)-oxides (Kurzweil et al., 2016). Perhaps one of the strongest pieces of evidence for oxygen availability at that time comes from the presence of extremely isotopically depleted kerogen within 2.72 to 2.59 Ga carbonates and shales in the Hamersley Province of Western Australia, the Kaapvaal Craton in South Africa, and the Superior Craton in Canada. Organic carbon  $\delta^{13}\text{C}$  values in these metasediments are as low as  $-60\text{‰}$  (Eigenbrode and Freeman, 2006; Hayes, 1983). The most  $^{13}\text{C}$ -depleted values have been ascribed to the assimilation of methane by chemolithoautotrophic, methanotrophic bacteria that in the modern world utilise electron acceptors such as  $\text{O}_2$ , sulfate ( $\text{SO}_4^{2-}$ ), nitrate ( $\text{NO}_3^-$ ) or even Mn(IV) and Fe(III) (Beal et al., 2009; Boetius et al., 2000; Cai et al., 2018; Ettwig et al., 2010; Ettwig et al., 2016). The presence of these metabolisms is a strong indication for the presence of  $\text{O}_2$  because oxygen is either used directly as the terminal electron acceptor (TEA), or is required in the formation of alternative electron acceptors such as sulfate, nitrate and Mn(IV). Oxygen is not necessary for methane oxidation coupled to Fe(III) reduction because the latter can be formed via anoxygenic photosynthesis. Nitrogen isotope compositions of kerogens in minimally altered shales from the Campbellrand-Malmani carbonate platform in South Africa and broadly correlative sedimentary succession in Western Australia (Hamersley

Group) show a significant rise in  $\delta^{15}\text{N}$  values between 2.67 and 2.50 Ga (Garvin et al., 2009; Godfrey and Falkowski, 2009). Exceptionally high  $\delta^{15}\text{N}$  values are also reported for the 2.72 Ga Tumbiana Formation (Thomazo et al., 2011). This positive shift has been interpreted as evidence for the onset of nitrification-denitrification reactions in the surface oceans (e.g., Beaumont and Robert, 1999). Stromatolitic assemblages in the 2.72 Ga Tumbiana Formation, Western Australia, were suggested to have been constructed by photoautotrophs that may have utilised oxygenic photosynthesis (Buick, 1992). More recent work has put forward the idea of filamentous bacteria, capable of gliding motility and phototaxis which tangle up upon contact, resulting in the formation of tufted mats. To date only a few microorganisms have been identified to be capable of such behavior, with cyanobacteria probably being the most prominent among them. Therefore, similar sedimentary structures in the Tumbiana Formation are a strong indicator of early cyanobacteria producing oxygen by 2.72 Ga (Flannery and Walter, 2012; Sim et al., 2012). Potential fossil assemblages of filamentous and coccoidal cyanobacterial colonies have been identified in the ca. 2.6 Gyr Campbellrand Group, South Africa (Altermann and Schopf, 1995). However, a poor degree of preservation and the relative simplicity of those microfossils have raised questions about whether an unambiguous identification of cyanobacteria can be made (Knoll, 2008, 2015), making the 1.9 Ga microfossils of the Belcher Islands, Canada, the earliest generally agreed upon fossils of cyanobacteria in the rock record (Hofmann, 1976).

## **2.2. Genetic evidence for an Archean evolution for cyanobacteria**

The early evolution of photosynthesis sometime in the Eoarchean (4.0–3.6 Ga) or Paleoarchean (3.6–3.2 Ga) likely occurred within bacterial lineages that are no longer extant. While this presents a challenge when studying the evolution of early phototrophs, biological evidence has already provided insights into both the evolution of the core proteins involved in oxygenic photosynthesis (Cardona, 2018; Cardona et al., 2018) and the appearance of cyanobacteria's common ancestor inferred from genomic data (Ponce-Toledo et al., 2017; Sánchez-Baracaldo, 2015; Sánchez-Baracaldo et al., 2017; Sánchez-Baracaldo et al., 2014; Schirromeister et al., 2015). For instance, recent studies support an early Archean origin of the core reaction center proteins (photosystem I and photosystem II, PSI and PSII, respectively), which are exclusively found in cyanobacteria and photosynthetic eukaryotes (Cardona et al., 2018). Biochemical and functional analysis of the sequence and structure of the core subunits of reaction centers of PSII predict that phototrophs already developed the capacity for water

oxidation in the Paleoproterozoic, probably before 3.22 Ga (Cardona et al., 2018). While it remains unclear how efficient such ancient processes would have been during the Archean, a recent study (Cardona et al., 2018) suggests evidence for low levels of oxygen being produced as the result of biological activity at this time. Other lines of evidence, such as the evolution of FtsH proteases, proteins specifically dedicated to the repair of PSII (D1 and D2), show that these proteins diverged early on, possibly between 3.8-3.5 Ga (Shao et al., 2018). This is significant because the oxygenic lineage of PSII-FtsH proteases diverged before FtsH proteases found in all the other groups of phototrophs (Shao et al., 2018). These findings support the view that genes associated with the photosynthetic process have co-evolved with key photosynthetic proteins (Shi et al., 2005), thus providing additional evidence for the early divergence of oxygenic phototrophs.

When looking at the biological record, it is worth noting that there are different levels of complexity when studying the early emergence of oxygenic phototrophs. At the gene level, the timing of the duplication event leading to the emergence of core reaction center proteins D1 and D2 at ~3.2 Ga (Cardona et al., 2018) implies that an inefficient water oxidation metabolism would have been present 0.8 Gyr before the GOE, and the origin of the crown cyanobacteria group (Blank and Sanchez-Baracaldo, 2010; Sánchez-Baracaldo, 2015; Schirmermeister et al., 2015). At the organismic level, phylogenomic and molecular clock analyses point to a much later origin of photosynthesis with most studies showing that the crown group of cyanobacteria appeared during the late Archean (Blank and Sanchez - Baracaldo, 2010; Sánchez-Baracaldo, 2015; Schirmermeister et al., 2015) or Paleoproterozoic (Shih et al., 2017; Shih et al., 2013). It is important to emphasise that while oxygenic phototrophy can be traced back to the early Archean, highly sophisticated forms of D1 proteins (G3 and G4 which are known to bind to the  $Mn_4CaO_5$  cluster or the water-splitting catalyst) are estimated to have originated near the GOE itself (Cardona et al., 2018).

### **2.3. Geological evidence for a Paleoproterozoic evolution of cyanobacteria**

As an alternative to an Archean evolution, it has been proposed that cyanobacteria evolved much closer to the GOE, in the Palaeoproterozoic. The GOE represents a transition from an atmosphere that was essentially devoid of free oxygen ( $O_2 \ll 10^{-5}$  PAL, 2 ppmv) to one with  $O_2$  concentrations  $>10^{-5}$  PAL. These estimates derive from the pioneering study of Farquhar et al. (2000) who discovered that marine sediments older than 2.45 Ga contain mass-independent

fractionations of sulfur (S-MIF), while younger rocks do not. Farquhar et al. (2010) hypothesized that the major source of the S-MIF signal is the photodissociation of  $\text{SO}_2$  into water-soluble (sulfate,  $\text{SO}_4^{2-}$ ) and water-insoluble fractions (elemental sulfur,  $\text{S}_8$ ) that are preserved when contrasting isotopic compositions of reduced and oxidized sulfur species are deposited from the atmosphere and incorporated into sedimentary rocks. The signature of S-MIF photochemistry is not only rapidly homogenized in an oxygenated environment, but ozone also inhibits  $\text{SO}_2$  photolysis by UVC irradiation. Indeed, Pavlov and Kasting (2002) computed that  $\text{O}_2$  levels as low as  $10^{-5}$  PAL would prevent MIF-S from reaching the sediments. The disappearance of S-MIF from various locations worldwide has now been constrained to between 2.45 and 2.32 Ga (Bekker et al., 2004; Gumsley et al., 2017; Guo et al., 2009; Luo et al., 2016; Papineau et al., 2007; Partridge et al., 2008; Williford et al., 2011), although the potential for minerals hosting the MIF signature to be cycled through terrestrial reservoirs and during subduction and volcanic processes means that MIF-S signals could be expected to be preserved for 10–100 million years after the GOE (Reinhard et al., 2013). Other lines of geological evidence for the GOE include the first occurrences of “red beds” (Chandler, 1980; Melezhik et al., 2005), copper deposits (Kirkham and Roscoe, 1993), iron rich paleosols (Rye and Holland, 1998), and the presence of extensive manganese deposits (see below) and phosphorites following the GOE (Bekker and Holland, 2012; Holland, 2005). Furthermore, well-rounded detrital pyrite, uraninite, and siderite grains are only found in clastic deposits before the GOE because these grains are unstable under oxic conditions (England et al., 2002; Hofmann et al., 2009; Rasmussen and Buick, 1999; Roscoe, 1996), suggesting that atmospheric oxygen levels would have been lower than  $3.2 \times 10^{-5}$  PAL (~40 nM; Johnson et al., 2014).

This rise of free atmospheric oxygen facilitated the onset of oxidative continental weathering reactions and increased the flux of dissolved sulfate and redox-sensitive trace elements to the oceans. Sulfate had two major sinks: (1) iron sulfide precipitation as a consequence of bacterial sulfate reduction in the water column, or (2) evaporitic precipitation of gypsum. In the first instance, Canfield (1998) proposed that increased levels of sulfide in the oceans effectively titrated out any remaining Fe(II) in seawater, leading to the end of IF deposition. Evidence in support of higher sulfide production comes from increasing fractionation between sulfur isotopes; values for  $^{34}\text{S}/^{32}\text{S}$  ( $\delta^{34}\text{S}$ ) are centered on mantle values (0‰) prior to around 2.45 Ga but then increase to around 25‰ after 2.45 Ga (Canfield and Farquhar, 2009). In

the second instance, primary sulfate evaporites are rarely reported before 2.45 Ga (Schröder et al., 2008), confirming insufficient dissolved sulfate availability before that time.

Temporal trends in trace metal composition in Archean and Paleoproterozoic marine sediments also support the timing of the GOE. For instance, a compilation of the Cr contents in IF showed a significant enrichment beginning at 2.45 Ga in the Weeli Wolli Formation (Konhauser et al., 2011). Given the poor solubility of Cr minerals, its mobilization and incorporation into IF indicates enhanced chemical weathering at that time, most likely associated with the evolution of aerobic continental pyrite oxidation. Similarly, a recent compilation of Cu isotopes in Precambrian marine sediments demonstrated a clear trend in the stable isotopes values whereby Cu isotopes in black shales after the GOE become progressively heavier. This trend has been attributed to world-wide changes in seawater composition, due to the combined effect of waning IF deposition, which prior to the GOE would have preferentially removed  $^{65}\text{Cu}$  with Fe(III) (oxyhydr)oxides, and increased oxidative supply of  $^{65}\text{Cu}$  derived from continental weathering due to preferential leaching of the heavier Cu isotope. This  $^{65}\text{Cu}$ , in turn, would have become incorporated into planktonic biomass that scavenged Cu from seawater (Fru et al., 2016).

The Mn(IV) deposits of the 2.22 Gyr Hotazel Formation in South Africa (since been re-dated to between 2.42 and 2.39 Ga; Gumsley et al., 2017) have traditionally been considered some of the best proof for the presence of oxygen (e.g., Tsikos and Moore, 1997) because the oxidation of dissolved Mn(II) to solid-phase Mn(IV) (oxyhydr)oxides is thought to require  $\text{O}_2$ , and the latter's concentration exerts direct control on the rate of Mn(II) oxidation (Tebo et al., 2005). Moreover, the Mn deposits contain a prominent negative cerium (Ce) anomaly that has generally been thought to indicate seawater that was partially oxygenated. A similar sequence of Mn-enrichments with positive Ce anomalies have also been recently reported from the uppermost Hamersley Group and overlying Turee Creek Group (Warchola et al., 2018). Where the story of Mn(II) oxidation really gets interesting is with the 2.45 Gyr Koegas Subgroup in South Africa, a mixture of chemical and clastic sediments where the BIF layers contain up to 17 wt% Mn. Johnson et al. (2013) suggested that the initial Mn(IV) (oxyhydr)oxide precursor phases were likely formed via Mn(II)-based phototrophy, a metabolism that thus far has not been documented to exist in natural settings. Those authors argued against  $\text{O}_2$  being the Mn(II) oxidant because of the presence of detrital pyrite grains and S-MIF in associated rocks, and importantly, that these



sediments must have formed prior to the rise of atmospheric O<sub>2</sub> even though the timing of these sediments falls within the GOE window.

The Johnson et al. (2013) study was not the first to suggest that there was minimal oxygen available on Earth prior to the GOE. Kopp et al. (2005) pointed out that the geological features of oxygen, such as red beds and paleosols, occurred immediately after the three glaciations recorded in the Huronian Supergroup of Canada (ending ~2.3 Ga) but before the 2.3–2.2 Ga Makganyene glaciations in South Africa (recall the Makganyene diamictites are now constrained to ca. 2.46 Ga as per Gumsley et al., 2017). Kopp et al. (2005) also argued that global O<sub>2</sub> production after 2.3 Ga triggered the collapse of a methane greenhouse and initiated the Snowball Earth event associated with the Makganyene diamictites. In their model, the timing of these events means that cyanobacteria likely evolved in the interval between the Huronian glaciations and the Makganyene glaciation (i.e., within a few million years); note with the new age constraints this could be up to 150 Myr. A subsequent modelling exercise by Ward et al. (2016) suggested that it might have taken as little as 100 Kyr following the emergence of cyanobacteria to initiate the GOE.

#### **2.4. Genetic evidence for a Paleoproterozoic evolution of cyanobacteria**

To determine when oxygenic photosynthesis evolved we can also examine when the photosystems essential for oxygenic photosynthesis evolved. However, there is still some debate as to how the common ancestor of extant cyanobacteria acquired the ability to photosynthesize considering that their closest relatives, melainabacteria, lack photosynthetic machinery (Battistuzzi et al., 2004; Soo et al., 2014). In the previous section we outlined the argument from those who advocate for an early origin for oxygenic photosynthesis where an early ancestral phototroph existed that contained both type I and type II reaction centres (RCs) and which subsequently saw selective loss of oxygenic photosynthesis (Cardona, 2015, 2016, 2017; Hohmann-Marriott and Blankenship, 2012). However, another school of thought maintains that the common ancestor of extant cyanobacteria was a non-phototroph that acquired the ability to photosynthesize (both PSI and PSII) after the divergence of the cyanobacteria from melainabacteria (Soo et al., 2017). This would suggest a rather late origin for oxygenic photosynthesis in the late Archean or early Paleoproterozoic between 2.6 to 2.5 Ga.

In short, the above studies argue that oxygenic photosynthesis evolved in the Paleoproterozoic. Ultimately, only the combination of in-depth geochemical analysis of the rock record together with molecular clock analyses can answer the question of when oxygenic photosynthesis developed. We would suggest, given careful evaluation of the previously discussed geochemical and molecular data, that oxygenic photosynthesis probably became of significance in the early Archean, perhaps as early as 0.8 Gyr before the GOE. However, the evidence presented does not explain why there was such a significant delay in the widespread oxygenation of the Earth's atmosphere and oceans. Moreover, it remains to be resolved where oxygenic photosynthesis developed. In the following section, we provide evidence which suggests that an offset between the evolution of oxygenic photosynthesis and the widespread oxygenation of the atmosphere can be explained by a terrestrial origin for early cyanobacteria.

### **2.5. A terrestrial origin for cyanobacteria**

There is a significant body of evidence which suggests that the evolution of cyanobacteria occurred in terrestrial habitats. Firstly, large-scale phylogenomic analyses have consistently shown that living relatives of early divergent cyanobacteria can be found in low salinity and terrestrial environments (Blank and Sanchez-Baracaldo, 2010; Larsson et al., 2011; Sanchez-Baracaldo et al., 2005; Shih et al., 2013). Furthermore, phylogenomic evidence suggests that cyanobacteria colonized marine environments independently at different times in Earth's history. In fact, marine cyanobacteria lineages do not form a natural group; they are instead nested within freshwater species, providing further evidence for independent colonization events into marine environments at different times in history (Sánchez-Baracaldo, 2015; Sánchez-Baracaldo et al., 2014). Evolutionary and molecular clock studies have found no evidence of marine planktonic cyanobacteria having any ancestors as early as the Paleoproterozoic (Sánchez-Baracaldo, 2015). Moreover, modern planktonic groups (e.g., *Prochlorococcus* and *Synechococcus*, *Crocospaera* clade, and *Trichodesmium*) only appeared during the Neoproterozoic (Sánchez-Baracaldo et al., 2014).

These genomic observations of a terrestrial origin for cyanobacteria are at odds with the long-held belief that colonization of the landmasses would be impossible prior to the accumulation of substantial amounts of oxygen in the atmosphere because, in the absence of an ozone shield, harmful UV radiation would bombard the Earth's surface (Berkner and Marshall,

1965). However, it now appears likely that early terrestrial microbial habitats could have been protected from UV bombardment by inhabiting endolithic environments (Bryce et al., 2015), growing under iron-enriched siliceous sediment (Pierson et al., 1993), or by precipitating their own mineralized crusts (e.g., Gauger et al., 2016; Mloszewska et al., 2018; Phoenix et al., 2006). Indeed, Phoenix et al. (2001) demonstrated that an iron-silica biomineral layer of only 150  $\mu\text{m}$  thickness was sufficient to attenuate all incoming UV-C radiation while still allowing for the transmittance of 400–700 nm wavelength light required to facilitate photosynthesis. In other words, terrestrial colonization should not have been inhibited by irradiation with high levels of ultraviolet light.

Trait evolution analyses show that the earliest cyanobacteria were unicellular and had small cell diameters (*Gloeobacter*, *Synechococcus*-like) but filamentous forms evolved relatively early on and likely resembled modern relatives of *Pseudanabaena* (Sánchez-Baracaldo, 2015). These filamentous forms would have represented a morphological innovation that facilitated the formation of microbial mats. Such mats are dense, highly productive ecosystems which would have enabled an increase in cyanobacteria's ecological dominance during the Proterozoic (Blank and Sanchez-Baracaldo, 2010; Schirrmester et al., 2013). Molecular clock analyses have also suggested that filamentous cyanobacteria appeared around the GOE (Battistuzzi et al., 2004; Ettwig et al., 2016; Soo et al., 2014), while most of the taxonomic and ecological diversity of extant cyanobacteria can be traced back to the late Paleoproterozoic and Mesoproterozoic (Sánchez-Baracaldo, 2015; Schirrmester et al., 2015).

Cyanobacterial lineages inhabited benthic, terrestrial and/or shelf environments for most of the Proterozoic with mat-dominated environments being even more common in the Precambrian than they are today as they are limited in extent by the activity of plants (which compete with mat formation) and animals (which graze on mats). The ubiquity of such environments is also reflected in the geological record which contains abundant examples of microbialites, including stromatolites, formed during the Archaean and Proterozoic (Grotzinger and Knoll, 1999; Peters et al., 2017; Stal, 2001; Walter et al., 1980), although whether or not these examples always represent cyanobacterial mats or whether they were produced by anoxygenic phototrophs is still an active area of debate (Fischer et al., 2016).

The early establishment of mat-forming filamentous cyanobacteria and subsequent dominance of benthic microbial communities likely restricted primary productivity to terrestrial habitats and ocean margins (Sánchez-Baracaldo, 2015; Sánchez-Baracaldo et al., 2014). However, it is unclear to which extent early terrestrial ecosystems contributed to global biogeochemical cycles (Thomazo et al., 2018). The formation of cyanobacteria-dominated biological soil crusts has been proposed as one scenario which could explain the observation of transient periods of mild oxygenation and oxidative weathering before the GOE (Kendall et al., 2015; Lalonde and Konhauser, 2015; Stüeken et al., 2012; Thomazo et al., 2018). Nonetheless, numerous analog studies have suggested that potential O<sub>2</sub> production from ancient microbial mats may have been limited by H<sub>2</sub>S, which can serve as an electron donor for anoxygenic photosynthesis and chemosynthesis, and thus enhance competition with cyanobacteria (Dick et al., 2018 and references therein). In general, it is believed that the global impact of oxygenic photosynthesis was likely negligible until cyanobacteria started colonizing marine habitats (Sánchez-Baracaldo et al., 2014). The emergence of planktonic groups during the late Meso- to early Neoproterozoic (ca. 0.92 to 0.67 Ga) would subsequently have had a major impact on global biogeochemical cycles as they contribute to at least 25% of marine productivity in today's oceans (Flombaum et al., 2013).

Marine planktonic cyanobacteria evolved comparatively late and early representatives were restricted to shelf environments for much of the Proterozoic (Sánchez-Baracaldo, 2015). The spatial restrictions of those environments would have limited the extent of primary production and the extent of its biogeochemical influence. Consequently, it would be expected that terrestrial or near-shore iron cycling would be impacted by rising oxygen before there were any discernible changes in the marine iron cycle. Only with the evolution of planktonic cyanobacteria and their spread into the ocean would there have been a more profound influence on the marine geochemical iron cycle. Evidence for this offset between the response of the terrestrial biosphere and the oxidation of the atmosphere in general can be found in the apparent discrepancy between the timing of widespread atmospheric oxygenation (as identified by the widespread disappearance of S-MIF), and earlier evidence for oxidative weathering on land (as discussed in the first sections of this review). Lalonde and Konhauser (2015) attribute this discrepancy to the production of oxygen by cyanobacteria in benthic habitats, attached to

sediments, rocks, soils or other natural solid substrates where oxidative weathering of the solid could proceed whilst in strong disequilibrium with the reducing atmosphere.

### **3. CONSEQUENCES OF OXYGENIC PHOTOSYNTHESIS FOR THE MARINE IRON CYCLE**

The evolution of oxygenic photosynthesis and the subsequent oxidation of Earth's atmosphere had dramatic effects on the entire web of reactions which characterize global biogeochemical cycling. No other element has been as central to the historical discussion of the atmospheric evolution of the Earth as iron. Certainly, the existence of extensive IFs deposited between 3.8 to 1.85 Ga can be used to trace the evolution of the marine redox state and marine geochemical cycling of iron. In the following sections, we discuss how the marine iron cycle evolved following the evolution and expansion of oxygenic photosynthesis and hypothesize how this evolution may have impacted the potential for different microbial iron-based metabolisms.

#### **3.1. Marine iron cycling before the evolution and expansion of cyanobacteria**

As outlined above, it is generally believed that the bulk early ocean waters were largely anoxic, with O<sub>2</sub> concentrations ranging from <1 to 10 μM (Olson et al., 2013). They were primarily ferruginous, with dissolved Fe(II) concentrations likely between 0.04 and 0.12mM (Canfield, 2005); compared to modern day dissolved Fe concentrations of <0.3 nM–2 nM (Boyd and Ellwood, 2010).

Traditionally the deposition of IFs has been attributed to the reaction of free molecular oxygen with Fe(II) (Cloud, 1973; Cloud, 1965). However, although evidence from the rock record and some molecular work points towards the antiquity of oxygenic photosynthesis (section 2.1/ 2.2), recent experimental evidence suggests that elevated Fe(II) concentrations (Swanner et al., 2015) and higher UV fluxes on early Earth (Mloszewska et al., 2018) might have impeded the distribution of early cyanobacteria beyond locally confined “oxygen oases” (Kendall et al., 2010; Olson et al., 2013). Therefore, the following discussion on early iron-cycling will be based on the assumption that prior to ~2.5 Ga the oceans had low dissolved oxygen (Hardisty et al., 2014; Olson et al., 2013).

As an alternative to the chemical oxidation of Fe(II) by free oxygen, photoferrotrophy – the photosynthetic process where anoxygenic phototrophs use Fe(II) as the electron acceptor for carbon fixation – was proposed (e.g., Garrels et al., 1973; Hartman, 1984). The metabolic by-product of this metabolism was likely a poorly soluble Fe(III) (oxyhydr)oxide (Kappler and Newman, 2004) or, since the Precambrian ocean contained elevated concentrations of silica (up to 2.2 mM, Maliva et al., 2005), a silica-ferrihydrite composite (Alibert, 2016; Fischer and Knoll, 2009; Konhauser et al., 2007) or Fe(III)-silica gel (Percak-Dennett et al., 2011; Wu et al., 2012). Alternate hypotheses propose that primary IF minerals were mostly ferrous iron-bearing minerals such as greenalite (e.g., Johnson et al., 2018; Rasmussen et al., 2017), but hydrogeological constraints do not support this (Robbins et al., 2019). Previous studies have also demonstrated that the trace element inventory of the ancient ocean would have been sufficient to support a microbial community large enough to deposit all Fe(III) in IFs (Konhauser et al., 2002; Konhauser et al., 2017b), and importantly, they would even have been able to do so under limiting light conditions (Kappler et al., 2005). Furthermore, a recent study suggested that even under nutrient limiting conditions, photoferrotrophs would have been able to outcompete early cyanobacteria and essentially oxidize all hydrothermally derived Fe(II) before it would have reached oxygenated surface waters (Jones et al., 2015).

There is also some evidence from the rock record suggesting the activity of photoferrotrophs during the deposition of IFs. This evidence reaches as far back as to the ca. 3.77 Ga Isua Supracrustal Belt (Czaja et al., 2013). Based on a modelling approach combined with independent S isotope data, Czaja et al. (2013) interpreted the positive and comparatively homogeneous  $\delta^{56}\text{Fe}$  values to be indicative of anoxygenic, iron-based photosynthesis. Similarly, positive  $\delta^{56}\text{Fe}$  values of between approx. 0.4 to 0.7‰ from the Nuvvuagittuq chemical sediments have been interpreted as being the result of partial Fe(II) oxidation by anoxygenic photosynthesis (Dauphas et al., 2007).

Photoferrotrophy is not the only microbial process leading to Fe(II) oxidation. Microbial Fe(II) oxidation coupled to nitrate reduction or oxygen reduction at low  $\mu\text{M}$  oxygen concentrations is also known (Melton et al., 2014). Microaerophilic Fe(II) oxidation is obviously excluded in a predominantly anoxic setting, but nitrate-dependent Fe(II) oxidation is an anaerobic process (Straub et al., 1996). Nitrate-dependent Fe(II) oxidation can either be enzymatically driven by microorganisms (He et al., 2016; Straub et al., 1996; Tominski et al., 2018) or

catalysed by the production of reactive N species formed as a by-product of denitrification (Klueglein and Kappler, 2013). However, the presence of oxidized N species such as nitrate is itself indicative of a more oxygenated ocean and thus is tightly linked to cyanobacterial evolution and expansion. The Mesoarchean N isotope record appears to consistently suggest an anaerobic nitrogen cycle dominated by nitrogen fixation (Zhang et al., 2014), for which the enzyme is proposed to have evolved before 3.2 Ga (Stüeken et al., 2015). Therefore, nitrate-dependent Fe(II) oxidation was probably unlikely to constitute a significant proportion of Fe(II) oxidation.

The oxidized iron formed by photoferrotrophs would have been precipitated in the form of mineral-cell aggregates (Wu et al., 2014), ultimately settling on the seafloor as precursor sediments to IFs (Konhauser et al., 2005). Experimental studies showed that these Fe(III) mineral-cell aggregates would have a stoichiometric excess of iron compared to the co-precipitated carbon (Posth et al., 2010). In other words, instead of the 4:1 Fe:C ratio predicted for photoferrotrophy, the aggregates could have had Fe:C ratios as high as 6:1. Such sediments would have been an ideal environment for dissimilatory Fe(III)-reducing (DIR) bacteria, which would have coupled the reduction of Fe(III) to the oxidation of the co-precipitated biomass, although some reduction of Fe(III) already during sedimentation could also be feasible. The significance of microbial Fe(III) mineral reduction for IF genesis was suggested many years ago (Walker, 1984), and molecular clock studies have suggested the antiquity of this metabolic process (Vargas et al., 1998). Indeed, there is ample evidence from the rock record, e.g., from the Eoarchean Isua Supracrustal Belt (Greenland), the Mesoarchean Mozaan Group (Pongola Supergroup, South Africa) or the Neoproterozoic IFs of the Hamersley Basin (Australia) and Transvaal Craton (South Africa), in the form of C- and Fe isotopic studies (Craddock and Dauphas, 2011; Czaja et al., 2010; Heimann et al., 2010; Johnson et al., 2008; Ossa et al., 2018; Steinhöfel et al., 2009) demonstrating the significance of DIR for early microbial iron cycling in IF sediments. Although it should be noted that an alternative, abiotic origin of magnetite in the Hamersley IF via thermal decomposition of siderite has been proposed (Rasmussen and Muhling, 2018).

Konhauser et al. (2005) suggested that under ideal circumstances as much as 70% of the initially precipitated Fe(III) minerals could have been reduced and cycled back into the water column as Fe(II). Their model suggested that fermenting bacteria and methanogens might have degraded biomass which was co-precipitated together with primary Fe(III) minerals and,

therefore, provided additional substrates for Fe(III)-reducers. There is significant evidence for the existence of methane-based metabolisms in the Archean, a process which requires access to fermentation products (e.g., H<sub>2</sub>, acetate, lactate). Thus, by extension, the presence of methanogens necessitates the presence of fermenters.

Methane was abundant prior to the GOE and molecular clock analyses suggest development of methanogenesis during the Eoarchean (Battistuzzi et al., 2004). Additionally, highly negative  $\delta^{13}\text{C}$  values in organic carbon have been interpreted as a sign of the activity of methane-oxidizing bacteria (methanotrophs) (Eigenbrode and Freeman, 2006; Hayes, 1983), which are thought to have evolved 3.1 Ga or later (Battistuzzi et al., 2004). Such a microbial methane cycle could clearly influence carbon cycling in these ancient oceans and potentially provide organic substrates for DIR. Furthermore, a recent in-situ study showed that methane oxidation can be coupled directly to Fe(III) reduction (Riedinger et al., 2014), which raises the possibility that methanotrophs could have contributed directly to an ancient iron cycle before the GOE (e.g., Konhauser et al., 2005). Alternatively, the mineralization of dead microbial biomass could have released ammonium, which could theoretically have provided a substrate for anaerobic ammonium oxidizing bacteria which can couple this reaction to Fe(III) reduction (Clément et al., 2005; Oshiki et al., 2013).

Given this literature, we propose that, if the origin of cyanobacteria was terrestrial and the expansion of cyanobacteria as planktonic forms was delayed as we suggest in section 2, iron cycling would have been controlled primarily by phototrophic Fe(II) oxidation and microbial Fe(III) reduction until the late Neoproterozoic (Fig. 1). In this scenario, photoferrotrophs provided a means of primary production and Fe(II) oxidation, with replenishment of Fe(II) from DIR closing the ancient iron cycle.



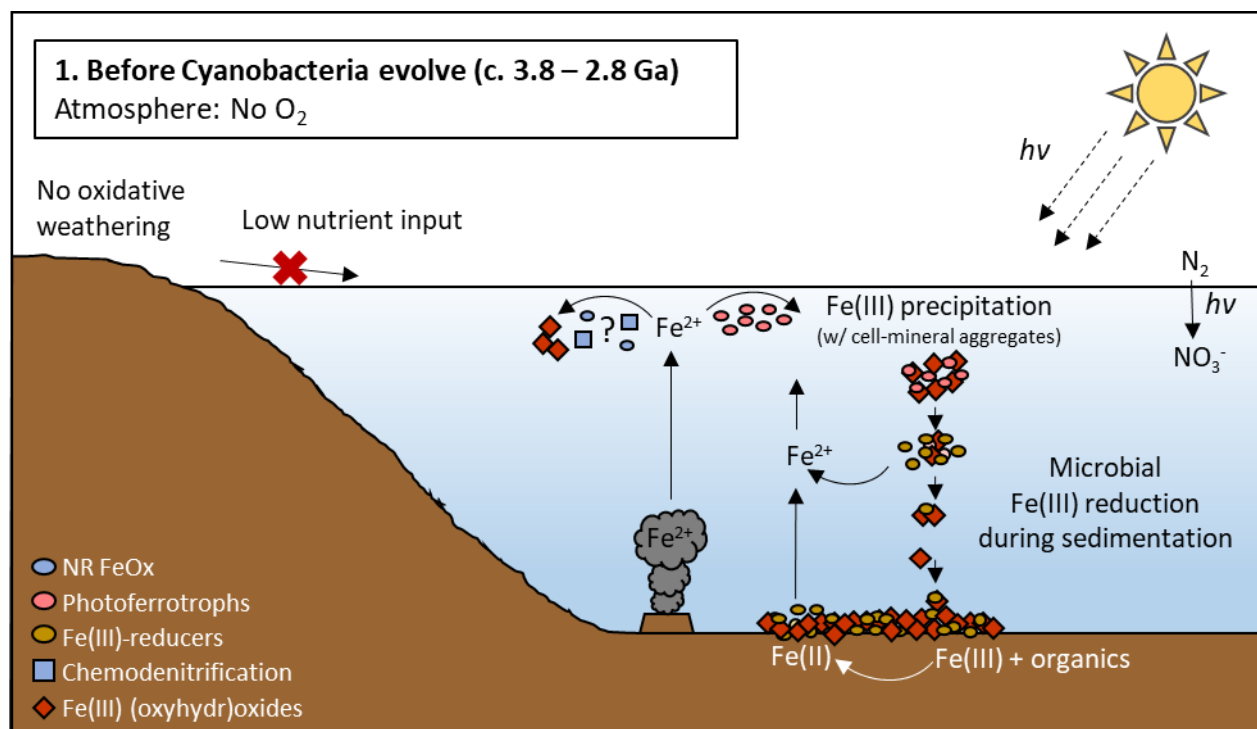


Fig. 1. Schematic of iron cycling in ancient oceans prior to the evolution of oxygenic photosynthesis. Anoxygenic phototrophy is the main mechanism of Fe(II) oxidation. Fe(II) is re-supplied by dissimilatory iron reduction occurring both in the sediment and the water column. There is a minor input of nitrate from atmospheric processes which could allow some nitrate dependent Fe(II) oxidation, but this process is likely a very minor contributor to iron cycling.

One factor which could have severely limited microbial iron cycling was the presence of H<sub>2</sub>S in the water column. H<sub>2</sub>S effectively titrates Fe(II) from solution and thus widespread euxinia (anoxic and sulfidic conditions) would have limited Fe(II) availability to iron-metabolizing microbes. Therefore, Fe(II):H<sub>2</sub>S ratios >1 would have been required for deposition of IFs and a widespread microbially-driven iron cycle (Kump and Seyfried, 2005). One key player in sulfate-turnover in the oceans are sulfate-reducing bacteria. The antiquity of this metabolic pathway is recorded in the S isotope record of sedimentary barites of the 3.6–3.2 Ga Barberton Greenstone Belt (South Africa; Roerdink et al., 2012); sedimentary barites, pyrite and sulfides from the ~3.5 Ga Dresser Formation (Western Australia; Ueno et al., 2008) and sedimentary barites of the 3.47 Ga North Pole area (Western Australia; Shen et al., 2009). While some sulfate might have been introduced to the Archean ocean by the photolysis of volcanic gases such as SO<sub>2</sub> (Farquhar et al., 2010; Roerdink et al., 2012), there was likely no additional inputs of sulfate to the early oceans before the evolution of oxygenic photosynthesis and the onset of widespread oxidative weathering (Konhauser et al., 2011). Consequently, the sulfate concentrations in the Archean ocean could have been as low as 10 μM (Zhelezinskaia et al.,

2014), and maybe even below 2.5  $\mu\text{M}$  (Crowe et al., 2014). If true, this means microbial sulfate reduction, while old, was an insignificant or at least severely spatially limited process during that time. Concomitant low  $\text{H}_2\text{S}$  concentrations would have resulted in minimal crossover between early Fe- and S-cycles until ca. 1.8 Ga (Canfield, 1998; Poulton et al., 2004).

### **3.2. Effect of cyanobacteria expansion on marine iron cycle**

It was suggested over a decade ago that a “whiff of oxygen” (Anbar et al., 2007) could have already existed prior to the GOE possibly leading to “pervasive oxygenation” along Archean coastlines by 2.6 Ga (Kendall et al., 2010), which is approximately 100–200 Ga before the GOE (arguably between ~2.45 and 2.32 Ga; Bekker et al., 2004; Farquhar et al., 2000; Konhauser et al., 2011). Evidence from the marine (Planavsky et al., 2014) and terrestrial (Crowe et al., 2013) rock record suggests that locally confined oxygenated areas could already have existed as far back as 3.0 Ga, forming local “oxygen oases”, with  $\text{O}_2$  concentrations between 1 to 10  $\mu\text{M}$  (Olson et al., 2013). In a recent study on the 2.98 to 2.85 Gyr Mozaan Group (White Mfolozi Inlier, Pongola Supergroup), Ossa et al. (2018) employed correlation analysis on Fe/Mn ratios and  $\delta^{56}\text{Fe}$  values as well as  $\delta^{98}\text{Mo}$  values. Based on their results they concluded that oxygen concentrations could even have exceeded the earlier maximum of 10  $\mu\text{M}$  in the Archean. This suggests that early cyanobacteria (and oxygen) slowly spread from terrestrial habitats, where they first developed (as discussed in section 2 of this review), via rivers and lacustrine environments to the oceans, where their expansion probably came to a (temporary) hold. With time, cyanobacteria spread from the marine littoral zone and became more abundant in the ancient ocean, resulting in an oxygenated surface ocean layer in the late Archean (Poulton and Canfield, 2011). A recent study has even demonstrated experimentally that the presence of ferric iron-silica colloids in the photic zone could have sheltered the plankton from incoming UV-C irradiation, thus allowing cyanobacteria to spread throughout more of the marine realm (Mloszewska et al., 2018).

Despite their early presence, cyanobacteria probably had no critical direct effect on marine iron cycling initially. Although the emergence and spread of early cyanobacteria would have pushed photoferrotrophs deeper into the water column (Fig. 2), this would not have influenced the means by which the initial Fe(III) mineral phases in IFs would have been deposited. The photoferrotrophs would have been more proximal to the hydrothermally derived

Fe(II) and could have, due to their adaptation to low light conditions (Kappler et al., 2005) and competitive advantage over cyanobacteria under nutrient limiting conditions (Jones et al., 2015), oxidized all Fe(II) before it would have reached oxygenated surface waters. Supporting evidence from the rock record is provided by a study from Haugaard et al. (2016) who suggested, based on iron isotope studies and paleo-environmental reconstructions, that photoferrotrophs could have deposited the primary Fe(III) mineral assemblages in the ~2.45 Gyr Joffre IF. Ultimately, the predominance of one oxidative process over the other is governed by the question of whether the redoxcline is above or below the photic depth. As long as the redoxcline remained above the photic depth, photoferrotrophy would have dominated Fe(II) oxidation and thus the deposition of IFs (Fig. 2). However, if the redoxcline moved below the photic depth (Fig. 3), abiotic oxidation of Fe(II) by O<sub>2</sub> produced via cyanobacteria and related dark Fe(II)-oxidizing mechanisms should have dominated Fe(II)-oxidation. Indeed, a recent study showed, that microaerophilic Fe(II)-oxidizing bacteria can compete with abiotic (chemical) Fe(II) oxidation in an O<sub>2</sub> concentration range from 5 μM to approx. 50 μM (Druschel et al., 2008; Lueder et al., 2017; Maisch et al., 2019). Lower O<sub>2</sub> concentrations limited enzymatic Fe(II) oxidation while higher concentrations resulted in chemical Fe(II) oxidation being dominant. Therefore, microaerophilic Fe(II)-oxidizing bacteria would have found ideal conditions under low O<sub>2</sub> conditions leading up to the GOE.

The rise of oxygen and expansion of oxygen oases would also have potentially led to an increase in the diversity of iron-respiring microorganisms. Those microbes which use O<sub>2</sub> as their TEA are in competition with the abiotic oxidation of Fe(II) by oxygen, and are therefore “microaerophiles” existing at oxic-anoxic interfaces where the biotic reaction can compete with the abiotic reaction (Druschel et al., 2008; Lueder et al., 2017). The significance of this metabolic pathway for IF deposition was first suggested by Holm (1989) and their potential contribution to the formation of IFs is discussed extensively by Chan et al. (2016) (Figs. 2 and 3). Modern nitrate-reducing Fe(II)-oxidizers contribute to Fe(II) oxidation either directly, by enzymatic oxidation of Fe(II) (Straub et al., 1996), or indirectly by production of reactive nitrogen species which react abiotically with Fe(II) in a process known as “chemodenitrification” (Klueglein and Kappler, 2013; Klueglein et al., 2014). In fact, it has recently been suggested that chemodenitrification may have led to significant fluxes of the greenhouse gas N<sub>2</sub>O in the Proterozoic (Stanton et al., 2018). Both microaerophilic and nitrate-reducing Fe(II)-oxidizing metabolisms require oxygen to be produced first, thus they would be limited in extent before the

evolution of cyanobacteria. However, with the spread of oxygen, both microaerophilic and nitrate-reducing Fe(II)-oxidizers would have become more significant for the marine microbial iron cycle (Figs. 2 and 3).

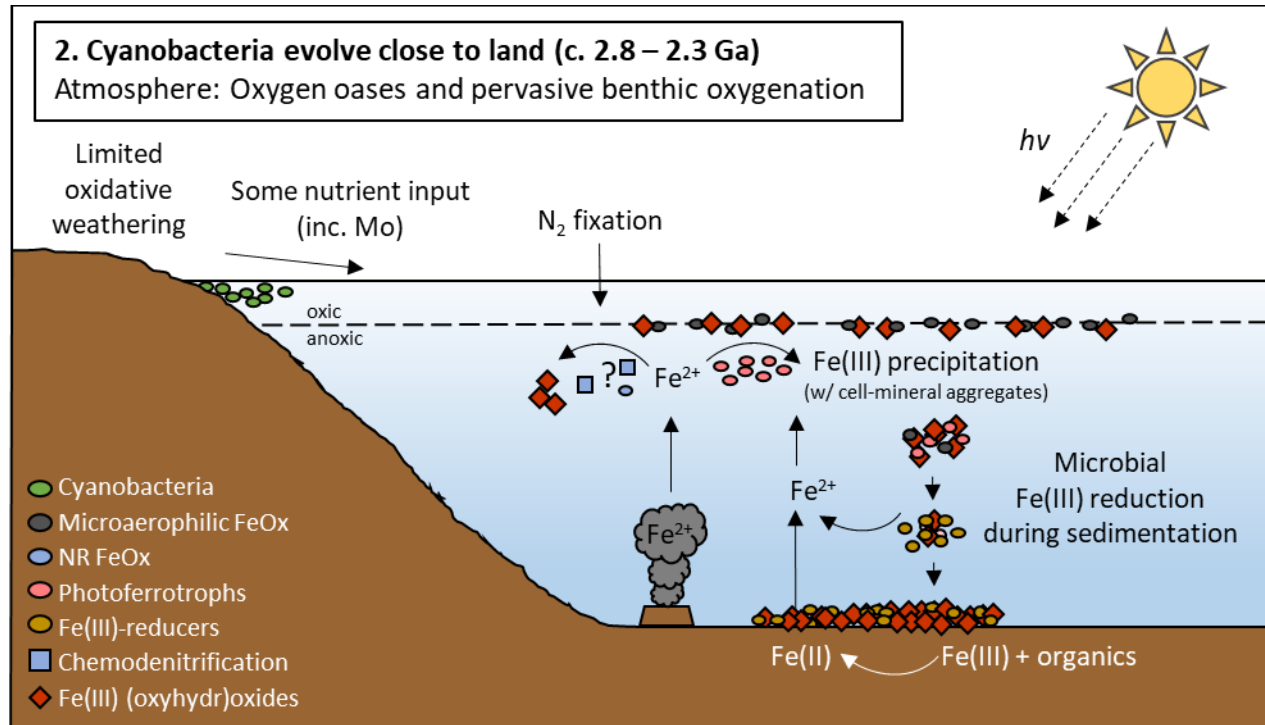


Fig. 2. Schematic of iron cycling in ancient oceans when oxygenic photosynthesis was limited to terrestrial or near-shore environments. Some redox stratification of the oceans could be possible enabling microaerophilic Fe(II)-oxidizers to become involved in the marine iron cycle. When the redoxcline remains above the photic zone, anoxygenic phototrophs remain the major driver of Fe(II) oxidation. Nitrogen fixation and an increase in atmospheric oxygen could enhance the contribution from nitrate-reducing Fe(II)-oxidizers.

The Neoproterozoic (2.8–2.5 Ga) has also been suggested to have been a time of major microbial Fe(III) respiration as a result of the combined deposition of Fe(III) (oxyhydr)oxides and organic carbon (Johnson et al., 2008). Thus, microbial Fe(III) mineral reduction remained a significant diagenetic process in the IFs deposited immediately prior to or during the GOE. Furthermore, additional studies add to the increasing pool of isotopic data (C, O and Fe) that highlight the importance of DIR for the ancient Fe cycle (Johnson et al., 2013; Steinhöfel et al., 2010; Teixeira et al., 2017). Based on the previous discussion, photoferrotrophs could still provide the primary means of Fe(II) oxidation, where replenishment of Fe(II) by DIR could act to close the ancient iron cycle (Fig. 2).

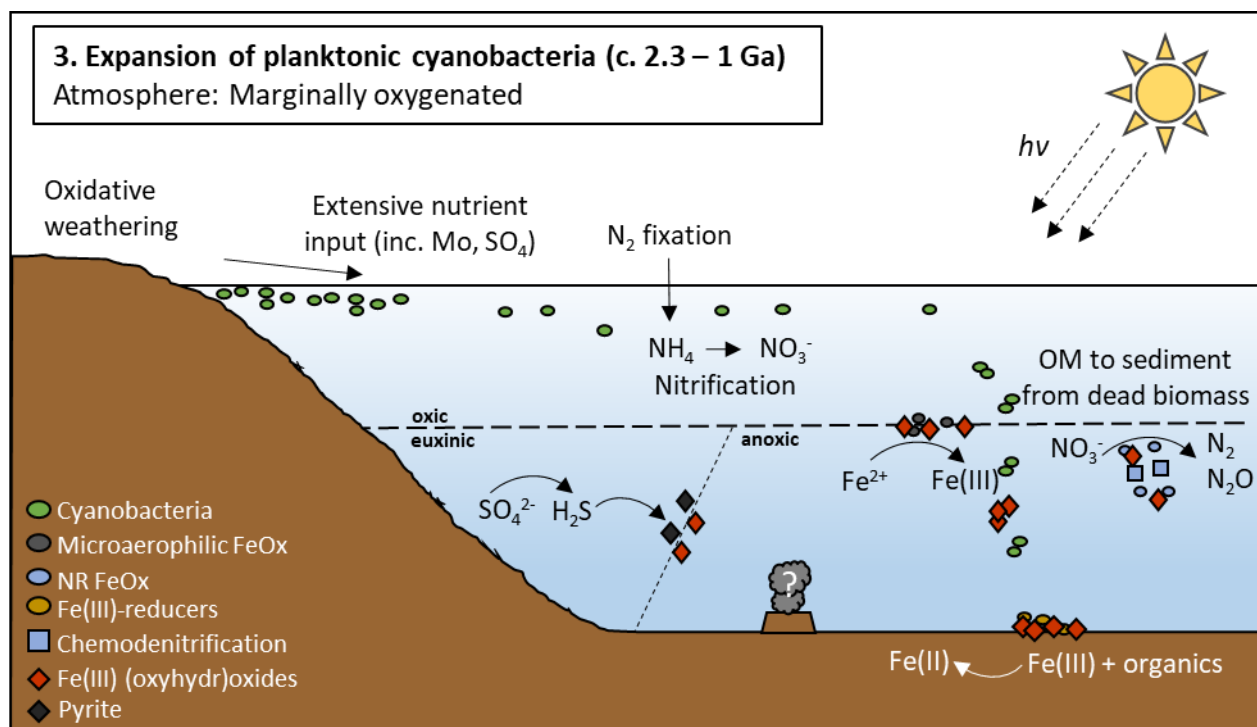


Fig. 3. Schematic of iron cycling in ancient oceans following the expansion of cyanobacteria in the marine realm. Atmospheric oxygenation is marginal with the deep oceans remaining anoxic. When the redoxcline is below the photic zone the contribution of anoxygenic phototrophs to iron cycling becomes negligible. Nitrate input increases, primarily from nitrification, as well as oxygen availability, which benefits microaerophilic and nitrate dependent Fe(II)-oxidizers. Hydrothermal input of iron may also have decreased around this time. Sulfate input from oxidative weathering led to sulfidic conditions in some near-shore areas which would lead to pyrite formation. IF deposition continues whilst the redoxcline remains above the depth of the shelf.

Other alternative iron-metabolizing pathways were potentially also affected by increasing concentrations of oxygen. For example, it has been suggested that a significant decrease in oceanic Ni concentrations prior to the GOE would have resulted in a decline in methanogens (Konhauser et al., 2009; Konhauser et al., 2015), which would have resulted in a decreased significance of methane-based Fe(III) reduction (Riedinger et al., 2014). Conversely, a decline in global methanogenesis and resulting higher availability of fermentation products (e.g., H<sub>2</sub>, acetate), otherwise used by methanogens (Blaut, 1994; Ferry, 1992), could have resulted in a more pronounced DIR. Consequently, a decrease in methane-dependent Fe(III) reduction would not necessarily have resulted in a decreased turnover of Fe(III) (oxyhydr)oxides. However, recent findings by Neubeck et al. (2016) showed that methane production in some species of methanogens was unaffected by Ni concentration, thereby suggesting that the influence of declining oceanic Ni concentrations on the global rates of methane production in the Precambrian is not straightforward. At the same time, the increase in biological N-fixation could have increased the significance of NH<sub>4</sub><sup>+</sup>-dependent Fe(III) reduction (Clément et al., 2005; Oshiki et

al., 2013). Therefore, other microbial processes (e.g. DIR and  $\text{NH}_4^+$ -dependent Fe(III) reduction) would become more important as a result of a shift in substrate availability.

The development of oxygenic photosynthesis and locally confined oxygen oases would not only have influenced the iron cycle significantly, but as a result of oxidative weathering, would also have resulted in increased pyrite dissolution (Konhauser et al., 2011), resulting in an increased sulfate (and nutrient) flux to the ocean (Fig. 2). Increased biomass production by early cyanobacteria within the oxygen oases together with an increased sulfate flux could have stimulated locally confined activity of sulfate-reducing bacteria along the paleo-shoreline and shelf regions, resulting in the development of locally confined sulfidic pools (Farquhar et al., 2010). Within those regions marine geochemical conditions would have been governed by the competition between Fe(II),  $\text{O}_2$ , organic matter input and  $\text{H}_2\text{S}$  accumulation (Reinhard et al., 2009). This period of marine evolution is interpreted to be recorded e.g. in the ~2.66 Gyr Jeerinah Formation (Hamersley Province, Western Australia; Scott et al., 2011) and the ~2.5 Gyr Mount McRae Shale (Reinhard et al., 2009). In these paleo-environments, locally confined euxinic conditions would have inhibited the upwelling Fe(II) from reaching the near-shore, resulting in the precipitation of FeS (Fig. 2). Consequently, Fe(II) would be inaccessible for microbial iron cycling. By contrast, the 2.5 Ga Mount McRae Shale shows N isotope signatures consistent with denitrification (Busigny et al., 2013), leading those authors to speculate about the existence of nitrate dependent iron oxidation.

In summary, when cyanobacteria expanded into the oceans, ferruginous conditions would likely still have existed in most areas of the Archean ocean. At some point in time, however, locally confined oxygen oases and increased sulfate input to the oceans resulting from early oxidative weathering would have turned parts of the continental margins and shelf regions euxinic, thereby suppressing microbial iron cycling. Additionally, oxygen oases would have enabled proliferation of Fe(II) oxidizers reliant on oxygen or nitrate, which we speculate could compete with photoferrotrophs in regions where the redox cline was still in the photic zone but would not be likely to dominate on a large scale.

### **3.3. Marine Fe cycle following GOE**

Following the evolution of planktonic cyanobacteria and their widespread expansion into the surface oceans, the production of  $\text{O}_2$  would have pushed the redoxcline below the photic zone

such that upwelling Fe(II) was oxidized abiotically before it could be available to photoferrotrophs (Fig. 3). Indeed, isotope evidence from the 2.3 to 2.2 Gyr Yuanjiacun IF suggests that by this time the oceans contained sufficient oxygen such that Fe(II) oxidation was not directly tied to the presence of cyanobacteria, yet the deep oceans remained ferruginous (Hou et al., 2014; Wang et al., 2016; Wang et al., 2015). Following the GOE, the waters overlying the continental shelf (around 150m deep) - where IFs were deposited (Trendall, 2002) - may have become sufficiently oxygenated that deposition of Superior-type IFs ceased as the upwelling hydrothermal Fe(II) was oxidized before reaching the shelf (Fig. 3). Although this could have led to IF deposition in deeper waters, the preservation potential of those sediments would be less than of IFs deposited on the stable shelf. The implications then are that IFs might be absent from the rock record, an observation borne out by the limited extent of major IFs deposited between ca. 2.4 and 1.9 Ga (Isley and Abbott, 1999; Konhauser et al., 2017).

Although the cessation of IF deposition during the above time interval was traditionally attributed to oxygenation of deep seawater (e.g., Holland, 1984), in the wake of the GOE, widespread oxidative weathering of pyrite on land would have resulted in an increased input of sulfate (and nutrients) to the oceans. Microbial turnover of sulfate and organic matter by sulfate-reducing bacteria in organic matter rich environments would have resulted in the formation of large quantities of H<sub>2</sub>S along the ocean margins (Canfield, 1998; Johnston et al., 2006; Kendall et al., 2011; Poulton et al., 2004), resulting in quantitative titration of upwelling Fe(II) from the water column and the end of IF deposition on the shelf.

Evidence from the 1.89 Gyr Gunflint and Biwabik IFs suggests that even in the Palaeoproterozoic, when the surface ocean was fully oxygenated, sporadically high fluxes of reductants (Fe(II)) from hydrothermal sources could still overwhelm the abiotic oxidation of Fe(II), resulting in Fe(II) accumulation and subsequent IF deposition on continental shelves (Planavsky et al., 2009). Under these conditions, oxygen produced by cyanobacteria clearly became the dominant oxidant for Fe(II) oxidation in the oceans. In turn, this would have resulted in a complete inhibition of Fe(II) oxidation by phototrophs in the surface ocean and restricted photoferrotrophs to a few specific sunlit, anoxic niches, such as coastal sediments and stratified lakes, much as they are today (Camacho et al., 2017). The competition between photoferrotrophs and cyanobacteria would also be confounded by the increase in nutrient input to the oceans from oxidative weathering, which would remove the competitive advantage photoferrotrophs had

enjoyed in the oligotrophic conditions widespread prior to the GOE (Jones et al., 2015; Robbins et al., 2016 for an extensive review on the ocean trace element budget). With a fully oxygenated photic zone, anoxygenic phototrophs would be unable to proliferate (Kappler et al., 2005) and “dark” Fe(II)-oxidizing metabolisms would become an increasingly important driver of microbially catalysed Fe(II) oxidation. In this scenario, microaerophilic Fe(II)-oxidizers may have dominated the Fe(II)-oxidizing community members along the deep redox-cline (Chan et al., 2016). As oxidative weathering on land increased, even more Mo would be introduced into the oceans, enhancing N-fixation, and potentially encouraging nitrate-reducing Fe(II)-oxidizers.

The significance of DIR for the marine iron cycle is recorded in several IFs deposited either directly in the wake of the GOE (e.g., the 2.3 to 2.2 Gyr Yuanjiacun IF; Hou et al., 2014; Wang et al., 2015) or during the approx. 1.8 Ga resurgence of IFs (e.g. the Sokoman IF or the Lake Superior IFs; Dodd et al., 2018; Planavsky et al., 2009; Raye et al., 2015). Alternatively, higher Mo concentrations (Thoby et al., 2019) would probably have furthered an increase in microbial Fe(III) reduction coupled to  $\text{NH}_4^+$  oxidation (Fe-ammo) below the deep redox-cline and in the sediments. This would additionally be stimulated by higher sedimentary ammonium fluxes from ammonification during burial due to increased microbial N-fixation in surface waters (Stüeken et al., 2015; Stüeken et al., 2016; Zerkle et al., 2006) and subsequent microbial degradation of organic carbon.

When the deep oceans became oxygenated (Fig. 4), hydrothermally derived Fe(II) would be precipitated directly around submarine vents much as it does today (e.g., Loihi, Hawaii; Karl et al., 1989). Marine iron cycling would be confined almost exclusively to sedimentary environments, with extremely low Fe(II) concentrations (and thus almost no microbial iron cycling) in the water column.



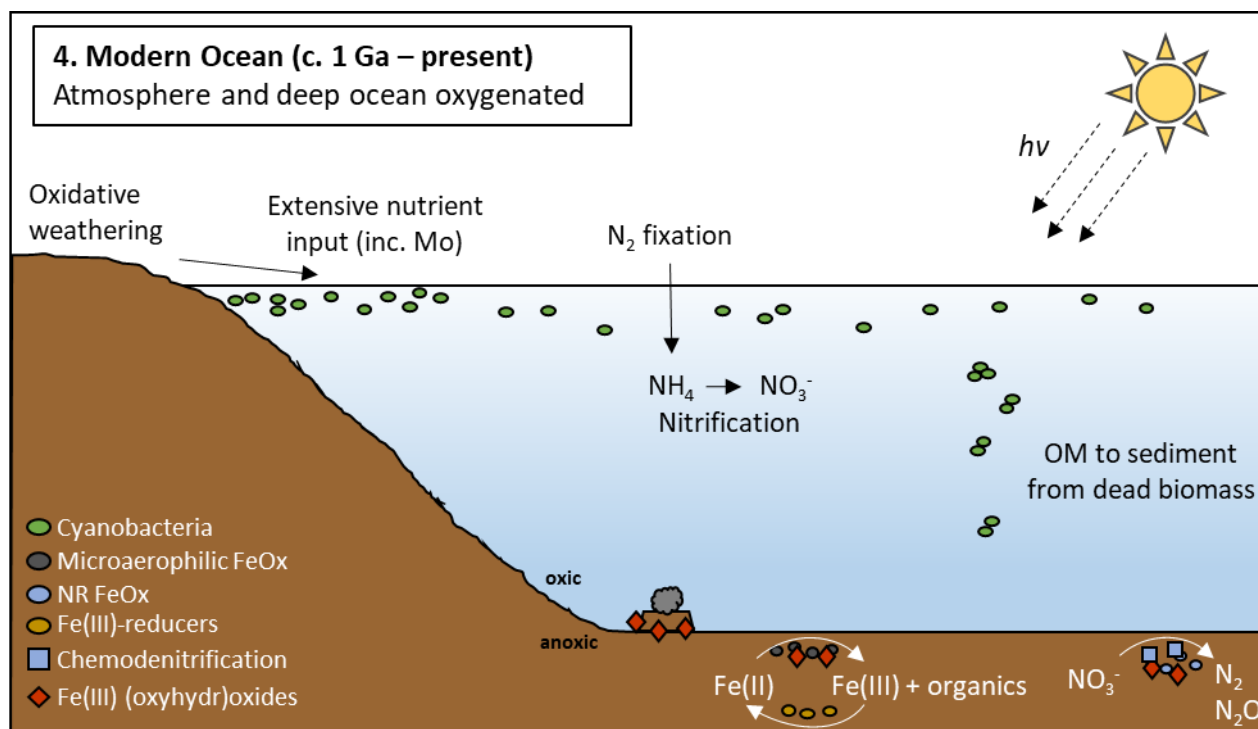


Fig. 4. Schematic of the marine iron cycle when oxygen penetration exceeds the depth of the shelf. Iron cycling proceeds similarly to today. Almost no Fe(II) can remain dissolved in the water column and most active iron cycling occurs in the sediments, or directly around hydrothermal vents.

#### 4. INFLUENCE OF OXYGENIC PHOTOSYNTHESIS ON TERRESTRIAL IRON CYCLING

While in section 2.5 we discussed the hypothesis of a potential terrestrial evolution of cyanobacteria, we now investigate how their oxygen production would have influenced an early terrestrial microbial iron cycle. Most of the knowledge on Archean and Proterozoic iron cycling comes from marine deposits, yet it is very likely that the evolution of oxygenic photosynthesis would have also had major consequences for terrestrial iron cycling. In this case we use the term terrestrial to refer to any exposed continental crust, regardless of whether it is aquatic or not. We therefore include rivers, lakes, streams and ponds under this definition as well as soils, sediments and exposed rock surfaces. Unfortunately, due to lower aerial extent of continental land masses in the Archean (compared to today) and resulting lower likelihood of preservation than the abundant marine deposits, the geological record of life on land during Earth's ancient history is significantly more patchy than that found in marine systems (Campbell and Davies, 2017; Flament et al., 2008, 2013; Rey and Coltice, 2008). Loss due to erosion is also high for terrestrial

deposits, meaning that those environments most likely to have had cyanobacterial communities were lost from the rock record.

What little understanding of terrestrial iron cycling we have comes from palaeosols - ancient soil horizons. Weathering of ancient soils under an anoxic atmosphere led to the mobilization and leaching of Fe(II). When oxygen is present, Fe(II) is oxidized and thus stabilized, preventing iron loss. It has been shown that before 2.4 Ga, palaeosols suffered significant iron loss whereas younger palaeosols generally show negligible loss of iron during weathering (Beukes et al., 2002; Rye and Holland, 1998). Although mobilization of iron from palaeosols can be explained by chemical processes (i.e., abiotic weathering of silicate minerals), the high abundance of aqueous Fe(II) implied by the observed iron mobilization in pre-GOE palaeosols allows us to speculate about the potential for iron-based metabolisms in these systems.

In modern terrestrial environments, Fe(II) is oxidized by the same three microbial processes as discussed in part 3 of this review: microaerophilic, anoxygenic phototrophic and nitrate dependent Fe(II) oxidation. In the modern environment, however, these processes are limited by the ubiquity of atmospheric oxygen which either competes with their metabolism (as in the case of microaerophilic Fe(II) oxidation) or even inhibits their activity completely because they are anaerobic (phototrophic and nitrate-reducing Fe(II) oxidation). In addition to benefitting from the dissolved Fe(II) produced and released from silicate weathering, these microorganisms are known to also directly oxidize crystalline Fe(II)-bearing minerals, including magnetite (Byrne et al., 2015), biotite (Shelobolina et al., 2012a), and clay minerals (Shelobolina et al., 2012b). On the other end of the iron cycle, given the relative paucity of TEAs such as  $O_2$ ,  $NO_3^-$  and  $SO_4^{2-}$  in the Precambrian, Fe(III) may have been one of the few electron acceptors available for ancient chemolithotrophs. In fact, it has been shown that close relatives of the last common ancestor of modern life had the ability to conduct DIR (Vargas et al., 1998). From the marine record it is clear that DIR played a significant role in marine iron cycling pre GOE (cross-reference to section 3), and there is no clear reason why this would not have been a plausible microbial metabolism on the early landmasses as well. It can, therefore, be proposed that pre-GOE palaeosols with low  $O_2$  and abundant Fe(II) would have represented an even more favourable environment for terrestrial microbial iron cycling than today, although the impact of such activity on global biogeochemistry may have been minor.

The palaeosol record also contains significant insights into ancient terrestrial biogeochemistry more generally. In the oldest palaeosol record, the 3.2 Gyr Moodies Group, Nabhan et al. (2016) observed contemporaneous formation of pedogenic sulfate nodules and secondary pyrite rims with  $\delta^{34}\text{S}_{\text{VCDT}}$  values between  $-20\%$  and  $-24.5\%$ , which they interpreted as evidence for microbial processing of sulfur during soil formation at that time. Of particular interest are paleosols found at several localities near Schagen (Mpumalanga Province, Eastern Transvaal Supergroup, South Africa) which were formed prior to 2.6 Ga. Their high organic C content (up to 1.4 wt%) in 20  $\mu\text{m}$  to 1 mm thick seams with  $\delta^{13}\text{C}_{\text{org}}$  values between  $-14.4$  and  $-17.4\%$  PDB not only indicates that microbial mats existed on the soil surface (Watanabe et al., 2000), but the retention of iron and the increased ratio of Fe(III)/Fe(II) with depth suggests that the mats were composed of cyanobacteria and that oxygen concentrations, at least locally, were  $>0.1\%$  PAL (Watanabe et al., 2004). Additional constraints on potential early terrestrial metabolisms is provided by a study on the 2.76 Gyr Mount Roe palaeosol, Western Australia (Rye and Holland, 2000). The authors describe isotopic evidence indicative of methanotrophy which they suggest occurred around ephemeral ponds. The presence of methanotrophs necessitates the presence of methane-producing microorganisms. Methane could have provided an additional substrate for microbial Fe(III) reduction where the oxidation of methane would have been coupled to microbial reduction of Fe(III) (Riedinger et al., 2014).

The terrestrial rock record also includes some evidence of aquatic terrestrial habitats on the early landmasses. For example, Homann et al. (2018) show direct fossil evidence for terrestrial microbial mats from a 3.22 Gyr fluvial deposit in the Moodies Group, South Africa. Buick (1992) and Stüeken et al. (2017) also provide textural and Mo isotopic evidence of oxygenic photosynthesis in 2.78 to 2.72 Gyr stromatolites of the Fortescue Group, Western Australia that were interpreted as having been formed in an ancient evaporitic lake. However, this interpretation is not unequivocal, as parts of the Tumbiana Formation were interpreted to represent coastal or shallow marine environments by previous work (Sakurai et al., 2005). Although these existing records do not directly imply a role for iron-metabolizing bacteria specifically, they do suggest an active microbial community which could consist of oxygenic or anoxygenic phototrophs, as well as active microbial nitrogen, sulfur and methane cycling. Crucially, all of these processes can potentially be linked to microbial iron cycling.

## 5. CONCLUSIONS

The exact timing of the evolution of oxygenic photosynthesis remains the subject of much debate, but the impact this biological innovation has ultimately had on the Earth's biogeochemistry is undeniably huge. A significant body of evidence suggests that this innovation first developed in terrestrial environments where cyanobacteria were responsible for “whiffs” of oxygen prior to the GOE. This would have had limited impact on the microbial iron cycle in the marine environment as the oceans would have remained primarily anoxic, and the microbial iron cycle would have been dominated by Fe(II) oxidation by anoxygenic phototrophs and Fe(III) reduction by DIR, much as it had been prior to the evolution of oxygenic photosynthesis. The subsequent evolution of planktonic cyanobacteria enabled expansion into the marine realm and led to progressive oxygenation of the atmosphere and oceans. Anoxygenic phototrophic Fe(II) oxidation likely remained the dominant mechanism of IF deposition until the redoxcline descended below the photic zone as anoxygenic phototrophs, which grow at lower light intensities, could oxidize upwelling Fe(II) before it reached cyanobacteria. Ultimately IF deposition would cease when the redoxcline descended below the depth of the shelf, and oxygen from oxidative photosynthesis would dominate Fe(II) removal from the water column. Increased availability of oxygen could have enabled expansion of new Fe(II)-oxidizing metabolisms such as microaerophilic and nitrate-reducing Fe(II)-oxidizers, but these are unlikely to have played a major role in precipitation of IFs. Under increasingly oxic conditions, however, these “dark” Fe(II)-oxidizing metabolisms would have found abundant niches in both marine and terrestrial systems where they could potentially influence the local biogeochemistry much as they continue to do today.

## ACKNOWLEDGEMENTS

This study was supported by grants from the German Research Foundation (DFG) to AK and CB, as well as grants to KK from the Natural Sciences and Engineering Research Council of Canada (NSERC). Funding support for PS-B came from a Royal Society University Research Fellowship.

---

**REFERENCES**

- Albut G., Babechuk M. G., Kleinhanns I. C., Bengner M., Beukes N. J., Steinhilber B., Smith A. J., Kruger S. J. and Schoenberg R. (2018) Modern rather than Mesoarchaeal oxidative weathering responsible for the heavy stable Cr isotopic signatures of the 2.95 Ga old Ijzermijn iron formation (South Africa). *Geochim. Cosmochim. Acta* **228**, 157-189.
- Alibert C. (2016) Rare earth elements in Hamersley BIF minerals. *Geochim. Cosmochim. Acta* **184**, 311-328.
- Altermann W. and Schopf J. W. (1995) Microfossils from the Neoproterozoic Campbell Group, Griqualand West Sequence of the Transvaal Supergroup, and their paleoenvironmental and evolutionary implications. *Precambrian Res.* **75**, 65-90.
- Anbar A. D., Duan Y., Lyons T. W., Arnold G. L., Kendall B., Creaser R. A., Kaufman A. J., Gordon G. W., Scott C. and Garvin J. (2007) A whiff of oxygen before the great oxidation event? *Science* **317**, 1903-1906.
- Battistuzzi F. U., Feijao A. and Hedges S. B. (2004) A genomic timescale of prokaryote evolution: insights into the origin of methanogenesis, phototrophy, and the colonization of land. *BMC Evol. Biol.* **4**, 44.
- Beal E. J., House C. H. and Orphan V. J. (2009) Manganese- and iron-dependent marine methane oxidation. *Science* **325**, 184-187.
- Beaumont V. and Robert F. (1999) Nitrogen isotope ratios of kerogens in Precambrian cherts: a record of the evolution of atmosphere chemistry? *Precambrian Res.* **96**, 63-82.
- Bekker A. and Holland H. D. (2012) Oxygen overshoot and recovery during the early Paleoproterozoic. *Earth Planet. Sci. Lett.* **317**, 295-304.
- Bekker A., Holland H. D., Wang P.-L., Rumble D., Stein H. J., Hannah J. L., Coetzee L. L. and Beukes N. J. (2004) Dating the rise of atmospheric oxygen. *Nature* **427**, 117-120.
- Berkner L. V. and Marshall L. (1965) On the origin and rise of oxygen concentration in the Earth's atmosphere. *J. Atmos. Sci.* **22**, 225-261.
- Beukes N. J., Dorland H., Gutzmer J., Nedachi M. and Ohmoto H. (2002) Tropical laterites, life on land, and the history of atmospheric oxygen in the Paleoproterozoic. *Geology* **30**, 491-494.
- Blank C. and Sánchez-Baracaldo P. (2010) Timing of morphological and ecological innovations in the cyanobacteria – a key to understanding the rise in atmospheric oxygen. *Geobiology* **8**, 1-23.
- Blaut M. (1994) Metabolism of methanogens. *Antonie Leeuwenhoek* **66**, 187-208.
- Boetius A., Ravensschlag K., Schubert C. J., Rickert D., Widdel F., Gieseke A., Amann R., Jørgensen B. B., Witte U. and Pfannkuche O. (2000) A marine microbial consortium apparently mediating anaerobic oxidation of methane. *Nature* **407**, 623-626.
- Boyd P. W. and Ellwood M. J. (2010) The biogeochemical cycle of iron in the ocean. *Nat. Geosci.* **3**, 675.
- Brasier M. D., Green O. R., Jephcoat A. P., Klepepe A. K., Van Kranendonk M. J., Lindsay J. F., Steele A. and Grassineau N. V. (2002) Questioning the evidence for Earth's oldest fossils. *Nature* **416**, 76-81.

- Bryce C. C., Horneck G., Rabbow E., Edwards H. G. and Cockell C. S. (2015) Impact shocked rocks as protective habitats on an anoxic early Earth. *Int. J. Astrobiol.* **14**, 115-122.
- Buick R. (1992) The antiquity of oxygenic photosynthesis: evidence from stromatolites in sulphate-deficient Archean lakes. *Science* **255**, 74-77.
- Buick R. (2010) Early life: Ancient acritarchs. *Nature* **463**, 885.
- Busigny V., Lebeau O., Ader M., Krapež B. and Bekker A. (2013) Nitrogen cycle in the Late Archean ferruginous ocean. *Chem. Geol.* **362**, 115-130.
- Byrne J. M., Klueglein N., Pearce C., Rosso K. M., Appel E. and Kappler A. (2015) Redox cycling of Fe(II) and Fe(III) in magnetite by Fe-metabolizing bacteria. *Science* **347**, 1473-1476.
- Cai C., Leu A. O., Xie G. J., Guo J., Feng Y., Zhao J. X., Tyson G. W., Yuan Z. and Hu S. (2018) A methanotrophic archaeon couples anaerobic oxidation of methane to Fe(III) reduction. *ISME J.* **12**, 1929-1939.
- Camacho A., Walter X. A., Picazo A. and Zopfi J. (2017) Photoferrotrophy: remains of an ancient photosynthesis in modern environments. *Front. Microbiol.* **8**, 323.
- Campbell I. H. and Davies D. R. (2017) Raising the continental crust. *Earth Planet. Sci. Lett.* **460**, 112-122.
- Canfield D. E. (1998) A new model for Proterozoic ocean chemistry. *Nature* **396**, 450-453.
- Canfield D. E. (2005) The early history of atmospheric oxygen: homage to Robert M. Garrels. *Annu. Rev. Earth Planet. Sci.* **33**, 1-36.
- Canfield D. E. and Farquhar J. (2009) Animal evolution, bioturbation, and the sulfate concentration of the oceans. *Proc. Natl. Acad. Sci.* **106**, 8123-8127.
- Cardona T. (2015) A fresh look at the evolution and diversification of photochemical reaction centers. *Photosynth. Res.* **126**, 111-134.
- Cardona T. (2016) Reconstructing the origin of oxygenic photosynthesis: do assembly and photoactivation recapitulate evolution? *Front. Plant Sci.* **7**, 257.
- Cardona T. (2017) Photosystem II is a chimera of reaction centers. *J. Mol. Evol.* **84**, 149-151.
- Cardona T. (2018) Early Archean origin of heterodimeric Photosystem I. *Heliyon* **4**, e00548.
- Cardona T., Sánchez-Baracaldo P., Rutherford A. W. and Larkum A. W. (2018) Early Archean origin of Photosystem II. *Geobiology* **17**, 127-150.
- Chan C. S., Emerson D. and Luther III G. W. (2016) The role of microaerophilic Fe-oxidizing micro-organisms in producing banded iron formations. *Geobiology* **14**, 509-528.
- Chandler F. W. (1980) Proterozoic redbed sequences of Canada. Energy, Mines and Resources Canada, Geological Survey of Canada.
- Clément J.-C., Shrestha J., Ehrenfeld J. G. and Jaffé P. R. (2005) Ammonium oxidation coupled to dissimilatory reduction of iron under anaerobic conditions in wetland soils. *Soil Biol. Biochem.* **37**, 2323-2328.

- Cloud P. E. (1965) Significance of the Gunflint (Precambrian) microflora photosynthetic oxygen may have had important local effects before becoming a major atmospheric gas. *Science* **148**, 27-35.
- Cloud P. E. (1973) Paleocological significance of the banded iron-formation. *Econ. Geol.* **68**, 1135-1143.
- Craddock P. R. and Dauphas N. (2011) Iron and carbon isotope evidence for microbial iron respiration throughout the Archean. *Earth Planet. Sci. Lett.* **303**, 121-132.
- Crowe S. A., Døssing L. N., Beukes N. J., Bau M., Kruger S. J., Frei R. and Canfield D. E. (2013) Atmospheric oxygenation three billion years ago. *Nature* **501**, 535-538.
- Crowe S. A., Paris G., Katsev S., Jones C., Kim S.-T., Zerkle A. L., Nomosatryo S., Fowle D. A., Adkins J. F. and Sessions A. L. (2014) Sulfate was a trace constituent of Archean seawater. *Science* **346**, 735-739.
- Czaja A. D., Johnson C. M., Beard B. L., Eigenbrode J. L., Freeman K. H. and Yamaguchi K. E. (2010) Iron and carbon isotope evidence for ecosystem and environmental diversity in the ~2.7 to 2.5 Ga Hamersley Province, Western Australia. *Earth Planet. Sci. Lett.* **292**, 170-180.
- Czaja A. D., Johnson C. M., Beard B. L., Roden E. E., Li W. and Moorbath S. (2013) Biological Fe oxidation controlled deposition of banded iron formation in the ca. 3770 Ma Isua Supracrustal Belt (West Greenland). *Earth Planet. Sci. Lett.* **363**, 192-203.
- Czaja A. D., Johnson C. M., Roden E. E., Beard B. L., Voegelin A. R., Nägler T. F., Beukes N. J. and Wille M. (2012) Evidence for free oxygen in the Neoproterozoic ocean based on coupled iron–molybdenum isotope fractionation. *Geochim. Cosmochim. Acta* **86**, 118-137.
- Dauphas N., Cates N. L., Mojzsis S. J. and Busigny V. (2007) Identification of chemical sedimentary protoliths using iron isotopes in the >3750 Ma Nuvvuagittuq Supracrustal Belt, Canada. *Earth Planet. Sci. Lett.* **254**, 358-376.
- Dick G. J., Grim S. L. and Klatt J. M. (2018) Controls on O<sub>2</sub> Production in Cyanobacterial Mats and Implications for Earth's Oxygenation. *Annu. Rev. Earth Planet. Sci.* **46**, 123-147.
- Dodd M. S., Papineau D., Grenne T., Slack J. F., Rittner M., Pirajno F., O'Neil J. and Little C. T. (2017) Evidence for early life in Earth's oldest hydrothermal vent precipitates. *Nature* **543**, 60.
- Dodd M. S., Papineau D., She Z., Fogel M. L., Nederbragt S. and Pirajno F. (2018) Organic remains in late Palaeoproterozoic granular iron formations and implications for the origin of granules. *Precambrian Res.* **310**, 133-152.
- Druschel G. K., Emerson D., Sutka R., Suchecki P. and Luther III G. W. (2008) Low-oxygen and chemical kinetic constraints on the geochemical niche of neutrophilic iron(II) oxidizing microorganisms. *Geochim. Cosmochim. Acta* **72**, 3358-3370.
- Eigenbrode J. L. and Freeman K. H. (2006) Late Archean rise of aerobic microbial ecosystems. *Proc. Natl. Acad. Sci.* **103**, 15759-15764.
- England G. L., Rasmussen B., Krapež B. and Groves D. I. (2002) Palaeoenvironmental significance of rounded pyrite in siliciclastic sequences of the Late Archaean Witwatersrand Basin: oxygen-deficient atmosphere or hydrothermal alteration? *Sedimentology* **49**, 1133-1156.

- Ettwig K. F., Butler M. K., Le Paslier D., Pelletier E., Mangenot S., Kuypers M. M., Schreiber F., Dutilh B. E., Zedelius J., de Beer D., Gloerich J., Wessels H. J. C. T., van Alen T., Luesken F., Wu M. L., van de Pas-Schoonen K. T., Op den Camp H. J. M., Janssen-Megens E. M., Francoijs K.-J., Stunnenberg H., Weissenbach J., Jetten M. S. M. and Strous M. (2010) Nitrite-driven anaerobic methane oxidation by oxygenic bacteria. *Nature* **464**, 543-548.
- Ettwig K. F., Zhu B., Speth D., Keltjens J. T., Jetten M. S. and Kartal B. (2016) Archaea catalyze iron-dependent anaerobic oxidation of methane. *Proc. Natl. Acad. Sci.* **113**, 12792-12796.
- Farquhar J., Bao H. and Thiemens M. (2000) Atmospheric influence of Earth's earliest sulfur cycle. *Science* **289**, 756-758.
- Farquhar J., Wu N., Canfield D. E. and Oduro H. (2010) Connections between sulfur cycle evolution, sulfur isotopes, sediments, and base metal sulfide deposits. *Econ. Geol.* **105**, 509-533.
- Fedo C. M. and Whitehouse M. J. (2002) Metasomatic origin of quartz-pyroxene rock, Akilia, Greenland, and implications for Earth's earliest life. *Science* **296**, 1448-1452.
- Ferry J. G. (1992) Biochemistry of methanogenesis. *Crit. Rev. Biochem. Mol. Biol.* **27**, 473-503.
- Fischer W. W., Hemp J. and Johnson J. E. (2016) Evolution of oxygenic photosynthesis. *Annu. Rev. Earth Planet. Sci.* **44**, 647-683.
- Fischer W. W. and Knoll A. H. (2009) An iron shuttle for deepwater silica in Late Archean and early Paleoproterozoic iron formation. *Geol. Soc. Am. Bull.* **121**, 222-235.
- Flament N., Coltice N. and Rey P. F. (2008) A case for late-Archean continental emergence from thermal evolution models and hypsometry. *Earth Planet. Sci. Lett.* **275**, 326-336.
- Flament N., Coltice N. and Rey P. F. (2013) The evolution of the  $^{87}\text{Sr}/^{86}\text{Sr}$  of marine carbonates does not constrain continental growth. *Precambrian Res.* **229**, 177-188.
- Flannery D. T. and Walter M. R. (2012) Archean tufted microbial mats and the Great Oxidation Event: new insights into an ancient problem. *Aust. J. Earth Sci.* **59**, 1-11.
- Flombaum P., Gallegos J. L., Gordillo R. A., Rincón J., Zabala L. L., Jiao N., Karl D. M., Li W. K., Lomas M. W. and Veneziano D. (2013) Present and future global distributions of the marine Cyanobacteria *Prochlorococcus* and *Synechococcus*. *Proc. Natl. Acad. Sci.* **110**, 9824-9829.
- Frei R., Crowe S. A., Bau M., Polat A., Fowle D. A. and Døssing L. N. (2016) Oxidative elemental cycling under the low O<sub>2</sub> Eoarchean atmosphere. *Sci. Rep.* **6**, 21058.
- Fru E. C., Rodríguez N. P., Partin C. A., Lalonde S. V., Andersson P., Weiss D. J., El Albani A., Rodushkin I. and Konhauser K. O. (2016) Cu isotopes in marine black shales record the Great Oxidation Event. *Proc. Natl. Acad. Sci.*, 201523544.
- Garrels R. M., Perry E. A. and Mackenzie F. T. (1973) Genesis of Precambrian iron-formations and the development of atmospheric oxygen. *Econ. Geol.* **68**, 1173-1179.
- Garvin J., Buick R., Anbar A. D., Arnold G. L. and Kaufman A. J. (2009) Isotopic evidence for an aerobic nitrogen cycle in the latest Archean. *Science* **323**, 1045-1048.
- Gauger T., Konhauser K. O. and Kappler A. (2016) Protection of nitrate-reducing Fe(II)-oxidizing bacteria from UV radiation by biogenic Fe(III) minerals. *Astrobiology* **16**, 301-310.



- Godfrey L. V. and Falkowski P. G. (2009) The cycling and redox state of nitrogen in the Archaean ocean. *Nat. Geosci.* **2**, 725.
- Grotzinger J. P. and Knoll A. H. (1999) Stromatolites in Precambrian carbonates: evolutionary mileposts or environmental dipsticks? *Annu. Rev. Earth Planet. Sci.* **27**, 313-358.
- Gumsley A. P., Chamberlain K. R., Bleeker W., Söderlund U., de Kock M. O., Larsson E. R. and Bekker A. (2017) Timing and tempo of the Great Oxidation Event. *Proc. Natl. Acad. Sci.* **114**, 1811-1816.
- Guo Q., Strauss H., Kaufman A. J., Schröder S., Gutzmer J., Wing B., Baker M. A., Bekker A., Jin Q. and Kim S.-T. (2009) Reconstructing Earth's surface oxidation across the Archean-Proterozoic transition. *Geology* **37**, 399-402.
- Hardisty D. S., Lu Z., Planavsky N. J., Bekker A., Philippot P., Zhou X. and Lyons T. W. (2014) An iodine record of Paleoproterozoic surface ocean oxygenation. *Geology* **42**, 619-622.
- Hartman H. (1984) The evolution of photosynthesis and microbial mats: A speculation on the banded iron formations. In *Microbial Mats: Stromatolites* (eds. Y. Cohen, R. W. Castenholz and H. O. Halvorson). Alan Liss, New York. pp. 451-453
- Haugaard R., Pecoits E., Lalonde S. V., Rouxel O. and Konhauser K. O. (2016) The Joffre banded iron formation, Hamersley Group, Western Australia: Assessing the palaeoenvironment through detailed petrology and chemostratigraphy. *Precambrian Res.* **273**, 12-37.
- Hayes J. (1983) Geochemical evidence bearing on the origin of aerobiosis, a speculative hypothesis. In *Earth's Earliest Biosphere: Its Origin and Evolution* (ed. J. W. Schopf). Princeton Univ. Press, Princeton, N. J., pp. 291-301
- He S., Tominski C., Kappler A., Behrens S. and Roden E. E. (2016) Metagenomic analyses of the autotrophic Fe(II)-oxidizing, nitrate-reducing enrichment culture KS. *Appl. Environ. Microbiol.* **82**, 2656-2668.
- Heimann A., Johnson C. M., Beard B. L., Valley J. W., Roden E. E., Spicuzza M. J. and Beukes N. J. (2010) Fe, C, and O isotope compositions of banded iron formation carbonates demonstrate a major role for dissimilatory iron reduction in ~2.5 Ga marine environments. *Earth Planet. Sci. Lett.* **294**, 8-18.
- Hofmann A., Bekker A., Rouxel O., Rumble D. and Master S. (2009) Multiple sulphur and iron isotope composition of detrital pyrite in Archaean sedimentary rocks: A new tool for provenance analysis. *Earth Planet. Sci. Lett.* **286**, 436-445.
- Hofmann H. J. (1976) Precambrian microflora, Belcher Islands, Canada: significance and systematics. *J. Paleontol.*, 1040-1073.
- Hohmann-Marriott M. F. and Blankenship R.E. (2012) The photosynthetic world. In *Photosynthesis. Advances in Photosynthesis and Respiration* (eds. J. J. Eaton-Rye, B. C. Tripathy and T. D. Sharkey). Springer, Dordrecht, pp. 3-32.
- Holland H. D. (1984) The chemical evolution of the atmosphere and oceans. Princeton University Press, Princeton, N. J.
- Holland H. D. (2005) Sea level, sediments and the composition of seawater. *Am. J. Sci.* **305**, 220-239.

- Holm N. G. (1989) The  $^{13}\text{C}^{12}\text{C}$  ratios of siderite and organic matter of a modern metalliferous hydrothermal sediment and their implications for banded iron formations. *Chem. Geol.* **77**, 41-45.
- Homann M., Heubeck C., Airo A. and Tice M. M. (2015) Morphological adaptations of 3.22 Ga-old tufted microbial mats to Archean coastal habitats (Moodies Group, Barberton Greenstone Belt, South Africa). *Precambrian Res.* **266**, 47-64.
- Homann M., Sansjofre P., Van Zuilen M., Heubeck C., Gong J., Killingsworth B., Foster I. S., Airo A., Van Kranendonk M. J. and Ader M. (2018) Microbial life and biogeochemical cycling on land 3,220 million years ago. *Nat. Geosci.* **11**, 665.
- Hou K., Li Y., Gao J., Liu F. and Qin Y. (2014) Geochemistry and Si–O–Fe isotope constraints on the origin of banded iron formations of the Yuanjiacun Formation, Lvliang Group, Shanxi, China. *Ore Geol. Rev.* **57**, 288-298.
- Isley A. E. and Abbott D. H. (1999) Plume-related mafic volcanism and the deposition of banded iron formation. *J. Geophys. Res. Solid Earth (1978–2012)* **104**, 15461-15477.
- Johnson C. M., Beard B. L., Klein C., Beukes N. J. and Roden E. E. (2008) Iron isotopes constrain biologic and abiologic processes in banded iron formation genesis. *Geochim. Cosmochim. Acta* **72**, 151-169.
- Johnson C. M., Ludois J. M., Beard B. L., Beukes N. J. and Heimann A. (2013) Iron formation carbonates: Paleooceanographic proxy or recorder of microbial diagenesis? *Geology* **41**, 1147-1150.
- Johnson J. E., Gerpheide A., Lamb M. P. and Fischer W. W. (2014) O<sub>2</sub> constraints from Paleoproterozoic detrital pyrite and uraninite. *Geol. Soc. Am. Bull.* **126**, 813-830.
- Johnson J. E., Muhling J. R., Cosmidis J., Rasmussen B. and Templeton A.S. (2018) Low-Fe(III) Greenalite Was a Primary Mineral From Neoproterozoic Oceans. *Geophys. Res. Lett.* **45**, 3182-3192.
- Johnson J. E., Webb S. M., Thomas K., Ono S., Kirschvink J. L. and Fischer W. W. (2013) Manganese-oxidizing photosynthesis before the rise of cyanobacteria. *Proc. Natl. Acad. Sci.* **110**, 11238-11243.
- Johnston D. T., Poulton S. W., Fralick P. W., Wing B. A., Canfield D. E. and Farquhar J. (2006) Evolution of the oceanic sulfur cycle at the end of the Paleoproterozoic. *Geochim. Cosmochim. Acta* **70**, 5723-5739.
- Jones C., Nomosatryo S., Crowe S. A., Bjerrum C. J. and Canfield D. E. (2015) Iron oxides, divalent cations, silica, and the early earth phosphorus crisis. *Geology* **43**, 135-138.
- Kappler A. and Newman D. K. (2004) Formation of Fe(III)-minerals by Fe(II)-oxidizing photoautotrophic bacteria. *Geochim. Cosmochim. Acta* **68**, 1217-1226.
- Kappler A., Pasquero C., Konhauser K. O. and Newman D. K. (2005) Deposition of banded iron formations by anoxygenic phototrophic Fe(II)-oxidizing bacteria. *Geology* **33**, 865-868.
- Karl D. M., Brittai, A. M. and Tilbroo, B. D. (1989) Hydrothermal and microbial processes at Loihi Seamount, a mid-plate hot-spot volcano. *Deep Sea Res. Part A. Oceanographic Research Papers* **36**, 1655-1673.

- Kendall B., Creaser R. A., Reinhard C. T., Lyons T. W. and Anbar A. D. (2015) Transient episodes of mild environmental oxygenation and oxidative continental weathering during the late Archean. *Sci. Adv.* **1**, e1500777.
- Kendall B., Gordon G. W., Poulton S. W. and Anbar A. D. (2011) Molybdenum isotope constraints on the extent of late Paleoproterozoic ocean euxinia. *Earth Planet. Sci. Lett.* **307**, 450-460.
- Kendall B., Reinhard C. T., Lyons T. W., Kaufman A. J., Poulton S. W. and Anbar A. D. (2010) Pervasive oxygenation along late Archaean ocean margins. *Nat. Geosci.* **3**, 647-652.
- Kirkham R. V. and Roscoe S. M. (1993) Atmospheric evolution and ore deposit formation. *Resour. Geol.* **15**, 1-17.
- Klueglein N. and Kappler A. (2013) Abiotic oxidation of Fe(II) by reactive nitrogen species in cultures of the nitrate-reducing Fe(II) oxidizer *Acidovorax* sp. BoFeN1 – questioning the existence of enzymatic Fe(II) oxidation. *Geobiology* **11**, 180-190.
- Klueglein N., Zeitvogel F., Stierhof Y.-D., Floetenmeyer M., Konhauser K. O., Kappler A. and Obst, M. (2014) Potential role of nitrite for abiotic Fe(II) oxidation and cell encrustation during nitrate reduction by denitrifying bacteria. *Appl. Environ. Microbiol.* **80**, 1051-1061.
- Knoll A. H. (2008) Cyanobacteria and Earth history. In *The cyanobacteria: Molecular Biology, Genomics, and Evolution* (eds. A. Herrero and E. Flores). Caister Academic Press, U.K. pp. 1-19
- Knoll A. H. (2015) Paleobiological perspectives on early microbial evolution. *Cold Spring Harb. Perspect. Biol.* **7**, a018093.
- Konhauser K. O., Newman D. K. and Kappler A. (2005) The potential significance of microbial Fe(III) reduction during deposition of Precambrian banded iron formations. *Geobiology* **3**, 167-177.
- Konhauser K. O., Planavsky N. J., Hardisty D. S., Robbins L. J., Warchola T. J., Hugaard R., Lalonde S. V., Partin C. A., Oonk P. B. H., Tsikos H., Lyons T. W., Bekker A. and Johnson C. M. (2017) Iron formations: A global record of Neoproterozoic to Palaeoproterozoic environmental history. *Earth Sci. Rev.* **172**, 140-177.
- Konhauser K. O., Hamade T., Raiswell R., Morris R. C., Ferris F. G., Southam G. and Canfield D. E. (2002) Could bacteria have formed the Precambrian banded iron formations? *Geology* **30**, 1079-1082.
- Konhauser K. O., Lalonde S. V., Amskold L. and Holland H. D. (2007) Was there really an Archean phosphate crisis? *Science* **315**, 1234-1234.
- Konhauser K. O., Lalonde S. V., Planavsky N. J., Pecoits E., Lyons T. W., Mojzsis S. J., Rouxel O. J., Barley M. E., Rosière C. and Fralick P. W. (2011) Aerobic bacterial pyrite oxidation and acid rock drainage during the Great Oxidation Event. *Nature* **478**, 369-373.
- Konhauser K. O., Pecoits E., Lalonde S. V., Papineau D., Nisbet E. G., Barley M. E., Arndt N. T., Zahnle K. and Kamber B. S. (2009) Oceanic nickel depletion and a methanogen famine before the Great Oxidation Event. *Nature* **458**, 750-753.
- Konhauser K. O., Robbins L. J., Alessi D. S., Flynn S. L., Gingras M. K., Martinez R. E., Kappler A., Swanner E. D., Li Y.-L., Crowe S. A., Planavsky N. J., Reinhard C. T. and

- Lalonde S. V. (2018) Phytoplankton contributions to the trace-element composition of Precambrian banded iron formations. *Geol. Soc. Am. Bull.* **130**, 941-951.
- Konhauser K. O., Robbins L. J., Pecoits E., Peacock C., Kappler A. and Lalonde S. V. (2015) The Archean Nickel Famine Revisited. *Astrobiology* **15**, 804-815.
- Kopp R. E., Kirschvink J. L., Hilburn I. A. and Nash C. Z. (2005) The Paleoproterozoic snowball Earth: a climate disaster triggered by the evolution of oxygenic photosynthesis. *Proc. Natl. Acad. Sci.* **102**, 11131-11136.
- Kump L. R. and Seyfried W. E. (2005) Hydrothermal Fe fluxes during the Precambrian: effect of low oceanic sulfate concentrations and low hydrostatic pressure on the composition of black smokers. *Earth Planet. Sci. Lett.* **235**, 654-662.
- Kurzweil F., Wille M., Gantert N., Beukes N. J. and Schoenberg R. (2016) Manganese oxide shuttling in pre-GOE oceans – evidence from molybdenum and iron isotopes. *Earth Planet. Sci. Lett.* **452**, 69-78.
- Lalonde S. V. and Konhauser K. O. (2015) Benthic perspective on Earth's oldest evidence for oxygenic photosynthesis. *Proc. Natl. Acad. Sci.* **112**, 995-1000.
- Larsson J., Nylander J. A. A. and Bergman B. (2011) Genome fluctuations in cyanobacteria reflect evolutionary, developmental and adaptive traits. *BMC Evol. Biol.* **11**, 1-21.
- Lueder U., Druschel G., Emerson D., Kappler A. and Schmidt C. (2017) Quantitative analysis of O<sub>2</sub> and Fe<sup>2+</sup> profiles in gradient tubes for cultivation of microaerophilic Iron(II)-oxidizing bacteria. *FEMS Microbiol. Ecol.* **94**, fix177.
- Luo G., Ono S., Beukes N. J., Wang D. T., Xie S. and Summons R. E. (2016) Rapid oxygenation of Earth's atmosphere 2.33 billion years ago. *Sci. Adv.* **2**, e1600134.
- Maisch M., Lueder U., Laufer K., Scholze C., Kappler A. and Schmidt C. (2019) Contribution of microaerophilic iron(II)-oxidizers to iron(III) mineral formation. *Environ. Sci. Technol.* **53**, 8197-8204.
- Maliva R. G., Knoll A. H. and Simonson B. M. (2005) Secular change in the Precambrian silica cycle: insights from chert petrology. *Geol. Soc. Am. Bull.* **117**, 835-845.
- McCollom T. M. and Seewald J. S. (2006) Carbon isotope composition of organic compounds produced by abiotic synthesis under hydrothermal conditions. *Earth Planet. Sci. Lett.* **243**, 74-84.
- Melezhik V. A., Fallick A. E., Rychanchik D. V. and Kuznetsov A. B. (2005) Palaeoproterozoic evaporites in Fennoscandia: implications for seawater sulphate, the rise of atmospheric oxygen and local amplification of the  $\delta^{13}\text{C}$  excursion. *Terra Nova* **17**, 141-148.
- Melton E. D., Swanner E. D., Behrens S., Schmidt C. and Kappler A. (2014) The interplay of microbially mediated and abiotic reactions in the biogeochemical Fe cycle. *Nat. Rev. Microbiol.* **12**, 797-808.
- Mloszewska A. M., Cole D. B., Planavsky N. J., Kappler A., Whitford D. S., Owttrim G. W. and Konhauser K. O. (2018) UV radiation limited the expansion of cyanobacteria in early marine photic environments. *Nat. Commun.* **9**, 1-8.
- Nabhan S., Wiedenbeck M., Milke R. and Heubeck C. (2016) Biogenic overgrowth on detrital pyrite in ca. 3.2 Ga Archean paleosols. *Geology* **44**, 763-766.

- Neubeck A., Sjöberg S., Price A., Callac N. and Schnürer A. (2016) Effect of nickel levels on hydrogen partial pressure and methane production in methanogens. *PloS one* **11**, e0168357.
- Olson S. L., Kump L. R. and Kasting J. F. (2013) Quantifying the areal extent and dissolved oxygen concentrations of Archean oxygen oases. *Chem. Geol.* **362**, 35-43.
- Oshiki M., Ishii S., Yoshida K., Fujii N., Ishiguro M., Satoh H. and Okabe S. (2013) Nitrate-dependent ferrous iron oxidation by anaerobic ammonium oxidation (anammox) bacteria. *Appl. Environ. Microbiol.* **79**, 4087-4093.
- Ossa F.O., Hofmann A., Wille M., Spangenberg J. E., Bekker A., Poulton S. W., Eickmann B. and Schoenberg R. (2018) Aerobic iron and manganese cycling in a redox-stratified Mesoarchean epicontinental sea. *Earth Planet. Sci. Lett.* **500**, 28-40.
- Papineau D., Mojzsis S. J. and Schmitt A. K. (2007) Multiple sulfur isotopes from Paleoproterozoic Huronian interglacial sediments and the rise of atmospheric oxygen. *Earth Planet. Sci. Lett.* **255**, 188-212.
- Partridge M. A., Golding S. D., Baublys K. A. and Young E. (2008) Pyrite paragenesis and multiple sulfur isotope distribution in late Archean and early Paleoproterozoic Hamersley Basin sediments. *Earth Planet. Sci. Lett.* **272**, 41-49.
- Pavlov A. A. and Kasting J. F. (2002) Mass-independent fractionation of sulfur isotopes in Archean sediments: strong evidence for an anoxic Archean atmosphere. *Astrobiology* **2**, 27-41.
- Percak-Dennett E. M., Beard B. L., Xu H., Konishi H., Johnson C. M. and Roden E. E. (2011) Iron isotope fractionation during microbial dissimilatory iron oxide reduction in simulated Archaean seawater. *Geobiology* **9**, 205-220.
- Peters S. E., Husson J. M. and Wilcots J. (2017) The rise and fall of stromatolites in shallow marine environments. *Geology* **45**, 487-490.
- Phoenix V. R., Konhauser K. O., Adams D. G. and Bottrell S. H. (2001) Role of biomineralization as an ultraviolet shield: Implications for Archean life. *Geology* **29**, 823-826.
- Phoenix V. R., Bennett P. C., Engel A. S., Tyler S. W. and Ferris F. G. (2006) Chilean high-altitude hot-spring sinters: a model system for UV screening mechanisms by early Precambrian cyanobacteria. *Geobiology* **4**, 15-28.
- Pierson B. K., Mitchell H. K. and Ruff-Roberts A. L. (1993) *Chloroflexus aurantiacus* and ultraviolet radiation: implications for archaean shallow-water stromatolites. *Orig. Life Evol. Biosph.* **23**, 243-260.
- Planavsky N. J., Rouxel O. J., Bekker A., Shapiro R., Fralick P. and Knudsen A. (2009) Iron-oxidizing microbial ecosystems thrived in late Paleoproterozoic redox-stratified oceans. *Earth Planet. Sci. Lett.* **286**, 230-242.
- Planavsky N. J., Asael D., Hofmann A., Reinhard C. T., Lalonde S. V., Knudsen A., Wang X., Ossa F. O., Pecoits E. and Smith A. J. (2014) Evidence for oxygenic photosynthesis half a billion years before the Great Oxidation Event. *Nat. Geosci.* **7**, 283-286.
- Ponce-Toledo R. I., Deschamps P., López-García P., Zivanovic Y., Benzerara K. and Moreira D. (2017) An early-branching freshwater cyanobacterium at the origin of plastids. *Curr. Biol.* **27**, 386-391.

- Posth N. R., Huelin S., Konhauser K. O. and Kappler A. (2010) Size, density and composition of cell–mineral aggregates formed during anoxygenic phototrophic Fe(II) oxidation: Impact on modern and ancient environments. *Geochim. Cosmochim. Acta* **74**, 3476-3493.
- Poulton S. W. and Canfield D. E. (2011) Ferruginous conditions: a dominant feature of the ocean through Earth's history. *Elements* **7**, 107-112.
- Poulton S. W., Fralick P. W. and Canfield D. E. (2004) The transition to a sulphidic ocean ~1.84 billion years ago. *Nature* **431**, 173-177.
- Rasmussen B. and Buick R. (1999) Redox state of the Archean atmosphere: evidence from detrital heavy minerals in ca. 3250–2750 Ma sandstones from the Pilbara Craton, Australia. *Geology* **27**, 115-118.
- Rasmussen B. and Muhling J. R. (2018) Making magnetite late again: evidence for widespread magnetite growth by thermal decomposition of siderite in Hamersley banded iron formations. *Precambrian Res.* **306**, 64-93.
- Rasmussen B., Muhling J. R., Suvorova A. and Krapež B. (2017) Greenalite precipitation linked to the deposition of banded iron formations downslope from a late Archean carbonate platform. *Precambrian Res.* **290**, 49-62.
- Raye U., Pufahl P. K., Kyser T. K., Ricard E. and Hiatt E. E. (2015) The role of sedimentology, oceanography, and alteration on the  $\delta^{56}\text{Fe}$  value of the Sokoman Iron Formation, Labrador Trough, Canada. *Geochim. Cosmochim. Acta* **164**, 205-220.
- Reinhard C. T., Planavsky N. J., Robbins L. J., Partin C. A., Gill B. C., Lalonde S. V., Bekker A., Konhauser K. O. and Lyons T. W. (2013) Proterozoic ocean redox and biogeochemical stasis. *Proc. Natl. Acad. Sci.* **110**, 5357-5362.
- Reinhard C. T., Raiswell R., Scott C., Anbar A. D. and Lyons T. W. (2009) A late Archean sulfidic sea stimulated by early oxidative weathering of the continents. *Science* **326**, 713-716.
- Rey P. F. and Coltice N. (2008) Neoproterozoic lithospheric strengthening and the coupling of Earth's geochemical reservoirs. *Geology* **36**, 635-638.
- Riedinger N., Formolo M. J., Lyons T. W., Henkel S., Beck A. and Kasten S. (2014) An inorganic geochemical argument for coupled anaerobic oxidation of methane and iron reduction in marine sediments. *Geobiology* **12**, 172-181.
- Robbins L. J., Funk S. P., Flynn S. L., Warchola T. J., Li Z., Lalonde S. V., Rostron B. J., Smith A. J. B., Beukes N. J., de Kock M. O., Heaman L. M., Alessi D. S. and Konhauser K. O. (2019) Hydrogeological constraints on the formation of Palaeoproterozoic banded iron formations. *Nat. Geosci.* **12**, 558-563.
- Robbins L. J., Lalonde S. V., Planavsky N. J., Partin C. A., Reinhard C. T., Kendall B., Scott C., Hardisty D. S., Gill B. C., Alessi D. S., Dupont C. L., Saito M. A., Crowe S. A., Poulton S. W., Bekker A., Lyons T. W. and Konhauser K. O. (2016) Trace elements at the intersection of marine biological and geochemical evolution. *Earth Sci. Rev.* **163**, 323-348.
- Roerdink D. L., Mason P. R., Farquhar J. and Reimer T. (2012) Multiple sulfur isotopes in Paleoproterozoic barites identify an important role for microbial sulfate reduction in the early marine environment. *Earth Planet. Sci. Lett.* **331**, 177-186.

- Roscoe S. M. (1996) Paleoplacer uranium gold. In *Geology of Canadian Mineral Deposits Types, vol P-1* (eds. O. R. Eckstrand, W. D. Sinclair and R. I. Thorpe.) Geological Society of America, The Geology of North America, Boulder. pp. 10-23.
- Rosing M. T. (1999)  $^{13}\text{C}$ -depleted carbon microparticles in > 3700-Ma sea-floor sedimentary rocks from West Greenland. *Science* **283**, 674-676.
- Rosing M. T. and Frei R. (2004) U-rich Archaean sea-floor sediments from Greenland – indications of > 3700 Ma oxygenic photosynthesis. *Earth Planet. Sci. Lett.* **217**, 237-244.
- Rye R. and Holland H. D. (1998) Paleosols and the evolution of atmospheric oxygen: a critical review. *Am. J. Sci.* **298**, 621-672.
- Rye R. and Holland H. D. (2000) Life associated with a 2.76 Ga ephemeral pond?: Evidence from Mount Roe# 2 paleosol. *Geology* **28**, 483-486.
- Sakurai R., Ito M., Ueno Y., Kitajima K. and Maruyama S. (2005) Facies architecture and sequence-stratigraphic features of the Tumbiana Formation in the Pilbara Craton, northwestern Australia: Implications for depositional environments of oxygenic stromatolites during the Late Archean. *Precambrian Res.* **138**, 255-273.
- Sánchez-Baracaldo P. (2015) Origin of marine planktonic cyanobacteria. *Sci. Rep.* **5**, 17418.
- Sánchez-Baracaldo P., Raven J. A., Pisani D. and Knoll A. H. (2017) Early photosynthetic eukaryotes inhabited low-salinity habitats. *Proc. Natl. Acad. Sci.* **114**, E7737-E7745.
- Sánchez-Baracaldo P., Ridgwell A. and Raven J. A. (2014) A neoproterozoic transition in the marine nitrogen cycle. *Curr. Biol.* **24**, 652-657.
- Sanchez-Baracaldo P., Hayes P. and Blank C. E. (2005) Morphological and habitat evolution in the Cyanobacteria using a compartmentalization approach. *Geobiology* **3**, 145-165.
- Satkoski A. M., Beukes N. J., Li W., Beard B. L. and Johnson C. M. (2015) A redox-stratified ocean 3.2 billion years ago. *Earth Planet. Sci. Lett.* **430**, 43-53.
- Schirmermeister B. E., de Vos J. M., Antonelli A. and Bagheri H. C. (2013) Evolution of multicellularity coincided with increased diversification of cyanobacteria and the Great Oxidation Event. *Proc. Natl. Acad. Sci.* **110**, 1791-1796.
- Schirmermeister B. E., Gugger M. and Donoghue P. C. (2015) Cyanobacteria and the Great Oxidation Event: evidence from genes and fossils. *Palaeontology* **58**, 769-785.
- Schröder S., Bekker A., Beukes N. J., Strauss H. and Van Niekerk H. S. (2008) Rise in seawater sulphate concentration associated with the Paleoproterozoic positive carbon isotope excursion: evidence from sulphate evaporites in the ~2.2–2.1 Gyr shallow-marine Lucknow Formation, South Africa. *Terra Nova* **20**, 108-117.
- Scott C. T., Bekker A., Reinhard C. T., Schnetger B., Krapež B., Rumble III D. and Lyons T. W. (2011) Late Archean euxinic conditions before the rise of atmospheric oxygen. *Geology* **39**, 119-122.
- Shao S., Cardona T. and Nixon P. (2018) Early emergence of the FtsH proteases involved in photosystem II repair. *Photosynthetica* **56**, 163-177.

- Shelobolina E. S., Xu H., Konishi H., Kukkadapu R., Wu T., Blöthe M. and Roden E. E. (2012a) Microbial lithotrophic oxidation of structural Fe(II) in biotite. *Appl. Environ. Microbiol.* **78**, 5746-5752.
- Shelobolina E.S., Konishi H., Xu H., Benzine J., Xiong M.Y., Wu T., Blöthe M. and Roden E. E. (2012b) Isolation of phyllosilicate–iron redox cycling microorganisms from an illite–smectite rich hydromorphic soil. *Front. Microbiol.* **3**, 134.
- Shen Y., Farquhar J., Masterson A., Kaufman A. J. and Buick R. (2009) Evaluating the role of microbial sulfate reduction in the early Archean using quadruple isotope systematics. *Earth Planet. Sci. Lett.* **279**, 383-391.
- Shi T., Bibby T. S., Jiang L., Irwin A. J. and Falkowski P. G. (2005) Protein interactions limit the rate of evolution of photosynthetic genes in cyanobacteria. *Mol. Biol. Evol.* **22**, 2179-2189.
- Shih P. M., Hemp J., Ward L. M., Matzke N. J. and Fischer W. W. (2017) Crown group Oxyphotobacteria postdate the rise of oxygen. *Geobiology* **15**, 19-29.
- Shih P. M., Wu D., Latifi A., Axen S. D., Fewer D. P., Talla E., Calteau A., Cai F., De Marsac N. T. and Rippka R. (2013) Improving the coverage of the cyanobacterial phylum using diversity-driven genome sequencing. *Proc. Natl. Acad. Sci.* **110**, 1053-1058.
- Siebert C., Kramers J., Meisel T., Morel P. and Nägler T. F. (2005) PGE, Re-Os, and Mo isotope systematics in Archean and early Proterozoic sedimentary systems as proxies for redox conditions of the early Earth. *Geochim. Cosmochim. Acta* **69**, 1787-1801.
- Sim M. S., Liang B., Petroff A. P., Evans A., Klepac-Ceraj V., Flannery D. T., Walter M. R. and Bosak T. (2012) Oxygen-dependent morphogenesis of modern clumped photosynthetic mats and implications for the Archean stromatolite record. *Geosciences* **2**, 235-259.
- Soo R. M., Hemp J., Parks D. H., Fischer W. W. and Hugenholtz P. (2017) On the origins of oxygenic photosynthesis and aerobic respiration in Cyanobacteria. *Science* **355**, 1436-1440.
- Soo R. M., Skennerton C. T., Sekiguchi Y., Imelfort M., Paech S. J., Dennis P. G., Steen J. A., Parks D. H., Tyson G. W. and Hugenholtz P. (2014) An expanded genomic representation of the phylum Cyanobacteria. *Genome Biol. Evol.* **6**, 1031-1045.
- Stal L. (2001) Coastal microbial mats: the physiology of a small-scale ecosystem. *South Afr. J. Bot.* **67**, 399-410.
- Stanton C. L., Reinhard C. T., Kasting J. F., Ostrom N. E., Haslun J. A., Lyons T. W. and Glass J. B. (2018) Nitrous oxide from chemodenitrification: A possible missing link in the Proterozoic greenhouse and the evolution of aerobic respiration. *Geobiology* **16**, 597-609.
- Steinboefel G., Horn I. and von Blanckenburg F. (2009) Micro-scale tracing of Fe and Si isotope signatures in banded iron formation using femtosecond laser ablation. *Geochim. Cosmochim. Acta* **73**, 5343-5360.
- Steinboefel G., von Blanckenburg F., Horn I., Konhauser K. O., Beukes N. J. and Gutzmer J. (2010) Deciphering formation processes of banded iron formations from the Transvaal and the Hamersley successions by combined Si and Fe isotope analysis using UV femtosecond laser ablation. *Geochim. Cosmochim. Acta* **74**, 2677-2696.
- Straub K. L., Benz M., Schink B. and Widdel F. (1996) Anaerobic, nitrate-dependent microbial oxidation of ferrous iron. *Appl. Environ. Microbiol.* **62**, 1458-1460.



- Stüeken E. E., Buick R., Anderson R. E., Baross J. A., Planavsky N. J. and Lyons T. W. (2017) Environmental niches and metabolic diversity in Neoproterozoic lakes. *Geobiology* **15**, 767-783.
- Stüeken E. E., Buick R., Guy B. M. and Koehler M. C. (2015) Isotopic evidence for biological nitrogen fixation by molybdenum-nitrogenase from 3.2 Gyr. *Nature* **520**, 666.
- Stüeken E. E., Catling D. C. and Buick R. (2012) Contributions to late Proterozoic sulphur cycling by life on land. *Nat. Geosci.* **5**, 722.
- Stüeken E. E., Kipp M. A., Koehler M. C. and Buick R. (2016) The evolution of Earth's biogeochemical nitrogen cycle. *Earth Sci. Rev.* **160**, 220-239.
- Swanner E. D., Mloszewska A. M., Cirpka O. A., Schoenberg R., Konhauser K. O. and Kappler A. (2015) Modulation of oxygen production in Proterozoic oceans by episodes of Fe(II) toxicity. *Nat. Geosci.* **8**, 126-130.
- Tebo B. M., Johnson H. A., McCarthy J. K. and Templeton A. S. (2005) Geomicrobiology of manganese(II) oxidation. *Trends Microbiol.* **13**, 421-428.
- Teixeira N. L., Caxito F. A., Rosière C. A., Pecoits E., Vieira L., Frei R., Sial A. N. and Poitrasson F. (2017) Trace elements and isotope geochemistry (C, O, Fe, Cr) of the Cauê iron formation, Quadrilátero Ferrífero, Brazil: Evidence for widespread microbial dissimilatory iron reduction at the Archean/Paleoproterozoic transition. *Precambrian Res.* **298**, 39-55.
- Thoby M., Konhauser K. O., Fralick P. W., Altermann W., Visscher P. T. and Lalonde S. V. (2019) Global importance of oxic molybdenum sinks prior to 2.6 Ga revealed by the Mo isotope composition of Precambrian carbonates. *Geology* **47**, 559-562.
- Thomazo C., Ader M. and Philippot P. (2011) Extreme <sup>15</sup>N-enrichments in 2.72-Gyr-old sediments: evidence for a turning point in the nitrogen cycle. *Geobiology* **9**, 107-120.
- Thomazo C., Couradeau E. and Garcia-Pichel F. (2018) Possible nitrogen fertilization of the early Earth Ocean by microbial continental ecosystems. *Nat. Commun.* **9**, 2530.
- Thomazo C., Nisbet E. G., Grassineau N. V., Peters M. and Strauss H. (2013) Multiple sulfur and carbon isotope composition of sediments from the Belingwe Greenstone Belt (Zimbabwe): A biogenic methane regulation on mass independent fractionation of sulfur during the Neoproterozoic? *Geochim. Cosmochim. Acta* **121**, 120-138.
- Tominski C., Heyer H., Lösekann-Behrens T., Behrens S. and Kappler A. (2018) Growth and population dynamics of the anaerobic Fe(II)-oxidizing and nitrate-reducing enrichment culture KS. *Appl. Environ. Microbiol.* **84**, e02173-17
- Trendall A. F. (2002) The significance of iron-formation in the Precambrian stratigraphic record. *Precambrian Sedimentary Environments: a Modern Approach to Depositional Systems*, *Spec. Publ. Internat. Assoc. Sedimentol.* **33**, 33-66.
- Tsikos H. and Moore J. M. (1997) Petrography and geochemistry of the Paleoproterozoic Hotazel Iron-Formation, Kalahari manganese field, South Africa; implications for Precambrian manganese metallogenesis. *Econ. Geol.* **92**, 87-97.
- Ueno Y., Ono S., Rumble D. and Maruyama S. (2008) Quadruple sulfur isotope analysis of ca. 3.5 Ga Dresser Formation: New evidence for microbial sulfate reduction in the early Archean. *Geochim. Cosmochim. Acta* **72**, 5675-5691.

- Van Zuilen M. A., Lepland A. and Arrhenius G. (2002) Reassessing the evidence for the earliest traces of life. *Nature* **418**, 627-630.
- Vargas M., Kashefi K., Blunt-Harris E. L. and Lovley D. R. (1998) Microbiological evidence for Fe(III) reduction on early Earth. *Nature* **395**, 65-67.
- Walker J. C. (1984) Suboxic diagenesis in banded iron formations. *Nature* **309**, 340-342.
- Walter M., Buick R. and Dunlop J. (1980) Stromatolites 3,400–3,500 Myr old from the North pole area, Western Australia. *Nature* **284**, 443-445.
- Wang C., Konhauser K. O., Zhang L., Zhai M. and Li W. (2016) Decoupled sources of the 2.3–2.2 Ga Yuanjiacun banded iron formation: Implications for the Nd cycle in Earth's early oceans. *Precambrian Res.* **280**, 1-13.
- Wang C., Zhang L., Dai Y. and Lan C. (2015) Geochronological and geochemical constraints on the origin of clastic meta-sedimentary rocks associated with the Yuanjiacun BIF from the Lüliang Complex, North China. *Lithos* **212**, 231-246.
- Warchola T. J., Lalonde S. V., Pecoits E., Von Gunten K., Robbins L. J., Alessi D. S., Philippot P. and Konhauser K. O. (2018) Petrology and geochemistry of the Boolgeeda Iron Formation, Hamersley Basin, Western Australia. *Precambrian Res.* **316**, 155-173.
- Ward L. M., Kirschvink J. L. and Fischer W. W. (2016) Timescales of oxygenation following the evolution of oxygenic photosynthesis. *Orig. Life Evol. Biosph.* **46**, 51-65.
- Watanabe Y., Martini J. E. and Ohmoto H. (2000) Geochemical evidence for terrestrial ecosystems 2.6 billion years ago. *Nature* **408**, 574.
- Watanabe Y., Stewart B. W. and Ohmoto H. (2004) Organic-and carbonate-rich soil formation ~2.6 billion years ago at Schagen, East Transvaal district, South Africa. *Geochim. Cosmochim. Acta* **68**, 2129-2151.
- Wille M., Kramers J. D., Nägler T. F., Beukes N. J., Schröder S., Meisel T., Lacassie J. and Voegelin A. (2007) Evidence for a gradual rise of oxygen between 2.6 and 2.5 Ga from Mo isotopes and Re-PGE signatures in shales. *Geochim. Cosmochim. Acta* **71**, 2417-2435.
- Williford K. H., Van Kranendonk M. J., Ushikubo T., Kozdon R. and Valley J. W. (2011) Constraining atmospheric oxygen and seawater sulfate concentrations during Paleoproterozoic glaciation: In situ sulfur three-isotope microanalysis of pyrite from the Turee Creek Group, Western Australia. *Geochim. Cosmochim. Acta* **75**, 5686-5705.
- Wu L., Percak-Dennett E. M., Beard B. L., Roden E. E. and Johnson C. M. (2012) Stable iron isotope fractionation between aqueous Fe(II) and model Archean ocean Fe–Si coprecipitates and implications for iron isotope variations in the ancient rock record. *Geochim. Cosmochim. Acta* **84**, 14-28.
- Wu W., Swanner E. D., Hao L., Zeitvogel F., Obst M., Pan Y. and Kappler A. (2014) Characterization of the physiology and cell–mineral interactions of the marine anoxygenic phototrophic Fe(II) oxidizer *Rhodovulum iodolum* – implications for Precambrian Fe(II) oxidation. *FEMS Microbiol. Ecol.* **88**, 503-515.
- Zerkle A. L., House C. H., Cox R. and Canfield D. E. (2006) Metal limitation of cyanobacterial N<sub>2</sub> fixation and implications for the Precambrian nitrogen cycle. *Geobiology* **4**, 285-297.

Zhang X., Sigman D. M., Morel F. M. and Kraepiel A. M. (2014) Nitrogen isotope fractionation by alternative nitrogenases and past ocean anoxia. *Proc. Natl. Acad. Sci.* **111**, 4782-4787.

Zhelezinskaia I., Kaufman A. J., Farquhar J. and Cliff J. (2014) Large sulfur isotope fractionations associated with Neoproterozoic microbial sulfate reduction. *Science* **346**, 742-744



## Questions and Goals

Banded Iron Formations (BIFs) provide a window into Earth's past, allowing to decipher past environmental processes and the evolution of microbial life. And yet, the complex interplay of environmental factors, microbial activity, diagenesis and low-grade metamorphism during their genesis makes it difficult to obtain a clear picture of the ancient Earth. Over a century of research has resulted in considerable advancement in our understanding of the mechanisms and the geochemical and biological constraints underlying the genesis of major BIFs of Archean to Paleoproterozoic age. The combined study of the BIF rock record, modern-day analogues for past environments and experimental studies have allowed us to develop and refine models for BIF genesis. Collectively, the majority of these studies point to a biogenic origin of major BIFs, where primary precipitates were formed either through the metabolic activity of anoxygenic photoautotrophic Fe(II)-oxidizing bacteria (photoferrotrophs) or the abiotic oxidation of Fe(II) via O<sub>2</sub> produced by early cyanobacteria. The properties and composition of these primary biogenic sediments would have been modified through subsequent processes like microbial Fe(III) reduction, followed by diagenesis and low-grade metamorphism.

However, past studies on BIF genesis often only focussed on resolving questions pertaining individual aspects such as (1) the geochemistry and the physical properties of the ocean they were deposited from, (2) the mechanism(s) underlying the formation of the primary precipitate, (3) the post-depositional alteration of these primary precipitates by microbial processes and diagenesis or (4) (low-grade) metamorphic processes. Rarely have studies considered a continuum of these aspects or their interaction with one another. Therefore, the goal of this PhD thesis was to obtain further insight into the interplay of the previously discussed factors. Specifically, the objectives of this PhD thesis were:

- (1) To quantify the influence of low-grade metamorphism (170°C, 1.2 kbar) on the post-depositional mobility of phosphate (PO<sub>4</sub><sup>3-</sup>) associated with primary Fe(III) (oxyhydr)oxides (**chapter 1**). BIFs are frequently used to constrain the geochemical

composition of the Archean to Paleoproterozoic ocean. For example, BIF P/Fe ratios are interpreted based on empirical partitioning coefficients to deduce ancient seawater  $\text{PO}_4^{3-}$  concentrations in order to constrain the size of the ancient marine biosphere and the extent of primary production. However, the influence of confounding factors such as low-grade metamorphism on the interpretation of the P/Fe ratios remains unexplored.

- (2) To determine the influence of temperature fluctuations on the metabolic activity of anoxygenic photoautotrophic Fe(II)-oxidizing bacteria (photoferrotrophs; **chapter 2**). Previous work suggested that such temperature fluctuations may act as unifying trigger for the alternating deposition of Fe- and Si-rich bands in BIFs by linking microbial Fe(II) oxidation during warm periods to abiotic Si precipitation during cold periods. We, therefore, wanted to verify the feasibility of a temperature cycling model for creating the characteristic banding in BIFs in a long-term experiment. An additional objective was to identify the mechanism(s) ultimately responsible for the separation of Fe and Si.
- (3) To determine the effect of repeated and dynamic microbial Fe redox cycling on the primary BIF mineral identity and the formation and properties of secondary minerals (**chapter 3**) and to examine the influence of increasing concentrations of Si on the Fe mineral (trans)formation. Although the individual role of photoferrotrophs and Fe(III)-reducing bacteria during the genesis of BIFs is well constrained, it remains unresolved how the direct interaction of both metabolisms influenced the initial deposition of BIFs and the formation of primary sediments. Specifically, it remains unclear if minerals such as siderite and magnetite are formed and maintained during dynamic and alternating microbial Fe redox cycles.







## Statement of personal contribution

### Chapter 1

#### **Phosphate remobilization from banded iron formations depends on metamorphic mineral transformations**

Manuel Schad, Maximilian Halama, Leslie J. Robbins, Tyler J. Warchola, Julian Tejada, Rainer Kirchhof, Stefan V. Lalonde, Elizabeth D. Swanner, Noah J. Planavsky, Harald Thorwarth, Muammar Mansor, Kurt O. Konhauser, Andreas Kappler

**Manuscript in preparation for publication in:** *Geological Society of America Bulletin*

The work described in this chapter was supported by grants from the German Research Foundation (DFG) to Prof. Andreas Kappler, grants from the Natural Science and Engineering Research Council (NSERC) to Prof. Kurt O. Konhauser, a Vanier Canada Graduate Scholarship (CGS) and a Donnelley Postdoctoral Fellowship from the Yale Institute of Biospheric Studies to Dr. Leslie J. Robbins, a NSERC CGS Master's to Tyler J. Warchola and grants from the Region of Brittany and LabexMER to Dr. Stefan Lalonde. The work in this chapter was supervised by Prof. Andreas Kappler and Prof. Kurt O. Konhauser.

The study was designed by Prof. Kurt O. Konhauser, Prof. Andreas Kappler and me. Prof. Harald Thorwarth advised us on experimental design for the best possible results during ICP-OES measurements.

Mineral syntheses were conducted, and samples prepared by Dr. Maximilian Halama, Tyler Warchola and me. The minerals were freeze-dried by Dr. Hartmut Schulz and Lars Grimm.

The freshly synthesized minerals were characterized with regards to their P, Si and Fe content by Dr. Stefan Lalonde, Dr. Julian Tejada and Dr. Rainer Kirchhof.

The experiments were run by Dr. Maximilian Halama and me.

<sup>57</sup>Fe Moessbauer analyses were performed by Dr. Maximilian Halama and me.  $\mu$ XRD analyses were conducted by Dr. Maximilian Halama and Natalia Jakus and the data analysed by me. Dr. James M. Byrne helped with the interpretation of <sup>57</sup>Fe Moessbauer and XRD data.

Phosphate extractions were performed by Dr. Maximilian Halama and me. Si and P contents of the washing solutions was quantified by Dr. Stefan Lalonde, Dr. Rainer Kirchhof and Dr. Julian Tejada.

Mineral digestions of initial minerals and metamorphic mineral products were performed by Dr. Rainer Kirchhof and Dr. Julian Tejada with the help of me. Dr. Rainer Kirchof and Dr. Julian Tejada performed the ICP-OES measurements on the mineral digestions.

Obtained results were discussed and analyzed in cooperation with Prof. Andreas Kappler and Prof. Kurt O. Konhauser. The manuscript was written by me with feedback and improvement by Prof. Andreas Kappler, Prof. Kurt O. Konhauser, Dr. Muammar Mansor, Dr. Leslie J. Robbins and Dr. Noah Planavsky.

The raw data underlying the organics-free, the glucose-containing and the vivianite-containing setups was obtained during the previous PhD work of Dr. Maximilian Halama (Halama M. (2016) Metamorphic origin of the mineralogy and geochemical signatures in banded iron formations. Ph.D. thesis. University of Tuebingen.). I re-analyzed, re-plotted and re-interpreted these data. They represent the foundation for and complement the data of the study presented here. Both old and new data will be published in a combined study. However, for the sake of this PhD thesis, the data obtained by Dr. Maximilian Halama are indicated/cited wherever they were used.

## Chapter 1

### **Phosphate remobilization from banded iron formations depends on metamorphic mineral transformations**

Manuel Schad<sup>a</sup>, Maximilian Halama<sup>a</sup>, Leslie J. Robbins<sup>b, c, d</sup>, Tyler J. Warchola<sup>b</sup>, Julian Tejada<sup>e</sup>,  
Rainer Kirchhof<sup>e</sup>, Stefan V. Lalonde<sup>f</sup>, Elizabeth D. Swanner<sup>g</sup>, Noah J. Planavsky<sup>c</sup>, Harald  
Thorwarth<sup>e</sup>, Muammar Mansor<sup>a</sup>, Kurt O. Konhauser<sup>b</sup>, Andreas Kappler<sup>a</sup>

<sup>a</sup> Geomicrobiology, Center for Applied Geosciences, University of Tübingen, 72076, Tübingen,  
Germany

<sup>b</sup> Department of Earth and Atmospheric Sciences, University of Alberta, Edmonton, AB T6G  
2E3, Canada

<sup>c</sup> Department of Geology and Geophysics, Yale University, New Haven, Connecticut 06511,  
USA

<sup>d</sup> Department of Geology, University of Regina, Regina, SK S4S 0A2, Canada

<sup>e</sup> University of Applied Forest Sciences Rottenburg, Schadenweilerhof, 72108 Rottenburg am  
Neckar, Germany

<sup>f</sup> European Institute for Marine Studies, CNRS-UMR6538 Laboratoire Domaines Océaniques,  
Technopôle Brest-Iroise, 29280 Plouzané, France

<sup>g</sup> Department of Geological and Atmospheric Sciences, Iowa State University, Ames, Iowa 50011,  
USA

**Manuscript in preparation for publication in:** *Geological Society of America Bulletin*

The published version of this chapter is available as:

Schad M., Halama M., Jakus N., Robbins L. J., Warchola T. J., Tejada J., Kirchof R., Lalonde S. V., Swanner E. D., Planavsky N. J., Thorwarth H., Mansor M., Konhauser K. O. and Kappler A. (2021). Phosphate remobilization from banded iron formations during metamorphic mineral transformations. *Chem. Geol.*, 120489. <https://doi.org/10.1016/j.chemgeo.2021.120489>.

**ABSTRACT**

Ratios of phosphorous (P) to iron (Fe) in Precambrian banded iron formations (BIFs) have previously been used to estimate dissolved seawater phosphate concentrations in the ancient oceans. Such studies rely on an assumed composition of the primary iron minerals, the concentrations of the major ions in seawater, and empirical partitioning coefficients for phosphate sorption to Fe(III) (oxyhydr)oxides. There is limited data, however, regarding the post-depositional stability of phosphate associated with presumed primary BIF iron minerals, such as ferrihydrite under low-grade metamorphic temperature and pressure conditions (170°C and 1.2 kbar). Here we experimentally formed ferrihydrite in the presence of silica, which was abundant in the Precambrian oceans, and then incubated it in the presence or absence of organic carbon ( $C_{org}$ ; either glucose or microbial biomass) as a proxy for ancient planktonic biomass. We found that the post-metamorphic mineral assemblage resulting from thermochemical Fe(III) reduction of Si-doped ferrihydrite depended on  $C_{org}$  reactivity: In the presence of highly reactive glucose siderite, magnetite, and vivianite were formed, with less than 1.2 mol.% of phosphate (0.5 M NaCl extractable) being mobilized. In contrast, the reaction of Si-doped ferrihydrite with less reactive microbial biomass resulted in the formation of hematite and siderite, but not vivianite, and approximately 10 mol.% of phosphate being remobilized into the sediment porewaters. Collectively, our data suggest that the fidelity with which BIFs record ancient oceanic phosphate concentrations depends on the mineralogy and diagenetic history of individual BIFs but should be reliable within 10%.



## 1. INTRODUCTION

Banded iron formations (BIFs) are iron-rich (15-40 wt.% Fe) and siliceous (40-60 wt.% SiO<sub>2</sub>) chemical sedimentary rocks that precipitated from seawater throughout the Precambrian eons, with the majority of preserved deposits having formed between 2.80 and 1.85 billion years ago (Ga) in the Neoproterozoic and Palaeoproterozoic eras (see Bekker et al., 2014; Konhauser et al., 2017 for reviews). The best-preserved BIF successions are remarkably uniform, composed mostly of chert (SiO<sub>2</sub>), magnetite (Fe<sub>3</sub>O<sub>4</sub>), and hematite (Fe<sub>2</sub>O<sub>3</sub>), with variable amounts of Fe-rich silicate minerals (e.g., greenalite, Fe<sub>3</sub>Si<sub>2</sub>O<sub>5</sub>(OH)<sub>4</sub>), carbonate minerals (e.g., siderite, FeCO<sub>3</sub>), and locally sparse sulfides (e.g., pyrite, FeS<sub>2</sub>). It is generally agreed that none of the minerals in BIF are primary in origin as the mineralogy of the original seafloor precipitate was not preserved. Instead, the minerals observed in BIFs today reflect multiple post-depositional alteration events that occurred under both diagenetic and metamorphic conditions. Diagenesis is considered here to include low-temperature processes (compaction, dewatering, recrystallization) beginning with the immediate burial of sediments, while metamorphism encompasses high-temperature transformations induced by deep burial, magmatic intrusions and compression by plate tectonics.

The iron oxides in BIFs are interpreted to have formed from an initial Fe(III) (oxyhydr)oxide phase precipitated from the photic zone via the metabolic activity of planktonic bacteria; however, alternative primary minerals such as greenalite (Muhling and Rasmussen, 2020; Rasmussen et al., 2017) and green rust (Halevy et al., 2017) have also been proposed. The classic, biological model invokes ferric iron precipitation occurring at the interface between reduced upwelling ferrous iron-rich waters and oxygenated shallow waters, with the oxygen being sourced from cyanobacteria or their predecessors (Cloud, 1973). Alternatively, anoxygenic photoautotrophic Fe(II)-oxidizing bacteria, known as photoferrotrophs, could have directly oxidized Fe(II) utilizing light energy and coupled this to the fixation of carbon (Hartman, 1984). Mass balance calculations even suggest that anoxygenic photoferrotrophy can account for most, if not all, Fe(III) deposited in BIF (Konhauser et al., 2002). In either case the composition of the primary Fe(III) (oxyhydr)oxide would have been a function of seawater chemistry ([Si] and [HCO<sub>3</sub><sup>-</sup>]) and Fe(II) oxidation rate, resulting in the formation of ferrihydrite, Fe(OH)<sub>3</sub>, goethite, α-FeO(OH), or a ferric-silica gel (see Konhauser et al., 2017 for review).

In many modern aquatic systems, primary production of organic matter is limited by phosphorus (Tyrrell, 1999). Phosphorus in the oceans is mostly present as inorganic phosphate ( $\text{PO}_4^{3-}$ ) with an average concentration of  $\sim 2 \mu\text{M}$  in modern ocean surface waters (Bruland et al., 2014; Levitus et al., 1993). Here, we use  $\text{PO}_4^{3-}$  to encompass all relevant protonation states at a given pH, and “P” when referring to the element phosphorus. While the abundance and distribution of  $\text{PO}_4^{3-}$  in the modern oceans is well understood, the concentration of  $\text{PO}_4^{3-}$  in the Precambrian marine systems, when BIF were being deposited, is a matter of ongoing debate. As  $\text{PO}_4^{3-}$  is the most-likely limiting nutrient on geological time scales (Reinhard et al., 2017; Tyrrell, 1999) this has obvious relevance to the size, and ultimately degree of primary productivity, that the Precambrian marine biosphere was capable of sustaining.

BIF may offer valuable insights for understanding Earth’s earliest P cycle, at least in terms of availability in near-shore, biologically productive depositional environments (e.g., shelf) where BIF accumulated: in other words, BIF cannot inform about bulk seawater [P] for which other lithological proxies (e.g., shales) are better suited. In this regard, a number of studies have examined P/Fe molar ratios in BIF by exploiting empirical distribution coefficients ( $K_D$ ) between dissolved  $\text{PO}_4^{3-}$  and the  $\text{PO}_4^{3-}$  adsorbed onto the surfaces of Fe(III) (oxyhydr)oxides (e.g., Bjerrum and Canfield, 2002; Jones et al., 2015; Konhauser et al., 2007; Planavsky et al., 2010). Low P/Fe ratios in BIF have been used to argue for a small, biologically available  $\text{PO}_4^{3-}$  reservoir, with estimated Archean [P] of 0.15 to  $0.6 \mu\text{M}$ . However, because the  $K_D$  value for  $\text{PO}_4^{3-}$  adsorption to ferrihydrite varies inversely with dissolved Si concentrations due to the competitive adsorption of aqueous Si species (Konhauser et al., 2007), it is also important to consider the evolution of the Si cycle when using P/Fe ratios as a paleoproxy (Planavsky et al., 2010). Indeed, when seawater [Si] approaches saturation with respect to amorphous silica (2.2 mM; Siever, 1992), predicted  $\text{PO}_4^{3-}$  concentrations increase from near 20% (Jones et al., 2015) to 100% (Konhauser et al., 2007) of the modern.

An additional uncertainty arises when considering that experimental first-order relationships for putative primary precipitates have been applied to a diagenetically altered and metamorphosed rock record. Therefore, a critical, but unresolved issue is whether the post-depositional alteration of a ferrihydrite-rich precursor sediment during both early diagenesis (mostly microbially-driven below  $120^\circ\text{C}$ ; (Kashefi and Lovley, 2000) and low-grade metamorphism (abiotic, at higher temperatures; (Halama et al., 2016; Köhler et al., 2013; Li et al.,



2013a; Posth et al., 2013) mobilized the seawater-sorbed  $\text{PO}_4^{3-}$ , and thus, whether the P/Fe ratios in BIF are a faithful, first-order representation of marine  $\text{PO}_4^{3-}$  concentrations. For instance, during diagenesis, the dehydration of ferrihydrite to hematite results in an increase of crystallinity and a decrease in surface area (Stanjek and Weidler, 1992), causing the release of  $\text{PO}_4^{3-}$  from the crystal structure to the sediment pore-waters (Wang et al., 2013b). Other processes potentially leading to the remobilization of  $\text{PO}_4^{3-}$  are; (1) dissimilatory ferric iron reduction (DIR) by sedimentary bacteria, resulting in the formation of magnetite (Li et al., 2011) or siderite (Köhler et al., 2013), and (2) the thermochemical reduction of Fe(III) coupled to  $\text{C}_{\text{org}}$  oxidation during low-grade metamorphism, similarly resulting in the formation of magnetite and siderite (Halama et al., 2016; Posth et al., 2013). In either instance, the  $\text{PO}_4^{3-}$  may be immobilized through the precipitation of either vivianite,  $\text{Fe}_3(\text{PO}_4)_2 \times 8 \text{H}_2\text{O}$  (Dijkstra et al., 2016; März et al., 2018) or carbonate fluorapatite,  $\text{Ca}_5(\text{PO}_4, \text{CO}_3)_3\text{F}$  (e.g. Alibert, 2016; Bekker et al., 2014) or the adsorption onto secondary magnetite (Daou et al., 2007). Yet, the effect of these processes on the  $\text{PO}_4^{3-}$  budget in primary BIF minerals has not yet been tested experimentally.

In this study, we built on previous simulated low-grade metamorphism experiments at 170°C and 1.2 kbar (Halama et al., 2016; Köhler et al., 2013; Posth et al., 2013; Robbins et al., 2015) to assess the diagenetic to low-grade metamorphic mobility of  $\text{PO}_4^{3-}$ , evaluated based on the ‘easily-extractable’ fraction. Incubations were conducted with; (1) different primary  $\text{PO}_4^{3-}$ -bearing Fe minerals (ferrihydrite and heat-treated ferrihydrite) synthesized at different dissolved silica concentrations (0, 0.5 or 1.6 mM Si, based on Zheng et al., 2016) and (2) in the absence or presence of organic  $\text{C}_{\text{org}}$  (labile glucose or recalcitrant microbial biomass). Biogenic and abiogenic vivianite, with and without glucose, were used as control setups to confirm the low-grade metamorphic stability of Fe(II) phosphates. To account for the potential release of  $\text{PO}_4^{3-}$  from microbial biomass, biomass controls were also incubated in separate setups with  $\text{PO}_4^{3-}$ - and Si-free ferrihydrite.

## 2. MATERIALS AND METHODS

### 2.1. Preparation of minerals, biomass and gold capsules

#### 2.1.1. Synthesis of primary $PO_4^{3-}$ -bearing minerals

A rationale for the experimental conditions, including the  $PO_4^{3-}$  and Si concentrations and initial minerals chosen, is provided in supplementary texts S1 and S2. An additional justification for the use of freeze-dried minerals and biomass to simulate an initially water-saturated sedimentary column is outlined in supplementary text S3.

**Ferrihydrite.** Ferrihydrite pre-loaded with  $PO_4^{3-}$  and Si was precipitated in three setups with the same  $PO_4^{3-}$  concentrations but three different Si concentrations following the methods of Schwertmann and Cornell (2008). First, 29.22 g of NaCl was dissolved in 1 L of ultra-pure  $H_2O$  (with a resistance of  $18.2 \text{ M}\Omega \times \text{cm}$  at  $25^\circ\text{C}$ ) to achieve an ionic strength of 0.5 M. Different silica concentrations of 0, 0.5, and 1.6 mM were achieved by adding 0, 0.1421 g, and 0.4567 g of sodium metasilicate nonahydrate ( $Na_2O_3Si \times 9H_2O$ ), respectively. The pH was set to  $<4$  by the addition of 1 M HCl before adding 20 mL of a Fe(III) stock solution (7.214 g  $Fe(NO_3)_3 \cdot 9H_2O$  dissolved in 100 mL ultra-pure  $H_2O$ ) and 2 mL of a certified 1000 ppm calibration standard for P. Depending on the Si concentration this results in Fe:Si:P ratios of approximately 55:0:1, 55:8:1 and 55:25:1, respectively, in the initial solution (all values normalized to P). Finally, the pH was increased to 8.3-8.6 with the incremental addition of 1 M KOH. After 3 h without stirring, the pH was readjusted to 8.3-8.6 and the minerals were centrifuged at 4229 g and freeze-dried.

**Heat-treated ferrihydrite.** Ferrihydrite was synthesized as described above, with the exception that after centrifugation the minerals were re-suspended in 0.1 L of a 0.5 M NaCl solution. This suspension was then heated to  $80^\circ\text{C}$  for 4 weeks in a closed bottle under occasional shaking. After 4 weeks the minerals were centrifuged at 4229 g and freeze-dried.

**Vivianite.** Synthetic vivianite was prepared following Al-Borno and Tomson (1994). Biogenic vivianite was produced by microbial reduction of  $C_6H_5FeO_7$  by *Shewanella oneidensis* MR-1 (Supplementary text S4; Veeramani et al., 2011). The synthetic and biogenic vivianite mineral suspensions were filtered and air-dried inside an anoxic glovebox (100%  $N_2$  atmosphere).

### 2.1.2. Preparation of microbial biomass

Non-heat-treated microbial biomass for simulated metamorphism experiments was prepared as described in Halama et al. (2016). Cells of *S. oneidensis* MR-1 were pelleted, washed and freeze-dried. The C content of the biomass was determined using an elemental analyzer (elemental Vario EL; Elementar Analysensysteme GmbH, Langenselbold, Germany). Freeze-dried biomass contained 45.1 wt.% C.

### 2.1.3. Mineral-organic carbon mixtures and gold capsule preparation

For simulated metamorphism experiments, pure minerals or mixtures of minerals and organic carbon ( $C_{\text{org}}$ ) were filled (under anoxic conditions in the case of vivianite) into gold capsules (diameter 2.1 mm, 0.2 mm wall thickness, 3 cm long). We used either bacterial biomass as proxy for recalcitrant  $C_{\text{org}}$  ( $C_{\text{recal}}$ ) or glucose as proxy for labile  $C_{\text{org}}$  ( $C_{\text{lab}}$ ). Capsules were then sealed and welded in air as previously described (e.g., Posth et al., 2013) before being placed in a high pressure/high temperature autoclave (SITEC-Sieber Engineering AG, Zurich, Switzerland) at 170°C and 1.2 kbar for 14 days. Primary Fe(III) (oxyhydr)oxides were mixed with  $C_{\text{org}}$  at an electron ratio of 0.6 to represent excess Fe(III) to biomass as per Posth et al. (2013). This ratio represents a limitation of electrons available for Fe(III) reduction coupled to  $C_{\text{org}}$  oxidation (i.e., the electrons from the oxidation of  $C_{\text{org}}$  are not sufficient for complete reduction of all Fe(III)) and is characteristic of Fe(III) mineral-cell aggregates produced by photoferrotrophs (Posth et al., 2010). An overview over all setups is provided in supplementary text S3.

## 2.2. Extractions and mineral digestions

### 2.2.1. Preparation of extraction vials

Extraction vials used for the extraction of ‘easily extractable’  $\text{PO}_4^{3-}$  (0.5 M NaCl) were soaked in 1 M HCl for 48 h, followed by 3 rinses with ultra-pure  $\text{H}_2\text{O}$  and air-dried.

### 2.2.2. NaCl extractions

After incubation in the autoclave, the gold capsules were brought into a glovebox (100%  $\text{N}_2$ ) and cut into 3 mm pieces. The ends of the capsules were then bent open and placed in 10 mL gas tight, acid-washed glass vials. To recover the ‘easily extractable’, remobilized  $\text{PO}_4^{3-}$ , 5 mL of 0.5 M NaCl solution was added to each vial. The vials were then placed in an ultrasonic bath for 20 min, centrifuged for 1 min at 1761 g and the supernatant recovered using a Pasteur pipette and

collected in a 50 ml Falcon tube. The extraction was repeated 5 times. The combined supernatants were then filtered (0.2  $\mu\text{m}$ ; Polyethersulfone, VWR International, USA), acidified with 69 % trace element grade  $\text{HNO}_3$  to a final concentration of 3 % and stored at 4°C in the dark until measurement by inductively coupled plasma-optical emission spectroscopy (ICP-OES, see below). For a specific setup, the experiments were performed either only once or in triplicates as detailed in Table 1 and supplementary text S3.

### 2.2.3. Mineral digestions

The elemental composition of all primary minerals was determined by ICP-OES (see below). Prior to ICP-OES measurements all Si-free minerals were dissolved by heating a 150 mg sample in 2 mL  $\text{HNO}_3$  (69%; trace element grade) to 70°C for 48 h.

Si-containing minerals were microwave digested in hydrofluoric acid (HF; Multiwave GO 3000 microwave digestion system, Anton Paar Ltd., Graz, Austria) using a protocol modified from ISO 16967:2015 (DIN Deutsches Institut für Normung e. V.). In short, 50 or 100 mg sample were amended with 1 mL of 30%  $\text{H}_2\text{O}_2$  and allowed to react for 5 min, 2.5 mL  $\text{HNO}_3$  (69%; supra quality) was added, allowed to react for 30 min and then 6 mL  $\text{HCl}$  (35%; supra quality) was added, and allowed to react for another 2 h. Samples were then digested at 190°C for 30 min with an initial heat ramping of 19°C  $\text{min}^{-1}$ . After cooling to room temperature, 1 mL of HF (40%; supra quality) was added, followed by a second microwave digest at 150°C for 15 min with an initial heat ramp of 10°C  $\text{min}^{-1}$ . Finally, after cooling down to room temperature, the HF was neutralized by the addition of 8 mL saturated  $\text{H}_3\text{BO}_3$  followed by a final microwave digest at 150°C for 10 min with an initial heat ramp of 15°C  $\text{min}^{-1}$ . The final digests were aliquoted to 50 mL with ultra-pure  $\text{H}_2\text{O}$  and measured in triplicate.

## 2.3. Analytical techniques

### 2.3.1. Elemental analysis and calculation of element remobilization

Concentrations of P, Si, and Fe in the NaCl extracts and in the mineral digests were determined by ICP-OES. Setups without  $\text{C}_{\text{org}}$ , setups with ferrihydrite and glucose, and setups with vivianite were analyzed using a Horiba Jobin Yvon Ultima 2 ICP-OES at the European Institute for Marine Studies in Brest, France. The remaining samples were analyzed with an ICP

---

Optical Emission Spectrometer series Spectro Blue with a model ASX-260 auto sampler and Argon humidifier at the University of Applied Forest Sciences Rottenburg, Germany.

The extent of remobilization of Fe, Si and  $\text{PO}_4^{3-}$  was determined by calculating the amount of substance ( $n$ ) in any given NaCl extraction supernatant or mineral digest, using previously determined concentrations. The extent of remobilization (in mol.%) was then set as the molar ratio of a given element in the NaCl extract in relation to the element in the initial solid phase, normalized to the capsule content ( $= n(\text{X}_{\text{extract}}) / n(\text{X}_{\text{solid}}) * 100$ ), where X represents the respective element.

Molar P/Fe ratios ( $= (n(\text{P}) / n(\text{Fe}))$ ) and molar Si/Fe ratios ( $= (n(\text{Si}) / n(\text{Fe}))$ ) of the starting material were calculated using P, Si and Fe concentrations determined by ICP-OES after dissolution of the minerals in nitric acid (69%  $\text{HNO}_3$ ) or after a mineral digest with hydrofluoric acid as described above.

### 2.3.2. Mineral identification by $^{57}\text{Fe}$ Moessbauer spectroscopy and $\mu\text{XRD}$

The mineral identity of all starting material and all metamorphic products was determined by  $^{57}\text{Fe}$  Moessbauer spectroscopy and  $\mu\text{XRD}$  as described in supplementary text S5.

## 3. RESULTS AND DISCUSSION

In order to determine how different Si concentrations might influence the metamorphic mineral transformation pathways and  $\text{PO}_4^{3-}$  mobility, we conducted low-grade metamorphism simulation experiments with  $\text{PO}_4^{3-}$ -preloaded ferrihydrite synthesized (1) in the absence of Si, (2) at low concentrations of Si (0.5 mM), and (3) at high concentrations of Si (1.6 mM). However, given the high similarity of the results between the low Si and high Si experiments, and in an effort to simplify the discussion, the focus will be on comparing the results for the high Si setups that are representative of an Archean ocean to the setups without Si that approximate conditions similar to modern oceans. Additionally, we used heat-treated ferrihydrite to determine how the increased temperatures associated with burial (during diagenesis) might influence mineral transformation pathways and the concomitant changes in  $\text{PO}_4^{3-}$  mobility. Finally, we varied the reactivity of the  $\text{C}_{\text{org}}$  used in order to determine how this may also influence mineral transformations and  $\text{PO}_4^{3-}$  remobilization.

### 3.1. Extent of $\text{PO}_4^{3-}$ remobilization

We found that the effect of low-grade metamorphism on  $\text{PO}_4^{3-}$  remobilization from primary ferrihydrite was independent of the presence of  $\text{C}_{\text{org}}$ . Both under (1)  $\text{C}_{\text{org}}$ -starved conditions, where biologically produced Fe(III) minerals and the microbial biomass which oxidized Fe(II) were deposited separately ( $\text{C}_{\text{org}}$ -free setups, FhP, FhPSi<sub>low</sub>, FhPSi<sub>high</sub>, e.g. Thompson et al., 2019), as well as under (2) conditions where primary minerals were deposited as microbial cell-Fe(III) mineral aggregates ( $\text{C}_{\text{recal}}$  setups: FhPC<sub>recal</sub>, FhPSi<sub>low</sub>C<sub>recal</sub>, FhPSi<sub>high</sub>C<sub>recal</sub>, Posth et al., 2010), we observed considerable metamorphic  $\text{PO}_4^{3-}$  remobilization of up to 9.8 mol.% (Tab. 1, Fig. 1). In contrast to  $\text{C}_{\text{org}}$ , the presence of Si showed a strong influence on metamorphic  $\text{PO}_4^{3-}$  remobilization. For the experiments performed in the absence of  $\text{C}_{\text{org}}$ ,  $\text{PO}_4^{3-}$  remobilization increased from 3.0 mol.% in the absence of Si (FhP) to 7.7 mol.% in the presence of Si (FhPSi<sub>high</sub>). Similarly, in the experiments performed with  $\text{C}_{\text{recal}}$ ,  $\text{PO}_4^{3-}$  remobilization increased from 5.2 mol.% in the absence of Si (FhPC<sub>recal</sub>) to 8.0 mol.% in the presence of Si (FhPSi<sub>high</sub>C<sub>recal</sub>, Tab. 1, Fig. 1). The higher  $\text{PO}_4^{3-}$  remobilization in the  $\text{C}_{\text{recal}}$  setups compared to the  $\text{C}_{\text{org}}$ -free setups can be explained by additional  $\text{PO}_4^{3-}$ -remobilization from biomass, which, on average, contributed 1.5 mol.%  $\text{PO}_4^{3-}$  to the overall  $\text{PO}_4^{3-}$  remobilized during low-grade metamorphism (based on experiments with  $\text{PO}_4^{3-}$ -free ferrihydrite, FhC<sub>recal</sub>, Tab. 1).

As a comparison to more recalcitrant organic carbon, and consistent with previous low-grade metamorphism studies (Halama et al., 2016; Köhler et al., 2013; Posth et al., 2013; Robbins et al., 2015), we mixed ferrihydrite with glucose as a proxy for labile  $\text{C}_{\text{org}}$  ( $\text{C}_{\text{lab}}$ ). Low-grade metamorphism using this experimental approach resulted in much lower metamorphic  $\text{PO}_4^{3-}$  remobilization (<1.5 mol.%, FhPC<sub>lab</sub>, FhPSi<sub>low</sub>C<sub>lab</sub>, FhPSi<sub>high</sub>C<sub>lab</sub>) compared to the previously discussed  $\text{C}_{\text{org}}$ -free and  $\text{C}_{\text{recal}}$  experiments and was largely independent of the Si concentration (Tab. 1, Fig. 1). Collectively these results suggest that metamorphic  $\text{PO}_4^{3-}$  remobilization was a function of the identity, and thus reactivity, of  $\text{C}_{\text{org}}$  rather than its presence or absence.

During pre-heating of P-loaded ferrihydrite to diagenetic temperatures (80°C), only a minor amount of  $\text{PO}_4^{3-}$  was mobilized (less than 0.5 mol.%  $\text{PO}_4^{3-}$ , see supplementary text S6). Increasing the temperature of the heat-treated ferrihydrite to low-grade metamorphic conditions (170°C) in the presence of  $\text{C}_{\text{recal}}$  (Fh<sub>heat</sub>PC<sub>recal</sub>, Fh<sub>heat</sub>PSi<sub>low</sub>C<sub>recal</sub>, Fh<sub>heat</sub>PSi<sub>high</sub>C<sub>recal</sub>) yielded  $\text{PO}_4^{3-}$  remobilization values that were comparable to the non-heat-treated  $\text{C}_{\text{recal}}$  setups (Tab. 1).

Table 1

Fractions of Fe and P released from the samples following after metamorphic pressure/temperature treatment. Fe and P were extracted from the post-incubation samples with 0.5 M NaCl, and are reported along with the initial and post-metamorphic mineralogical composition of each sample. “Recalcitrant”  $C_{org}$  ( $C_{recal}$ ) refers to treatments where  $C_{org}$  was derived from the biomass of *Shewanella*. “Labile”  $C_{org}$  ( $C_{lab}$ ) refers to treatments where glucose used as biomass proxy. “Low Si” refers to a Si concentration of 0.5 mM, “high Si” to a Si concentration of 1.6 mM. Where errors are given values are the mean of triplicates  $\pm$  1 standard deviation; all other values are single measurements. \*data adapted from Halama (2016).

Initial mineralogy	Sample composition	Released element		Post-metamorphic mineralogy
		Fe [mol.%]	P [mol.%]	
Ferrihydrite	Fh $C_{recal}$	0.0 $\pm$ 0.0	1.5 $\pm$ 0.7	Hematite (100%)
	FhP *	0.0	3.0	Hematite (100%)
	FhPC $_{recal}$	0.0 $\pm$ 0.0	5.2 $\pm$ 0.1	Siderite (3.7%), Hematite (96.3%)
	FhPC $_{lab}$ *	0.5	0.5	Siderite (9.6%), Magnetite (90.4%)
	FhPSi $_{low}$ *	0.0	9.4	Ferrihydrite (69.4%), Hematite (30.6%)
	FhPSi $_{low}C_{recal}$	0.0 $\pm$ 0.0	9.8 $\pm$ 0.6	Siderite (12%), Hematite (88%)
	FhPSi $_{low}C_{lab}$ *	0.2	0.4	Siderite (17.0%), Magnetite (83.0%)
	FhPSi $_{high}$ *	0.0	7.7	Ferrihydrite (88.8%), Hematite (11.2%)
	FhPSi $_{high}C_{recal}$	0.0 $\pm$ 0.0	8.0 $\pm$ 0.9	Siderite (9.2%), Ferrihydrite (17.4%), Hematite (73.4%)
	FhPSi $_{high}C_{lab}$ *	0.2	1.2	Siderite (23%), Fe(II)-phosphate (28.5%), Ferrihydrite (16.0%), Magnetite (32.5%)
Heat-treated ferrihydrite	Fh $_{heat}PC_{recal}$	0.0 $\pm$ 0.0	4.8 $\pm$ 0.1	Siderite (7%), Hematite (93%)
	Fh $_{heat}PSi_{low}C_{recal}$	0.0 $\pm$ 0.0	6.4 $\pm$ 0.2	Siderite (10.1%), Fe(II)-phosphate (7.2%), Hematite (72.8%)
	Fh $_{heat}PSi_{high}C_{recal}$	0.0 $\pm$ 0.0	10.7 $\pm$ 2.0	Siderite (8.8%), Fe(II)-phosphate (13.0%), Ferrihydrite (15.7%), Hematite (62.6%)
Synthetic vivianite	Viv $_{synth}$ *	0.2	0.3	Phosphoferrite (100%)
	Viv $_{synth}C_{labile}$ *	0.1	0.1	Phosphoferrite, Lipscombite, Fe <sub>2</sub> PO <sub>4</sub> O
Biogenic vivianite	Viv $_{bio}$ *	1.7	0.3	Vivianite (100%)

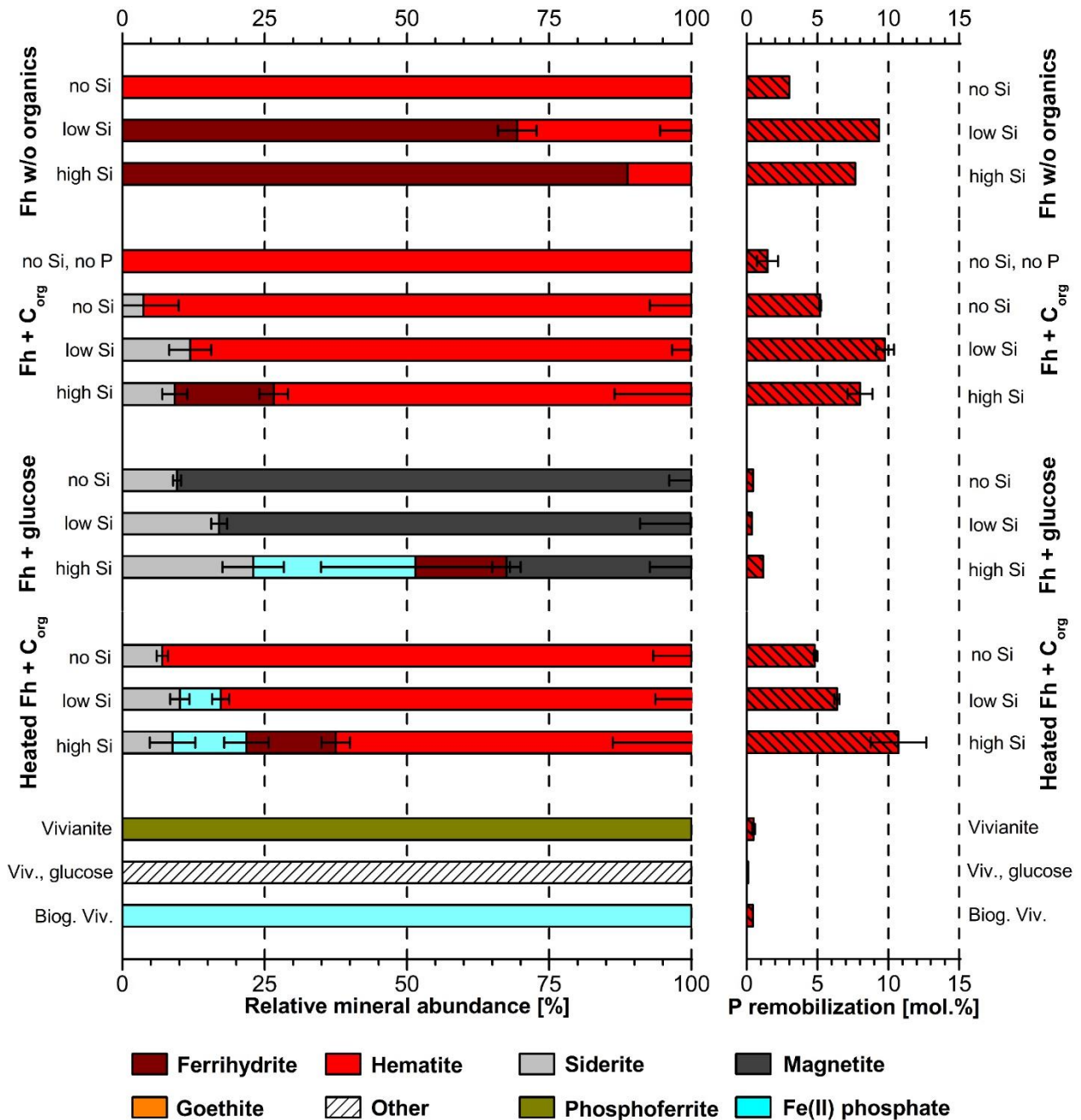


Fig. 1. Relative Fe mineral abundances (based on  $^{57}\text{Fe}$  Moessbauer spectroscopy) relative to the extent of metamorphically induced  $\text{PO}_4^{3-}$  remobilization.  $\text{C}_{\text{org}}$  refers to recalcitrant, *Shewanella*-derived organic carbon used during low-grade metamorphism experiments. Fh refers to ferrihydrite. Error bars in mineral abundances depict uncertainties in the corresponding spectral areas of the Moessbauer fit. Where errors are given for the P remobilization, data are means from triplicate measurements  $\pm 1$  standard deviation; otherwise data represent single measurements. “Fh w/o organics”, “Fh + glucose” and vivianite setups represent data adapted from Halama (2016).



### 3.2. Controls on mineral transformation pathways

An overview over all experimental setups is provided in supplementary text S3, along with a detailed characterization of the primary minerals in supplementary text S6. Generally, the identity of the primary minerals synthesized initially was neither influenced by the presence nor the concentration of Si or  $\text{PO}_4^{3-}$ . Additionally, the heating of ferrihydrite to 80°C prior to metamorphic incubations did not induce mineral transformation.

Similar to  $\text{PO}_4^{3-}$  remobilization, the metamorphic mineral transformations were characterized by a dichotomous behavior: while simulated low-grade metamorphism of ferrihydrite incubated in the absence of  $\text{C}_{\text{org}}$ , or as an admixture with  $\text{C}_{\text{recal}}$ , resulted in the formation of hematite as the predominant mineral product (Fig. 1), mixtures of ferrihydrite and  $\text{C}_{\text{lab}}$  resulted in the formation of magnetite. A detailed discussion of the various mineral transformation pathways and their dependence on the varied  $\text{C}_{\text{org}}$  sources and Si concentrations is provided in supplementary text S8. Briefly, in the absence of any  $\text{C}_{\text{org}}$ , mineral transformations were driven by non-redox, pressure- and temperature-dependent reactions. Hematite was the main metamorphic mineral product (Fig. 1, Tab. 1) and formed via the dehydration of ferrihydrite (Cornell and Schwertmann, 2003). However, increasing concentrations of Si resulted in increasing stabilization and preservation of the ferrihydrite (Fig. 1, Tab. 1), confirming environmental observations of similar mineral systems (Toner et al., 2012). In the presence of  $\text{C}_{\text{recal}}$ , thermochemical reduction of Fe(III) to Fe(II) was coupled to the oxidation of  $\text{C}_{\text{org}}$  to  $\text{CO}_2$ . However, no magnetite was found among the metamorphic mineral products. Instead, hematite was the primary mineral product. The inhibition of magnetite formation in experiments with  $\text{C}_{\text{recal}}$  can be attributed to complex organic compounds adsorbing onto the surface of primary Fe(III) minerals and thus inhibiting the adsorption of Fe(II) required for the solid-state conversion to magnetite (Halama et al., 2016). Again, similar as in the absence of organic compounds, we observed a preservation of ferrihydrite with increasing Si concentration ( $\text{FhPSi}_{\text{high}}\text{C}_{\text{recal}}$ , Fig. 1, Tab. 1). Siderite was the sole Fe(II)-bearing mineral product identified and likely formed through the reaction of Fe(II) with inorganic carbon resulting from the oxidation of organic compounds (Halama et al., 2016; Köhler et al., 2013; Posth et al., 2013). Interestingly, we observed the formation of vivianite in experiments with Si-bearing heat-treated ferrihydrite ( $\text{Fh}_{\text{heat}}\text{PSi}_{\text{low}}\text{C}_{\text{recal}}$ ,  $\text{Fh}_{\text{heat}}\text{PSi}_{\text{high}}\text{C}_{\text{recal}}$ , supplementary text S8). Vivianite, a mineral frequently found in modern anoxic sedimentary environments (e.g. Dijkstra et al., 2018b; Dijkstra et al., 2016; Rothe et al., 2016),

was likely formed through the reaction of Fe(II) released from ferrihydrite via redox reactions and  $\text{PO}_4^{3-}$  released from both  $\text{C}_{\text{org}}$  and primary Fe(III) during simulated low-grade metamorphism (supplementary text S8).

In contrast to the experiments with  $\text{C}_{\text{recal}}$ , experiments with  $\text{C}_{\text{lab}}$  resulted in the formation of magnetite and siderite. Magnetite was likely formed via solid-state conversion of Fe(III), caused by the adsorption of Fe(II), stemming from thermochemical Fe(III) reduction, to the remaining Fe(III) minerals (Fig. 1, Hansel et al., 2003). Similar to the experiments with  $\text{C}_{\text{recal}}$ , increasing Si concentrations stabilized the ferrihydrite against heat-induced metamorphic transformation and, comparable to experiments with heat-treated ferrihydrite, induced vivianite formation ( $\text{FhPSi}_{\text{high}}\text{C}_{\text{lab}}$ , Fig. 1, Tab. 1).

### **3.3. Controls on $\text{PO}_4^{3-}$ remobilization: mineral transformation pathways**

Generally, the mineral transformation pathways under metamorphic conditions controlled the extent of  $\text{PO}_4^{3-}$  remobilization.  $\text{PO}_4^{3-}$  remobilization was higher when either only hematite (no  $\text{C}_{\text{org}}$ ), hematite and siderite ( $\text{C}_{\text{recal}}$ ) or hematite together with siderite and vivianite ( $\text{C}_{\text{recal}}$  and heat-treated ferrihydrite) were formed.  $\text{PO}_4^{3-}$  mobilization was lower when magnetite along with vivianite was formed.

#### *3.3.1. Influence of hematite formation on $\text{PO}_4^{3-}$ remobilization*

In both  $\text{C}_{\text{org}}$ -free ( $\text{FhP}$ ,  $\text{FhPSi}_{\text{low}}$ ,  $\text{FhPSi}_{\text{high}}$ ) as well as in setups containing  $\text{C}_{\text{recal}}$  ( $\text{FhPC}_{\text{recal}}$ ,  $\text{FhPSi}_{\text{low}}\text{C}_{\text{recal}}$ ,  $\text{FhPSi}_{\text{high}}\text{C}_{\text{recal}}$ ), hematite was the main metamorphic mineral product. However, increasing concentrations of Si resulted in increased preservation of ferrihydrite (Fig. 1, supplementary text S8). The slightly higher  $\text{PO}_4^{3-}$  remobilization in the  $\text{C}_{\text{recal}}$  setups compared to the  $\text{C}_{\text{org}}$ -free setups cannot be explained by siderite formation, since the extent of  $\text{PO}_4^{3-}$  remobilization does not correlate with the extent of siderite formation. Reasons might either be additional  $\text{PO}_4^{3-}$  remobilization from biomass or the high affinity of complex organics to Fe(III) (oxyhydr)oxides (Gu et al., 1996; Gu et al., 1994; Schad et al., 2019) that prevent  $\text{PO}_4^{3-}$ , which was mobilized during low-grade metamorphism, from re-adsorbing to the Fe(III) (oxyhydr)oxides.

$\text{PO}_4^{3-}$  remobilization during transformation of  $\text{PO}_4^{3-}$ -loaded ferrihydrite to hematite can be explained by two combined factors. First, hematite has a specific surface area (SSA) that is

approximately 50 times lower than ferrihydrite (Cornell and Schwertmann, 2003), resulting in a decreased availability of  $\text{PO}_4^{3-}$  sorption sites and  $\text{PO}_4^{3-}$  release upon transformation (Wang et al., 2013b). Second, co-precipitated and/or adsorbed Si lowers the point of zero charge (PZC) of primary Fe(III) minerals and hematite (Kingston et al., 1972; Konhauser et al., 2007; Schwertmann and Fechter, 1982; Sigg and Stumm, 1981) and thus prevents re-adsorption of the mobilized  $\text{PO}_4^{3-}$ . However, there are two points counter-arguing these two lines of argumentation. First, a previous study reported that  $\text{PO}_4^{3-}$  can be retained in the crystal structure of hematite up to a maximum P/Fe ratio of 0.03 (Galvez et al., 1999). The maximum P/Fe ratio in our primary minerals is 0.01 (supplementary text S6), which is three times lower than the reported maximum ratio of 0.03. Therefore, even upon complete transformation of ferrihydrite to hematite,  $\text{PO}_4^{3-}$  should have been retained in the crystal structure or remain adsorbed (see e.g. FhP, Tab. 1). Second, in the FhPSi<sub>low</sub>, FhPSi<sub>high</sub> and FhPSi<sub>high</sub>C<sub>recal</sub> setups, up to 89% of the initial ferrihydrite is preserved. Thus, based on the much higher SSA of ferrihydrite compared to hematite, the  $\text{PO}_4^{3-}$  remobilization should have been minimal, even when considering the previously described  $\text{PO}_4^{3-}$ -repulsing effect of Si.

However, a closer analysis of the Moessbauer spectrometry hyperfine parameters of the hematite formed in the various setups may offer a potential explanation for  $\text{PO}_4^{3-}$  remobilization during transformation of  $\text{PO}_4^{3-}$ -loaded ferrihydrite to hematite. Generally, increasing Si concentrations resulted in a decrease in the mean magnetic hyperfine field parameter ( $B_{\text{hf}}$ , Fig. 2A), suggesting lower magnetic (structural) ordering possibly due to inhibited crystal growth induced by adsorbed and/ or co-precipitated Si (Campbell et al., 2002; Rzepa et al., 2016). This is supported by wider reflections of Si-containing hematite in the respective X-ray diffractograms (supplementary text S8), which suggests lower crystallinity and smaller particle size with increasing Si concentration. Furthermore, the decrease in  $B_{\text{hf}}$  shows a good overall correlation with increasing  $\text{PO}_4^{3-}$  remobilization ( $R^2 = 0.65$ , Fig. 2B). We, therefore, contend that with decreasing particle size and a corresponding increase in the surface to volume ratio, more  $\text{PO}_4^{3-}$  would have been exposed at the particle surface during low-grade metamorphism. This prevents the hematite from retaining  $\text{PO}_4^{3-}$  up to maximum P/Fe ratio of 0.03 during mineral transformation. Consequently, since Si outcompetes  $\text{PO}_4^{3-}$  for sorption sites (Konhauser et al., 2007), especially at neutral pH and high Si-loading relative to  $\text{PO}_4^{3-}$  (Hiemstra, 2018; Hilbrandt et al., 2019), and is immobilized through polymerization during low-grade metamorphism,  $\text{PO}_4^{3-}$

is preferentially remobilized. Following remobilization, the  $\text{PO}_4^{3-}$  would be unable re-adsorb onto the hematite due to the decline in the PZC induced by Si.

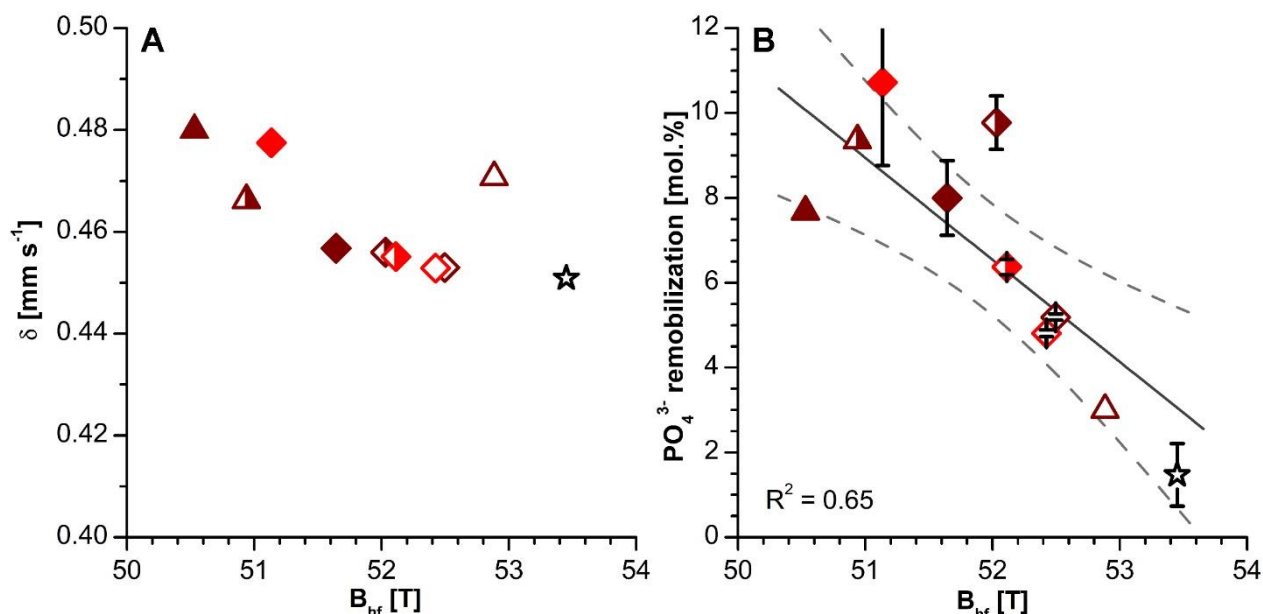


Fig. 2. Moessbauer spectroscopic analyses of hematite formed during low-grade metamorphism. Panel (A) shows isomer shift ( $\delta$ ) relative to the mean magnetic hyperfine field ( $B_{\text{hf}}$ ; weighted average of multiple sextets, see supplementary text S7) at 140 K. Panel (B) shows mean magnetic hyperfine field ( $B_{\text{hf}}$ ) plotted against  $\text{PO}_4^{3-}$  remobilization. The  $B_{\text{hf}}$  at 140 K depends on Si (and  $\text{PO}_4^{3-}$ ) concentration of starting ferrihydrite. Open symbols: Si-free hematite; half-filled symbols: low Si hematite; closed symbols: high Si hematite. Brown color marks hematite resulting from non-heat-treated ferrihydrite, red color is hematite resulting from heat-treated ferrihydrite. Diamonds: Incubation in the presence of  $C_{\text{recal}}$ ; triangles: Incubation in the absence of  $C_{\text{org}}$ . The black open star marks incubation with Si- and  $\text{PO}_4^{3-}$ -free ferrihydrite in the presence of  $C_{\text{recal}}$ . Where error bars are given, they mark mean from triplicates  $\pm$  standard deviation. Solid line is linear regression. Dashed lines mark 95 % confidence interval. “Incubation in the absence of  $C_{\text{org}}$ ” represent data adapted from Halama (2016).

This, however, does not explain the high degree of  $\text{PO}_4^{3-}$  remobilization despite a high degree of ferrihydrite preservation. In this regard a study by Stanjek and Weidler (1992) showed that ferrihydrite can undergo significant dehydration upon heating with a concomitant decrease in SSA without formation of more crystalline mineral phases. Indeed, Wang et al. (2013a) showed that with increasing crystal size and resultant decrease in SSA and pore space volume, the  $\text{PO}_4^{3-}$  adsorption capacity of ferrihydrite decreases by >40%, which would explain the high extent of  $\text{PO}_4^{3-}$  remobilization observed in our study despite Si-induced ferrihydrite preservation. Additionally,  $\text{PO}_4^{3-}$  remobilization would have been further amplified by Si-induced changes in the PZC, preventing  $\text{PO}_4^{3-}$  immobilization through re-adsorption onto the remaining ferrihydrite.

### 3.3.2. *Influence of magnetite and vivianite formation on $PO_4^{3-}$ remobilization*

The lowest extent of  $PO_4^{3-}$  remobilization was observed when ferrihydrite was transformed to magnetite or a mixture of magnetite and vivianite, where less  $PO_4^{3-}$  was remobilized in the FhPC<sub>lab</sub> setup (0.5 mol.%) compared to the FhPSi<sub>high</sub>C<sub>lab</sub> setup (1.2 mol.%, Fig. 1, Tab. 1). One explanation for this generally low extent of  $PO_4^{3-}$  remobilization in setups with magnetite formation is  $PO_4^{3-}$  re-adsorption to, or co-precipitation with, freshly formed magnetite (Daou et al., 2007). The relatively higher  $PO_4^{3-}$  remobilization in the FhPSi<sub>high</sub>C<sub>lab</sub> can be explained by (1) a higher extent of thermochemical Fe(III) reduction (62.3% compared to 39.7%) due to higher primary mineral reactivity (supplementary text S8), (2) a lower extent of magnetite formation (32.5% compared to 90.4% in FhPC<sub>lab</sub>), and (3) Si lowering the PZC of both primary Fe(III) minerals and metamorphic mineral products, thus preventing the re-adsorption of  $PO_4^{3-}$  onto the metamorphic mineral products. However, considering the combined effect of all three factors one would expect a higher  $PO_4^{3-}$  remobilization. On the one hand, a considerable amount of the  $PO_4^{3-}$  likely reacted with the freshly formed Fe(II) and was ultimately immobilized as vivianite (approx. 30% of the mineral product), thus mitigating increased  $PO_4^{3-}$  remobilization (Fig. 1, Tab. 1). On the other hand, both Moessbauer and XRD results suggest that the magnetite formed in the presence of Si has a smaller particle size (supplementary text S8). Therefore, the resulting higher SSA and reactivity in combination with the reported high affinity of  $PO_4^{3-}$  for magnetite might have partially offset the adverse effects of Si on  $PO_4^{3-}$  adsorption observed for pure Fe(III) minerals. This would have resulted in  $PO_4^{3-}$  being adsorbed to the freshly formed magnetite.

### 3.3.3. *Influence of diagenetic heating pre-treatment of ferrihydrite (at 80°C) on $PO_4^{3-}$ remobilization*

Experiments with heat-treated ferrihydrite represent the approach most comparable to the genesis of BIF as it combines initial co-precipitation of  $PO_4^{3-}$  with the primary ferrihydrite mineral, followed by a first-stage diagenetic heating exposure of the ferrihydrite and final low-grade metamorphism. In the absence of Si, diagenetic heating of the ferrihydrite to 80°C had minimal effect on  $PO_4^{3-}$  remobilization, i.e., both the minerals formed and extent of  $PO_4^{3-}$  remobilized were essentially the same in the Fh<sub>heat</sub>PC<sub>recal</sub> and FhPC<sub>recal</sub> setups. In the presence of low concentrations of Si (Fh<sub>heat</sub>PSi<sub>low</sub>C<sub>recal</sub>),  $PO_4^{3-}$  remobilization was suppressed (6.4 mol.%)

compared to the equivalent setup where the ferrihydrite had not undergone diagenetic heating (9.8 mol.%, FhPSi<sub>low</sub>C<sub>recal</sub>, Fig. 1, Tab. 1). This is best explained by the formation of vivianite through reaction of freshly formed Fe(II) with PO<sub>4</sub><sup>3-</sup>. However, in the high Si setup (Fh<sub>heat</sub>PSi<sub>high</sub>C<sub>recal</sub>) we observed a much higher extent of PO<sub>4</sub><sup>3-</sup> remobilization (10.7 mol.%) despite the presence of 13 % vivianite in the post-incubation mineral assemblage (Fig. 1, Tab. 1). Due to the formation of vivianite one would expect less PO<sub>4</sub><sup>3-</sup> remobilization compared to the equivalent setup with non-heat-treated ferrihydrite (FhPSi<sub>high</sub>C<sub>recal</sub>, 8 mol.%, Fig. 1, Tab.1). A potential explanation is again offered by the comparison of the mean hyperfine field (B<sub>hf</sub>) values in the Moessbauer spectra of the hematite in the Fh<sub>heat</sub>PSi<sub>low</sub>C<sub>recal</sub>, Fh<sub>heat</sub>PSi<sub>high</sub>C<sub>recal</sub> and FhPSi<sub>high</sub>C<sub>recal</sub> setups, i.e., their degree of magnetic (structural) ordering in relation to the PO<sub>4</sub><sup>3-</sup> remobilization (Fig. 2B). Fh<sub>heat</sub>PSi<sub>high</sub>C<sub>recal</sub> has an approximately 0.7 T and 1 T lower B<sub>hf</sub> value compared to FhPSi<sub>high</sub>C<sub>recal</sub> and Fh<sub>heat</sub>PSi<sub>low</sub>C<sub>recal</sub>, respectively. Together with the wider reflections in the respective X-ray diffractogram (supplementary text S8), this suggests that the hematite in this particular setup has a lower degree of structural ordering with lower crystallinity, smaller particle size and higher SSA. Following our arguments above concerning hematite formation, this implies that the higher surface exposure and resulting PO<sub>4</sub><sup>3-</sup> remobilization should have offset the PO<sub>4</sub><sup>3-</sup> immobilization by vivianite formation, resulting in a higher net PO<sub>4</sub><sup>3-</sup> remobilization.

### 3.4. Stability of low-grade metamorphic vivianite

In order to verify the likelihood of the formation and preservation of a Fe(II) phosphate mineral by thermochemical reduction of PO<sub>4</sub><sup>3-</sup>-loaded ferrihydrite and concomitant PO<sub>4</sub><sup>3-</sup> immobilization, we examined the metamorphic stability of vivianite. To this end we subjected both synthetic and biogenic vivianite to low-grade metamorphic conditions, and then determined associated mineral transformations and quantified PO<sub>4</sub><sup>3-</sup> remobilization.

Both synthetic (Vi<sub>synth</sub>) and biogenic vivianite (Vi<sub>bio</sub>) were identified as sole Fe(II) mineral phase by Moessbauer spectroscopy (Fig. 3A and B, supplementary text S7), with additional minor amounts of Fe(III) (6.7% and 8.3%, respectively) being present after mineral synthesis. While the biogenic vivianite was largely X-ray amorphous, the synthetic vivianite showed reflections suggestive of phosphoferrite in addition to sharp reflections indicative of crystalline vivianite (Fig. 3C).

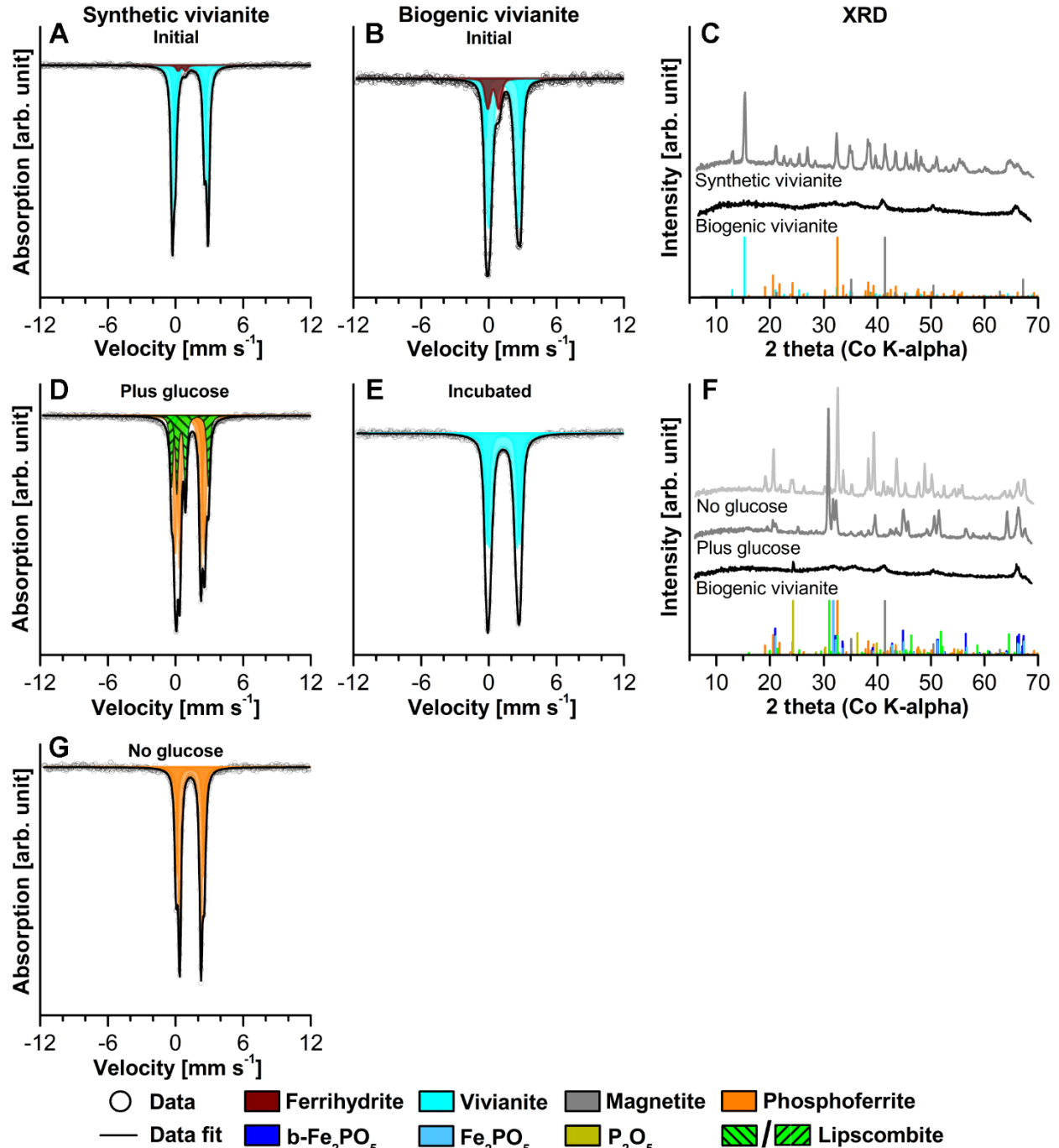


Fig. 3. Mössbauer spectra and X-ray diffractograms of primary (synthetic and biogenic vivianite, A-C) and vivianite incubated at 170°C and 1.2 kbar for 14 days (D-G). Synthetic vivianite was either mixed with glucose (D) or incubated without addition of any organics (G). Mössbauer spectra were collected at 140 K. Data shown are adapted from Halama (2016).

$\text{Vi}_{\text{bio}}$  showed high thermal resistance under our low-grade metamorphism conditions; it did not transform into a secondary mineral phase (Fig. 3E) and remained X-ray amorphous (Fig. 3F). However, based on previous work, the dehydration of vivianite to phosphoferrite ( $\text{Fe}_3(\text{PO}_4)_2 \times 3 \text{H}_2\text{O}$ ) would have been expected (Frost et al., 2003). It thus appears that the  $\text{C}_{\text{org}}$

co-precipitated with  $Viv_{bio}$  stabilized it against metamorphic transformation. In contrast hereto,  $Viv_{synth}$  that contains no  $C_{org}$ , quantitatively transformed into phosphoferrite (Fig. 3G, Mattievich and Danon, 1977) as expected per Frost et al. (2003). Furthermore, the  $Viv_{synth}$  with admixed  $C_{lab}$  ( $Viv_{synth}C_{lab}$ ) showed formation of lipscombite ( $Fe(II)Fe(III)_2PO_4(OH)_2CO_3$ ), a mixed valent Fe phosphate (Fig. 3D, Rouzies and Millet, 1993; Vochten and De Grave, 1981) in addition to phosphoferrite, suggesting that some reaction with the Fe(III) leftover from the mineral synthesis had taken place. XRD analysis revealed the presence of two additional mixed valent Fe mineral phases (Fig. 3F), providing further evidence for the formation of mixed-valent Fe phosphates due to reaction of primary vivianite with Fe(III) (Fig. 3A).

Independent of the secondary mineral transformation, the  $PO_4^{3-}$  remobilization from vivianite was generally less than 0.3 mol.% for all setups (Fig. 1, Tab. 1). Therefore, in agreement with previous results, our data suggest that vivianite would have been stable under low-grade metamorphic conditions, thus effectively immobilizing  $PO_4^{3-}$  liberated during thermochemical Fe(III) reduction.

Recently, Alibert (2016) reported the putative presence of vivianite in the Hamersley Basin BIFs of Western Australia, however, to our knowledge this is the only study so far to report the presence of vivianite in BIFs. One potential explanation for the absence of vivianite in the BIF rock record could be the sulfidic dissolution of vivianite during the diagenesis and metamorphism of BIFs (e.g. Dijkstra et al., 2018a). Although sulfate and thus also sulfide would have been a trace constituent during the deposition of BIFs (Crowe et al., 2014), the presence of sulfides as trace minerals in BIFs has been reported (e.g. Bekker et al., 2014). It is therefore possible that vivianite might initially have been formed during low-grade metamorphism and that reactions with sulfide during the later metamorphic process would have resulted in its dissolution and removal. Alternatively, a  $PO_4^{3-}$  mineral that has frequently been reported as trace constituent from BIFs of various ages is apatite (e.g. Bekker et al., 2014; Li et al., 2011; Li et al., 2013b; Nutman and Friend, 2006; Papineau et al., 2011; Papineau et al., 2010; Pecoits et al., 2009). In a recent study Hao et al. (2020) suggested that at temperatures exceeding 100°C vivianite could react irreversibly with calcite, resulting in the formation of apatite. Our simplified experimental approach, however, precluded testing this potential metamorphic pathway. While our experimental data suggest the formation and stability of vivianite under low-grade metamorphic conditions it seems plausible that apatite might have been formed during the subsequent



metamorphism of vivianite. In either case the  $\text{PO}_4^{3-}$  remobilized from the primary Fe(III) minerals would have been immobilized through the formation of secondary authigenic  $\text{PO}_4^{3-}$  minerals, thus preserving the  $\text{PO}_4^{3-}$  signal in the rock record.

### 3.5. Implications of metamorphic remobilization for the ancient $\text{PO}_4^{3-}$ budget

The release of  $\text{PO}_4^{3-}$  during the metamorphic transformation of primary Fe(III) (oxyhydr)oxides formed in an Archean to Paleoproterozoic ocean rich in Si (Jones et al., 2015; Zheng et al., 2016) is governed by several inter-dependent factors, including (1) the reactivity of the  $\text{C}_{\text{org}}$  present, (2) the extent to which  $\text{C}_{\text{org}}$  would have been co-precipitated with Fe(III) minerals, and (3) the presence of Si. However, while the presence of Si in general had a major impact on  $\text{PO}_4^{3-}$  remobilization, we did not observe a pronounced difference in  $\text{PO}_4^{3-}$  mobilization between low and high Si concentrations (Fig. 1).

Our results suggest that metamorphic remobilization of  $\text{PO}_4^{3-}$  would have been independent of the presence of  $\text{C}_{\text{org}}$  as long as Fe(III) minerals (hematite with or without preserved ferrihydrite) were the predominant metamorphic product(s), in which case up to 10 mol.% of the  $\text{PO}_4^{3-}$  was remobilized. Considering BIF metamorphism, this would have resulted in the modification of the P/Fe ratios in the solids since  $\text{PO}_4^{3-}$  would have been remobilized from the Fe minerals into sediment porewaters (Fig. 4). Consequently, the inferred ancient seawater  $\text{PO}_4^{3-}$  concentrations based on the BIF mineral record may reflect an underestimation (Bjerrum and Canfield, 2002; Konhauser et al., 2007; Planavsky et al., 2010).

While the extent of  $\text{C}_{\text{org}}$ -Fe(III) mineral association during low-grade metamorphism did not influence  $\text{PO}_4^{3-}$  remobilization, the reactivity of the biomass had a profound influence on the metamorphic mineralogy and the extent of  $\text{PO}_4^{3-}$  remobilization. From this we conclude that if more labile organic compounds reached metamorphic depth, magnetite and vivianite may have formed instead of hematite (Fig. 4) resulting in an effective sequestration of  $\text{PO}_4^{3-}$ . Accordingly, we suggest that when magnetite and phosphate minerals are found in BIFs, they likely record ancient ocean  $\text{PO}_4^{3-}$  concentrations with high fidelity. However, while labile organic compounds like acetate have been reported in BIFs (Li et al., 2011), their lability necessitates that metamorphic magnetite formation took place early during metamorphism since they would likely have reacted first and thus not been available anymore for later mineral transformations.

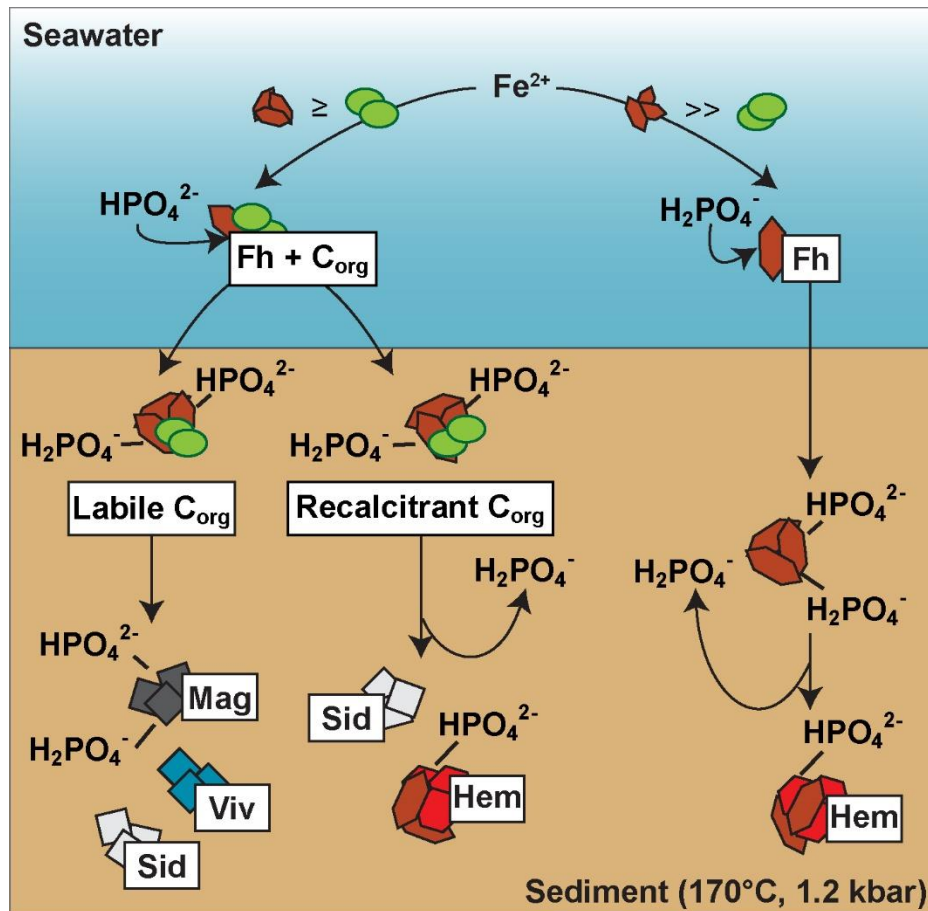


Fig. 4. Mineral transformation and  $\text{PO}_4^{3-}$  re-/immobilization pathways in BIF during metamorphism after deposition of  $\text{PO}_4^{3-}$ -loaded Fe(III) (oxyhydr)oxide particles (Fh: ferrihydrite; Hem: hematite; Sid: siderite; Mag: magnetite; Viv: vivianite;  $\text{C}_{\text{org}}$ : organic carbon).  $\text{PO}_4^{3-}$  binds to ferrihydrite formed by chemical or microbial oxidation in the upper water column and the  $\text{PO}_4^{3-}$ -loaded Fe(III) (oxyhydr)oxides are deposited with or without associated  $\text{C}_{\text{org}}$ . When ferrihydrite is buried with labile  $\text{C}_{\text{org}}$ ,  $\text{PO}_4^{3-}$ -loaded magnetite, vivianite and siderite are formed, while ferrihydrite buried with recalcitrant  $\text{C}_{\text{org}}$  is transformed into hematite and siderite and some  $\text{PO}_4^{3-}$  is released to interstitial waters and possibly to seawater. Similarly,  $\text{C}_{\text{org}}$ -free ferrihydrite is transformed to hematite and some of the  $\text{PO}_4^{3-}$  is released to interstitial waters and possibly to seawater. Adapted from Halama (2016).

Using experimentally derived  $K_D$  values determined by Jones et al. (2015) and P/Fe ratios of pre-GOE Iron Formations from Planavsky et al. (2010), we re-calculated ancient ocean  $\text{PO}_4^{3-}$  concentrations in seawater overlying the continental shelf (supplementary text S12). If ancient seawater Si concentrations approached saturation with regards to cristobalite, seawater  $\text{PO}_4^{3-}$  would have averaged 0.10  $\mu\text{M}$ . For Si concentrations approaching amorphous Si saturation,  $\text{PO}_4^{3-}$  would have averaged 0.55  $\mu\text{M}$ . For ancient calcite seas and aragonite seas  $\text{PO}_4^{3-}$  concentrations would fall within this range with 0.21  $\mu\text{M}$  and 0.34  $\mu\text{M}$ , respectively. These values should be particularly reliable in the case of magnetite and/ or Fe phosphate formation. Nonetheless, even when considering a  $\text{PO}_4^{3-}$  remobilization of up to 10 mol.%, resulting in slightly higher  $\text{PO}_4^{3-}$  concentrations (ranging from 0.11  $\mu\text{M}$  to 0.61  $\mu\text{M}$ ), the results of our study generally support an

ancient ocean overall low in  $\text{PO}_4^{3-}$  (Hao et al., 2020; Jones et al., 2015). To our knowledge there is no prior experimental evidence for the formation of Fe(II) phosphate minerals under conditions representative of thermally immature (sub-greenschist facies) BIFs and there is only one study where vivianite has been reported from the rock record under comparable conditions (Alibert, 2016). This scarcity is in spite of the apparently important role Fe(II) phosphates appear to have played in suppressing low-grade metamorphic  $\text{PO}_4^{3-}$  remobilization and their high preservation potential. This further supports the idea of  $\text{PO}_4^{3-}$ -limitation in shallow shelf waters in the Archean to Paleoproterozoic, given that the formation of vivianite would have required pore water concentrations exceeding  $1 \mu\text{M}$  (Derry, 2015). However, such an interpretation would necessitate that the lack of vivianite observed in BIFs to date is not a result of vivianite sulfidation during the genesis of BIFs, a process often observed in modern sedimentary environments (e.g. Dijkstra et al., 2018a), but rather the metamorphic reaction of vivianite with calcite leading to the formation of apatite (Hao et al., 2020).

#### 4. CONCLUSIONS

As P is often considered to be the limiting nutrient on geological timescales (e.g. Reinhard et al., 2017; Tyrrell, 1999), and depressed concentrations may have been a requisite for maintaining a low oxygenation state in the Earth's middle ages (Laakso and Schrag, 2018), there is great interest in reconstructing the history of P bioavailability over the course of Earth's history. Low  $\text{PO}_4^{3-}$  concentrations in Earth's primitive oceans would almost certainly have had profound implications for the evolution of the biosphere and the protracted oxygenation of Earth's surface environments. This is highlighted by a number of recent Earth systems modeling papers that have discussed the consequences of low  $\text{PO}_4^{3-}$  during the Proterozoic. A recent assessment by Laakso and Schrag (2018) tested P limitation over geological timescales in a quantitative framework by modeling the effect of nutrient limitation on net primary productivity (NPP) in the Proterozoic; their models of NPP point to P as being the most likely nutrient to have limited the Proterozoic biosphere. Similarly, Ozaki et al. (2019) employed a statistical approach in constraining Proterozoic  $\text{O}_2$  levels from a 1-D box model of ocean biogeochemistry. Those authors found that net  $\text{O}_2$  production was limited to a fraction of modern levels, in large part due to widespread phosphorus limitation. The scarcity of P has also been invoked in the maintenance of low

atmospheric O<sub>2</sub> levels in the Neoproterozoic (Guilbaud et al., 2020). While the findings of Guilbaud et al. (2020) are at odds with the Neoproterozoic increase in P identified by Reinhard et al. (2017), these studies collectively highlight the importance of constraining ancient P levels for constraining both the activity of Earth's emergent biosphere, and the protracted oxygenation of Earth's oceans and atmosphere. While many of these examples have been focused on the Proterozoic, their implications likely extend to the Archean and Paleoproterozoic, a period in Earth's history where BIF deposition is a hallmark of ocean chemistry.

Given the potential implications for the evolution of oxygenic photosynthesis and related changes in the oxidation state on the Earth's atmosphere-ocean system, the interpretation of the P/Fe ratios in the Archean to early Paleoproterozoic BIF rock record and deduced ocean PO<sub>4</sub><sup>3-</sup> concentrations have been highly debated (e.g. Bjerrum and Canfield, 2002; Jones et al., 2015; Konhauser et al., 2007; Planavsky et al., 2010). Where previous studies focussed on the interpretation of rock record P/Fe ratios employing empirical K<sub>D</sub> values based on putative primary Fe precipitates, we extended this approach beyond the initial deposition and included low-grade metamorphism, a mechanism responsible for the post-depositional alteration of BIF sediments. We found that the metamorphic mineral transformation pathway of PO<sub>4</sub><sup>3-</sup>-loaded ferrihydrite containing varying concentrations of Si was largely independent of the quantity of C<sub>org</sub> but instead was heavily influenced by C<sub>org</sub> reactivity. The presence of highly reactive C<sub>org</sub> resulted in the formation of magnetite and vivianite, effectively immobilizing PO<sub>4</sub><sup>3-</sup> (<1.5 mol.% remobilization). By contrast, the absence of C<sub>org</sub> or presence of less reactive C<sub>org</sub> resulted in the formation of hematite with concomitant higher PO<sub>4</sub><sup>3-</sup> remobilization (<10 mol.%). Our results thus suggest that the primary BIF mineralogy and changes thereof (e.g. during metamorphism) generally exerted a minor control on the P contained in BIF, albeit some variation between BIF of different mineralogical composition (predominantly hematite-rich vs. magnetite-rich) could have occurred. Therefore, BIF apparently report past ocean P with high fidelity, collectively pointing to depressed levels relative to modern, between 0.1 μM and 1 μM. However, it remains unknown to which extent the associated biomass might have influenced the BIF P content. A recent study showed that the same phytoplankton which formed BIFs might also have supplied essentially all trace elements contained in BIF (Konhauser et al., 2018). Yet, it remains unresolved to which extent e.g. P was assimilated by such phytoplankton and to which extent phytoplankton-derived

biomass in turn would have been associated with primary Fe(III) minerals and thus ultimately sequestered in BIFs.

## ACKNOWLEDGMENTS

This study was supported by grant KA 1736/24-1 from the German Research Foundation (DFG) and a Natural Sciences and Engineering Research Council (NSERC) grant to KOK. LJR gratefully acknowledges a Vanier Canada Graduate Scholarship (CGS) and Donnelley Postdoctoral Fellowship from the Yale Institute of Biospheric Studies, and TJW a NSERC CGS Master's. SVL acknowledges support from the Region of Brittany and LabexMER. The authors would further like to thank Dr. James M. Byrne for help with the interpretation of Moessbauer and XRD data. Natalia Jakus is acknowledged for help with the  $\mu$ XRD measurements and XRD data interpretation.

## REFERENCES

- Al-Borno A. and Tomson M. B. (1994) The temperature dependence of the solubility product constant of vivianite. *Geochim. Cosmochim. Acta* **58**, 5373-5378.
- Alibert C. (2016) Rare earth elements in Hamersley BIF minerals. *Geochim. Cosmochim. Acta* **184**, 311-328.
- Bekker A., Planavsky N., Rasmussen B., Krapez B., Hofmann A., Slack J., Rouxel O. and Konhauser K. O. (2014) Iron formations: Their origins and implications for ancient seawater chemistry. In *Treatise on Geochemistry, second ed. Vol. 9* (eds. H. D. Holland and K. K. Turekian). Elsevier, Netherlands. pp. 561-628.
- Bjerrum C. J. and Canfield D. E. (2002) Ocean productivity before about 1.9 Gyr ago limited by phosphorus adsorption onto iron oxides. *Nature* **417**, 159-162.
- Bruland K. W., Middag R. and Lohan M. C., 2014. Controls of trace metals in seawater. In *Treatise on Geochemistry, second ed. Vol. 8*, (eds. H. D. Holland and K. K. Turekian). Elsevier, Netherlands. pp.19-55.
- Campbell A. S., Schwertmann U., Stanjek H., Friedl J., Kyek A. and Campbell P. A. (2002) Si incorporation into hematite by heating Si-ferrihydrite. *Langmuir* **18**, 7804-7809.
- Cloud P. E. (1973) Paleoecological significance of the banded iron-formation. *Econ. Geol.* **68**, 1135-1143.
- Cornell R. M. and Schwertmann U. (2003) *The Iron Oxides: Structure, Properties, Reactions, Occurrences and Uses*. Wiley-VCH Verlag, Weinheim.

- Crowe S. A., Paris G., Katsev S., Jones C., Kim S.-T., Zerkle A. L., Nomosatryo S., Fowle D. A., Adkins J. F., Sessions A. L., Farquhar J. and Canfield D. E. (2014) Sulfate was a trace constituent of Archean seawater. *Science* **346**, 735-739.
- Daou T. J., Begin-Colin S., Grenèche J.-M., Thomas F., Derory A., Bernhardt P., Legaré P. and Pourroy G. (2007) Phosphate adsorption properties of magnetite-based nanoparticles. *Chem. Mat.* **19**, 4494-4505.
- Derry L. A. (2015) Causes and consequences of mid-Proterozoic anoxia. *Geophys. Res. Lett.* **42**, 8538-8546.
- Dijkstra N., Hagens M., Egger M. J. and Slomp C. P. (2018a) Post-depositional formation of vivianite-type minerals alters sediment phosphorus records. *Biogeosciences* **15**, 861-883.
- Dijkstra N., Kraal P., Séguret M. J. M., Flores M. R., Gonzalez S., Rijkenberg M. J. A. and Slomp C. P. (2018b) Phosphorus dynamics in and below the redoxcline in the Black Sea and implications for phosphorus burial. *Geochim. Cosmochim. Acta* **222**, 685-703.
- Dijkstra N., Slomp C. P. and Behrends T. (2016) Vivianite is a key sink for phosphorus in sediments of the Landsort Deep, an intermittently anoxic deep basin in the Baltic Sea. *Chem. Geol.* **438**, 58-72.
- DIN Deutsches Institut für Normung e. V. (2015) *Solid biofuels – Determination of major elements – Al, Ca, Fe, Mg, P, K, Si, Na and Ti (ISO 16967:2015)*. German version EN ISO 16967:2015;75.160.10. 10772 Berlin: Beuth Verlag GmbH.
- Frost R. L., Weier M. L., Martens W., Klopogge J. T. and Ding Z. (2003) Dehydration of synthetic and natural vivianite. *Thermochim. Acta* **401**, 121-130.
- Galvez N., Barron V. and Torrent J. (1999) Effect of phosphate on the crystallization of hematite, goethite, and lepidocrocite from ferrihydrite. *Clays Clay Miner.* **47**, 304-311.
- Gu B., Mehlhorn T. L., Liang L. and McCarthy J. F. (1996) Competitive adsorption, displacement, and transport of organic matter on iron oxide: I. Competitive adsorption. *Geochim. Cosmochim. Acta* **60**, 1943-1950.
- Gu B., Schmitt J., Chen Z., Liang L. and McCarthy J. F. (1994) Adsorption and desorption of natural organic matter on iron oxide: mechanisms and models. *Environ. Sci. Technol.* **28**, 38-46.
- Guilbaud R., Poulton S. W., Thompson J., Husband K. F., Zhu M., Zhou Y., Shields G. A. and Lenton T. M. (2020) Phosphorus-limited conditions in the early Neoproterozoic ocean maintained low levels of atmospheric oxygen. *Nat. Geosci.* **13**, 296-301.
- Halama M. (2016) Metamorphic origin of the mineralogy and geochemical signatures in banded iron formations. Ph.D. thesis. University of Tuebingen.
- Halama M., Swanner E. D., Konhauser K. O. and Kappler A. (2016) Evaluation of siderite and magnetite formation in BIFs by pressure-temperature experiments of Fe(III) minerals and microbial biomass. *Earth Planet. Sci. Lett.* **450**, 243-253.
- Halevy I., Alesker M., Schuster E. M., Popovitz-Biro R. and Feldman Y. (2017) A key role for green rust in the Precambrian oceans and the genesis of iron formations. *Nat. Geosci.* **10**, 135-139.

- Hansel C. M., Benner S. G., Neiss J., Dohnalkova A., Kukkadapu R. K. and Fendorf S. (2003) Secondary mineralization pathways induced by dissimilatory iron reduction of ferrihydrite under advective flow. *Geochim. Cosmochim. Acta* **67**, 2977-2992.
- Hao J., Knoll A. H., Huang F., Schieber J., Hazen R. M. and Daniel I. (2020) Cycling phosphorus on the Archean Earth: Part II. Phosphorus limitation on primary production in Archean ecosystems. *Geochim. Cosmochim. Acta* **280**, 360-377.
- Hartman H. (1984) The evolution of photosynthesis and microbial mats: A speculation on the banded iron formations. In *Microbial Mats: Stromatolites* (eds. Y. Cohen, R. W. Castenholz and H. O. Halvorson). Alan Liss, New York. pp. 451-453.
- Hiemstra T. (2018) Ferrihydrite interaction with silicate and competing oxyanions: geometry and hydrogen bonding of surface species. *Geochim. Cosmochim. Acta* **238**, 453-476.
- Hilbrandt I., Lehmann V., Zietzschmann F., Ruhl A. S. and Jekel M. (2019) Quantification and isotherm modelling of competitive phosphate and silicate adsorption onto micro-sized granular ferric hydroxide. *RSC Adv.* **9**, 23642-23651.
- Jones C., Nomosatryo S., Crowe S. A., Bjerrum C. J. and Canfield D. E. (2015) Iron oxides, divalent cations, silica, and the early earth phosphorus crisis. *Geology* **43**, 135-138.
- Kashefi K. and Lovley D. R. (2000) Reduction of Fe(III), Mn(IV), and toxic metals at 100°C by *Pyrobaculum islandicum*. *Appl. Environ. Microbiol.* **66**, 1050-1056.
- Kingston F. J., Posner A. M. and Quirk J. P. (1972) Anion adsorption by goethite and gibbsite: I. The role of the proton in determining adsorption envelopes. *Eur. J. Soil Sci.* **23**, 177-192.
- Köhler I., Konhauser K. O., Papineau D., Bekker A. and Kappler A. (2013) Biological carbon precursor to diagenetic siderite with spherical structures in iron formations. *Nat. Commun.* **4**, 1741.
- Konhauser K. O., Planavsky N. J., Hardisty D. S., Robbins L. J., Warchola T. J., Haugaard R., Lalonde S. V., Partin C. A., Oonk P. B. H., Tsikos H., Lyons T. W., Bekker A. and Johnson C. M. (2017) Iron formations: A global record of Neoproterozoic to Palaeoproterozoic environmental history. *Earth Sci. Rev.* **172**, 140-177.
- Konhauser K. O., Hamade T., Raiswell R., Morris R. C., Ferris F. G., Southam G. and Canfield D. E. (2002) Could bacteria have formed the Precambrian banded iron formations? *Geology* **30**, 1079-1082.
- Konhauser K. O., Lalonde S. V., Amskold L. and Holland H. D. (2007) Was there really an Archean phosphate crisis? *Science* **315**, 1234-1234.
- Konhauser K. O., Robbins L. J., Alessi D. S., Flynn S. L., Gingras M. K., Martinez R. E., Kappler A., Swanner E. D., Li Y.-L., Crowe S. A., Planavsky N. J., Reinhard C. T. and Lalonde S. V. (2018) Phytoplankton contributions to the trace-element composition of Precambrian banded iron formations. *Geol. Soc. Am. Bull.* **130**, 941-951.
- Laakso T. A. and Schrag D. P. (2018) Limitations on limitation. *Global Biogeochem. Cycles* **32**, 486-496.
- Levitus S., Conkright M. E., Reid J. L., Najjar R. G. and Mantyla A. (1993) Distribution of nitrate, phosphate and silicate in the world oceans. *Prog. Oceanogr.* **31**, 245-273.

- Li Y.-L., Konhauser K. O., Cole D. R. and Phelps T. J. (2011) Mineral ecophysiological data provide growing evidence for microbial activity in banded-iron formations. *Geology* **39**, 707-710.
- Li Y.-L., Konhauser K. O., Kappler A. and Hao X.-L. (2013a) Experimental low-grade alteration of biogenic magnetite indicates microbial involvement in generation of banded iron formations. *Earth Planet. Sci. Lett.* **361**, 229-237.
- Li Y.-L., Sun S. and Chan L. S. (2013b) Phosphogenesis in the 2460 and 2728 million-year-old banded iron formations as evidence for biological cycling of phosphate in the early biosphere. *Ecol. Evol.* **3**, 115-125.
- März C., Riedinger N., Sena C. and Kasten S. (2018) Phosphorus dynamics around the sulphate-methane transition in continental margin sediments: Authigenic apatite and Fe (II) phosphates. *Mar. Geol.* **404**, 84-96.
- Mattievich E. and Danon J. (1977) Hydrothermal synthesis and Mössbauer studies of ferrous phosphates of the homologous series  $\text{Fe}_3^{2+}(\text{PO}_4)_2(\text{H}_2\text{O})_n$ . *J. Inorg. Nucl. Chem.* **39**, 569-580.
- Muhling J. R. and Rasmussen B. (2020) Widespread deposition of greenalite to form Banded Iron Formations before the Great Oxidation Event. *Precambrian Res.* **339**, 105619.
- Nutman A. P. and Friend C. R. (2006) Petrography and geochemistry of apatites in banded iron formation, Akilia, W. Greenland: Consequences for oldest life evidence. *Precambrian Res.* **147**, 100-106.
- Ozaki K., Reinhard C. T. and Tajika E. (2019) A sluggish mid-Proterozoic biosphere and its effect on Earth's redox balance. *Geobiology* **17**, 3-11.
- Papineau D., De Gregorio B. T., Cody G. D., O'Neil J., Steele A., Stroud R. M. and Fogel M. L. (2011) Young poorly crystalline graphite in the >3.8-Gyr-old Nuvvuagittuq banded iron formation. *Nat. Geosci.* **4**, 376-379.
- Papineau D., De Gregorio B. T., Stroud R. M., Steele A., Pecoits E., Konhauser K. O., Wang J. and Fogel M. L. (2010) Ancient graphite in the Eoarchean quartz-pyroxene rocks from Akilia in southern West Greenland II: Isotopic and chemical compositions and comparison with Paleoproterozoic banded iron formations. *Geochim. Cosmochim. Acta* **74**, 5884-5905.
- Pecoits E., Gingras M. K., Barley M. E., Kappler A., Posth N. R. and Konhauser K. O. (2009) Petrography and geochemistry of the Dales Gorge banded iron formation: Paragenetic sequence, source and implications for palaeo-ocean chemistry. *Precambrian Res.* **172**, 163-187.
- Planavsky N. J., Rouxel O. J., Bekker A., Lalonde S. V., Konhauser K. O., Reinhard C. T. and Lyons T. W. (2010) The evolution of the marine phosphate reservoir. *Nature* **467**, 1088-1090.
- Posth N. R., Huelin S., Konhauser K. O. and Kappler A. (2010) Size, density and composition of cell-mineral aggregates formed during anoxygenic phototrophic Fe(II) oxidation: Impact on modern and ancient environments. *Geochim. Cosmochim. Acta* **74**, 3476-3493.
- Posth N. R., Kohler I., Swanner E. D., Schröder C., Wellmann E., Binder B., Konhauser K. O., Neumann U., Berthold C., Nowak M. and Kappler A. (2013) Simulating Precambrian banded iron formation diagenesis. *Chem. Geol.* **362**, 66-73.



- Rasmussen B., Muhling J. R., Suvorova A. and Krapež B. (2017) Greenalite precipitation linked to the deposition of banded iron formations downslope from a late Archean carbonate platform. *Precambrian Res.* **290**, 49-62.
- Reinhard C. T., Planavsky N. J., Gill B. C., Ozaki K., Robbins L. J., Lyons T. W., Fischer W. W., Wang C., Cole D. B. and Konhauser K. O. (2017) Evolution of the global phosphorus cycle. *Nature* **541**, 386.
- Robbins L. J., Swanner E. D., Lalonde S. V., Eickhoff M., Paranich M. L., Reinhard C. T., Peacock C. L., Kappler A. and Konhauser K. O. (2015) Limited Zn and Ni mobility during simulated iron formation diagenesis. *Chem. Geol.* **402**, 30-39.
- Rothe M., Kleeberg A. and Hupfer M. (2016) The occurrence, identification and environmental relevance of vivianite in waterlogged soils and aquatic sediments. *Earth Sci. Rev.* **158**, 51-64.
- Rouzies D. and Millet J. M. M. (1993) Mössbauer study of synthetic oxidized vivianite at room temperature. *Hyperfine Interact.* **77**, 19-28.
- Rzepa G., Pieczara G., Gawel A., Tomczyk A. and Zalecki R. (2016) The influence of silicate on transformation pathways of synthetic 2-line ferrihydrite. *J. Therm. Anal. Calorim.* **125**, 407-421.
- Schad M., Halama M., Bishop B., Konhauser K. O. and Kappler A. (2019) Temperature fluctuations in the Archean ocean as trigger for varve-like deposition of iron and silica minerals in banded iron formations. *Geochim. Cosmochim. Acta* **265**, 386-412.
- Schwertmann U. and Cornell R. M. (2008) Iron oxides in the laboratory. John Wiley & Sons.
- Schwertmann U. and Fechter H. (1982) The point of zero charge of natural and synthetic ferrihydrites and its relation to adsorbed silicate. *Clay Miner.* **17**, 471-476.
- Siever R. (1992) The silica cycle in the Precambrian. *Geochim. Cosmochim. Acta* **56**, 3265-3272.
- Sigg L. and Stumm W. (1981) The interaction of anions and weak acids with the hydrous goethite ( $\alpha$ -FeOOH) surface. *Colloids Surf.* **2**, 101-117.
- Stanjek H. and Weidler P. (1992) The effect of dry heating on the chemistry, surface area, and oxalate solubility of synthetic 2-line and 6-line ferrihydrites. *Clay Miner.* **27**, 397-411.
- Thompson K. J., Kenward P. A., Bauer K. W., Warchola T., Gauger T., Martinez R., Simister R. L., Michiels C. C., Lirós M., Reinhard C. T., Kappler A., Konhauser K. O. and Crowe S. A. (2019) Photoferrotrophy, deposition of banded iron formations, and methane production in Archean oceans. *Sci. Adv.* **5**, eaav2869.
- Toner B. M., Berquó T. S., Michel F. M., Sorensen J. V., Templeton A. S. and Edwards K. J. (2012) Mineralogy of iron microbial mats from Loihi Seamount. *Front. Microbiol.* **3**, 118.
- Tyrrell T. (1999) The relative influences of nitrogen and phosphorus on oceanic primary production. *Nature* **400**, 525-531.
- Veeramani H., Alessi D. S., Suvorova E. I., Lezama-Pacheco J. S., Stubbs J. E., Sharp J. O., Dippon U., Kappler A., Bargar J. R. and Bernier-Latmani R. (2011) Products of abiotic U(VI) reduction by biogenic magnetite and vivianite. *Geochim. Cosmochim. Acta* **75**, 2512-2528.
- Vochten R. and De Grave E. (1981) Crystallographic, Mössbauer and electrokinetic study of synthetic lipscombite. *Phys. Chem. Miner.* **7**, 197-203.

- Wang X., Li W., Harrington R., Liu F., Parise J. B., Feng X. and Sparks D. L. (2013a) Effect of ferrihydrite crystallite size on phosphate adsorption reactivity. *Environ. Sci. Technol.* **47**, 10322-10331.
- Wang X., Liu F., Tan W., Li W., Feng X. and Sparks D. L. (2013b) Characteristics of phosphate adsorption-desorption onto ferrihydrite: comparison with well-crystalline Fe (hydr)oxides. *Soil Sci.* **178**, 1-11.
- Zheng X.-Y., Beard B. L., Reddy T. R., Roden E. E. and Johnson C. M. (2016) Abiologic silicon isotope fractionation between aqueous Si and Fe(III)-Si gel in simulated Archean seawater: Implications for Si isotope records in Precambrian sedimentary rocks. *Geochim. Cosmochim. Acta* **187**, 102-122.

---

## SUPPLEMENTAL INFORMATION

### **Phosphate remobilization from banded iron formations depends on metamorphic mineral transformations**

Manuel Schad<sup>a</sup>, Maximilian Halama<sup>a</sup>, Leslie J. Robbins<sup>b, c, d</sup>, Tyler J. Warchola<sup>b</sup>, Julian Tejada<sup>e</sup>,  
Rainer Kirchhof<sup>e</sup>, Stefan V. Lalonde<sup>f</sup>, Elizabeth D. Swanner<sup>g</sup>, Noah J. Planavsky<sup>c</sup>, Harald  
Thorwarth<sup>e</sup>, Muammar Mansor<sup>a</sup>, Kurt O. Konhauser<sup>b</sup>, Andreas Kappler<sup>a</sup>

<sup>a</sup> Geomicrobiology, Center for Applied Geosciences, University of Tübingen, 72076, Tübingen,  
Germany

<sup>b</sup> Department of Earth and Atmospheric Sciences, University of Alberta, Edmonton, AB T6G  
2E3, Canada

<sup>c</sup> Department of Geology and Geophysics, Yale University, New Haven, Connecticut 06511,  
USA

<sup>d</sup> Department of Geology, University of Regina, Regina, SK S4S 0A2, Canada

<sup>e</sup> University of Applied Forest Sciences Rottenburg, Schadenweilerhof, 72108 Rottenburg am  
Neckar, Germany

<sup>f</sup> European Institute for Marine Studies, CNRS-UMR6538 Laboratoire Domaines Océaniques,  
Technopôle Brest-Iroise, 29280 Plouzané, France

<sup>g</sup> Department of Geological and Atmospheric Sciences, Iowa State University, Ames, Iowa 50011,  
USA

**Manuscript in preparation for publication in:** *Geological Society of America Bulletin*

## APPENDIX

## APPENDIX A

### 1. TEXT S1: DEPOSITIONAL SETTING OF BANDED IRON FORMATIONS AND DEDUCED EXPERIMENTAL DESIGN AND CONDITIONS

The mineralogical, sedimentological and geochemical framework for BIF deposition has been extensively reviewed elsewhere (e.g. Bekker et al., 2014; Bekker et al., 2010; Beukes and Gutzmer, 2008; Klein, 2005; Konhauser et al., 2017). However, below we will line out which specific assumptions our experiments are based on.

Laterally and vertically extensive BIFs (Superior-type BIF after Gross, 1980) were deposited throughout the Mesoarchean to Paleoproterozoic. Prime examples are the extensively studied BIFs of the Hamersley basin in Western Australia and Transvaal basin of South Africa (e.g. Beukes and Gutzmer, 2008). However, BIFs of similar age are also found in Brazil and India. The high amount of Fe (15-40 wt.% Fe) and Si (40-60 wt.% SiO<sub>2</sub>) as well as their high chemical purity, marked by minimal detrital input (<1 wt.% Al<sub>2</sub>O<sub>3</sub>, low concentrations of crustal elements Ti, Zn, Th, Hf, Sc <20 ppm; Klein, 2005; Konhauser et al., 2017), their generally low degree of deformation, lateral continuity and absence of current- or wave-generated structures poses some unique restrictions on the environment they were deposited from.

First, the ocean from which the BIFs were deposited was enriched in Fe<sup>2+</sup> with concentrations ranging from 0.03 to 0.5 mM (Holland, 1973; Morris, 1993). Rare-earth element and yttrium compositions suggest that the Fe contained in BIFs was hydrothermally derived (e.g. Planavsky et al., 2010a) and likely supplied to depositional areas either through upwelling (Holland, 1973) or hydrothermal plumes (Isley, 1995; Isley and Abbott, 1999). However, this necessitates an ocean-atmosphere system which was anoxic (Catling and Zahnle, 2020) to permit the transport of vast amounts of dissolved Fe<sup>2+</sup>. O<sub>2</sub> concentrations prior to the great oxidation event are generally considered to have been low (~1 μM; Hardisty et al., 2014), although locally confined O<sub>2</sub> oases have been reported where concentration exceeded 10 μM (Olson et al., 2013). Si concentration have been estimated to have at least approached saturation with regards to cristobalite (0.67 mM), possibly even saturation with regards to amorphous Si (2.2 mM; Maliva et al., 2005; Siever, 1992). However, more recent estimates range from 0.5 to 1.6 mM (Jones et al., 2015; Zheng et al., 2016). Furthermore, the ocean is considered to have contained low

dissolved  $\text{SO}_4^{2-}$  ( $<1 \mu\text{M}$ ; Crowe et al., 2014), have been temperate (max.  $50^\circ\text{C}$ ; Krissansen-Totton et al., 2018) with a pH slightly lower than today (6.2-7.7, increasing through time; Halevy and Bachan, 2017; Krissansen-Totton et al., 2018) but comparable salinity (3-5%; Marty et al., 2018). Nutrients, like e.g.  $\text{PO}_4^{3-}$ , contained in BIFs today were likely initially derived from continental weathering and supplied by riverine transport (Hao et al., 2020a; Hao et al., 2020b; Hao et al., 2017a, b). Further important sources of nutrients might have been pyroclastic material (e.g. Haugaard et al., 2016) or upwelling hydrothermal fluids derived from submarine volcanism (Barley et al., 1997; Isley and Abbott, 1999).

Major BIFs were deposited once stable cratons had developed. Based on their general association with carbonates and shales, it has been suggested that they were deposited on continental margins in stable nearshore shelf environments (e.g. Beukes and Gutzmer, 2008; Gross, 1980; Trendall, 2002) even though bathymetric depth and individual sequence stratigraphy may vary. However, the general absence of current- or wave-generated structures requires a relative deep-water setting below storm-wave base ( $>200 \text{ m}$  in modern environments; Boggs Jr, 2014).

The mineral assemblages found in BIFs today contain hematite, magnetite, carbonates (e.g. siderite, ankerite), various Fe(II)/Fe(III) silicates (e.g. stilpnomelane, riebeckite, minnesotaite, greenalite), pyrite and chert (Klein, 2005). However, it is generally agreed upon that none of these minerals are primary but rather represent diagenetic and metamorphic overprinting. The least metamorphosed BIFs experienced sub-greenschist facies burial metamorphism with a maximum pressure of 1.2 kbar and temperatures ranging from  $100$  to  $300^\circ\text{C}$  in the Hamersley basin (Klein and Gole, 1981; Smith et al., 1982), although pressures of 1.5 kbar and temperatures between  $300$  and  $360^\circ\text{C}$  have also been described. Maximum temperatures reported for the Transvaal basin are up to  $170^\circ\text{C}$  (Miyano and Beukes, 1984). Therefore, we set the pressure/temperature conditions in our low-grade metamorphism experiments to 1.2 kbar and a maximum temperature of  $170^\circ\text{C}$ .

Phosphorous as nutrient of interest in our study is found at molar P/Fe ratios from below 0.01 to a maximum of approximately 0.02 in BIFs of Mesoarchean to Paleoproterozoic age (e.g. Planavsky et al., 2010b; Robbins et al., 2016). Therefore, we set the maximum value of 0.02 as the upper limit for the minerals synthesized for the use in our experiments.

## **2. TEXT S2: CHOICE OF STARTING MINERALS – Fe(III) (OXYHYDR)OXIDES VS: Fe(II)-SILICATES AND MIXED-VALENT Fe SPECIES**

The nature of the primary mineral precipitates that formed the precursor phase to BIFs is probably one of the most debated questions among researchers concerned with reconstructing the Precambrian Earth. This question is not a trivial one, since these reconstructions are mostly based on the analysis of the ancient rock record, which requires a detailed knowledge of the chemical and physical interactions between the primary constituents at the point of their formation.

Many researchers favor a model where Fe(III) (oxyhydr)oxides formed the precursor mineral phase to BIFs (see e.g. Konhauser et al., 2017) and a vast amount of studies trying to reconstruct Paleo-seawater chemistry is based on this proposition. However, recent years have seen a renewed interest in the search for alternative models and there is an increasing body of literature suggesting Fe(II)-silicates, such as greenalite, not Fe(III) (oxyhydr)oxides might have been the precursor mineral to BIF (e.g. Johnson et al., 2018; Muhling and Rasmussen, 2020; Rasmussen et al., 2015; Rasmussen et al., 2013; Rasmussen et al., 2019; Rasmussen et al., 2017). These minerals would have been precipitated directly from the water column when  $\text{Fe}^{2+}$  and  $\text{SiO}_{2,\text{aq}}$  transported in acidic hydrothermal plumes mixed with cooler and more alkaline seawater, leading decreased Fe(II) and Si solubility. This would have promoted rapid nucleation of Fe(II)-silicate nanoparticles, which aggregated and accumulated on the seafloor either as silt-sized floccules or amorphous mud (Rasmussen et al., 2017). This is supported by an experimental study by Tosca et al. (2016) who synthesized a Fe(II)-silica gel under experimental conditions aimed at simulating a Precambrian ocean. Such a process would also exclude two major problems associated with the primary Fe(III) (oxyhydr)oxide theory: (1) The contradiction between a rock record starved of organic carbon (e.g. Klein and Beukes, 1989) and an oxidative mechanism potentially linked to microbial activity (Kappler et al., 2005; Konhauser et al., 2002), resulting in a close association between Fe(III) minerals and microbial biomass. (2) Preservation of an oxidized mineral in an otherwise reduced and Fe(II)-rich ocean. Instead it was suggested that Fe(III) is secondary in origin, formed either through the percolation of oxidizing fluids during ore-forming processes (Rasmussen et al., 2014) or thermal decomposition of primary greenalite (Rasmussen et al., 2016).

However, this hypothesis also has several important caveats: (1) The conditions facilitating the formation of greenalite are poorly constrained. While geochemical modelling suggests that greenalite may form at pH 7 and  $\text{Fe}^{2+}$  and Si concentrations relevant to the Precambrian ocean (Johnson et al., 2018), the experimental work of Tosca et al. (2016) required a pH exceeding 7.5 for the precipitation of greenalite. On the one hand this may indicate a kinetic limitation for the precipitation of greenalite at a lower pH. On the other hand, the pH applied in the experimental study is at odds with the pH of the Precambrian ocean, which is assumed to have been lower than today in the range of 6.2-7.2 during the Archean. Only at the Archean-Paleoproterozoic boundary it is assumed to have increased to 6.5-7.7 (Halevy and Bachan, 2017; Krissansen-Totton et al., 2018). Furthermore, a recent study demonstrated based on (hydro)geological constraints that, while secondary oxidation of greenalite by percolating fluids might have been an important process locally, it is unlikely to have been of significance on a basin scale (Robbins et al., 2019), especially in BIFs rich in iron oxides (hematite and magnetite).

Nonetheless, the wide-spread occurrence of greenalite in some BIFs makes it difficult to argue against it being of significance during BIF deposition. However, the formation of greenalite might have been restricted to environments with a higher pH than average seawater. Some potential scenarios envisioned are for example the precipitation of greenalite along an alkalinity chemocline (Beukes and Gutzmer, 2008). Also, high primary production linked to oxygenic photosynthesis either near the paleoshore or in the upper layers of the water column could have resulted in increased  $\text{CO}_2$ -fixation, locally driving the pH to values above 9 (Ibelings and Maberly, 1998; Ji et al., 2020; Verspagen et al., 2014). Depending on basin geometry and currents, this could potentially have created the conditions/ alkalinity chemocline necessary for greenalite precipitation. Another process, which would have permitted the formation of greenalite, is the microbial reduction of primary Fe(III) (oxyhydr)oxide minerals by dissimilatory Fe(III)-reducing bacteria during diagenesis. This microbial process would have provided the slightly alkaline conditions and concentrations of  $\text{Fe}^{2+}$  and Si required for greenalite formation even in BIFs rich in Fe oxides. Therefore, while there is a precedence for greenalite as a primary mineral product in some BIFs, it is considered unlikely to have been the primary mineral phase in the oxide-rich BIFs considered in our study.

A second putative precursor mineral phase to BIFs is green rust, a mixed-valent Fe(II)-Fe(III) hydroxide, which may have been formed through partial oxidation of  $\text{Fe}^{2+}$  by low

concentrations of O<sub>2</sub> (Halevy et al., 2017; Koeksoy et al., 2019) or through the transformation of Fe(III) (oxyhydr)oxides either by microbes (Zegeye et al., 2012) or abiotically through the reaction with Fe<sup>2+</sup> (Li et al., 2017). This is of significance since bioessential nutrients like phosphate (Bocher et al., 2004; Hansen and Poulsen, 1999) and Ni (Zegeye et al., 2012), display a higher affinity for green rust than they do for Fe(III) (oxyhydr)oxides, with important implications for the interpretation of their aqueous concentration in the Precambrian ocean as derived from the BIF rock record. Importantly, upon aging green rust transforms into minerals found in BIFs today, such as magnetite, siderite, Fe-bearing silicates (stilpnomelane or minnesotaite) as well as Fe(III) (oxyhydr)oxides (Halevy et al., 2017; Li et al., 2017; Zegeye et al., 2012), which have been implicated as being the precursor mineral phase to hematite. However, a recent study by Han et al. (2020a) demonstrated that photoautotrophic Fe(II)-oxidizing bacteria, which have been suggested to having played a key role in the deposition of BIFs (Kappler et al., 2005; Konhauser et al., 2002), can also oxidize green rust. This raises questions about to which extent green rust might actually have settled on the seafloor without having been altered already in the water column.

The third group of putative precursor minerals is based on the proposition that BIF deposition was initiated by the oxidation of Fe<sup>2+</sup> contained in the water column either chemically by O<sub>2</sub> produced by early cyanobacteria (e.g. Cloud, 1973; Cloud, 1965) or enzymatically by photoautotrophic Fe(II)-oxidizing bacteria (photoferrotrophy; Kappler et al., 2005; Konhauser et al., 2002; Widdel et al., 1993). There is a wide consensus, that either Fe(III) (oxyhydr)oxides (e.g. Ahn and Buseck, 1990; Beukes and Gutzmer, 2008; Kappler and Newman, 2004; Kaufman et al., 1990; Klein and Beukes, 1989; Pecoits et al., 2009; Sun et al., 2015), a Si-containing ferrihydrite phase (e.g. Alibert, 2016; Fischer and Knoll, 2009) or a Fe(III)-Si gel (Percak-Dennett et al., 2011; Zheng et al., 2016) would have formed as a result of such oxidative processes and most of the paleo-reconstructions derived from the interpretation of the BIF rock record are based on the prevalence of such a mineral phase.

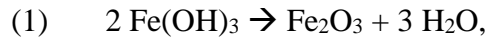
However, this hypothesis has been questioned based on the instability of an oxidized mineral phase being present in an otherwise reducing (Fe(II)-containing) ocean. Indeed, there is ample evidence for the transformation of Fe(III) (oxyhydr)oxides like ferrihydrite into secondary minerals like lepidocrocite, goethite, green rust or magnetite either through the abiotic reaction with Fe(II) (e.g. Hansel et al., 2003; Li et al., 2017; Zachara et al., 2002) or by microbial Fe(III)



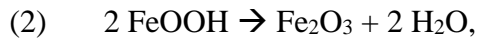
reduction (e.g. Han et al., 2020b; Kukkadapu et al., 2004; O'Loughlin et al., 2010). On the other hand, it has been shown that co-precipitated biomass, as it would have been present from the microbes catalyzing photoferrotrophy (Posth et al., 2010), can retard or even completely inhibit the secondary transformation of a primary Fe(III) (oxyhydr)oxide by Fe(II) (e.g. Chen et al., 2015; Han et al., 2020b; Jones et al., 2009; ThomasArrigo et al., 2018; Zhou et al., 2018). A similar stabilizing effect has been described for Si (e.g. Cismasu et al., 2011; Jones et al., 2009; Senn et al., 2017; Voegelin et al., 2010), which would have been abundant in the ancient ocean (e.g. Maliva et al., 2005). Therefore, it appears reasonable to assume, that primary Fe(III) (oxyhydr)oxides would have been preserved while settling through the water column. Consequently, the remobilization of  $\text{PO}_4^{3-}$  from these Fe(III) (oxyhydr)oxides during low-grade metamorphism will be the focus of our study.

### 3. TEXT S3: RATIONAL BEHIND “WATER FREE” SETUP AND OVERVIEW OVER EXPERIMENTAL SETUPS

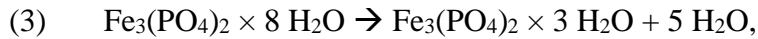
Due to the use of closed gold capsules to simulate low-grade metamorphism, it was not possible to use water-saturated mineral suspensions: The presence of water during the arc-welding of the gold capsules essentially resulted in the destruction of the area of the gold capsule that came in contact with the electrode during the welding process, making it impossible to close the gold capsules. Therefore, we decided to use freeze-dried minerals instead. Although this seems to be in contrast with our proposition of simulating an initially water-saturated sediment column, water should still be liberated and thus be present during low-grade metamorphism according to the following reactions:



which describes the dehydration of ferrihydrite during the transformation to hematite,



which describes the dehydration of goethite to hematite and



which describe the dehydration of vivianite following Frost et al. (2003b).

This is underpinned by the content of the gold capsules being wet upon completion of the low-grade metamorphism and opening of the gold capsules.

Table S1

Overview over experimental setups and respective abbreviations. “Recalcitrant” C<sub>org</sub> is referring to *Shewanella*-derived microbial biomass. “Labile” C<sub>org</sub> is referring to glucose as biomass proxy. \*data per Halama (2016).

Mineral	Heat pre-treatment	P	Si	C <sub>org</sub> source	Replicates	Abbreviation
Ferrihydrite			no	recalcitrant	3	FhC <sub>recalcitrant</sub>
Ferrihydrite *		X	no		1	FhP
Ferrihydrite *		X	low		1	FhPSi <sub>low</sub>
Ferrihydrite *		X	high		1	FhPSi <sub>high</sub>
Ferrihydrite *		X	no	labile	1	FhPC <sub>labile</sub>
Ferrihydrite *		X	low	labile	1	FhPSi <sub>low</sub> C <sub>labile</sub>
Ferrihydrite *		X	high	labile	1	FhPSi <sub>high</sub> C <sub>labile</sub>
Ferrihydrite		X	no	recalcitrant	3	FhPC <sub>recalcitrant</sub>
Ferrihydrite		X	low	recalcitrant	3	FhPSi <sub>low</sub> C <sub>recalcitrant</sub>
Ferrihydrite		X	high	recalcitrant	3	FhPSi <sub>high</sub> C <sub>recalcitrant</sub>
Ferrihydrite	X	X	no	recalcitrant	3	Fh <sub>heat</sub> PC <sub>recalcitrant</sub>
Ferrihydrite	X	X	low	recalcitrant	3	Fh <sub>heat</sub> PSi <sub>low</sub> C <sub>recalcitrant</sub>
Ferrihydrite	X	X	high	recalcitrant	3	Fh <sub>heat</sub> PSi <sub>high</sub> C <sub>recalcitrant</sub>
Goethite		X	no	recalcitrant	3	GtPC <sub>recalcitrant</sub>
Goethite		X	low	recalcitrant	3	GtPSi <sub>low</sub> C <sub>recalcitrant</sub>
Synthetic vivianite *					1	Viv <sub>synth</sub>
Synthetic vivianite *				labile	1	Viv <sub>synth</sub> C <sub>labile</sub>
Biogenic vivianite *					1	Viv <sub>bio</sub>

#### 4. TEXT S4: SYNTHESIS OF BIOGENIC VIVIANITE

The heterotrophic Fe(III)-reducing strain *Shewanella oneidensis* MR-1 was pre-cultivated on agar plates prepared from sterile LB-medium (10 g L<sup>-1</sup> peptone, 5 g L<sup>-1</sup> yeast extract, 6 g L<sup>-1</sup> NaCl, 12 g L<sup>-1</sup> agar). After 24 h at 28°C, single colonies were transferred to 50 mL sterile liquid LB medium (10 g L<sup>-1</sup> peptone, 5 g L<sup>-1</sup> yeast extract, 6 g L<sup>-1</sup> NaCl) in 250 mL flasks. The inoculated liquid medium was incubated at 28°C for 14 h on a shaker at 150 rpm.

For production of biogenic vivianite, *Shewanella oneidensis* MR-1 was cultivated in anoxic medium containing 1.36 g NaCl, 1.24 g MgCl<sub>2</sub> × 6H<sub>2</sub>O, 0.16 g CaCl<sub>2</sub> × 2H<sub>2</sub>O, 0.8 g Na<sub>2</sub>SO<sub>4</sub>, 0.3 g NH<sub>4</sub>Cl, 0.6 g KCl, 5 g Na<sub>2</sub>CO<sub>3</sub>, 1 g yeast extract, 9 g lactic acid and 4 g HEPES buffer in 2 L high-purity H<sub>2</sub>O (with a resistance of 18.2 MΩ × cm at 25°C), which was prepared using a Widdel flask. The medium was autoclaved and made anoxic by flushing with N<sub>2</sub>/CO<sub>2</sub> (v/v, 90/10) after autoclaving. After cooling, the medium was separated equally into two sterilized 2 L Schott bottles. Anoxic and sterile Fe(III)-citrate solution was added to the medium to an initial concentration of 50 mM. NaH<sub>2</sub>PO<sub>4</sub> was added to a concentration of 5 mM. The medium was inoculated with 1% inoculum from the pre-cultivated cell suspensions. The Fe(III) reduction was monitored by quantifying the Fe(II) concentrations using the ferrozine assay (Stookey, 1970). Vivianite was collected when no further Fe(III) reduction occurred.

---

## 5. TEXT S5: MINERALOGICAL ANALYSIS

### 5.1. Quantification and identification of Fe minerals by Moessbauer spectroscopy

Gold capsules were opened and samples were filled into Plexiglas holders with an inner-diameter of 1.5 cm in an anoxic (100% N<sub>2</sub> atmosphere) glovebox and spread evenly in the holders to form a thin disc. The samples were stored in anoxic (100% N<sub>2</sub>) SCHOTT bottles at -20°C. They were taken out of respective SCHOTT bottles just before measurements and inserted into a closed-cycle exchange gas cryostat (Janis cryogenics). The spectra were recorded at 77 K for primary Fe(III) minerals and 140 K for incubated minerals in transmission geometry using a constant acceleration drive system (WissEL) in the Geomicrobiology group at the Center for Applied Geosciences, University of Tuebingen. A <sup>57</sup>Co source embedded in a Rhodium matrix was used as gamma radiation source. The sample spectra were calibrated against a 7-μm-thick α-<sup>57</sup>Fe foil at room temperature. The RECOIL software suite (University of Ottawa, Canada) was used for the calibration and spectra modeling using Voigt-based line shapes (Rancourt and Ping, 1991). The Lorentz half-width-half-maximum value was kept constant at the line width determined from the minimum line width of the third and fourth peak of the calibration foil in the models, and the Gauss' sigma parameter was used to account for line broadening. The relative proportion of the areas covered by the doublets and sextets of the total area of the Moessbauer spectrum is equivalent to the relative abundance of Fe in a particular crystal lattice site to the total Fe.

### 5.2. Identification of minerals by μXRD

Gold capsules were opened in a glovebox with 100% N<sub>2</sub> atmosphere. The sample material was collected from the gold capsules and ground with an agate mortar and pestle. A small aliquot was put on a silicon wafer and stored in N<sub>2</sub>-filled preserving jars until μXRD analysis under ambient atmospheric conditions (within a few minutes to avoid oxidation of O<sub>2</sub>-sensitive Fe minerals). A Bruker D8 Discover GADDS XRD<sup>2</sup>-microdiffractometer (Bruker AXS GmbH, Karlsruhe, Germany) from the Applied Mineralogy group at the University of Tübingen was used for μXRD equipped with a Co-anode with a Co-Kα wavelength of 1.79030 Å, a primary graphite monochromator, and a 2-dimensional HI-STAR-detector (Bruker Vântec 500, Bruker AXS GmbH, Karlsruhe, Germany). Crystalline minerals were identified by using the Match! Software

for phase identification from powder diffraction (Match!, Crystal Impact, Bonn, Germany, version 3.9.0.158).

## 6. TEXT S6: CHARACTERIZATION OF PRIMARY Fe(III) MINERALS

Prior to simulated low-grade metamorphism experiments, the primary Fe(III) minerals (ferrihydrite, heat-treated ferrihydrite, and goethite) were characterized by  $\mu$ XRD,  $^{57}\text{Fe}$  Moessbauer spectroscopy and ICP-OES. This allowed for a detailed characterization of their mineralogy, crystallinity, and chemical composition (molar P/Fe and Si/Fe ratios).

### 6.1. Ferrihydrite

Analysis of the primary ferrihydrites (FhP, FhPSi<sub>low</sub>, and FhPSi<sub>high</sub>) revealed that the addition of  $\text{PO}_4^{3-}$  and Si did not affect the primary mineral identity: independent of the initial Si concentration, the Moessbauer spectra suggest the presence of a short-range ordered (SRO) Fe(III) mineral, with hyperfine parameters indicative of ferrihydrite (Fig. S1 A-C, Text S7; Eickhoff et al., 2014; Murad, 1996). Additionally,  $\mu$ XRD analysis suggest that X-ray amorphous Fe(III) minerals were formed, with the only reflections in the diffractogram being due to the presence of halite (NaCl; Fig. S1 D). However, while the center shift stayed constant for ferrihydrite synthesized at differing Si concentrations, the quadrupole splitting increased slightly from  $0.78 \text{ mm s}^{-1}$  to  $0.85 \text{ mm s}^{-1}$  with increasing Si concentration, suggesting Si-induced structural disordering of the ferrihydrite with increasing Si concentrations (Cismasu et al., 2014; Senn et al., 2015; van Genuchten et al., 2014). A similar effect was observed for the addition of  $\text{PO}_4^{3-}$ : ferrihydrite synthesized in the absence of  $\text{PO}_4^{3-}$  and Si (referred to as “Fh” hereafter) exhibited the lowest quadrupole splitting ( $0.7 \text{ mm s}^{-1}$ , Text S7) of all ferrihydrites synthesized, which implies that it had the highest crystallinity (Murad et al., 1988).

ICP-OES analysis of the primary ferrihydrite revealed that  $\text{PO}_4^{3-}$  adsorption and/or co-precipitation during mineral synthesis was non-quantitative, resulting in P/Fe ratios of approximately 0.01 in the mineral product independent of the Si concentration (P/Fe = 0.018 in synthesis solution). Si/Fe ratios in the primary ferrihydrite were 0, 0.04 and 0.2, respectively and thus, similar to  $\text{PO}_4^{3-}$ , Si adsorption and/ or co-precipitation was non-quantitative.

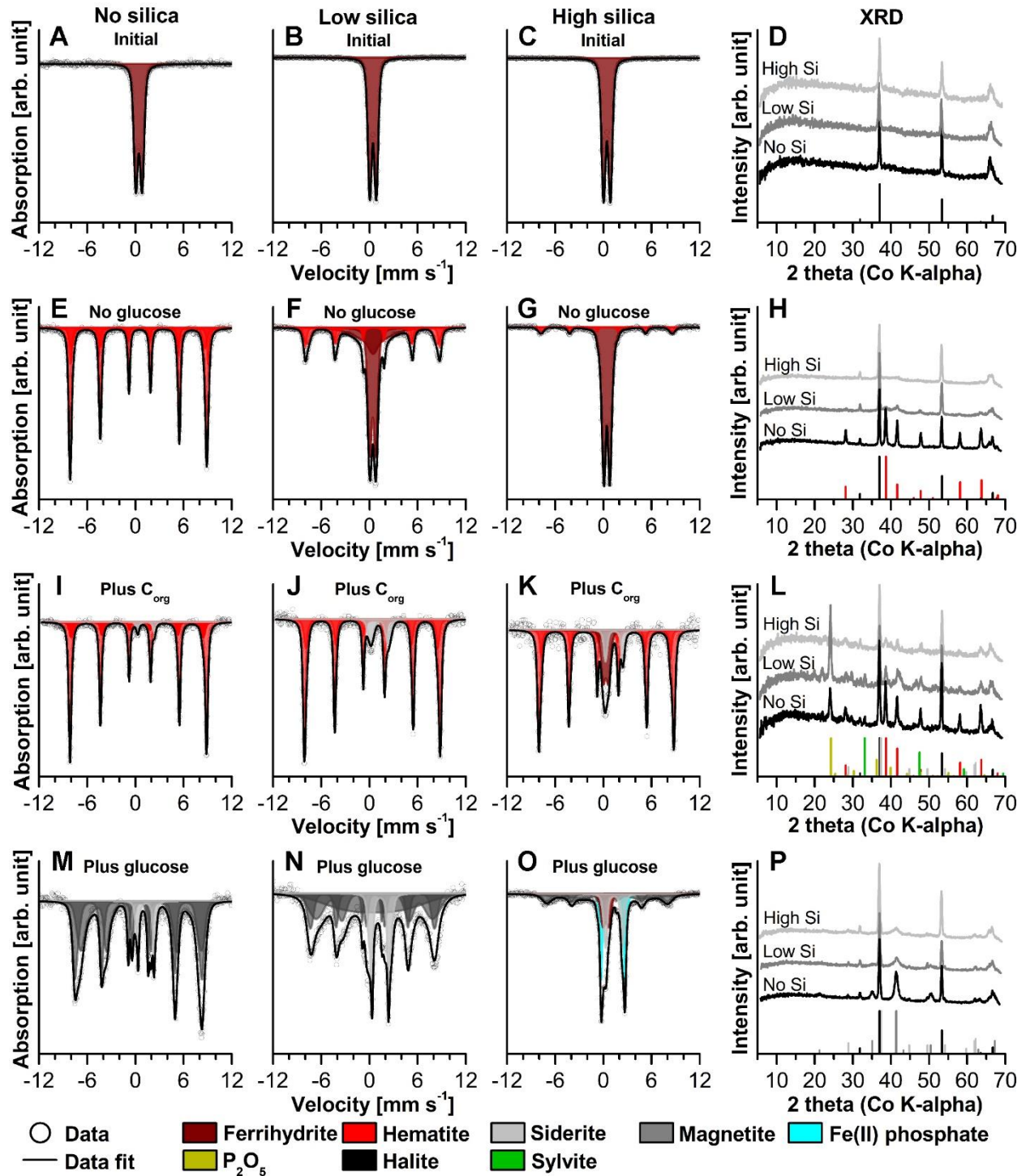


Fig. S1. Mössbauer spectra and X-ray diffractograms of primary ferrihydrite (with no, low or high silica; A-D) and ferrihydrite after incubation at  $170^\circ\text{C}$  and 1.2 kbar for 14 days in the absence of any organics (E-H), in the presence of recalcitrant, *Shewanella*-derived organic carbon ( $C_{\text{org}}$ , I-L) or in the presence of glucose as proxy for labile organic carbon (M-P). Mössbauer spectra for starting minerals were collected at 77 K, spectra for incubated minerals were collected at 140 K. Exception is the low Si + glucose setup (N) for which the spectrum was collected at 77 K due to difficulties of fitting the 140 K spectrum. The presence of halite and sylvite is due to mineral synthesis in a seawater ionic strength solution (0.5 M NaCl) and the use of KOH during mineral synthesis, respectively. Panels E-H and M-P represent data adapted from Halama (2016).



## 6.2. Heat-treated ferrihydrite

In order to test how early diagenetic mineral transformation, e.g., by moderate heating, during burial might have affected  $\text{PO}_4^{3-}$  remobilization from primary ferrihydrite, in one set of experiments  $\text{PO}_4^{3-}$ - and Si-loaded ferrihydrite were heated to  $80^\circ\text{C}$  prior to the metamorphism experiments.

Independent of the Si concentration of the primary ferrihydrite, the Mössbauer spectra of the heat-treated ferrihydrite ( $\text{Fh}_{\text{heatP}}$ ,  $\text{Fh}_{\text{heatPSi}_{\text{low}}}$  and  $\text{Fh}_{\text{heatPSi}_{\text{high}}}$ , hereafter) suggested the presence of a SRO Fe(III) mineral, likely ferrihydrite (Fig. S2 A-C, Eickhoff et al., 2014). No mineral phase transformation had taken place, which would have been indicated by either magnetic ordering of the mineral phase (development of a sextet in the Mössbauer spectrum) or reflections appearing in the X-ray diffractogram. This agrees with previous studies which suggested that both Si and  $\text{PO}_4^{3-}$  (Senn et al., 2017; Toner et al., 2012) can inhibit or slow mineral ageing and recrystallization. However, although the mineral product remained X-ray amorphous (Figure 2D), Mössbauer spectroscopy revealed a shift in the quadrupole splitting to lower values for all three Si concentrations to between  $0.70 \text{ mm s}^{-1}$  ( $\text{Fh}_{\text{heatP}}$ ) and  $0.79 \text{ mm s}^{-1}$  ( $\text{Fh}_{\text{heatPSi}_{\text{high}}}$ ; Text S7. This suggests that the minerals had undergone some degree of structural re-ordering (Murad et al., 1988).

Additionally, the heat treatment did not have an apparent effect on the  $\text{PO}_4^{3-}$  remobilization (maximum of 0.34 mol.%  $\text{PO}_4^{3-}$  mobilization for  $\text{Fh}_{\text{heatPSi}_{\text{high}}}$ ) but induced a 5.3 mol.% remobilization of Si from  $\text{Fh}_{\text{heatPSi}_{\text{high}}}$ . Generally, this suggests that ferrihydrite, when formed under conditions relevant for the Archean ocean, might have been preserved during the initial stage of sediment diagenesis, depending on the geothermal gradient applied ( $20\text{-}50^\circ\text{C km}^{-1}$ ; Grotzinger and Jordan, 2016) until a depth of at least 1.5 km. Furthermore, the stabilizing effect of Si against mineral transformation would also have prevented  $\text{PO}_4^{3-}$  remobilization associated with crystal aging and mineral transformation (Senn et al., 2017).

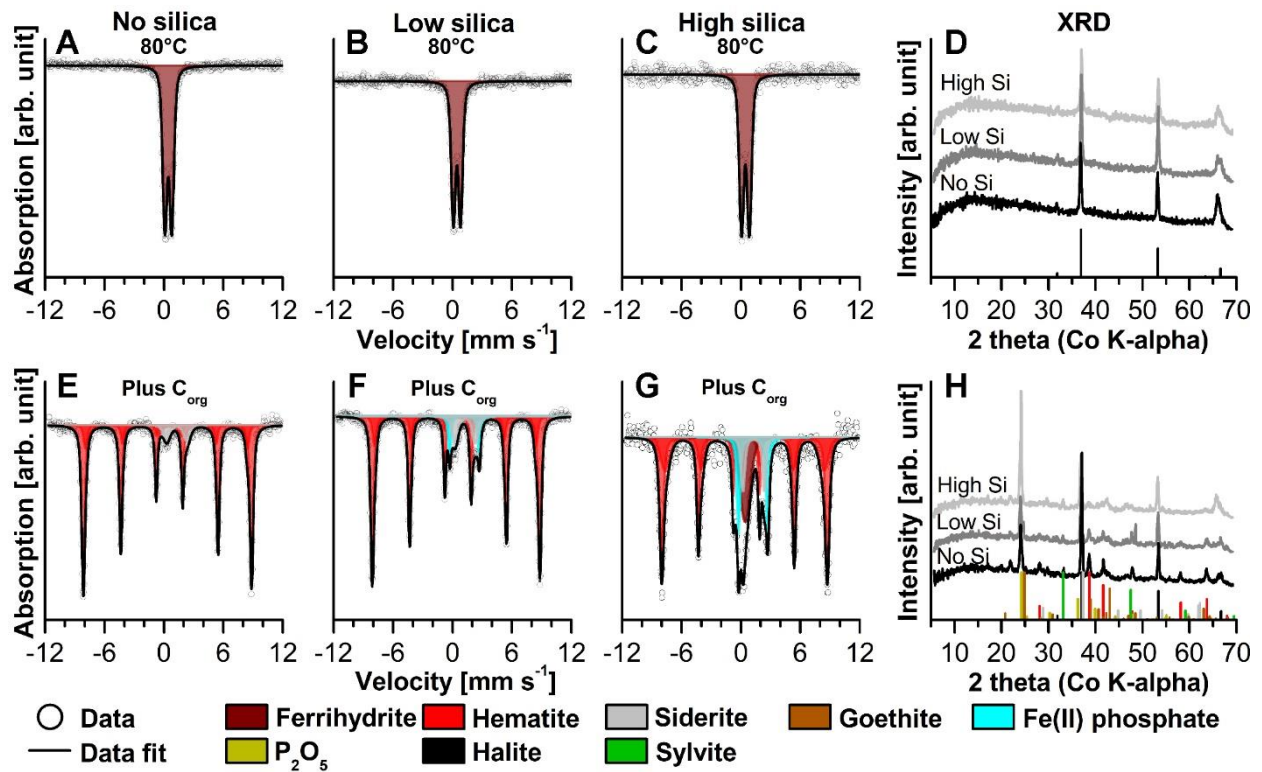


Fig. S2. Moessbauer spectra and X-ray diffractograms of heat-treated ferrihydrite (A-D) and heat-treated ferrihydrite after incubation at 170°C and 1.2 kbar for 14 days in the presence of recalcitrant, *Shewanella*-derived organic carbon ( $C_{org}$ , E-H). Moessbauer spectra for starting materials (first row) were collected at 77 K, spectra for incubated mixtures were collected at 140 K. The presence of halite and sylvite is due to mineral synthesis in a seawater ionic strength solution (0.5 M NaCl) and the use of KOH during mineral synthesis, respectively.

---

## 7. TEXT S7: MOESSBAUER FITTING PARAMETERS

Individual mineral phases were identified using  $^{57}\text{Fe}$  Moessbauer spectroscopy applying the criteria described below. However, all values given may be subject to change due to inclusion of foreign ions in the crystal lattice or association of minerals with organic matter.

- **Fe(III) minerals:**

- **Short-range ordered Fe(III) minerals:** SRO Fe(III) minerals, usually ferrihydrite, were identified by their narrow paramagnetic doublet with a center shift of  $0.45 \pm 0.01 \text{ mm s}^{-1}$  and quadrupole splitting of  $0.7\text{-}0.86 \text{ mm s}^{-1}$ . Both, the addition of  $\text{PO}_4^{3-}$  and Si resulted in an increase in the quadrupole splitting parameter, resulting in observed values at the higher end of the range given.
- **Goethite:** Goethite was identified by the presence of a magnetically ordered component (sextet) in the Mössbauer spectrum. A center shift of  $0.47 \pm 0.02 \text{ mm s}^{-1}$  in combination with a quadrupole shift of  $-0.12 \pm 0.03 \text{ mm s}^{-1}$  was characteristic of primary and metamorphically transformed goethite. The hyperfine field of primary goethite was between 46-47 T. In metamorphically transformed goethite this value increased and was in the range of 48-48.5 T.
- **Hematite:** Hematite was identified by the presence of a wide magnetically ordered sextet with hyperfine field values between 50 T to over 53 T. These values generally decreased with increasing Si concentrations. The center shift displayed values of  $0.45 \pm 0.03 \text{ mm s}^{-1}$ . The quadrupole shift was dependent on the presence of  $\text{PO}_4^{3-}$ , where it was positive with a value of approx.  $0.2 \text{ mm s}^{-1}$  in the absence of  $\text{PO}_4^{3-}$  and negative in the range of  $-0.07$  to  $-0.16 \text{ mm s}^{-1}$  when  $\text{PO}_4^{3-}$  was present.

- **Mixed-valent Fe minerals:**

- **Lipscombite:** Lipscombite as a mixed-valent Fe mineral was identified through its combination of a narrow (Fe(III)) and a wide (Fe(II)) paramagnetic doublet.
- **Magnetite:** Magnetite was identified by its characteristic double sextet in the Mössbauer spectrum, which describe the tetrahedrally and octahedrally coordinated Fe unit cell, respectively. Tetrahedrally coordinated Fe displays a low center shift

value of  $0.37 \pm 0.02 \text{ mm s}^{-1}$ , a quadrupole shift value of  $0-0.06 \text{ mm s}^{-1}$  and a hyperfine field value between 47-50 T. The octahedrally coordinated Fe usually has a center shift of  $0.75 \pm 0.05 \text{ mm s}^{-1}$ , a zero or negative quadrupole shift of down to  $-0.13 \text{ mm s}^{-1}$  and hyperfine field values that are approximately 2 T lower than for the tetrahedrally coordinated Fe in the range of 46-47.5 T.

- **Fe(II) minerals:**

- **Siderite:** Siderite was identified by a wide paramagnetic doublet with a center shift of  $1.35 \pm 0.05 \text{ mm s}^{-1}$  and quadrupole splitting of  $2-2.2 \text{ mm s}^{-1}$ .
- **Vivianite:** Vivianite was identified by its characteristic wide double doublet. Generally, vivianite doublets display a lower center shift than siderite ( $<1.3 \text{ mm s}^{-1}$ ) but a higher quadrupole splitting with the narrower doublet displaying values in the range of  $2.5-2.6 \text{ mm s}^{-1}$  and the wider doublet values  $>2.9 \text{ mm s}^{-1}$ .
- **Phosphoferrite:** Being a dehydration product of vivianite, phosphoferrite is characterized by a similar combination of two wide paramagnetic doublets. However, while the center shift shows comparable values to vivianite, the quadrupole splitting is lower with the narrow paramagnetic doublet having values of  $1.8-1.9 \text{ mm s}^{-1}$  and the wide doublet displaying values between  $2.5-2.6 \text{ mm s}^{-1}$ .

Table S2

Hyperfine parameters for primary Fe minerals. Results of the fitting spectra.  $\delta$  – isomer shift,  $\Delta E_Q$  – quadrupole splitting,  $\varepsilon$  – quadrupole shift (for sextets only),  $B_{hf}$  – hyperfine magnetic field, R. A. – relative abundance of the mineral phase at the given temperature,  $\pm$  - error in the relative abundance,  $\chi^2$  indicates the goodness of fit. Abbreviations of samples are per Table S1. “SPM Goethite” is “superparamagnetic goethite”. \*data per Halama (2016).

Sample	Temp [K]	Phase	$\delta$ [mm s <sup>-1</sup> ]	$\Delta E_Q$ [mm s <sup>-1</sup> ]	$\varepsilon$ [mm s <sup>-1</sup> ]	$B_{hf}$ [T]	R. A. [%]	$\pm$	$\chi^2$	HWHM
Fh	77	SRO Fe(III)	0.46	0.70	-	-	100	0	0.56	0.127
FhP	77	SRO Fe(III)	0.45	0.78	-	-	100	0	0.94	0.132
FhPSi <sub>low</sub>	77	SRO Fe(III)	0.45	0.8	-	-	100	0	4.5	0.132
FhPSi <sub>high</sub>	77	SRO Fe(III)	0.45	0.85	-	-	100	0	11.01	0.132
Fh <sub>heat</sub> P	77	SRO Fe(III)	0.45	0.7	-	-	100	0	1.04	0.13
Fh <sub>heat</sub> PSi <sub>low</sub>	77	SRO Fe(III)	0.46	0.73	-	-	100	0	0.82	0.13
Fh <sub>heat</sub> PSi <sub>high</sub>	77	SRO Fe(III)	0.46	0.79	-	-	100	0	0.66	0.13
GtP	77	Goethite	0.48	-	-0.12	46.5	100	0	3.17	0.13
GtPSi <sub>low</sub>	77	Goethite	0.48	-	-0.12	46.15	84.8	2.3	2.03	0.13
		SPM Goethite	0.42	-	-0.15	30.92	15.2	2.3		
GtPSi <sub>high</sub>	77	SRO Fe(III)	0.46	0.86	-	-	100	0	1.94	0.138
Viv <sub>synth</sub> *	140	Vivianite A	1.27	2.58	-	-	34.67	0.59	0.70	0.133
		Vivianite B	1.30	3.17	-	-	62.76	0.62		
		SRO Fe(III)	0.57	0.65	-	-	2.57	0.37		
Viv <sub>bio</sub> *	140	Vivianite A	1.29	2.56	-	-	72.50	3.10	0.73	0.134
		Vivianite B	1.29	3.13	-	-	15.60	3.30		
		SRO Fe(III)	0.41	0.97	-	-	11.85	0.95		

Table S3

Hyperfine parameters for Fe mineral products of low-grade metamorphism. Results of the fitting spectra.  $\delta$  – isomer shift,  $\Delta E_Q$  – quadrupole splitting,  $\epsilon$  – quadrupole shift (for sextets only),  $B_{\text{hf}}$  – hyperfine magnetic field, R. A. – relative abundance of the mineral phase at the given temperature,  $\pm$  - error in the relative abundance,  $\chi^2$  indicates the goodness of fit. Abbreviations of samples are per Table S1. All samples were measured at 140K. \*Sample FhPSi<sub>high</sub>C<sub>labile</sub> was measured at 77K due to difficulties of fitting the 140K spectrum. \*<sup>2</sup> data adapted per Halama (2016).

Sample	Phase	$\delta$ [mm s <sup>-1</sup> ]	$\Delta E_Q$ [mm s <sup>-1</sup> ]	$\epsilon$ [mm s <sup>-1</sup> ]	$B_{\text{hf}}$ [T]	R. A. [%]	$\pm$	$\chi^2$	HWHM
FhP * <sup>2</sup>	Hematite	0.47	-	-0.11	52.78	60	11	0.99	0.134
	Hematite	0.45	-	-0.07	51.53	19	11		
	Hematite	0.48	-	0.03	53.15	21.5	7.8		
FhPSi <sub>low</sub> * <sup>2</sup>	SRO Fe(III) mineral	0.43	0.76	-	-	45.1	2.1	1.79	0.134
	SRO Fe(III) transition phase	0.41	-	-0.06	14.25	24.3	1.3		
	Hematite	0.46	-	-0.07	51.98	12.3	2.7		
	Hematite	0.47	-	-0.09	50.24	18.3	2.8		
	Hematite	0.44	0.78	-	-	88.8	0		
FhPSi <sub>high</sub> * <sup>2</sup>	Hematite	0.48	-	-0.07	50.53	11.2	0	1.91	0.131
	Hematite	0.45	-	0.20	53.45	100	0	1.49	0.146
FhC <sub>recalcitrant</sub>	Hematite	0.45	-	0.20	53.45	100	0	1.49	0.146
	Siderite	1.34	2.07	-	-	3.7	0.6	0.78	0.146
FhPC <sub>recalcitrant</sub>	Hematite	0.46	-	-0.10	52.74	83.3	3.6		
	Hematite	0.39	-	-0.16	50.93	13	3.7	0.86	0.146
FhPSi <sub>low</sub> C <sub>recalcitrant</sub>	Siderite	1.29	2.17	-	-	11.9	3.7		
	Hematite	0.46	-	-0.10	52.46	66	16		
	Hematite	0.43	-	-0.12	50.75	22	17		
FhPSi <sub>high</sub> C <sub>recalcitrant</sub>	Siderite	1.36	2.16	-	-	9.2	2.2	0.54	0.146
	SRO Fe(III) mineral	0.32	0.68	-	-	17.4	2.5		
	Hematite	0.46	-	-0.09	52.12	58.6	6.2		
	Hematite	0.44	-	-0.12	49.76	14.8	7.3		
FhPC <sub>labile</sub> * <sup>2</sup>	Siderite	1.33	2.09	-	-	9.6	0.7	0.89	0.134
	Magnetite (tetrahedral)	0.37	-	0.01	48.41	44.0	1.9		
	Magnetite (octahedral)	0.75	-	-0.02	45.05	46.4	2.0		

Table S3 continued

Sample	Phase	$\delta$ [mm s <sup>-1</sup> ]	$\Delta E_Q$ [mm s <sup>-1</sup> ]	$\epsilon$ [mm s <sup>-1</sup> ]	$B_{hf}$ [T]	R. A. [%]	$\pm$	$\chi^2$	HWHM
FhPSi <sub>low</sub> C <sub>labile</sub> *2	Siderite	1.35	2.31	-	-	17.0	1.4	0.77	0.134
	Magnetite?	0.57	7.64	-	-	31.6	3.4		
	Magnetite (tetrahedral)	0.37	-	0.03	47.90	19.5	2.2		
	Magnetite (octahedral)	0.71	-	-0.08	44.93	31.8	3.3		
*FhPSi <sub>high</sub> C <sub>labile</sub> *2	SRO Fe(III) mineral	0.32	0.75	-	-	16	2.5	0.64	0.131
	Siderite	1.33	2.14	-	-	23	5.4		
	Vivianite A	1.22	2.65	-	-	2.1	8.8		
	Vivianite B	1.22	2.97	-	-	26.4	7.8		
	Magnetite (tetrahedral)	0.45	-	0.02	46.71	13.7	2.6		
	Magnetite (octahedral)	0.89	-	-0.13	35.83	18.8	4.7		
Fh <sub>heat</sub> PC <sub>recalcitrant</sub>	Siderite	1.31	2.04	-	-	7	1	0.75	0.146
	Hematite	0.46	-	-0.10	52.71	79.9	3.3		
	Hematite	0.42	-	-0.15	50.69	13.1	3.4		
Fh <sub>heat</sub> PSi <sub>low</sub> C <sub>recalcitrant</sub>	Siderite	1.30	2.06	-	-	10.1	1.7	0.85	0.146
	Fe(II) phosphate	1.22	2.99	-	-	7.2	1.5		
	Hematite	0.46	-	-0.10	52.50	67.2	3.2		
	Hematite	0.42	-	-0.12	50.43	15.6	3.2		
Fh <sub>heat</sub> PSi <sub>high</sub> C <sub>recalcitrant</sub>	Siderite	1.29	2.15	-	-	8.8	4	0.61	0.146
	SRO Fe(III) mineral	0.44	0.75	-	-	15.7	2.5		
	Fe(II)phosphate	1.24	2.95	-	-	13	3.9		
	Hematite	0.46	-	-0.09	51.90	40.6	6.5		
	Hematite	0.52	-	-0.15	49.72	22	7.4		

Table S3 continued

Sample	Phase	$\delta$ [mm s <sup>-1</sup> ]	$\Delta E_Q$ [mm s <sup>-1</sup> ]	$\epsilon$ [mm s <sup>-1</sup> ]	$B_{hf}$ [T]	R. A. [%]	$\pm$	$\chi^2$	HWHM
GtPC <sub>recalcitrant</sub>	Siderite	1.33	1.99	-	-	10.1	0.8	0.88	0.146
	Goethite	0.50	-	-0.07	46.62	22.9	3.4		
	Goethite	0.45	-	-0.13	48.23	67	3.2		
GtPSi <sub>low</sub> C <sub>recalcitrant</sub>	Siderite	1.33	2.00	-	-	9.9	1.1	0.74	0.146
	Goethite	0.47	-	-0.10	46.19	26.7	5.1		
	Goethite	0.45	-	-0.13	48.16	63.4	4.8		
Viv <sub>bio</sub> * <sup>2</sup>	Vivianite A	1.28	2.46	-	-	58	20	0.54	0.129
	Vivianite B	1.30	2.95	-	-	42	20		
Viv <sub>synth</sub> * <sup>2</sup>	Phosphoferrite A	1.32	1.89	-	-	63.4	0.8	0.66	0.129
	Phosphoferrite B	1.30	2.50	-	-	36.6	0.8		
Viv <sub>synth</sub> C <sub>labile</sub> * <sup>2</sup>	Phosphoferrite A	1.31	1.86	-	-	33.9	0.6	1.04	0.127
	Phosphoferrite B	1.28	2.60	-	-	34.8	0.7		
	Lipscombite (Fe(III))	0.51	0.75	-	-	16	0.3		
	Lipscombite (Fe(II))	1.30	3.28	-	-	15.4	0.5		



---

## 8. TEXT S8: METAMORPHIC MINERAL TRANSFORMATION

### 8.1. Metamorphic mineral transformations in dependence of $C_{\text{org}}$ quantity and quality, Si concentrations and diagenetic heating

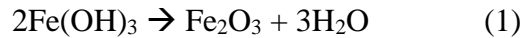
We expect the mineral transformations driven by low-grade metamorphism to be driven by several interdependent factors: First, the extent of association between primary minerals and biomass, which likely was determined wither by different putative Fe(II)-oxidizing mechanisms during BIF genesis or by variability in metamorphic (mineral) products formed by microorganisms. Second, the reactivity of  $C_{\text{org}}$ , where e.g. fermentation could have broken down complex (recalcitrant,  $C_{\text{recal}}$ )  $C_{\text{org}}$  into more labile and reactive ( $C_{\text{lab}}$ )  $C_{\text{org}}$ . In the presence of  $C_{\text{org}}$ , metamorphic mineral transformations include:(1) thermochemical Fe(III) reduction, where  $C_{\text{org}}$  serves as a reducing agent for Fe(III), (2) the reaction of Fe(II) with the precursor ferric(oxyhydroxide) or other reaction products such as  $\text{CO}_2$ , and (3) non-redox based pressure/temperature-driven mineral transformations. In the absence of  $C_{\text{org}}$ , non-redox based mineral transformations result from increased pressure and temperature during burial. Third, variable association of primary minerals with Si, resulting in different Si/Fe ratios. Finally, primary minerals, such as ferrihydrite, would likely have experienced diagenetic heating prior to low-grade metamorphism. This heating might either have resulted in thermal “healing” of the minerals or mineral transformation into thermodynamically more stable minerals, resulting in higher crystallinity and lower reactivity due to decreased specific surface area (SSA). In order to simplify the discussion, the focus will largely be placed on comparing the results of the two end-member scenarios, the high Si setups that represent conditions mimicking an Archean ocean relative to the no Si setups that are more applicable to modern ocean surface water.

#### 8.1.1. *Metamorphic mineral transformation in the absence of $C_{\text{org}}$*

To quantify the influence of low-grade metamorphism on the  $\text{PO}_4^{3-}$  remobilization from  $C_{\text{org}}$  limited systems (Thompson et al., 2019), where Fe(III) minerals and biomass would potentially have been deposited separately, we subjected Si-containing (FhPSi<sub>low</sub> and FhPSi<sub>high</sub>) and Si-free ferrihydrite (FhP) to low-grade metamorphic conditions without the addition of any  $C_{\text{org}}$  (supplementary text S3).

Mineral transformations in the  $C_{\text{org}}$ -free setups was solely driven by non-redox, pressure-temperature driven reactions. Ferrihydrite transformation depended on the amount of Si present

during the mineral synthesis, where increasing concentrations of Si resulted in increasing amounts of primary ferrihydrite being preserved (Fig S1). Analysis of the Mössbauer spectrum of FhPSi<sub>high</sub> revealed that approximately 89% of the ferrihydrite was preserved (based on the spectral area, Fig. S1 G) and 11% of the initially present ferrihydrite dehydrated to hematite following equation (1) (Cornell and Schwertmann, 2003),



Ferrihydrite was identified by its narrow paramagnetic doublet (Murad et al., 1988), while hematite was identified by its characteristically wide magnetically ordered sextet in the Mössbauer spectrum (Cornell and Schwertmann, 2003; Ericsson et al., 1986; Posth et al., 2013). The mineralogy was confirmed with  $\mu$ XRD (Fig. S1 H, supplementary text S7). The low extent of ferrihydrite transformation suggests that Si had an inhibitory effect on the metamorphic transformation of ferrihydrite to hematite (Campbell et al., 2002; Carlson and Schwertmann, 1981; Toner et al., 2012). This could potentially be related to Fe-O-Si bonds that need to be broken before ferrihydrite can be transformed to hematite (Campbell et al., 2002; Carlson and Schwertmann, 1981; Glasauer et al., 2000). Alternatively, Si can prevent recrystallization and aggregation of ferrihydrite (nano-)particles, which would be required for further structural ordering (Rzepa et al., 2016). Indeed, hematite formed in the presence of high concentrations of Si shows wide reflections in the corresponding X-ray diffractogram, indicative of low crystallinity (Fig. S1 H). Additionally, the higher hyperfine field parameter (51.3-53.2 T compared to 50.5 T in the high Si setup) and sharper reflections in the X-ray diffractogram of the Si-free hematite further suggest that incorporation of Si into the crystal structure, or its adsorption, inhibits magnetic ordering and crystal growth (Campbell et al., 2002). Consistent with the suggested mechanism, the extent of hematite formation increased to 30.6% in FhPSi<sub>low</sub> and ferrihydrite was quantitatively transformed to hematite in the absence of Si (FhP, Fig. S1 E and F, supplementary text S7). X-ray diffractograms additionally showed narrower reflections representative of hematite with decreasing Si concentration (Fig. S1 H).

### 8.1.2. *Metamorphic mineral transformation in the presence of C<sub>recal</sub>*

In order to further determine how low-grade metamorphism would influence PO<sub>4</sub><sup>3-</sup> remobilization from primary ferrihydrite if it would have been deposited as cell-Fe(III) mineral

aggregates, e.g. as a result of photoferrotrophy (Posth et al., 2010), and thus in thight association with  $C_{\text{org}}$ , we incubated ferrihydrite in the presence of  $C_{\text{recal}}$ .

Incubation of ferrihydrite synthesized in the absence of both Si and  $\text{PO}_4^{3-}$  ( $\text{Fh}C_{\text{recal}}$ ) resulted in its quantitative transformation into hematite through previously described mechanisms (Posth et al., 2013). However, in comparison to other, Si and  $\text{PO}_4^{3-}$  bearing, hematites it had a slightly ( $\sim 0.7$  T, supplementary text S7) higher hyperfine field parameter, indicating that, similar to Si (Toner et al., 2012),  $\text{PO}_4^{3-}$  may inhibit mineral ordering and transformation (Paige et al., 1997; Senn et al., 2017), albeit to a lesser extent at concentrations used here.

Compared to the setups without admixed  $C_{\text{org}}$ ,  $\text{Fh}PC_{\text{recal}}$ ,  $\text{FhPSi}_{\text{low}}C_{\text{recal}}$  and  $\text{FhPSi}_{\text{high}}C_{\text{recal}}$  showed additional redox reactions occurring during low-grade metamorphism in which the thermochemical reduction of Fe(III) to Fe(II) was coupled to the oxidation of  $C_{\text{org}}$ , resulting in  $\text{CO}_2$  formation. The reaction of this  $\text{CO}_2$  with freshly formed Fe(II) resulted in the formation of siderite (Halama et al., 2016; Köhler et al., 2013; Posth et al., 2013) as identified by a wide paramagnetic doublet in the Mössbauer spectra (Fig. S1 I-K, supplementary text S7, Posth et al., 2013) and by  $\mu\text{XRD}$  (Fig. S1 L). The extent of thermochemical Fe(III) reduction, as marked by siderite formation, ranged from 3.7% ( $\text{Fh}PC_{\text{recal}}$ ) to 12% ( $\text{FhPSi}_{\text{low}}C_{\text{recal}}$ , supplementary text S7). The second major mineral product identified in all three setups was hematite (Fig. S1 I-K, supplementary text S7, Cornell and Schwertmann, 2003; Ericsson et al., 1986; Posth et al., 2013), which was formed through previously described mechanisms. With increasing Si concentrations, the value of the mean magnetic hyperfine field decreased (supplementary text S7), which together with wider reflections in the X-ray diffractogram (Fig. S1 L) suggests decreasing magnetic and structural ordering, lower crystallinity and potentially smaller crystallite size, resulting in higher SSA. In addition to siderite and hematite, 17.4% of the primary ferrihydrite was preserved in the  $\text{FhPSi}_{\text{high}}C_{\text{recal}}$  setup (Fig. S1 K). However, compared to non-incubated ferrihydrite it displayed a decrease in both center shift and quadrupole splitting, suggesting that it had undergone some recrystallization or structural ordering, potentially into poorly crystalline lepidocrocite (supplementary text S7, Murad et al., 1988; Murad and Cashion, 2004; Murad and Schwertmann, 1984). For all three setups the X-ray diffractogram suggested the presence of  $\text{P}_2\text{O}_5$ , presumably in form of a polymer or a surface group (Fig. S1 L).

### 8.1.3. *Metamorphic mineral transformation in the presence of $C_{lab}$*

We also considered the scenario where more labile  $C_{org}$  was preserved to a depth where it could act as a reducing agent for primary BIF minerals during low-grade metamorphism; for instance, acetate (a common by-product of for example glucose fermentation or microbial Fe(III) reduction) has been reported from the rock record (Li et al., 2011). Here, we used glucose as a proxy for labile  $C_{org}$  during low-grade metamorphism of ferrihydrite in order to determine how this would influence metamorphic mineral transformation and resulting  $PO_4^{3-}$  remobilization consistent with previous diagenesis studies (Halama et al., 2016; Köhler et al., 2013; Posth et al., 2013; Robbins et al., 2015).

Our data show that low-grade metamorphic transformation of  $FhPSi_{high}C_{lab}$  resulted in the formation of magnetite (32.5% of the spectral area as determined by Mössbauer spectroscopy; Fig S1 O, Text S7; e.g. Byrne et al., 2016). However, the magnetite formed was poorly crystalline and distorted, as indicated by line broadening in the Mössbauer spectrum (Fig S1 O). Additionally, wide reflections in the X-ray diffractogram suggest low crystallinity (Fig. S1 P). Magnetite was likely formed via solid-state conversion, where Fe(II) formed via the thermochemical reduction of Fe(III), subsequently adsorbed onto hematite (Hansel et al., 2003). The poor crystallinity of the magnetite suggests that during this process adsorbed and/or co-precipitated Si limited the extent to which Fe(II) was able to interact with the mineral surface, probably either by limiting available surface sites or Si complexation with Fe polymers (Cismasu et al., 2014), thus limiting the extent of mineral transformation and re-crystallization (Jones et al., 2009). Moessbauer spectroscopy also suggested the formation of siderite, which accounted for 23% of the spectral area (Fig S1 O; supplementary text S7). Furthermore, the presence of two additional wide doublets suggests the presence of a second Fe(II) mineral phase, possibly vivianite (Forsyth et al., 1970), which accounted for 28.5% of the spectral area. However, no reflections for vivianite were visible in the X-ray diffractogram (Fig. S1 P), indicating that if present, vivianite was poorly crystalline. The formation of vivianite has frequently been described from anoxic (sedimentary) environments rich in  $PO_4^{3-}$  (e.g. Dijkstra et al., 2018; Dijkstra et al., 2016; Hsu et al., 2014; O'Connell et al., 2015; Poulton and Canfield, 2006; Rothe et al., 2016), where it forms through the reaction of Fe(II) with  $PO_4^{3-}$ . However, the two Fe(II) doublets in vivianite often have comparable spectral areas (1:1 to 1:2 ratio; e.g. Amthauer and Rossman, 1984; Forsyth et al., 1970; Manning et al., 1999; Rouzies and Millet, 1993). Therefore,

the interpretation of this mineral phase as vivianite is not unequivocal because the ratio deviates considerably (ratio of approx. 1:13). An alternative interpretation with regards to vivianite is provided in supplementary text S9. Although this alternative interpretation achieved a similar goodness of fit ( $X^2$ ) and a ratio between the spectral areas lower than 1:2, which is characteristic for vivianite, it resulted in higher uncertainties in the relative abundances of the mineral phases. Consequently, we maintain the interpretation provided here. In addition to magnetite, siderite and vivianite, 16% of the initial ferrihydrite was preserved, as identified by Mössbauer spectroscopy (Fig. S1 O, supplementary text S7).

In contrast to the FhPSi<sub>high</sub> setup, both vivianite and preserved ferrihydrite were absent in FhPC<sub>lab</sub> and FhPSi<sub>low</sub>C<sub>lab</sub> and we only observed in the formation of siderite and magnetite (Fig. S1 M and P, supplementary text S7). Consistent with the previously discussed inhibitory effect of Si on the solid state conversion of ferrihydrite to magnetite (Hansel et al., 2003), the extent of magnetite formation was much larger in the Si-free setup (90.4% and 83% for no and low Si, respectively, compared to 32.5%, Fig. S1 M, supplementary text S7). Additionally, the decreasing Si concentrations resulted in the formation of higher crystallinity magnetite as indicated by increasingly clearly defined, undistorted double sextets in the Moessbauer spectrum (e.g. Byrne et al., 2016) and narrower reflections in the X-ray diffractogram (Fig. S1 M, N and P).

Noticeably, the presence of Si, while partially inhibiting the formation of magnetite in the high Si setup (1.6 mM), also seemed to have increased the overall reducibility of the ferrihydrite. This is reflected in the lower extent of thermochemical Fe(III) reduction of 39.7% in the Si-free setup (FhPC<sub>labile</sub>) compared to the high Si setup (FhPSi<sub>high</sub>C<sub>labile</sub>), where 62.3% of the Fe(III) was reduced (Fig. S1 M-O, supplementary text S7), a value close to the 60% Fe(III) reduction expected based on the electron ratio used ( $C/Fe = 0.6$ ). The extent of Fe(III) reduction is the sum of Fe(II) contained in all reduced Fe mineral phases and thus encompasses siderite, vivianite and magnetite (one third of its spectral area, based on the ideal magnetite stoichiometry). The higher reducibility of Si-containing ferrihydrite is probably due to a smaller ferrihydrite particle size in the presence of Si (Vempati et al., 1990) resulting in higher SSA and thus higher intrinsic reactivity (Jones et al., 2009; Postma, 1993).

#### 8.1.4. *Metamorphic mineral transformation following diagenetic heating*

In order to determine the transformation of and  $\text{PO}_4^{3-}$  remobilization from ferrihydrite that had undergone moderate heating ( $80^\circ\text{C}$ ) during early diagenesis, we subjected mixtures of diagenetic ferrihydrite and recalcitrant  $\text{C}_{\text{org}}$  to simulate low-grade metamorphism. In the presence of high concentrations of Si ( $\text{Fh}_{\text{heat}}\text{PSi}_{\text{high}}\text{C}_{\text{recal}}$ ), this resulted in the thermochemical reduction of ~22% of the initially present Fe(III) as estimated based on Mössbauer spectroscopy (Fig S2 G). This is more than 2 times the amount of Fe(III) reduced in the corresponding experiment  $\text{FhPSi}_{\text{high}}\text{C}_{\text{recal}}$  without any prior heat-treatment (Fig. S1 K), although generally the same minerals were formed. Siderite, which accounted for 8.8% of the spectral area, as well as hematite (Fig. S2 G, supplementary text S7, Ericsson et al., 1986; Posth et al., 2013), were identified by Mössbauer spectroscopy. Broad reflections in the X-ray diffractogram suggested hematite was poorly crystalline (Fig. S2 H). Furthermore, ferrihydrite accounted for 15.7% of the spectral area (Fig S2 G, supplementary text S7), suggesting that it was partially stabilized by Si during low-grade metamorphism (Campbell et al., 2002; Carlson and Schwertmann, 1981; Toner et al., 2012). A second Fe(II) mineral phase accounted for 13.0% of the spectral area and was identified as Fe(II) phosphate, potentially vivianite, based on its hyperfine parameters (Fig. S2 G, supplementary text S7, Forsyth et al., 1970). However, we were not able to identify this mineral by  $\mu\text{XRD}$ , thus it was likely poorly crystalline. In addition, the previously in setups with  $\text{C}_{\text{recal}}$  described  $\text{P}_2\text{O}_5$  phase was identified by  $\mu\text{XRD}$ .

Simulated metamorphism of  $\text{Fh}_{\text{heat}}\text{PC}_{\text{recal}}$  resulted in both the formation of siderite (Posth et al., 2013) and hematite (Cornell and Schwertmann, 2003), whose narrow reflections in the X-ray diffractogram suggest it to be of higher crystallinity than the hematite formed from the high-Si heat-treated ferrihydrite (Fig. S2 E and H). However, in contrast to simulated low-grade metamorphism of  $\text{Fh}_{\text{heat}}\text{PSi}_{\text{high}}\text{C}_{\text{recal}}$ , no formation of vivianite was observed. Additionally, with only 7% Fe(III) reduced to Fe(II) (present as siderite; Fig. S2 E, supplementary text S7), the extent of thermochemical Fe(III) reduction was much lower and thus essentially comparable to  $\text{FhPSi}_{\text{high}}\text{C}_{\text{recal}}$  and  $\text{FhPC}_{\text{recal}}$ . Therefore, the heat-induced changes in the primary ferrihydrite alone had no direct influence on metamorphic transformation of the diagenetic (heat-treated) ferrihydrite. Yet, it begs the question what caused the higher reducibility of the Si-containing ferrihydrite (~22% Fe(II) compared to 7% Fe(II)) and the formation of vivianite during low-grade metamorphism of  $\text{Fh}_{\text{heat}}\text{PSi}_{\text{high}}\text{C}_{\text{recal}}$ . One potential explanation might be that not only the Fe(III)

---

minerals but also the associated Si would have been subject to alteration during the heat pretreatment preceding the simulated low-grade metamorphism. Consequently, the Si associated with the Fe(III) minerals would potentially have been subject to polymerization prior to low-grade metamorphism (Goto, 1956; Iler, 1979; Krauskopf, 1956). The ferrihydrite particles could have catalyzed this process by acting as nucleation sites where the initially present monomers would have been transformed into oligomers and ultimately polymers (Swedlund et al., 2010; Swedlund et al., 2011; Swedlund and Webster, 1999). Consequently, during the following low-grade metamorphism the already present Si polymers would have limited further Fe polymerization (Pokrovski et al., 2003) and ferrihydrite particle aggregation necessary for mineral growth and transformation into hematite. This would have resulted in a lower overall crystallinity and smaller particle size compared to  $\text{Fh}_{\text{heat}}\text{PC}_{\text{recal}}$ ,  $\text{FhPC}_{\text{recal}}$ , and  $\text{FhP}$  as suggested by wide reflections in the X-ray diffractogram (Fig. S1 L, Fig. S2 H) and indicated by a narrower hyperfine field in the Mössbauer spectrum (supplementary text S7; Rzepa et al., 2016). The lower crystallinity and smaller particle size would have caused an increased particle reactivity (Anschutz and Penn, 2005; Jones et al., 2009; Wang et al., 2013), resulting in the observed higher thermochemical Fe(III) reduction with concomitant  $\text{PO}_4^{3-}$  release and formation of vivianite through the reaction of  $\text{PO}_4^{3-}$  and Fe(II) (e.g. Dijkstra et al., 2018; Dijkstra et al., 2016).

## 9. TEXT S9: ALTERNATIVE INTERPRETATION OF MOESSBAUER SPECTRA FOR FhPSi<sup>high</sup>C<sub>lab</sub>, Fh<sup>heat</sup>PSi<sup>low</sup>C<sub>crecal</sub> AND Fh<sup>heat</sup>PSi<sup>high</sup>C<sub>crecal</sub>

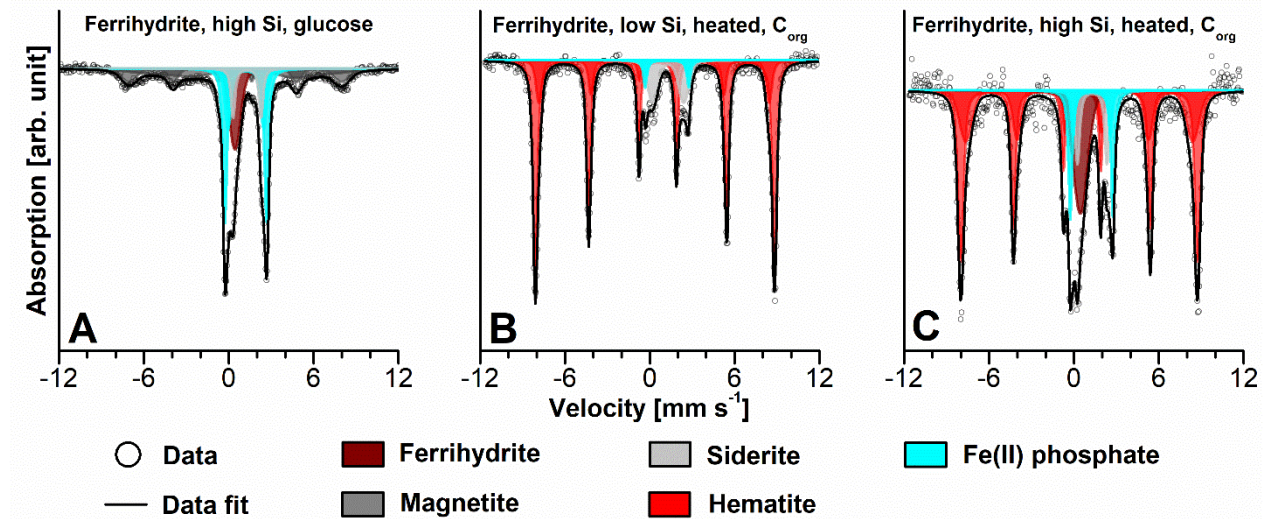


Fig. S3. Alternative interpretation of vivianite-containing  $^{57}\text{Fe}$  Moessbauer spectra. Mineral mixtures were subjected to simulated low-grade metamorphism at  $170^\circ\text{C}$  and 1.2 kbar for 14 days. Specifics of the primary minerals and organics used are displayed in the heading of the respective panels. Spectra were collected at 140 K. Panel A represents data adapted from Halama (2016).

The interpretation of the Moessbauer spectra given here clearly identified vivianite as second Fe(II) mineral phase in addition to siderite and generally achieved a comparable goodness of fit. However, the individual error in the relative abundances of the mineral phases is much higher than for the interpretations provided in the main text (compare parameters in supplementary text S7).



Table S4

Hyperfine parameters. Results of the fitting spectra.  $\delta$  – isomer shift,  $\Delta E_Q$  – quadrupole splitting,  $\varepsilon$  – quadrupole shift (for sextets only),  $B_{\text{hf}}$  – hyperfine magnetic field, R. A. – relative abundance of the mineral phase at the given temperature,  $\pm$  - error in the relative abundance,  $\chi^2$  indicates the goodness of fit. \*data adapted from Halama (2016).

Sample	Temp [K]	Phase	$\delta$ [mm s <sup>-1</sup> ]	$\Delta E_Q$ [mm s <sup>-1</sup> ]	$\varepsilon$ [mm s <sup>-1</sup> ]	$B_{\text{hf}}$ [T]	R. A. [%]	$\pm$	$\chi^2$	HWHM
A *	140	SRO Fe(III)	0.44	0.56	-	-	16.2	4.6	0.62	0.131
		Siderite	1.30	1.98	-	-	8.9	5.1		
		Vivianite	1.22	2.52	-	-	15.0	18.0		
		Vivianite	1.21	2.96	-	-	28.0	14.0		
		Magnetite	0.46	-	0.02	46.69	13.7	4.1		
		Magnetite	0.93	-	-0.15	36.09	19.0	6.4		
		Siderite	1.30	2.19	-	-	12	15		
B	140	Vivianite	1.22	2.94	-	-	2	83	0.88	0.146
		Vivianite	1.21	3.08	-	-	3	82		
		Hematite	0.46	-	-0.1	52.50	67	80		
		Hematite	0.42	-	-0.12	50.4	16	19		
		SRO Fe(III)	0.44	0.72	-	-	15.7	3.5		
C	140	Siderite	1.28	2.09	-	-	7.4	4.2	0.61	0.146
		Vivianite	1.25	2.64	-	-	3.7	9.9		
		Vivianite	1.24	3.02	-	-	10.8	8.3		
		Hematite	0.46	-	-0.1	51.93	39.5	9.3		
		Hematite	0.49	-	-0.13	49.76	22.9	9.3		
		SRO Fe(III)	0.44	0.72	-	-	15.7	3.5		

## **10. TEXT S10: PO<sub>4</sub><sup>3-</sup> MOBILIZATION DURING METAMORPHIC GOETHITE TRANSFORMATION**

Besides ferrihydrite, other, more crystalline Fe(III) (oxyhydr)oxides such as goethite and lepidocrocite could also have been important as BIF precursor minerals. Therefore, in order to evaluate the potential of goethite as a BIF precursor mineral and to quantify the impact of a higher mineral crystallinity on the initial PO<sub>4</sub><sup>3-</sup> co-precipitation and/or adsorption, we synthesized goethite in the presence of three different Si and one fixed PO<sub>4</sub><sup>3-</sup>.

### **10.1. Methods**

#### *10.1.1. Goethite synthesis*

Goethite was synthesized following (Schwertmann and Cornell, 2008). Briefly, the same P, Si and NaCl concentrations as for the ferrihydrite synthesis were used. The resulting Fe:Si:P ratios were approximately 771:0:1, 771:8:1 and 771:25:1, respectively, for the different Si concentrations. Ultra-pure 18.2 MΩ × cm H<sub>2</sub>O was deoxygenated for 30 minutes by bubbling with N<sub>2</sub>. NaCl, PO<sub>4</sub><sup>3-</sup> and Si were added, and the pH was set to <4 before addition of 9.9 g FeCl<sub>2</sub> × 4 H<sub>2</sub>O under a constant backstream of N<sub>2</sub>. Next, 110 mL of a 1 M NaHCO<sub>3</sub> solution was added and the N<sub>2</sub> replaced by air (21% O<sub>2</sub>) at a flow rate of 30-40 mL min<sup>-1</sup> under constant stirring, resulting in complete oxidation after 48 h. The resultant precipitates were centrifuged at 4229 g and freeze-dried.

### **10.2. Results and Discussion**

#### *10.2.1. Characterization of primary goethite*

More crystalline Fe(III) (oxyhydr)oxides such as goethite could also have been important as BIF precursor minerals: note, lepidocrocite may also have been a primary phase, but as the less stable polymorph of goethite, we do not explicitly consider it here. While the slow oxidation of Fe<sup>2+</sup>, either by low concentrations of O<sub>2</sub> or through the activity of photoferrotrophs, could have formed lepidocrocite or goethite (Cornell and Schwertmann, 2003; Posth et al., 2014), higher Archean pCO<sub>2</sub> levels (Catling and Zahnle, 2020) should have favored the formation of goethite (Cornell and Schwertmann, 2003; Larese-Casanova et al., 2010). To evaluate the potential remobilization of PO<sub>4</sub><sup>3-</sup> during metamorphism, we first synthesized goethite at the same Si and PO<sub>4</sub><sup>3-</sup> concentrations described above.

We found that goethite formation (referred to as GtP, GtPSi<sub>low</sub>, and GtPSi<sub>high</sub> from hereon) was insensitive to PO<sub>4</sub><sup>3-</sup> at the ratio utilized in this study (molar P/Fe = 0.0013 in the synthesis solution), as only goethite were detected by both Mössbauer spectroscopy and  $\mu$ XRD (Fig. S4 A and D, Text S7; Larese-Casanova et al., 2010; Quin et al., 1988). This suggests that the influence of PO<sub>4</sub><sup>3-</sup> is concentration-dependent; this was also suggested by Quin et al. (1988) who found that only at molar P/Fe ratios exceeding 0.007 did PO<sub>4</sub><sup>3-</sup> suppress the formation of goethite. However, in the presence of low concentrations of Si (0.5 mM) the Mössbauer spectrum required a second, collapsed, sextet to obtain an optimal fit (Fig. S4 B, Text S7). This, together with less intense but wider reflections in the X-ray diffractogram (Fig. S4 D), suggests that Si partially restricted the structural ordering of goethite, resulting in decreased crystallinity and smaller particle sizes (Larese-Casanova et al., 2010; Murad, 1982; Quin et al., 1988). In contrast, the formation of goethite was completely inhibited in the presence of high concentrations of Si (1.6 mM) and an X-ray amorphous Fe(III) mineral was formed instead. Mössbauer spectroscopy indicated the presence of a SRO Fe(III) mineral phase whose hyperfine parameters were suggestive of ferrihydrite (Fig S4 C and D, Text S7, Eickhoff et al., 2014), which likely formed due to inhibited Fe(III) polymerization and constrained crystal growth in the presence of high Si concentrations (Cismasu et al., 2011; Voegelin et al., 2010). Thus, the Si concentrations exhibited a strong influence on goethite formation.

ICP-OES results suggest, that, comparable to ferrihydrite, PO<sub>4</sub><sup>3-</sup> removal during the initial synthesis was non-quantitative with P/Fe ratios of 0.0008, 0.0006 and 0.0006 for GtP, GtPSi<sub>low</sub> and GtPSi<sub>high</sub>, respectively. Similarly, Si removal was non-quantitative, with no Si being found in GtPSi<sub>low</sub> (Si/Fe = 0) and only approximately 66% (Si/Fe = 0.0213) of the Si present during the synthesis found in GtPSi<sub>high</sub>.

Our results suggest that the relevance of goethite as a primary mineral for BIF deposition and its impact on an early P cycle would have been strongly governed by seawater Si concentrations. If the early ocean would have been at saturation with respect to cristobalite (dissolved Si = 0.67 mM), goethite might have been formed, but if seawater Si concentrations approached saturation with regards to amorphous silica (2.2 mM Si), then goethite formation would have been inhibited and instead a ferrihydrite-like mineral phase would have been preferentially formed. Consequently, due the similarity of this SRO Fe(III) mineral with the

previously described ferrihydrite and the expected comparable mineral transformation pathways, GtPSi<sub>high</sub> was omitted from the simulated low-grade metamorphism experiments.

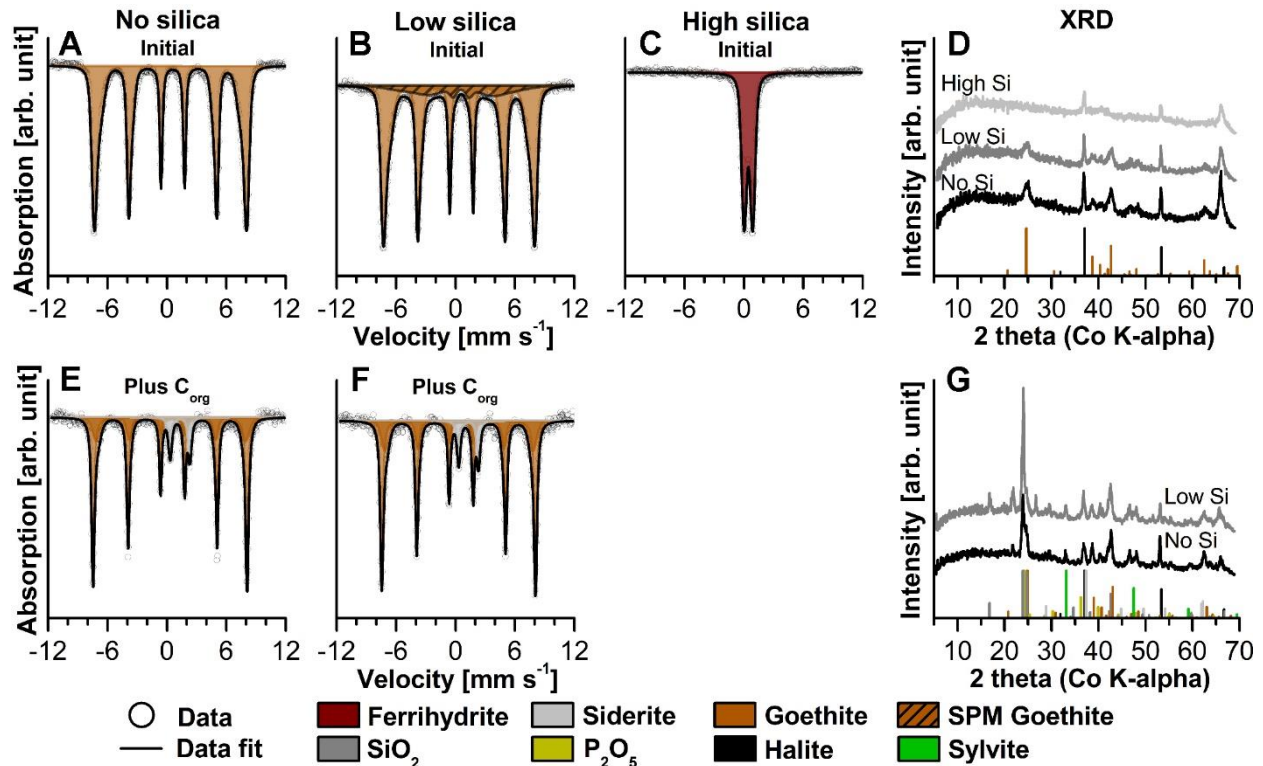


Fig. S4. Moessbauer spectra and X-ray diffractograms of primary goethite (A-D) and goethite after incubation at 170°C and 1.2 kbar for 14 days in the presence of recalcitrant, *Shewanella*-derived organic carbon ( $C_{org}$ , E-H). Moessbauer spectra for starting materials (A-C) were collected at 77 K, spectra for incubated mixtures (E-G) were collected at 140 K. The presence of halite and sylvite is due to mineral synthesis in a seawater ionic strength solution (0.5 M NaCl) and the use of KOH during mineral synthesis, respectively.

### 10.2.2. Metamorphic $PO_4^{3-}$ remobilization depends on Si concentration

In order to further quantify the influence of low-grade metamorphism on the  $PO_4^{3-}$  remobilization from the goethite formed, we subjected mixtures of goethite and recalcitrant  $C_{org}$  to low-grade metamorphic conditions (GtPSi<sub>low</sub> $C_{recal}$  and GtPC<sub>recal</sub> hereon after). Low-grade metamorphism of  $PO_4^{3-}$ -loaded goethite in the presence of  $C_{recal}$  resulted in only 2.1 mol.% of the initially present  $PO_4^{3-}$  being remobilized in the GtPSi<sub>low</sub> $C_{recal}$  setup and 1.1 mol.% in the GtPC<sub>recal</sub> setup. Following the line of argument in the main text, where 1.5 mol.%  $PO_4^{3-}$  were released from microbial biomass, the majority of this  $PO_4^{3-}$  is probably related to thermochemical oxidation/ degradation of biomass.

### 10.2.3. Metamorphic mineral transformation is independent of Si concentration

Simulated low-grade metamorphism of both, GtPSi<sub>low</sub>C<sub>recal</sub> and GtPC<sub>recal</sub>, resulted in the thermochemical reduction of approx. 10% of the primary goethite (Fig. S4 E and F, supplementary text S7). The resulting Fe(II)-containing mineral phase was identified as siderite by Mössbauer spectroscopy (Fig. S4 E and F, supplementary text S7, Posth et al., 2013). In both cases the only other Fe mineral phase identified by <sup>57</sup>Fe Moessbauer spectroscopy based on its characteristic hyperfine parameters was goethite (Fig. S4 E and F, supplementary text S7, Larese-Casanova et al., 2010; Quin et al., 1988). No further transformation to hematite had taken place, suggesting increased thermal stability of goethite under low-grade metamorphic conditions at the experimental timescale compared to the ferrihydrite used in our other experiments. This high thermal stability of goethite has been reported elsewhere (e.g. Gualtieri and Venturelli, 1999; Liu et al., 2013; Wolska and Schwertmann, 1989), where goethite only started to transform into hematite between 180 and 250°C. However, compared to the primary goethite, the metamorphosed goethite consisted of several magnetically ordered components and required two sextets for an optimal fit (Fig. S4 E and F, supplementary text S7). The second sextet showed a shift in the mean magnetic hyperfine field parameter to higher values. In the case of GtPC<sub>recal</sub> for example, it was approx. 1.7 T higher than the first sextet (48.23 T compared to 46.5 T, supplementary text S7), suggesting increased magnetic ordering (higher crystallinity) probably due to partial structural rearrangement of the primary goethite at higher temperatures (Frost et al., 2003a). This is corroborated by  $\mu$ XRD results, where metamorphosed goethite showed narrower reflections than freshly synthesized goethite, suggesting an increase in crystallinity (Fig. S4 G).

### 10.2.4. Metamorphic PO<sub>4</sub><sup>3-</sup> remobilization is independent of mineral transformation

The role of mineralogical changes in goethite and related effects on PO<sub>4</sub><sup>3-</sup> mobility during simulated low-grade metamorphism is ambiguous. On the one hand PO<sub>4</sub><sup>3-</sup> remobilization in the experiments with goethite can be explained by PO<sub>4</sub><sup>3-</sup> release from microbial biomass. However, even though goethite has a lower SSA than ferrihydrite (Cornell and Schwertmann, 2003), we would have expected PO<sub>4</sub><sup>3-</sup> released from biomass to be re-adsorbed to goethite when Si was absent, resulting in re-adsorption of PO<sub>4</sub><sup>3-</sup> (see previous discussion in supplementary text S8 and main text for effect of Si on PZC and PO<sub>4</sub><sup>3-</sup> sorption). One possibility could be that complex

organic, which have a high affinity for Fe(III) (oxyhydr)oxides (Gu et al., 1996; Gu et al., 1994; Schad et al., 2019), prevented the re-adsorption of  $\text{PO}_4^{3-}$  to goethite.

On the other hand, the low amount of  $\text{PO}_4^{3-}$  being remobilized compared to setups with ferrihydrite is likely directly related to the higher thermal stability of goethite. For example, in the  $\text{GtPSi}_{\text{low}}\text{C}_{\text{recal}}$  setup, where we identified a super paramagnetic mineral phase, partial recrystallization at high temperatures would potentially have resulted in some loss of SSA (Schwertmann et al., 1985; Strauss et al., 1997), causing some  $\text{PO}_4^{3-}$  to be remobilized. However, this decrease in SSA should have been much lower than during the ferrihydrite to hematite transformation (Cornell and Schwertmann, 2003), resulting in lower  $\text{PO}_4^{3-}$  remobilization. The additional  $\text{PO}_4^{3-}$  remobilization we observed in the  $\text{GtPSi}_{\text{low}}\text{C}_{\text{recal}}$  setup compared to the  $\text{GtPC}_{\text{recal}}$  setup is likely due to the PZC-lowering effect of Si (Kingston et al., 1972; Schwertmann and Fechter, 1982; Sigg and Stumm, 1981) and due to immobilization of Si through polymerization (Hilbrandt et al., 2019), as suggested by the formation of a crystalline  $\text{SiO}_2$  species (Fig. S4 G). The combined effect of both processes would effectively have prevented the mobilized  $\text{PO}_4^{3-}$  from being re-adsorbed.

Overall, these results indicate, that, while the formation of goethite might have been limited to low Si environments, its presence would have resulted in a depressed  $\text{PO}_4^{3-}$  levels associated with the primary mineral phase (supplementary text S11) and lower  $\text{PO}_4^{3-}$  remobilization during low-grade metamorphism. However, care should be taken in the interpretation of the goethite-related results as different mineral synthesis pathways resulted in different molar P/Fe and Si/Fe ratios. This likely influenced the mineral transformation pathways and relative coverage of available surface sites on primary Fe(III) minerals with  $\text{PO}_4^{3-}$  or Si.

## 11. TEXT S11: RAW ICP-OES DATA; CALCULATED PO<sub>4</sub><sup>3-</sup> REMOBILIZATION AND MOLAR P/Fe AND Si/Fe RATIOS

Raw data for ICP-OES measurements of NaCl extractions and mineral digests and calculated molar Si/Fe and P/Fe ratios as well as extent of P remobilization will be made available on <https://www.pangaea.de/>.

## 12. TEXT S12: ANCIENT SEAWATER PO<sub>4</sub><sup>3-</sup> CONCENTRATIONS

Ancient seawater PO<sub>4</sub><sup>3-</sup> concentrations were calculated employing empirical K<sub>D</sub> values determined by Jones et al. (2015) to BIF P/Fe ratios per Planavsky et al. (2010b). Calculated concentrations will be made available on <https://www.pangaea.de/>.

## REFERENCES

- Ahn J. H. and Buseck P. R. (1990) Hematite nanospheres of possible colloidal origin from a Precambrian banded iron formation. *Science* **250**, 111-113.
- Alibert C. (2016) Rare earth elements in Hamersley BIF minerals. *Geochim. Cosmochim. Acta* **184**, 311-328.
- Amthauer G. and Rossman G. R. (1984) Mixed valence of iron in minerals with cation clusters. *Phys. Chem. Miner.* **11**, 37-51.
- Anschutz A. J. and Penn R. L. (2005) Reduction of crystalline iron(III) oxyhydroxides using hydroquinone: Influence of phase and particle size. *Geochem. Trans.* **6**, 60.
- Barley M. E., Pickard A. L. and Sylvester, P. J. (1997) Emplacement of a large igneous province as a possible cause of banded iron formation 2.45 billion years ago. *Nature* **385**, 55-58.
- Bekker A., Planavsky N., Rasmussen B., Krapez B., Hofmann A., Slack J., Rouxel O. and Konhauser K. O. (2014) Iron formations: Their origins and implications for ancient seawater chemistry. In *Treatise on Geochemistry, second ed. Vol. 9* (eds. H. D. Holland and K. K. Turekian). Elsevier, Netherlands. pp. 561-628.
- Bekker A., Slack J. F., Planavsky N., Krapež B., Hofmann A., Konhauser K. O. and Rouxel O. J. (2010) Iron formation: the sedimentary product of a complex interplay among mantle, tectonic, oceanic, and biospheric processes. *Econ. Geol.* **105**, 467-508.
- Beukes N. J. and Gutzmer J. (2008) Origin and paleoenvironmental significance of major iron formations at the Archean-Paleoproterozoic boundary. *Rev. Econ. Geol.* **15**, 5-47.
- Bocher F., Géhin A., Ruby C., Ghanbaja J., Abdelmoula M. and Génin J.-M. R. (2004) Coprecipitation of Fe(II-III) hydroxycarbonate green rust stabilised by phosphate adsorption. *Solid State Sci.* **6**, 117-124.

- Boggs Jr S. (2014) *Principles of sedimentology and stratigraphy*, 5<sup>th</sup> international ed., Pearson Education Ltd, Harlow.
- Byrne J. M., Van Der Laan G., Figueroa A. I., Qafoku O., Wang C., Pearce C. I., Jackson M., Feinberg J., Rosso K.M. and Kappler A. (2016) Size dependent microbial oxidation and reduction of magnetite nano-and micro-particles. *Sci. Rep.* **6**, 1-13.
- Campbell A. S., Schwertmann U., Stanjek H., Friedl J., Kyek A. and Campbell P. A. (2002) Si incorporation into hematite by heating Si-ferrihydrite. *Langmuir* **18**, 7804-7809.
- Carlson L. and Schwertmann U. (1981) Natural ferrihydrites in surface deposits from Finland and their association with silica. *Geochim. Cosmochim. Acta* **45**, 421-425,427-429.
- Catling D. C. and Zahnle K. J. (2020) The Archean atmosphere. *Sci. Adv.* **6**, eaax1420.
- Chen C., Kukkadapu R. and Sparks D. L. (2015) Influence of Coprecipitated Organic Matter on Fe<sup>2+</sup><sub>(aq)</sub>-Catalyzed Transformation of Ferrihydrite: Implications for Carbon Dynamics. *Environ. Sci. Technol.* **49**, 10927-10936.
- Cismasu A. C., Michel F. M., Tcaciuc A. P. and Brown G. E. (2014) Properties of impurity-bearing ferrihydrite III. Effects of Si on the structure of 2-line ferrihydrite. *Geochim. Cosmochim. Acta* **133**, 168-185.
- Cismasu A. C., Michel F. M., Tcaciuc A. P., Tyliczszak T. and Brown Jr G. E. (2011) Composition and structural aspects of naturally occurring ferrihydrite. *C. R. Geosci.* **343**, 210-218.
- Cloud P. E. (1965) Significance of the Gunflint (Precambrian) microflora photosynthetic oxygen may have had important local effects before becoming a major atmospheric gas. *Science* **148**, 27-35.
- Cloud P. E. (1973) Paleoecological significance of the banded iron-formation. *Econ. Geol.* **68**, 1135-1143.
- Cornell R. M. and Schwertmann U. (2003) *The Iron Oxides: Structure, Properties, Reactions, Occurrences and Uses*. Wiley-VCH Verlag, Weinheim.
- Crowe S. A., Paris G., Katsev S., Jones C., Kim S.-T., Zerkle A. L., Nomosatryo S., Fowle D. A., Adkins J. F., Sessions A. L., Farquhar J. and Canfield D. E. (2014) Sulfate was a trace constituent of Archean seawater. *Science* **346**, 735-739.
- Dijkstra N., Kraal P., Séguret M. J. M., Flores M. R., Gonzalez S., Rijkenberg M. J. A. and Slomp C. P. (2018) Phosphorus dynamics in and below the redoxcline in the Black Sea and implications for phosphorus burial. *Geochim. Cosmochim. Acta* **222**, 685-703.
- Dijkstra N., Slomp C. P. and Behrends T. (2016) Vivianite is a key sink for phosphorus in sediments of the Landsort Deep, an intermittently anoxic deep basin in the Baltic Sea. *Chem. Geol.* **438**, 58-72.
- Eickhoff M., Obst M., Schröder C., Hitchcock A. P., Tyliczszak T., Martinez R. E., Robbins L. J., Konhauser K. O. and Kappler A. (2014) Nickel partitioning in biogenic and abiogenic ferrihydrite: the influence of silica and implications for ancient environments. *Geochim. Cosmochim. Acta* **140**, 65-79.
- Ericsson T., Krisnamurthy A. and Srivastava B. K. (1986) Morin-transition in Ti-substituted hematite: A Mössbauer study. *Phys. Scr.* **33**, 88.



- Fischer W. W. and Knoll A. H. (2009) An iron shuttle for deepwater silica in Late Archean and early Paleoproterozoic iron formation. *Geol. Soc. Am. Bull.* **121**, 222-235.
- Forsyth J. B., Johnson, C. E. and Wilkinson, C. (1970) The magnetic structure of vivianite,  $\text{Fe}_3(\text{PO}_4)_2 \cdot 8 \text{H}_2\text{O}$ . *J. Phys. C Solid State* **3**, 1127.
- Frost R. L., Ding Z. and Ruan H. D. (2003a) Thermal analysis of goethite. *J. Therm. Anal. Calorim.* **71**, 783-797.
- Frost R. L., Weier M. L., Martens W., Kloprogge J. T. and Ding Z. (2003b) Dehydration of synthetic and natural vivianite. *Thermochim. Acta* **401**, 121-130.
- Glasauer S. M., Hug P., Weidler P. G. and Gehring A. U. (2000) Inhibition of sintering by Si during the conversion of Si-rich ferrihydrite to hematite. *Clay Clay Miner.* **48**, 51-56.
- Goto K. (1956) Effect of pH on polymerization of silicic acid. *J. Phys. Chem.* **60**, 1007-1008.
- Gross G. A. (1980) A classification of iron formations based on depositional environments. *Can. Mineral.* **18**, 215-222.
- Grotzinger, J. and Jordan, T. (2016) *Press/Siever Allgemeine Geologie*. Springer-Verlag, Heidelberg.
- Gu B., Mehlhorn T. L., Liang L. and McCarthy J. F. (1996) Competitive adsorption, displacement, and transport of organic matter on iron oxide: I. Competitive adsorption. *Geochim. Cosmochim. Acta* **60**, 1943-1950.
- Gu B., Schmitt J., Chen Z., Liang L. and McCarthy J. F. (1994) Adsorption and desorption of natural organic matter on iron oxide: mechanisms and models. *Environ. Sci. Technol.* **28**, 38-46.
- Gualtieri A. F. and Venturelli P. (1999) In situ study of the goethite-hematite phase transformation by real time synchrotron powder diffraction. *Am. Mineral.* **84**, 895-904.
- Halama M. (2016) Metamorphic origin of the mineralogy and geochemical signatures in banded iron formations. Ph.D. thesis. University of Tuebingen.
- Halama M., Swanner E. D., Konhauser K. O. and Kappler A. (2016) Evaluation of siderite and magnetite formation in BIFs by pressure-temperature experiments of Fe(III) minerals and microbial biomass. *Earth Planet. Sci. Lett.* **450**, 243-253.
- Halevy I., Alesker M., Schuster E. M., Popovitz-Biro R. and Feldman Y. (2017) A key role for green rust in the Precambrian oceans and the genesis of iron formations. *Nat. Geosci.* **10**, 135-139.
- Halevy I. and Bachan A. (2017) The geologic history of seawater pH. *Science* **355**, 1069-1071.
- Han X., Tomaszewski E. J., Sorwat J., Pan Y., Kappler A. and Byrne, J. M. (2020a) Oxidation of green rust by anoxygenic phototrophic Fe(II)-oxidising bacteria. *Geochem. Perspect. Lett.* **12**, 52-57.
- Han X., Tomaszewski E. J., Sorwat J., Pan Y., Kappler A. and Byrne J. M. (2020b) Effect of Microbial Biomass and Humic Acids on Abiotic and Biotic Magnetite Formation. *Environ. Sci. Technol.* **54**, 4121-4130.

- Hansel C. M., Benner S. G., Neiss J., Dohnalkova A., Kukkadapu R. K. and Fendorf, S. (2003) Secondary mineralization pathways induced by dissimilatory iron reduction of ferrihydrite under advective flow. *Geochim. Cosmochim. Acta* **67**, 2977-2992.
- Hansen H. C. B. and Poulsen I. F. (1999) Interaction of synthetic sulphate “green rust” with phosphate and the crystallization of vivianite. *Clay Clay Miner.* **47**, 312-318.
- Hao J., Knoll A. H., Huang F., Hazen R. M. and Daniel I. (2020a) Cycling phosphorus on the Archean Earth: Part I. Continental weathering and riverine transport of phosphorus. *Geochim. Cosmochim. Acta* **273**, 70-84.
- Hao J., Knoll A. H., Huang F., Schieber J., Hazen R. M. and Daniel I. (2020b) Cycling phosphorus on the Archean Earth: Part II. Phosphorus limitation on primary production in Archean ecosystems. *Geochim. Cosmochim. Acta* **280**, 360-377.
- Hao J., Sverjensky D. A. and Hazen R. M. (2017a) Mobility of nutrients and trace metals during weathering in the late Archean. *Earth Planet. Sci. Lett.* **471**, 148-159.
- Hao J., Sverjensky D. A. and Hazen R. M. (2017b) A model for late Archean chemical weathering and world average river water. *Earth Planet. Sci. Lett.* **457**, 191-203.
- Hardisty D. S., Lu Z., Planavsky N. J., Bekker A., Philippot P., Zhou X. and Lyons T. W. (2014) An iodine record of Paleoproterozoic surface ocean oxygenation. *Geology* **42**, 619-622.
- Haugaard R., Pecoits E., Lalonde S. V., Rouxel O. and Konhauser K. O. (2016) The Joffre banded iron formation, Hamersley Group, Western Australia: Assessing the palaeoenvironment through detailed petrology and chemostratigraphy. *Precambrian Res.* **273**, 12-37.
- Hilbrandt I., Lehmann V., Zietzschmann F., Ruhl A. S. and Jekel M. (2019) Quantification and isotherm modelling of competitive phosphate and silicate adsorption onto micro-sized granular ferric hydroxide. *RSC Adv.* **9**, 23642-23651.
- Holland H. D. (1973) The oceans; a possible source of iron in iron-formations. *Econ. Geol.* **68**, 1169-1172.
- Hsu T.-W., Jiang W.-T. and Wang Y. (2014) Authigenesis of vivianite as influenced by methane-induced sulfidization in cold-seep sediments off southwestern Taiwan. *J. Asian Earth Sci.* **89**, 88-97.
- Ibelings B. W. and Maberly S. C. (1998) Photoinhibition and the availability of inorganic carbon restrict photosynthesis by surface blooms of cyanobacteria. *Limnol. Oceanogr.* **43**, 408-419.
- Iler R. K. (1979) *The chemistry of silica: solubility, polymerization, colloid and surface properties, and biochemistry*. Wiley, New York.
- Isley A. E. (1995) Hydrothermal plumes and the delivery of iron to banded iron formation. *J. Geol.* **103** 169-185.
- Isley A. E. and Abbott D. H. (1999) Plume-related mafic volcanism and the deposition of banded iron formation. *J. Geophys. Res. Solid Earth* **104**, 15461-15477.
- Ji X., Verspagen J. M., Van de Waal D. B., Rost B. and Huisman J. (2020) Phenotypic plasticity of carbon fixation stimulates cyanobacterial blooms at elevated CO<sub>2</sub>. *Sci. Adv.* **6**, eaax2926.

- Johnson J. E., Muhling J. R., Cosmidis J., Rasmussen B. and Templeton A. S. (2018) Low-Fe(III) Greenalite Was a Primary Mineral From Neoproterozoic Oceans. *Geophys. Res. Lett.* **45**, 3182-3192.
- Jones A. M., Collins R. N., Rose J. and Waite T. D. (2009) The effect of silica and natural organic matter on the Fe(II)-catalysed transformation and reactivity of Fe(III) minerals. *Geochim. Cosmochim. Acta* **73**, 4409-4422.
- Jones C., Nomosatryo S., Crowe S. A., Bjerrum C. J. and Canfield D. E. (2015) Iron oxides, divalent cations, silica, and the early earth phosphorus crisis. *Geology* **43**, 135-138.
- Kappler A. and Newman D. K. (2004) Formation of Fe(III)-minerals by Fe(II)-oxidizing photoautotrophic bacteria. *Geochim. Cosmochim. Acta* **68**, 1217-1226.
- Kappler A., Pasquero C., Konhauser K. O. and Newman D. K. (2005) Deposition of banded iron formations by anoxygenic phototrophic Fe(II)-oxidizing bacteria. *Geology* **33**, 865-868.
- Kaufman A. J., Hayes J. and Klein C. (1990) Primary and diagenetic controls of isotopic compositions of iron-formation carbonates. *Geochim. Cosmochim. Acta* **54**, 3461-3473.
- Kingston F. J., Posner A. M. and Quirk, J. P. (1972) Anion adsorption by goethite and gibbsite: I. The role of the proton in determining adsorption envelopes. *J. Soil Sci.* **23**, 177-192.
- Klein C. (2005) Some Precambrian banded iron-formations (BIFs) from around the world: Their age, geologic setting, mineralogy, metamorphism, geochemistry, and origins. *Am. Mineral.* **90**, 1473-1499.
- Klein C. and Beukes N. J. (1989) Geochemistry and sedimentology of a facies transition from limestone to iron-formation deposition in the early Proterozoic Transvaal Supergroup, South Africa. *Econ. Geol.* **84**, 1733-1774.
- Klein C. and Gole M. J. (1981) Mineralogy and petrology of parts of the Marra Mamba iron formation, Hamersley Basin, Western Australia. *Am. Mineral.* **66**, 507-525.
- Koeksoy E., Sundman A., Byrne J. M., Lohmayer R., Planer-Friedrich B., Halevy I., Konhauser K. O. and Kappler A. (2019) Formation of green rust and elemental sulfur in an analogue for oxygenated ferro-euxinic transition zones of Precambrian oceans. *Geology* **47**, 211-214.
- Köhler I., Konhauser K. O., Papineau D., Bekker A. and Kappler A. (2013) Biological carbon precursor to diagenetic siderite with spherical structures in iron formations. *Nat. Commun.* **4**, 1741.
- Konhauser K. O., Planavsky N. J., Hardisty D. S., Robbins L. J., Warchola T. J., Hugaard R., Lalonde S. V., Partin C. A., Oonk P. B. H., Tsikos H., Lyons T. W., Bekker A. and Johnson C. M. (2017) Iron formations: A global record of Neoproterozoic to Palaeoproterozoic environmental history. *Earth Sci. Rev.* **172**, 140-177.
- Konhauser K. O., Hamade T., Raiswell R., Morris R. C., Ferris F. G., Southam G. and Canfield D. E. (2002) Could bacteria have formed the Precambrian banded iron formations? *Geology* **30**, 1079-1082.
- Krauskopf K. B. (1956) Dissolution and precipitation of silica at low temperatures. *Geochim. Cosmochim. Acta* **10**, 1-26.

- Krissansen-Totton J., Arney G. N. and Catling D. C. (2018) Constraining the climate and ocean pH of the early Earth with a geological carbon cycle model. *Proc. Natl. Acad. Sci.* **115**, 4105-4110.
- Kukkadapu R. K., Zachara J. M., Fredrickson J. K. and Kennedy D. W. (2004) Biotransformation of two-line silica-ferrihydrite by a dissimilatory Fe(III)-reducing bacterium: formation of carbonate green rust in the presence of phosphate. *Geochim. Cosmochim. Acta* **68**, 2799-2814.
- Larese-Casanova P., Haderlein S. B. and Kappler A. (2010) Biomineralization of lepidocrocite and goethite by nitrate-reducing Fe(II)-oxidizing bacteria: effect of pH, bicarbonate, phosphate, and humic acids. *Geochim. Cosmochim. Acta* **74**, 3721-3734.
- Li Y.-L., Konhauser K. O., Cole D. R. and Phelps T. J. (2011) Mineral ecophysiological data provide growing evidence for microbial activity in banded-iron formations. *Geology* **39**, 707-710.
- Li Y.-L., Konhauser K. O. and Zhai M. (2017) The formation of magnetite in the early Archean oceans. *Earth Planet. Sci. Lett.* **466**, 103-114.
- Liu H., Chen T., Zou X., Qing C. and Frost R. L. (2013) Thermal treatment of natural goethite: Thermal transformation and physical properties. *Thermochim. Acta* **568**, 115-121.
- Maliva R. G., Knoll A. H. and Simonson B. M. (2005) Secular change in the Precambrian silica cycle: insights from chert petrology. *Geol. Soc. Am. Bull.* **117**, 835-845.
- Manning P. G., Prepas E. E. and Serediak M. S. (1999) Pyrite and vivianite intervals in the bottom sediments of eutrophic Baptiste Lake, Alberta, Canada. *Can. Mineral.* **37**, 593-601.
- Marty B., Avice G., Bekaert D. V. and Broadley M. W. (2018) Salinity of the Archaean oceans from analysis of fluid inclusions in quartz. *C. R. Geosci.* **350**, 154-163.
- Miyano T. and Beukes N. J. (1984) Phase relations of stilpnomelane, ferri-annite, and riebeckite in very low-grade metamorphosed iron-formations. *South Afr. J. Geol.* **87**, 111-124.
- Morris R. C. (1993) Genetic modelling for banded iron-formation of the Hamersley Group, Pilbara Craton, Western Australia. *Precambrian Res.* **60**, 243-286.
- Muhling J. R. and Rasmussen B. (2020) Widespread deposition of greenalite to form Banded Iron Formations before the Great Oxidation Event. *Precambrian Res.* **339**, 105619.
- Murad E. (1982) The characterization of goethite by Mössbauer spectroscopy. *Am. Mineral.* **67**, 1007-1011.
- Murad E. (1996) Magnetic properties of microcrystalline iron(III) oxides and related materials as reflected in their Mössbauer spectra. *Phys. Chem. Miner.* **23**, 248-262.
- Murad E., Bowen L., Long G. and Quin T. (1988) Influence of crystallinity on magnetic ordering in natural ferrihydrites. *Clay Miner.* **23**, 161-173.
- Murad E. and Cashion J. (2004), *Mössbauer Spectroscopy of Environmental Materials and Their Industrial Utilization*. Springer, New York.
- Murad E. and Schwertmann U. (1984) The influence of crystallinity on the Mössbauer spectrum of lepidocrocite. *Mineral. Mag.* **48**, 507-511.

- O'Connell D. W., Jensen M. M., Jakobsen R., Thamdrup B., Andersen T. J., Kovács A. and Hansen H. C. B. (2015) Vivianite formation and its role in phosphorus retention in Lake Ørn, Denmark. *Chem. Geol.* **409**, 42-53.
- O'Loughlin E. J., Gorski C. A., Scherer M. M., Boyanov M. I. and Kemner K. M. (2010) Effects of oxyanions, natural organic matter, and bacterial cell numbers on the bioreduction of lepidocrocite ( $\gamma$ -FeOOH) and the formation of secondary mineralization products. *Environ. Sci. Technol.* **44**, 4570-4576.
- Olson S. L., Kump L. R. and Kasting J. F. (2013) Quantifying the areal extent and dissolved oxygen concentrations of Archean oxygen oases. *Chem. Geol.* **362**, 35-43.
- Paige C. R., Snodgrass W. J., Nicholson R. V., Scharer J. M. and He Q. H. (1997) The effect of phosphate on the transformation of ferrihydrite into crystalline products in alkaline media. *Water Air Soil Pollut.* **97**, 397-412.
- Pecoits E., Gingras M. K., Barley M. E., Kappler A., Posth N. R. and Konhauser K. O. (2009) Petrography and geochemistry of the Dales Gorge banded iron formation: Paragenetic sequence, source and implications for palaeo-ocean chemistry. *Precambrian Res.* **172**, 163-187.
- Percak-Dennett E. M., Beard B. L., Xu H., Konishi H., Johnson C. M. and Roden E. E. (2011) Iron isotope fractionation during microbial dissimilatory iron oxide reduction in simulated Archean seawater. *Geobiology* **9**, 205-220.
- Planavsky N. J., Bekker A., Rouxel O. J., Kamber B., Hofmann A., Knudsen A. and Lyons T. W. (2010a) Rare earth element and yttrium compositions of Archean and Paleoproterozoic Fe formations revisited: new perspectives on the significance and mechanisms of deposition. *Geochim. Cosmochim. Acta* **74**, 6387-6405.
- Planavsky N. J., Rouxel O. J., Bekker A., Lalonde S. V., Konhauser K. O., Reinhard C. T. and Lyons T. W. (2010b) The evolution of the marine phosphate reservoir. *Nature* **467**, 1088-1090.
- Pokrovski G. S., Schott J., Farges F. and Hazemann J. L. (2003) Iron(III)-silica interactions in aqueous solution: insights from X-ray absorption fine structure spectroscopy. *Geochim. Cosmochim. Acta.* **67**, 3559-3573.
- Posth N. R., Canfield D. E. and Kappler A. (2014) Biogenic Fe(III) minerals: from formation to diagenesis and preservation in the rock record. *Earth Sci. Rev.* **135**, 103-121.
- Posth N. R., Huelin S., Konhauser K. O. and Kappler A. (2010) Size, density and composition of cell-mineral aggregates formed during anoxygenic phototrophic Fe(II) oxidation: Impact on modern and ancient environments. *Geochim. Cosmochim. Acta* **74**, 3476-3493.
- Posth N. R., Kohler I., Swanner E.D., Schröder C., Wellmann E., Binder B., Konhauser K. O., Neumann U., Berthold C., Nowak M. and Kappler A. (2013) Simulating Precambrian banded iron formation diagenesis. *Chem. Geol.* **362**, 66-73.
- Postma D. (1993) The reactivity of iron oxides in sediments: a kinetic approach. *Geochim. Cosmochim. Acta* **57**, 5027-5034.
- Poulton S. W. and Canfield D. E. (2006) Co-diagenesis of iron and phosphorus in hydrothermal sediments from the southern East Pacific Rise: Implications for the evaluation of paleoseawater phosphate concentrations. *Geochim. Cosmochim. Acta* **70**, 5883-5898.

- Quin T. G., Long G. J., Benson C. G., Mann S. and Williams R. J. (1988) Influence of silicon and phosphorus on structural and magnetic properties of synthetic goethite and related oxides. *Clay Clay Miner.* **36**, 165-175.
- Rancourt D. G. and Ping J. Y. (1991) Voigt-based methods for arbitrary-shape static hyperfine parameter distributions in Mössbauer spectroscopy. *Nucl. Instrum. Methods Phys. Res. B* **58**, 85-97.
- Rasmussen B., Krapež B. and Meier D. B. (2014) Replacement origin for hematite in 2.5 Ga banded iron formation: Evidence for postdepositional oxidation of iron-bearing minerals. *Geol. Soc. Am. Bull.* **126**, 438-446.
- Rasmussen B., Krapež B., Muhling J. R. and Suvorova A. (2015) Precipitation of iron silicate nanoparticles in early Precambrian oceans marks Earth's first iron age. *Geology* **43**, 303-306.
- Rasmussen B., Meier D. B., Krapež B. and Muhling J. R. (2013) Iron silicate microgranules as precursor sediments to 2.5-billion-year-old banded iron formations. *Geology* **41**, 435-438.
- Rasmussen B., Muhling J. R. and Fischer W. W. (2019) Evidence from laminated chert in banded iron formations for deposition by gravitational settling of iron-silicate muds. *Geology* **47**, 167-170.
- Rasmussen B., Muhling J. R., Suvorova A. and Krapež B. (2016) Dust to dust: evidence for the formation of "primary" hematite dust in banded iron formations via oxidation of iron silicate nanoparticles. *Precambrian Res.* **284**, 49-63.
- Rasmussen B., Muhling J. R., Suvorova A. and Krapež B. (2017) Greenalite precipitation linked to the deposition of banded iron formations downslope from a late Archean carbonate platform. *Precambrian Res.* **290**, 49-62.
- Robbins L. J., Funk S. P., Flynn S. L., Warchola T. J., Li Z., Lalonde S. V., Rostron B. J., Smith A. J. B., Beukes N. J., de Kock M. O., Heaman L. M., Alessi D. S. and Konhauser K. O. (2019) Hydrogeological constraints on the formation of Palaeoproterozoic banded iron formations. *Nat. Geosci.* **12**, 558-563.
- Robbins L. J., Lalonde S. V., Planavsky N. J., Partin C. A., Reinhard C. T., Kendall B., Scott C., Hardisty D. S., Gill B. C., Alessi D. S., Dupont C. L., Saito M. A., Crowe S. A., Poulton S. W., Bekker A., Lyons T. W. and Konhauser K. O. (2016) Trace elements at the intersection of marine biological and geochemical evolution. *Earth Sci. Rev.* **163**, 323-348.
- Robbins L. J., Swanner E. D., Lalonde S. V., Eickhoff M., Paranich M. L., Reinhard C. T., Peacock C. L., Kappler A. and Konhauser K. O. (2015) Limited Zn and Ni mobility during simulated iron formation diagenesis. *Chem. Geol.* **402**, 30-39.
- Rothe M., Kleeberg A. and Hupfer M. (2016) The occurrence, identification and environmental relevance of vivianite in waterlogged soils and aquatic sediments. *Earth Sci. Rev.* **158**, 51-64.
- Rouzies D. and Millet J. M. M. (1993) Mössbauer study of synthetic oxidized vivianite at room temperature. *Hyperfine Interact.* **77**, 19-28.
- Rzepa G., Pieczara G., Gawel A., Tomczyk A. and Zalecki R. (2016) The influence of silicate on transformation pathways of synthetic 2-line ferrihydrite. *J. Therm. Anal. Calorim.* **125**, 407-421.

- Schad M., Halama M., Bishop B., Konhauser K. O. and Kappler A. (2019) Temperature fluctuations in the Archean ocean as trigger for varve-like deposition of iron and silica minerals in banded iron formations. *Geochim. Cosmochim. Acta* **265**, 386-412.
- Schwertmann U., Cambier P. and Murad E. (1985) Properties of goethites of varying crystallinity. *Clay Clay Miner.* **33**, 369-378.
- Schwertmann U. and Cornell R. M. (2008) *Iron oxides in the laboratory*. John Wiley & Sons.
- Schwertmann U. and Fechter H. (1982) The point of zero charge of natural and synthetic ferrihydrites and its relation to adsorbed silicate. *Clay Miner.* **17**, 471-476.
- Senn A.-C., Kaegi R., Hug S. J., Hering J. G., Mangold S. and Voegelin A. (2015) Composition and structure of Fe(III)-precipitates formed by Fe(II) oxidation in water at near-neutral pH: Interdependent effects of phosphate, silicate and Ca. *Geochim. Cosmochim. Acta* **162**, 220-246.
- Senn A.-C., Kaegi R., Hug S. J., Hering J. G., Mangold S. and Voegelin A. (2017) Effect of aging on the structure and phosphate retention of Fe(III)-precipitates formed by Fe(II) oxidation in water. *Geochim. Cosmochim. Acta* **202**, 341-360.
- Siever R. (1992) The silica cycle in the Precambrian. *Geochim. Cosmochim. Acta* **56**, 3265-3272.
- Sigg L. and Stumm W. (1981) The interaction of anions and weak acids with the hydrous goethite ( $\alpha$ -FeOOH) surface. *Colloids Surface* **2**, 101-117.
- Smith R. E., Perdrix J. and Parks T. (1982) Burial metamorphism in the Hamersley basin, Western Australia. *J. Petrol.* **23**, 75-102.
- Stookey L. L. (1970) Ferrozine---a new spectrophotometric reagent for iron. *Anal. Chem.* **42**, 779-781.
- Strauss R., Brümmer G. and Barrow N. (1997) Effects of crystallinity of goethite: I. Preparation and properties of goethites of differing crystallinity. *Eur. J. Soil Sci.* **48**, 87-99.
- Sun S., Konhauser K. O., Kappler A. and Li Y.-L. (2015) Primary hematite in Neoproterozoic oceans. *Geol. Soc. Am. Bull.* **127**, 850-861.
- Swedlund P. J., Miskelly G.M. and McQuillan A. J. (2010) Silicic Acid Adsorption and Oligomerization at the Ferrihydrite-Water Interface: Interpretation of ATR-IR Spectra Based on a Model Surface Structure. *Langmuir* **26**, 3394-3401.
- Swedlund P. J., Sivaloganathan S., Miskelly G. M. and Waterhouse G. I. (2011) Assessing the role of silicate polymerization on metal oxyhydroxide surfaces using X-ray photoelectron spectroscopy. *Chem. Geol.* **285**, 62-69.
- Swedlund P. J. and Webster J. G. (1999) Adsorption and polymerisation of silicic acid on ferrihydrite, and its effect on arsenic adsorption. *Water Res.* **33**, 3413-3422.
- Thomas-Arrigo L. K., Byrne J. M., Kappler A. and Kretzschmar R. (2018) Impact of Organic Matter on Iron(II)-Catalyzed Mineral Transformations in Ferrihydrite-Organic Matter Coprecipitates. *Environ. Sci. Technol.* **52**, 12316-12326.
- Thompson K. J., Kenward P. A., Bauer K. W., Warchola T., Gauger T., Martinez R., Simister, R. L., Michiels C. C., Llíros M., Reinhard C. T., Kappler A., Konhauser K. O. and Crowe S. A.

- (2019) Photoferrotrophy, deposition of banded iron formations, and methane production in Archean oceans. *Sci. Adv.* **5**, eaav2869.
- Toner B. M., Berquó T. S., Michel F. M., Sorensen J. V., Templeton A. S. and Edwards K. J. (2012) Mineralogy of iron microbial mats from Loihi Seamount. *Front. Microbiol.* **3**, 118.
- Tosca N. J., Guggenheim S. and Pufahl P. K. (2016) An authigenic origin for Precambrian greenalite: Implications for iron formation and the chemistry of ancient seawater. *Geol. Soc. Am. Bull.* **128**, 511-530.
- Trendall, A. F. (2002) The significance of iron-formation in the Precambrian stratigraphic record. *Precambrian Sedimentary Environments: a Modern Approach to Depositional Systems*, *Spec. Publ. Internat. Assoc. Sedimentol.* **33**, 33-66.
- van Genuchten C. M., Peña J., Amrose S. E. and Gadgil A. J. (2014) Structure of Fe(III) precipitates generated by the electrolytic dissolution of Fe(0) in the presence of groundwater ions. *Geochim. Cosmochim. Acta* **127**, 285-304.
- Vempati R. K., Loeppert R. H. and Coker D. L. (1990) Mineralogy and reactivity of amorphous Si-ferrihydrites. *Solid State Ion.* **38**, 53-61.
- Verspagen J. M., Van de Waal D. B., Finke J. F., Visser P. M., Van Donk E. and Huisman J. (2014) Rising CO<sub>2</sub> levels will intensify phytoplankton blooms in eutrophic and hypertrophic lakes. *PLoS one* **9**, e104325.
- Voegelin A., Kaegi R., Frommer J., Vantelon D. and Hug S. J. (2010) Effect of phosphate, silicate, and Ca on Fe(III)-precipitates formed in aerated Fe(II)- and As(III)-containing water studied by X-ray absorption spectroscopy. *Geochim. Cosmochim. Acta* **74**, 164-186.
- Wang X., Li W., Harrington R., Liu F., Parise J. B., Feng X. and Sparks D. L. (2013) Effect of ferrihydrite crystallite size on phosphate adsorption reactivity. *Environ. Sci. Technol.* **47**, 10322-10331.
- Widdel F., Schnell S., Heising S., Ehrenreich A., Assmus B. and Schink B. (1993) Ferrous iron oxidation by anoxygenic phototrophic bacteria. *Nature* **362**, 834-836.
- Wolska E. and Schwertmann U. (1989) Nonstoichiometric structures during dehydroxylation of goethite. *Z. Kristallogr. Cryst. Mater.* **189**, 223-237.
- Zachara J. M., Kukkadapu R. K., Fredrickson J. K., Gorby Y. A. and Smith S. C. (2002) Biomineralization of poorly crystalline Fe(III) oxides by dissimilatory metal reducing bacteria (DMRB). *Geomicrobiol. J.* **19**, 179-207.
- Zegeye A., Bonneville S., Benning L. G., Sturm A., Fowle D. A., Jones C., Canfield D. E., Ruby C., MacLean L. C., Nomosatryo S., Crowe S. A. and Poulton S. W. (2012) Green rust formation controls nutrient availability in a ferruginous water column. *Geology* **40**, 599-602.
- Zheng X.-Y., Beard B. L., Reddy T. R., Roden E. E. and Johnson C. M. (2016) Abiologic silicon isotope fractionation between aqueous Si and Fe(III)-Si gel in simulated Archean seawater: Implications for Si isotope records in Precambrian sedimentary rocks. *Geochim. Cosmochim. Acta* **187**, 102-122.
- Zhou Z., Latta D. E., Noor N., Thompson A., Borch T. and Scherer M. M. (2018) Fe(II)-Catalyzed Transformation of Organic Matter-Ferrihydrite Coprecipitates: A Closer Look Using Fe Isotopes. *Environ. Sci. Technol.* **52**, 11142-11150.







## Statement of personal contribution

### Chapter 2

#### Temperature fluctuations in the Archean ocean as trigger for varve-like deposition of iron and silica minerals in banded iron formations

Manuel Schad, Maximilian Halama, Brendan Bishop, Kurt O. Konhauser, Andreas Kappler

**Published in:** *Geochimica et Cosmochimica Acta* **265** (2019) 386-412

The work described in this chapter was supported by grants from the German Research Foundation (DFG) to Prof. Andreas Kappler and grants from the Natural Science and Engineering Research Council (NSERC) to Prof. Kurt O. Konhauser. The work in this chapter was supervised by Prof. Andreas Kappler, Prof. Kurt O. Konhauser.

The study was designed and conceptualized by me with the help of Prof. Andreas Kappler, Prof. Kurt O. Konhauser and Dr. Maximilian Halama. Dr. Hartmut Schulz, Dr. Aleksandra Mloszewska, Dr. Wenfang Wu, Dr. Stefan Lalonde, Dr. Leslie J. Robbins and Tyler Warchola provided background information, feedback and advice for the experimental design.

The bacterial cultures used in this study were provided by Lars Grimm and Wiebke Ruschmeier. The experiments, including sample preparation and analyses were conducted by me. Geochemical modelling was performed with the help of Dr. Leslie J. Robbins.

Scanning electron microscopy sample preparation and analyses were performed by me with help of Dr. Hartmut Schulz and Dr. James M. Byrne.

$^{57}\text{Fe}$  Moessbauer analyses were carried out by me with help of Dr. James M. Byrne and Dr. Markus Maisch.

$\mu\text{XRD}$  analysis was preformed by Dr. Markus Maisch.

Zeta-potential analyses and development of measurement protocols were performed by me with the help of Ellen Röhm.

Potentiometric titrations were carried out and analyzed by Brendan Bishop.

Obtained results were discussed and analyzed in cooperation with Prof. Andreas Kappler, Prof. Kurt O. Konhauser and Dr. Maximilian Halama. The paper was written by me with feedback and improvement by Prof. Andreas Kappler and Prof. Kurt O. Konhauser. The manuscript was reviewed by 5 anonymous reviewers.

The raw data underlying Figure 1 and Figure 2 of this paper were obtained during my preceding Master thesis and re-analyzed, re-plotted and re-interpreted during my PhD thesis for the purposed of this study.

## Chapter 2

### Temperature fluctuations in the Archean ocean as trigger for varve-like deposition of iron and silica minerals in banded iron formations

Manuel Schad<sup>a</sup>, Maximilian Halama<sup>a</sup>, Brendan Bishop<sup>b</sup>, Kurt O. Konhauser<sup>b</sup>, Andreas Kappler<sup>a</sup>

<sup>a</sup> Geomicrobiology, Center for Applied Geosciences, University of Tübingen, 72076, Tübingen, Germany

<sup>b</sup> Department of Earth and Atmospheric Sciences, University of Alberta, Edmonton, AB T6G 2E3, Canada

**Published in:** *Geochimica et Cosmochimica Acta* **265** (2019) 386-412

Schad M., Halama M., Bishop B., Konhauser K. O. and Kappler, A. (2019). Temperature fluctuations in the Archean ocean as trigger for varve-like deposition of iron and silica minerals in banded iron formations. *Geochim. Cosmochim. Acta*, **265**, 386-412.

<https://doi.org/10.1016/j.gca.2019.08.031>.



---

**ABSTRACT**

Banded iron formations (BIFs) are Fe- and Si-rich chemical sediments that were deposited in the oceans throughout the Archean Eon (4.0–2.5 billion years ago; Ga). Despite extensive research pertaining to their composition, mineralogy and depositional settings, the mechanism(s) leading to their characteristic layering is still a matter of debate. Recently, it has been proposed that temperature fluctuations could have acted as the unifying trigger for the precipitation and deposition of Fe(III)-mineral-rich layers mediated by phototrophic Fe(II)-oxidizing bacteria during warm periods and the deposition of silica (SiO<sub>2</sub>)-rich layers by abiotic precipitation of dissolved silica during cold periods. To verify the feasibility of such a mechanism, we conducted laboratory experiments with the marine phototrophic Fe(II)-oxidizing bacterium *Rhodovulum iodosum* under simulated Archean ocean conditions. The temperature was cycled between 26°C (warm period) and 5°C (cold period) to mimic temperature fluctuations in the past. Our results showed that *R. iodosum* readily oxidized Fe(II) during warm periods resulting in the formation of an orange-brown Fe(III) mineral layer, whereas it was inactive during cold periods. Conversely, silica largely stayed in solution during warm periods but was precipitated abiotically as an amorphous, gel-like layer during cold periods, enhanced by Si addition that led to Si oversaturation. Most importantly, during Fe(III) mineral precipitation, most silica stayed in solution leading to an independent precipitation of the Fe- and Si-rich layers. This is due to inhibition of silica sorption onto the biogenic Fe-minerals caused by sorption of microbially derived organic matter that contains negatively-charged carboxyl/phosphodiester groups. Analyses of precipitation rates and theoretical sedimentological considerations suggest that this process could explain the banding in BIFs on the microband level and produce sediments of similar thicknesses as found in nature.





## 1. INTRODUCTION

Banded Iron Formations (BIFs) are Fe- and Si-rich marine sedimentary deposits which were mainly formed during the Archean and early Paleoproterozoic until ca. 1.8 Ga (Bekker et al., 2010; Bekker et al., 2014; Konhauser et al., 2017). They are frequently laminated on a range of scales that include; (1) macrobands which can be several meters in thickness, (2) mesobands which are usually of a few centimeters in thickness, and (3) microbands which range from the millimeter to sub-millimeter scale and have been proposed to represent an annual cycle of iron and silica precipitation (Trendall and Blockley, 1970). These microbands have also been referred to as chemical varves, where one Fe-rich and one Si-rich layer together represent one year of precipitation (Trendall, 2002). Recently, diurnal nanobands have also been hypothesized (Li, 2014). Compositionally, BIF are characterized by an average redox state of  $\text{Fe}^{2.4+}$  representing their variable Fe(II)- and Fe(III)-bearing mineralogy (e.g. hematite, magnetite, siderite and Fe-silicates; Klein and Beukes, 1992), by a low organic carbon content (<0.5 wt.%) and a Fe-content of 20–40 wt.% and silica-content of 40–50 wt.%  $\text{SiO}_2$  (Trendall, 2002). The most extensive “Superior-type” BIFs are in the Hamersley Range of Western Australia. It is several hundred meters thick,  $10^5 \text{ km}^2$  in aerial extent and contains  $>10^{13} \text{ t}$  of Fe (Isley, 1995; Isley and Abbott, 1999). Due to the lack of current- or wave-related sedimentological features, Superior-type BIFs were likely deposited in depths of more than 100 m (Trendall, 2002) on the continental shelf (Beukes, 1973; Morris and Horwitz, 1983; Klein, 2005).

It is widely accepted that microorganisms were directly or indirectly involved in the initial oxidation and hydrolysis of seawater Fe(II) to form the Fe(III) (oxyhydr)oxide precursor phase to BIF – see Rasmussen et al. (2013, 2015, 2017) for an alternate opinion. The classic model invokes ferric iron precipitation occurring at the interface between oxygenated shallow waters and reduced upwelling iron-rich waters; the oxygen being sourced from cyanobacteria, or their predecessors (Cloud, 1965, 1973). These photoautotrophs would have flourished when nutrients were available and passively induced the precipitation of Fe(III) (oxyhydr)oxides through their metabolic activity. Alternatively, anoxygenic photoautotrophic Fe(II)-oxidizing bacteria (known as photoferrotrophs) could have directly oxidized Fe(II) and coupled this to the fixation of carbon by light energy (Hartman, 1984; Kappler and Newman, 2004). Konhauser et al. (2002, 2018) suggested that photoferrotrophs might have accounted for most, if not all, Fe(III) deposited in BIF, while iron isotopes in the oldest BIF (the 3.8 Isua Supracrustal Belt in Greenland) suggest

the most parsimonious explanation for Fe(II) oxidation was photoferrotrophy (Czaja et al., 2013). Kappler et al. (2005) further showed that the photoferrotrophs could have oxidized all hydrothermally derived Fe(II) before it reached surface waters, even with the simultaneous presence of cyanobacteria in the oxic layer above. The adaptation to low-light conditions would have given photoferrotrophs a competitive advantage over early cyanobacteria which likely inhabited surface waters, especially since cyanobacteria would have had higher phosphate requirements (Jones et al., 2015) and the ferruginous conditions prevailing in the Precambrian ocean might have been toxic to cyanobacteria (Swanner et al., 2015a). Studies that focused on the ecophysiology of photoferrotrophs (Hegler et al., 2008; Posth et al., 2008) support the notion that they could have prospered in a temperate Precambrian ocean. Moreover, Wu et al. (2014) showed that Fe(II) oxidation rates were not significantly influenced by silica concentrations relevant for the Precambrian ocean. Recent work on modern day analogues for the Precambrian ocean further showed that photoferrotrophs play a key role in their bacterial communities and in the turnover of Fe(II) (e.g. Crowe et al., 2008; Walter et al., 2014; Koeksoy et al., 2016).

One key characteristic of BIFs is the consistency of the alternating Fe- and Si-rich layers. Previous studies suggested that it is possible to correlate microbands over almost 100 km between different cores (Trendall and Blockley, 1970; Ewers and Morris, 1981). If true, the consistency with which these alternating layers were deposited requires a comparable ocean chemistry over much of the depositional basin, and it suggests a unifying trigger for the deposition of Fe-rich and Si-rich layers. The mechanisms suggested for being responsible for BIF banding are divided into primary, secondary or diagenetic. Primary mechanisms imply the precipitation and the banding resulted from some form of periodicity, such as seasonal upwelling of Fe(II)-rich ocean bottom waters onto the continental shelf (e.g. Ewers and Morris, 1981; Morris, 1993). Posth et al. (2008) took the idea one step further by incorporating the role of plankton. They postulated that photoferrotrophs would have been active at temperatures between 20 and 25°C, for example in summer or during periods of warm climate. This would have resulted in the formation of layers consisting of biogenic Fe(III) (oxyhydr)oxides, while silica would have largely remained soluble. In modern oceans, the seasonal temperature changes may reach up to 6–10°C, although larger differences might be possible based on local differences in incoming ocean currents and upwelling areas (Pickard and Emery, 1982). Glacial/inter-glacial differences are smaller with between 2–3°C warming/cooling, however, seasonal differences in

---

temperate regions during these times might have been  $>12^{\circ}\text{C}$  (Pflaumann et al., 2003; MARGO, 2009). Therefore, upon cooling of the ocean (e.g. up to  $10\text{--}15^{\circ}\text{C}$ ), either due to incoming cold ocean currents or seasonal changes (Emery et al., 2006), microbial activity would have diminished and amorphous silica could have precipitated abiotically. When the ocean temperature rose again, e.g., in spring, the photoferrotrophs would have resumed their metabolic activity. These estimates are well within estimates given for the Archean ocean, which supposedly was temperate (Krissansen-Totton et al., 2018; Galili et al., 2019) with temperatures ranging from  $10\text{--}33^{\circ}\text{C}$  (Kasting et al., 2006). Thus, this model offers a relatively simple explanation for the wide-scale continuous deposition of Fe-rich and Si-rich micro-bands in BIFs.

Secondary mechanisms invoke mechanical forcing as dominant processes for the alternating deposition of Fe-rich and Si-rich layers in BIF. For instance, Krapež et al. (2003) and Pickard et al. (2004) suggested that BIF precursor sediments might have been transported to a deep-sea BIF depositional basin by either turbidity or deep-sea density currents. Thus, micro-banding in BIF would represent compacted density current lamination. Post-depositional processes during burial and diagenesis include the compaction of initial BIF sediments resulting in the formation of Fe-rich layers and the vertical escape of the silica which then would have precipitated on top (e.g. Trendall and Blockley, 1970; Dimroth and Chauvel, 1973; Beukes, 1984). Others have suggested that the layers depleted in Fe might represent the post-depositional activity of Fe(III)-reducing bacteria, resulting in remobilization of Fe(II) from the sediment and formation of Si-rich layers (Nealson and Myers, 1990). This could potentially have been controlled by fluctuations in photosynthetic activity with variations in organic matter deposition on the seafloor, resulting in microbial reduction of Fe(III) minerals with this organic matter, its remobilization as Fe(II), and the formation Si-rich layers (Hashizume et al., 2016). Recently, Eglseder et al. (2018) suggested a process where dissolution-precipitation would have resulted in the liberation of hematite particles from their silica matrix. These particles would have accumulated in parallel layers forming microbands, where new hematite particles were formed by non-classical crystallization pathways.

Considering the likelihood that photosynthetic Fe(II)-oxidizing bacteria contributed to BIF, it was our aim to further investigate the primary layering-model involving microbial activity, specifically the fate of Fe(III) and silica during the active growing season. This aspect is not as straightforward as initially proposed in the Posth et al. (2008) model because it has since been

suggested that primary Fe(III) minerals could have acted as a shuttle for silica to BIF sediments (Fischer and Knoll, 2009), while other studies have speculated that Fe(II) oxidation in the presence of dissolved silica could have resulted in the formation of a homogeneous, single-phase Fe(III)-silica gel, where Fe and silica are tightly bound and do not form separate silica and Fe(III) (oxyhydr)oxide phases (Doelsch et al., 2001; Percak-Dennett et al., 2011). Zheng et al. (2016) concluded that the primary precipitate of BIFs might therefore have been a Fe(III)-silica gel. Consequently, if the alternating banding of Fe- and Si-rich layers was indeed of primary origin, this would require a mechanism by which the sorption of silica to the primary Fe(III) mineral precipitates can be prevented. Although there is evidence from the rock record in the form of trace element and isotope geochemistry from individual Si- and Fe-rich micro-bands suggesting distinct sources and mechanisms of silica and Fe precipitation (e.g. Frei and Polat, 2007; Bau and Alexander, 2009; Steinhoefel et al., 2010; Viehmann et al., 2014), to date no model has provided a satisfactory answer on why Fe and silica were deposited independently and consistently over large areas.

For our experiments we envisioned an Archean ocean before the development of widespread oxygenic photosynthesis, in which anoxygenic Fe(II)-metabolizing bacteria, such as photoferrotrophs, were primarily responsible for the deposition of BIFs. In order to test whether the model developed by Posth et al. (2008) can be validated with what we now know about Fe-silica interactions, we cultivated the marine photoferrotroph *Rhodovulum iodosum* under conditions relevant for an Archean ocean. We performed precipitation experiments where we followed geochemical parameters, recorded the development of the layering in the experiments and identified the mineral precipitates formed. Furthermore, in order to elucidate whether cell-derived biomass associated with the Fe(III) minerals results in changes in surface charge or properties, and whether this could prevent co-precipitation of Fe(III) minerals and amorphous silica, we conducted zeta-potential ( $\zeta$ -potential) measurements and potentiometric titrations on the cell-Fe(III)-mineral aggregates formed during microbial Fe(II) oxidation. Finally, in order to evaluate how the tested model could have contributed to the deposition of BIFs, we took our experimental data and extrapolated them to the ca. 2.5 billion-year-old Hamersley Group in Western Australia as a model depositional basin for BIF.

---

## 2. MATERIALS AND METHODS

### 2.1. Source of microorganisms, culturing medium and growth conditions

*R. iodosum* is a marine photoferrotroph belonging to the purple bacteria and placed amongst the  $\alpha$ -Proteobacteria. It was first isolated from a mud flat of the Jadebusen (North Sea) (Straub et al., 1999). The culture used was obtained from the Deutsche Sammlung von Mikroorganismen und Zellkulturen (DSMZ) in Germany (DSM 12328T) and kept in our laboratory collection for several years. Although it survives and grows at a wide range of temperatures between 10 and 35°C, it has a relatively narrow optimum where it shows the highest Fe(II) oxidation activity between 20 and 25°C.

*R. iodosum* was cultivated on marine phototroph medium which was prepared as outlined in Wu et al. (2014), but with the following modifications: (1) To simulate Archean seawater silica concentrations, 0.5684 g L<sup>-1</sup> Na<sub>2</sub>SiO<sub>3</sub> × 9 H<sub>2</sub>O was added to achieve a final silica concentration of 2 mM (Maliva et al., 2005). (2) Instead of 22 mM sodium bicarbonate, we added 30 mM as primary buffer and the pH was adjusted to 7.0. (3) No FeCl<sub>3</sub> was added to the trace metal solution, and instead Fe(II) was added as an anoxic and sterile 1 M FeCl<sub>2</sub> × 4 H<sub>2</sub>O stock solution (Hegler et al., 2008) at an initial concentration of 5 mM. Although this initial Fe(II) concentration is higher than the Fe(II) concentrations assumed for the Archean ocean (up to 0.5 mM; Holland, 1973; Morris, 1993), this high concentration was necessary to perform the experiments within a reasonable timeframe. (4) The medium was filtered once after the addition of Fe(II) to remove any Fe(II)-carbonate and -phosphate precipitates formed. The filtered medium was then transferred into 1L SCHOTT glass bottles and the headspace exchanged with N<sub>2</sub>/CO<sub>2</sub> (90:10, v/v) for 5 min. Therefore, in order to achieve maximum removal of minerals that are expected to form from the added Fe(II), phosphate and bicarbonate, the medium was placed at 5°C for at least 48 h. Following the formation of greenish-grey precipitates (likely siderite or vivianite; Hohmann et al., 2009), after 48 h, the pH of the medium was adjusted to 6.8 to simulate the circumneutral pH of the Archean seawater (Halevy and Bachan, 2017). Any forming precipitates were removed by filtration (Millipore filter, 0.22 mm) in an anoxic glovebox (100% N<sub>2</sub> atmosphere), and the headspace was again exchanged for N<sub>2</sub>/CO<sub>2</sub> (90:10, v/v). Filtration of the medium resulted in a removal of ~30% of the initially added Fe<sup>2+</sup> and ~31% of the added Si(OH)<sub>4</sub>. Consequently, the resulting starting concentration in the experiment was ~3.5 mM Fe<sup>2+</sup> and ~1.4 mM monomeric

silica. For stock cultures of *R. iodosum* 25 mL of medium were transferred into 58 mL serum bottles. Stock cultures were inoculated with 4% inoculum and incubated at 26°C in a light incubator with a 40-W incandescent light bulb.

## 2.2. Experimental set-up

In our experiments we aimed at simulating an Archean ocean prior to the development of widespread oxygenic photosynthesis in which anoxygenic photosynthetic Fe(II)-oxidizing bacteria would have accounted for most, if not all, Fe(II) being oxidized. To test whether temperature cycles can couple the biotically mediated precipitation of Fe(III) mineral layers during warm periods to the abiotic precipitation of silica during cold periods, we conducted precipitation experiments where we cycled the temperature between 26°C and 5°C – the temperature extremes exhibited by this species. This temperature change of 21°C is within the temperature range that was suggested for ancient oceans (between 10 and 33°C; Kasting et al., 2006), but crucially from an experimental perspective, these temperatures were chosen to demonstrate the feasibility of this mechanism within a reasonable timeframe. In total we simulated two warm periods (26°C in the light) and one cold period (5°C in the dark) over a period of 168 days in the main experiment. We also performed experiments specifically designed to investigate: (1) *R. iodosum*'s ability to oxidize Fe(II) at low temperatures, (2) *R. iodosum*'s ability to commence Fe(II) oxidation once it had been exposed to low temperatures, and (3) the effect of low temperatures and silica oversaturation on the chemical precipitation of amorphous silica.

### 2.2.1. First warm period – Fe(II) oxidation prior to silica precipitation

The main temperature cycling experiments were run in biotic triplicates with one additional abiotic (not inoculated) control. The abiotic control was set up to emphasize the key role of microbial Fe(II)-oxidizing activity and temperature in triggering the alternating deposition of Fe- and Si-rich layers by showing that in the absence of living cells no Fe(III) (oxyhydr)oxide formation will take place. 18 mL of filtered Fe(II)- and silica-containing medium (as described in Section 2.1) were transferred into 20 mL headspace vials in an anoxic glovebox (100% N<sub>2</sub>), stoppered with butyl rubber stoppers, brought out of the glovebox and the headspace exchanged for N<sub>2</sub>/CO<sub>2</sub> (90:10, v/v).

To initiate the biogenic precipitation of Fe(III) minerals, the biotic triplicates were inoculated with 5% (approximately  $7.5 \times 10^7$  cells mL<sup>-1</sup>) of a *R. iodosum* culture pre-grown on filtered medium containing 3.5 mM Fe(II) and 1.4 mM of silica (as described in Section 2.1) after an equal amount of medium was removed. The removed medium was subsequently used for Fe<sup>2+</sup> and monomeric silica quantification. The cultures were pre-grown in the presence of silica to adapt them to Si-rich conditions. All headspace vials were placed in a light incubator at 26°C and sampled every 5–6 days for Fe<sup>2+</sup> and monomeric silica quantification as described below. Once all Fe(II) was oxidized, an aliquot of medium was removed from each vial so that 8 mL remained. The supernatant removed was then used to quantify the remaining Fe<sup>2+</sup> and monomeric silica. The vials were subsequently refilled with filtered Fe(II)- and silica-containing medium in an anoxic glovebox (100% N<sub>2</sub>) to 18 mL, where care was taken to not disturb the already sedimented mineral layer. The headspace was exchanged for N<sub>2</sub>/CO<sub>2</sub> (90:10, v/v), each vial was sampled again for Fe<sup>2+</sup> and monomeric silica concentrations and then placed at 26 °C in the light. These steps were repeated until a clearly visible ca. 0.5–1 mm thick Fe(III) mineral layer had developed (Fig. 1A).

### 2.2.2. Cold period – abiotic silica precipitation

Once a sufficiently thick Fe(III) mineral layer had developed in the main experiment, monomeric silica (to a final concentration of ca. 4 mM) was added from a 50 mM Na<sub>2</sub>SiO<sub>3</sub> × 9 H<sub>2</sub>O stock solution (~pH 12.8) to test whether amorphous silica precipitation would already take place at this concentration (Tab. A.1, day 35). The monomeric silica solution was freshly prepared, adjusted to circumneutral pH using 1 M HCl in an anoxic glovebox (100% N<sub>2</sub> atmosphere) and 1.44 mL immediately added to the headspace vials. The neutralization was necessary to maintain the neutral pH of the medium and prevent the added monomeric silica from immediately being precipitated upon addition to the medium. The volume of 18 mL in the headspace vials was maintained by removing an amount of medium equal to the amount of silica solution added while also accounting for the volume removed during sampling. The removed medium was used for Fe<sup>2+</sup> and monomeric silica quantification and pH monitoring. After addition of the silica, the headspace vials were given 1 hour to equilibrate at room temperature in the light, the headspace was exchanged for N<sub>2</sub>/CO<sub>2</sub> (90:10, v/v) and sampled again for Fe<sup>2+</sup> and monomeric silica quantification. The headspace vials were then placed at 5°C in the dark.

Although amorphous silica precipitation would have been expected based on known solubility values (1.3 mM at 5°C; Gunnarsson and Arnórsson, 2000), no amorphous silica precipitation was observed at day 54. This lack of amorphous silica precipitation is potentially attributed to slow silica precipitation kinetics (Krauskopf, 1956 and references therein) or a lack of nucleation sites necessary for initiating the polymerization and precipitation of silica. Therefore, to identify the concentration of monomeric silica necessary to complete the experiment within a reasonable timeframe, we varied the concentration of the added monomeric silica (Table A.1), and from day 93 onwards, 8 mM monomeric silica were added repeatedly once the concentration dropped below 2 mM to create the amorphous silica layer. Care was taken to not disturb any layering that had already developed. During the entire time the headspace vials were kept at 5°C in the dark. The sampling frequency for Fe<sup>2+</sup> and monomeric silica quantification was adjusted from initially 7 days to 3 or 4 days to better resolve the development of the monomeric silica concentration.

Additionally, we investigated (1) how oversaturation with regards to amorphous silica would influence silica precipitation at low temperatures and (2) how the presence of cells, Fe(II) and light would influence the amorphous silica layer being formed. All complementary experiments were performed using the silica-containing marine phototroph medium in the same headspace vials using the general experimental setup. To answer the first question, Fe(II)-free marine phototroph medium was used. Fe(II) was omitted in this particular experiment in order to rule out any effect on silica precipitation by interaction of Fe(II) and silica during the formation of Fe(II)-silicates. This allowed to specifically determine the influence of temperature on silica precipitation. The experiment was divided into four setups each consisting of triplicates. To half of the setups neutralized monomeric silica was added to a final concentration of 8 mM as described before. The other half did not receive any additional silica and thus only contained approximately 1.4 mM monomeric silica. For each silica concentration half of the setups were incubated at 26°C and light and the other half at 5°C and light. Samples for dissolved monomeric silica quantification were taken before addition of additional monomeric silica and directly after addition of monomeric silica. During the first 12 h of the experiment samples were taken every 2–4 h, after 24 h, and every 2–3 days thereafter.

To answer the second question, the Fe(II)-containing marine phototroph medium was used. The experiment was set up as biotic triplicates containing 5% (0.9 mL) *R. iodosum*, pre-



grown on Fe(II)- and silica-containing medium, and one abiotic (non-inoculated) control. Neutralized monomeric silica was added to all headspace vials to achieve a final concentration of 8 mM. All headspace vials were incubated at 5°C and light. Samples for Fe<sup>2+</sup> and dissolved monomeric silica quantification were taken before addition of cells and monomeric silica and directly afterwards. Thereafter, samples were taken continuously every 2–3 days.

Furthermore, we determined whether *R. iodosum* would be able to oxidize Fe(II) under low temperature (5°C) conditions. The experiment consisted of a biotic triplicate containing 5% (0.9 mL) *R. iodosum*, pre-grown on Fe(II)- and silica-containing medium, and one abiotic (non-inoculated) control and was incubated continuously under light and at 5°C. Samples for Fe<sup>2+</sup> and dissolved monomeric silica quantification were taken immediately before and directly after the addition of *R. iodosum* cells and every 2–3 days thereafter.

### 2.2.3. Second warm period – Fe(II) oxidation following silica precipitation at low temperatures

Once a clearly visible 2–3 cm thick amorphous silica layer had developed in the main temperature cycling experiment, an aliquot of the supernatant (medium) was removed so that 14.1 mL remained in each headspace vial. The removed volume was used for Fe<sup>2+</sup> and monomeric silica quantification and pH monitoring. For the precipitation of the second Fe(III) mineral layer, 3.15 mL of filtered Fe(II)- and silica-containing medium was added to the biotic triplicates and 4.05 mL to the abiotic controls in an anoxic glovebox (100% N<sub>2</sub> atmosphere). The headspace was exchanged for N<sub>2</sub>/CO<sub>2</sub> (90:10, v/v), all headspace vials were sampled again for Fe<sup>2+</sup> and monomeric silica, and the biotic triplicates were re-inoculated with 5% (0.9 mL) of a pre-grown *R. iodosum* stock culture which resulted in approximately  $7.5 \times 10^7$  cells mL<sup>-1</sup> (Wu et al., 2014). The medium was exchanged to balance the loss of nutrients during the previous oxidation step, the dilution of the medium during the addition of the monomeric silica solution and supply new Fe(II) for growth of *R. iodosum*. A re-inoculation with new *R. iodosum* cells was deemed necessary as prolonged cold temperature and darkness (79 days), as well as dilution of the medium during the addition of the silica solution, potentially damaged the cells so that a fraction of them were possibly no longer viable. To simulate the second warm period all headspace vials were placed in a light incubator at 26°C and sampled every 3–4 days for Fe<sup>2+</sup> and monomeric silica quantification. 3 mL of medium were repeatedly exchanged as described before

(including Fe<sup>2+</sup> and monomeric silica quantification as well as pH monitoring) once the Fe(II) oxidation was completed until a clearly visible Fe(III) mineral layer had developed.

Finally, to determine whether *R. iodosum* would be able to recover from cold stress, we performed an experiment with Fe(II)- and silica-containing marine phototroph medium. The experiment was set up as biotic triplicates containing 5% (0.9 mL) *R. iodosum* pre-grown on Fe(II)- and silica-containing medium, with one abiotic (not inoculated) control. The headspace vials were incubated at 26°C and light until approximately half of the initial Fe(II) was oxidized. Thereafter, the headspace vials were transferred to 5°C and light, kept under these conditions for 10 days, and then transferred back to 26°C and light where they were incubated until all Fe(II) was oxidized. Samples for Fe<sup>2+</sup> and dissolved monomeric silica were taken before addition of *R. iodosum* and directly after inoculation. Thereafter, samples were taken every 2–3 days.

### **2.3. Fe analysis and calculation of maximum oxidation rates**

For Fe<sup>2+</sup> quantification 100 µL of sample was taken from the headspace vials under a constant N<sub>2</sub>/CO<sub>2</sub> (90:10, v/v) stream, fixed in 900 µL 1 M HCl and stored at 5°C until analysis. For the quantification of Fe<sup>2+</sup> the ferrozine assay was used (Stookey, 1970). The absorbance at 562 nm was measured with a microtiter plate reader (Multiskan GO Microplate Spectrophotometer with internal software (SkanIT RE for Multiskan GO 3.2)).

The maximum oxidation rates were determined by linear regression analysis through the steepest 2 or when possible, steepest 3 points of the Fe<sup>2+</sup> curve at a given time point.

### **2.4. Silica analysis**

For silica analysis 50 µL of sample were taken from the headspace vials under a constant N<sub>2</sub>/CO<sub>2</sub> (90:10, v/v) stream, diluted either 1:20 or 1:40 with MilliQ<sup>®</sup> water to not exceed the maximum concentration of 80 µM for the assay and measured as soon as possible after sampling. For quantification of monomeric silica, a modified protocol of the molybdenum blue method from Strickland and Parsons (1972) was used. To 1 mL of diluted sample 40 µL acid molybdate solution was added, mixed by shaking and allowed to react for 15 minutes at room temperature. Thereafter, 40 µL of oxalic acid were added, mixed by shaking and 20 µL of ascorbic acid added immediately afterwards. The blue color was allowed to develop for 60 min at room temperature. 200 µL of sample were then measured spectrophotometrically at 810 nm in black-walled micro-

titer plates using a Multiskan GO Microplate Spectrophotometer with internal software (SkanIT RE for Multiskan GO 3.2).

## 2.5. Zeta-potential ( $\zeta$ -potential) measurements

*R. iodosum* was cultivated as described above in 100 mL serum bottles containing 50 mL anoxic marine phototroph medium without additional silica. To compare the  $\zeta$ -potential of biogenic Fe(III) minerals produced by the Fe(II)-oxidizing strain *R. iodosum* to abiotically precipitated Fe(III) minerals, pressurized 0.22  $\mu$ m-filtered air (with 21% O<sub>2</sub>) was added to serum bottles with the same Fe(II)-containing medium but not inoculated with *R. iodosum* to oxidize the Fe(II) abiotically leading to the precipitation of abiogenic Fe(III) minerals.

Samples of biogenic and abiogenic Fe(III) minerals were diluted with 10 mM HEPES-buffered MilliQ<sup>®</sup> water, which was adjusted to pH 6.8 in order to have the same pH as in the initial medium. To test the influence of the geochemical composition of the marine medium on the  $\zeta$ -potential values, abiogenic ferrihydrite (Schwertmann and Cornell, 2008) and biogenic Fe(III) minerals produced by *R. iodosum* were mixed with a modified version of the above described marine phototroph medium which was mixed at different ratios with 10 mM HEPES buffered MilliQ<sup>®</sup> water (medium only, 10:1, 1:1, 1:10 and MilliQ<sup>®</sup> water only). For the modified marine phototroph medium, the medium was prepared under air, no medium additives were added, the bicarbonate buffer was replaced by a 10 mM HEPES buffer, and the pH was adjusted to 6.8. All measurements were conducted using a Zetasizer Nano ZSP (Malvern, Herrenberg, Germany) with Zetasizer Nano Series disposable folded capillary cells (DTS1070; Malvern, Herrenberg, Germany).

## 2.6. Potentiometric titrations of Fe(III) mineral-cell aggregates

For potentiometric titrations, *R. iodosum* was cultivated as described above in silica-free medium. Upon completion of Fe(II) oxidation (determined by the Ferrozine method), the remaining medium including free cells was removed anoxically after shaking and inverting the culture and allowing the cell-Fe(III)-mineral aggregates to settle. Thereafter, fresh Fe(II)-free medium was added, the bottle was shaken gently, the cell-mineral-aggregates allowed to re-settle, and the medium supernatant removed again. This washing step was repeated twice to remove any free cells from solution in order to only have cell-Fe(III)-mineral aggregates for the titrations. After the last washing step, the samples were suspended in 0.01 M NaNO<sub>3</sub> and centrifuged for 10

min at 10,000 g, after which the  $\text{NaNO}_3$  was decanted and wet mass of sample was determined. Then, 0.075 g of the cell-mineral aggregates were suspended in 30 mL of 0.01 M  $\text{NaNO}_3$  for a concentration of  $2.5 \text{ g L}^{-1}$  (wet mass) and purged with  $\text{N}_2$  gas for 15 min prior to and during the titration in order to establish and maintain a  $\text{CO}_2$  free environment. The titrations were performed on a Metrohm Titrando 905 using a Metrohm pH probe calibrated to pH 4, 7, and 10 using commercially available buffers (Fisher Scientific). Initially, the solution was acidified to pH 3 using 0.1 M HCl, followed by an “up” titration where the pH of the solution was increased to pH 9 by incrementally adding aliquots of 0.1 M NaOH, with the amount of titrant and pH recorded with each addition. Once pH 9 was achieved, a “down” titration was performed to return the pH to 3 by adding aliquots of 0.1 M HCl to test the reversibility of proton binding and to observe for any hysteresis due to dissolution of the aggregates. All titrations were performed using “dynamic mode” where the titrator adds a variable amount of titrant depending on the instantaneous buffering capacity of the system, with additions only being made once the pH electrode achieved a stability of  $0.2 \text{ mV s}^{-1}$ .

The titration data was evaluated in terms of the concentration of base added to the system and modeled using a least-squares optimization method to solve for both site densities and  $\text{pK}_a$  values within a fixed interval using FITEQL v 4.0 (Herbelin and Westall, 1999). Models employing 2–4 proton-binding sites were tested in FITEQL, with a 2-site model having the best fit to the experimental titration data.

## **2.7. $^{57}\text{Fe}$ Moessbauer spectroscopy**

Samples for Fe(III) mineral identification were taken from the experiments as liquid mineral suspensions and filtered through  $0.45 \text{ }\mu\text{m}$  Luer-lock filters and fixed on Kapton tape. The samples were loaded into a closed-cycle exchange gas cryostat (Janis cryogenics). Spectra were collected at 77 K and 5 K in transmission geometry using a constant acceleration drive system (WissEL) in the Geomicrobiology group at Center for Applied Geosciences, University of Tuebingen. A  $^{57}\text{Co}$  source embedded in a Rhodium matrix was used as  $\gamma$ -radiation source. The spectra were calibrated against a  $7 \text{ }\mu\text{m}$  thick  $\alpha\text{-}^{57}\text{Fe}$  foil at room temperature. The RECOIL software suite (University of Ottawa, Canada) was used for the calibration and spectra modeling using Voigt-based line shapes was performed (Rancourt and Ping, 1991). The Lorentz half-width-half-maximum was kept constant at  $0.14 \text{ mm s}^{-1}$  as determined by using the minimum line

width of the third and fourth peak of the calibration foil in the models. The Gauss' sigma parameter was used to account for line broadening. The relative proportion of the areas covered by each doublet and sextet of the total spectrum is corresponding to the relative abundance of Fe in a particular crystal lattice site.

## 2.8. $\mu$ XRD measurements

For  $\mu$ XRD measurements an aliquot of the mineral suspensions was sampled from the experiment, the cell-Fe(III)-mineral aggregates were harvested by centrifugation (1761 g) and vacuum-dried. A small aliquot of this mineral powder was put on a silicon wafer.  $\mu$ XRD measurements were conducted using a 2D-Microdiffractometer (Bruker D8 Discover with GADDS,  $\mu$ -XRD<sup>2</sup>, Bruker AXS GmbH, Karlsruhe, Germany) available in the Geoscience Department at the University of Tuebingen. The instrument was equipped with a Co-anode as X-ray source with a Co-K $\alpha$  wavelength of 1.79030 Å, a primary graphite monochromator and a 2D detector with 40° angle cover (Bruker Vântec 500, Bruker AXS GmbH, Karlsruhe, Germany). Reflection patterns were collected for 120 seconds per angle setting. Reflection pattern analysis and mineral identification was carried out using the Match!© program for phase identification from powder diffraction (Match!, Crystal Impact, Bonn, Germany).

## 2.9. Scanning electron microscopy (SEM)

For SEM imaging, *R. iodosum* was cultivated as previously described in 100 mL serum bottles containing either silica-free or silica-containing marine phototroph medium. In order to compare the morphology of the cell-Fe(III) mineral aggregates formed by *R. iodosum* to abiotically precipitated Fe(III) minerals, pressurized, 0.22  $\mu$ m-filtered air (21% oxygen) was added to serum bottles with the same Fe(II)-containing medium but not inoculated with *R. iodosum*. Samples for SEM were fixed in glutaraldehyde (final concentration 2.5%) overnight, washed twice with MilliQ<sup>®</sup> water, and mounted on Poly-L-lysine covered glass slides. The samples were prepared by serial dehydration with ethanol (30%, 70%, 95%, each 5 minutes and 2x 100%, each 30 minutes), treated with hexamethyldisilazan (HMDS, 2 times 30 seconds) and dried by evaporation at room temperature and ambient pressure (Zeitvogel et al., 2017). Samples were coated with a ~15 nm Pt-layer using a Balzers Union Med 010 (Bal-Tec, Balzers, Liechtenstein) sputter coater. SEM analysis was performed at the Center for Applied Geosciences, University of Tuebingen, using a LEO 1450 VP (Zeiss) equipped with an Everhart-Thornley SE-

Detector. Secondary electron (SE) imaging was performed at an acceleration voltage of 7 kV with a working distance of 8 mm. The pressure was targeted at  $8 * 10^{-6}$  mbar. No elemental analysis by EDS was performed.

### **2.10. Fe(III) mineral aggregates size analysis**

For Fe(III) mineral aggregate size determination, the ImageJ software was used to analyze the aggregates visualized in SEM micrographs. To randomize the particles counted, horizontal, vertical and diagonal lines were drawn from the top left corner of the picture and all aggregates along these lines measured. For all aggregates the distance between the two points the farthest away from each other were measured. In order to obtain some statistical significance at least 100 aggregates were analyzed. It has to be noted that aggregate size analysis by SEM is a 2D technique and does not consider potential differences in size in the z-axis.

### **2.11. Modelling of mineral saturation states and aqueous speciation**

Geochemical modelling was performed for the low-temperature stage of the precipitation experiments in order to determine the aqueous speciation of silica and compare the mineral saturation states of amorphous silica and greenalite under the given silica and Fe(II) concentrations and geochemical composition of the medium used in the experiment. For equilibrium speciation modelling Visual MINTEQ vs. 3.1 was used employing a solubility product for greenalite of  $\log K_{sp} = 27.70$  calculated based on Tosca et al. (2016).

## **3. RESULTS**

### **3.1. Development of Fe(III) and silica mineral layers at fluctuating temperatures**

In order to demonstrate the alternating precipitation of Fe(III) and silica minerals, we incubated Fe(II)- and silica-containing medium with the phototrophic Fe(II)-oxidizing bacterium *Rhodovulum iodosum* and cycled the temperature between 26°C and 5°C. The basic idea of the experimental setup was (1) to investigate how the presence of silica concentrations near the saturation stated of amorphous silica (ca. 2 mM) affect microbial Fe(II) oxidation at warm temperatures and whether this would affect the formation of Fe(III) mineral layers, and (2) to explore the effect of lowering the temperature on the precipitation of silica in the presence of high concentrations of dissolved  $Fe^{2+}$  and how lowering the temperature would affect the activity

of *R. iodosum*. For silica precipitation at low temperatures, silica concentrations above the saturation limit of ca. 2 mM were necessary, in our case ca. 8 mM, to overcome the kinetic limitations for precipitation and to observe precipitation in experimentally reasonable timeframes of several weeks. Similarly, higher  $\text{Fe}^{2+}$  concentrations of 2–3 mM, compared to the ca. 0.5 mM  $\text{Fe}^{2+}$  concentration assumed for the Archean ocean, were necessary to precipitate a sufficient quantity of Fe(III) minerals within the experimental timeframe.

Photos of the precipitating Fe mineral and amorphous silica layers were taken in order to record the banding development. The activity of the phototrophic Fe(II)-oxidizing bacterium *R. iodosum* at 26°C in the light resulted in the formation of orange-colored Fe(III) mineral precipitates. After 54 days, during which fresh Fe(II)- and silica-containing medium had been added 4 times to simulate constant input in ancient oceans of  $\text{Fe}^{2+}$  from hydrothermal activity and silica from the continents (Hamade et al., 2003), an approximately 1 mm thick Fe(III) mineral layer developed (Fig. 1A). During the same time the abiotic (not inoculated) setup remained colorless and only a minor amount of pale greyish-green precipitates formed (inset Fig. 1A). This corresponded to a removal of aqueous Fe(II) of only 7% compared to the amount that was oxidized and precipitated by the photoferrotrophs. After the development of the Fe(III) mineral layer by day 54, more monomeric silica was added to all setups which were then transferred to 5°C resulting in the supersaturation of the medium with respect to amorphous silica. After 126 days, a clearly defined amorphous silica layer had developed (Fig. 1B). This amorphous silica layer was visible in both the biotic vials that contained *R. iodosum* cells, as well as in the abiotic setups. Following the addition of new medium, re-inoculation of the biotic setups with *R. iodosum*, and the transfer back to 26°C and light, caused a second Fe(III) mineral layer to precipitate on top of the amorphous silica layer. This layer was again visible as orange-colored Fe(III) minerals in the biotic setups (Fig. 1C). The alternating layers of Fe(III) minerals and amorphous silica remained stable and clearly distinct on a macroscopic level until the end of the experiment, although the thickness of the silica layer decreased slightly from approximately 3 cm to 2.5 cm due to density-driven compaction.

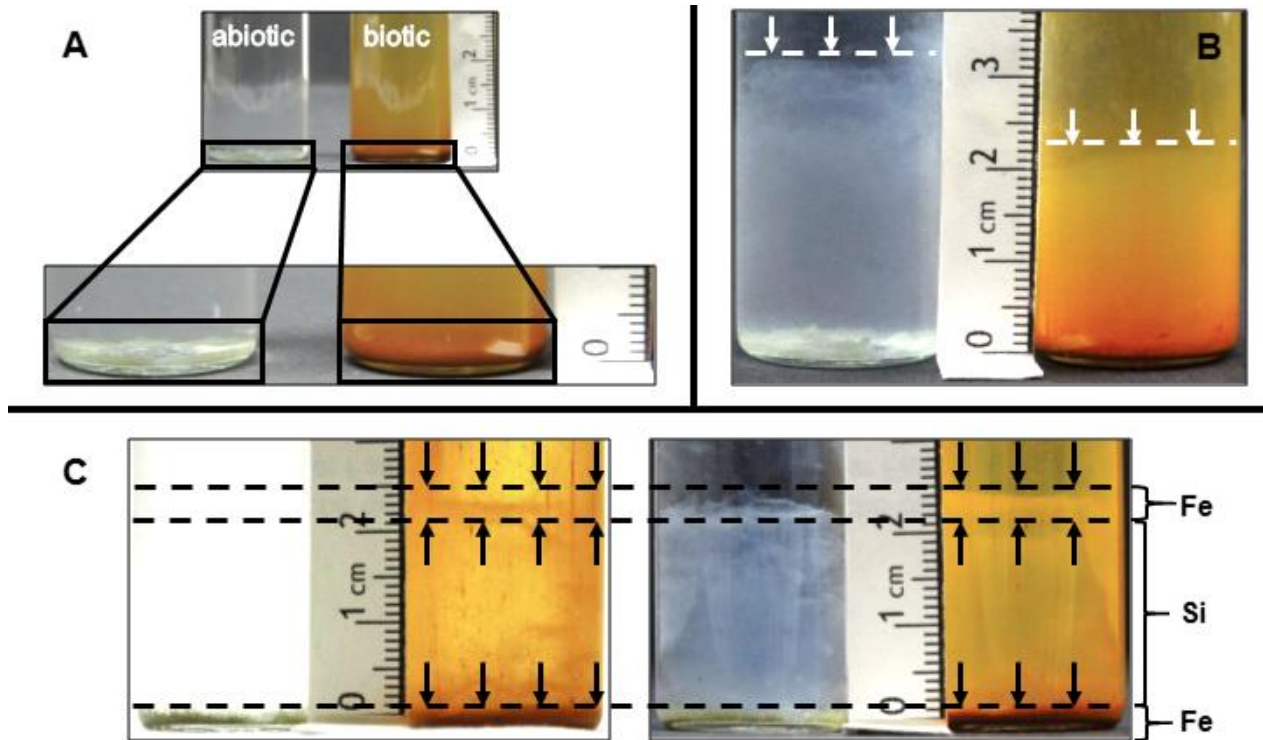


Fig. 1. Development of iron- and silica-layering over time. (A) Shows microbially mediated deposition of a Fe(III) mineral layer by the activity of the phototrophic Fe(II)-oxidizer *R. iodosum* at 26°C compared to the abiotic setup. The upper picture in (A) shows Fe(II) oxidation and formation of Fe(III) minerals which is evident by the development of orange-colored minerals after 43 days. The lower picture in (A) shows close-ups that demonstrate the precipitation of the orange Fe(III) minerals in the biotic but not in the abiotic setups. (B) Shows the abiotic precipitation of amorphous silica at 5°C after 126 days in the biotic setups (right) as well as in the abiotic, not-inoculated setup (left). The white dashed line and arrows indicate the upper limit of the amorphous silica layer. Please note that the white band in the biotic setup is difficult to see in the right photograph due to the orange minerals that stick to the glass wall. (C) Shows the deposition of an orange-colored Fe(III) mineral layer (2.1–2.5 cm) on top of the previously precipitated amorphous silica layer (0.1–2.1 cm) in the biotic setup after 168 days. The precipitation of Fe(III) minerals in biotic setups is mediated by *R. iodosum* at 26°C during a second warm period. A bright (left picture) and dark (right picture) background were chosen in order to better visualize the difference between the Fe and silica layers. Respective layers are marked by black dashed lines, arrows and braces with labelling.

### 3.2. Fe(III) mineral formation by microbial phototrophic Fe(II) oxidation and abiotic silica precipitation

In addition to the physical changes during the deposition of alternating Fe(III)- and silica-rich layers, we also followed the underlying changes in the geochemistry of our experimental solution. Specifically, we measured changes in concentrations of the dissolved species, Fe<sup>2+</sup> and monomeric silica.

During the first warm incubation period, *R. iodosum* oxidized ca. 2.0–2.5 mM of dissolved Fe<sup>2+</sup> within 4–7 days (Fig. 2, upper panel until day 35) yielding initial average Fe(II) oxidation rates of ca. 0.3 mM d<sup>-1</sup> (between day 0 and 13) and maximum Fe(II) oxidation rates of



0.6 mM d<sup>-1</sup>. Fe(II) removal from solution mediated by *R. iodosum* was >96%. Although there was some removal of monomeric silica from solution together with the Fe(III) minerals during Fe(II) oxidation, approximately 1.0 mM monomeric silica stayed in solution all the time (Fig. 2). No Fe(II) oxidation was observed in the abiotic control during the first warm period as indicated by the absence of orange-colored precipitates (Fig. 1A).

During the cold period between days 54 and 133 (Fig. 2), monomeric silica was added in 5 spikes to the biotic setups, each resulting in measured monomeric silica concentrations of >4 mM (day 99). Concentrations of monomeric silica decreased quickly (within 3–6 days) to an overall average of 1.7 mM (Fig. 2). The average monomeric silica concentration immediately before adding a new silica spike was 1.6 mM. Maximum removal rates of monomeric silica ranged from 0.3–0.5 mM d<sup>-1</sup>. The Fe<sup>2+</sup> concentration in the biotic setup remained at approximately 0 mM as expected due to the absence of fresh Fe<sup>2+</sup> addition. The monomeric silica concentrations in the abiotic control essentially equaled those in the biotic setups. The Fe<sup>2+</sup> concentration in the abiotic setup (that was ca. 3.5–3.7 mM before silica addition) decreased significantly after the first addition of monomeric silica from 3.5 mM to 1.2 mM. This is likely due to the removal of Fe(II)-containing medium prior to the addition of neutralized monomeric

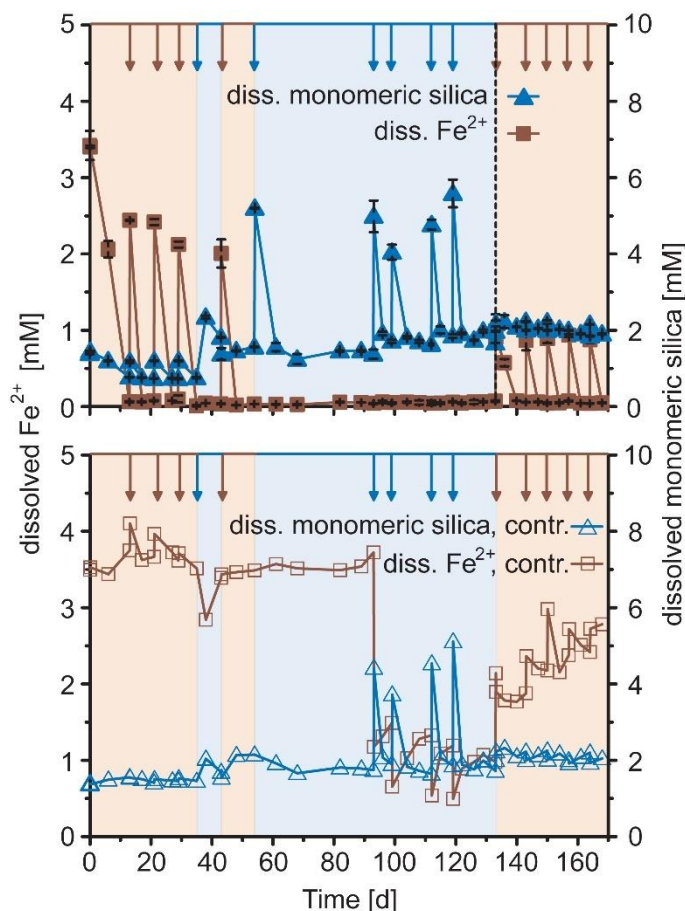


Fig. 2. Variations in dissolved Fe<sup>2+</sup> and monomeric silica concentrations over time during temperature cycles under simulated Archean ocean conditions. The top panel shows the biotic setups, while the bottom panel shows the abiotic (non-inoculated) setup. Orange arrows mark removal of supernatant and addition of new microbial growth medium with ca. 3.5 mM of Fe<sup>2+</sup> and ca. 1.4 mM of monomeric silica. Blue arrows mark addition of monomeric silica solution. Orange shaded areas mark incubation at 26°C and light. Blue shaded areas mark incubation at 5°C in the dark. Vertical black dashed line marks re-inoculation with *R. iodosum* in the biotic replicates. Data shown for biotic setups are the mean of triplicates ± standard deviation. Data of abiotic controls are single measurements.

silica and potentially the precipitation of some Fe(II)-silicates; it further decreased during the subsequent additions of monomeric silica to a value of ca. 1 mM. Prior to each addition of neutralized monomeric silica solution between 8% and 40% of the existing solution was removed. Consequently, at the end of the cold phase only about 34% of the initial solution was still present in each vial. Similarly, as proposed above, Fe<sup>2+</sup> would have been removed from solution to a final concentration of approximately 1.2 mM. All other nutrients and solutes were diluted in a similar manner.

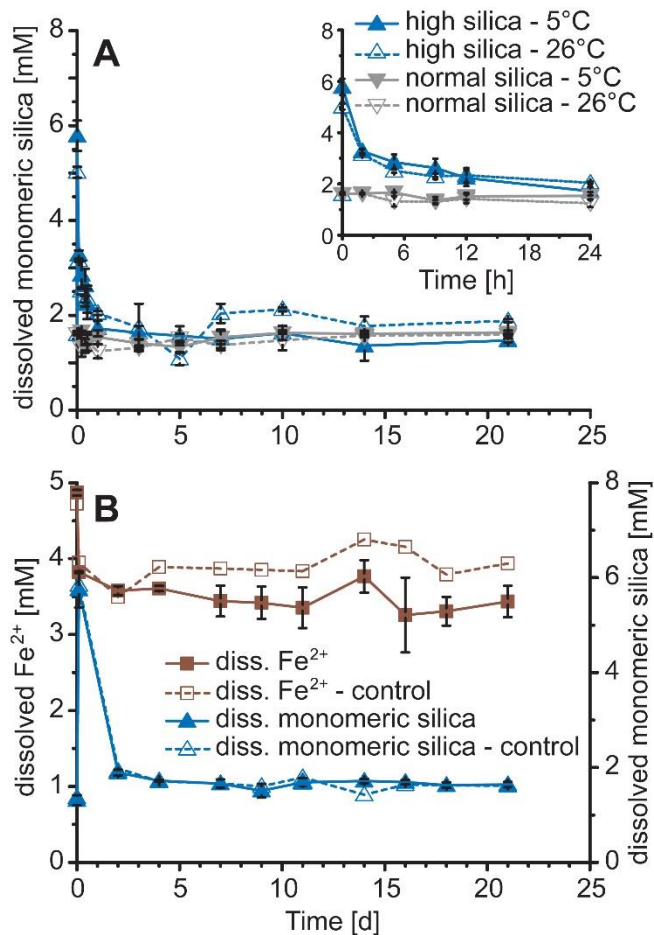


Fig. 3. Development of dissolved monomeric silica concentration over time during: (A) silica precipitation kinetics experiments at 5°C and 26°C in light and (B) dissolved Fe<sup>2+</sup> and monomeric silica concentrations during silica precipitation in the presence of *R. iodosum*, dissolved Fe<sup>2+</sup> at 5°C and light. The insert in (A) shows the development of dissolved monomeric silica during the first 24 h. Data shown in (A) are the mean from triplicates  $\pm$  standard deviation. In (B) data for biotic setups are the mean from triplicates  $\pm$  standard deviation while the data for the abiotic (non-inoculated) control represent single measurements.

Since a high degree of silica oversaturation was necessary to overcome the kinetic limitation of amorphous silica precipitation in the main experiment, we performed additional experiments to: (1) compare the kinetics of silica precipitation at different silica concentrations and temperatures to determine the effect of amorphous silica oversaturation during the cold period, and (2) determine the combined influence of Fe(II), cells and light on amorphous silica precipitation during the cold period. The silica precipitation kinetics experiments (Fig. 3, panel A) showed that at elevated initial monomeric silica concentrations (8 mM), 74.5% (at 5°C) and 80.8% (at 26°C) of the silica were removed during the first 24 h of the experiment. Monomeric silica polymerization/removal rates showed no significant differences for 5°C and 26°C ( $0.56 \pm 0.09$  mM h<sup>-1</sup> and  $0.48 \pm 0.02$  mM h<sup>-1</sup>, respectively;  $p =$

0.2073). However, the final equilibrium concentration at day 21 differed significantly ( $p = 0.0001$ ) with  $1.47 \pm 0.04$  mM at  $5^{\circ}\text{C}$  and  $1.89 \pm 0.03$  mM at  $26^{\circ}\text{C}$ . By comparison, setups with only  $\sim 1.4$  mM dissolved monomeric silica present initially showed no silica precipitation independent of the temperature and the concentration remained constant for the duration of the experiment.

The second experiment, which was designed to test the influence of Fe(II), cells and light on amorphous silica precipitation during the cold period (Fig. 3, panel B), showed an initial strong decrease of  $\text{Fe}^{2+}$  after the removal of  $\text{Fe}^{2+}$ -containing medium and the addition of neutralized monomeric silica from approximately 4.9 mM  $\text{Fe}^{2+}$  to 3.9 mM  $\text{Fe}^{2+}$ . Over the course of the experiment the  $\text{Fe}^{2+}$  concentration further decreased to approximately 3.5 mM. Nonetheless, no visible formation of Fe(III) (oxyhydr)oxides was observed. The  $\text{Fe}^{2+}$  concentration in the abiotic control stayed constant after the initial decrease. The dissolved monomeric silica concentration showed a strong decrease after the first 48 h and remained constant for the remainder of the experiment.

Additionally, we determined the influence of low temperatures ( $5^{\circ}\text{C}$ ) on the ability of *R. iodosum* to oxidize Fe(II) and whether the formation of Fe(III) (oxyhydr)oxides would be expected under these conditions. Therefore, the temperature was kept constant at  $5^{\circ}\text{C}$  while keeping the vials illuminated (Fig. 4, panel A). The biotic triplicates showed a slight decrease in  $\text{Fe}^{2+}$  from an initial concentration of approximately 4.9 mM to 4.2 mM at the end of the experiment. However, no visible orange-

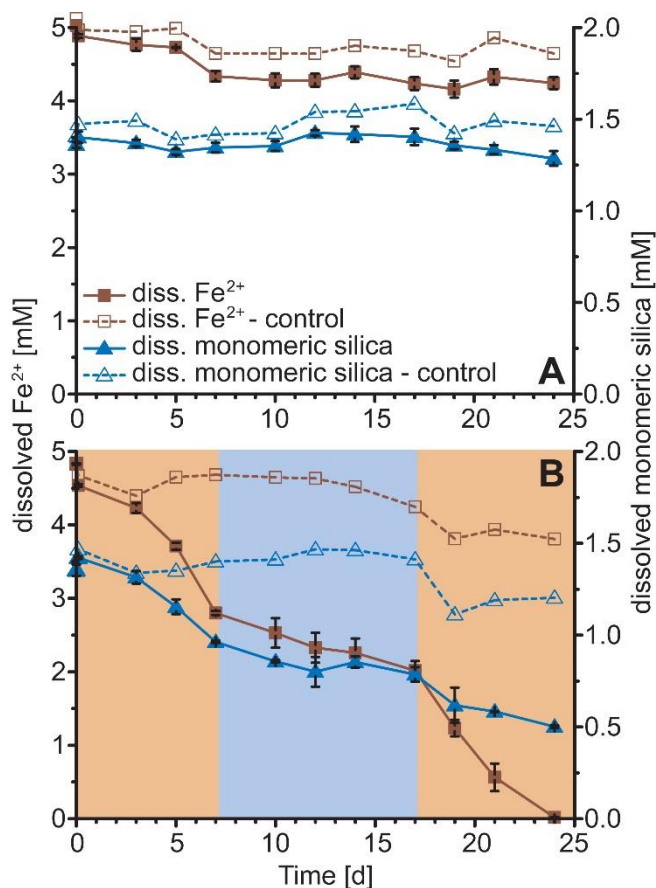


Fig. 4. Development of dissolved  $\text{Fe}^{2+}$  and monomeric silica concentrations over time for: (A) incubation of *R. iodosum* at  $5^{\circ}\text{C}$  and light, and (B) incubation of *R. iodosum* under changing temperature conditions and light. Data for biotic setups are the mean from triplicates  $\pm$  standard deviation while the data for the abiotic (non-inoculated) controls represent single measurements. Orange shaded areas in panel (B) represent incubation at  $26^{\circ}\text{C}$ , while blue shaded areas mark incubation at  $5^{\circ}\text{C}$ .

colored Fe(III) (oxyhydr)oxides were observed. The Fe<sup>2+</sup> concentration in the abiotic (non-inoculated) control decreased slightly from an initial concentration of approximately 5 mM to a final concentration of approximately 4.7 mM. The Fe(II) oxidation rates of the biotic triplicates and the abiotic control showed only a minor deviation with 0.03 mM d<sup>-1</sup> and 0.02 mM d<sup>-1</sup>, respectively. The dissolved monomeric silica concentration remained constant over the course of the experiment for both the biotic triplicates and the abiotic (non-inoculated) abiotic control.

During the second warm period of the main experiment (days 133–168, Fig. 2), *R. iodosum* oxidized approximately 0.9 mM of Fe<sup>2+</sup> in the biotic setups within 4 to 7 days, yielding maximum oxidation rates of ca. 0.2 mM d<sup>-1</sup> (Fig. 2). Fe(II) oxidation is also indicated by the precipitation of orange-colored Fe(III) minerals on top of the amorphous silica layer (Fig. 1C). The removal of Fe<sup>2+</sup> from solution was >92%. In contrast to the first warm period, the monomeric silica concentrations during the second warm period remained at amorphous silica saturation (2.2 mM). These values are approximately 35% higher than the initial monomeric silica concentration at the beginning of the experiment and almost 24% higher than corresponding average values during the cold period. It thus appears that the amount of monomeric silica removed during Fe(II) oxidation is affected by the amount of Fe<sup>2+</sup> oxidized, and as expected, the remaining concentration of monomeric silica is influenced by the high and low temperatures. At the same time the remaining dissolved Fe<sup>2+</sup> concentration in the abiotic setup increased consistently from 1.9 mM on day 133 to 2.8 mM at the end of the experiment. The abiotic setup showed similar trends in monomeric silica concentrations as the biotic setups, i.e., changing silica solubility at low vs. high temperatures controls silica precipitation and thus the remaining silica concentrations in solution.

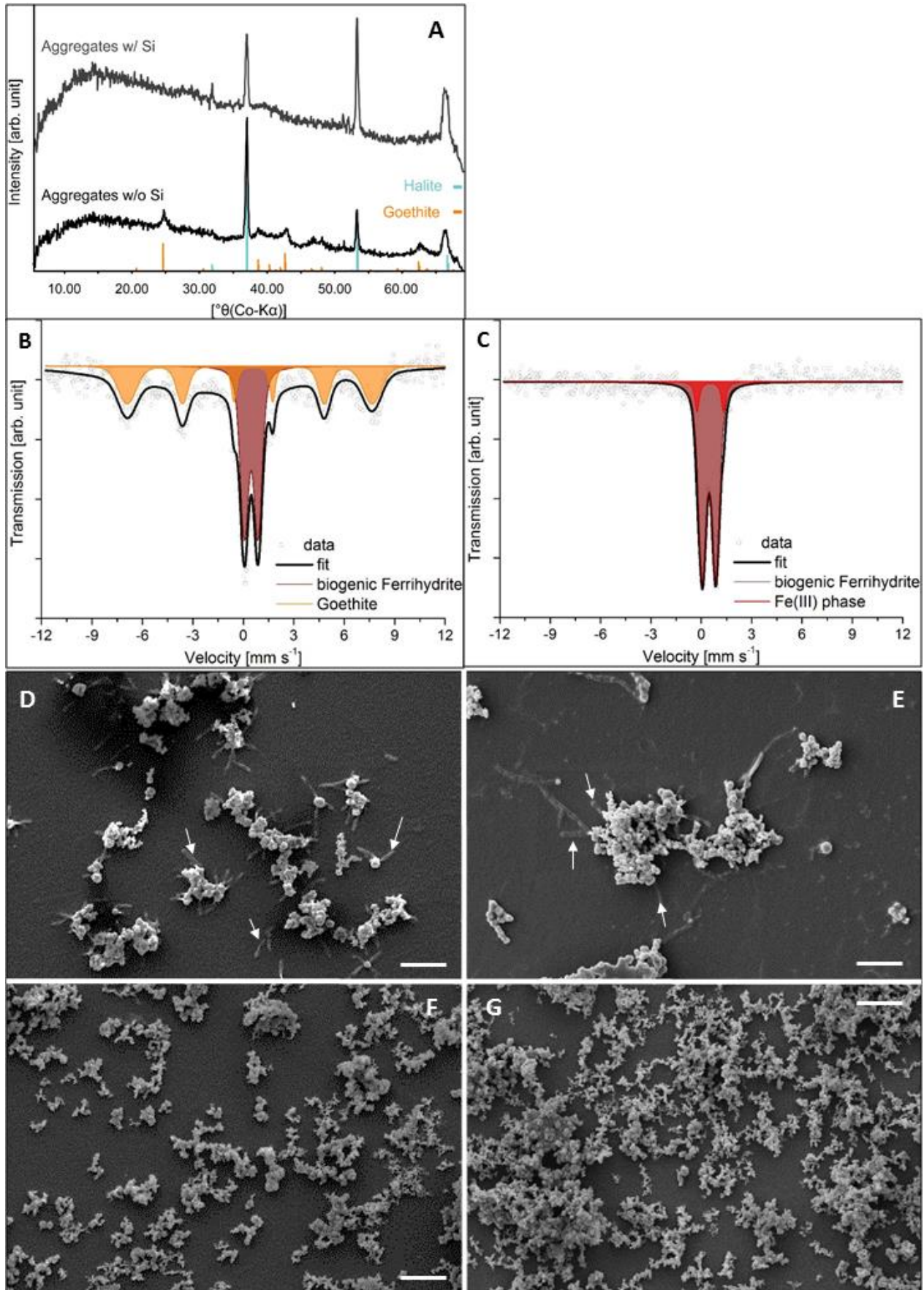
Crucial to the temperature cycling model envisioned in our study is the ability of *R. iodosum* to recover and resume Fe(II) oxidation after a prolonged phase of cold temperatures. Therefore, we performed an additional experiment under varying temperature conditions to verify the ability of *R. iodosum* to resume Fe(II) oxidation after inactivity during a cold period (Fig. 4, panel B). *R. iodosum* showed rapid initial Fe(II) oxidation with rates of  $0.36 \pm 0.02$  mM d<sup>-1</sup>, rates similar to the main experiment (Fig. 2, day 0–13), and formation of orange-colored Fe(III) (oxyhydr)oxides during the first warm period (Fig. 4B, 26°C, day 0–7). During the following cold period (Fig. 4B, 5°C, day 7–17) the Fe(II) oxidation rate decreased to  $0.07 \pm 0.01$  mM d<sup>-1</sup>, resulting in a decrease of the Fe<sup>2+</sup> concentration from approximately 2.8–2.0 mM. The increase in

temperature to 26°C during the second warm period (Fig. 4B, day 17–24) resulted in *R. iodosum* oxidizing Fe(II) at rates comparable to the first warm period ( $0.36 \pm 0.04 \text{ mM d}^{-1}$ ), showing that *R. iodosum* would theoretically be able to recover from prolonged cold stress. During the first warm period, approximately 32% of the initially present dissolved monomeric silica was removed from solution. During the following cold period and the second warm period another 18% and 15% dissolved monomeric silica, respectively, were removed from solution. The Fe<sup>2+</sup> and dissolved monomeric silica concentrations of the abiotic (non-inoculated) control remained relatively constant until the end of the experiment.

### 3.3. Properties of Fe(III) mineral precipitates

To identify the mechanism which led to the separate precipitation of Fe- and Si-rich minerals, we analyzed the mineral identity, structure and morphology, as well as the charge ( $\zeta$ -potential) of the primary minerals formed either by *R. iodosum* or by abiotic reaction of Fe<sup>2+</sup> with O<sub>2</sub>. The X-ray diffractograms of the precipitates formed in the presence of *R. iodosum*, both in the absence as well as in the presence of dissolved silica, showed reflections representative for NaCl, stemming from the salt-rich marine medium (Fig. 5A). The sample taken from Fe(III) mineral precipitates formed in the absence of silica showed additional reflections representative of goethite, where the broad base, relatively low intensity and signal quality suggest goethite being present in a low crystalline form. The Fe(III) mineral precipitates formed in the presence of silica showed no additional reflections and were X-ray amorphous with regard to the Fe-bearing mineralogy.





← Fig. 5. Identity and structure of biogenic and abiogenic Fe(III) mineral precipitates. (A) shows X-ray diffractograms of Fe(III) minerals formed by *R. iodosum* in the presence and absence of silica. (B) and (C) show Moessbauer spectra collected at 77 K (data for 5 K measurements is shown in the supporting information). Circles represent collected data points while the solid black lines represent the fit. (B/C) represent spectra collected from Fe(III) minerals precipitated by *R. iodosum* in the absence of silica (B) and presence of silica (C). (D-G) SEM micrographs taken from Fe(III) minerals either precipitated by *R. iodosum* in the absence of silica (D), Fe(III) minerals precipitated by *R. iodosum* in the presence of silica (E), abiogenic Fe(III) minerals precipitated by addition of O<sub>2</sub> to silica-free medium (F), and abiogenic Fe(III) minerals precipitated by addition of O<sub>2</sub> to silica-containing medium (G). The size bar in all SEM micrographs is 5 μm. Cells are indicated by white arrows.

Both biogenic Fe(III) minerals formed by *R. iodosum* in the absence or presence of silica were additionally identified by Moessbauer spectroscopy. For the minerals precipitated in the absence of silica, two distinct mineral phases were identified in the Moessbauer spectrum measured at 77 K (Fig. 5B). A mineral phase identified as biogenic ferrihydrite by its paramagnetic doublet and fitting parameters (Table 1; Eickhoff et al., 2014) made up for 52.5% of all minerals present. The second mineral phase, which made up 47.5% of the fit, was most closely related to goethite and identified by its parameters (Table 1) as well as its partial magnetic ordering and collapsed sextet (Halama et al., 2016). This interpretation was supported by Moessbauer spectra obtained at 5 K (Appendix A, Fig. A.1). The biogenic minerals precipitated in the presence of silica (Fig. 5C) consisted mainly of ferrihydrite (90.8%), which was identified by its paramagnetic doublet, an isomer shift of 0.46 mm s<sup>-1</sup> and a quadrupole shift of 0.80 mm s<sup>-1</sup> in the spectrum measured at 77 K (Eickhoff et al., 2014; Halama et al., 2016). A second, hitherto unidentified Fe(III) phase comprised 9.2% of the fitting (Table 1). However, this second mineral phase was not found in Moessbauer spectra obtained at 5 K. Here, biogenic ferrihydrite made up for 100% of the fit and was identified by its parameters (Appendix A, Table A.2).

Table 1

Moessbauer spectroscopy data obtained at 77 K for biogenic Fe(III) minerals precipitated by *R. iodosum* in the presence or absence of silica. <sup>1</sup>IS = isomer shift, <sup>2</sup>QS = quadrupole shift, <sup>3</sup>B<sub>hf</sub> = hyperfine field, <sup>4</sup>Fh = ferrihydrite.

	IS <sup>1</sup> [mm s <sup>-1</sup> ]	QS <sup>2</sup> [mm s <sup>-1</sup> ]	B <sub>hf</sub> <sup>3</sup> [T]	Area [%]
<b>No silica</b>				
Biog. Fh <sup>4</sup>	0.46	0.81	-	52.5
Goethite	0.48	-0.11	45.19	47.5
<b>With silica</b>				
Biogenic Fh <sup>4</sup>	0.46	0.80	-	90.8
Fe(III) phase	0.53	1.58	-	9.2

Based on SEM analyses, cell-Fe(III) mineral aggregates precipitated in the absence of silica generally showed close association between cells and minerals (Fig. 5D). Aggregate sizes were  $7.6 \pm 5.2$   $\mu\text{m}$  as determined by electron microscopy. The surface of the minerals was rough and needle-like, forming bulb-like structures. Compared to the biogenic cell-Fe(III) mineral aggregates precipitated in the absence of silica, the biogenic aggregates formed in the presence of silica showed less cells associated with the minerals. Furthermore, the minerals formed by bacteria in the presence of silica were smooth and appeared to consist of bulb-like shapes that stuck together (Fig. 5E). Their average size was  $10.3 \pm 9.3$   $\mu\text{m}$ . However, in both cases, despite being associated with the Fe(III) minerals, the cells generally seemed to be free of mineral precipitates. Calculated settling velocities, based on a density of  $2 \text{ g cm}^{-3}$  (Posth et al., 2010), for aggregates formed in the absence of silica were  $0.56 \text{ m h}^{-1}$  and  $1.03 \text{ m h}^{-1}$  for aggregates formed in the presence of silica. However, it must be pointed out that using SEM (a 2D technique) for aggregate size analysis likely introduced a size analysis bias into our measurements in that the aggregate sizes reported above likely differ from the true aggregate sizes. Consequently, the settling velocities calculated above would also either be faster or slower, resulting in uncertainty regarding the water column residence time of the aggregates.

Abiotic aggregates precipitated by  $\text{O}_2$  in the absence of silica showed a similar mineral shape and morphology as their biogenic equivalents but with individual aggregates being more intertwined and linked to each other (Fig. 5F). The average size of the abiotic Fe(III) mineral aggregates was  $8.6 \pm 7.6$   $\mu\text{m}$ . The abiotic Fe(III) mineral aggregates precipitated in the presence of silica appeared to be the smallest of all aggregates investigated (Fig. 5G). However, the individual small aggregates were so intertwined and associated with each other that individual aggregate sizes could not be accurately measured.

To determine whether cells or cell debris co-precipitated with the Fe(III) minerals might influence the surface charge of the minerals, thus preventing the silica from becoming sorbed, we performed  $\zeta$ -potential measurements (with samples diluted 1:10 with 10 mM HEPES-buffered MilliQ<sup>®</sup> water). The measurements showed that the surface charge for biogenic Fe(III) mineral-cell aggregates produced by *R. iodosum* was very negative with  $-23.5 \pm 1.4$  mV, while the abiotically precipitated Fe(III) minerals showed much less negative values of  $-16.3 \pm 0.7$  mV (Fig. 6A). This suggests that in blank water containing HEPES buffer the biogenic Fe(III) minerals are expected to be less likely to bind negatively charged silica than the abiotic Fe(III) minerals.



---

In order to apply particle reactivity in terms of BIF, it is further important to determine the particle surface charge under relevant ancient ocean marine conditions. When taking this into account, we found that for an increasing ratio of marine medium to MilliQ<sup>®</sup> water, the  $\zeta$ -potential of 2-line ferrihydrite (corresponding to the abiogenic Fe(III) minerals) increased from  $-12.5 \pm 2.6$  mV for MilliQ<sup>®</sup> water to only  $-3.7 \pm 0.4$  mV (1:1 ratio medium to MilliQ<sup>®</sup> water) and to  $-1.7 \pm 3.4$  mV for medium only (Fig. 6B). These results clearly suggest that under marine water (ancient ocean) conditions, the abiogenic Fe(III) minerals are almost neutrally charged and are expected to bind the negatively charged silica ions to a large extent. This is in contrast to the biogenic Fe(III) minerals formed by *R. iodosum* where the average  $\zeta$ -potential value  $-27.4 \pm 1.4$  mV in MilliQ<sup>®</sup> water increased to  $-21.3 \pm 1.6$  mV for a 1:1 ratio mixture of MilliQ<sup>®</sup> water to medium and to  $-17.8 \pm 2.0$  mV for medium only (Fig. 6B). This shows that even when the geochemical composition of the seawater is considered, the biogenic cell-Fe(III) mineral aggregates remain negatively charged in contrast to the abiotic Fe(III) minerals, resulting in an expected repulsion of silica (or at least binding to a much lesser extent) and thus potentially allowing the formation of alternating Fe- and Si-rich mineral layers.

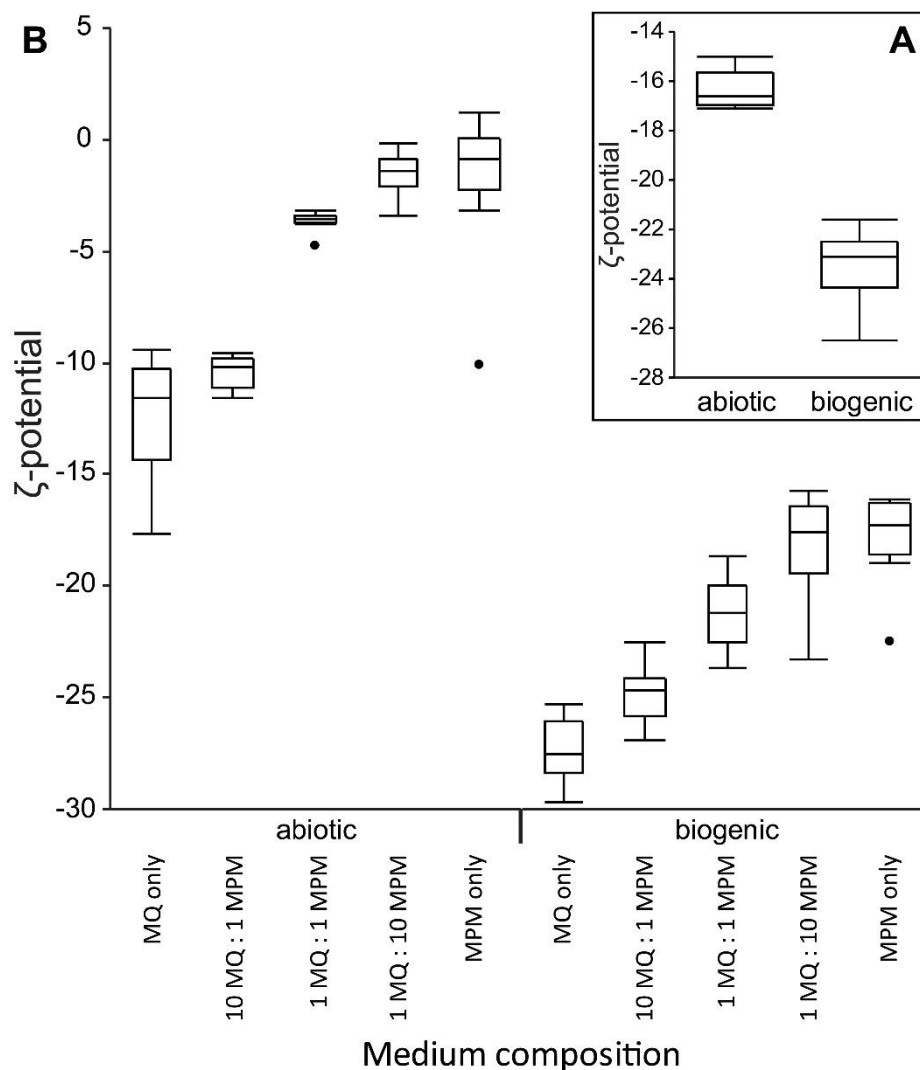


Fig. 6. Surface charge of Fe(III) minerals given as  $\zeta$ -potential. All measurements represent replicate measurements where  $n = 9$ . The insert (A) shows the  $\zeta$ -potential of abiotic Fe(III) minerals compared to biogenic Fe(III) minerals formed by *R. iodosum* obtained in pure MilliQ<sup>®</sup> water (MQ). The large plot (B) shows the  $\zeta$ -potential of 2-line ferrihydrite compared to biogenic Fe(III) minerals formed by *R. iodosum* depending on the geochemical composition of the medium, ranging from pure MilliQ<sup>®</sup> water (MQ), different water-medium mixtures, to pure marine phototroph medium (MPM).

### 3.4. Surface reactivity of the cell-mineral aggregates

Potentiometric titrations were performed in conjunction with FITEQL modeling to determine the  $pK_a$  and site concentrations of surface active functional groups for the *R. iodosum* Fe(III) mineral-cell aggregates. Protonation models invoking 2–4 sites were tested in FITEQL, with a model employing two proton active surface functional sites providing the only converging fit in FITEQL. The site  $pK_a$  and site concentration per gram of Fe(III) mineral-cell aggregate are presented in Table 2, with the values for site 1 being 3.35 and  $4.96 \times 10^{-5}$ , respectively; while site

2 had a  $pK_a$  value of 8.50 and a site concentration per gram of  $1.42 \times 10^{-4}$ , over twice as abundant as site 1. Site 1 likely corresponds to carboxyl/phosphodiester groups, whereas site 2 corresponds to amino groups.

Table 2

$pK_a$  and site concentration per gram of Fe(III) mineral-cell aggregates for replicate measurements displayed as mean from triplicates  $\pm$  standard deviation. A 2-site FITEQL model was employed to fit the titration data. <sup>1</sup>Assignment of functional groups is tentative and based on references (Cox et al., 1999; Sokolov et al., 2001; Martinez et al., 2002; Liu et al., 2015).

Surface site	Mean $pK_a$	Site concentration [ $10^{-4}$ mol $g^{-1}$ aggregates	Suggested functional group <sup>1</sup>
1	$3.35 \pm 0.49$	$0.50 \pm 0.01$	carboxyl/phosphodiester
2	$8.80 \pm 0.02$	$1.42 \pm 0.22$	amino

Fig. 7 shows the titration data for  $2.5 \text{ g L}^{-1}$  Fe(III) mineral-cell aggregate plotted in terms of the difference in mol added of 0.1 M HCl and 0.1 M NaOH per gram of Fe(III) mineral-cell aggregates. The slope of the titration curve at any point gives the instantaneous buffering capacity of the Fe(III) mineral-cell aggregates, corresponding to the rate of deprotonation of its surface. The areas with the greatest slope correspond to the regions where buffering capacity of each site is highest, which correlates with the functional group  $pK_a$  values.

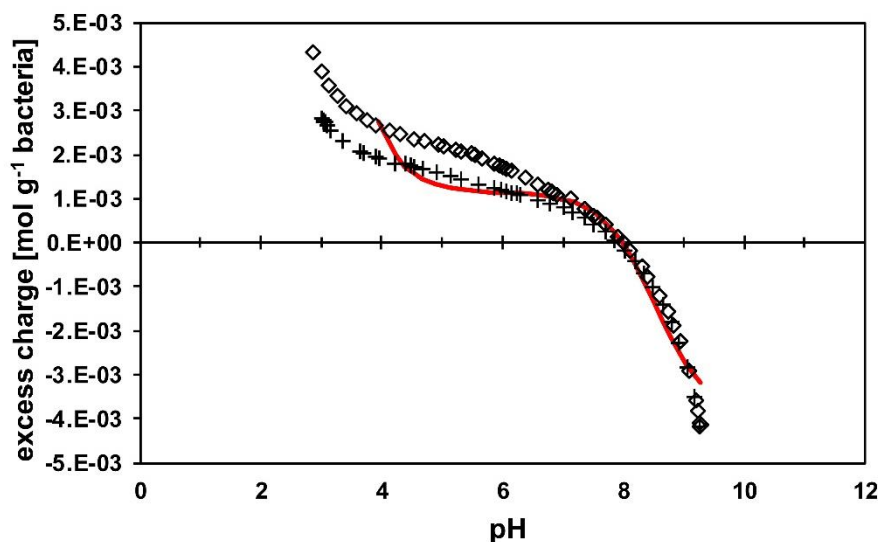
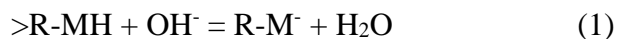


Fig. 7. Titration curve for Fe(III) mineral-cell aggregates plotted in terms of mol of base subtracted from mol of acid added per gram of bacteria (excess charge) for the pH 3 to 9 and 9 to 3 titrations. Crosses represent the forward (pH 3–9) titration while open diamonds represent the reverse (pH 9–3) titration. The FITEQL model is plotted in red with the inflection points being the  $pK_a$  values.

The titration data demonstrate that the Fe(III) mineral-cell aggregates have a high buffering capacity between each of the two  $pK_a$  values, where a large addition of titrant produces

a comparably minor change in pH. Minimal hysteresis was observed between the “up” and “down” titrations, further indicating limited dissolution and cell damage between titrations, and that the protonation/deprotonation of the cell wall functional groups were reversible. The mass action equation for the deprotonation of the generalized surface functional group is given by:



where M represents the surface functional group attached to the surface (>R) of the Fe(III) mineral-cell aggregate. As shown by Eq. (1), the addition  $OH^-$  (i.e. increasing pH) causes deprotonation of the surface ligands, leaving them with a negative surface charge. As pH increases, the surface of the Fe(III) mineral-cell aggregates becomes progressively deprotonated, causing a net negative surface charge. This is corroborated by the  $\zeta$ -potential measurements which show a highly negative surface charge for the biogenic Fe(III) mineral-cell aggregates.

### 3.5. Mineral saturation states

In order to determine silica speciation and the saturation states of the different silica minerals and Fe(II)-silicates at different temperatures, we performed geochemical modelling based on the composition of the marine phototroph medium and the Fe(II) and monomeric silica present in the experiments.

The results of the geochemical modelling (Table 3) showed that no formation of greenalite is expected under the experimental conditions. However, both a decrease in temperature from 26°C to 5°C or an increase in the monomeric silica concentration (as during the cold period or in experiments with silica oversaturation) increased the potential for greenalite formation. For the initial medium composition (3.5 mM  $Fe^{2+}$  and ~1.4 mM dissolved monomeric silica) a temperature decrease from 26°C to 5°C resulted in a change from a slight undersaturation with respect to amorphous silica to a slight oversaturation with respect to amorphous silica. In experiments with a high degree of silica oversaturation (cold phase precipitation experiment and silica precipitation kinetic experiment), the formation of amorphous silica was generally expected when a decrease in temperature lowered the solubility of amorphous silica. The model generally predicted the presence of cristobalite and quartz on the basis of their lower solubility and higher thermodynamic stability, however, in reality both crystallize from an amorphous silica precursor through dissolution-reprecipitation reactions

(Williams et al., 1985). The major dissolved silica species in all simulations was  $\text{H}_4\text{SiO}_4$  and generally accounted for >99%.

Table 3

Summary of saturation indices (SI) calculated with Visual MINTEQ vs. 3.1 for the initial marine phototroph medium (medium) and Si oversaturation experiments, based on pH, geochemical composition of the medium and temperature.

Mineral	Initial medium		Si oversaturation (8 mM)	
	SI, 26°C	SI, 5°C	SI, 26°C	SI, 5°C
Greenalite	-2.16	-2.02	-0.64	-0.51
$\text{SiO}_2$ (am, gel)	-0.09	0.09	0.67	0.85
$\text{SiO}_2$ (am, ppt)	-0.06	0.14	0.70	0.90
Cristobalite	0.55	0.81	0.55	1.57
Quartz	1.19	1.50	1.95	2.25

## 4. DISCUSSION

### 4.1. Fe(II) oxidation by *R. iodosum* in the presence of Si and mineral (trans)formation

Several studies have suggested an important role of phototrophic Fe(II)-oxidizing bacteria (photoferrotrophs) during the deposition of Archean BIF and emphasized their potential role in the formation of these ancient sedimentary deposits (Widdel et al., 1993; Ehrenreich and Widdel, 1994; Konhauser et al., 2002; Kappler et al., 2005; Li et al., 2011; Jones et al., 2015). Analysis of the BIF rock record even suggests their activity as early as ca. 3.8 Ga (Mloszewska et al., 2012; Czaja et al., 2013; Martinez et al., 2016). While we appreciate that microaerophilic Fe(II)-oxidizing bacteria could have contributed to BIF deposition once there was sufficient oxygen available to fuel their metabolism (Holm, 1987; Konhauser et al., 2002; Smith et al., 2013; Chan et al., 2016), for the scope of our study we specifically envision an Archean ocean devoid of oxygen.

In order to investigate the alternating deposition of Fe- and Si-rich mineral layers and to simulate an Archean ocean environment with elevated  $\text{Fe}^{2+}$  (Poulton and Canfield, 2011) and silica concentrations (Maliva et al., 2005), we grew *R. iodosum* in a marine medium starting with 3.5 mM  $\text{Fe}^{2+}$  and 1.4 mM monomeric silica during warm and cold periods. Additionally, during the cold period of the main experiment and selected control experiments (see Figs. 2 and 3), 8 mM dissolved monomeric silica were added. *R. iodosum* showed maximum oxidation rates of up to 0.6 mM d<sup>-1</sup> during the first warm period and maximum rates of 0.2 mM d<sup>-1</sup> during the

second warm period. No obvious lag phase was observed in both cases. In fact, during the first warm period 28% of the initial  $\text{Fe}^{2+}$  was already oxidized within 6 days, while during the second warm period 42% of the initially present  $\text{Fe}^{2+}$  was oxidized within 3 days. This is in contrast to previous work which observed a lag phase of 7–9 days for the same strain (Straub et al., 1999; Wu et al., 2014). A potential explanation for this observation is that pre-cultivation, and therefore, a high degree of adaptation of our strain, occurred prior to our experiments, resulting in a lack of an obvious lag phase in the experiments. Our data also suggests that the presence of ca. 1.4 mM monomeric silica does not negatively influence Fe(II) oxidation, which is in line with observations from previous studies (Posth et al., 2008; Wu et al., 2014; Gauger et al., 2016). Gauger et al. (2016) and Wu et al. (2017) also showed that the presence of dissolved monomeric silica actually increased Fe(II) oxidation rates, potentially by reducing toxicity effects related to high  $\text{Fe}^{2+}$  concentrations in the presence of light (Bird et al., 2013; Swanner et al., 2015a). The maximum oxidation rate determined for the first warm period (Fig. 2) correlates well with the results of other studies where photoferrotrophs were grown in silica-containing medium. They found comparable oxidation rates for other marine photoferrotrophs (Swanner et al., 2015b; Laufer et al., 2017) or freshwater photoferrotrophs grown in Si-rich conditions with comparable  $\text{Fe}^{2+}$  concentrations (Konhauser et al., 2007). The maximum oxidation rates of 0.2  $\text{mM d}^{-1}$  derived for the second warm period are comparable to results of Wu et al. (2014) who reported rates of 0.25  $\text{mM d}^{-1}$  for  $\text{Fe}^{2+}$  concentrations of 0.7 mM.

Overall the oxidation rates determined in our study agree well with previous results and suggest that photoferrotrophs could have been active under the high Fe and silica conditions relevant for an Archean ocean. Although those previous studies, and our work here as well, showed that oxidation rates of photoferrotrophs depend on the initial Fe(II) concentration (Hegler et al., 2008; Wu et al., 2014), the experimental data presented here add to an increasing pool of indirect evidence which suggests that photoferrotrophs could have been active in an Archean ocean and could have facilitated the deposition of BIFs.

The validity of the temperature-dependent model for the alternating precipitation of Fe and silica layers in BIFs envisioned in the present study additionally depends on a predicted low activity of photoferrotrophs at low temperatures. Although the individual influence of  $\text{Fe}^{2+}$  concentration, light intensity and temperature on photoferrotrophic Fe(II) oxidation rates have been investigated in the past (e.g. Hegler et al., 2008; Posth et al., 2008; Wu et al., 2014), no

study exists that investigated the combination of these factors. In this regard, our study provides a first step to resolve this knowledge gap by showing that the model strain *R. iodosum* was significantly less active at low temperatures. By extension these results suggest that photoferrotrophs should essentially be inactive if not only the temperature is lowered but especially and even more under low Fe(II) conditions, thereby allowing a separate deposition of Si-rich layers in BIFs.

There is considerable agreement that the precursor minerals to BIFs were likely poorly crystalline or amorphous Fe(III) (oxyhydr)oxides (Konhauser et al., 2002; Kappler et al., 2005; Klein, 2005; Posth et al., 2014; Sun et al., 2015; Robbins et al., 2019) or a silica-containing ferrihydrite (Percak-Dennett et al., 2011; Alibert, 2016; Zheng et al., 2016). The mineralogical data obtained in this study provide support for this claim as a poorly crystalline, X-ray amorphous Fe(III) phase, most likely ferrihydrite, as well as fine-grained goethite were found. This is principally in line with previous studies with *R. iodosum* (Wu et al., 2014; Swanner et al., 2015b; Wu et al., 2017), although we found no lepidocrocite, which could potentially be attributed to the higher bicarbonate ( $\text{HCO}_3^-$ ) concentration used in the present study, promoting the formation of goethite over lepidocrocite (Larese-Casanova et al., 2010). Additionally, the Fe mineralogy showed a clear dependence on the presence or absence of silica. While a mixture of ferrihydrite and goethite was formed in the medium containing no silica, the presence of silica clearly prevented the formation of more crystalline mineral phases, resulting in the formation of ferrihydrite only. This effect has been observed in the past (Cornell et al., 1987; Jones et al., 2009; Toner et al., 2012; Eickhoff et al., 2014) and is probably related to silica blocking sorption sites for Fe(II), thereby preventing Fe(II)-catalyzed transformation of ferrihydrite into thermodynamically more stable minerals like goethite (Posth et al., 2014).

The constant settling of primary Fe(III) (oxyhydr)oxides produced by photoferrotrophs through the water column could have been subjected to further secondary mineral transformations, e.g., reaction with  $\text{Fe}^{2+}$  sourced from hydrothermal vent sites and transported to the shelf regions where BIFs were deposited. The reaction between primary Fe(III) (oxyhydr)oxides and  $\text{Fe}^{2+}$  could have resulted in the formation of meta-stable green rust and perhaps the formation of nanosized magnetite as secondary minerals (Li et al., 2017; Koeksoy et al., 2019). Alternatively, Fe(III)-reducing bacteria could have used the co-precipitated organic carbon to (partially) reduce the primary Fe(III) minerals forming secondary Fe(II)-bearing

minerals such as magnetite. Such a mechanism was initially proposed by Walker (1984) and independently confirmed by experimental studies and C and Fe isotope analysis of the BIF rock record (e.g. Heimann et al., 2010; Steinhoefel et al., 2010; Craddock and Dauphas, 2011; Li et al., 2013). However, recent work has shown that a close association of ferrihydrite and organic matter may inhibit Fe atom exchange between Fe(II) and ferrihydrite (ThomasArrigo et al., 2017), thus preventing the formation of more crystalline mineral phases during the abiotic reaction of ferrihydrite-organic matter coprecipitates with Fe(II) (ThomasArrigo et al., 2018; Zhou et al., 2018). Consequently, organic matter coprecipitated with biogenic Fe(III) minerals could have prevented the secondary transformation of minerals such as magnetite. Indeed, the minerals formed were generally closely associated with bacterial cells, forming cell-Fe(III)-mineral aggregates. Nevertheless, many of the cells remained free of encrustation, which appears to be a common feature for photoferrotrophs (Kappler and Newman, 2004; Schaedler et al., 2009; Posth et al., 2010; Wu et al., 2014; Gauger et al., 2015; Gauger et al., 2016; Laufer et al., 2017).

Results from this study and others demonstrate that different strains associate with Fe(III) minerals to different extents, and in some cases become partially encrusted. For example, in a study by Kappler and Newman (2004) the freshwater photoferrotroph *R. ferrooxidans* strain SW2 showed partial association of minerals with cells during the initial growth phase but none after several months of incubation. Laufer et al. (2017) reported a close association between cells of a marine photoferrotroph and Fe(III) minerals where the cells remained free of any mineral encrustation, which is comparable to results by Wu et al. (2014) with the marine photoferrotroph *R. iodolum*. Other studies with photoferrotrophs showed that cells were only loosely attached to Fe(III) minerals or not associated at all (Hegler et al., 2008; Schaedler et al., 2009). This has implications for the use of different bacterial strains as model strains for BIF deposition. Depending on the extent to which cells and Fe(III) minerals are co-precipitated, different C:Fe ratios in the settling aggregates and the sediments will be obtained. Consequently, depending on the strain which is being used in different studies, contradicting conclusions might be drawn on the importance of biomass for the trace element budget (Konhauser et al., 2018), co-precipitation and sorption of trace elements to biogenic Fe(III) (oxyhydr)oxides (e.g. Eickhoff et al., 2014) or post-depositional and (early) diagenetic (microbial) processes (Posth et al., 2013; Posth et al., 2014; Halama et al., 2016). Moreover, the characteristics of the aggregates formed not only depend on whole cells co-precipitated with the Fe(III) minerals but also on cell debris and



organic molecules which are either released upon cell death or actively excreted by living cells. For example, *R. iodosum* has been shown in previous studies to form EPS (Wu et al., 2014). Therefore, it seems conceivable that a mixture of those organic compounds and cells might influence the characteristics of the minerals and in particular the mineral surface in a way which leads to the separate deposition of Fe(III) minerals and silica.

#### 4.2. Abiotic silica mineral saturation, precipitation and formation of silica layers in BIF

The Archean ocean was not only ferruginous but also rich in silica, with concentrations of up to 2.2 mM (saturation with respect to amorphous silica; Maliva et al., 2005); this is reflected in the high silica content of BIFs - up to 50 wt.% SiO<sub>2</sub> (Trendall, 2002). According to the model initially suggested by Posth et al. (2008), the precipitation of the Si-rich layers in BIFs was triggered by a decrease in temperature causing supersaturation with regards to amorphous silica. We therefore simulated the precipitation of amorphous silica under conditions relevant for the Archean ocean triggered by a decrease in temperature and performed complementary experiments where we determined silica precipitation kinetics and the influence of the presence of *R. iodosum*, Fe<sup>2+</sup> and light on the formation of these silica layers.

We also used geochemical modelling to assess whether our experimental conditions with Fe<sup>2+</sup> and silica led to the formation of amorphous silica or Fe-silicates such as greenalite (e.g. Rasmussen et al., 2013; Rasmussen et al., 2015; Tosca et al., 2016; Rasmussen et al., 2017; Johnson et al., 2018). Our modelling results suggested that under the given geochemical conditions no greenalite formation is to be expected, independent of the temperature, and amorphous silica should be the dominant silica species being formed. However, in contrast to our experimental results, the geochemical modeling showed that there was a temperature dependence for amorphous silica formation at 1.4 mM where at higher temperatures (26°C) the solution was undersaturated with regards to amorphous silica and only at lower temperatures (5°C) did silica precipitate, as expected based on Gunnarsson and Arnórsson (2000).

Another factor which could potentially influence the formation of the initial amorphous silica layers is the activity of photoferrotrophs at low temperatures which could lead to the coprecipitation of some Fe(III) (oxyhydr)oxides with the amorphous silica. Based on our experimental results, only minor activity of photoferrotrophs during cold periods is expected. Additionally, although minor Fe(II) oxidation occurred in silica precipitation experiments with *R.*

*iodosum*, Fe<sup>2+</sup> and light at low temperature, no Fe(III) (oxyhydr)oxides were detected, suggesting the formation of almost pure amorphous silica layers.

One critical point about our experiments is that a certain degree of oversaturation with regards to amorphous silica (8 mM dissolved monomeric silica, approximately 4× the saturation of amorphous silica) was necessary to achieve silica precipitation and the formation of an amorphous silica layer. Consequently, it seems likely that the silica precipitated as a result of this oversaturation instead of the temperature change, as suggested by our abiotic silica precipitation experiments (Fig. 3) and the results of our geochemical modelling (Table 3). One potential reason for this lack of silica precipitation after several weeks in the experiments to create alternating layers of Fe(III) minerals and amorphous silica (Figs. 1 and 2) could be a lack of nucleation sites that are necessary to initiate the silica precipitation, resulting in a much higher silica concentration needed for the formation of an amorphous silica layer. Theoretically, the already present cell-Fe(III) mineral aggregates deposited at the bottom of the vials could have served as nucleation for silica precipitation. However, based on visual inspection, the presence of those cell-Fe(III) mineral aggregates did not seem to have induced any silica nucleation. One potential reason could be the presence of organic matter produced by the bacteria, which would have prevented the initial sorption of silica onto the Fe(III) minerals (as lined out below in Section 4.3). Another potential reason for the absence of silica precipitation could be that the formation of silica gels at neutral pH is very slow (Krauskopf, 1956 and references therein). Moreover, silicification takes place in three discrete steps (Iler, 1979) where silica polymers are first formed (explaining the fast decline in dissolved monomeric silica concentration), these polymers then slowly increase in size until the polymers grow into chains and networks, and finally they form a visible amorphous silica gel. However, these results are at odds with the silica precipitation control experiments, where we observed the same rapid decline in dissolved monomeric silica (Fig. 3), but a visible amorphous silica layer formed already after 3–5 days. Currently we have no explanation for this discrepancy. In addition, our silica precipitation control experiments showed that the decrease in temperature from 26°C to 5°C, while slightly accelerating the removal of monomeric silica from solution, had no further effect on silica precipitation (Fig. 3). Instead, rather than influencing the initial silica precipitation kinetics, lowering the temperature from 26°C to 5°C resulted in a significant decrease in the equilibrium concentration of dissolved monomeric silica at 5°C compared to 26°C ( $1.47 \pm 0.04$  mM and  $1.89 \pm 0.03$  mM, respectively;

Fig. 3). This suggests that in order to precipitate amorphous silica from solution oversaturation was required in our experiments. In summary, while temperature certainly modulated the activity of photoferrotrophs and therefore Fe(III) mineral precipitation, based on our experiments silica precipitation required (in addition to lower temperatures) either a high degree of oversaturation or the presence of nucleation sites, such as bacterial cells, to precipitate amorphous silica layers.

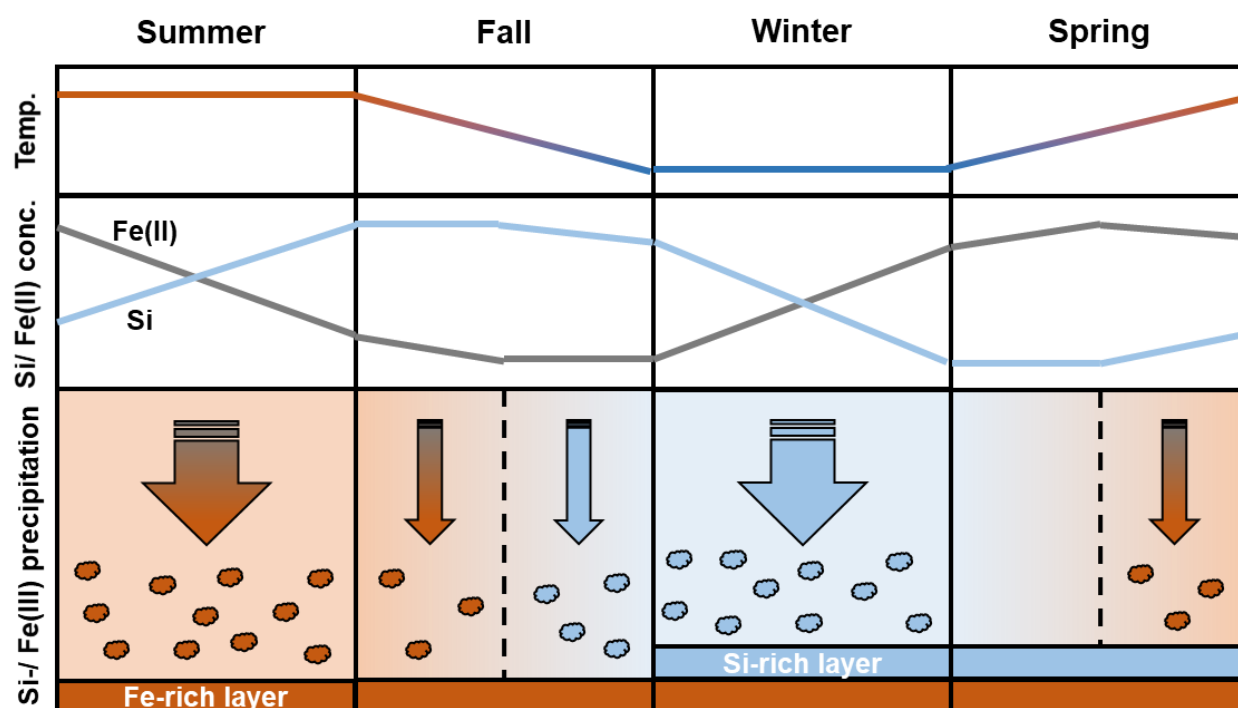


Fig. 8. Course of Fe and silica precipitation depending on temperature. Orange colors indicate high temperatures and Fe(III) precipitation, blue colors correspond to cold temperatures and silica precipitation; grey color shows dissolved Fe(II) concentration. Arrows pointing downwards represent Fe(III) or silica precipitation. The thickness of the arrows represents the extent of Fe(III) or silica precipitation. During **summer** there is extensive Fe(III) mineral precipitation due to the activity of photoferrotrophs, leading to the formation of Fe(III)-rich layers and depletion of the Fe(II) reservoir. At the same time, due to higher solubility at higher temperatures and due to riverine and/or hydrothermal input, the silica reservoir is increased during summer. As the temperature starts to decrease in **autumn**, the photoferrotrophs become less active, resulting in decreased Fe(III) mineral precipitation. At the same time due to decreasing temperature the replenishment with regards to silica slows down and eventually as the temperature gets too cold, amorphous silica starts to precipitate. Meanwhile, the Fe(II) reservoir, which was mostly depleted by the activity of the photoferrotrophs during summer starts to be increase again. In **winter**, due oversaturation with regards to silica, extensive silica precipitation and formation of Si-rich layers takes place. Silica precipitation stops once the silica concentration drops below the equilibrium value at low temperature. Meanwhile, due to the inactivity of the photoferrotrophs, the Fe(II) reservoir is replenished. In **spring**, due to higher temperature no more silica is being precipitated, allowing both the Fe(II) and silica reservoir continue and start to being refilled, respectively. Once the temperature gets high enough the photoferrotrophs become re-activated and they start oxidizing Fe(II).

In order to create an amorphous silica layer, we envision a model (as in Fig. 8) where during the warm period (spring and summer), while the photoferrotrophs are active, the silica reservoir increases. With the onset of autumn, the photoferrotrophs become less active due to lower temperatures and silica starts to precipitate. In winter significant silica precipitation takes

place leading to the formation of Si-rich layers, while the photoferrotrophs are mostly inactive and the Fe<sup>2+</sup> reservoir replenishes. Once the equilibrium concentration at low temperatures is reached, no further silica precipitation takes place. With the increase in temperature in the spring the photoferrotrophs resume their metabolic activity resulting in the onset of Fe(III) mineral precipitation and formation of the next Fe-rich layer while the dissolved monomeric silica reservoir replenishes during the warm period.

#### **4.3. Mechanism responsible for separated deposition of Fe- and Si-rich layers in BIFs**

The previous study by Posth et al. (2008), and the results of the present study, suggest minor co-precipitation of silica and Fe(III) minerals. This implies that temperature might have acted as the unifying trigger for the alternating deposition of Si- and Fe-rich layers in BIFs. However, in addition to temperature, another factor must be responsible for the reduced silica binding to the Fe(III) minerals, as the absence of silica-Fe-co-precipitation (as previously reported by Percak-Dennett et al., 2011; Zheng et al., 2016), and the independent precipitation of Fe-rich and Si-rich layers initially remained unclear. Based on our experimental results we suggest that organic molecules, cell debris, and whole cells which were co-precipitated with the Fe(III) minerals led to changes in the mineral surface properties, minimizing sorption of silica to the Fe(III) minerals, thus preventing co-precipitation of silica. To identify the underlying mechanism(s) and to support our hypothesis that organics formed by microorganisms caused the decreased removal of silica from solution, we performed SEM analysis,  $\zeta$ -potential measurements, and potentiometric titrations of the Fe(III) mineral-cell aggregates.

SEM micrographs showed that *R. iodosum* cells are generally closely associated with the Fe(III) minerals. Natural organic matter (NOM) and EPS are known to have a strong affinity towards Fe(III) (oxyhydr)oxides (Gu et al., 1994; Phoenix et al., 2003; Amstaetter et al., 2012; Shimizu et al., 2013; Hao et al., 2016; Sundman et al., 2017), which suggests that the cells and/or EPS produced by *R. iodosum* (Wu et al., 2014) bind iron as well and might significantly influence the characteristics of the Fe(III) minerals formed and the extent to which Fe(III) minerals and silica are co-precipitated. Indeed,  $\zeta$ -potential measurements showed that the presence of biomass significantly lowered the surface charge of the Fe(III) mineral-cell aggregates ( $-23.5 \pm 1.4$  mV) compared to an abiotic Fe(III) mineral ( $-16.3 \pm 0.7$  mV). This is most likely related to carboxyl/phosphodiester groups as identified by our titration experiments, and previously demonstrated by

Martinez et al. (2016), which make the surface of the Fe(III) mineral-cell aggregates more negative. It has been previously shown that NOM or humic substances can lower the  $\zeta$ -potential of e.g. hydrous Al oxides or ferrihydrite significantly, when sorbed to or co-precipitated with such minerals (Pommerenk and Schafran, 2005; Angelico et al., 2014). Furthermore, the sorption of other anions, such as phosphate, was shown to be decreased by up to 40% in NOM-containing systems compared to NOM-free systems (Davis, 1982). Consequently, our experimental results suggest that the reaction of organic matter produced by *R. iodosum*, together with Fe(III) minerals, lowers the surface charge of the Fe(III) mineral-cell aggregates, making them more negatively-charged. Based on these experimental results it would be expected for any anion to be electrostatically repulsed by the negatively charged surface. Yet based on our modelling results >99% of the silica should be present as  $\text{Si}(\text{OH})_4$  which is the predominant species at  $\text{pH} < 9$  (e.g. Sjöberg, 1996; Tan et al., 2013). Nevertheless, despite deprotonation at high pH values, silica still possesses a point of zero charge of 3 due to external silanol groups (Williams and Crerar, 1985). Consequently, dissolved silica should have a residual negative surface charge under our experimental conditions resulting in some electrostatic repulsion between the Fe(III) minerals surface and silica oligo- and polymers which potentially formed. Furthermore, it has been determined that silica dimers ( $\text{H}_5\text{Si}_2\text{O}_7^-$ ) have a  $\text{pK}_a$  value of -5.0 (Svensson et al., 1986; Felmy et al., 2001), suggesting a significant part of negatively-charged dimers being present in aquatic systems. Another relevant process is the blocking of hydroxyl groups responsible for the formation of Fe-O-Si linkages (Carlson and Schwertmann, 1981; Doelsch et al., 2001) and the sorption of silica to Fe(III) minerals by bidentate, binuclear linkages (Pokrovski et al., 2003; Hiemstra et al., 2007; Swedlund et al., 2010). Irrespective of the exact process, we suggest that co-precipitated organic matter would inhibit the sorption of silica to the Fe(III) mineral-cell aggregates and, therefore, lead to the separate deposition of Fe- and Si-rich layers in BIFs (Fig. 9).

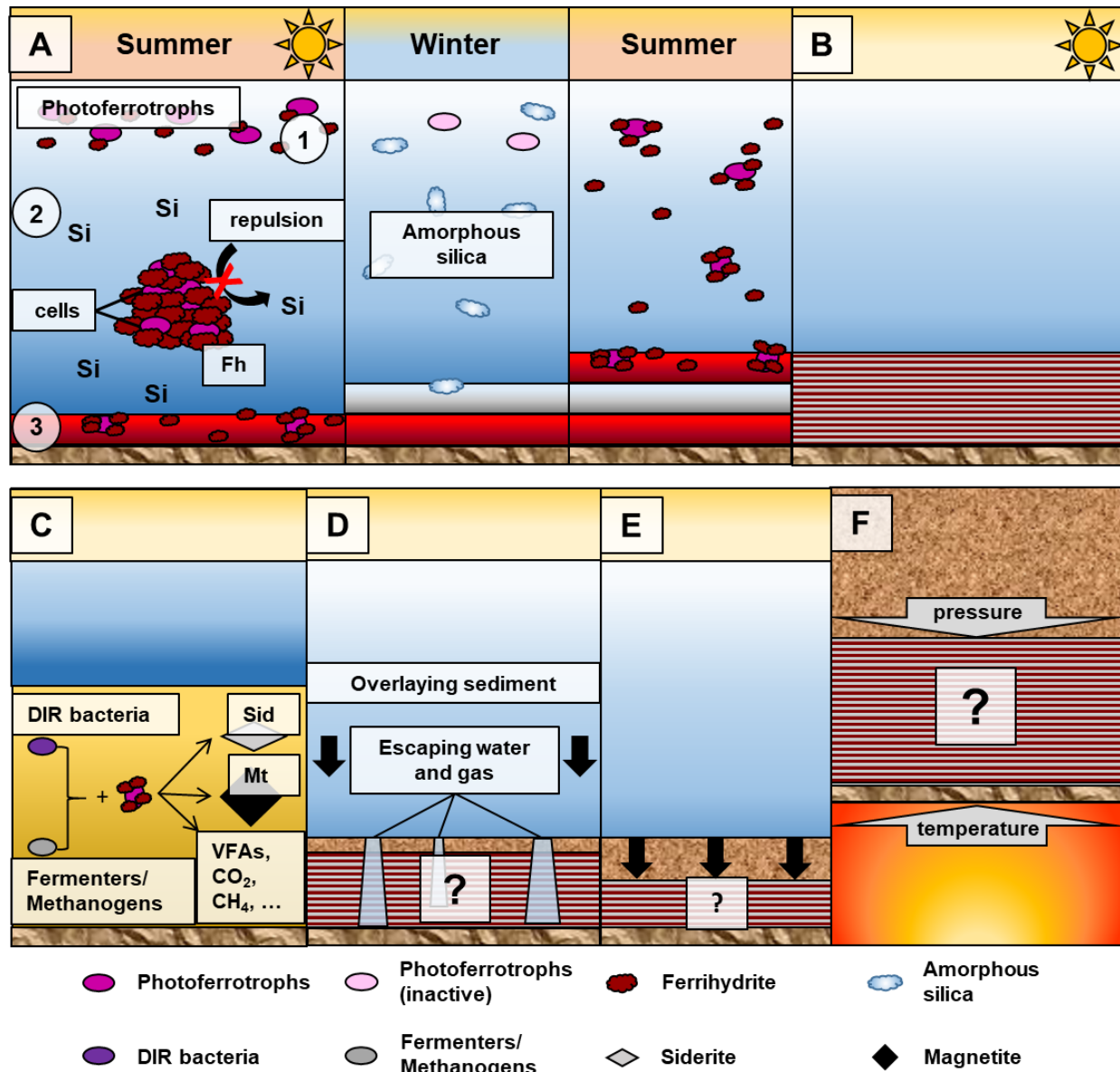


Fig. 9. Overview of diagenetic history of mineral layering in BIFs. (A) Photoferrotrophs are metabolically active during summer and/or warm periods and oxidize  $Fe^{2+}$  (1). This leads to the formation Fe(III) mineral-cell aggregates, where the co-precipitated/sorbed biomass prevents the silica from being bound to the freshly formed Fe(III) minerals (2). Accumulation of Fe(III) mineral-cell aggregates leads to the formation of Fe-rich layers during warm periods (3). During winter/cold periods the photoferrotrophs become metabolically inactive, leading either to decreased Fe(II) oxidation or completely inhibiting it. Due to the lower solubility at lower temperatures amorphous silica spontaneously precipitates from the water column, thereby forming Si-rich layers. Upon increasing temperature, the photoferrotrophs become active again, leading to renewed Fe(II) oxidation and formation of Fe-rich layers. (B) Over several  $10^5$  to  $10^6$  years of repetitive warm and cold periods or seasons lead to the formation of layered primary BIF sediments. (C) After deposition of Fe(III) mineral-cell aggregates, the co-precipitated biomass is degraded by fermenting bacteria and methanogens, thereby supplying the necessary organic substrates (volatile fatty acids, VFAs) for microbial Fe(III) reduction (DIR), leading to the formation of secondary minerals, such as siderite and magnetite. (D & E) The pressure of overlying sediment layers leads to the compaction and burial of the BIF sediments, probably accompanied by (vertical) escape of pore water and or gasses (D), silicification of the silica layers and beginning formation of secondary (Fe) minerals. (F) Upon deep burial, late-stage diagenesis and low-grade metamorphism lead to the formation of secondary Fe minerals, such as siderite, magnetite and hematite. Depending on the previous diagenetic history, the banding should remain stable under these conditions.

Although our experimental data suggest that sorption of microbially-derived organic matter to the Fe(III) (oxyhydr)oxide minerals would have reduced, or even prevented, sorption and co-precipitation of silica, some uncertainties remain. Strikingly, the first and second warm periods show a different silica-co-precipitation behavior. During the first warm period between 36% and 47% of the dissolved monomeric silica was co-precipitated or sorbed with the Fe(III) minerals during microbial Fe(II) oxidation, while in the second warm period virtually no silica co-precipitation was observed. Based on results for the initial Fe(II) oxidation of the first warm period, Fe- and silica-precipitation would not be independent and the Fe(III) (oxyhydr)oxides act as a shuttle for silica (Fischer and Knoll, 2009). Unfortunately, due to experimental restrictions, the Fe(II) concentrations used in the present study (several mM) were an order of magnitude higher than estimated for the Archean ocean ( $\sim 0.5$  mM Fe<sup>2+</sup>; Holland, 1973; Morris, 1993). For comparison, Konhauser et al. (2007) had Fe<sup>2+</sup> concentrations two times lower and the concentrations used by Posth et al. (2008) were approximately 7 times lower than in the present study. In both studies silica was only co-precipitated with the Fe(III) minerals to a minor extent, which suggests that silica-co-precipitation is dependent on the initial Fe:Si ratio.

During the initial Fe(II) oxidation step during the first warm period 3.5 mM Fe<sup>2+</sup> were completely oxidized (until day 13, Fig. 2). Upon addition of new medium on days 13, 21, 29 and 43 (Fig. 2), the amount of Fe<sup>2+</sup> added was only between 2.0 and 2.5 mM. This relatively lower amount of Fe<sup>2+</sup> being completely oxidized resulted in the amount of silica being co-precipitated to decrease from initially approximately 50% (day 0–13, Fig. 2) to below 40% (days 13–17, 21–27, 29–35, 43–48; Fig. 2). Thus, at higher initial Fe<sup>2+</sup> concentrations the organics formed were unable to block all the sorption sites for the silica. Consequently, a comparably low removal of between 40% and 50% monomeric silica from solution could represent a contribution of sorption of microbially-derived biomolecules to the decreased drawdown of silica with biogenic ferrihydrite. Throughout the second warm period (day 133–168, Fig. 2) maximum Fe<sup>2+</sup> concentrations were only at around 0.9 mM (Fig. 2) and, therefore, much lower than during the first warm period (2.0–3.5 mM Fe<sup>2+</sup>, Fig. 2). Importantly, no silica co-precipitation was noted during the second warm period, despite the Fe<sup>2+</sup> being completely oxidized. This further confirms the hypothesis that at higher initial Fe<sup>2+</sup> concentrations, the cell-derived organics are not able to block all sorption sites for silica, resulting in an increased co-precipitation of silica and Fe(III) minerals, whereas at low Fe<sup>2+</sup> concentrations, directly relevant for Archean oceans, all surface

sites at the Fe(III) (oxyhydr)oxide particles are covered by organics and minimal silica-removal is observed. Consequently, the initially observed high silica co-precipitation would represent an experimental bias, not representative for the overall mechanism as assumed for the Archean ocean where photoferotrophs would have contributed to BIF deposition.

Overall, we propose a model where Fe(III) minerals are co-precipitated as aggregates with cells, cell debris, and other organic compounds such as EPS. These organic compounds influence the surface of the aggregates in that they turn them more negative or block surface functional groups of the Fe(III) minerals. This ultimately results in the inhibition of silica sorption leading to a separate deposition of Fe- and Si-rich layers in BIFs (Fig. 9).

#### **4.4. Varve-like deposition of alternating Fe- and Si-rich layers in the Hamersley BIF as a result of temperature cycles**

Extended temperature cycling experiments were conducted in order to determine whether the initial model proposed by Posth et al. (2008) could have resulted in the alternating deposition of Fe- and Si-rich layers in BIFs. The experimental setup aimed at simulating the Archean ocean as closely as possible and showed that temperature cycles linking photoferotrophy during warm periods to abiotic silica precipitation during cold periods results in the development of alternating layers of Fe(III) and silica minerals, similar to those found as microbands in BIFs. However, some of the experimental conditions (determined by constraints due to the chosen experimental setup), namely full light saturation and comparably high Fe<sup>2+</sup> concentrations (low mM range) are potentially at odds with the depositional conditions assumed for the Archean ocean. However, although we conducted our experiments under full light conditions and specifically envision an ocean devoid of free oxygen, where there would have been no need for photoferotrophs to move deeper into the water column in order to being able to compete with other Fe(II)-oxidizing mechanisms, it has been suggested that photoferotrophs could have even been active at lower light intensities at approximately 100 m water depth (Kappler et al., 2005). We, therefore, took a more conservative approach to investigate the minimum requirements under which photoferotrophs could still deposit BIFs, while still being able to draw important conclusions regarding the potential mechanisms being responsible for the alternating deposition of Fe- and Si-rich layers in BIFs.



In order to quantify whether our proposed model would still be of significance for BIF deposition under the relevant conditions discussed above, we extrapolated our experimental results to the rock record, focusing on the Hamersley Group in Western Australia. The Fe(II) oxidation rates obtained from the first warm periods were determined from Fe(II) concentrations one order of magnitude higher than assumed for the Archean ocean. Therefore, we specifically focused on the Fe(II) oxidation rates determined for the second warm period where the Fe(II) concentrations (~0.8–0.9 mM) were of the same order of magnitude as in the Archean ocean and consequently the data obtained would be more comparable. Furthermore, we adjusted the Fe(II) oxidation rates used to low light intensity values (as outlined below) to showcase that photoferrotrophs might have been active deeper in the water column of the Archean ocean. The key variables for the following calculations are summarized in Table 4.

Table 4  
Variables used for verification of the temperature cycling model.

Variable		Reference
Hamersley depositional area	11 <sup>11</sup> m <sup>2</sup>	Konhauser et al. (2002)
Average depth of Hamersley basin	500 m	Trendall (2002)
Depth of seasonal thermocline	100 m	Pinet (2011)
Photic depth	100 m	Pinet (2011)
Fe <sup>2+</sup> concentration	0.02-0.5 mM	Holland (1973); Morris (1993)
Fe(II) oxidation rate	0.2 mM d <sup>-1</sup>	Experimental data
Fe(II) oxidation rate at 20% efficiency	0.04 mM d <sup>-1</sup>	Adapted from Kappler et al. (2005)
Layer thickness of photoferrotrophic community	10.4 m	Calculated following Kappler et al. (2005)

One requirement for the deposition of Fe-rich layers is the supply of Fe(II) at rates sufficient to sustain ongoing Fe(II) oxidation. Assuming that the Hamersley Basin can be approximated by a simple box we calculated a theoretical layer thickness for a photoferrotrophic community required to oxidize all Fe(II) before it reaches the surface of the ocean based on Kappler et al. (2005). Further assuming the maximum Fe<sup>2+</sup> concentration in the Archean was 0.5 mM (Holland, 1973; Morris, 1993), using an adapted Fe(II) oxidation rate of 0.04 mM d<sup>-1</sup> and the theoretically predicted eddy diffusion coefficient for the modern ocean (as given in Kappler et al., 2005), the photoferrotrophic community would have a uniform thickness of 10.4 m over the whole basin (Table 4). Furthermore, based on the oxidation rate given and the total volume of

water contained in this photoferrotrophic community layer stretched over the entire basin,  $5.6 * 10^{10}$  mol Fe(II)  $d^{-1}$  would be oxidized by a *R. iodosum* community. Using the  $Fe^{2+}$  concentration given in Table 4 and the volume of the layer, we calculated the total  $Fe^{2+}$  initially contained in this layer to be  $7 * 10^{11}$  mol. Therefore, the amount of  $Fe^{2+}$  oxidized by a *R. iodosum* community would equal 8% of the total  $Fe^{2+}$  present in the respective layer being oxidized each day. Again assuming that the basin can be approximated by a simple box, applying this 8% to the layer thickness of the photoferrotrophic community (10.4 m) would result in a ca. 0.8 m thick part of this layer (8% of 10.4 m) being depleted in  $Fe^{2+}$  each day. Assuming homogeneous  $Fe^{2+}$  distribution, Fe(II) oxidation and upwelling, an upwelling rate of ca. 0.8 m  $d^{-1}$  would be required to sustain continuous Fe(II) oxidation. This calculated value is within the same order of magnitude as upwelling rates observed in modern upwelling areas (up to 3.0 m  $d^{-1}$ ; Kadko and Johns, 2011; Kadko, 2017), supporting the plausibility of the assumptions made.

Based on this calculation, it seems feasible that photoferrotrophs could have continuously oxidized  $Fe^{2+}$  in an Archean ocean during warm periods (Fig. 9A.1). Additionally, it needs to be determined whether the amount of  $Fe^{2+}$  oxidized would have been sufficient to ultimately result in the BIF layer thicknesses observed today. The  $5.6 * 10^{10}$  mol  $Fe^{2+}$  oxidized by *R. iodosum* each day would correspond to  $2.04 * 10^{13}$  mol  $Fe^{2+}$  being oxidized each year. Based on a molar mass of 107 g  $mol^{-1}$  for ferrihydrite ( $Fe(OH)_3$ ), this would correspond to  $2.18 * 10^{15}$  g ferrihydrite  $yr^{-1}$  deposited over the whole Hamersley basin or  $2.18 * 10^4$  g ferrihydrite  $m^{-2} yr^{-1}$ . Based on a previously determined density of 2 g  $cm^{-3}$  ( $2 * 10^6$  g  $m^{-3}$ ) for Fe(III) mineral-cell aggregates (Posth et al., 2010), this would result in a yearly deposited layer thickness of 0.0109 m  $yr^{-1}$  or 10.9 mm  $yr^{-1}$  in the initial sediment (Fig. 9A.3); this is one magnitude higher than calculated by Konhauser et al. (2002) and Kappler et al. (2005) but can be attributed to slightly higher Fe(II) oxidation rates.

After having determined that a photoferrotrophic community would have been able to deposit a sufficiently thick primary Fe(III) mineral layer, it remains to be determined whether the seasonal cooling of the Archean ocean could have resulted in the deposition of silica layers which would ultimately be of comparable layer thicknesses as found in BIFs today. However, because the silica concentrations necessary to precipitate amorphous silica, the scale, and the duration of our experiments were so fundamentally different from what is assumed for the Archean ocean, the following paragraphs containing discussion on silica precipitation should be seen as a thought

experiment only. Nonetheless, with regards to the maximum amount of silica being precipitated during the cool-down of the ocean the 0.5 mM difference between the silica concentration determined experimentally during the second warm period (ca. 2.1 mM) and the cold period (ca. 1.6 mM), values comparable to known literature values for silica solubility at the respective temperatures (Gunnarsson and Arnórsson, 2000), seem to be a reasonable approach. Based on those and literature values, we expect that little or no further amorphous silica is being precipitated once the lower temperature limit is reached. Since we consider temperature as the major driver for the alternating deposition of Fe- and Si-rich layers, only the depth of the ocean which is affected by temperature changes (thermocline at ca. 100 m in modern oceans; Pinet, 2011) will be taken into account for silica precipitation. From the layer affected by seasonal temperature changes extrapolated over the entire basin ( $10^{11} \text{ m}^2$ ),  $0.5 * 10^{13} \text{ mol}$  amorphous silica  $\text{yr}^{-1}$  ( $50 \text{ mol}$  amorphous silica  $\text{m}^{-2}$ ) could be deposited during a respective cold period or winter (Fig. 9A). Using the molar mass of  $60 \text{ g mol}^{-1}$  for  $\text{SiO}_2$  this would result in a yearly precipitation of  $3 * 10^{14} \text{ g}$  amorphous silica ( $3 * 10^3 \text{ g}$  amorphous silica  $\text{m}^{-2} \text{ yr}^{-1}$ ). Based on the density for amorphous silica of  $2.2 \text{ g cm}^{-3}$  (Renner and Zemek, 1973) and water a weighted average of  $1.24 \text{ g cm}^{-3}$  (assuming 80% water content) was calculated for the initial silica precipitates. Applying this density, a layer thickness of 2.42 mm was calculated.

Over the course of several  $10^5$ – $10^6$  years alternating warm and cold periods could have resulted in the formation of layered primary sediments (Fig. 9B). However, once the initial wet, unconsolidated Fe(III)-rich sedimentary layers were deposited, several post-depositional processes would have changed the layer thickness. On the one hand there were microbial processes. Konhauser et al. (2005) suggested that 70% of the initially precipitated Fe(III) minerals might have been reduced by Fe(III)-reducing bacteria and cycled back into the water column (Fig. 9C). Therefore, the calculated layer thickness for the Fe(III) mineral layers would be reduced from  $10.9 \text{ mm yr}^{-1}$  to  $3.27 \text{ mm yr}^{-1}$ . Furthermore, taking into account that the initially precipitated Fe-rich sediments were compacted by the mass of overlaying sediment layers (Fig. 9D and E), the Fe-layer thickness would be further reduced by 75% (Altermann and Nelson, 1998) to  $0.82 \text{ mm yr}^{-1}$ . This value corresponds closely to the mean varve thickness calculated by Trendall and Blockley (1970) of 0.65 mm, and is within one order of magnitude of previous estimates of  $0.033 \text{ mm yr}^{-1}$  compacted BIF sedimentation rate for the Fe-layer (Pickard, 2002).

Similar to the Fe-mineral layers, the silica layers would have been subject to post-depositional processes. Based on our experimental results the silica layers contained more water compared to the Fe(III) mineral layers (Fig. 1). This is further supported by preliminary experiments where a 2-line ferrihydrite suspension and a monomeric silica solution were added alternately to the marine phototroph medium in experimental tubes and subsequently centrifuged. After centrifugation, the formed amorphous silica layers showed a strong compaction while the formed Fe mineral layers showed only minor compaction (if any at all; data not shown). Consequently, we applied a higher compaction of 95% for the silica layers, as suggested for the compaction of BIFs by Trendall and Blockley (1970). This resulted in the silica layer thickness being reduced from  $2.42 \text{ mm yr}^{-1}$  to  $0.12 \text{ mm yr}^{-1}$ , which is well within the mm to sub-mm range which has been suggested for BIF silica-microbands (Trendall and Blockley, 1970). Additionally, when considering that one Si-rich layer containing up to 50 wt.% of  $\text{SiO}_2$  (Trendall, 2002) was of continuous thickness, stretched laterally over the whole Hamersley area and had an average density of chert ( $2.7 \text{ g cm}^{-3}$ ), it would contain  $1.7 * 10^{13} \text{ g SiO}_2$ . This value is within one order of magnitude of the value calculated based on the temperature-driven decrease of the monomeric silica concentration for a cold period as discussed above, which supports the validity of the assumptions taken for the calculations of the silica layer thicknesses.

In summary, the calculated layer thicknesses for Fe- and Si-rich layers based on the experimental data suggest that biannual temperature changes might have led to the formation of microbands in BIFs (Trendall and Blockley, 1970). Furthermore, we apply the definition of Trendall (2002), where one Fe- and one Si-rich layer together make up one microband and thus represent one year of precipitation, i.e., a chemical varve. Consequently, the layer thickness for both layers would decrease to 0.31 mm and 0.06 mm for the Fe- and Si-rich layers for half a year of deposition, respectively. In combination this would result in 0.37 mm compacted yearly sedimentation rate. For  $10^6$  years this would result in a BIF of 370 m vertical extent. Of course, these results only apply when considering that BIFs were deposited continuously without any depositional hiatuses. When assuming varves as mode of deposition for BIFs, the results of our study are within the range of other sedimentation rates found. Trendall and Blockley (1970) estimated the average thickness of one Fe- and silica-layer couplet to be 0.65 mm in the Dales Gorge Member of the Brockman Iron Formation in Western Australia, which would result in a depositional thickness of 650 m after  $10^6$  - years. Klein and Beukes (1989) derived a deposition

---

rate of  $570 \text{ m Myr}^{-1}$  for the BIF in the Campbellrand-Kuruman transition zone, Transvaal Supergroup, South Africa, while Morris (1993) estimated the deposition rate of the BIFs of the Hamersley group, Pilbara Craton, Western Australia to have been  $890 \text{ m Myr}^{-1}$ . Other estimates for the same BIF are given by Trendall et al. (2004) with  $180 \text{ m Myr}^{-1}$ . Overall, the values calculated based on our experimental results are well in line with compacted sedimentation rates estimated from the BIF rock record. Accordingly, we suggest that biannual temperature cycles, as originally envisioned by Posth et al. (2008), would have contributed significantly to the deposition of BIFs. Varves would, therefore, have been the most likely mode of deposition for BIFs on the microband scale, leading to the formation of BIFs as we observe them today.

## 5. CONCLUSIONS

In modern environments, temperature changes play an important role in controlling biologic (microbial) and abiogenic processes. Our study suggests that seasonal (or periodical) temperature changes could have played an equally important role in the Archean ocean during the deposition of BIFs. Although temperature changes certainly had a major control over the activity of Fe(II)-oxidizing bacteria (photoferrotrophs), our experimental results provide no conclusive evidence that temperatures as low as  $5^{\circ}\text{C}$  would have had any direct influence on abiotic silica precipitation. Instead a high degree of silica oversaturation was necessary to form an amorphous silica layer. This is in contrast to some of our experimental results and geochemical modelling which suggest that lower temperatures would have resulted in lower equilibrium concentrations of monomeric silica and ultimately should have resulted in silica precipitation given that a solution is saturated with regards to amorphous silica at  $26^{\circ}\text{C}$ . Therefore, abiotic silica precipitation is either extremely slow and thus not testable at the experimental (time)scale or for example nucleation points are necessary to initiate silica precipitation.

While the exact mechanism underlying abiotic silica precipitation is currently unknown, we suggest that some coprecipitation of biomass with the Fe(III) minerals occurred and changed the characteristics of the precipitates in a way which prevented sorption of silica to the Fe(III) minerals, thus ultimately causing a separation of Fe- and Si-rich layers in BIFs. To our knowledge this is the first study utilizing marine microbial strains for this kind of BIF deposition simulation experiments and thus confirms that these bacteria could have been active in an anoxic,

Fe- and Si-rich Archean ocean. Most importantly, seasonal temperature changes represent a simple unifying mechanism which could have controlled biological and abiotic processes on a basin scale and, therefore, represent a plausible means to explain the large-scale continuity of the banding in BIFs and therefore suggesting the banding in BIFs to be of primary origin.

Although the experimental data suggest that temperature cycles may have contributed significantly to the development of the characteristic lamination in BIFs, it is certain that other processes contributed to the ultimate appearance of Fe- and Si-rich layers in BIFs as we see them today (Fig. 9). For example, not all banding in BIF is on the micron- to millimeter scale, and not all banding is between iron and silica-rich minerals. Moreover, any model on BIF must also take into account the mesobanding and macrobanding which rely on decadal to longer time scales. One important parameter which potentially determined the predominance of either Fe- or Si-rich layers is the supply of  $\text{Fe}^{2+}$  to BIF depositional areas: Higher  $\text{Fe}^{2+}$  fluxes would have resulted in the deposition of dominantly Fe-rich layers and masked silica precipitation, while lower  $\text{Fe}^{2+}$  fluxes would have resulted in a decline or secession of microbial activity and led to the formation of more and vertically more extensive Si-rich layers. Prolonged warm periods could also have resulted in the predominance and formation of vertically more extensive of Fe-rich layers, while periods of prolonged subaerial volcanism might have favored the formation of vertically more extensive Si-rich layers by suppressing the formation of Fe(III) (oxyhydr)oxides by Fe(II)-metabolizing bacteria. Additionally, a recent study suggested that Milankovitch forcing would have exerted a major control on past climate oscillations on a scale of 0.41 Myr and 1.4 to 1.6 Myr, thereby influencing the composition of BIFs on a large scale (Lantink et al., 2019).

It is also unclear to which extent post-depositional processes altered the initial BIF sediment. Konhauser et al. (2005) suggested that up to 70% of the initial Fe(III) mineral precipitates could have been reduced by microbial activity and cycled back into the water column. This could potentially also have led to a release of silica from the aggregates which could then have been recycled back into the water column. If dissolution took place within the sediment itself, silica could have become concentrated in the pore space, thereby enhancing silicification and consequently either (1) disrupting any clear layering or (2) stabilizing the layering during further diagenesis and metamorphism. Abiogenic diagenetic processes would also have influenced the primary layering. It seems conceivable based on the differences in density between the primary Fe(III) minerals and amorphous silica that the much denser Fe(III) minerals should

displace and potentially disrupt any amorphous silica layer. Additionally, it would be expected that the pressure of the overlaying sediment column would lead to the compaction and vertical escape of water and dissolved silica (Fig. 9D and E). In either case it would be required that the silica layers silicify and solidify early during the diagenesis as proposed by Ewers and Morris (1981) in order to remain stable and consistent during the diagenetic history. Last but not least, it is unclear how deep burial and low-grade metamorphism would have influenced the stability of the laminated primary sediment and how the primary layering would have been preserved under such conditions.

## **ACKNOWLEDGMENTS**

The authors would like to thank Dr. H. Schulz for advice and support with SEM analysis and providing information on seasonal and glacial/inter-glacial temperature changes in modern oceans. Dr. J.M. Byrne is thanked for help with preparation of SEM samples and analysis and interpretation of Moessbauer spectra. M. Maisch is acknowledged for help with analysis of Moessbauer spectra and conducting  $\mu$ XRD analysis. Dr. A. Mloszewska, Dr. W. Wu, Dr. S. Lalonde, Dr. L. Robbins and T. Warchola are further acknowledged for fruitful discussions and advice on the experimental design. This study was supported by grants from the German Research Foundation (DFG) to AK and a Natural Sciences and Engineering Research Council (NSERC) grant to KOK.

## REFERENCES

- Alibert C. (2016) Rare earth elements in Hamersley BIF minerals. *Geochim. Cosmochim. Acta* **184**, 311–328.
- Altermann W. and Nelson D. R. (1998) Sedimentation rates, basin analysis and regional correlations of three Neoproterozoic and Palaeoproterozoic sub-basins of the Kaapvaal craton as inferred from precise U-Pb zircon ages from volcanoclastic sediments. *Sediment. Geol.* **120**, 225–256.
- Amstatter K., Borch T. and Kappler A. (2012) Influence of humic acid imposed changes of ferrihydrite aggregation on microbial Fe (III) reduction. *Geochim. Cosmochim. Acta* **85**, 326–341.
- Angelico R., Ceglie A., He J.-Z., Liu Y.-R., Palumbo G. and Colombo C. (2014) Particle size, charge and colloidal stability of humic acids coprecipitated with ferrihydrite. *Chemosphere* **99**, 239–247.
- Bau M. and Alexander B. W. (2009) Distribution of high field strength elements (Y, Zr, REE, Hf, Ta, Th, U) in adjacent magnetite and chert bands and in reference standards FeR-3 and FeR-4 from the Temagami iron-formation, Canada, and the redox level of the Neoproterozoic ocean. *Precambrian Res.* **174**, 337–346.
- Bekker A., Slack J. F., Planavsky N., Krapež B., Hofmann A., Konhauser K. O. and Rouxel O. J. (2010) Iron formation: the sedimentary product of a complex interplay among mantle, tectonic, oceanic, and biospheric processes. *Econ. Geol.* **105**, 467–508.
- Bekker A., Planavsky N., Rasmussen B., Krapež B., Hofmann A., Slack J., Rouxel O. and Konhauser K. O. (2014) Iron formations: Their origins and implications for ancient seawater chemistry. In *Treatise on Geochemistry, second ed. Vol. 9* (eds. H. D. Holland and K. K. Turekian). Elsevier, Netherlands. pp. 561–628.
- Beukes N. J. (1973) Precambrian iron-formations of southern Africa. *Econ. Geol.* **68**, 960–1004.
- Beukes N. J. (1984) Sedimentology of the Kuruman and Griquatown iron-formations, Transvaal Supergroup, Griqualand West, South Africa. *Precambrian Res.* **24**, 47–84.
- Bird L. J., Coleman M. L. and Newman D. K. (2013) Iron and copper act synergistically to delay anaerobic growth of bacteria. *Appl. Environ. Microbiol.* **79**, 3619–3627.
- Carlson L. and Schwertmann U. (1981) Natural ferrihydrites in surface deposits from Finland and their association with silica. *Geochim. Cosmochim. Acta* **45**, 421–425, 427–429.
- Chan C. S., Emerson D. and Luther, III, G. W. (2016) The role of microaerophilic Fe-oxidizing micro-organisms in producing banded iron formations. *Geobiology* **14**, 509–528.
- Cloud P. E. (1965) Significance of the Gunflint (Precambrian) microflora photosynthetic oxygen may have had important local effects before becoming a major atmospheric gas. *Science* **148**, 27–35.
- Cloud P. E. (1973) Paleocological significance of the banded iron-formation. *Econ. Geol.* **68**, 1135–1143.



- Cornell R. M., Giovanoli R. and Schindler P. W. (1987) Effect of silicate species on the transformation of ferrihydrite into goethite and hematite in alkaline media. *Clays Clay Miner.* **35**, 21–28.
- Cox J. S., Smith D. S., Warren L. A. and Ferris F. G. (1999) Characterizing heterogeneous bacterial surface functional groups using discrete affinity spectra for proton binding. *Environ. Sci. Technol.* **33**, 4514–4521.
- Craddock P. R. and Dauphas N. (2011) Iron and carbon isotope evidence for microbial iron respiration throughout the Archean. *Earth Planet. Sci. Lett.* **303**, 121–132.
- Crowe S. A., Jones C., Katsev S., Magen C., O'Neill A. H., Sturm A., Canfield D. E., Haffner G. D., Mucci A. and Sundby B. (2008) Photoferrotrophs thrive in an Archean Ocean analogue. *Proc. Natl. Acad. Sci.* **105**, 15938–15943.
- Czaja A. D., Johnson C. M., Beard B. L., Roden E. E., Li W. and Moorbath S. (2013) Biological Fe oxidation controlled deposition of banded iron formation in the ca. 3770 Ma Isua Supracrustal Belt (West Greenland). *Earth Planet. Sci. Lett.* **363**, 192–203.
- Davis J. A. (1982) Adsorption of natural dissolved organic matter at the oxide/water interface. *Geochim. Cosmochim. Acta* **46**, 2381–2393.
- Dimroth E. and Chauvel J. J. (1973) Petrography of the Sokoman iron formation in part of the central Labrador trough, Quebec, Canada. *Geol. Soc. Am. Bull.* **84**, 111–134.
- Doelsch E., Stone W. E., Petit S., Masion A., Rose J., Bottero J.-Y. and Nahon D. (2001) Speciation and crystal chemistry of Fe(III) chloride hydrolyzed in the presence of SiO<sub>4</sub> ligands. 2. Characterization of Si-Fe aggregates by FTIR and <sup>29</sup>Si solid-state NMR. *Langmuir* **17**, 1399–1405.
- Eggsleder M., Cruden A. R., Tomkins A. G., Wilson S. A. and Langendam A. D. (2018) Colloidal origin of microbands in banded iron formations. *Geochem. Perspect. Lett.* **6**, 43–49.
- Ehrenreich A. and Widdel F. (1994) Anaerobic oxidation of ferrous iron by purple bacteria, a new type of phototrophic metabolism. *Appl. Environ. Microbiol.* **60**, 4517–4526.
- Eickhoff M., Obst M., Schröder C., Hitchcock A. P., Tyliczszak T., Martinez R. E., Robbins L. J., Konhauser K. O. and Kappler A. (2014) Nickel partitioning in biogenic and abiogenic ferrihydrite: the influence of silica and implications for ancient environments. *Geochim. Cosmochim. Acta* **140**, 65–79.
- Emery W. J., Talley L. D. and Pickard G. L. (2006) Descriptive physical oceanography. Elsevier, Amsterdam.
- Ewers W. E. and Morris R. C. (1981) Studies of the Dales Gorge member of the Brockman iron formation, Western Australia. *Econ. Geol.* **76**, 1929–1953.
- Felmy A. R., Cho H., Rustard J. R. and Mason M. J. (2001) An aqueous thermodynamic model for polymerized silica species to high ionic strength. *J. Solution Chem.* **30**, 509–525.
- Fischer W. W. and Knoll A. H. (2009) An iron shuttle for deepwater silica in Late Archean and early Paleoproterozoic iron formation. *Geol. Soc. Am. Bull.* **121**, 222–235.
- Frei R. and Polat A. (2007) Source heterogeneity for the major components of ~3.7 Ga Banded Iron Formations (Isua Greenstone Belt, Western Greenland): tracing the nature of interacting water masses in BIF formation. *Earth Planet. Sci. Lett.* **253**, 266–281.

- Galili N., Shemesh A., Yam R., Brailovsky I., Sela-Adler M., Schuster E. M., Collom C., Bekker A., Planavsky N., Macdonald F. A., Pr at A., Rudmin M., Trela W., Stuesson U., Heikoop J. M., Aurell M., Ramajo J. and Halevy I. (2019) The geologic history of seawater oxygen isotopes from marine iron oxides. *Science* **365**, 469–473.
- Gauger T., Konhauser K. O. and Kappler A. (2015) Protection of phototrophic iron(II)-oxidizing bacteria from UV irradiation by biogenic iron(III) minerals: implications for early Archean banded iron formation. *Geology* **43**, 1067–1070.
- Gauger T., Byrne J. M., Konhauser K. O., Obst M., Crowe S. and Kappler A. (2016) Influence of organics and silica on Fe(II) oxidation rates and cell–mineral aggregate formation by the green-sulfur Fe(II)-oxidizing bacterium *Chlorobium ferrooxidans* KoFox – Implications for Fe(II) oxidation in ancient oceans. *Earth Planet. Sci. Lett.* **443**, 81–89.
- Gu B., Schmitt J., Chen Z., Liang L. and McCarthy J. F. (1994) Adsorption and desorption of natural organic matter on iron oxide: mechanisms and models. *Environ. Sci. Technol.* **28**, 38–46.
- Gunnarsson I. and Arn rsson S. (2000) Amorphous silica solubility and the thermodynamic properties of H<sub>4</sub>SiO<sub>4</sub> in the range of 0° to 350°C at P<sub>sat</sub>. *Geochim. Cosmochim. Acta* **64**, 2295–2307.
- Halama M., Swanner E. D., Konhauser K. O. and Kappler A. (2016) Evaluation of siderite and magnetite formation in BIFs by pressure–temperature experiments of Fe(III) minerals and microbial biomass. *Earth Planet. Sci. Lett.* **450**, 243–253.
- Halevy I. and Bachan A. (2017) The geologic history of seawater pH. *Science* **355**, 1069–1071.
- Hamade T., Konhauser K. O., Raiswell R., Goldsmith S. and Morris R. C. (2003) Using Ge/Si ratios to decouple iron and silica fluxes in Precambrian banded iron formations. *Geology* **31**, 35–38.
- Hao L., Guo Y., Byrne J. M., Zeitvogel F., Schmid G., Ingino P., Li J., Neu T. R., Swanner E. D. and Kappler A. (2016) Binding of heavy metal ions in aggregates of microbial cells, EPS and biogenic iron minerals measured in-situ using metal- and glycoconjugates-specific fluorophores. *Geochim. Cosmochim. Acta* **180**, 66–96.
- Hartman, H. (1984) The evolution of photosynthesis and microbial mats: A speculation on the banded iron formations. In *Microbial Mats: Stromatolites* (eds. Y. Cohen, R. W. Castenholz and H. O. Halvorson). Alan Liss, New York. pp. 451–453.
- Hashizume K., Pinti D. L., Orberger B., Cloquet C., Jayananda M. and Soyama H. (2016) A biological switch at the ocean surface as a cause of laminations in a Precambrian iron formation. *Earth Planet. Sci. Lett.* **446**, 27–36.
- Herbelin A.L. and Westall J.C. (1999) FITEQL 4.0: A computer program for determination of chemical equilibrium constants from experimental data.
- Hegler F., Posth N. R., Jiang J. and Kappler A. (2008) Physiology of phototrophic iron(II)-oxidizing bacteria: implications for modern and ancient environments. *FEMS Microbiol. Ecol.* **66**, 250–260.
- Heimann A., Johnson C. M., Beard B. L., Valley J. W., Roden E. E., Spicuzza M. J. and Beukes N. J. (2010) Fe, C, and O isotope compositions of banded iron formation carbonates

- demonstrate a major role for dissimilatory iron reduction in ~2.5 Ga marine environments. *Earth Planet. Sci. Lett.* **294**, 8–18.
- Hiemstra T., Barnett M. O. and van Riemsdijk W. H. (2007) Interaction of silicic acid with goethite. *J. Colloid Interface Sci.* **310**, 8–17.
- Hohmann C., Winkler E., Morin G. and Kappler A. (2009) Anaerobic Fe(II)-oxidizing bacteria show As resistance and immobilize As during Fe(III) mineral precipitation. *Environ. Sci. Technol.* **44**, 94–101.
- Holland H. D. (1973) The oceans; a possible source of iron in iron-formations. *Econ. Geol.* **68**, 1169–1172.
- Holm N. G. (1987) Biogenic influences on the geochemistry of certain ferruginous sediments of hydrothermal origin. *Chem. Geol.* **63**, 45–57.
- Iler R. K. (1979) The chemistry of silica: solubility, polymerization, colloid and surface properties, and biochemistry. Wiley.
- Isley A. E. (1995) Hydrothermal plumes and the delivery of iron to banded iron formation. *J. Geol.* **103**, 169–185.
- Isley, A. E. and Abbott, D. H. (1999) Plume-related mafic volcanism and the deposition of banded iron formation. *J. Geophys. Res. Solid Earth* (1978–2012) **104**, 15461–15477.
- Johnson J. E., Muhling J. R., Cosmidis J., Rasmussen B. and Templeton A. S. (2018) Low-Fe(III) greenalite was a primary mineral from neoproterozoic oceans. *Geophys. Res. Lett.* **45**, 3182–3192.
- Jones A. M., Collins R. N., Rose J. and Waite T. D. (2009) The effect of silica and natural organic matter on the Fe(II)-catalysed transformation and reactivity of Fe (III) minerals. *Geochim. Cosmochim. Acta* **73**, 4409–4422.
- Jones C., Nomosatryo S., Crowe S. A., Bjerrum C. J. and Canfield D. E. (2015) Iron oxides, divalent cations, silica, and the early earth phosphorus crisis. *Geology* **43**, 135–138.
- Kadko D. (2017) Upwelling and primary production during the US GEOTRACES East Pacific Zonal Transect. *Glob. Biogeochem. Cycles* **31**, 218–232.
- Kadko D. and Johns W. (2011) Inferring upwelling rates in the equatorial Atlantic using <sup>7</sup>Be measurements in the upper ocean. *Deep Sea Res. Part I: Oceanogr. Res. Pap.* **58**, 647–657.
- Kappler A. and Newman D. K. (2004) Formation of Fe(III)-minerals by Fe(II)-oxidizing photoautotrophic bacteria. *Geochim. Cosmochim. Acta* **68**, 1217–1226.
- Kappler A., Pasquero C., Konhauser K. O. and Newman D. K. (2005) Deposition of banded iron formations by anoxygenic phototrophic Fe(II)-oxidizing bacteria. *Geology* **33**, 865–868.
- Kasting J. F., Howard M. T., Wallmann K., Veizer J., Shields G. and Jaffrés J. (2006) Paleoclimates, ocean depth, and the oxygen isotopic composition of seawater. *Earth Planet. Sci. Lett.* **252**, 82–93.
- Klein C. (2005) Some Precambrian banded iron-formations (BIFs) from around the world: Their age, geologic setting, mineralogy, metamorphism, geochemistry, and origins. *Am. Mineral.* **90**, 1473–1499.

- Klein C. and Beukes N. J. (1989) Geochemistry and sedimentology of a facies transition from limestone to iron-formation deposition in the early Proterozoic Transvaal Supergroup, South Africa. *Econ. Geol.* **84**, 1733–1774.
- Klein C. and Beukes N. J. (1992) Time distribution, stratigraphy, and sedimentologic setting, and geochemistry of Precambrian iron-formations. In *The Proterozoic Biosphere: A Multidisciplinary Study* (eds. J. W. Schopf and C. Klein). Cambridge Univ. Press, New York, pp. 139–146.
- Koeksoy E., Halama M., Konhauser K. O. and Kappler A. (2016) Using modern ferruginous habitats to interpret Precambrian banded iron formation deposition. *Int. J. Astrobiol.* **15**, 205–217.
- Koeksoy E., Sundman A., Byrne J. M., Lohmayer R., Planer-Friedrich B., Halevy I., Konhauser K. O. and Kappler A. (2019) Formation of green rust and elemental sulfur in an analogue for oxygenated ferro-euxinic transition zones of Precambrian oceans. *Geology* **47**, 211–214.
- Konhauser K. O., Hamade T., Raiswell R., Morris R. C., Ferris F. G., Southam G. and Canfield D. E. (2002) Could bacteria have formed the Precambrian banded iron formations?. *Geology* **30** 1079–1082.
- Konhauser K. O., Newman D. K. and Kappler A. (2005) The potential significance of microbial Fe(III) reduction during deposition of Precambrian banded iron formations. *Geobiology* **3**, 167–177.
- Konhauser K. O., Amskold L., Lalonde S. V., Posth N. R., Kappler A. and Anbar A. (2007) Decoupling photochemical Fe(II) oxidation from shallow-water BIF deposition. *Earth Planet. Sci. Lett.* **258**, 87–100.
- Konhauser K. O., Planavsky N. J., Hardisty D. S., Robbins L. J., Warchola T. J., Haugaard R., Lalonde S. V., Partin C. A., Oonk P. B. H., Tsikos H., Lyons T. W., Bekker A. and Johnson C. M. (2017) Iron formations: A global record of Neoproterozoic to Palaeoproterozoic environmental history. *Earth Sci. Rev.* **172**, 140–177.
- Konhauser K. O., Robbins L. J., Alessi D. S., Flynn S. L., Gingras M. K., Martinez R. E., Kappler A., Swanner E. D., Li Y.-L., Crowe S. A., Planavsky N. J., Reinhard C. T. and Lalonde S. V. (2018) Phytoplankton contributions to the trace-element composition of Precambrian banded iron formations. *Geol. Soc. Am. Bull.* **130**, 941–951.
- Krapež B., Barley M. E. and Pickard A. L. (2003) Hydrothermal and resedimented origins of the precursor sediments to banded iron formation: sedimentological evidence from the Early Palaeoproterozoic Brockman Supersequence of Western Australia. *Sedimentology* **50**, 979–1011.
- Krauskopf K. B. (1956) Dissolution and precipitation of silica at low temperatures. *Geochim. Cosmochim. Acta* **10**, 1–26.
- Krissansen-Totton J., Arney G. N. and Catling D. C. (2018) Constraining the climate and ocean pH of the early Earth with a geological carbon cycle model. *Proc. Natl. Acad. Sci.* **115**, 4105–4110.
- Lantink M. L., Davies J. H., Mason P. R., Schaltegger U. and Hilgen F. J. (2019) Climate control on banded iron formations linked to orbital eccentricity. *Nat. Geosci.* **12**, 369–374.

- Larese-Casanova P., Haderlein S. B. and Kappler A. (2010) Biomineralization of lepidocrocite and goethite by nitrate-reducing Fe(II)-oxidizing bacteria: effect of pH, bicarbonate, phosphate, and humic acids. *Geochim. Cosmochim. Acta* **74**, 3721–3734.
- Laufer K., Niemeyer A., Nikeleit V., Halama M., Byrne J. M. and Kappler A. (2017) Physiological characterization of a halotolerant anoxygenic phototrophic Fe(II)-oxidizing green-sulfur bacterium isolated from a marine sediment. *FEMS Microbiol. Ecol.* **93**, fix054.
- Li Y.-L. (2014) Micro- and nanobands in late Archean and Palaeoproterozoic banded-iron formations as possible mineral records of annual and diurnal depositions. *Earth Planet. Sci. Lett.* **391**, 160–170.
- Li Y.-L., Konhauser K. O., Cole D. R. and Phelps T. J. (2011) Mineral ecophysiological data provide growing evidence for microbial activity in banded-iron formations. *Geology* **39**, 707–710.
- Li Y.-L., Konhauser K. O., Kappler A. and Hao X.-L. (2013) Experimental low-grade alteration of biogenic magnetite indicates microbial involvement in generation of banded iron formations. *Earth Planet. Sci. Lett.* **361**, 229–237.
- Li Y.-L., Konhauser K. O. and Zhai M. (2017) The formation of magnetite in the early Archean oceans. *Earth Planet. Sci. Lett.* **466**, 103–114.
- Liu Y., Alessi D. S., Owtrim G. W., Petrash D. A., Mloszewska A. M., Lalonde S. V., Martinez R. E., Zhou Q. and Konhauser K. O. (2015) Cell surface reactivity of *Synechococcus* sp. PCC 7002: implications for metal sorption from seawater. *Geochim. Cosmochim. Acta* **169**, 30–44.
- Maliva R. G., Knoll A. H. and Simonson B. M. (2005) Secular change in the Precambrian silica cycle: insights from chert petrology. *Geol. Soc. Am. Bull.* **117**, 835–845.
- MARGO Project Members (2009) Constraints on the magnitude and patterns of ocean cooling at the Last Glacial Maximum. *Nat. Geosci.* **2**, 127–132.
- Martinez R. E., Smith D. S., Kulczycki E. and Ferris F. G. (2002) Determination of intrinsic bacterial surface acidity constants using a Donnan shell model and a continuous pK<sub>a</sub> distribution method. *J. Colloid Interface Sci.* **253**, 130–139.
- Martinez R. E., Konhauser K. O., Paunova N., Wu W., Alessi D. S. and Kappler A. (2016) Surface reactivity of the anaerobic phototrophic Fe(II)-oxidizing bacterium *Rhodovulum iodolum*: Implications for trace metal budgets in ancient oceans and banded iron formations. *Chem. Geol.* **442**, 113–120.
- Mloszewska A. M., Pecoits E., Cates N. L., Mojzsis S. J., O’Neil J., Robbins L. J. and Konhauser K. O. (2012) The composition of Earth’s oldest iron formations: the Nuvvuagittuq Supracrustal Belt (Québec, Canada). *Earth Planet. Sci. Lett.* **317**, 331–342.
- Morris R. C. (1993) Genetic modelling for banded iron-formation of the Hamersley Group, Pilbara Craton Western Australia. *Precambrian Res.* **60**, 243–286.
- Morris R. C. and Horwitz R. C. (1983) The origin of the iron-formation-rich Hamersley Group of Western Australia - deposition on a platform. *Precambrian Res.* **21**, 273–297.
- Nealson K. H. and Myers C. R. (1990) Iron reduction by bacteria: a potential role in the genesis of banded iron formations. *Am. J. Sci.* **290**, 35–45.

- Percak-Dennett E. M., Beard B. L., Xu H., Konishi H., Johnson C. M. and Roden E. E. (2011) Iron isotope fractionation during microbial dissimilatory iron oxide reduction in simulated Archaean seawater. *Geobiology* **9**, 205–220.
- Pflaumann U., Sarnthein M., Chapman M., d'Abreu L., Funnell B., Huels M., Kiefer T., Maslin M., Schulz H., Swallow J., van Kreveld S., Vautravers M., Vogelsang E. and Weinelt M. (2003) Glacial North Atlantic: sea-surface conditions reconstructed by GLAMAP 2000. *Paleoceanography* **18**.
- Phoenix V. R., Konhauser K. O. and Ferris F. G. (2003) Experimental study of iron and silica immobilization by bacteria in mixed Fe-Si systems: Implications for microbial silicification in hot-springs. *Can. J. Earth Sci.* **40**, 1669–1678.
- Pickard A. L. (2002) SHRIMP U-Pb zircon ages of tuffaceous mudrocks in the Brockman Iron Formation of the Hamersley Range, Western Australia\*. *Aust. J. Earth Sci.* **49**, 491–507.
- Pickard A. L., Barley M. E. and Krapež B. (2004) Deep-marine depositional setting of banded iron formation: sedimentological evidence from interbedded clastic sedimentary rocks in the early Palaeoproterozoic Dales Gorge Member of Western Australia. *Sediment. Geol.* **170**, 37–62.
- Pickard G. L. and Emery W. J. (1982) *Descriptive Physical Oceanography: An Introduction*, 4th enlarged ed. Pergamon Press.
- Pinet P. R. (2011) *Invitation to oceanography*. Jones & Bartlett Publishers.
- Pokrovski G. S., Schott J., Farges F. and Hazemann J. L. (2003) Iron(III)-silica interactions in aqueous solution: Insights from X-ray absorption fine structure spectroscopy. *Geochim. Cosmochim. Acta.* **67**, 3559–3573.
- Pommerenk P. and Schafran G. C. (2005) Adsorption of inorganic and organic ligands onto hydrous aluminum oxide: evaluation of surface charge and the impacts on particle and NOM removal during water treatment. *Environ. Sci. Technol.* **39**, 6429–6434.
- Posth N. R., Hegler F., Konhauser K. O. and Kappler A. (2008) Alternating Si and Fe deposition caused by temperature fluctuations in Precambrian oceans. *Nat. Geosci.* **1**, 703–708.
- Posth N. R., Huelin S., Konhauser K. O. and Kappler A. (2010) Size, density and composition of cell–mineral aggregates formed during anoxygenic phototrophic Fe(II) oxidation: Impact on modern and ancient environments. *Geochim. Cosmochim. Acta* **74**, 3476–3493.
- Posth N. R., Konhauser K. O. and Kappler A. (2013) Microbiological processes in banded iron formation deposition. *Sedimentology* **60**, 1733–1754.
- Posth N. R., Canfield D. E. and Kappler A. (2014) Biogenic Fe(III) minerals: from formation to diagenesis and preservation in the rock record. *Earth Sci. Rev.* **135**, 103–121.
- Poulton S. W. and Canfield D. E. (2011) Ferruginous conditions: a dominant feature of the ocean through Earth's history. *Elements* **7**, 107–112.
- Rancourt D. G. and Ping J. Y. (1991) Voigt-based methods for arbitrary-shape static hyperfine parameter distributions in Mössbauer spectroscopy. *Nucl. Instrum. Meth. B* **58**, 85–97.
- Rasmussen B., Meier D. B., Krapež B. and Muhling J. R. (2013) Iron silicate microgranules as precursor sediments to 2.5-billion-year-old banded iron formations. *Geology* **41**, 435–438.

- Rasmussen B., Krapež B., Muhling J. R. and Suvorova A. (2015) Precipitation of iron silicate nanoparticles in early Precambrian oceans marks Earth's first iron age. *Geology* **43**, 303–306.
- Rasmussen B., Muhling J. R., Suvorova A. and Krapež B. (2017) Greenalite precipitation linked to the deposition of banded iron formations downslope from a late Archean carbonate platform. *Precambrian Res.* **290**, 49–62.
- Renner O. and Zemek J. (1973) Density of amorphous silicon films. *Czechoslovak J. Phys.* **23**, 1273–1276.
- Robbins L. J., Funk S. P., Flynn S. L., Warchola T. J., Li Z., Lalonde S. V., Rostron B. J., Smith A. J. B., Beukes N. J., de Kock M. O., Heaman L. M., Alessi D. S. and Konhauser K. O. (2019) Hydrogeological constraints on the formation of Palaeoproterozoic banded iron formations. *Nat. Geosci.* **12**, 558–563.
- Schaedler S., Burkhardt C., Hegler F., Straub K. L., Miot J., Benzerara K. and Kappler A. (2009) Formation of cell-iron-mineral aggregates by phototrophic and nitrate-reducing anaerobic Fe(II)-oxidizing bacteria. *Geomicrobiol. J.* **26**, 93–103.
- Schwertmann U. and Cornell R. M. (2008) Iron oxides in the laboratory. John Wiley & Sons.
- Shimizu M., Zhou J., Schroöder C., Obst M., Kappler A. and Borch T. (2013) Dissimilatory reduction and transformation of ferrihydrite-humic acid coprecipitates. *Environ. Sci. Technol.* **47**, 13375–13384.
- Sjöberg S. (1996) Silica in aqueous environments. *J. Non Cryst. Solids* **196**, 51–57.
- Smith A. J. B., Beukes N. J. and Gutzmer J. (2013) The composition and depositional environments of Mesoarchean iron formations of the West Rand Group of the Witwatersrand Supergroup, South Africa. *Econ. Geol.* **108**, 111–134.
- Sokolov I., Smith D. S., Henderson G. S., Gorby Y. A. and Ferris F. G. (2001) Cell surface electrochemical heterogeneity of the Fe(III)-reducing bacteria *Shewanella putrefaciens*. *Environ. Sci. Technol.* **35**, 341–347.
- Steinboefel G., von Blanckenburg F., Horn I., Konhauser K. O., Beukes N. J. and Gutzmer J. (2010) Deciphering formation processes of banded iron formations from the Transvaal and the Hamersley successions by combined Si and Fe isotope analysis using UV femtosecond laser ablation. *Geochim. Cosmochim. Acta* **74**, 2677–2696.
- Stookey L. L. (1970) Ferrozine - a new spectrophotometric reagent for iron. *Anal. Chem.* **42**, 779–781.
- Straub K. L., Rainey F. A. and Widdel F. (1999) *Rhodovulum iodosum* sp. nov. and *Rhodovulum robiginosum* sp. nov., two new marine phototrophic ferrous-iron-oxidizing purple bacteria. *Int. J. Syst. Bacteriol.* **49**, 729–735.
- Strickland J. D. H. and Parsons T. R. (1972) *A practical handbook of seawater analysis*. Fisheries Research Board of Canada, 167, Ottawa.
- Sun S., Konhauser K. O., Kappler A. and Li Y.-L. (2015) Primary hematite in Neoproterozoic to Paleoproterozoic oceans. *Geol. Soc. Am. Bull.* **127**, 850–861.
- Sundman A., Byrne J. M., Bauer I., Menguy N. and Kappler A. (2017) Interactions between magnetite and humic substances: redox reactions and dissolution processes. *Geochem. Trans.* **18**, 6.

- Svensson I. L., Sjöberg S. and Öhman L.-O. (1986) Polysilicate equilibria in concentrated sodium silicate solutions. *J. Chem. Society Faraday Trans. 1* **82**, 3635–3646.
- Swanner E. D., Mloszewska A. M., Cirkpa O. A., Schoenberg R., Konhauser K. O. and Kappler A. (2015a) Modulation of oxygen production in Archaean oceans by episodes of Fe(II) toxicity. *Nat. Geosci.* **8**, 126–130.
- Swanner E. D., Wu W., Schoenberg R., Byrne J., Michel F. M., Pan Y. and Kappler A. (2015b) Fractionation of Fe isotopes during Fe (II) oxidation by a marine photoferrotroph is controlled by the formation of organic Fe-complexes and colloidal Fe fractions. *Geochim. Cosmochim. Acta* **165**, 44–61.
- Swedlund P. J., Miskelly G. M. and McQuillan A. J. (2010) Silicic Acid Adsorption and Oligomerization at the Ferrihydrite-Water Interface: interpretation of ATR-IR Spectra Based on a Model Surface Structure. *Langmuir* **26**, 3394–3401.
- Tan H., Skinner W. and Addai-Mensah J. (2013) pH-mediated interfacial chemistry and particle interactions in aqueous chlorite dispersions. *Chem. Eng. Res. Des.* **91**, 448–456.
- ThomasArrigo L. K., Mikutta C., Byrne J. M., Kappler A. and Kretzschmar R. (2017) Iron(II)-catalyzed iron atom exchange and mineralogical changes in iron-rich organic freshwater flocs: an iron isotope tracer study. *Environ. Sci. Technol.* **51**, 6897–6907.
- ThomasArrigo L. K., Byrne J. M., Kappler A. and Kretzschmar R. (2018) Impact of organic matter on iron(II)-catalyzed mineral transformations in ferrihydrite-organic matter coprecipitates. *Environ. Sci. Technol.* **52**, 12316–12326.
- Toner B. M., Berquó T. S., Michel F. M., Sorensen J. V., Templeton A. S. and Edwards K. J. (2012) Mineralogy of iron microbial mats from Loihi Seamount. *Front. Microbiol.* **3**, 118.
- Tosca N. J., Guggenheim S. and Pufahl P. K. (2016) An authigenic origin for Precambrian greenalite: Implications for iron formation and the chemistry of ancient seawater. *Geol. Soc. Am. Bull.* **128**, 511–530.
- Trendall, A. F. (2002) The significance of iron-formation in the Precambrian stratigraphic record. *Precambrian Sedimentary Environments: a Modern Approach to Depositional Systems*, *Spec. Publ. Internat. Assoc. Sedimentol.* **33**, 33-66.
- Trendall A. F. and Blockley J. B. (1970) The iron formations of the Hamersley Group, Western Australia, with special reference to the associated crocidolite. *Western Austr. Geol. Surv., Bull.*, **119**, 353 pp.
- Trendall A. F., Compston W., Nelson D. R., De Laeter J. R. and Bennett V. C. (2004) SHRIMP zircon ages constraining the depositional chronology of the Hamersley Group, Western Australia\*. *Aust. J. Earth Sci.* **51**, 621–644.
- Viehmann S., Hoffmann J. E., Münker C. and Bau M. (2014) Decoupled Hf-Nd isotopes in Neoproterozoic seawater reveal weathering of emerged continents. *Geology* **42**, 115–118.
- Walker J. C. (1984) Suboxic diagenesis in banded iron formations. *Nature* **309**, 340–342.
- Walter X. A., Picazo A., Miracle M. R., Vicente E., Camacho A., Aragno M. and Zopfi J. (2014) Phototrophic Fe(II)-oxidation in the chemocline of a ferruginous meromictic lake. *Front. Microbiol.* **5**, 713.



- 
- Widdel F., Schnell S., Heising S., Ehrenreich A., Assmus B. and Schink B. (1993) Ferrous iron oxidation by anoxygenic phototrophic bacteria. *Nature* **362**, 834–836.
- Williams L. A. and Crerar D. A. (1985) Silica diagenesis; II, general mechanisms. *J. Sediment. Res.* **55**, 312–321.
- Williams L. A., Parks G. A. and Crerar D. A. (1985) Silica diagenesis; I, solubility controls. *J. Sediment. Res.* **55**, 301–311.
- Wu W., Swanner E. D., Hao L., Zeitvogel F., Obst M., Pan Y. and Kappler A. (2014) Characterization of the physiology and cell–mineral interactions of the marine anoxygenic phototrophic Fe(II) oxidizer *Rhodovulum iodolum* – implications for Precambrian Fe(II) oxidation. *FEMS Microbiol. Ecol.* **88**, 503–515.
- Wu W., Swanner E. D., Kleinmanns I. C., Schoenberg R., Pan Y. and Kappler A. (2017) Fe isotope fractionation during Fe(II) oxidation by the marine photoferrotroph *Rhodovulum iodolum* in the presence of Si - implications for Precambrian iron formation deposition. *Geochim. Cosmochim. Acta.* **211**, 307–321.
- Zeitvogel F., Burkhardt C. J., Schroepel B., Schmid G., Ingino P. and Obst M. (2017) Comparison of preparation methods of bacterial cell-mineral aggregates for SEM imaging and analysis using the model system of *Acidovorax* sp. BoFeN1. *Geomicrobiol. J.* **34**, 317–327.
- Zheng X. Y., Beard B. L., Reddy T. R., Roden E. E. and Johnson C. M. (2016) Abiologic silicon isotope fractionation between aqueous Si and Fe(III)–Si gel in simulated Archean seawater: implications for Si isotope records in Precambrian sedimentary rocks. *Geochim. Cosmochim. Acta* **187**, 102–122.
- Zhou Z., Latta D. E., Noor N., Thompson A., Borch T. and Scherer M. M. (2018) Fe(II)-catalyzed transformation of organic matter-ferrihydrite coprecipitates: a closer look using Fe isotopes. *Environ. Sci. Technol.* **52**, 11142–11150.



## SUPPLEMENTAL INFORMATION

### **Temperature fluctuations in the Archean ocean as trigger for varve-like deposition of iron and silica minerals in banded iron formations**

Manuel Schad<sup>a</sup>, Maximilian Halama<sup>a</sup>, Brendan Bishop<sup>b</sup>, Kurt O. Konhauser<sup>b</sup>, Andreas Kappler<sup>a</sup>

<sup>a</sup> Geomicrobiology, Center for Applied Geosciences, University of Tübingen, 72076, Tübingen,  
Germany

<sup>b</sup> Department of Earth and Atmospheric Sciences, University of Alberta, Edmonton, AB T6G  
2E3, Canada

**Published in:** *Geochimica et Cosmochimica Acta* **265** (2019) 386-412,  
<https://doi.org/10.1016/j.gca.2019.08.031>.

## APPENDIX

---

**Appendix A**
**Supplementary information: Volume of monomeric silica solution added.**

Table A.1

Overview about the volumes of monomeric Si solution added to the parallel setups (“low”, “intermediate” and “high”) during the formation of the amorphous Si layer. Monomeric Si was added from a 50 mM anoxic  $\text{Na}_2\text{SiO}_3 \cdot 9 \text{H}_2\text{O}$  stock solution. Numbers 1 to 3 represent biotic triplicates, while number 4 represents the abiotic (non-inoculated) control. In this table the volume of monomeric Si added is listed, not the concentration of dissolved monomeric Si measured.

Timepoint [d]	Si(OH) <sub>4</sub> solution added [mL]											
	“low“				“intermediate“				“high“			
	1	2	3	4	1	2	3	4	1	2	3	4
35	1.44	1.44	1.44	1.44	1.44	1.44	1.44	1.44	1.44	1.44	1.44	1.44
54	1.44	1.44	0	0	2.88	2.88	0	0	5.76	5.76	0	0
93	5.76	5.76	7.2	7.2	4.32	4.32	7.2	7.2	1.44	1.44	7.2	7.2
99	2.88	2.88	2.88	2.88	2.88	2.88	2.88	2.88	2.88	2.88	2.88	2.88
112	2.88	2.88	2.88	2.88	2.88	2.88	2.88	2.88	2.88	2.88	2.88	2.88
119	2.88	2.88	2.88	2.88	2.88	2.88	2.88	2.88	2.88	2.88	2.88	2.88
Total volume added (mL)	17.28	17.28	17.28	17.28	17.28	17.28	17.28	17.28	17.28	17.28	17.28	17.28

---

## Supplementary information: 5 K Moessbauer data

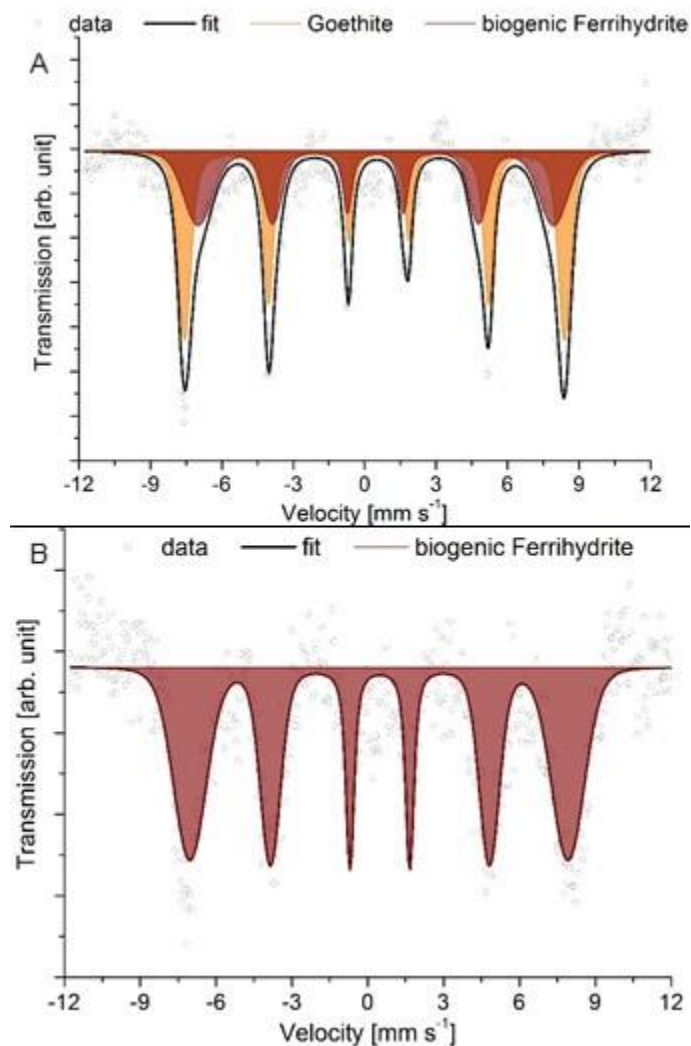


Fig. A.1: Moessbauer spectra collected at 5 K. Light grey circles represent collected data points while the solid black lines and the colored areas represent the fit. (A) represents a spectrum collected from Fe(III) minerals precipitated by *R. iodosum* in the absence of Si. (B) represents a spectrum collected from Fe(III) minerals precipitated by *R. iodosum* in the presence of Si.

Table A.2

Data obtained by Moessbauer spectroscopy at 5 K for biogenic Fe(III) minerals precipitated by *R. iodosum* in the presence or absence of Si. <sup>1</sup>isomer shift, <sup>2</sup>quadrupole shift, <sup>3</sup>hyperfine field, <sup>4</sup>ferrihydrite.

	<b>IS<sup>1</sup></b> [mm/s]	<b>QS<sup>2</sup></b> [mm/s]	<b>B<sub>hf</sub><sup>3</sup></b> [T]	<b>Area</b> [%]
<b>No silica</b>				
	0.50	-0.09	49.5	56
	0.46	0.01	46.3	44
<b>With silica</b>				
Biogenic Fh <sup>4</sup>	0.46	-0.02	46.4	100







## Statement of personal contribution

### Chapter 3

#### **Microbial Fe cycling in a simulated Precambrian ocean environment: Implications for secondary mineral (trans)formation and deposition during BIF genesis**

Manuel Schad, James M. Byrne, Laurel K. ThomasArrigo, Ruben Kretzschmar, Kurt O. Konhauser, Andreas Kappler

**Manuscript in preparation for publication in:** *Geochimica et Cosmochimica Acta*

The work described in this chapter was supported by grants from the German Research Foundation (DFG) to Prof. Andreas Kappler and grants from the Natural Science and Engineering Research Council (NSERC) to Prof. Kurt O. Konhauser. The work in this chapter was supervised by Prof. Andreas Kappler, Prof. Kurt O. Konhauser.

The study was designed and conceptualized by me with the help of Prof. Andreas Kappler, Prof. Kurt O. Konhauser.

The bacterial cultures used in this study were provided by Lars Grimm. The experiments including sample preparation and analyses were conducted by me. Dr. Yuge Bai and Katrin Wunsch provided experimental support during sampling and subsequent sample analysis.

Flow cytometry was conducted with the help of Dr. Casey Bryce and Lars Grimm.

HPLC measurements were performed by Ellen Röhm.

Light and fluorescence microscopy was performed by me with the advice of Lars Grimm.

Scanning electron microscopy sample preparation and analyses were performed by me with the help of Dr. Hartmut Schulz, Dr. James M. Byrne and Timm Bayer.

$^{57}\text{Fe}$  Moessbauer analysis was carried out by me with the help of Dr. James M. Byrne.

XRD analysis was performed by Prof. Ruben Kretzschmar and Dr. Laurel ThomasArrigo.

Dr. James M. Byrne, Dr. M. Muehe, Dr. C. Bryce, Dr. M. Maisch, M. Patzner and J. Sorwat provided advice on experimental design and data interpretation.

Obtained results were discussed and analyzed in cooperation with Prof. Andreas Kappler and Prof. Kurt O. Konhauser. The manuscript was written by me with feedback and improvement by Prof. Andreas Kappler, Dr. James M. Byrne and Dr. Yuge Bai.

## Chapter 3

### **Microbial Fe cycling in a simulated Precambrian ocean environment: Implications for secondary mineral (trans)formation and deposition during BIF genesis**

Manuel Schad<sup>a</sup>, James M. Byrne<sup>a,b</sup>, Laurel K. ThomasArrigo<sup>c</sup>, Ruben Kretzschmar<sup>c</sup>, Kurt O. Konhauser<sup>d</sup>, Andreas Kappler<sup>a</sup>

<sup>a</sup> Geomicrobiology, Center for Applied Geosciences, University of Tuebingen, Tuebingen, Germany

<sup>b</sup> Now: School of Earth Sciences, University of Bristol, Bristol, United Kingdom

<sup>c</sup> Soil Chemistry, Department of Environmental Systems Science, ETH Zürich, Zürich, Switzerland

<sup>d</sup> Department of Earth and Atmospheric Sciences, University of Alberta, Edmonton, Canada

**Manuscript in preparation for publication in:** *Geochimica et Cosmochimica Acta*

A modified version of this chapter has been submitted to *Geochimica et Cosmochimica Acta*.



---

**ABSTRACT**

Banded Iron Formations (BIFs) contain a variety of Fe-bearing minerals such as hematite, magnetite, siderite and Fe<sup>II</sup>-/Fe<sup>III</sup>-containing silicates. It has been suggested that dissimilatory Fe(III)-reducing bacteria (DIRB) could have transformed primary Fe(III) (oxyhydr)oxide minerals in the sediment into secondary magnetite and siderite. However, it is unknown, to which extent this mineral transformation would already have taken place in the water column, where the Fe<sup>2+</sup> released could have been re-oxidized, thus closing the Fe cycling. To test this, we conducted Fe cycling experiments with marine phototrophic Fe(II)-oxidizing bacteria and DIRB under conditions mimicking the Precambrian ocean water column to elucidate whether such microbial Fe cycling could have taken place. We followed secondary mineral formation over three consecutive redox cycles (oxidation followed by reduction) over a time interval of up to 58 days to determine which mineral phases would ultimately have settled as BIF forming sediments. We used wet geochemical methods to follow Fe speciation, dissolved silica and volatile fatty acid (VFA) concentrations, determined cell-mineral associations using fluorescence and electron microscopy and characterized the mineralogy using <sup>57</sup>Fe-Moessbauer spectroscopy and XRD. Our results showed that both the absence of silica and an increasing number of Fe cycles favored the formation of more crystalline minerals like goethite. However, in the presence of high concentrations of monomeric silica as suggested for ancient oceans (2.2 mM), only short-range ordered (SRO) Fe(III) minerals were observed, which did not transform into more thermodynamically stable Fe(III) phases such as goethite during repeated Fe cycling. No magnetite formation was observed in any of the setups. Instead increasing Si concentrations favored the formation of increasing quantities of Fe(II) minerals such as siderite and/or Fe(II)-silicates. Microscopy revealed a tight association between microbial biomass and minerals formed. Silica analysis showed co-precipitation of silica during Fe(II) oxidation and a release of Si during Fe(III) reduction, suggesting an important role of co-precipitated biomass as well as silica for secondary mineral formation by either constraining crystal growth and/or inhibiting Fe(II)-induced mineral transformation. Overall our results imply that microbial Fe cycling during Fe mineral settling through the photic zone in a Precambrian ocean would have already resulted in the partial transformation of primary Fe(III) (oxyhydr)oxides into Fe(II) minerals such as siderite and/or Fe(II)-silicates in the water column. This would have resulted in the accumulation of mixtures of ferrihydrite-silica composite and Fe(II) minerals in the initial BIF forming

sediments. By contrast, magnetite would have been formed during subsequent sediment diagenesis.

## 1. INTRODUCTION

The geochemistry of the Archean to early Paleoproterozoic ocean was fundamentally different from the modern ocean. Prior to the Great Oxidation Event (GOE) when the Earth's atmosphere accumulated significant levels of oxygen for the first time (Lyons et al., 2014), the bulk ocean was essentially anoxic with O<sub>2</sub> concentrations below 1 μM (Hardisty et al., 2014). Low O<sub>2</sub> in combination with low sulfate/sulfide concentrations (Crowe et al., 2014) and an increased hydrothermal Fe flux (Kump and Seyfried, 2005) allowed the buildup of high concentrations of hydrothermally derived dissolved Fe(II) (Fe<sup>2+</sup>) of between 0.03 and 0.5 mM (Holland, 1973; Morris, 1993). Similarly, the early ocean would have been enriched in dissolved Si, ranging from 0.67 mM (saturation with respect cristobalite) to 2.2 mM. (saturation with respect to amorphous silica; Maliva et al., 2005; Siever, 1992), although a recent study suggested lower concentrations (0.5-1.6 mM; Zheng et al., 2016).

These conditions are reflected in the composition of major Banded Iron Formations (BIFs), marine chemical sedimentary deposits which were mainly deposited during the Neoarchean and early Paleoproterozoic (Konhauser et al., 2017). They predominantly consist of Fe (15-40 wt.%) and Si (40-60 wt.%; Trendall, 2002), deposited in alternating layers resulting in the characteristic banding (Trendall and Blockley, 1970). BIFs contain little organic carbon (<0.5 wt.%; Gole and Klein, 1981) and minimal detrital input (<1 wt.% Al<sub>2</sub>O<sub>3</sub>, <20 ppm Ti, Zr, Th, Hf, Sc; Konhauser et al., 2017). Their chemical composition, lateral continuity, high degree of preservation and general association with carbonates and shales suggest that BIFs were deposited in nearshore shelf environments on the margins of stable cratons. However, the absence of wave- or current-generated structures indicates deposition in depths >200 m (Bekker et al., 2010; Trendall, 2002). Mineralogically the least metamorphosed BIFs consist of hematite, magnetite, carbonates (ankerite, siderite) and chert with varying contributions of Fe<sup>II</sup>Fe<sup>III</sup>-silicates (e.g. greenalite, stilpnomelane, riebeckite and minnesotaite) and pyrite (Klein, 2005). The presence of both oxidized and reduced Fe minerals gives BIFs an average oxidation state of Fe<sup>2.4+</sup> (Klein and Beukes, 1992). Consensus is that none of the minerals found in BIFs today are primary but rather a product of diagenetic and metamorphic alteration of the initially deposited minerals.

The composition of these precursor mineral phases is highly debated. Both (partially) reduced minerals such as greenalite (e.g. Rasmussen et al., 2017) and oxidized minerals such as

Fe(III) (oxyhydr)oxides have been suggested (Alibert, 2016; Beukes and Gutzmer, 2008; Pecoits et al., 2009). However, many researchers seem to be in favor of the deposition of Fe(III) (oxyhydr)oxides as precursors to BIF Fe oxides, whose deposition has traditionally been explained by the oxidation of Fe<sup>2+</sup> via O<sub>2</sub> produced by cyanobacteria (Cloud, 1973). Alternatively, anoxygenic photoautotrophic Fe(II)-oxidizing bacteria (photoferrotrophs) could have driven early primary production by coupling Fe(II) oxidation to CO<sub>2</sub> fixation by harvesting light energy (Hartman, 1984). Konhauser et al. (2002) suggested that this process could have accounted for most if not all Fe initially deposited in BIFs in form of ferrihydrite, a ferrihydrite-Si composite or goethite (Alibert, 2016; Beukes and Gutzmer, 2008; Kappler and Newman, 2004; Pecoits et al., 2009), co-precipitated with bacterial cells (Posth et al., 2010).

These cell-Fe(III) mineral aggregates would have provided an ideal habitat for bacteria able to couple carbon oxidation to Fe(III) reduction (dissimilatory Fe(III) reduction, DIR; Lovley and Phillips, 1986, 1988), potentially resulting in the formation of secondary minerals such as siderite and magnetite (Lovley, 1991), minerals commonly found in BIFs today. Additionally, the organic carbon utilized would have been oxidized to CO<sub>2</sub>, hence offering a plausible explanation for the low organic carbon content in BIFs. The significance of microbial Fe(III) reduction for the genesis of BIFs was first hypothesized by Walker (1984) and later further conceptualized by Nealson and Myers (1990). C, O and Fe isotope studies have since stressed the importance of DIR for the post-depositional alteration of BIFs (e.g. Craddock and Dauphas, 2011; Heimann et al., 2010; Johnson et al., 2003; Johnson et al., 2008; Steinhöfel et al., 2010; Teixeira et al., 2017; Wang et al., 2015). Further evidence for DIR is provided by detailed sedimentological and petrographic work which emphasizes an early paragenetic origin of magnetite (e.g. Beukes and Gutzmer, 2008 and references therein, Pecoits et al., 2009) as well as by crystallochemical data suggesting magnetite crystals contained in BIFs to display similarities to modern biogenic magnetite (Li et al., 2011).

This has important implications since experimental results have cast doubt on a metamorphic origin of magnetite, where its formation was limited to experiments conducted with highly reactive glucose as biomass proxy (Halama et al., 2016). In the presence of complex biomass, however, hematite and siderite were the main metamorphic products. More recent work has emphasized the possibility of magnetite formation through thermal decomposition of siderite at temperatures exceeding 200°C (Rasmussen and Mühling, 2018) but the significance of this



---

mineral transformation pathway for the least metamorphosed BIFs remains unclear. Alternatively, magnetite could have been the product of a reaction between primary Fe(III) (oxyhydr)oxides and hot (>50°C) Fe(II)-rich hydrothermal fluids (Li et al., 2017). However, both Si (Cismasu et al., 2014; Jones et al., 2009), which would have been abundant in the ancient ocean, as well as organic matter contained in cell-Fe(III) mineral aggregates (Han et al., 2020), have shown to retard or even inhibit Fe(II)-induced mineral transformation to mixed-valent Fe minerals. In contrast hereto, magnetite formed by Fe(III)-reducing bacteria and exposed to metamorphic pressure-temperature conditions exhibited high thermal stability (Li et al., 2013), suggesting its preservation during low-grade metamorphism and thus pointing to a microbial origin for magnetite.

In summary, there is strong precedence for the formation of primary cell-Fe(III) mineral aggregates by photoferrotrophs and subsequent diagenetic alteration of these mineral aggregates by DIR during the genesis of BIF. Konhauser et al. (2005) estimated that up to 70% of the initially deposited Fe(III) might have been reduced microbially and cycled back into the water column, resulting in the formation of secondary biogenic magnetite and siderite (Han et al., 2020). However, it is unclear how a continuous microbial Fe cycle, i.e. the combination of photoferrotrophy and microbial DIR, during the sedimentation of cell-Fe(III) mineral aggregates would have influenced the secondary mineralogy of BIFs. Specifically, it remains unclear (1) how Fe(II)-oxidizing and Fe(III)-reducing bacteria would have interacted during repeated and dynamic microbial Fe cycling, (2) how this would have influenced the nature and composition of primary BIF sediments, (3) if there was indeed the formation and preservation of siderite and magnetite, and (4) in case magnetite was formed microbially, when and where during the deposition of BIFs its formation would have occurred. To test this, we conducted experiments simulating the Precambrian ocean chemistry where we co-cultivated marine photoferrotrophs and marine Fe(III)-reducing bacteria. We followed geochemical parameters, mineral identity and composition of cell-mineral aggregates over time and placed our experimental data into the context of BIF deposition applying some simplified calculations regarding the water column residence time of these cell-mineral aggregates.

## 2. MATERIALS AND METHODS

### 2.1. Source of microorganisms, culturing medium and growth conditions

*Chlorobium* sp. strain N1 is a marine photoferrotroph belonging to the green-sulfur bacteria, which was isolated from Norsminde Fjord, Denmark (Laufer et al., 2017; Laufer et al., 2016). A marine Fe(III)-reducing enrichment culture, which showed a 99% sequence similarity to *Shewanella colwelliana*, was obtained from the same field site (Laufer et al., 2016). Both cultures have been kept in our laboratory culture collection since their isolation.

Both cultures were routinely cultivated on artificial seawater medium (ASW; Laufer et al., 2016) buffered by 30 mM bicarbonate under a N<sub>2</sub>/CO<sub>2</sub> (90:10) headspace. The pH was set to 7.1 aimed at simulating the circumneutral pH of the Precambrian ocean (Halevy and Bachan, 2017; Krissansen-Totton et al., 2018). Additionally, to obtain Si concentrations covering the range of concentrations assumed for the Precambrian ocean (0.67 to 2.2 mM, saturation with respect to cristobalite and amorphous silica, respectively; (Maliva et al., 2005; Siever, 1992), 0.19 g L<sup>-1</sup> and 0.63 g L<sup>-1</sup> Na<sub>2</sub>SiO<sub>3</sub> × 9 H<sub>2</sub>O, respectively, were added. For the cultivation of *Chlorobium* sp. strain N1 the ASW was additionally amended with 5 mM Fe(II) (1 M FeCl<sub>2</sub> × 4 H<sub>2</sub>O stock solution; (Hegler et al., 2008). This Fe(II) concentration is approximately one order of magnitude higher than the maximum concentration assumed for the Precambrian ocean (0.5 mM; Holland, 1973; Morris, 1993) but was necessary to obtain enough Fe minerals for analysis. All media amended with Si and/ or Fe(II) were placed at 5°C for >48h to maximize the removal of any silicate or Fe(II) carbonate or phosphate (likely siderite or vivianite; Hohmann et al., 2009) which may have formed. Hereafter, the pH was re-adjusted to 7.1 when necessary, the precipitates removed by sterile filtration (polyethersulfone, 0.22 μm pore size Steritop filter unit, Millipore, Merck KGaA, Darmstadt, Germany) inside an anoxic glovebox (100% N<sub>2</sub> atmosphere) and the headspace exchanged for N<sub>2</sub>/CO<sub>2</sub> (90/10). The extent of Fe(II) and Si(OH)<sub>4</sub> removal during filtration of Fe(II)-containing medium used in our experiments is detailed in Table 1.

Table 1  
Extent of Fe(II) and Si(OH)<sub>4</sub> removal during filtration of Fe(II)-containing ASW.

Medium	Expected concentration		Final concentration		Loss upon filtration	
	Fe(II) [mM]	Si(OH) <sub>4</sub> [mM]	Fe(II) [mM]	Si(OH) <sub>4</sub> [mM]	Fe(II) [%]	Si(OH) <sub>4</sub> [%]
ASW, no Si	5.00	0.00	4.75	0.00	5.00	0.00
ASW, low Si	5.00	0.67	4.40	0.71	12.00	0.00
ASW, high Si	5.00	2.20	4.23	1.43	15.40	35.00

All stock cultures were grown in 250 mL serum bottles containing 100 mL growth medium. Stock cultures of *Chlorobium* sp. strain N1 were grown on Fe(II)-containing ASW with 0 mM, 0.67 mM and 2.2 mM Si, respectively. Cultures were incubated at 20°C in light using a 40-W incandescent light bulb.

Stock cultures of the Fe(III)-reducing enrichment culture were grown routinely on ASW containing either no Si, 0.67 mM Si or 2.2 mM Si, respectively, with 5 mM of 2-line ferrihydrite (Schwertmann and Cornell, 2008) as terminal electron acceptor (TEA) and 5 mM lactate as electron donor and C source. However, cultures used for the inoculation the experiments were grown on 20 mM fumarate as TEA and 10 mM lactate as electron donor and C source for at least two generations to minimize the amount of Fe transferred to the experiment. All cultures were incubated in the dark at room temperature (RT).

## 2.2. Experimental setup

### 2.2.1. Preparation of the inoculum

*Chlorobium* sp. strain N1 was inoculated directly from a stationary phase culture grown on Fe(II) with the respective Si concentration (0 mM, 0.67 mM or 2.2 mM). Cell numbers of all cultures were quantified by flow cytometry prior to inoculation.

For the Fe(III)-reducing enrichment culture, cultures grown on fumarate and lactate were harvested by centrifugation at 1761 g and washed 3 times with a sterile 30 mM bicarbonate buffer to remove any remaining metabolic products. Afterwards the cultures were resuspended in ASW of the respective Si concentration, made anoxic by flushing with N<sub>2</sub>/CO<sub>2</sub> (90:10) and stored at RT. The cell suspensions were used within 48 h of preparation. Cell numbers of all cultures were quantified by flow cytometry prior to inoculation.

### 2.2.2. *Microbial Fe cycling experiments*

Since it is practically impossible to setup a 100 m water column experiment in the laboratory to follow Fe cycling during sedimentation, we simulated the processes that occur during sedimentation in 250 mL serum bottles containing 100 mL Fe(II)-containing ASW. The small amount of precipitates formed prevents artifacts resulting from redox stratification that would occur in thick layers of mineral sediments. Our experimental setup, therefore, allows us to simulate redox and mineral transformation processes occurring in sedimenting Fe mineral particles. One third of all bottles did not contain any added Si to represent modern ocean Si concentrations. One third contained 0.67 mM Si (low Si) to represent the lower limit of the ancient ocean Si concentrations and the last third contained 2.2 mM (high Si) to simulate the upper limit of assumed Si concentrations (Maliva et al., 2005; Siever, 1992). All experiments were run in biotic triplicates with one abiotic control. We performed 3 consecutive microbial Fe cycles each consisting of an oxidative half cycle (activity of photoferrotrophs in light) and a reductive half cycle (activity of Fe(III)-reducing bacteria in dark) over a period of maximum 58 days.

The first oxidative half cycle was initiated by the addition of 1% inoculum (*v/v*, 1 mL) of *Chlorobium* sp. strain N1 grown on the respective Si concentrations to the biotic triplicates (Fig. 1). Quantification of *Chlorobium* sp. strain N1 cell numbers by flow cytometry was not possible. However, based on Laufer et al. (2017), where twice the Fe(II) concentration of our experiments was used, approximately  $4 \times 10^8$  cells mL<sup>-1</sup> were added. The second and third oxidative half cycle were initiated by transferring the cultures from dark to light conditions without addition of new cells. For the oxidative half cycles all cultures were incubated at 20°C in light. Samples were taken prior to inoculation, after inoculation and at regular time intervals during the experiment as described below. The oxidative half cycles were considered finished once >95% of the initial Fe(II) was oxidized (as determined by the ferrozine assay).

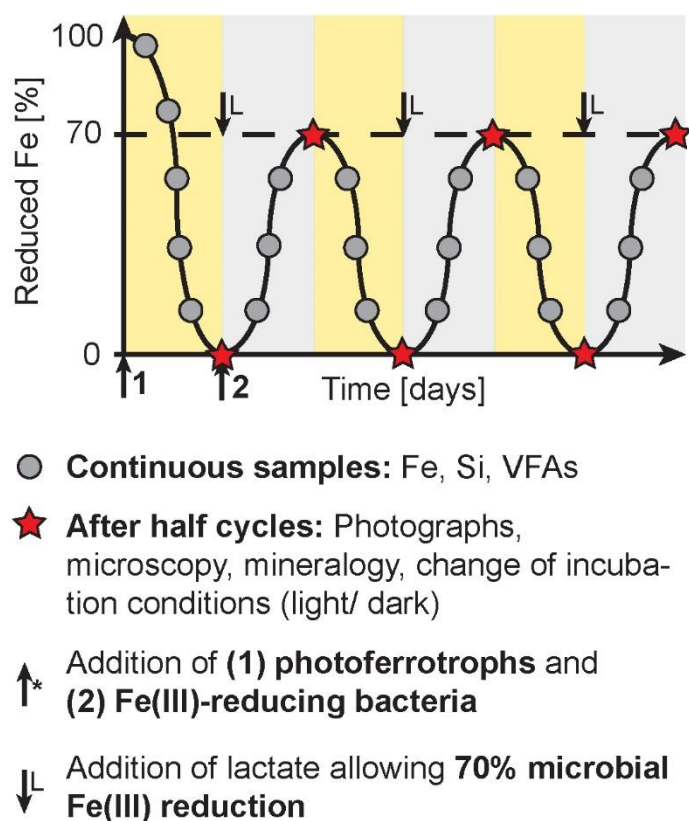


Fig. 1. Overview over experimental setup of cycling experiment with alternating oxidative and reductive periods and sampling pattern (grey dots and red stars). Yellow shaded areas mark oxidative periods by incubation in light at 20°C. Grey shaded areas mark reductive periods by incubation in the dark at RT.

lactate to a concentration that again allowed for up to 70% Fe(III) reduction and were transferred to dark conditions. No new cells were added after the first reductive half cycle. Samples were taken prior to and after inoculation and lactate addition and at regular time intervals during the experiment as described in the following section. The reductive half cycles were terminated once 70% Fe(III) reduction had been achieved (determined by ferrozine assay) and the cultures were transferred back to light conditions.

### 2.2.3. Sampling and sample processing

All sampling was performed in an anoxic glovebox (100% N<sub>2</sub> atmosphere). Samples for wet geochemistry were taken continuously throughout the experiments and include samples for Fe concentration and redox speciation, dissolved Si and volatile fatty acids (VFAs). Samples for light and electron microscopy and mineral identification by XRD and <sup>57</sup>Fe Moessbauer spectroscopy were taken at the end of each half cycle (Fig. 1).

The first reductive half cycle was initiated by the addition of 0.1% inoculum (v/v, 0.1 mL), thus approximately  $1 \times 10^7$  cells mL<sup>-1</sup>, from the Fe(III)-reducing enrichment culture cell suspensions (Fig. 1). Additionally, lactate was added at a concentration (~1-1.2 mM, depending on the Fe<sup>2+</sup> concentration after filtration) that would theoretically allow for 70% of the Fe(III) to be reduced to Fe(II) (per Konhauser et al., 2005; based on the initial Fe(II) concentration, assuming that all Fe(II) was oxidized). During reductive conditions, all cultures were wrapped in Al foil and incubated at RT in the dark. The second and third reductive half cycles were initiated by the addition of

For wet geochemical samples, approximately 1 mL of sample was taken from each serum bottle after vigorous shaking. For total Fe quantification, a 100  $\mu\text{L}$  aliquot of the whole sample (solid + liquid) was digested in 900  $\mu\text{L}$  1 M HCl for 1 hour, centrifuged (12,100 g) and the supernatant preserved for further analysis. The remaining total sample (~900  $\mu\text{L}$ , solid + liquid) was centrifuged (12100 g) and 100  $\mu\text{L}$  of the supernatant was stabilized in 900  $\mu\text{L}$  1 M HCl for dissolved Fe quantification, 50  $\mu\text{L}$  of the supernatant was diluted with 950  $\mu\text{L}$  Milli-Q<sup>®</sup> water (Merck KGaA, Darmstadt, Germany) for dissolved Si quantification and the remaining supernatant was separated and preserved for VFA quantification. Samples for Fe speciation and quantification were kept at 5°C until further analysis. Samples for dissolved Si were measured as soon as possible after sampling. Samples for VFA quantification were stored at -20°C until further analysis.

For light and fluorescent microscopy, approximately 10  $\mu\text{L}$  sample was taken, transferred to a microscope slide and mixed with 1  $\mu\text{L}$  of SYTO<sup>®</sup> 9 green fluorescent dye (LIVE/DEAD<sup>™</sup> BacLight<sup>™</sup> Bacterial Viability and Counting Kit, Thermo Fisher Scientific Inc., Waltham, Massachusetts, USA), incubated for 10 minutes in the dark and immediately analyzed.

Samples for scanning electron microscopy (SEM) were fixed with glutaraldehyde (final concentration 2.5%) over night at 4°C. Subsequently, they were washed twice with Milli-Q<sup>®</sup> water, mounted on poly-L-lysine covered glass slides and sequentially dehydrated with increasing concentrations of EtOH (30, 50, 70, and 95%, 5 minutes each, 2 x 100%, 30 minutes each) and finally with hexamethyldisilazane (HMDS, 2 x 30 seconds). Thereafter samples were left to dry in air at ambient pressure. Dried samples were mounted onto Al stubs using conductive carbon tape and coated with a ~15 nm Pt-layer using a Balzers Union Med 010 sputter coater (Bal-Tec, Balzers, Liechtenstein). Samples were store in a drying cabinet until analysis.

Samples for mineral analysis by <sup>57</sup>Fe Moessbauer spectroscopy and XRD were prepared by filtration onto 0.45  $\mu\text{m}$  filter papers which were embedded in Kapton tape and stored in anoxic (100% N<sub>2</sub>) air-tight bottles at -20°C until analysis.

#### 2.2.4. *Characterization of primary precipitates (formed after first oxidative half-cycle)*

For the characterization of primary precipitates (cell-Fe(III) mineral precipitates formed after the first oxidative half-cycle) additional serum bottles (biotic triplicates, no control) were set up as detailed at the beginning of section 2.2.2 for the oxidative half cycles. Once all Fe(II) was

---

oxidized (>95%, as determined by the ferrozine assay) the content of all serum bottles was harvested quantitatively and further processed for mineralogy and aggregate size analysis (see below) as well as organic carbon content and surface charge as detailed in supplementary text S1.

## 2.3. Analytical techniques

### 2.3.1. Cell counts

Cell numbers of both, *Chlorobium* sp. strain N1 and the Fe(III)-reducing enrichment culture were determined by flow cytometry (Attune NxT Flow Cytometer, Thermo Fisher Scientific Inc., Waltham, Massachusetts, USA) using 200  $\mu\text{L}$  sample in 96-well plates.

It was not possible to obtain reliable cell numbers for *Chlorobium* sp. strain N1 due to poor staining of the cells and a high background signal. A complete description of the various experimental approaches and parameters modified during sample preparation is given in the supplementary text S2.

Samples for the Fe(III)-reducing cultures were prepared by sequential dilution of a 100  $\mu\text{L}$  sample from the culture with 30 mM bicarbonate buffer (up to  $10^{-3}$ ). BacLight™ green bacterial stain (Thermo Fisher Scientific Inc., Waltham, Massachusetts, USA) was added at a concentration of 1  $\mu\text{L mL}^{-1}$  and incubated in the dark for 15 minutes prior to measurement.

### 2.3.2. Wet geochemistry

#### 2.3.2.1. Fe analysis and calculation of maximum Fe(II) oxidation and Fe(III) reduction rates

Fe concentration and redox were determined using a modified protocol for the ferrozine assay (Stookey, 1970) as detailed in Hegler et al. (2008). The absorption at 562 nm was measured using a Multiskan GO Microplate Spectrophotometer with internal software (SkanIT RE for Multiskan GO 3.2; Thermo Fisher Scientific Inc., Waltham, Massachusetts, USA).

Maximum Fe(II) oxidation and Fe(III) reduction rates were calculated by linear regression analysis through the steepest 3 points of the total Fe(II) curve at a given timepoint.

### 2.3.2.2. Si analysis

Quantification of dissolved monomeric Si was performed using a modified protocol of the molybdenum blue method developed by Strickland and Parsons (1972). In short, 40  $\mu\text{L}$  acid molybdate solution was added to 1 mL of sample, mixed by shaking and the yellow color allowed to develop for 15 minutes. 40  $\mu\text{L}$  oxalic acid was then added to bind excess molybdate and eliminate the influence of phosphate in the sample, mixed by shaking and 20  $\mu\text{L}$  ascorbic acid added immediately. After mixing the blue color was allowed to develop for 60 minutes. 200  $\mu\text{L}$  were transferred into a black-walled micro-titer plate and the absorption measured at 810 nm using a Multiskan GO Microplate Spectrophotometer with internal software (SkanIT RE for Multiskan GO 3.2; Thermo Fisher Scientific Inc., Waltham, Massachusetts, USA).

### 2.3.2.3. High pressure liquid chromatography (HPLC)

VFAs were quantified using a Shimadzu prominence (Shimadzu Corp., Kyoto, Japan) HPLC system equipped with a Biorad Aminex HPX87H column with 5 mM  $\text{H}_2\text{SO}_4$  as eluent and a diode-array detector. The flow rate was set to 0.6 ml  $\text{min}^{-1}$ .

## 2.3.3. *Microscopy*

### 2.3.3.1. Fluorescence and light microscopy

Fluorescence microscopy was performed on fresh samples using a Leica DM5500 epifluorescence microscope (Leica Microsystems GmbH, Wetzlar, Germany) at 40x magnification.

### 2.3.3.2. Scanning electron microscopy (SEM)

SEM imaging for investigation of mineral morphology and cell-mineral associations was performed at the Center for Light-Matter Interaction, Sensors & Analytics (LISA+) at the University of Tuebingen, Germany. Secondary electron (SE) images were obtained using a JEOL JSM-6500F field emission SEM with a Schottky field emitter (JEOL Ltd., Tokyo, Japan). The instrument was operated at an acceleration voltage of 5 kV with a working distance of 10 mm. No elemental analysis by EDS was performed.

SEM imaging for particle size analysis was performed at the Center for Applied Geosciences, University of Tuebingen, Germany. SE imaging was performed using a LEO 1450



VP (Carl Zeiss AG, Oberkochen, Germany) equipped with an Everhart-Thornley SE-Detector. The instrument was operated at an acceleration voltage of 7 kV and a working distance of 8 mm. No elemental analysis by EDS was performed.

#### 2.3.4. Mineral identification

##### 2.3.4.1. $^{57}\text{Fe}$ Moessbauer spectroscopy

$^{57}\text{Fe}$  Moessbauer spectroscopy was performed at the Geomicrobiology group, Center for Applied Geosciences, University of Tuebingen. The anoxic bottles the samples were stored in were opened just prior to loading the sample into the instrument. The samples were loaded into the Mössbauer instrument and inserted into a closed-cycle exchange gas cryostat (Janis cryogenics, Janis Research Company LLC, Woburn, Massachusetts, USA) under a backflow of He. Spectra were collected using a constant acceleration drive system (WissEl, Starnberg, Germany) operated in transmission mode with a  $^{57}\text{Co}$  source embedded in a Rh matrix as  $\gamma$ -radiation source. The spectra of samples obtained at the end of the oxidative half cycles were collected at 77 K. The spectra of samples obtained at the end of the reductive half cycles were collected at 140 K. All spectra were calibrated against a 7  $\mu\text{m}$  thick  $\alpha$ - $^{57}\text{Fe}$  foil measured at RT. The Recoil software (University of Ottawa) was used to fit measured spectra using a Voigt-based fitting routine (Rancourt and Ping, 1991). The Lorentz half-width-half-maximum (HWHM) was determined using the minimum line width of the third and fourth peak of the calibration. The HWHM was fixed at 0.127  $\text{mm s}^{-1}$ . The hyperfine parameters describing individual samples fits are detailed in supplementary text S3.

##### 2.3.4.2. X-ray diffraction (XRD)

XRD analysis was conducted at the Soil Chemistry group, Institute of Biogeochemistry and Pollutant Dynamics, ETH Zürich, Switzerland. XRD analysis was performed on the same samples analyzed by  $^{57}\text{Fe}$  Moessbauer spectroscopy. Samples stemming from oxidative half-cycles were handled in ambient atmosphere, samples stemming from reductive half-cycles were handled inside an anoxic glovebox ( $\text{N}_2$  atmosphere,  $<1$  ppm  $\text{O}_2$ ). Kapton tape-sealed samples were opened, dried biomineral residue carefully scraped off the filter papers and/or Kapton tape and collected in 0.5 mL Eppendorf tubes. The dry material was resuspended in approximately 20  $\mu\text{L}$  (anoxic) EtOH and pipetted onto a polished silicon wafer (Sil'tronix Silicon Technologies,

Archamps, France). Samples from reductive half-cycles were secured in an air-tight sample holder with integrated beam knife.

Samples were analyzed on a Bruker D8 Advance XRD in Bragg-Brentano geometry using Cu K $\alpha_{1,2}$  radiation ( $\lambda = 1.5418 \text{ \AA}$ , 40 kV and 40 mA) and a high-resolution energy-dispersive 1-D detector (LYNXEYE). Diffractograms were recorded from 10 to 70°2 $\theta$  with a step size of 0.02°2 $\theta$  and 6 s acquisition time per step. Data analysis was performed using the CrystalDiffract 6 software (EVA/TOPAS, Bruker) in combination with the PDF2 database (The International Centre for Diffraction Data) and crystallographic information files (CIF) for halite and goethite obtained from the Inorganic Crystal Structure Database (FIZ Karlsruhe).

### 2.3.5. *Aggregate size analysis and calculation of settling velocity*

Stoke's law was used to calculate the settling velocity of the primary Fe(III) mineral-cell aggregates (aggregates formed during the first oxidative half-cycle). The aggregate size was determined in SEM micrographs by measuring the longest axis for any given aggregate. The aggregates measured were randomized by drawing a vertical, a diagonal and a horizontal line from the top left corner of any given image and measuring all aggregates along those lines. In order to obtain some statistical significance, the size of at least 100 aggregates was determined using the ImageJ software. In case of an insufficient amount of aggregates all aggregates were measured. Due to lacking consideration of size variations in z direction by 2D imaging with SEM, the results may be biased.

### 2.3.6. *Statistical analyses*

All statistical analyses were performed using IBM® SPSS® Statistics Version 26 (IBM Corp., Armonk, New York, USA).

## 3. RESULTS

### 3.1. **Microbial Fe(II) oxidation and Fe(III) reduction in dependence of Si concentrations**

The main objectives of our study were (1) to determine how Fe-metabolizing microorganisms would have interacted under conditions relevant for early Earth, e.g. through their mutual influence on each other's metabolic activity, either directly by providing substrates

or potentially also indirectly through biochemical cues, and (2) to evaluate how an early microbial Fe cycle would have influenced the (trans)formation of the Fe mineralogy accumulated in BIF depositional environments. We, therefore, conducted experiments in which we co-cultivated the marine photoferrotroph *Chlorobium* sp. strain N1 and a marine Fe(III)-reducing enrichment culture under conditions which simulate the proposed geochemistry of an early ocean. In these experiments, we monitored microbial activity by following changes in solution geochemistry including dissolved and total Fe, dissolved Si and VFAs.

For all three setups, no Si (0 mM), low Si (0.67 mM) and high Si (2.2 mM), three full microbial Fe redox cycles were performed. Oxidative half cycles were considered completed when  $\geq 95\%$  Fe(II) was oxidized and reductive half cycles completed when  $\geq 70\%$  of the initially oxidized Fe(II) was reduced again (as per Konhauser et al., 2005).

For the first oxidative half cycle (day 0-18) all three setups showed an initial lag time of 4 days (Fig. 2A, D and G). Thereafter, the Fe(II) in all setups was completely oxidized within 10 days. Maximum Fe(II) oxidation rates decreased slightly with increasing Si concentrations ( $0.79 \pm 0.11$  mM d<sup>-1</sup>,  $0.76 \pm 0.07$  mM d<sup>-1</sup> and  $0.57 \pm 0.03$  mM d<sup>-1</sup>, Fig. 3). Total 1 M HCl extractable Fe concentrations showed contrasting trends for different Si concentrations: While the high Si setup showed (within error) no decrease in total Fe from days 1-18 (suggesting that all Fe in the minerals formed was HCl-extractable), it decreased from approximately 4.5 mM to between 2 to 2.5 mM and to approximately 0.5 mM in the low Si and no Si setups, respectively. Since 1 M HCl extracts mostly short-range ordered Fe minerals, this suggests the presence of more highly crystalline Fe(III) minerals with decreasing Si concentration and in the absence of Si (Fig. 2B, E and H). The Si containing setups showed, concomitant with Fe(II) oxidation, a sharp decrease in dissolved Si concentrations:  $56 \pm 1.6\%$  of the initial 0.72 mM Si were removed from solution in the low Si setup until day 18, which is comparable in extent to the high Si setup where the dissolved Si decreased from  $1.40 \pm 0.02$  mM to  $0.83 \pm 0.02$  mM (Fig. 2D and G).

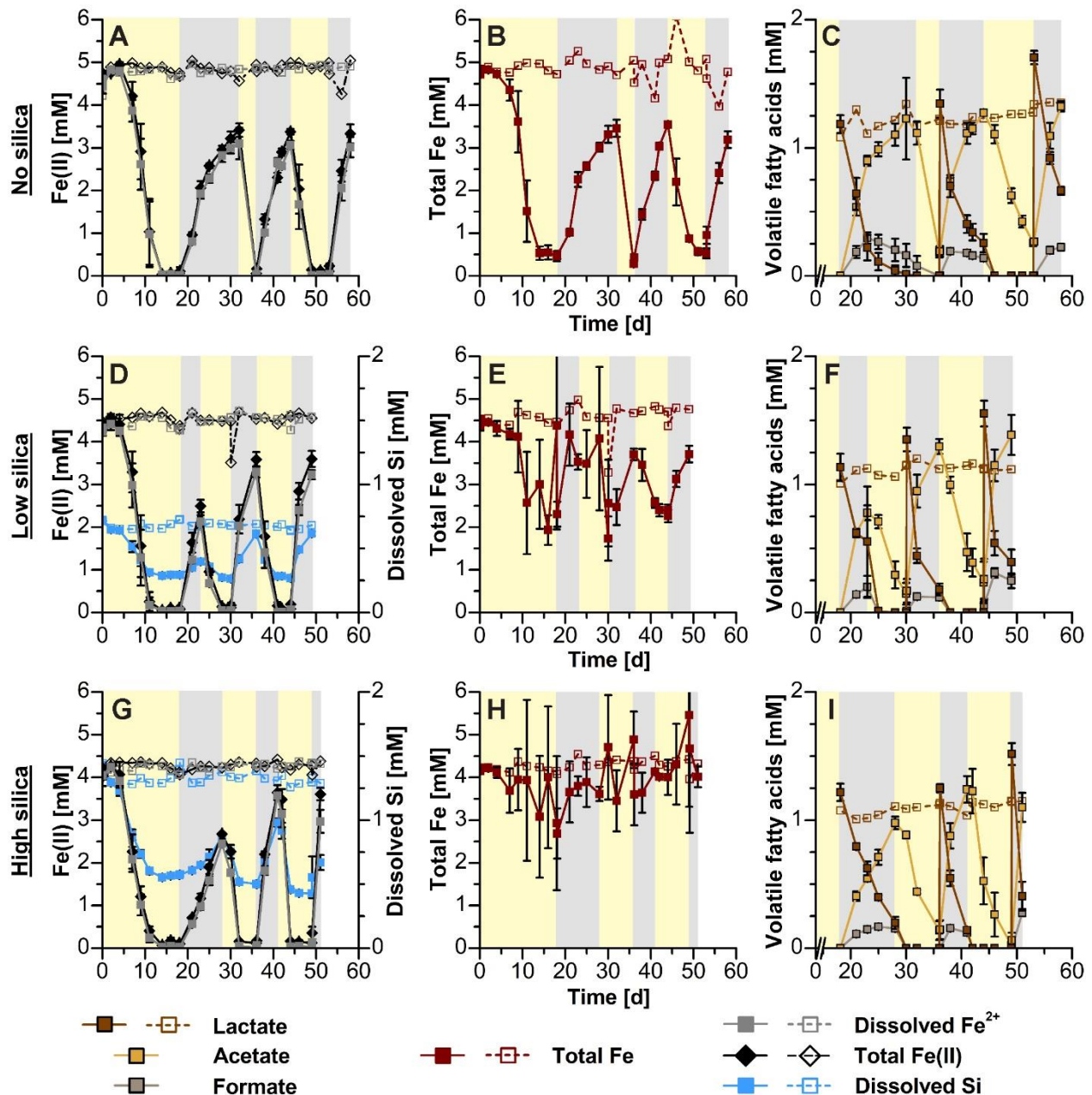


Fig. 2. Variations in wet geochemical parameters (fatty acids, total Fe, total and dissolved Fe(II), dissolved Si) over time during microbial Fe cycling experiments. The top row shows the results of the Si-free setup, the middle row results of the low Si setup and the bottom row the results of the high Si setup. Closed symbols with solid lines are biotic triplicates. Open symbols with dashed lines are abiotic controls. Yellow shaded areas mark incubation at 20°C in light. Grey shaded areas mark incubation at RT in dark. Data shown for biotic setups are mean from triplicates  $\pm$  standard deviation. Abiotic controls are single measurements.

Upon completion of the first oxidative half cycle, the biotic triplicates of all setups were inoculated with the Fe(III)-reducing enrichment culture and all bottles (including abiotic, non-inoculated controls) were amended with lactate to a concentration that could theoretically allow for 70% of the oxidized Fe(II) to be reduced again. Fe(III) reduction was initiated by transferring all bottles to the dark. In the low Si setup, around 60% of the Fe(III) was reduced within 5 days

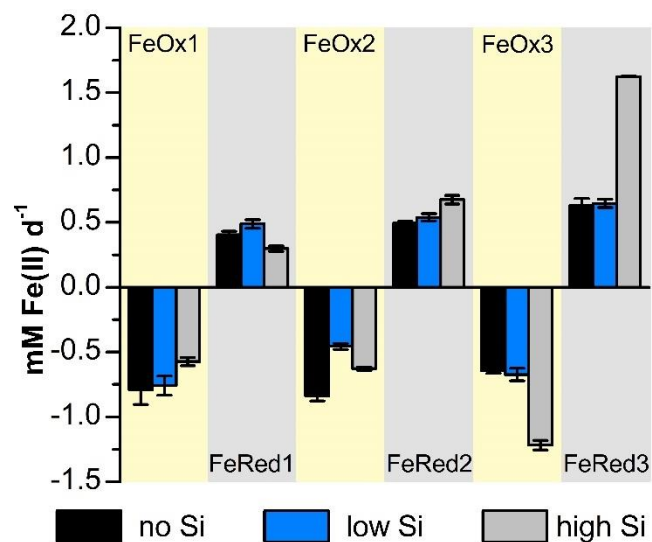
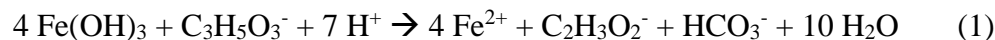


Fig. 3. Maximum Fe(III) reduction (positive values) and Fe(II) oxidation rates (negative values). Rates were calculated by linear regression analysis through the steepest 3 points of the total Fe(II) curve at a given timepoint. Values are the mean from biotic triplicates. For the calculation of the maximum rates two outliers were removed: 1.27 mM d<sup>-1</sup> for the second reductive half cycle of the high Si setup and 2.06 mM d<sup>-1</sup> for the third oxidative half cycle of the high Si setup.

it increased slightly from approximately 2.2 mM to 3.5 mM in the low Si setup and increased considerably from 0.5 to 3.5 mM (thus essentially mimicking Fe(II) concentrations) in the no Si setup (Figure 2B, E, H). These results suggest that independent of the crystallinity of the minerals formed by microbial Fe(II) oxidation, they remained accessible for microbial Fe(III) reduction. In all cases the recycled Fe(II) was mostly present as dissolved Fe(II) (Fe<sup>2+</sup>, >85%), thus both, the formation of Fe(II)-containing minerals and adsorption of Fe(II) to the remaining Fe(III) (oxyhydr)oxides was limited (Fig. 2A, D, G). Microbial Fe(III) reduction was linked to incomplete lactate oxidation and acetate and formate formation (Fig. 2C, F, I). The ratio of Fe(III) reduced to lactate oxidized was below the expected 4:1 ratio (equation 1), ranging from 3.02 ± 0.65 (low Si) to 3.56 ± 0.14 (high Si).



For the Si-containing setups dissolution of Fe(III) minerals during microbial Fe(III) reduction resulted in the remobilization of 24.6 ± 5.9% (low Si) and 35.1 ± 3.3% (high Si) of the Si immobilized during the previous oxidative half cycle, resulting in aqueous Si concentrations of 0.40 ± 0.01 mM and 0.87 ± 0.01 mM, respectively.

(day 18-23), followed by the high Si setup (>60% in 10 days, day 18-28) and the Si-free setup (>70% in 14 days, day 18-32; Fig. 2A, D, G). This is partially reflected by the maximum Fe(III) reduction rates, which was the highest for the low Si setup (0.49 ± 0.03 mM d<sup>-1</sup>), followed by the no Si and high Si setup, with 0.41 ± 0.03 mM d<sup>-1</sup> and 0.30 ± 0.02 mM d<sup>-1</sup>, respectively. Similar to the oxidative half cycle, total 1 M HCl-extractable Fe concentrations depended on the Si concentration: In the high Si setup, the total extractable Fe concentrations remained constant, while

After incubation under dark conditions during the first reductive half cycle, there was no lag time when shifting to the second oxidative half cycle (days 32-36 for no Si setup, days 23-30 for low Si and days 28-36 for high Si). Fe(II) oxidation was faster than during the first oxidative half cycle: In the second cycle  $\geq 95\%$  Fe(II) was oxidized in 4 days (no Si, high Si) or 5 days (low Si), respectively (Fig. 2A, D, G). This is reflected in slightly higher maximum Fe(II) oxidation rates for the no Si and high Si setups of  $0.84 \pm 0.04 \text{ mM d}^{-1}$  and  $0.63 \pm 0.01 \text{ mM d}^{-1}$ , respectively (Fig. 3). In contrast, the maximum Fe(II) oxidation rate of the low Si setup decreased to  $0.46 \pm 0.02 \text{ mM d}^{-1}$ . Total 1 M HCl-extractable Fe concentrations followed the same trends as during the first oxidative half cycle (Fig. 2B, E, H). Similar to the first oxidative half cycle, the dissolved Si concentration decreased from  $0.40 \pm 0.01 \text{ mM}$  to  $0.26 \pm 0.01 \text{ mM}$  ( $33.8 \pm 4.0\%$  removal) and from  $0.87 \pm 0.01 \text{ mM}$  to  $0.50 \pm 0.00 \text{ mM}$  ( $42.3 \pm 0.5\%$  removal) during Fe(II) oxidation, for the low Si and high Si setup, respectively. Additionally, in all biotic triplicates formate formed during as well as the lactate remaining after the previous reductive half cycle were metabolized completely during the oxidative half cycle, while approximately  $0.1 \text{ mM}$  acetate remained in solution (Fig. 2C, F, I).

Upon completion of the second oxidative half cycle, all biotic triplicates were amended with lactate again and all bottles transferred to dark conditions, thus initiating the second reductive half cycle (day 36-44 no Si setup, day 30-36 low Si setup, day 36-41 high Si setup). The maximum Fe(III) reduction rates increased compared to the first reductive half cycle with  $0.50 \pm 0.01 \text{ mM d}^{-1}$ ,  $0.54 \pm 0.03 \text{ mM d}^{-1}$  and  $0.68 \pm 0.03 \text{ mM d}^{-1}$  for the no Si, low Si and high Si setups, respectively (Fig. 3). Again, the Fe(II) formed during microbial Fe(III) reduction was mainly present as  $\text{Fe}^{2+}$  ( $>90\%$ ). Furthermore, total extractable Fe concentrations followed the same trends already observed for the first reductive half cycle (Fig. 2B, E, H). The oxidation of lactate was incomplete (as also observed during the first cycle) and resulted in the formation of acetate and formate (Fig. 2C, F, I). Compared to the first reductive half cycle the ratio of Fe(III) reduced to lactate oxidized decreased to between  $2.74 \pm 0.11$  (no Si) and  $3.20 \pm 0.25$  (high Si). The microbial reduction of Fe(III) minerals also resulted in an extensive release of Si into solution ( $0.61 \pm 0.01 \text{ mM}$  dissolved Si,  $264.1 \pm 43.3\%$  increase, low Si and  $0.98 \pm 0.03 \text{ mM}$  dissolved Si,  $130.8 \pm 10.8\%$  increase, high Si; Fig. 2D, G).

During the third and last oxidative half cycle (days 44-49 for the no Si, days 36-44 for the low Si and days 41-49 for the high Si setup) Fe(II) oxidation was fastest in the high Si setup ( $\geq 95\%$

Fe(II) oxidation within two days) and slower for the no Si and low Si setups with 5 and 6 days respectively being required for complete Fe(II) oxidation (Fig. 2A, D, G). This is reflected in the maximum Fe(II) oxidation rates, which were  $1.22 \pm 0.04 \text{ mM d}^{-1}$ ,  $0.65 \pm 0.02 \text{ mM d}^{-1}$  and  $0.67 \pm 0.05 \text{ mM d}^{-1}$  for the high Si, no Si and low Si setups respectively, the last two thus being comparable to the second oxidative half cycle (Fig. 3). Total Fe as well as fatty acid concentrations followed the same trends as during the previous oxidative half cycles (Fig. 2B + C, E + F, H + I). Additionally, dissolved Si concentrations decreased to  $0.27 \pm 0.01 \text{ mM}$  ( $56.5 \pm 0.9\%$  removal) in the low Si and to  $0.43 \pm 0.02 \text{ mM}$  ( $56.4 \pm 2.4\%$  removal) in the high Si setup (Fig. 2D, F).

The final reductive half cycle (days 54-59 for the no Si, days 44-49 for the low Si and days 49-51 for the high Si setup) was generally the fastest, with 5 days required to recycle  $\geq 70\%$  of the previously oxidized Fe(II) by the no and low Si setups and only 2 days required by the high Si setup (Fig. 2A, D, G). This is mirrored by higher maximum Fe(III) reduction rates of  $0.63 \pm 0.06 \text{ mM d}^{-1}$ ,  $0.65 \pm 0.03 \text{ mM d}^{-1}$  and  $1.63 \pm 0.00 \text{ mM d}^{-1}$  for the no, low and high Si setup, respectively (Fig. 3). Comparable to the previous two reductive half cycles the Fe(II) formed was mainly present as  $\text{Fe}^{2+}$  ( $>80\%$ ) and total extractable Fe concentrations followed the trends observed for the first two cycles (Fig. 2B, E, H). Fe(III) reduction was linked to incomplete lactate oxidation (Fig. 2C, F, I), where the ratio of Fe(III) reduced to lactate oxidized further decreased to on average below 3 for all Si concentrations. Upon Fe(III) mineral dissolution the dissolved Si concentration increased back to final values of  $0.62 \pm 0.02 \text{ mM}$  in the low Si setup and  $0.67 \pm 0.06 \text{ mM}$  in the high Si setup (Fig. 2D, G).

In summary, our wet geochemical data suggest that co-cultivation of photoferrotrophs and Fe(III)-reducing bacteria facilitates microbial Fe cycling independent of the Si concentration. Overall, the high Si setup showed the fastest Fe cycling (38 days), followed by the low Si setup (40 days) and the no Si setup (50 days), when considering only the time in which Fe was actively metabolized, thus the time until  $\geq 95\%$  Fe(II) was oxidized or  $\geq 70\%$  Fe(III) was reduced. All three setups showed faster Fe(II) oxidation and Fe(III) reduction with an increasing number of microbial Fe redox cycles. This is reflected by an overall significant (positive) effect of an increasing number of Fe cycles on the maximum Fe(III) reduction rates, which increased over time (see supplementary text S4).

However, the effect of the number of Fe cycles on the maximum Fe(II) oxidation rates was different depending on the presence of Si, and rates either decreased over time (no Si), were not affected (low Si) or increased (high Si; see supplementary text S4). Si did not significantly influence the maximum Fe(II) oxidation rates during the first oxidative half cycle and even had an adverse effect during first reductive half cycle if present at high concentrations (see supplementary text S4). However, by the second reductive half cycle this effect was inverted and high Si concentrations resulted in significantly higher maximum oxidation and reduction rates throughout the remaining experiment compared to the no Si and low Si setups. In contrast, low Si concentrations had no pronounced effect on the maximum rates over the duration of the experiment (see supplementary text S4).

Furthermore, differing Si concentrations seemed to influence the crystallinity of the Fe(III) minerals formed during the oxidative half cycles, where the crystallinity was highest in the no Si setup and lowest in the high Si setup (Fig. 4). However, during all reductive half cycles no crystalline Fe(II)-containing minerals (like magnetite) seemed to have been formed since generally >80% of the Fe(II) was present as Fe<sup>2+</sup>. In spite of the high degree of mineral dissolution during microbial Fe(III) reduction, dissolved Si concentrations seemed to be strongly affected by the Fe mineral (trans)formations, resulting in a significant decrease in dissolved Si in both the low Si setup (paired t-test,  $t = 10.961$ ,  $df = 2$ ,  $P = 0.008$ ) and high Si setup (paired t-test,  $t = 19.282$ ,  $df = 2$ ,  $P = 0.003$ ):  $14.0 \pm 2.2\%$  and  $52.2 \pm 4.4\%$  of the initially present dissolved Si,  $0.72 \pm 0.00$  mM and  $1.40 \pm 0.02$  mM, respectively, were removed from solution over the course of microbial Fe cycling (Fig. 4).



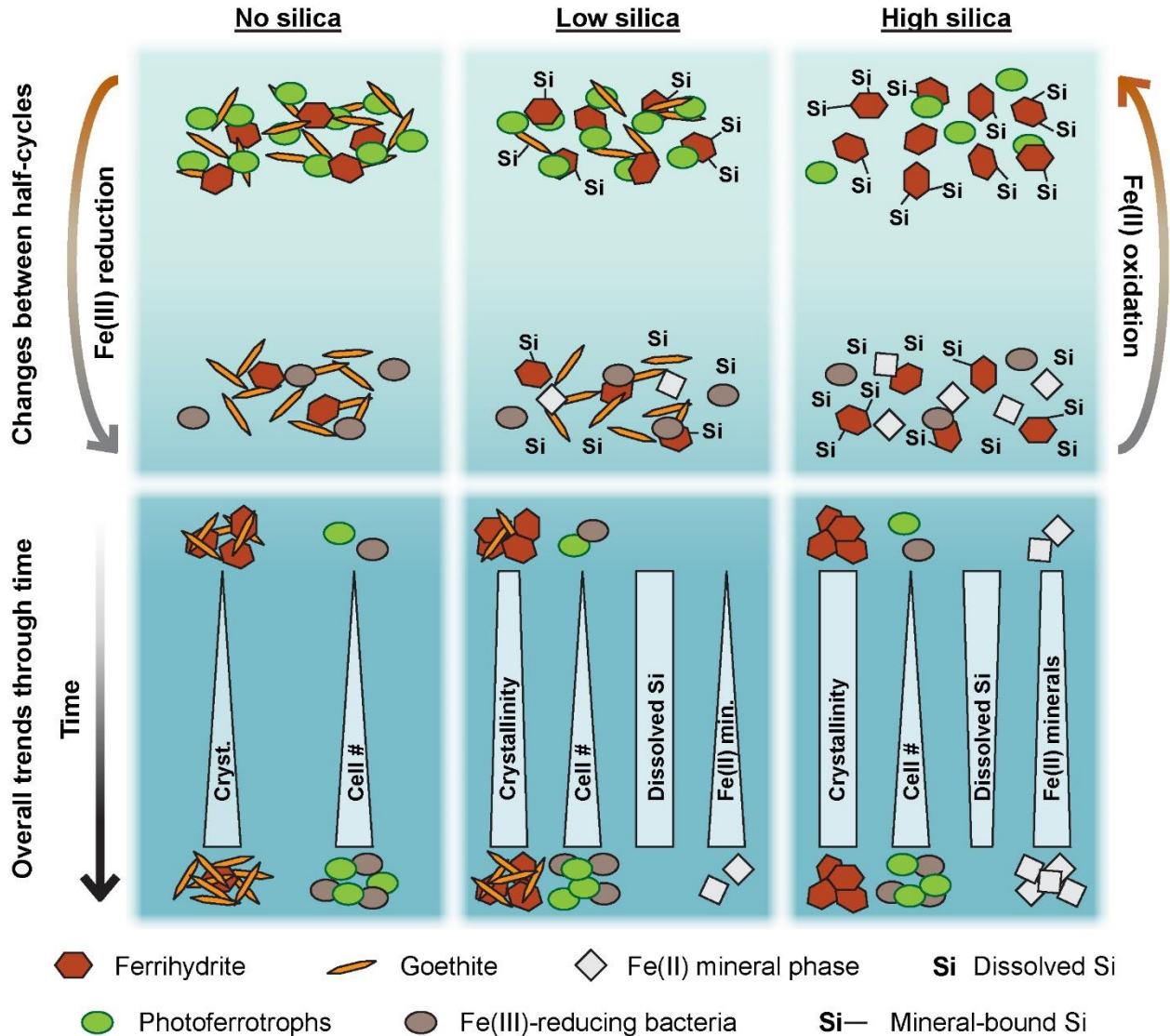


Fig. 4. Overview of the experimental results. Orange shaded areas mark oxidizing conditions, grey shaded areas reducing conditions. The number of individual symbols as well as their association with each other reflect the actual results. The extent of change in the width of the bars in the bottom row should be considered proportional to the changes of the parameters during the experiments.

### 3.2. Characterization of the cell-mineral aggregates (trans)formed during microbial Fe cycling

In order to determine the extent and type of cell-mineral associations during microbial Fe cycling as well as the size and morphology of cell-mineral-aggregates formed, we performed fluorescence as well as scanning electron microscopy on samples obtained at the end of each individual half cycle.

### 3.2.1. Cell-mineral associations – fluorescence and light microscopy

Generally, during oxidative half cycles, orange colored minerals were formed and fluorescence microscopy showed that there was a close association between cells and minerals (Fig. 5A-C, G-I, Fig. S2). At the end of the third oxidative half cycle the color of the minerals formed in the Si-free setup had changed from a bright orange (suggestive of a short-range ordered (SRO) Fe(III) mineral phase) to a dark yellow or ochre (suggestive of goethite, Fig. 5G, Schwertmann and Cornell, 2008). In contrast, the minerals formed during reductive half cycle were dark brown or black and less cells were associated with the Fe minerals and more free cells were present (Fig. 5D-F, J-L). Although the dark brown to black color of the minerals formed was indicative of the presence of mixed-valent Fe minerals such as magnetite, they were not magnetic, thus arguing against the presence of magnetite in our experiments (Fig. 5D-F, J-L, Fig. S2). Furthermore, based on the fluorescence microscopy conducted the overall cell densities appear to have increased over three consecutive microbial Fe cycles, resulting in both a higher number of mineral-associated and free cells during the last microbial Fe cycle (Fig. 4, Fig. 5G-L).

In addition to the number of Fe cycles, Si also seemed to influence the extent to which cells were associated with the Fe minerals. Overall, the low Si setup showed highest extent of cell-mineral associations throughout the experiment and the lowest number of free cells (Fig. 4, Fig. 5B, E, H, K, Fig. S2). In comparison, the extent of cell-mineral association in the Si-free setup seemed to be less visible despite the fact that there appeared to be a higher number of free cells during the last microbial Fe cycle (oxidative and reductive half cycle) (Fig. 5G and J). Finally, the high Si setup showed the lowest extent of cell-mineral associations over all three microbial Fe cycles (Fig. 5C, F, I, L, Fig. S2) and an initially intermediate number of free cells. The number of free cells, however, strongly increased over three consecutive microbial Fe cycles and was higher during reductive rather than during oxidative half cycles (e.g. Fig. 5I and L). Interestingly, the high Si setup seemed to form biofilm like structures after the second oxidative half cycle, which were initially attached to the mineral precipitates formed but were easily suspended upon shaking. These biofilms were either marked by a dense network of minerals (Fig. S2C) or close association/ accumulation of cells under the microscope (Fig. 5I).

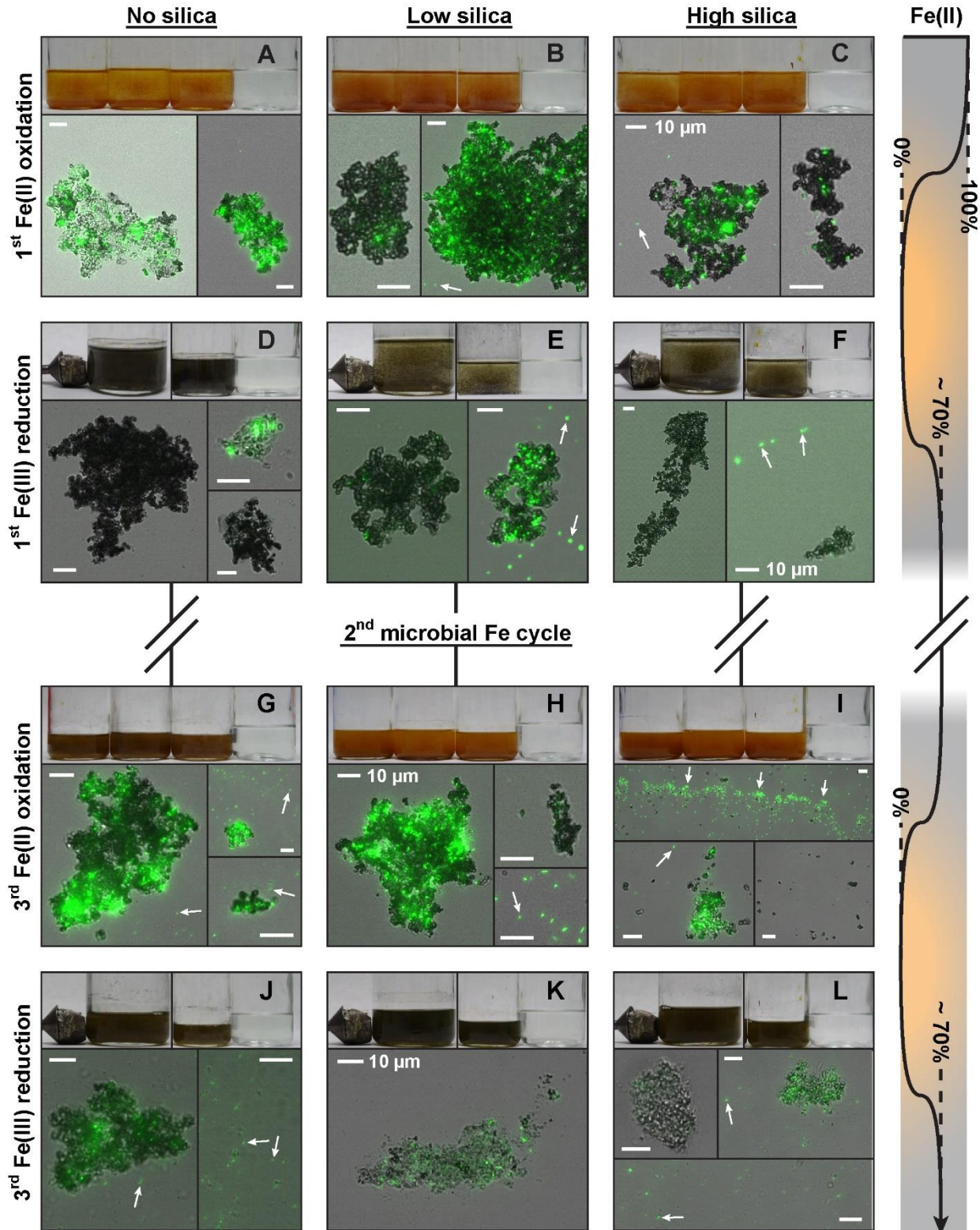


Fig. 5. Overlay of fluorescence and light microscopy images showing cells (green) and mineral particles (dark) over the course of three microbial Fe cycles. The different panels show oxidative half cycles (odd row numbers) and reducing half cycles (even numbers) for Si-free (first column), low Si (second column) and high Si (last column) setups. Orange colors mark oxidizing conditions, grey colors reducing conditions. The magnet in panels D, E, F, J, K and L was placed next to the bottles in order to test for the presence of magnetic minerals like magnetite. All scale bars are 10 μm.

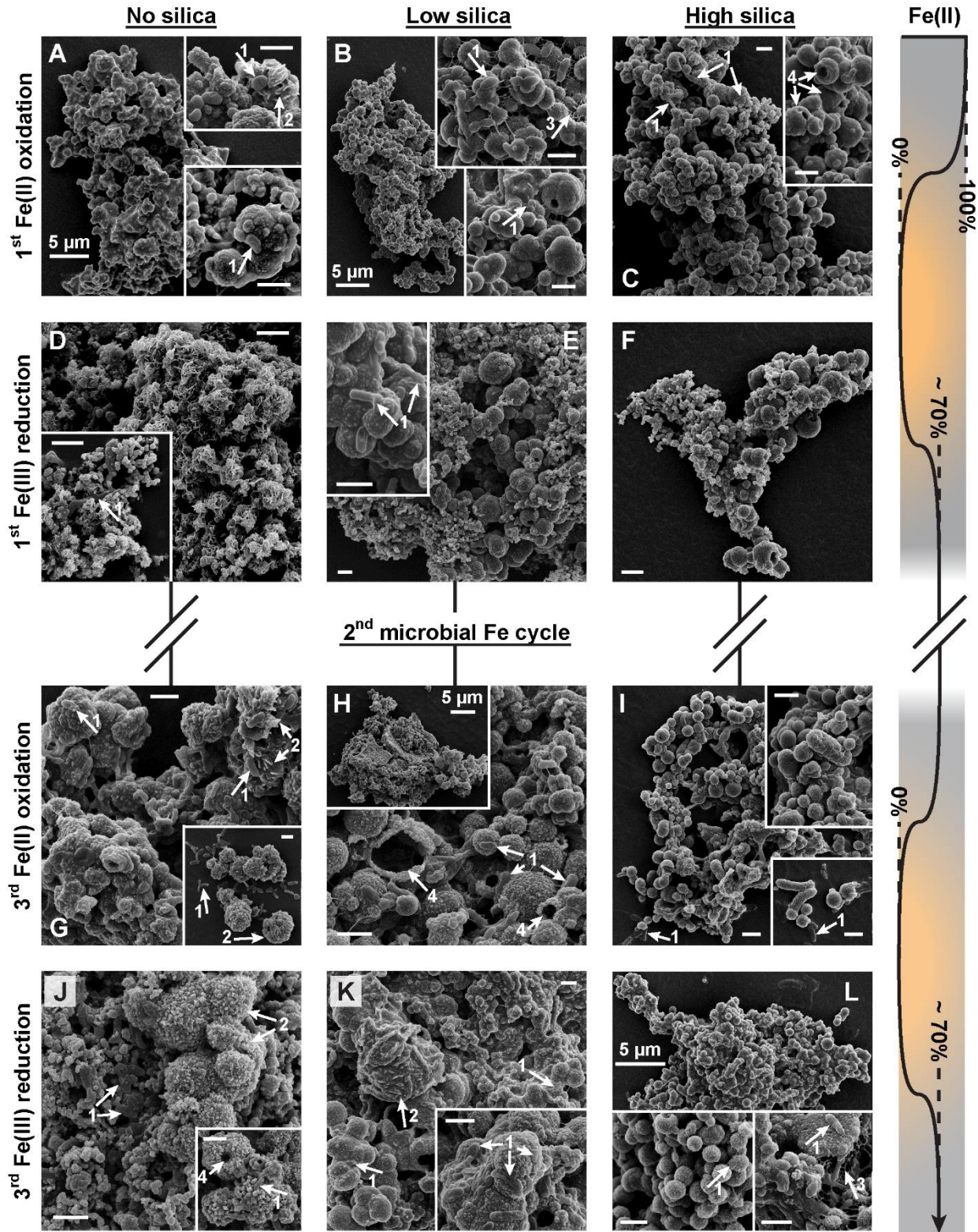
### 3.2.2. Morphology and size of cell-mineral aggregates – scanning electron microscopy (SEM)

#### 3.2.2.1. *Morphology of cell-mineral aggregates (trans)formed during repeated microbial Fe cycling*

SEM analysis confirmed the trends observed by fluorescence microscopy: There was generally a close association between cells and minerals during oxidative half cycles and comparatively few cells associated with the minerals during reductive half cycles (Fig. 6, Fig. S3). All cells found were free of encrustation. However, there appeared to be slight differences in cell morphology, with photoferrotrophs being smaller ( $\sim 1 \mu\text{m}$ ) and bean-shaped (e.g. Fig. 6A-C) whereas Fe(III)-reducers were longer ( $1.5\text{-}2 \mu\text{m}$ ) and rod-shaped (e.g. inset Fig. 6D, number 1, inset Fig. S3D, number 1). Furthermore, the number of cells associated with minerals seemed to be lowest in the high Si setup (Fig. 4, Fig. 6C, F, I, L, Fig. S3) and highest in the low Si setup (Fig. 6B, E, H, K, Fig. S3) and similar to the fluorescence microscopy cell numbers seemed to increase through time (Fig. 6, third Fe cycle, Fig. S3).

→ Fig. 6. SEM micrographs of cell-mineral aggregates formed during alternating oxidative and reductive half cycles. The different panels show oxidative half cycles (odd row numbers) and reducing half cycles (even numbers) for Si-free (first column), low Si (second column) and high Si (last column) setups. Orange colors mark oxidizing conditions, grey colors reducing conditions. Arrows labelled with number 1 indicate cells, arrows labelled with 2 higher crystalline parts of the cell-mineral aggregates, arrows labelled with number 3 remains of putative exopolysaccharides and arrows labelled with number 4 hollow mineral spheres. Unless stated otherwise all scale bars are  $1 \mu\text{m}$ .





The mineral morphology showed distinct differences depending on the Si concentration and number of microbial Fe cycles. The minerals initially formed during the first oxidative half cycle were either amorphous without clear structure (Fig. 6A) or had a needle- or platelet-like appearance (inset Fig. 6A, number 2). Additionally, especially in the Si-containing setups, the aggregates seemed to consist of spheres of various sizes with a smooth surface (approximately 0.5-2  $\mu\text{m}$  diameter; Fig. 6A-C), some of which appeared to be hollow (inset Fig. 6C, number 4) or attached to each other by fibrous structures, probably remainders of exopolysaccharides (top inset, Fig. 6B, number 3, Wu et al., 2014). During the following reductive half cycle the aggregates formed in the Si-free setup were dominated by needle- or platelet-shaped minerals, while the aggregates in the Si-containing setups retained their spherical structure (Fig. 6D-F). However, the spheres in the low Si setup seemed to have a rougher surface compared to the oxidative half cycle (Fig. 6E). Additionally, the spheres seemed to be separated into two size categories being either 0.5-2  $\mu\text{m}$  in size or smaller than 0.2  $\mu\text{m}$ . Over time there was a marked increase in the crystallinity of the aggregates formed in the no Si setup marked by an increasing amount of needle- or platelet-shaped minerals (Fig. 4, Fig. 6G, Fig. S3A and D) or cauliflower-like appearance of the spheres formed. In the low Si setup, minerals underwent a similar trend, with spheres equally showing increasing surface roughness (Fig. 4, Fig. 6H and K, Fig. S3B and E) and occasionally platelet-like structures (Fig. 6K, number 2). The minerals formed in the high Si setup did not undergo any changes over time and generally consisted of smooth spheres (Fig. 4, Fig. 6I and L, Fig. S3C and F). However, mineral aggregates consisting of hollow spheres, similar to the ones found for the first oxidative half cycle, were repeatedly observed in the Si-containing setups (Fig. 6H, Fig. S3C and E). Similarly, the previously described cobweb-like structures were also consistently found in the Si-containing setups (Fig. 6H, I and L, Fig. S3B and C), where they generally seemed to connect individual mineral spheres.

#### 3.2.2.2. *Size and sedimentation rate of primary cell-Fe(III) mineral aggregates*

In order to calculate the settling velocity of the cell-mineral aggregates formed during microbial Fe cycling and thus ultimately the time these aggregates would have required to settle on the seafloor, we measured the size of the primary cell-Fe(III) mineral aggregates (after the first oxidative half cycle). However, using a 2D technique (SEM) to determine the size of our cell-Fe(III) mineral aggregates likely biased our results by not considering the third dimension. The following results should thus be considered as conservative estimates.

The mean aggregate size for the Si-free aggregates was  $30.45 \pm 21.56 \mu\text{m}$  (median =  $25.97 \mu\text{m}$ ). The aggregates formed in the low Si and high Si setups were both significantly smaller (one-way ANOVA,  $F = 15.233$ ,  $df = 2, 329$ ,  $P < 0.001$ , Tamhane post-hoc test,  $\alpha = 0.05$ ) with  $17.90 \pm 16.40 \mu\text{m}$  (median =  $12.95 \mu\text{m}$ ) and  $16.01 \pm 12.72 \mu\text{m}$  (median =  $13.23 \mu\text{m}$ ), respectively. Based on these values we calculated the sedimentation rate by applying Stoke's law (equation 2),

$$v_p = \frac{2}{9} \times \frac{r^2 \times g \times (\rho_p - \rho_f)}{\mu} \quad (2),$$

where  $v_p$  [ $\text{m s}^{-1}$ ] is the terminal velocity,  $r$  [ $\text{m}$ ] is the radius of the particle,  $g$  [ $\text{m s}^{-2}$ ] is the gravitational force,  $\rho_p$  [ $\text{kg m}^{-3}$ ] the density of the particle,  $\rho_f$  [ $\text{kg m}^{-3}$ ] the density of the fluid and  $\mu$  [ $\text{kg m}^{-1} \text{s}^{-1}$ ] the dynamic viscosity of the fluid. While Stoke's law is best applied to spherical particles, we nonetheless used it as an approximation for our irregularly shaped cell-Fe(III) mineral aggregates. Particle densities were assigned based on previous work of Posth et al. (2010). Although the Si-free aggregates showed the highest organic carbon content (see supplementary text S1) and would thus be estimated to have the lowest density, we also considered the Si-co-precipitation during Fe(III) mineral formation. We, therefore, used a density of  $2.4 \text{ g cm}^{-3}$  for the Si-free aggregates, a density of  $2.2 \text{ g cm}^{-3}$  for the low Si aggregates and a density of  $2.0 \text{ g cm}^{-3}$  for the high Si aggregates. Calculated sedimentation rates were  $3.45 \pm 4.69 \text{ m h}^{-1}$  (median =  $1.67 \text{ m h}^{-1}$ ) for the Si-free,  $1.25 \pm 2.35 \text{ m h}^{-1}$  (median =  $0.35 \text{ m h}^{-1}$ ) for the low Si and  $0.73 \pm 1.51 \text{ m h}^{-1}$  (median =  $0.31 \text{ m h}^{-1}$ ) for the high Si cell-Fe(III) mineral aggregates.

### 3.3. Mineral (trans)formation during microbial Fe cycling

In order to determine which (Fe) minerals were formed during microbial Fe cycling and how differing Si concentrations may have influenced the identity of the minerals formed we analyzed solid samples taken at the end of every half cycle by  $^{57}\text{Fe}$  Moessbauer spectroscopy and XRD.

After the first oxidative half cycle three mineral phases were identified in the setup without Si: A narrow paramagnetic doublet with a isomer shift ( $\delta$ ) of  $0.45 \text{ mm s}^{-1}$  and quadrupole splitting ( $\Delta E_Q$ ) of  $0.70 \text{ mm s}^{-1}$  suggested the presence of a short-range ordered (SRO) Fe(III) (oxyhydr)oxide, which accounted for 13.9% of the spectral area. This doublet could either represent a single mineral entity such as ferrihydrite (Eickhoff et al., 2014; Murad and Schwertmann, 1980) or a complex mixture consisting of a continuum of ferrihydrite, akageneite

and/ or lepidocrocite (Laufer et al., 2017). The magnetically ordered component of the Moessbauer spectrum was dominated by goethite (47.4% of the spectral area) and was identified by hyperfine parameters ( $\delta = 0.50 \text{ mm s}^{-1}$ , quadrupole shift ( $\epsilon$ ) = -0.13 and hyperfine field ( $B_{\text{hf}}$ ) = 46.6 T, (Pantke et al., 2012). However, in order to obtain an optimal fit, a second magnetically ordered component in the form of collapsed sextet (poorly ordered magnetic component), suggestive of a highly structurally distorted, poorly crystalline mineral phase (Chen and Thompson, 2018; Eusterhues et al., 2008), was required (Fig. 7A and B). The presence of goethite was confirmed by XRD, but no other crystalline mineral phases were detected. In contrast, the Moessbauer spectra of the low Si and high Si setups both consisted of a single narrow paramagnetic doublet with hyperfine parameters suggestive of ferrihydrite (Fig. 7E and H, supplementary text S3, Eickhoff et al., 2014; Gauger et al., 2016; Murad and Schwertmann, 1980). The higher quadrupole splitting of  $0.84 \text{ mm s}^{-1}$  and  $0.86 \text{ mm s}^{-1}$  for the low Si and high Si setup, respectively, compared to the Si-free setup are suggestive decreased crystallinity (Murad, 1996; Murad et al., 1988). This is probably due to inhibited particles growth and increased structural strain/ disorder in the ferrihydrite particles due to co-precipitated silica (Cismasu et al., 2014; Cismasu et al., 2011; Eickhoff et al., 2014). No crystalline Fe mineral phases were detected by XRD (Fig. 7F and I).



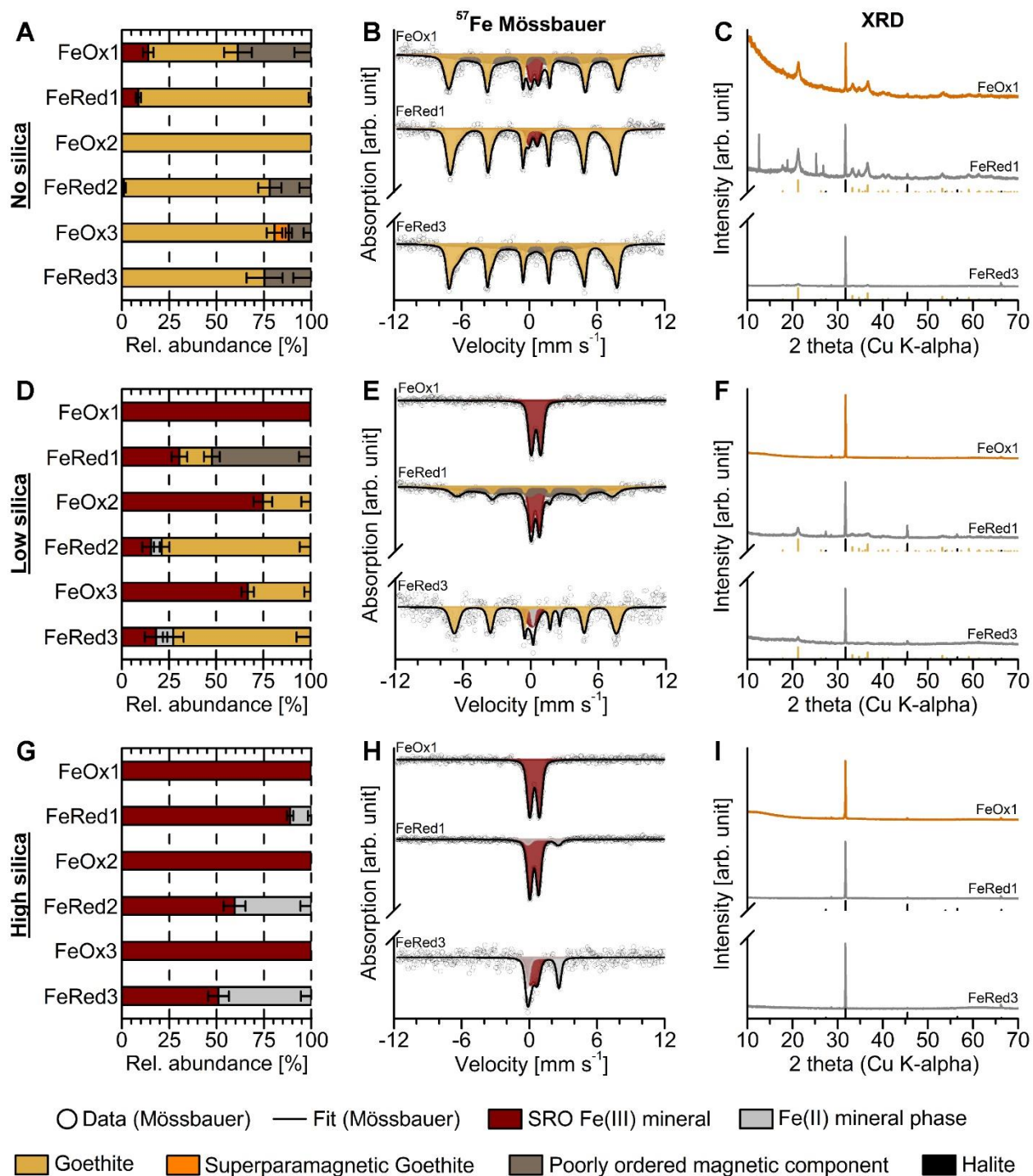


Fig. 7. Relative Fe mineral abundance (based on  $^{57}\text{Fe}$  Moessbauer analysis),  $^{57}\text{Fe}$  Moessbauer spectra and X-ray diffractograms of mineral products taken at the end of the oxidative and reductive half cycles. Panels A-C show selected results of the no Si setup, D-F results of the low Si setup and G-I results of the high Si setup. Error bars in the relative mineral abundances are based on the error of the relative abundance in the Moessbauer fit. Orange colors in the X-ray diffractograms mark mineral products of oxidative half cycles. Grey colors mark mineral products of the reductive half cycles.

After the first reductive half cycle, the mineralogy in the Si-free setup was dominated by goethite (91.3%, magnetically ordered sextet, Fig. 7B, supplementary text S3, Dippon et al.,

2015). A second mineral phase, whose narrow paramagnetic doublet is suggestive of a SRO Fe(III) mineral like ferrihydrite (Fig. 7B, supplementary text S3, Dippon et al., 2015; Shimizu et al., 2013), which accounted for 8.7% of the spectral area. The formation of goethite was independently confirmed by XRD analysis (Fig. 7D). In addition to goethite XRD analysis suggests the presence of a second, unknown, Fe mineral phase, potentially a variety of green rust. The low Si setup was dominated by a poorly ordered magnetic component (>50%), which, based on its hyperfine parameters, was likely a structurally distorted, nano-sized Fe(III) mineral phase that had not undergone complete magnetic ordering (Fig. 7D and E, supplementary text S3, Chen and Thompson, 2018; Eusterhues et al., 2008). However, due to the generally poor signal-to-noise ratio of the Moessbauer spectra, likely due to a high amount of co-precipitated organics, the interpretation remained inconclusive. Additionally, microbial Fe(III) reduction resulted in the formation of some goethite (17.2%, clearly defined sextet, Fig. 7D and E, supplementary text S3) and a SRO Fe(III) mineral phase, likely ferrihydrite (narrow paramagnetic doublet, Fig. 7D and E, supplementary text S3, Dippon et al., 2015; Shimizu et al., 2013). The presence of goethite was confirmed by XRD, but no other crystalline Fe mineral phases were detected (Fig. 7F). In the high Si setup, no formation of any crystalline mineral phases was observed. The Moessbauer spectrum consisted of two paramagnetic doublets. The narrow paramagnetic doublet suggested the presence of a SRO Fe(III) mineral phase, e.g. ferrihydrite, while the wide paramagnetic doublet, which accounted for approximately 10% of the spectral area, and had hyperfine parameters ( $\delta = 1.23 \text{ mm s}^{-1}$  and  $\Delta E_Q = 2.70 \text{ mm s}^{-1}$ ) suggestive of a Fe(II) mineral phase (Fig. 7G and H, Murad, 2010). Specifically, the Moessbauer hyperfine parameters are suggestive of a phyllosilicate (Pollak and Stevens, 1986), which potentially formed through the reaction of  $\text{Fe}^{2+}$  and Si present in our growth medium. Alternatively, the presence of high concentrations of both  $\text{Fe}^{2+}$  and bicarbonate (sourced from the primary buffer), could also have facilitated the formation of siderite. An added difficulty which precluded the clear identification of the Fe(II) mineral was the high NaCl content of our samples: For example the main identifiable siderite reflection ([1 0 4]; d-spacing  $2.798 \text{ \AA}$ ,  $32^\circ 2\theta$ ) is directly next to the often very large halite reflection ([0 0 2]; d-spacing  $2.825 \text{ \AA}$ ,  $31.7^\circ 2\theta$ ). The unambiguous identification/confirmation of the Fe(II) mineral phase by XRD was therefore not possible. However, independent of the exact nature of the Fe(II) mineral, based on the absence of identifiable reflections in the X-ray diffractogram the mineral was likely poorly crystalline.

Moessbauer and XRD analysis support the results of our SEM analysis: Both increasing number of microbial Fe redox cycles and Si concentration seemed to have influenced the mineral crystallinity (Fig. 4). Following the first microbial Fe cycle, Moessbauer spectra of the Si-free setup were generally fully magnetically ordered (sextets) and the mineralogy dominated by goethite, which was independently confirmed by XRD (supplementary text S3, Fig. 7A-C, Fig. S4A and B). The mean magnetic hyperfine field parameter of the goethite (trans)formed during both oxidizing and reducing half cycles increased with an increasing number of microbial Fe cycles (Fig. S5B and D), suggesting that the goethite underwent increasing structural (magnetic) ordering over time. However, in order to achieve an optimal fit the sextet describing goethite in the Moessbauer spectra required an additional component with a mean hyperfine field value which was lower than for the first component. This indicates that although structural (magnetic) ordering generally increased, mineral growth/ structural ordering was partially constricted, probably by co-precipitated organics. The amount of goethite was higher during the oxidative half cycles (80-100%) than during the reductive half cycles (~75%). The remaining up to 25% consisted of the previously described poorly ordered magnetic component of putative nano-crystalline nature (Fig. 7A).

In contrast to the setup without Si the Moessbauer spectra of the low Si setup generally consisted of a mixture of paramagnetic doublets (SRO Fe(III) and Fe(II) minerals) and a magnetically ordered sextet (goethite), with the latter becoming more abundant over time. Over the course of three consecutive microbial Fe cycles the amount of goethite formed increased (Fig. 7D-E, Fig. S4C and D) and was higher during reductive compared to oxidative half cycles. During oxidative half cycles the amount of goethite formed ranged from 25.2% to 33.3%. During the reductive half cycles it increased from initially 17.2% to 72.8% at the end of the third reductive half cycle. The higher amount of goethite present during the reductive half cycles suggests that the SRO Fe(III) mineral phase was preferentially reduced during microbial Fe(III) reduction. In addition to goethite, a Fe(II) mineral phase was formed during microbial Fe(III) reduction in increasing quantities (5.7% during the second, 9.1% during the third reductive half cycle; Fig. 7D and E, Fig. S4C). As before, a clear identification of the Fe(II) mineral phase was not possible, making both the formation of siderite and a Fe(II)-silicate equally possible. A decrease in the quadrupole splitting value and an increase in the mean magnetic hyperfine field parameter suggest increased structural ordering of both the SRO Fe(III) mineral phase and

goethite over time, respectively (Fig. S5). However, the mean magnetic hyperfine field value of the goethite formed in the presence of Si was lower than for the goethite formed in the absence of Si (Fig. S5B and D), thus suggesting lower structural ordering of the former.

Finally, the high Si setup showed no changes in mineral crystallinity and the mineral product of both oxidative and reductive half cycles remained X-ray amorphous (Fig. 7I, Fig. S4F). The Fe(III) mineral phase consisted entirely of SRO Fe(III) minerals, while a clear identification of the Fe(II) mineral phase was not possible (either siderite and/or an Fe(II) silicate; Fig. 7G and H, Fig. S4E). The amount of Fe(II) minerals increased over time from 11.2% at the end of the first reductive half cycle to 49.0% at the end of the third reductive half cycle (Fig. 4, Fig. 7G). Although the mineral products remained X-ray amorphous a decrease in the isomer shift and quadrupole splitting values of the SRO Fe(III) minerals suggests that they had undergone some degree of structural ordering/ increase in crystallinity (Murad, 1996; Murad et al., 1988) over time (Fig. S5A and C).

## 4. DISCUSSION

### 4.1. Interaction of photoferrotrophs and Fe(III) reducers during microbial Fe cycling

Photoferrotrophy has been implicated as a major mechanism having driven the deposition of the Neoproterozoic to early Paleoproterozoic BIFs. Similarly, microbial Fe(III) reduction has been considered as an important mechanism in the post-depositional alteration of primary BIF sediments (see e.g. Konhauser et al., 2017 for review). However, their individual importance would also have been determined by their ability to thrive under the environmental conditions given and their interactions with other microbial players present during the deposition of BIFs. One of the major questions driving our study was therefore how photoferrotrophs and Fe(III)-reducing bacteria would have interacted during microbial Fe cycling in an early ocean? Before speculating on the extent and manner of the interaction between photoferrotrophs and Fe(III)-reducing bacteria, it seems appropriate to first probe the individual performance under simulate Precambrian ocean conditions.

#### 4.1.1. Influence of microbial Fe cycling on Fe(II) oxidation by *Chlorobium* sp. N1 – the role of fatty acids and Si

During oxidative half cycles we observed two major particularities. (1) A concurrent decrease of dissolved Fe(II) and fatty acids either formed during (formate/ acetate) or remaining after (lactate) microbial Fe(III) reduction (Fig. 2) and (2) differences in the development of maximum Fe(II) oxidation rates depending on the Si concentration (Fig. 3).

Photoferrotrophs are known for their metabolic flexibility and their growth on organic substrates such as acetate and lactate (as well as formate) has previously been reported (e.g. Ehrenreich and Widdel, 1994; Heising et al., 1999; Laufer et al., 2017; Straub et al., 1999). Furthermore, previous studies have shown that the cultivation of photoferrotrophs on co-substrates (Fe(II) + organic acid or H<sub>2</sub>) may result in higher cell numbers compared to Fe(II) only (e.g. Heising et al., 1999; Melton et al., 2014). While the use of acetate has not been reported for *Chlorobium* sp. strain N1, the fast consumption of lactate upon restoring light condition suggests that it used lactate along with Fe(II) as electron donor (Laufer et al., 2017), leading to the higher cell numbers we deduced from fluorescent and electron micrographs (Fig. 5 and 6). Yet, we cannot rule out that it may also have used acetate, which seems feasible given the genetic potential within the family of Chlorobiaceae (Imhoff, 2014). Alternatively, Laufer et al. (2017) showed that *Chlorobium* sp. strain N1 can be grown on more complex substrates such as yeast extract, while genome sequencing conducted by Bryce et al. (2019) found the potential for several fermentation pathways in *Chlorobium* sp. strain N1. Collectively these results suggest that *Chlorobium* sp. strain N1 may have used more complex organics formed during the microbial Fe cycling in our experiments, thus explaining the increase in cell numbers we found over the course of multiple Fe cycles.

Given this overall increase in cell numbers and comparable consumption of fatty acids in all three setups, we would also have expected a uniform development in the maximum Fe(II) oxidation rates. Instead, comparable to previous studies (e.g. Gauger et al., 2016; Wu et al., 2017) increasing Si concentrations resulted in increasing maximum Fe(II) oxidation rates. In general, the maximum Fe(II) oxidation rates we observed in our study (between  $0.46 \pm 0.02$  mM d<sup>-1</sup> and  $1.22 \pm 0.04$  mM d<sup>-1</sup>) were within the range of published Fe(II) oxidation rates for photoferrotrophs (0.1-4.5 mM d<sup>-1</sup>; Gauger et al., 2016; Hegler et al., 2008; Jiao et al., 2005;

Kappler and Newman, 2004; Laufer et al., 2017; Peng et al., 2019a; Straub et al., 1999; Wu et al., 2014) and within the metabolic capability of our strain used (max. rate 0.77 mM Fe(II) d<sup>-1</sup>; Laufer et al., 2017). One potential explanation for the increased Fe(II) oxidation rates at high Si concentrations could be the Fe(II)-mitigating effect that has been ascribed to Si previously (Gauger et al., 2016). We further observed a tight coupling between Fe(II) oxidation and a decrease in dissolved Si, suggesting the adsorption and/or co-precipitation during Fe(II) oxidation, similar to naturally occurring Fe(III) minerals (e.g. Cismasu et al., 2011; Parfitt et al., 1992; Schwertmann and Fechter, 1982). The resulting changes in point of zero charge (PZC; Schwertmann and Fechter, 1982) or occupation of surface functional groups could prevent the co-precipitation with or adsorption of trace elements and nutrients onto Fe(III) (oxyhydr)oxides. Various trace elements, nutrients and heavy metals have been shown to have a high affinity to be adsorbed to Fe(III) (oxyhydr)oxides (Das et al., 2013; Eickhoff et al., 2014; Gustafsson, 2003; Konhauser et al., 2007; Lack et al., 2002; Rout et al., 2012) and could thus become biolimiting in the absence of Si, therefore limiting microbial activity over time.

Other studies have found a high affinity of trace elements biofilms, exopolysaccharides (EPS) or organic-mineral composites (e.g. Ferris et al., 1989; Hao et al., 2016; Moon and Peacock, 2012; Zhu et al., 2010), structures we observed in the presence of low concentrations of Si to a limited extent but especially at high Si concentrations. High concentrations of Si and formation of EPS could thus act synergistically to provide consistent access to the nutrients and trace elements required by the photoferrotrophs.

#### *4.1.2. Influence of microbial Fe cycling on Fe(III) reduction by a marine Fe(III)-reducing enrichment culture – the effect of Si and electron shuttling*

The opposite site of the microbial Fe cycling during our experiments showed a similar complexity with a variety of factors such as media composition, mineralogy, electron shuttles, reduction rates and oxyanions showing a strong interdependence (a more complete compilation of factors influencing microbial Fe(III) reduction is provided in the work of O’Loughlin et al., 2019 and Dong et al., 2020). This makes it difficult to directly compare our results to previous studies and we will thus focus on explaining microbial Fe(III) reduction within the framework of microbial Fe cycling in our study.

During our microbial Fe cycling experiments the stoichiometry of microbial Fe(III) reduction consistently deviated from the expected 4:1 ratio of Fe(III) reduced to lactate oxidized and ranged from  $3.56 \pm 0.14$  to  $2.74 \pm 0.11$ , values comparable to experimental values obtained by e.g. Roden and Zachara (1996). We attribute this deviation to the incorporation of C into cell biomass, as suggested by the general increase in cell numbers observed over the course of our experiments (Fig. 5 and 6, Fig. S2 and S3).

These increasing cell numbers are also reflected in the linear increase of maximum Fe(III) reduction rates over the course of the experiment in the Si-free and low Si setups (Fig. 3). Slightly higher maximum Fe(III) reduction rates in the low Si setup compared to the Si-free setup can be explained by the lower mineral crystallinity in the low Si compared to the setup without Si (Fig. 7). SRO Fe(III) mineral phases have been shown to be more readily accessible by Fe(III)-reducing bacteria compared to higher crystalline Fe(III) minerals such as goethite (Bonneville et al., 2009; Postma, 1993; Roden, 2003; Roden and Zachara, 1996). An exception is the first reductive half cycle of the high Si setup. Even though the initial crystallinity was the lowest (no goethite formed), which should theoretically have resulted in the highest reactivity towards microbial Fe(III) reduction (Bonneville et al., 2009; Jones et al., 2009; Kraal et al., 2019; Postma, 1993; Roden, 2003; Roden and Zachara, 1996), it initially had the lowest maximum Fe(III) reduction rate.

Paradoxically, the incorporation of Si, which should have resulted in an increased reactivity towards reductive dissolution by microbial Fe(III) reduction, might actually have initially restricted microbial Fe(III) reduction in the high Si setup during. It has been suggested that at high Si concentrations Si-ferrihydrite composites display increased stability against reductive dissolution and transformation, thus limiting bioavailability (Cismasu et al., 2014). This is probably due to a reduced availability reactive surface sites caused by Si adsorption, resulting in lower maximum Fe(III) reduction rates (Roden, 2003). Furthermore, it has also been shown that  $\text{Fe}^{2+}$  adsorbed to mineral surfaces can retard or even inhibit microbial Fe(III) reduction in the absence of chelating or electron shuttling moieties (Roden and Urrutia, 2002; Roden and Zachara, 1996). Other studies have suggested that Si, similar to adsorbed Fe(II), is mostly present as a surface layer when associated with ferrihydrite (Dyer et al., 2010; Dyer et al., 2012; Swedlund and Webster, 1999). Therefore, Si, when present at high concentrations, may have a comparable

surface passivating effect, thus explaining the lower maximum Fe(III) reduction rate during the first reductive half cycle.

Interestingly, the high Si setup showed the most pronounced increase in maximum Fe(III) reduction rates over the course of the experiment, deviating clearly from the other two setups (Fig. 3). One potential explanation for this diverging trend is the development of EPS or biofilm like structures in response to poor accessibility of Fe(III) during the first reductive half cycle (Fig. 5 and 6). This is reflected by a sharp decrease in the Fe(III) reduction stoichiometry compared to the other two setups, from  $3.56 \pm 0.14$  during the first reductive half cycle to  $2.95 \pm 0.27$  during the third reductive half cycle, suggesting that a considerable amount of C was invested in the synthesis of biomolecules. Kotloski and Gralnick (2013) showed that *S. oneidensis* MR-1 is able to produce flavins to facilitate extracellular electron shuttling, which could help overcoming accessing Si-containing Fe(III) minerals as terminal electron acceptor. Studies have further shown that elevated C/Fe ratios lead to higher Fe(III) reduction by *Shewanella* species by facilitating more efficient electron shuttling (e.g. Cooper et al., 2017; Poggenburg et al., 2016; Poggenburg et al., 2018; Shimizu et al., 2013). An aided effect of the higher abundance of organics could be the complexation of substantial amounts of Fe(II) which would result in enhanced microbial Fe(III) reduction (e.g. Kügler et al., 2019; Royer et al., 2002; Urrutia et al., 1998).

#### *4.1.3. Mutual benefit of photoferrotrophy and microbial Fe(III) reduction – stimulation of growth and metabolic activity*

The co-cultivation of photoferrotrophs and Fe(III)-reducing bacteria, especially in the presence of Si, resulted in a highly dynamic microbial Fe cycle. In addition to the previously discussed factors, the simultaneous presence of both types of bacteria resulted in the mutual stimulation of both growth and activity.

The most obvious mutual benefit is the use of the respective metabolic products of the cycling partner. The metabolic activity of the photoferrotroph resulted in the formation of Fe(III) minerals and  $C_{org}$ , which in turn were used by the Fe(III)-reducing bacterium. Conversely, the metabolic activity of Fe(III)-reducing bacteria resulted in the release of Fe(II) and lower molecular weight organic compounds such as acetate, which were both used by the photoferrotroph. The resulting concurrent activity of photoferrotrophs and Fe(III)-reducing



---

bacteria potentially resulted in a “cryptic” Fe cycle (Berg et al., 2016; Peng et al., 2019b) during oxidative half cycles, thus explaining depressed or stagnant maximum Fe(II) oxidation rates following the first oxidative half cycle.

However, the benefits of this microbial Fe cycle may stretch beyond a mutual supply of growth substrates (Cooper et al., 2020). While the use of co-substrates might certainly be beneficial to the individual metabolism by stimulating growth, the constant consumption of the metabolic products by the Fe cycling partner would certainly also have prevented product inhibition. Furthermore, the excretion of metabolites by photoferrotrophs and Fe(III)-reducing bacteria might also have triggered a mutualistic metabolic response, thus stimulating the growth and activity of each partner (Cooper et al., 2020). This is especially evident when microbial Fe cycling is taking place in the presence of high concentrations of Si, where the development of the maximum Fe(II) oxidation and Fe(III) reduction rates deviates from the linearity the other setups show. The poor accessibility of Si-containing ferrihydrite during the first reductive half cycle might have prompted a combined metabolic response by photoferrotrophs and Fe(III) reducers, leading to increased secretion of EPS and electron shuttling moieties such as flavins. The resulting capture of the metabolic products as well as nutrients and trace elements in these organic structures would have resulted in them being readily accessible, thus accelerating microbial Fe cycling.

An additional factor which might have influenced the dynamics of the microbial Fe cycling (on the long run) is the frequency of Fe cycling and the resulting constant supply of substrates. Interestingly, the dynamicity of the Fe cycling might thus have been self-reinforcing: We observed that over time the length of the half cycles in our experiments became shorter and the maximum rates with which Fe was metabolized increased (Fig. 2 and 3), especially in the presence of Si. Barcellos et al. (2018) suggested that higher maximum Fe(III) reduction rates in high periodicity Fe cycles might be related to microbes maintaining their activity due to frequent pulses of reactive substrate. Furthermore, the frequent cycling of the Fe minerals would also have prevented sustained crystal growth. Our combined mineralogical and SEM analyses suggest that even when goethite was formed, its particle growth was constricted and it likely was of low crystallinity (see further discussion below). The overall low crystallinity of goethite and the dominance of SRO Fe(III) (oxyhydr)oxides in the presence of Si likely resulted in increased bioavailability, therefore sustaining highly dynamic microbial Fe cycling. Based on our

integrated results we thus conclude that microbial Fe cycling in the water column of an Archean to early Paleoproterozoic ocean would have been highly dynamic.

#### **4.2. Changes in composition of cell-mineral aggregates during microbial Fe cycling – Fe-organic-Si dynamics**

The high dynamicity of the microbial Fe cycling also had a profound influence on the composition and transformation of the cell-mineral aggregates and related changes in mineral crystallinity, mineral-C<sub>org</sub> and mineral-Si associations. During our experiments we observed tightly coupled Fe mineral formation and C<sub>org</sub> dynamics, where microbial biomass was co-precipitated with Fe(III) (oxyhydr)oxides during Fe(II) oxidation and released from Fe minerals during Fe(III) mineral reduction. The same trend was observed for the association of Si with Fe minerals. The main factor determining Fe mineral crystallinity was the Si concentration. Si either retarded (low Si concentration) or completely inhibited the formation of crystalline mineral phases (high Si concentration) over several alternating oxidative and reductive half cycles.

##### *4.2.1. Influence of microbial Fe cycling on C<sub>org</sub>-Fe mineral association*

The oxidation of Fe(II) by *Chlorobium* sp. strain N1 resulted in the formation of cell-Fe(III) aggregates, structures that have already been found to be formed by photoferrotrophs in previous studies (Gauger et al., 2016; Hegler et al., 2008; Jiao et al., 2005; Kappler and Newman, 2004; Laufer et al., 2017; Posth et al., 2010; Schaedler et al., 2009; Wu et al., 2014). However, the extent of cell-mineral association depended on the Si concentration: In the absence of Si or at low Si concentrations cells and Fe(III) (oxyhydr)oxides were closely associated with each other. By contrast, at high Si concentrations there were only few cells associated with the Fe(III) mineral precipitates (compare also Schad et al., 2019). Additionally, we observed the formation of organic structures suggestive of EPS in the Si containing setups. The formation of EPS has been observed in previous studies on photoferrotrophs and has been suggested to prevent cell encrustation by Fe(III) minerals (Hao et al., 2016; Martinez et al., 2016; Schaedler et al., 2009; Wu et al., 2014).

Microbial Fe(III) reduction resulted in a release of C<sub>org</sub> from cell-Fe(III) mineral aggregates. Although we did not specifically determine dissolved organic carbon (DOC) concentrations, the mineral aggregates remaining after microbial Fe(III) reduction showed a much lower number of associated cells compared to Fe(II) oxidation. The release of C<sub>org</sub> during

microbial Fe(III) reduction can either be explained by a decrease in available mineral surface area or the breaking of bonds between the mineral surface and organics (Pan et al., 2016). Previous studies reported an increase in DOC of between approximately 13% (Pan et al., 2016) and close to 55% (Adhikari et al., 2017) upon microbial reduction of co-precipitates consisting of ferrihydrite and different organic compounds depending on the C/Fe ratio. Adhikari et al. (2017) further observed a depletion in aromatic or carboxylic moieties in the desorbed organic compounds, suggesting their preferential association with Fe minerals. This may explain contrasting results of a study by Mejia et al. (2018) who observed no release  $C_{org}$  from co-precipitates of highly aromatic humic acid (HA) and ferrihydrite. The effect of  $C_{org}$  on microbial Fe(III) reduction and the extent to which it is released from Fe(III) minerals during microbial reduction thus appears to be related to its chemical composition. In this regard a further characterization of the  $C_{org}$  formed during our Fe cycling experiments would have helped to better understand the processes influencing its re-/ immobilization.

#### 4.2.2. *Competitive sorption of $C_{org}$ and Si onto Fe(III) minerals during microbial Fe cycling*

Si displayed large fluctuations in its aqueous concentrations during microbial Fe cycling, marked by decreasing concentrations during Fe(II) oxidation and increasing concentrations during microbial Fe(III) reduction. Si has a high affinity for Fe(III) minerals (e.g. Sigg and Stumm, 1981; Swedlund and Webster, 1999), thus explaining the decreasing concentrations during Fe(II) oxidation. Similar to  $C_{org}$  the release of Si back into solution during microbial Fe(III) reduction can be explained by the decrease in available reactive surface sites, leading to the destruction of surface complexes between Fe(III) minerals and monosilicic acid (e.g. Cismasu et al., 2014; Pokrovski et al., 2003; Wang et al., 2018).

Although the overall behavior of Si during microbial Fe cycling was similar in the low Si and high Si setups, they showed an important difference: The high Si setup showed a higher overall extent of Si removal ( $52.17 \pm 4.40\%$ ) over three microbial Fe cycles compared to the low Si setup ( $13.99 \pm 2.18\%$ ), despite the release of Si back into solution during the reductive half cycles. In a previous study we showed, that the co-precipitation of  $C_{org}$  in cell-Fe(III) mineral aggregates likely reduces the extent of Si co-precipitation with Fe(III) minerals (Schad et al., 2019). The higher amount of co-precipitated  $C_{org}$  (cells, probably EPS) in the low Si setup should, therefore, offer a straight-forward explanation for the lower overall Si co-precipitation. However,

compared with our previous study the adsorption of  $C_{org}$  and Si onto Fe(III) (oxyhydr)oxides showed differences depending on the Si concentration. At low concentrations of Si  $C_{org}$  had a competitive advantage over Si, resulting in lower Si sorption, while at high concentrations of Si the opposite was the case. These results are in line with a previous study by Davis et al. (2001), which showed that the exposure of ferrihydrite to increasing concentrations of Si resulted in decreasing amounts of fulvic acid being adsorbed onto ferrihydrite thereafter. Further insight into the competition between  $C_{org}$  and Si for Fe(III) mineral reactive surface sites is provided by a study of Dyer et al. (2012). They proposed that at higher Si concentrations the sorption of Si onto Fe(III) mineral particles will take place earlier during Fe(III) mineral particle formation than at lower Si concentrations. Applied to our study, this means that in the low Si setup Si sorption would have taken place later, thus allowing  $C_{org}$  to bind to the Fe(III) minerals. In the high Si setup on the other hand, the Si would have directly been adsorbed to the freshly formed Fe(III) minerals, thus forming a Si surface layer (Dyer et al., 2010; Dyer et al., 2012), which prevented the adsorption of  $C_{org}$ .

The difference in the extent of Si removal between the low Si and high Si setup can thus be explained by a concentration-dependent competition for sorption sites between Si and  $C_{org}$ : at low Si concentrations  $C_{org}$  is preferentially adsorbed, thus preventing Si sorption. The reverse applies to high Si concentrations, resulting in a higher extent of Si removal from solution. An additional explanation for the higher extent of Si removal in the high Si setup is the potential for Si polymerization. Fe(III) (oxyhydr)oxides can act as catalysts for Si polymerization (Swedlund et al., 2010; Swedlund and Webster, 1999). Once a critical surface saturation is achieved first oligomers and later polymers are formed (Swedlund et al., 2010; Wang et al., 2018), which are not detectable by the spectrophotometric assay employed in our study.

#### *4.2.3. Combined influence of $C_{org}$ , Si and microbial Fe cycling on Fe mineral crystallinity*

In our study we found a close association of  $C_{org}$  and Si with Fe(III) minerals during microbial Fe cycling (see preceding discussion). Both are known to retard or even inhibit Fe(II)-induced secondary mineral transformation and the formation of more crystalline Fe(III) minerals either by blocking reactive surface sites or by complexing Fe(II) (e.g. Jones et al., 2009; Schwertmann et al., 2004; ThomasArrigo et al., 2017; Zhou et al., 2018). For  $C_{org}$  it was further shown that both the inhibitory effect and the mineral transformation pathway depended on the

type of  $C_{org}$  co-precipitated with the Fe(III) mineral (e.g. ThomasArrigo et al., 2018; Zhou et al., 2018) as well as on the C/Fe ratio (e.g. Chen et al., 2015; ThomasArrigo et al., 2018). In our study experiments conducted in the absence of Si still showed the formation of goethite, suggesting that the C/Fe ratio of the cell-Fe(III) mineral aggregates formed by our photoferrotroph was too low to completely inhibit mineral transformation. Instead, some surface functional groups were still available for Fe(II)-mineral interactions and only due to the cumulative effect of  $C_{org}$  and Si we observed a decrease in the crystallinity of the Fe(III) minerals formed at increasing Si concentrations.

Depending on the Si concentration the mineralogy of the different setups (no Si, low Si, high Si) further showed differing trends in their crystallinity over 3 consecutive microbial Fe cycles. The Si-free and low Si setups, in line with previous work (e.g. Thompson et al., 2006; Tomaszewski et al., 2016), both showed an increase in mineral crystallinity with increasing numbers of Fe cycles, where the low Si setup retained a lower crystalline mineralogy than the setup without Si (Fig. 6). The increase in mineral crystallinity over several microbial Fe cycles can be explained the preferential use of poorly crystalline minerals by Fe(III)-reducing microbes (e.g. Bonneville et al., 2009; Bonneville et al., 2004; Roden, 2003; Roden and Zachara, 1996). This process might have been further enhanced by pre-existing Fe(III) minerals acting as nucleation seeds for the formation of crystalline Fe(III) minerals (Dippon et al., 2012; Larese-Casanova et al., 2012). In contrast to the setup without Si and the low Si setup, no crystalline mineral phases were formed in the high Si setup over time. Additionally, the high Si setup showed the highest Fe(II) oxidation and Fe(III) reduction rates over time. Faster Fe(II) oxidation results in the formation of more structurally distorted Fe(III) minerals which are more susceptible to microbial Fe(III) reduction (Chen et al., 2018). Furthermore, shorter redox oscillations lead to increased maximum Fe(III) reduction rates (Barcellos et al., 2018), resulting in decreased interaction time between dissolved Fe(II) and remaining Fe(III) minerals, thus preventing the formation of crystalline Fe(III) minerals like goethite.

#### **4.3. Where is the magnetite?**

Magnetite is a secondary mineral often formed during microbial reduction of Fe(III) (oxyhydr)oxides by marine Fe(III)-reducing bacteria (e.g. Benaiges-Fernandez et al., 2019; Li et al., 2019) and a major Fe mineral found in BIFs today (Bekker et al., 2014; Klein, 2005;

Konhauser et al., 2017). Magnetite has further been reported to be formed in the water column of ferruginous lakes that are studied as modern-day analogues to the Precambrian ocean (e.g. Bauer et al., 2020; Zegeye et al., 2012). It has been hypothesized to be formed through the solid-state conversion of Fe(III) minerals, such as ferrihydrite, following the adsorption of Fe(II) to the mineral surface (Hansel et al., 2005; Hansel et al., 2003). Based on the prevalence of magnetite in BIFs and in the water column of modern-day analogues, we would also have expected the formation of magnetite following the microbial Fe cycling in our experiments. However, the mineral product in our cycling experiments conducted under conditions relevant for an Archean to early Paleoproterozoic ocean was instead dominated by ferrihydrite ( $\text{Fe}^{\text{III}}(\text{OH})_3$ ), which was (partially) replaced by goethite ( $\alpha\text{-Fe}^{\text{III}}\text{OOH}$ ) when Si was omitted from the experiments, and a Fe(II) mineral phase consisting either of siderite ( $\text{Fe}^{\text{II}}\text{CO}_3$ ) or a Fe(II)-silicate (e.g. greenalite,  $\text{Fe}_6\text{Si}_4\text{O}_{10}(\text{OH})_8$ ) or a mixture thereof.

In our experiments we observed a tight association between Fe(III) minerals, microbially-derived  $\text{C}_{\text{org}}$  and Si. The inhibitory effect of organic matter (Amstaetter et al., 2012; Chen et al., 2015; Eusterhues et al., 2014; Poggenburg et al., 2016; Poggenburg et al., 2018; Shimizu et al., 2013; ThomasArrigo et al., 2017; Zhou et al., 2018) and Si (e.g. Cismasu et al., 2014; Jones et al., 2009; Kukkadapu et al., 2004; Sergent et al., 2011) on magnetite formation during abiotic (Fe(II)-induced) and microbially driven Fe(III) mineral reduction is well recognized. However, these studies also showed that the inhibitory effect was dependent on concentration of either  $\text{C}_{\text{org}}$  or Si and at lower C/Fe and Si/Fe ratios magnetite formation still took place. Magnetite formation has been found to require a Fe(II) loading in excess of 1 mmol  $\text{g}^{-1}$  ferrihydrite, while goethite formation only requires the presence of 40  $\mu\text{M}$  Fe(II) ( $\sim 0.1$  mmol  $\text{g}^{-1}$  ferrihydrite; Hansel et al., 2005), which potentially explains the prevalence of goethite over magnetite in our Fe cycling experiments. Interestingly, Han et al. (2020) found considerable ( $>50\%$ ) magnetite formation upon microbial reduction of cell-Fe(III) mineral aggregates formed by *Rhodobacter ferrooxidans* SW2. Therefore, co-precipitated organics alone cannot explain the inhibited magnetite formation. Instead, based on our previous discussion, it is likely a combined effect of co-precipitated  $\text{C}_{\text{org}}$  and high concentrations of Si approaching the upper limit of concentrations suggested for the Archean to Paleoproterozoic ocean (saturation with regards to amorphous silica; Maliva et al., 2005; Siever, 1992). However, this does not explain the absence of magnetite formation at Si

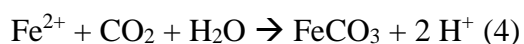
concentrations approaching the lower limit of expected ancient seawater Si concentrations (saturation with regards to cristobalite), as some mineral transformation evidently still took place.

An additional factor potentially influencing magnetite formation in our experiments is time. During our experiments redox conditions oscillated with a high frequency on the timescale of weeks to days, thus severely limiting the time available for the reaction between Fe(II) and extant Fe(III) minerals. Previous studies found that magnetite formation may require more than 30 days (e.g. Han et al., 2020; Roden and Zachara, 1996). This long timespan clearly exceeds the mineral residence times in our highly dynamic microbial cycling experiments, which would consequently preclude magnetite formation.

The effect of this limited Fe(II)-mineral interaction would have been amplified by the complexation of freshly reduced Fe(II) by  $C_{org}$ . There is strong precedence in the literature for Fe(II) complexation by organics such as AQDS, ferrozine, NTA or natural organic matter (NOM) and DOC in general (Adhikari et al., 2017; Daugherty et al., 2017; Kügler et al., 2019; Roden and Urrutia, 1999; Royer et al., 2002; Urrutia et al., 1998) during microbial Fe(III) reduction. Our experimental data suggest that some of the bacterially derived  $C_{org}$  was released back into solution during reductive half cycles (see previous section). This  $C_{org}$  likely complexed the freshly formed Fe(II), as suggested by the high amount of dissolved Fe(II) (>80%) we measured at the end of the reductive half cycles, thus preventing the adsorption of Fe(II) onto Fe(III) minerals required for magnetite formation (see equation 3).



The identity of the Fe(II) mineral phase that formed during microbial Fe(III) reduction remains unclear. Concurrent with the reductive dissolution of cell-Fe(III) mineral aggregates the labile  $C_{org}$  (provided as lactate) was oxidized to  $\text{CO}_2$  (equation 1), thus increasing alkalinity. Furthermore, during our cycling experiments we observed increasing Fe(III) reduction rates over time and with increasing Si concentration. The combination of increasing alkalinity and high biogenic Fe(II) flux could thus have favored the formation of siderite (equation 4)



over magnetite as major Fe(II)-bearing mineral (Stumm and Morgan, 1996; Zachara et al., 2002). However, it is unclear if the mineralization of the lactate provided (1-1.2 mM) would have been

sufficient to effectively suppress the formation of magnetite, since previous studies found that an excess of 10 mM bicarbonate is required to do so (Hansel et al., 2005). It appears more likely that the 30 mM bicarbonate added as primary buffer was the decisive factor for siderite formation. This high bicarbonate concentration likely also favored the formation of goethite in our setups without or low Si (Carlson and Schwertmann, 1990; Larese-Casanova et al., 2010; Zachara et al., 2011).

An alternative Fe(II) mineral to siderite which could have been formed during microbial Fe(III) reduction and is of high relevance for BIF genesis is a Fe(II)-silicate. However, previous work suggested that the formation of Fe(II)-silicates such as greenalite requires alkaline pH values (7.5-8 or higher; e.g. Beukes and Gutzmer, 2008; Halevy et al., 2017; Klein, 2005; Rasmussen et al., 2020; Tosca et al., 2016). This is at odds with the slightly acidic to circumneutral pH conditions of an Archean to early Paleoproterozoic ocean we aimed at simulating in our experiments (Halevy and Bachan, 2017; Krissansen-Totton et al., 2018). Yet, there are two potential mechanisms which might have facilitated the formation of Fe(II)-silicates. On the one hand, the simultaneous release of Fe<sup>2+</sup> and Si during microbial Fe(III) reduction and the accompanying increase in pH could have created micro-environments in which the formation of Fe(II)-silicates would have been possible. On the other hand, microbial cells and/or EPS could have acted as nucleation sites for Fe-silicate precipitation, thus enabling mineral precipitation despite unfavorable geochemical conditions (compare e.g. Fein et al., 2002; Fortin and Ferris, 1998; Fortin et al., 1998; Konhauser et al., 1993; Konhauser et al., 1994).

Based on our experimental results we deem the formation of magnetite during BIF deposition in the water column of a Neoproterozoic to early Paleoproterozoic ocean highly unlikely. The highly dynamic conditions resulting from an effective microbial Fe cycling would have precluded the reaction time necessary for magnetite formation, especially when considering the potential inhibitory high concentrations of Si (Maliva et al., 2005; Siever, 1992) and co-precipitation of microbially derived C<sub>org</sub> with primary Fe(III) (oxyhydr)oxides. Instead, high concentrations of Si and the higher *p*CO<sub>2</sub> during that time (Catling and Zahnle, 2020; Krissansen-Totton et al., 2018) as well as increased alkalinity following microbial Fe(III) reduction would have driven the system towards the formation of siderite and/or Fe(II)-silicates, potentially also allowing the formation of goethite at seawater Si concentrations approaching the saturation with regards to cristobalite.



#### 4.4. The relevance of microbial Fe cycling for the deposition of BIFs

##### 4.4.1. Factors controlling microbial Fe cycling during BIF deposition

The extent to which microbial Fe cycling during the deposition of BIFs would have influenced the secondary mineral (trans)formation is determined by three major factors: (1) Depth of the photic zone, (2) particle size and resulting sedimentation rate, and (3) the maximum Fe(II) oxidation and Fe(III) reduction rates. These factors would have determined the residence time of mineral particles within the photic zone and how many Fe cycles these particles could have undergone before leaving the photic zone.

The maximum depth of the photic zone over the shelf is influenced by the particle loading in the water column (bacteria, minerals, organics, etc.). In modern oceans 95% of the light is absorbed within the first approximately 100 m of the water column. In turbid coastal waters this depth may be reduced to a few meters (Hempel et al., 2016; Stewart, 2008). In the Black Sea, anoxygenic phototrophs have been reported to occur in depths between 60 and 120 m (Manske et al., 2005; Repeta et al., 1989). Crowe et al. (2008) reported the presence of putative photoferrotrophs from depths between 110 and 120 m in Lake Matano (Indonesia), a modern-day analogue for ferruginous Archean oceans. In contrast hereto Lirós et al. (2015) reported >90% of the photosynthetically active light to have been absorbed within the first 10 m of the ferruginous water column of Kabuno Bay, Lake Kivu, Eastern Africa (DR Kongo) with peak bacteriochlorophyll *a* concentrations between 10 and 12 m water depth. In order to address these contrasting conditions, we will consider two endmember scenarios where (1) photoferrotrophy occurs until depths of 100 m before mineral particles exit the photic zone and (2) photoferrotrophs are only active within the top 10 m of the water column.

Considering these two endmember scenarios, microbial Fe cycling linking photoferrotrophy and microbial Fe(III) reduction could have taken place during 5% (10 m photic depth) to 50% (100 m photic depth) of the time required by cell-Fe(III) mineral aggregates to be deposited seafloor (depth of the shelf,  $\geq 200$  m; Tab. 2, Supplementary text S8). Due to experimental constraints to obtain a sufficient quantity of Fe minerals for analysis, the Fe concentrations we used in our experiments exceeded the concentrations assumed for the Precambrian by approximately an order of magnitude (0.03-0.5 mM; Holland, 1973; Morris, 1993). Therefore, instead of trying to adapt our experimentally derived maximum rates to lower

Fe concentrations, we compare the time required for 3 microbial Fe cycles in our experiments to the time theoretically required by the mineral particles to sink through the photic zone. Despite the discrepancy in the Fe(II) concentrations this should thus still provide us with an estimate about the extent of microbial Fe cycling (the number of cycles) in the water column during the deposition of BIFs.

Table 2

Summary of sedimentation rates, water column residence time and parameters determining microbial Fe cycling inside the photic zone for Si concentrations bracketing expected Precambrian ocean concentrations (0.67-2.2 mM Si). Calculated values are based on results for particle size and sedimentation rate (see section 3.2.2.2, supplementary text S1).  $n = 148$  for “low Si” and  $n = 135$  for “high Si”. A full breakdown of all calculations is provided in supplementary text S8. <sup>a</sup> Based on 3 microbial Fe cycles performed in our experiments. We define the time until either  $\geq 95\%$  of the Fe(II) was oxidized or  $\geq 70\%$  of the initially oxidized Fe(II) was reduced again as “metabolically active”, <sup>b</sup> Assuming BIFs were deposited at the depth of the shelf, at depths exceeding modern storm-wave base, <sup>c</sup> Based on 3 microbial Fe cycles performed in our experiments.

	Low Si		High Si	
Time metabolically active [d] <sup>a</sup>	40		38	
	<b>Mean</b>	<b>Median</b>	<b>Mean</b>	<b>Median</b>
Aggregate size [ $\mu\text{m}$ ]	17.90	12.95	16.01	13.23
Sedimentation rate [ $\text{m h}^{-1}$ ]	1.25	0.35	0.73	0.31
Water column residence time [d] <sup>b</sup>	196.63	23.51	155.01	27.12
<b>10 m photic zone</b>				
Time inside photic zone [d]	9.83	1.18	7.75	1.36
Number of Fe cycles <sup>c</sup>	0.74	0.09	0.61	0.11
Time outside photic zone [d]	186.80	22.33	147.26	25.77
<b>100 m photic zone</b>				
Time Inside photic zone [d]	98.32	11.76	77.50	13.56
Number of Fe cycles <sup>c</sup>	7.37	0.88	6.12	1.07
Time outside photic zone [d]	98.32	11.76	77.50	13.56

The results of our estimates regarding the extent of microbial Fe cycling occurring at different Si concentrations are summarized in Table 2 and we will focus on the high Si setup in the following. If the photic zone was relatively shallow (10 m), for example as result of a volcanic eruption, bacterial plumes or closer to the shore as a result of increased particle input, then microbial Fe cycling likely only played a minor role. The average photic zone residence time of cell-mineral aggregates would have been approximately 8 days, where the majority of the aggregates would have passed through the photic zone in only 1.36 days, allowing for less than one microbial Fe cycle (Tab. 2, Supplementary text S8). If, on the other hand, the photic zone

---

extended to approximately 100 m, the influence of microbial Fe cycling would have been much more prominent. The average photic zone residence time of any given aggregate would have increased to ca. 80 days, with the majority of aggregates exiting the photic zone after ca. 14 days. Consequently, individual aggregates might on average have been cycled up to 6 times, with the majority having been cycled at least once before leaving the photic zone. Our values bracket and are in good agreement with results of Bauer et al. (2020), who estimated that Fe(II) in the Malili lake system (as modern-day analogue to the Precambrian ocean) is cycled 2-3 times before being removed from the system through sedimentation and burial.

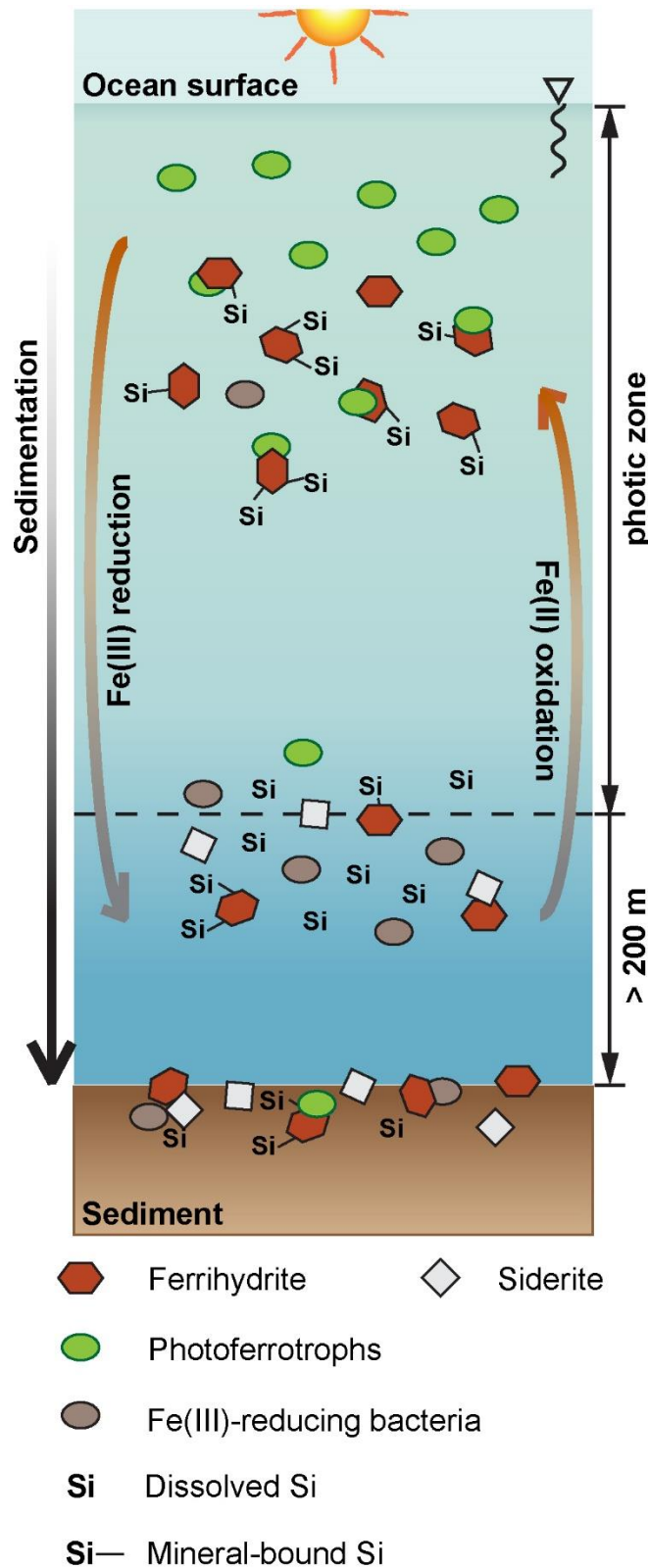
Another consequence of the attenuation of light with increasing water depth is that this influences the relative importance of photoferrotrophy vs. microbial Fe(III) reduction. In our experiments, the oxidative half cycles were performed at or close to light saturation, which generally resulted in net Fe(II) oxidation during oxidative half cycles. However, considering decreasing light availability at increasing water depth, the efficacy with which Fe(II) is oxidized photosynthetically will also be reduced. Indeed, Kappler et al. (2005) suggested that at 100 m depth the rate with which Fe(II) is oxidized would be only 20% of the surface level. By contrast, Fe(III)-reducing bacteria would be unaffected by changing light levels. Therefore, depending on the water depth, the extent to which Fe is cycled within and below the photic zone would be affected.

An additional factor expected to influence Fe cycling is the use of co-substrates by photoferrotrophs, i.e. the parallel use of Fe(II) and fatty acids (see section 4.1). Past studies showed that the parallel presence of both Fe(II) and fatty acids may increase cell numbers (Melton et al., 2014), leading to enhanced Fe(II) oxidation, or, depending on the substrate preference, fatty acids may be consumed before Fe(II), thus delaying Fe(II) oxidation. Similarly, Croal et al. (2009) found that the presence of a co-substrate ( $H_2$ ) limited Fe(II) oxidation by their tested photoferrotrophic strains. Additionally, high frequency redox oscillations have been found to increase the rate with which Fe(III)-reducing bacteria reduce Fe(III) (e.g. Barcellos et al., 2018; Ginn et al., 2017). This has been attributed to the ability of bacteria to maintain their activity during shorter redox oscillations and to their constant stimulation by repeated pulses of substrate. In reverse this indicates that the constant re-supply of Fe(II) would have a similar stimulating effect on photoferrotrophs, thus enhancing the efficacy with which they re-oxidize the Fe(II),

resulting in a highly efficient microbial Fe cycle even at reduced light conditions deeper in the photic zone.

#### *4.4.2. Consequences of microbial Fe cycling for the mineralogy and composition of primary BIF sediments*

The composition of the primary BIF sediment would have been heavily dependent on the frequency of microbial Fe cycling during the initial deposition of BIFs and the seawater Si concentration. At high seawater Si concentrations (approaching saturation with regards to amorphous Si, 2.2 mM) and moderate water column Fe cycling (1 full cycle) during the deposition of BIFs, the composition of the primary sediment would have been dominated by a primary SRO Fe(III) (oxyhydr)oxide (e.g., ferrihydrite; see also Alibert, 2016; Beukes and Gutzmer, 2008; Pecoits et al., 2009; Sun et al., 2015) with an admixture of up to 10% of a Fe(II) mineral (siderite and or Fe(II)-silicate). On the other hand, if there would have been extensive Fe cycling (up to 6 full cycles), the primary sediment would have consisted of up to 50% of a Fe(II) mineral phase (siderite and/or Fe(II)-silicate) and an SRO Fe(III) (oxyhydr)oxide. By contrast, at low seawater Si concentrations (saturation with regards to cristobalite, 0.67 mM) the Fe(III) mineral phase would have consisted of a mixture of a SRO Fe(III) mineral (ferrihydrite) and goethite. Additionally, compared to high seawater Si concentrations the formation of an Fe(II) mineral phase would have been limited: In case of moderate water column Fe cycling (1 full cycle) no Fe(II) mineral phase would have been formed and even during extensive Fe cycling (up to 6 full cycles) the extent of Fe(II) mineral formation would not have exceeded 10%. However, both at low and high seawater Si concentrations the reductive dissolution of the Fe(III) mineral phase during microbial Fe(III) reduction would have resulted in the release of C<sub>org</sub> and Si from the cell-mineral aggregates (Fig. 8).



← Figure 8: Microbial Fe cycling occurring in the water column during the deposition of BIFs. Hydrothermally derived  $\text{Fe}^{2+}$  is oxidized by photoferrotrophs, resulting in the co-precipitation of ferrihydrite (Fh),  $\text{C}_{\text{org}}$  (microbial cells, EPS) and Si. These cell-Fe(III) mineral aggregates are then reduced by Fe(III)-reducing bacteria within the water column, resulting in the reduction of Fh, the formation of siderite and the concomitant release of Si and  $\text{C}_{\text{org}}$  from the aggregates. The co-occurrence of photoferrotrophs and Fe(III)-reducing bacteria results in a highly dynamic microbial Fe cycling. With waning light intensity deeper in the water column the Fe cycling is increasingly dominated by microbial Fe(III) reduction and ceases once individual cell-mineral aggregates sink below the photic depth, resulting in the deposition of ferrihydrite and siderite at the ocean floor together with  $\text{C}_{\text{org}}$  and Si, albeit the latter two are to some extent released from the aggregates during water column Fe cycling.

Various petrographic and isotope geochemical studies on the BIF rock record suggest that siderite was formed through microbial Fe(III) reduction during diagenesis (e.g. Beukes, 1973; Fischer et al., 2009; Heimann et al., 2010; Johnson et al., 2003; Johnson et al., 2008; Johnson et al., 2013; Pecoits et al., 2009). By contrast, other studies have suggested siderite to be a primary seawater precipitate (e.g. Beukes and Klein, 1990; Beukes et al., 1990; Kaufman et al., 1990). We strike a middle ground and suggest that siderite might have been formed through microbial Fe cycling in the water column. *In-situ* measurements performed on samples of the Hamersley BIF, Western Australia,

showed that carbonate REE + Y patterns partially resemble modern-day seawater REE + Y (Alibert, 2016). Carbonate specific extractions performed on the Asbestos Hills iron formations

(Griqualand-West Basin, South Africa) by Oonk et al. (2018) revealed strong similarities between carbonate REE + Y and modern seawater. Finally, Frost et al. (2007) suggested that Fe isotope fractionation in carbonates is virtually unaffected by low-grade metamorphism. Collectively these three studies support the possibility of siderite formation in the water column by Fe cycling occurring during BIF deposition.

Based on our experimental data the formation of a Fe(II)-silicate instead of siderite during microbial Fe cycling could also have been possible. Previous studies have advanced the idea that a Fe(II)-silicate such as greenalite instead of Fe(III) (oxyhydr)oxides could have been the primary seawater precipitate during BIF deposition thus forming the precursor sediment to BIFs (e.g. Muhling and Rasmussen, 2020; Rasmussen et al., 2017). This view has been contested based on the alkaline pH required for its formation (see discussion in section 4.3) and the low probability of basin-scale secondary oxidation (Robbins et al., 2019). However, microbial Fe(III) reduction during microbial Fe cycling in the water column would have generated the geochemical conditions required for the precipitation of Fe(II)-silicates (see section 4.3). Consequently, even though Fe(III) (oxyhydr)oxides would have been the primary seawater precipitate, Fe(II)-silicates might have been an important secondary mineral and, depending on the extent of the microbial Fe cycling, potentially a major mineral phase in the primary BIF sediments (see also Johnson et al., 2018).

In contrast to siderite and/or Fe(II)-silicates, magnetite likely formed later during sediment diagenesis since the water column residence time of cell-mineral aggregates outside the photic zone was likely too short for microbial magnetite formation (median <30 days, Tab. 2, time required >30 days, see e.g. Han et al., 2020). Alternatively, ferrihydrite could have reacted abiotically with hydrothermally derived Fe<sup>2+</sup> deeper in the water column (Li et al., 2017), which would have been facilitated through the release of Si and C<sub>org</sub> from cell-mineral aggregates during microbial Fe cycling. Magnetite has been found to structurally overgrow hematite and siderite (e.g. Ayres, 1972; Beukes and Gutzmer, 2008; Ewers and Morris, 1981; Pecoits et al., 2009), thus rather supporting its formation later in the paragenetic sequence either during sediment diagenesis (microbial, e.g. Craddock and Dauphas, 2011; Johnson et al., 2008; Steinhoefel et al., 2009) or low-grade metamorphism.

## 5. CONCLUSIONS

Past experimental studies aimed at evaluating the mechanisms underlying the (trans-) formation of BIFs often considered only a single mechanism concerning either (1) the initial mineral deposition, biotically by photoferrotrophs or cyanobacteria or abiotically through precipitation of Fe(II)-silicates, or (2) post-depositional alteration during (microbial) diagenesis or low-grade metamorphism. Here we experimentally determined how and to which extent two such mechanisms suggested to have played a major role in the genesis of BIFs, photoferrotrophy and microbial Fe(III) reduction, may have interacted during the genesis of BIFs. To this end, we co-cultivated a marine photoferrotroph and a marine Fe(III)-reducing culture under conditions relevant for the Precambrian ocean. We specifically determined (1) how Fe(II)-oxidizing and Fe(III)-reducing bacteria would have interacted during repeated and dynamic microbial Fe cycling, (2) how this would have influenced the nature, composition and mineralogy of primary BIF sediments.

We found that the co-cultivation of photoferrotrophs and Fe(III)-reducing bacteria resulted in highly dynamic microbial Fe cycling, which persisted over several consecutive Fe cycles. Generally, Fe(II) oxidation resulted in the co-precipitation of microbially derived organics, Fe(III) minerals (ferrihydrite and/ or goethite) and Si, whereas Fe(III) reduction resulted in the reductive dissolution of Fe(III) minerals, the release of organics and Si and (depending on the Si concentration) the formation of varying amounts of a Fe(II) mineral phase consisting of siderite and/or Fe(II)-silicates. While siderite and Fe(II)-silicates might thus be considered as having formed during microbial Fe cycling in the water column during BIF deposition, we found no evidence for magnetite formation in any of our experiments. We attribute this to the combined influence of high frequency Fe cycling, co-precipitation of  $C_{org}$  during Fe(II) oxidation and Fe(II) complexation by  $C_{org}$  during Fe(III) reduction as well as an inhibitory effect of co-precipitated Si. This is in line with previous studies which suggested ferrihydrite (hematite) and siderite to be of an early diagenetic or primary origin (e.g. Alibert, 2016; Beukes and Gutzmer, 2008; Heimann et al., 2010; Kaufman et al., 1990; Pecoits et al., 2009; Sun et al., 2015). Furthermore, although our study suggests that Fe(III) minerals instead of the Fe(II)-silicates (see e.g. Muhling and Rasmussen, 2020; Rasmussen et al., 2017) would have been the primary seawater precipitate, we stress that water column Fe cycling could have facilitated the formation of secondary Fe(II)-silicates and their subsequent deposition on the seafloor.

During the genesis of BIFs, magnetite formation would likely have been facilitated by the longer sedimentological timescales after deposition as compared to the short timescale and highly dynamic processes occurring in our experiments. Magnetite formation could have been enabled by the release of  $C_{org}$  and Si during Fe cycling in the water column, which would have decreased the inhibiting effect both would have had on magnetite formation. Similarly, a lower  $C_{org}$  content and lower temperatures on the ocean floor likely also resulted in lower Fe(III) reduction rates, leading to a more moderate Fe(II) production, thus ultimately facilitating the formation of magnetite (e.g. Zachara et al., 2002). Furthermore, upon deeper burial, seawater infiltration into the sediment would have become increasingly limited and, therefore, also the supply of seawater-derived  $HCO_3^-$ , preventing siderite formation and resulting in an increasing abundance of  $Fe^{2+}$  available for solid-state conversion of ferrihydrite to magnetite.

Our study thus suggests that while ferrihydrite as well as siderite and/or Fe(II)-silicates likely formed during microbial Fe cycling in the water column, magnetite formed during BIF sediment diagenesis. However, despite a wealth of studies concerned with the factors influencing microbial Fe(III) reduction and accompanying Fe mineral transformations, the origin of magnetite in BIFs remains enigmatic. Future studies tailored to mimicking the conditions underlying BIF genesis are thus required. These studies should specifically focus on: (1) the co-occurrence of  $C_{org}$  and Si and their co-precipitation with Fe(III) (oxyhydr)oxides depending on the  $C_{org}$  and Si concentrations. (2) determining the influence of parameters such as light saturation and the presence of co-substrates on the dominance of photoferrotrophy vs microbial Fe(III) reduction. (3) varying timescales, the extent of Si-Fe mineral and  $C_{org}$ -Fe mineral association as well as the reactivity of the  $C_{org}$  present during microbial Fe(III) reduction. The reactivity of  $C_{org}$  is an especially important factor, since it not only determines the initial availability of  $C_{org}$  for microbial metabolisms but the reactivity of the  $C_{org}$  is also expected to decrease during the diagenetic and metamorphic history of BIFs. Consequently, if any  $C_{org}$  reached metamorphic depth we would expect it to be highly complex and stable. We, therefore, deem a metamorphic origin for magnetite in the least metamorphosed BIFs highly unlikely, which is corroborated by recent experimental results (Halama et al., 2016). However, the co-deposition of ferrihydrite with siderite might have facilitated magnetite formation through thermal decomposition of siderite (Rasmussen and Muhling, 2018) even though this process



usually occurs at temperatures and pressures exceeding those of the least metamorphosed BIFs and its importance thus remains to be determined.

## ACKNOWLEDGMENTS

The authors would like to thank Dr. Y. Bai and K. Wunsch for their experimental support. Dr. Y. Bai is further thanked for her comments which helped to improve this manuscript. Dr. H. Schulz and T. Bayer are acknowledged for advice and support with SEM analysis. The authors would further like to thank Dr. C. Bryce and L. Grimm for their help with flow cytometry. Ellen Röhm is acknowledged for her help with HPLC measurements. Dr. M. Muehe, Dr. C. Bryce, Dr. M. Maisch, M. Patzner and J. Sorwat are further acknowledged for fruitful discussions on experimental design and data interpretation. This study was supported by grants from the German Research Foundation (DFG) to AK and a Natural Sciences and Engineering Research Council (NSERC) grant to KOK.

## REFERENCES

- Adhikari D., Zhao Q., Das K., Mejia J., Huang R., Wang X., Poulson S. R., Tang Y., Roden E. E. and Yang Y. (2017) Dynamics of ferrihydrite-bound organic carbon during microbial Fe reduction. *Geochim. Cosmochim. Acta* **212**, 221-233.
- Alibert C. (2016) Rare earth elements in Hamersley BIF minerals. *Geochim. Cosmochim. Acta* **184**, 311-328.
- Amstaetter K., Borch T. and Kappler A. (2012) Influence of humic acid imposed changes of ferrihydrite aggregation on microbial Fe(III) reduction. *Geochim. Cosmochim. Acta* **85**, 326-341.
- Ayres D. (1972) Genesis of iron-bearing minerals in banded iron formation mesobands in the Dales Gorge Member, Hamersley Group, Western Australia. *Econ. Geol.* **67**, 1214-1233.
- Barcellos D., Cyle K. T. and Thompson A. (2018) Faster redox fluctuations can lead to higher iron reduction rates in humid forest soils. *Biogeochemistry* **137**, 367-378.
- Bauer K. W., Byrne J. M., Kenward P., Simister R. L., Michiels C. C., Friese A., Vuillemin A., Henny C., Nomosatryo S., Kallmeyer J., Kappler A., Smit M. A., Francois R. and Crowe S. A. (2020) Magnetite biomineralization in ferruginous waters and early Earth evolution. *Earth Planet. Sci. Lett.* **549**, 116495.
- Bekker A., Planavsky N., Rasmussen B., Krapez B., Hofmann A., Slack J., Rouxel O. and Konhauser K. O. (2014) Iron formations: Their origins and implications for ancient seawater

- chemistry. In *Treatise on Geochemistry, second ed. Vol. 9* (eds. H. D. Holland and K. K. Turekian). Elsevier, Netherlands. pp. 561-628.
- Bekker A., Slack J. F., Planavsky N., Krapež B., Hofmann A., Konhauser K. O. and Rouxel O. J. (2010) Iron formation: the sedimentary product of a complex interplay among mantle, tectonic, oceanic, and biospheric processes. *Econ. Geol.* **105**, 467-508.
- Benaiges-Fernandez R., Palau J., Offeddu F. G., Cama J., Urmeneta J., Soler J. M. and Dold B. (2019) Dissimilatory bioreduction of iron(III) oxides by *Shewanella loihica* under marine sediment conditions. *Mar. Environ. Res.* **151**, 104782.
- Berg J. S., Michellod D., Pjevac P., Martinez-Perez C., Buckner C. R., Hach P. F., Schubert C. J., Milucka J. and Kuypers M. M. (2016) Intensive cryptic microbial iron cycling in the low iron water column of the meromictic Lake Cadagno. *Environ. Microbiol.* **18**, 5288-5302.
- Beukes N. J. (1973) Precambrian iron-formations of southern Africa. *Econ. Geol.* **68**, 960-1004.
- Beukes N. J. and Gutzmer J. (2008) Origin and paleoenvironmental significance of major iron formations at the Archean-Paleoproterozoic boundary. *Rev. Econ. Geol.* **15**, 5-47.
- Beukes N. J. and Klein C. (1990) Geochemistry and sedimentology of a facies transition - from microbanded to granular iron-formation - in the early Proterozoic Transvaal Supergroup, South Africa. *Precambrian Res.* **47**, 99-139.
- Beukes N. J., Klein C., Kaufman A. J. and Hayes J. (1990) Carbonate petrography, kerogen distribution, and carbon and oxygen isotope variations in an early Proterozoic transition from limestone to iron-formation deposition, Transvaal Supergroup, South Africa. *Econ. Geol.* **85**, 663-690.
- Bonneville S., Behrends T. and Van Cappellen P. (2009) Solubility and dissimilatory reduction kinetics of iron(III) oxyhydroxides: a linear free energy relationship. *Geochim. Cosmochim. Acta* **73**, 5273-5282.
- Bonneville S., Van Cappellen P. and Behrends T. (2004) Microbial reduction of iron(III) oxyhydroxides: effects of mineral solubility and availability. *Chem. Geol.* **212**, 255-268.
- Bryce C., Blackwell, N., Straub D., Kleindienst S. and Kappler A. (2019) Draft genome sequence of *Chlorobium* sp. strain N1, a marine Fe(II)-oxidizing green sulfur bacterium. *Microbiol. Resour. Announc.* **8**.
- Carlson L. and Schwertmann U. (1990) The effect of CO<sub>2</sub> and oxidation rate on the formation of goethite versus lepidocrocite from an Fe(II) system at pH 6 and 7. *Clay Miner.* **25**, 65-71.
- Catling D. C. and Zahnle K. J. (2020) The Archean atmosphere. *Sci. Adv.* **6**, eaax1420.
- Chen C., Kukkadapu R. and Sparks D. L. (2015) Influence of Coprecipitated Organic Matter on Fe<sup>2+</sup><sub>(aq)</sub>-Catalyzed Transformation of Ferrihydrite: Implications for Carbon Dynamics. *Environ. Sci. Technol.* **49**, 10927-10936.
- Chen C., Meile C., Wilmoth J., Barcellos D. and Thompson A. (2018) Influence of pO<sub>2</sub> on iron redox cycling and anaerobic organic carbon mineralization in a humid tropical forest soil. *Environ. Sci. Technol.* **52**, 7709-7719.
- Chen C. and Thompson A. (2018) Ferrous iron oxidation under varying pO<sub>2</sub> levels: the effect of Fe(III)/Al(III) oxide minerals and organic matter. *Environ. Sci. Technol.* **52**, 597-606.

- Cismasu A. C., Michel F. M., Tcaciuc A. P. and Brown G. E. (2014) Properties of impurity-bearing ferrihydrite III. Effects of Si on the structure of 2-line ferrihydrite. *Geochim. Cosmochim. Acta* **133**, 168-185.
- Cismasu A. C., Michel F. M., Tcaciuc A. P., Tyliczszak T. and Brown G. E. (2011) Composition and structural aspects of naturally occurring ferrihydrite. *C. R. Geosci.* **343**, 210-218.
- Cloud P. E. (1973) Paleoecological significance of the banded iron-formation. *Econ. Geol.* **68**, 1135-1143.
- Cooper R. E., Eusterhues K., Wegner C.-E., Totsche K. U. and Küsel K. (2017) Ferrihydrite-associated organic matter (OM) stimulates reduction by *Shewanella oneidensis* MR-1 and a complex microbial consortia. *Biogeosciences* **14**.
- Cooper R. E., Wegner C.-E., Kügler S., Poulin R. X., Ueberschaar N., Wurlitzer J. D., Stettin D., Wichard T., Pohnert G. and Küsel K. (2020) Iron is not everything: unexpected complex metabolic responses between iron-cycling microorganisms. *ISME J.* **14**, 2675-2690.
- Craddock P. R. and Dauphas N. (2011) Iron and carbon isotope evidence for microbial iron respiration throughout the Archean. *Earth Planet. Sci. Lett.* **303**, 121-132.
- Croal L. R., Jiao Y., Kappler A. and Newman D. K. (2009) Phototrophic Fe(II) oxidation in an atmosphere of H<sub>2</sub>: implications for Archean banded iron formations. *Geobiology* **7**, 21-24.
- Crowe S. A., Jones C., Katsev S., Magen C., O'Neill A. H., Sturm A., Canfield D. E., Haffner G. D., Mucci A., Sundby B. and Fowle D. A. (2008) Photoferrotrophs thrive in an Archean Ocean analogue. *Proc. Natl. Acad. Sci.* **105**, 15938-15943.
- Crowe S. A., Paris G., Katsev S., Jones C., Kim S.-T., Zerkle A. L., Nomosatryo S., Fowle D. A., Adkins J. F., Sessions A. L., Farquhar J. and Canfield D. E. (2014) Sulfate was a trace constituent of Archean seawater. *Science* **346**, 735-739.
- Das S., Hendry M. J. and Essilfie-Dughan J. (2013) Adsorption of selenate onto ferrihydrite, goethite, and lepidocrocite under neutral pH conditions. *Appl. Geochem.* **28**, 185-193.
- Daugherty E. E., Gilbert B., Nico P. S. and Borch, T. (2017) Complexation and redox buffering of iron(II) by dissolved organic matter. *Environ. Sci. Technol.* **51**, 11096-11104.
- Davis C. C., Knocke W. R. and Edwards M. (2001) Implications of aqueous silica sorption to iron hydroxide: mobilization of iron colloids and interference with sorption of arsenate and humic substances. *Environ. Sci. Technol.* **35**, 3158-3162.
- Dippon U., Pantke C., Porsch K., Larese-Casanova P. and Kappler A. (2012) Potential function of added minerals as nucleation sites and effect of humic substances on mineral formation by the nitrate-reducing Fe(II)-oxidizer *Acidovorax* sp. BoFeN1. *Environ. Sci. Technol.* **46**, 6556-6565.
- Dippon U., Schmidt C., Behrens S. and Kappler A. (2015) Secondary mineral formation during ferrihydrite reduction by *Shewanella oneidensis* MR-1 depends on incubation vessel orientation and resulting gradients of cells, Fe<sup>2+</sup> and Fe minerals. *Geomicrobiol. J.* **32**, 878-889.
- Dong Y., Sanford R. A., Boyanov M. I., Flynn T. M., O'Loughlin E. J., Kemner K. M., George S., Fouke K. E., Li S., Huang D., Li S. and Fouke B. W. (2020) Controls on Iron Reduction

- and Biomineralization over Broad Environmental Conditions as Suggested by the Firmicutes *Orenia metallireducens* Strain Z6. *Environ. Sci. Technol.* **54**, 10128-10140.
- Dyer L. G., Fawell P. D., Newman O. and Richmond W. R. (2010) Synthesis and characterisation of ferrihydrite/silica co-precipitates. *J. Colloid Interface Sci.* **348**, 65-70.
- Dyer L. G., Chapman K. W., English P., Saunders M. and Richmond W. R. (2012) Insights into the crystal and aggregate structure of Fe<sup>3+</sup> oxide/silica co-precipitates. *Am. Mineral.* **97**, 63-69.
- Ehrenreich A. and Widdel F. (1994) Anaerobic oxidation of ferrous iron by purple bacteria, a new type of phototrophic metabolism. *Appl. Environ. Microbiol.* **60**, 4517-4526.
- Eickhoff M., Obst M., Schröder C., Hitchcock A. P., Tyliczszak T., Martinez R. E., Robbins L. J., Konhauser K. O. and Kappler A. (2014) Nickel partitioning in biogenic and abiogenic ferrihydrite: the influence of silica and implications for ancient environments. *Geochim. Cosmochim. Acta* **140**, 65-79.
- Eusterhues K., Hädrich A., Neidhardt J., Küsel K., Keller T., Jandt K. and Totsche K. (2014) Reduction of ferrihydrite with adsorbed and coprecipitated organic matter: microbial reduction by *Geobacter bremensis* vs. abiotic reduction by Na-dithionite. *Biogeosciences* **11**, 4953.
- Eusterhues K., Wagner F. E., Häusler W., Hanzlik M., Knicker H., Totsche K. U., Kögel-Knabner I. and Schwertmann U. (2008) Characterization of ferrihydrite-soil organic matter coprecipitates by X-ray diffraction and Mössbauer spectroscopy. *Environ. Sci. Technol.* **42**, 7891-7897.
- Ewers W. E. and Morris R. C. (1981) Studies of the Dales Gorge member of the Brockman iron formation, Western Australia. *Econ. Geol.* **76**, 1929-1953.
- Fein J. B., Scott S. and Rivera N. (2002) The effect of Fe on Si adsorption by *Bacillus subtilis* cell walls: insights into non-metabolic bacterial precipitation of silicate minerals. *Chem. Geol.* **182**, 265-273.
- Ferris F. G., Schultze S., Witten T. C., Fyfe W. S. and Beveridge T. J. (1989) Metal interactions with microbial biofilms in acidic and neutral pH environments. *Appl. Environ. Microbiol.* **55**, 1249-1257.
- Fischer W. W., Schroeder S., Lacassie J. P., Beukes N. J., Goldberg T., Strauss H., Horstmann U. E., Schrag D. P. and Knoll A. (2009) Isotopic constraints on the Late Archean carbon cycle from the Transvaal Supergroup along the western margin of the Kaapvaal Craton, South Africa. *Precambrian Res.* **169**, 15-27.
- Fortin, D. and Ferris, F. G. (1998) Precipitation of iron, silica, and sulfate on bacterial cell surfaces. *Geomicrobiol. J.* **15**, 309-324.
- Fortin D., Ferris F. G. and Scott S. D. (1998) Formation of Fe-silicates and Fe-oxides on bacterial surfaces in samples collected near hydrothermal vents on the Southern Explorer Ridge in the northeast Pacific Ocean. *Am. Mineral.* **83**, 1399-1408.
- Frost C. D., von Blanckenburg F., Schoenberg R., Frost B. R. and Swapp S. M. (2007) Preservation of Fe isotope heterogeneities during diagenesis and metamorphism of banded iron formation. *Contrib. Mineral. Petrol.* **153**, 211.

- Gauger T., Byrne J. M., Konhauser K. O., Obst M., Crowe S. A. and Kappler, A. (2016) Influence of organics and silica on Fe(II) oxidation rates and cell–mineral aggregate formation by the green-sulfur Fe(II)-oxidizing bacterium *Chlorobium ferrooxidans* KoFox–Implications for Fe(II) oxidation in ancient oceans. *Earth Planet. Sci. Lett.* **443**, 81-89.
- Ginn B., Meile C., Wilmoth J., Tang Y. and Thompson A. (2017) Rapid iron reduction rates are stimulated by high-amplitude redox fluctuations in a tropical forest soil. *Environ. Sci. Technol.* **51**, 3250-3259.
- Gole M. J. and Klein C. (1981) Banded iron-formations through much of Precambrian time. *J. Geol.* **89** 169-183.
- Gustafsson J. P. (2003) Modelling molybdate and tungstate adsorption to ferrihydrite. *Chem. Geol.* **200**, 105-115.
- Halama M., Swanner E. D., Konhauser K. O. and Kappler A. (2016) Evaluation of siderite and magnetite formation in BIFs by pressure–temperature experiments of Fe(III) minerals and microbial biomass. *Earth Planet. Sci. Lett.* **450**, 243-253.
- Halevy I., Alesker M., Schuster E. M., Popovitz-Biro R. and Feldman Y. (2017) A key role for green rust in the Precambrian oceans and the genesis of iron formations. *Nat. Geosci.* **10**, 135-139.
- Halevy I. and Bachan A. (2017) The geologic history of seawater pH. *Science* **355**, 1069-1071.
- Han X., Tomaszewski E. J., Sorwat J., Pan Y., Kappler A. and Byrne J. M. (2020) Effect of Microbial Biomass and Humic Acids on Abiotic and Biotic Magnetite Formation. *Environ. Sci. Technol.* **54**, 4121-4130.
- Hansel C. M., Benner S. G. and Fendorf S. (2005) Competing Fe(II)-induced mineralization pathways of ferrihydrite. *Environ. Sci. Technol.* **39**, 7147-7153.
- Hansel C. M., Benner S. G., Neiss J., Dohnalkova A., Kukkadapu R. K. and Fendorf S. (2003) Secondary mineralization pathways induced by dissimilatory iron reduction of ferrihydrite under advective flow. *Geochim. Cosmochim. Acta* **67**, 2977-2992.
- Hao L., Guo Y., Byrne J. M., Zeitvogel F., Schmid G., Ingino P., Li J., Neu T. R., Swanner E. D. and Kappler A. (2016) Binding of heavy metal ions in aggregates of microbial cells, EPS and biogenic iron minerals measured in-situ using metal-and glycoconjugates-specific fluorophores. *Geochim. Cosmochim. Acta* **180**, 66-96.
- Hardisty D. S., Lu Z., Planavsky N. J., Bekker A., Philippot P., Zhou X. and Lyons T. W. (2014) An iodine record of Paleoproterozoic surface ocean oxygenation. *Geology* **42**, 619-622.
- Hartman H. (1984) The evolution of photosynthesis and microbial mats: A speculation on the banded iron formations. In *Microbial Mats: Stromatolites* (eds. Y. Cohen, R. W. Castenholz and H. O. Halvorson). Alan Liss, New York. pp. 451-453
- Hegler F., Posth N. R., Jiang J. and Kappler A. (2008) Physiology of phototrophic iron(II)-oxidizing bacteria: implications for modern and ancient environments. *FEMS Microbiol. Ecol.* **66**, 250-260.
- Heimann A., Johnson C. M., Beard B. L., Valley J. W., Roden E. E., Spicuzza M. J. and Beukes, N. J. (2010) Fe, C, and O isotope compositions of banded iron formation carbonates

- demonstrate a major role for dissimilatory iron reduction in ~2.5 Ga marine environments. *Earth Planet. Sci. Lett.* **294**, 8-18.
- Heising S., Richter L., Ludwig W. and Schink B. (1999) *Chlorobium ferrooxidans* sp. nov., a phototrophic green sulfur bacterium that oxidizes ferrous iron in coculture with a “*Geospirillum*” sp. strain. *Arch. Microbiol.* **172**, 116-124.
- Hempel G., Bischof K. and Hagen W. (2016) *Faszination Meeresforschung: Ein ökologisches Lesebuch, second ed.* Springer-Verlag, Berlin, Heidelberg.
- Hohmann C., Winkler E., Morin G. and Kappler A. (2009) Anaerobic Fe(II)-oxidizing bacteria show As resistance and immobilize As during Fe(III) mineral precipitation. *Environ. Sci. Technol.* **44**, 94-101.
- Holland H. D. (1973) The oceans; a possible source of iron in iron-formations. *Econ. Geol.* **68**, 1169-1172.
- Imhoff J F. (2014) The family *Chlorobiaceae*. In *The Prokaryotes* (eds. Rosenberg E., DeLong E. F., Lory S., Stackebrandt E. and Thompson F.). Springer-Verlag, Berlin-Heidelberg.
- Jiao Y., Kappler A., Croal L. R. and Newman D. K. (2005) Isolation and characterization of a genetically tractable photoautotrophic Fe(II)-oxidizing bacterium, *Rhodopseudomonas palustris* strain TIE-1. *Appl. Environ. Microbiol.* **71**, 4487-4496.
- Johnson C. M., Beard B. L., Beukes N. J., Klein C. and O'Leary J. M. (2003) Ancient geochemical cycling in the Earth as inferred from Fe isotope studies of banded iron formations from the Transvaal Craton. *Contrib. Mineral. Petrol.* **144**, 523-547.
- Johnson C. M., Beard B. L., Klein C., Beukes N. J. and Roden E. E. (2008) Iron isotopes constrain biologic and abiologic processes in banded iron formation genesis. *Geochim. Cosmochim. Acta* **72**, 151-169.
- Johnson C. M., Ludois J. M., Beard B. L., Beukes N. J. and Heimann, A. (2013) Iron formation carbonates: Paleooceanographic proxy or recorder of microbial diagenesis? *Geology* **41**, 1147-1150.
- Johnson J. E., Muhling J. R., Cosmidis J., Rasmussen B. and Templeton A. S. (2018) Low - Fe(III) Greenalite Was a Primary Mineral From Neoproterozoic Oceans. *Geophys. Res. Lett.* **45**, 3182-3192.
- Jones A. M., Collins R. N., Rose J. and Waite T. D. (2009) The effect of silica and natural organic matter on the Fe(II)-catalysed transformation and reactivity of Fe(III) minerals. *Geochim. Cosmochim. Acta* **73**, 4409-4422.
- Kappler A. and Newman D. K. (2004) Formation of Fe(III)-minerals by Fe(II)-oxidizing photoautotrophic bacteria. *Geochim. Cosmochim. Acta* **68**, 1217-1226.
- Kappler A., Pasquero C., Konhauser K. O. and Newman D. K. (2005) Deposition of banded iron formations by anoxygenic phototrophic Fe(II)-oxidizing bacteria. *Geology* **33**, 865-868.
- Kaufman A. J., Hayes J. and Klein C. (1990) Primary and diagenetic controls of isotopic compositions of iron-formation carbonates. *Geochim. Cosmochim. Acta* **54**, 3461-3473.
- Klein C. (2005) Some Precambrian banded iron-formations (BIFs) from around the world: Their age, geologic setting, mineralogy, metamorphism, geochemistry, and origins. *Am. Miner.* **90**, 1473-1499.

- Klein C. and Beukes N. J. (1992) Proterozoic iron-formations. In *Developments in Precambrian Geology, Vol. 10* (ed. K. C. Condie). Elsevier, Netherlands. pp. 383-418.
- Konhauser K. O., Fyfe W. S., Ferris F. G. and Beveridge T. J. (1993) Metal sorption and mineral precipitation by bacteria in two Amazonian river systems: Rio Solimoes and Rio Negro, Brazil. *Geology* **21**, 1103-1106.
- Konhauser K. O., Newman D. K. and Kappler A. (2005) The potential significance of microbial Fe(III) reduction during deposition of Precambrian banded iron formations. *Geobiology* **3**, 167-177.
- Konhauser K. O., Planavsky N. J., Hardisty D. S., Robbins L. J., Warchola T. J., Haugaard R., Lalonde S. V., Partin C. A., Oonk P. B. H., Tsikos H., Lyons T. W., Bekker A. and Johnson C. M. (2017) Iron formations: A global record of Neoproterozoic to Palaeoproterozoic environmental history. *Earth Sci. Rev.* **172**, 140-177.
- Konhauser K. O., Schultze-Lam S., Ferris F. G., Fyfe W. S., Longstaffe F. J. and Beveridge T. J. (1994) Mineral precipitation by epilithic biofilms in the Speed River, Ontario, Canada. *Appl. Environ. Microbiol.* **60**, 549-553.
- Konhauser K. O., Hamade T., Raiswell R., Morris R. C., Ferris F. G., Southam G. and Canfield D. E. (2002) Could bacteria have formed the Precambrian banded iron formations? *Geology* **30**, 1079-1082.
- Konhauser K. O., Lalonde S. V., Amskold L. and Holland H. D. (2007) Was there really an Archean phosphate crisis? *Science* **315**, 1234-1234.
- Kotloski N. J. and Gralnick J. A. (2013) Flavin electron shuttles dominate extracellular electron transfer by *Shewanella oneidensis*. *MBio* **4**.
- Kraal P., van Genuchten C. M., Behrends T. and Rose A. L. (2019) Sorption of phosphate and silicate alters dissolution kinetics of poorly crystalline iron (oxyhydr) oxide. *Chemosphere* **234**, 690-701.
- Krissansen-Totton J., Arney G. N. and Catling D. C. (2018) Constraining the climate and ocean pH of the early Earth with a geological carbon cycle model. *Proc. Natl. Acad. Sci.* **115**, 4105-4110.
- Kügler S., Cooper R. E., Wegner C.-E., Mohr J. F., Wichard T. and Küsel K. (2019) Iron-organic matter complexes accelerate microbial iron cycling in an iron-rich fen. *Sci. Total Environ.* **646**, 972-988.
- Kukkadapu R. K., Zachara J. M., Fredrickson J. K. and Kennedy D. W. (2004) Biotransformation of two-line silica-ferrihydrite by a dissimilatory Fe(III)-reducing bacterium: formation of carbonate green rust in the presence of phosphate. *Geochim. Cosmochim. Acta* **68**, 2799-2814.
- Kump L. R. and Seyfried W. E. (2005) Hydrothermal Fe fluxes during the Precambrian: effect of low oceanic sulfate concentrations and low hydrostatic pressure on the composition of black smokers. *Earth Planet. Sci. Lett.* **235**, 654-662.
- Lack J. G., Chaudhuri S. K., Kelly S. D., Kemner K. M., O'Connor S. M. and Coates J. D. (2002) Immobilization of radionuclides and heavy metals through anaerobic bio-oxidation of Fe(II). *Appl. Environ. Microbiol.* **68**, 2704-2710.

- Larese-Casanova P., Haderlein S. B. and Kappler A. (2010) Biomineralization of lepidocrocite and goethite by nitrate-reducing Fe(II)-oxidizing bacteria: effect of pH, bicarbonate, phosphate, and humic acids. *Geochim. Cosmochim. Acta* **74**, 3721-3734.
- Larese-Casanova P., Kappler A. and Haderlein S. B. (2012) Heterogeneous oxidation of Fe(II) on iron oxides in aqueous systems: Identification and controls of Fe(III) product formation. *Geochim. Cosmochim. Acta* **91**, 171-186.
- Laufer K., Niemeyer A., Nikeleit V., Halama M., Byrne J. M. and Kappler A. (2017) Physiological characterization of a halotolerant anoxygenic phototrophic Fe(II)-oxidizing green-sulfur bacterium isolated from a marine sediment. *FEMS Microbiol. Ecol.* **93**, fix054.
- Laufer K., Nordhoff M., Røy H., Schmidt C., Behrens S., Jørgensen B. B. and Kappler A. (2016) Coexistence of microaerophilic, nitrate-reducing, and phototrophic Fe(II) oxidizers and Fe(III) reducers in coastal marine sediment. *Appl. Environ. Microbiol.* **82**, 1433-1447.
- Li X., Zeng X., Qiu D., Zhang Z., Chen J. and Shao Z. (2019) Dissimilatory Iron [Fe (III)] Reduction by a Novel Fermentative, Piezophilic Bacterium *Anoxybacter fermentans* DY22613T Isolated from East Pacific Rise Hydrothermal Sulfides. *Geomicrobiol. J.* **36**, 291-302.
- Li Y.-L., Konhauser K. O., Cole D. R. and Phelps T. J. (2011) Mineral ecophysiological data provide growing evidence for microbial activity in banded-iron formations. *Geology* **39**, 707-710.
- Li Y.-L., Konhauser K. O., Kappler A. and Hao X.-L. (2013) Experimental low-grade alteration of biogenic magnetite indicates microbial involvement in generation of banded iron formations. *Earth Planet. Sci. Lett.* **361**, 229-237.
- Li Y.-L., Konhauser K. O. and Zhai M. (2017) The formation of magnetite in the early Archean oceans. *Earth Planet. Sci. Lett.* **466**, 103-114.
- Llirós M., García-Armisen T., Darchambeau F., Morana C., Triadó-Margarit X., Inceoğlu Ö., Borrego C. M., Bouillon S., Servais P. and Borges A. V. (2015) Pelagic photoferrotrophy and iron cycling in a modern ferruginous basin. *Sci. Rep.* **5**, 13803.
- Lovley D. R. (1991) Magnetite formation during microbial dissimilatory iron reduction. In *Iron biominerals* (eds. R. B. Frankel and R. P. Blakemore). Springer, Boston. pp. 151-166.
- Lovley D. R. and Phillips E. J. (1986) Organic matter mineralization with reduction of ferric iron in anaerobic sediments. *Appl. Environ. Microbiol.* **51**, 683-689.
- Lovley D. R. and Phillips E. J. (1988) Novel mode of microbial energy metabolism: organic carbon oxidation coupled to dissimilatory reduction of iron or manganese. *Appl. Environ. Microbiol.* **54**, 1472-1480.
- Lyons T. W., Reinhard C. T. and Planavsky N. J. (2014) The rise of oxygen in Earth's early ocean and atmosphere. *Nature* **506**, 307-315.
- Maliva R. G., Knoll A. H. and Simonson B. M. (2005) Secular change in the Precambrian silica cycle: insights from chert petrology. *Geol. Soc. Am. Bull.* **117**, 835-845.
- Manske A. K., Glaeser J., Kuypers M. M. and Overmann J. (2005) Physiology and phylogeny of green sulfur bacteria forming a monospecific phototrophic assemblage at a depth of 100 meters in the Black Sea. *Appl. Environ. Microbiol.* **71**, 8049-8060.



- Martinez R. E., Konhauser K. O., Paunova N., Wu W., Alessi D. S. and Kappler A. (2016) Surface reactivity of the anaerobic phototrophic Fe(II)-oxidizing bacterium *Rhodovulum iodolum*: Implications for trace metal budgets in ancient oceans and banded iron formations. *Chem. Geol.* **442**, 113-120.
- Mejia J., He S., Yang Y., Ginder-Vogel M. and Roden E. E. (2018) Stability of ferrihydrite-humic acid coprecipitates under iron-reducing conditions. *Environ. Sci. Technol.* **52**, 13174-13183.
- Melton E. D., Schmidt C., Behrens S., Schink B. and Kappler A. (2014) Metabolic flexibility and substrate preference by the Fe(II)-oxidizing purple non-sulphur bacterium *Rhodospseudomonas palustris* strain TIE-1. *Geomicrobiol. J.* **31**, 835-843.
- Moon E. M. and Peacock C. L. (2012) Adsorption of Cu(II) to ferrihydrite and ferrihydrite-bacteria composites: importance of the carboxyl group for Cu mobility in natural environments. *Geochim. Cosmochim. Acta* **92**, 203-219.
- Morris R. C. (1993) Genetic modelling for banded iron-formation of the Hamersley Group, Pilbara Craton, Western Australia. *Precambrian Res.* **60**, 243-286.
- Muhling J. R. and Rasmussen B. (2020) Widespread deposition of greenalite to form Banded Iron Formations before the Great Oxidation Event. *Precambrian Res.* **339**, 105619.
- Murad E. (1996) Magnetic properties of microcrystalline iron(III) oxides and related materials as reflected in their Mössbauer spectra. *Phys. Chem. Miner.* **23**, 248-262.
- Murad E. (2010) Mossbauer spectroscopy of clays, soils and their mineral constituents. *Clay Miner.* **45**, 413-430.
- Murad E., Bowen L., Long G. and Quin T. (1988) Influence of crystallinity on magnetic ordering in natural ferrihydrites. *Clay Miner.* **23**, 161-173.
- Murad E. and Schwertmann U. (1980) The Mössbauer spectrum of ferrihydrite and its relations to those of other iron oxides. *Am. Mineral.* **65**, 1044-1049.
- Nealson K. H. and Myers C. R. (1990) Iron reduction by bacteria: a potential role in the genesis of banded iron formations. *Am. J. Sci.* **290**, 35-45.
- O'Loughlin E. J., Gorski C. A., Flynn T. M. and Scherer M. M. (2019) Electron Donor Utilization and Secondary Mineral Formation during the Bioreduction of Lepidocrocite by *Shewanella putrefaciens* CN32. *Minerals* **9**, 434.
- Oonk P. B. H., Mason P. R. D., Tsikos H. and Bau M. (2018) Fraction-specific rare earth elements enable the reconstruction of primary seawater signatures from iron formations. *Geochim. Cosmochim. Acta* **238**, 102-122.
- Pan W., Kan J., Inamdar S., Chen C. and Sparks D. (2016) Dissimilatory microbial iron reduction release DOC (dissolved organic carbon) from carbon-ferrihydrite association. *Soil Biol. Biochem.* **103**, 232-240.
- Pantke C., Obst M., Benzerara K., Morin G., Ona-Nguema G., Dippon U. and Kappler A. (2012) Green Rust Formation during Fe(II) Oxidation by the Nitrate-Reducing *Acidovorax* sp. Strain BoFeN1. *Environ. Sci. Technol.* **46**, 1439-1446.
- Parfitt R., Van der Gaast S. and Childs C. (1992) A structural model for natural siliceous ferrihydrite. *Clays Clay Miner.* **40**, 675-581.

- Pecoits E., Gingras M. K., Barley M. E., Kappler A., Posth N. R. and Konhauser K. O. (2009) Petrography and geochemistry of the Dales Gorge banded iron formation: Paragenetic sequence, source and implications for palaeo-ocean chemistry. *Precambrian Res.* **172**, 163-187.
- Peng C., Bryce C., Sundman A., Borch T. and Kappler A. (2019a) Organic matter complexation promotes Fe(II) oxidation by the photoautotrophic Fe(II)-oxidizer *Rhodopseudomonas palustris* TIE-1. *ACS Earth Space Chem.* **3**, 531-536.
- Peng C., Bryce C., Sundman A. and Kappler A. (2019b) Cryptic cycling of complexes containing Fe(III) and organic matter by phototrophic Fe(II)-oxidizing bacteria. *Appl. Environ. Microbiol.* 85:e02826-18.
- Poggenburg C., Mikutta R., Sander M., Schippers A., Marchanka A., Dohrmann R. and Guggenberger G. (2016) Microbial reduction of ferrihydrite-organic matter coprecipitates by *Shewanella putrefaciens* and *Geobacter metallireducens* in comparison to mediated electrochemical reduction. *Chem. Geol.* **447**, 133-147.
- Poggenburg C., Mikutta R., Schippers A., Dohrmann R. and Guggenberger G. (2018) Impact of natural organic matter coatings on the microbial reduction of iron oxides. *Geochim. Cosmochim. Acta* **224**, 223-248.
- Pokrovski G. S., Schott J., Farges F. and Hazemann J. L. (2003) Iron(III)-silica interactions in aqueous solution: insights from X-ray absorption fine structure spectroscopy. *Geochim. Cosmochim. Acta.* **67**, 3559-3573.
- Pollak H. and Stevens J. G. (1986) Phyllosilicates: a Mössbauer evaluation. *Hyperfine Interact.* **29**, 1153-1156.
- Posth N. R., Huelin S., Konhauser K. O. and Kappler A. (2010) Size, density and composition of cell-mineral aggregates formed during anoxygenic phototrophic Fe(II) oxidation: Impact on modern and ancient environments. *Geochim. Cosmochim. Acta* **74**, 3476-3493.
- Postma D. (1993) The reactivity of iron oxides in sediments: a kinetic approach. *Geochim. Cosmochim. Acta* **57**, 5027-5034.
- Rancourt D. G. and Ping J. Y. (1991) Voigt-based methods for arbitrary-shape static hyperfine parameter distributions in Mössbauer spectroscopy. *Nucl. Instrum. Methods Phys. Res. Section B* **58**, 85-97.
- Rasmussen B., Muhling J. R. and Fischer W. W. (2020) Greenalite Nanoparticles in Alkaline Vent Plumes as Templates for the Origin of Life. *Astrobiology*.
- Rasmussen B. and Muhling J. R. (2018) Making magnetite late again: evidence for widespread magnetite growth by thermal decomposition of siderite in Hamersley banded iron formations. *Precambrian Res.* **306**, 64-93.
- Rasmussen B., Muhling J. R., Suvorova A. and Krapež B. (2017) Greenalite precipitation linked to the deposition of banded iron formations downslope from a late Archean carbonate platform. *Precambrian Res.* **290**, 49-62.
- Repeta D. J., Simpson D. J., Jorgensen B. B. and Jannasch H. W. (1989) Evidence for anoxygenic photosynthesis from the distribution of bacterio-chlorophylls in the Black Sea. *Nature* **342**, 69-72.

- Robbins L. J., Funk S. P., Flynn S. L., Warchola T. J., Li Z., Lalonde S. V., Rostron B. J., Smith A. J. B., Beukes N. J., de Kock M. O., Heaman L. M., Alessi D. S. and Konhauser K. O. (2019) Hydrogeological constraints on the formation of Palaeoproterozoic banded iron formations. *Nat. Geosci.* **12**, 558-563.
- Roden E. E. (2003) Fe(III) oxide reactivity toward biological versus chemical reduction. *Environ. Sci. Technol.* **37**, 1319-1324.
- Roden E. E. and Urrutia M. M. (1999) Ferrous iron removal promotes microbial reduction of crystalline iron(III) oxides. *Environ. Sci. Technol.* **33**, 1847-1853.
- Roden E. E. and Urrutia M. M. (2002) Influence of biogenic Fe(II) on bacterial crystalline Fe(III) oxide reduction. *Geomicrobiol. J.* **19**, 209-251.
- Roden E. E. and Zachara J. M. (1996) Microbial reduction of crystalline iron(III) oxides: influence of oxide surface area and potential for cell growth. *Environ. Sci. Technol.* **30**, 1618-1628.
- Rout K., Mohapatra M. and Anand S. (2012) 2-Line ferrihydrite: synthesis, characterization and its adsorption behaviour for removal of Pb(II), Cd(II), Cu(II) and Zn(II) from aqueous solutions. *Dalton Trans.* **41**, 3302-3312.
- Royer R. A., Burgos W. D., Fisher A. S., Unz R. F. and Dempsey B. A. (2002) Enhancement of biological reduction of hematite by electron shuttling and Fe(II) complexation. *Environ. Sci. Technol.* **36**, 1939-1946.
- Schad M., Halama M., Bishop B., Konhauser K. O. and Kappler A. (2019) Temperature fluctuations in the Archean ocean as trigger for varve-like deposition of iron and silica minerals in banded iron formations. *Geochim. Cosmochim. Acta* **265**, 386-412.
- Schaedler S., Burkhardt C., Hegler F., Straub K., Miot J., Benzerara K. and Kappler A. (2009) Formation of cell-iron-mineral aggregates by phototrophic and nitrate-reducing anaerobic Fe(II)-oxidizing bacteria. *Geomicrobiol. J.* **26**, 93-103.
- Schwertmann U. and Cornell R. M. (2008) *Iron oxides in the laboratory*. John Wiley & Sons.
- Schwertmann U. and Fechter H. (1982) The point of zero charge of natural and synthetic ferrihydrites and its relation to adsorbed silicate. *Clay Miner.* **17**, 471-476.
- Schwertmann U., Friedl J. and Kyek A. (2004) Formation and properties of a continuous crystallinity series of synthetic ferrihydrites (2- to 6-line) and their relation to FeOOH forms. *Clays Clay Miner.* **52**, 221-226.
- Sergent A.-S., Jorand F. and Hanna K. (2011) Effects of Si-bearing minerals on the nature of secondary iron mineral products from lepidocrocite bioreduction. *Chem. Geol.* **289**, 86-97.
- Shimizu M., Zhou J., Schröder C., Obst M., Kappler A. and Borch T. (2013) Dissimilatory reduction and transformation of ferrihydrite-humic acid coprecipitates. *Environ. Sci. Technol.* **47**, 13375-13384.
- Siever R. (1992) The silica cycle in the Precambrian. *Geochim. Cosmochim. Acta* **56**, 3265-3272.
- Sigg L. and Stumm W. (1981) The interaction of anions and weak acids with the hydrous goethite ( $\alpha$ -FeOOH) surface. *Colloid. Surface.* **2**, 101-117.

- Steinhoefel G., Horn I. and von Blanckenburg F. (2009) Micro-scale tracing of Fe and Si isotope signatures in banded iron formation using femtosecond laser ablation. *Geochim. Cosmochim. Acta* **73**, 5343-5360.
- Steinhoefel G., von Blanckenburg F., Horn I., Konhauser K. O., Beukes N. J. and Gutzmer J. (2010) Deciphering formation processes of banded iron formations from the Transvaal and the Hamersley successions by combined Si and Fe isotope analysis using UV femtosecond laser ablation. *Geochim. Cosmochim. Acta* **74**, 2677-2696.
- Stewart R. H. (2008) *Introduction to physical oceanography*. Robert H. Stewart.
- Stookey L. L. (1970) Ferrozine - a new spectrophotometric reagent for iron. *Anal. Chem.* **42**, 779-781.
- Straub K. L., Rainey F. A. and Widdel F. (1999) *Rhodovulum iodosum* sp. nov. and *Rhodovulum robiginosum* sp. nov., two new marine phototrophic ferrous-iron-oxidizing purple bacteria. *Int. J. Syst. Bacteriol.* **49**, 729-735.
- Strickland J. D. H. and Parsons T. R. (1972) *A practical handbook of seawater analysis*. Fisheries Research Board of Canada, 167, Ottawa.
- Stumm W. and Morgan J. J. (1996) *Aquatic Chemistry: chemical equilibria and rates in natural waters, third ed.* John Wiley & Sons, New York.
- Sun S., Konhauser K. O., Kappler A. and Li Y.-L. (2015) Primary hematite in Neoproterozoic to Paleoproterozoic oceans. *Geol. Soc. Am. Bull.* **127**, 850-861.
- Swedlund P. J., Miskelly G. M. and McQuillan A. J. (2010) Silicic Acid Adsorption and Oligomerization at the Ferrihydrite-Water Interface: Interpretation of ATR-IR Spectra Based on a Model Surface Structure. *Langmuir* **26**, 3394-3401.
- Swedlund P. J. and Webster J. G. (1999) Adsorption and polymerisation of silicic acid on ferrihydrite, and its effect on arsenic adsorption. *Water Res.* **33**, 3413-3422.
- Teixeira N. L., Caxito F. A., Rosière C. A., Pecoits E., Vieira L., Frei R., Sial A. N. and Poitras F. (2017) Trace elements and isotope geochemistry (C, O, Fe, Cr) of the Cauê iron formation, Quadrilátero Ferrífero, Brazil: Evidence for widespread microbial dissimilatory iron reduction at the Archean/Paleoproterozoic transition. *Precambrian Res.* **298**, 39-55.
- ThomasArrigo L. K., Byrne J. M., Kappler A. and Kretzschmar R. (2018) Impact of Organic Matter on Iron(II)-Catalyzed Mineral Transformations in Ferrihydrite-Organic Matter Coprecipitates. *Environ. Sci. Technol.* **52**, 12316-12326.
- ThomasArrigo L. K., Mikutta C., Byrne J. M., Kappler A. and Kretzschmar R. (2017) Iron(II)-Catalyzed Iron Atom Exchange and Mineralogical Changes in Iron-rich Organic Freshwater Flocs: An Iron Isotope Tracer Study. *Environ. Sci. Technol.* **51**, 6897-6907.
- Thompson A., Chadwick O. A., Rancourt D. G. and Chorover, J. (2006) Iron-oxide crystallinity increases during soil redox oscillations. *Geochim. Cosmochim. Acta* **70**, 1710-1727.
- Tomaszewski E. J., Cronk S. S., Gorski C. A. and Ginder-Vogel M. (2016) The role of dissolved Fe(II) concentration in the mineralogical evolution of Fe(hydr)oxides during redox cycling. *Chem. Geol.* **438**, 163-170.

- Tosca N. J., Guggenheim S. and Pufahl P. K. (2016) An authigenic origin for Precambrian greenalite: Implications for iron formation and the chemistry of ancient seawater. *Geol. Soc. Am. Bull.* **128**, 511-530.
- Trendall, A. F. (2002) The significance of iron-formation in the Precambrian stratigraphic record. *Precambrian Sedimentary Environments: a Modern Approach to Depositional Systems, Spec. Publ. Internat. Assoc. Sedimentol.* **33**, 33-66.
- Trendall A. F. and Blockley J. B. (1970) The iron formations of the Hamersley Group, Western Australia, with special reference to the associated crocidolite. *Western Austr. Geol. Surv., Bull.*, **119**, 353 pp.
- Urrutia M. M., Roden E. E., Fredrickson J. K. and Zachara J. M. (1998) Microbial and surface chemistry controls on reduction of synthetic Fe(III) oxide minerals by the dissimilatory iron-reducing bacterium *Shewanella alga*. *Geomicrobiol. J.* **15**, 269-291.
- Walker J. C. (1984) Suboxic diagenesis in banded iron formations. *Nature* **309**, 340-342.
- Wang C., Konhauser K. O. and Zhang L. (2015) Depositional environment of the Paleoproterozoic Yuanjiacun banded iron formation in Shanxi Province, China. *Econ. Geol.* **110**, 1515-1539.
- Wang X., Kubicki J. D., Boily J.-F., Waychunas G. A., Hu Y., Feng X. and Zhu M. (2018) Binding geometries of silicate species on ferrihydrite surfaces. *ACS Earth Space Chem.* **2**, 125-134.
- Wu W., Swanner E. D., Hao L., Zeitvogel F., Obst M., Pan Y. and Kappler A. (2014) Characterization of the physiology and cell-mineral interactions of the marine anoxygenic phototrophic Fe(II) oxidizer *Rhodovulum iodolum* – implications for Precambrian Fe(II) oxidation. *FEMS Microbiol. Ecol.* **88**, 503-515.
- Wu W., Swanner E. D., Kleinhanns I. C., Schoenberg R., Pan Y. and Kappler A. (2017) Fe isotope fractionation during Fe(II) oxidation by the marine photoferrotroph *Rhodovulum iodolum* in the presence of Si - implications for Precambrian iron formation deposition. *Geochim. Cosmochim. Acta* **211**, 307-321.
- Zachara J. M., Kukkadapu R. K., Fredrickson J. K., Gorby Y. A. and Smith S. C. (2002) Biomineralization of poorly crystalline Fe(III) oxides by dissimilatory metal reducing bacteria (DMRB). *Geomicrobiol. J.* **19**, 179-207.
- Zachara J. M., Kukkadapu R. K., Peretyazhko T., Bowden M., Wang C., Kennedy D. W., Moore D. and Arey B. (2011) The mineralogic transformation of ferrihydrite induced by heterogeneous reaction with bio-reduced anthraquinone disulfonate (AQDS) and the role of phosphate. *Geochim. Cosmochim. Acta* **75**, 6330-6349.
- Zegeye A., Bonneville S., Benning L. G., Sturm A., Fowle D. A., Jones C., Canfield D. E., Ruby C., MacLean L. C., Nomosatryo S., Crowe S. A. and Poulton S. W. (2012) Green rust formation controls nutrient availability in a ferruginous water column. *Geology* **40**, 599-602.
- Zheng X.-Y., Beard B. L., Reddy T. R., Roden E. E. and Johnson C. M. (2016) Abiologic silicon isotope fractionation between aqueous Si and Fe(III)-Si gel in simulated Archean seawater: Implications for Si isotope records in Precambrian sedimentary rocks. *Geochim. Cosmochim. Acta* **187**, 102-122.

- Zhou Z., Latta D. E., Noor N., Thompson A., Borch T. and Scherer M. M. (2018) Fe(II)-Catalyzed Transformation of Organic Matter-Ferrihydrite Coprecipitates: A Closer Look Using Fe Isotopes. *Environ. Sci. Technol.* **52**, 11142-11150.
- Zhu J., Pigna M., Cozzolino V., Caporale A. G. and Violante A. (2010) Competitive sorption of copper(II), chromium(III) and lead(II) on ferrihydrite and two organomineral complexes. *Geoderma* **159**, 409-416.

## SUPPLEMENTAL INFORMATION

### **Microbial Fe cycling in a simulated Precambrian ocean environment: Implications for secondary mineral (trans)formation and deposition during BIF genesis**

Manuel Schad<sup>a</sup>, James M. Byrne<sup>a,b</sup>, Laurel K. ThomasArrigo<sup>c</sup>, Ruben Kretzschmar<sup>c</sup>, Kurt O. Konhauser<sup>d</sup>, Andreas Kappler<sup>a</sup>

<sup>a</sup> Geomicrobiology, Center for Applied Geosciences, University of Tuebingen, Tuebingen, Germany

<sup>b</sup> Now: School of Earth Sciences, University of Bristol, Bristol, United Kingdom

<sup>c</sup> Soil Chemistry, Department of Environmental Systems Science, ETH Zürich, Zürich, Switzerland

<sup>d</sup> Department of Earth and Atmospheric Sciences, University of Alberta, Edmonton, Canada

**Manuscript in preparation for publication in:** *Geochimica et Cosmochimica Acta*

## APPENDIX

## 1. SUPPLEMENTARY TEXT S1: CHARACTERIZATION OF PRIMARY MINERAL PRECIPITATES

In addition to mineralogical and aggregate size analysis, primary precipitates (cell-Fe(III) mineral aggregates formed after the first oxidative half cycle) were also analyzed with respect to total organic carbon (TOC) content and mineral surface charge.

The TOC content of the cell-Fe(III) mineral aggregates was quantified using an elemental analyzer (elemental Vario EL; Elementar Analysensysteme GmbH, Langenselbold, Germany). The surface charge of cell-Fe(III) mineral aggregates was determined as zeta-potential using a Zetasizer Nano ZSP (Malvern, Herrenberg, Germany) with Zetasizer Nano Series disposable folded capillary cells (DTS1070, Malvern, Herrenberg, Germany), following previously developed protocols (Schad et al., 2019).

The results of aggregate size analysis, TOC and zeta-potential measurements are summarized in table S1 and figure S1.

Table S1

Summary of extended characteristics of primary precipitates formed during the first oxidative half cycle. Where errors are given, they represent the mean  $\pm$  standard deviation. Values in parentheses represent the median. Where no errors are given, values represent single measurements. Sample size for aggregate size analysis is indicated below in Fig. S1. Sample size for zeta-potential measurements is  $n = 9$ .

	<b>0 mM Si</b>	<b>0.67 mM Si</b>	<b>2.2 mM Si</b>
Aggregate size [ $\mu\text{m}$ ]	$30.45 \pm 21.56$ (25.97)	$17.90 \pm 16.40$ (12.95)	$16.01 \pm 12.72$ (13.23)
TOC [wt.%]	3.01	1.90	2.14
Zeta-potential [mV]	$-13.2 \pm 3.0$	$-19.7 \pm 4.1$	$-16.2 \pm 0.4$



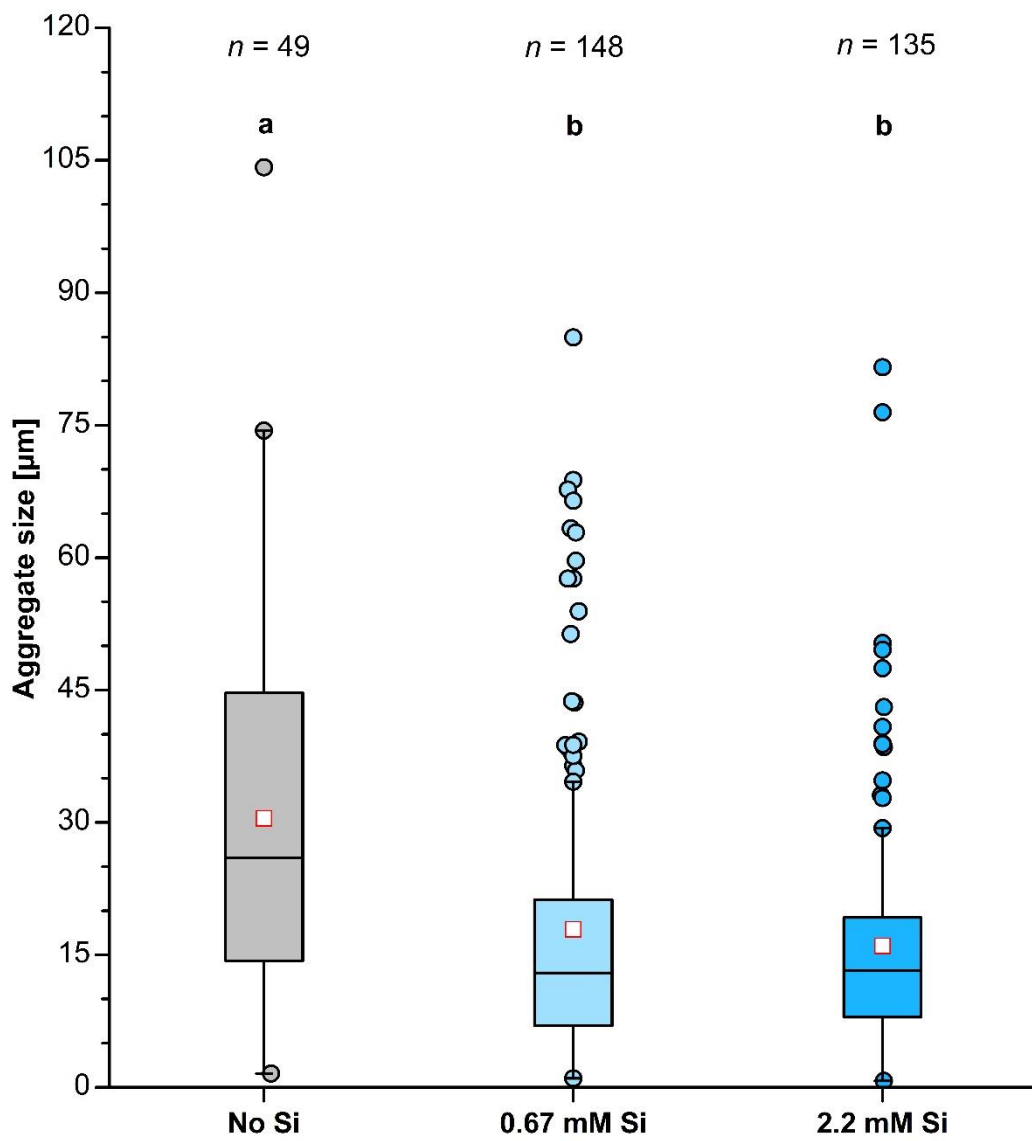


Fig. S1. Aggregate size distribution of cell-Fe(III) mineral aggregates formed by microbial Fe(II) oxidation ~5 mM Fe(II) by *Chlorobium* sp. strain N1 at different Si concentrations. Aggregate size was determined by 2D SEM analysis. Red open square in boxplot is mean value. Lowercase letters mark statistically significant differences in aggregate sizes between different setups.

## 2. SUPPLEMENTARY TEXT S2: ANALYSIS OF *Chlorobium* sp. N1 CELL NUMBERS BY FLOW CYTOMETRY

Samples of *Chlorobium* sp. N1 were prepared by mixing 200  $\mu\text{L}$  sample with 600  $\mu\text{L}$  oxalate solution (2.8 g ammonium oxalate monohydrate and 1.5 g oxalic acid in 0.1 L MilliQ<sup>®</sup> water) and allowed to react for 3 minutes to dissolved the Fe(III) minerals. Then, 1.2 mL 30 mM bicarbonate buffer were added, mixed by shaking and centrifuged for 15 minutes at 14,680  $g$ . After centrifugation the supernatant was decanted and the remaining pellet resuspended in 1 mL 30 mM bicarbonate buffer. Thereafter, BacLight<sup>™</sup> green bacterial stain (Thermo Fisher Scientific Inc., Waltham, Massachusetts, USA) was added at a concentration of 1  $\mu\text{L mL}^{-1}$  and allowed to react for 5 minutes in the dark prior to measurement.

Due to poor mineral dissolution, the first step of the protocol concerned with mineral dissolution was modified. The revised protocol included 100 mM Fe(II) ethylenediammonium sulphate (Fe(II)-EDAS) as catalyst for mineral dissolution. The first step now consisted of mixing 200  $\mu\text{L}$  sample with 540  $\mu\text{L}$  oxalate solution and 60  $\mu\text{L}$  Fe(II)-EDAS. The remaining procedure remained unchanged.

The revised protocol resulted in complete Fe(III) mineral dissolution but poor staining of the bacterial cells. The following steps were carried out in order to improve the staining of the bacterial cells, all of which proofed to be inadequate:

- 1) Changed to strength of the buffer from 30 mM to 10 mM,
- 2) Reduce the  $g$ -forces used during centrifugation to half of the initial protocol to better preserve the cells,
- 3) Vary the amount of buffer used to resuspend the pellet prior to staining the cells (50  $\mu\text{L}$ , 100  $\mu\text{L}$  or 400  $\mu\text{L}$ ),
- 4) Increase the amount of stain used from 1  $\mu\text{L mL}^{-1}$  to 2  $\mu\text{L mL}^{-1}$ ,
- 5) Increase the staining time from 5 minutes to first 10 and finally 15 minutes,
- 6) Change the order of staining and buffer addition, either (1) add the stain directly after centrifugation and only add the buffer afterwards or (2) add some buffer, then add the

stain and let the mixture react for 15 minutes in the dark and then fill to final volume with the buffer.

### 3. SUPPLEMENTARY TEXT S3: MOESSBAUER FITTING PARAMETERS

Table S2

Hyperfine parameters for minerals formed during alternating microbial Fe redox cycles.  $\delta$  – isomer shift,  $\Delta E_Q$  – quadrupole splitting,  $\epsilon$  – quadrupole shift (for sextets only),  $B_{\text{hf}}$  – hyperfine magnetic field, R.A. – relative abundance of the mineral phase at the given temperature,  $\pm$  – error in the relative abundance,  $\chi^2$  indicates the goodness of fit, HWHM – half-width at half-maximum, SRO Fe(III) mineral – short-range ordered Fe(III) mineral, SPM Goethite – superparamagnetic goethite.

Sample	Temp. [K]	Phase	$\delta$ [mm s <sup>-1</sup> ]	$\Delta E_Q$ [mm s <sup>-1</sup> ]	$\epsilon$ [mm s <sup>-1</sup> ]	$B_{\text{hf}}$ [T]	R.A. [%]	$\pm$	$\chi^2$	HWHM [mm s <sup>-1</sup> ]
<b>No silica</b>										
1 <sup>st</sup> oxidative half cycle	77	SRO Fe(III) mineral	0.45	0.70	-	-	13.9	2.8	0.63	0.127
		Goethite	0.50	-	-0.13	46.6	47.4	7.3		
		Poorly ordered magn. component	0.64	-	0.02	35.0	38.7	8.9		
2 <sup>nd</sup> oxidative half cycle	77	Goethite	0.48	-	-0.11	47.0	100.0	0.0	0.77	0.127
3 <sup>rd</sup> oxidative half cycle	77	SPM Goethite	0.66	1.07	-	-	7.5	1.7	0.51	0.127
		Goethite	0.48	-	-0.13	47.0	80.6	4.1		
		Poorly ordered magn. component	0.76	-	-0.62	25.2	11.9	4.0		
1 <sup>st</sup> reductive half cycle	140	SRO Fe(III) mineral	0.33	0.76	-	-	8.7	1.3	0.69	0.127
		Goethite	0.46	-	-0.12	44.4	91.3	1.3		
2 <sup>nd</sup> reductive half cycle	140	Fe(II) mineral phase	1.29	2.91	-	-	1.1	1.0	0.58	0.127
		Goethite	0.45	-	-0.13	44.9	77.0	6.1		
		Poorly ordered magn. component	-0.17	-	-0.64	27.9	21.8	6.1		
3 <sup>rd</sup> reductive half cycle	140	Goethite	0.46	-	-0.13	44.4	75.3	9.5	0.58	0.127
		Poorly ordered magn. component	-0.04	-	-0.69	24.6	24.7	9.5		
<b>Low silica</b>										
1 <sup>st</sup> oxidative half cycle	77	SRO Fe(III) mineral	0.47	0.84	-	-	100.0	0.0	0.56	0.127
2 <sup>nd</sup> oxidative half cycle	77	SRO Fe(III) mineral	0.47	0.84	-	-	74.8	4.9	0.57	0.127
		Goethite	0.42	-	-0.08	45.2	25.2	4.9		
3 <sup>rd</sup> oxidative half cycle	77	SRO Fe(III) mineral	0.47	0.82	-	-	66.7	3.3	0.59	0.127
		Goethite	0.47	-	-0.17	46.6	33.3	3.3		

Table S3 continued

Sample	Temp. [K]	Phase	$\delta$ [mm s <sup>-1</sup> ]	$\Delta E_Q$ [mm s <sup>-1</sup> ]	$\epsilon$ [mm s <sup>-1</sup> ]	$B_{hf}$ [T]	R.A. [%]	$\pm$	$X^2$	HWHM [mm s <sup>-1</sup> ]
1 <sup>st</sup> reductive half cycle	140	SRO Fe(III) mineral	0.41	0.74	-	-	30.5	4.1	0.67	0.127
		Goethite	0.47	-	-0.12	42.8	17.2	4.2		
		Poorly ordered magn. component	0.49	-	-0.28	32.2	52.4	6.2		
2 <sup>nd</sup> reductive half cycle	140	SRO Fe(III) mineral	0.28	0.95	-	-	15.4	4.6	0.62	0.127
		Fe(II) mineral phase	1.40	2.37	-	-	5.7	4.1		
		Goethite	0.46	-	-0.17	42.7	78.9	5.7		
3 <sup>rd</sup> reductive half cycle	140	SRO Fe(III) mineral	0.11	0.75	-	-	18.1	6.0	0.50	0.127
		Fe(II) mineral phase	1.40	2.37	-	-	9.1	5.5		
		Goethite	0.50	-	-0.09	44.6	72.8	7.4		
<b>High silica</b>										
1 <sup>st</sup> oxidative half cycle	77	SRO Fe(III) mineral	0.47	0.86	-	-	100.0	0.0	0.54	0.127
2 <sup>nd</sup> oxidative half cycle	77	SRO Fe(III) mineral	0.47	0.85	-	-	100.0	0.0	0.64	0.127
3 <sup>rd</sup> oxidative half cycle	77	SRO Fe(III) mineral	0.47	0.84	-	-	100.0	0.0	0.66	0.127
1 <sup>st</sup> reductive half cycle	140	SRO Fe(III) mineral	0.44	0.78	-	-	88.8	1.7	0.74	0.127
		Fe(II) mineral phase	1.23	2.70	-	-	11.2	1.7		
2 <sup>nd</sup> reductive half cycle	140	SRO Fe(III) mineral	0.43	0.70	-	-	59.5	5.7	0.56	0.127
		Fe(II) mineral phase	1.23	2.87	-	-	40.5	5.7		
3 <sup>rd</sup> reductive half cycle	140	SRO Fe(III) mineral	0.39	0.65	-	-	51.0	5.5	0.56	0.127
		Fe(II) mineral phase	1.22	2.81	-	-	49.0	5.5		

---

#### 4. SUPPLEMENTARY TEXT S4: STATISTICAL ANALYSES OF WET GEOCHEMICAL RESULTS

Since the number Fe cycles seemed to influence the kinetics of the microbial Fe redox transformation, we wanted to know if observed changes in rates were significant.

For the setup without Si the maximum Fe(II) oxidation rate of the last oxidative half cycle was significantly lower than during the second oxidative half cycle (one-way ANOVA,  $F = 6.558$ ,  $df = 2, 6$ ,  $P = 0.031$ , Tamhane post-hoc test,  $\alpha = 0.05$ ). Similarly the maximum Fe(III) reduction rate of the last reductive half cycle was significantly higher than during the previous two reductive half cycles (one-way ANOVA,  $F = 28.647$ ,  $df = 2, 6$ ,  $P = 0.001$ , Tukey HSD post-hoc test,  $\alpha = 0.05$ ).

For the low Si setup there were no clear trends regarding increasing or decreasing maximum Fe(II) oxidation rates with an increasing number of microbial Fe cycles. However, statistical analysis suggested that the maximum Fe(II) oxidation rate of the second oxidative half cycle was significantly lower than for the previous and for the following oxidative half cycle (one-way ANOVA,  $F = 26.623$ ,  $df = 2, 6$ ,  $P = 0.001$ , Tukey HSD post-hoc test,  $\alpha = 0.05$ ). Conversely, the maximum Fe(III) reduction rates showed a significant increase during the last reductive half cycle (one-way ANOVA,  $F = 18.989$ ,  $df = 2, 6$ ,  $P = 0.003$ , Tukey HSD post-hoc test,  $\alpha = 0.05$ ).

Finally, for the high Si setup the maximum Fe(II) oxidation rate during the final oxidative half cycle was significantly higher than during the previous oxidative half cycle (one-way ANOVA,  $F = 363.245$ ,  $df = 2, 5$ ,  $P < 0.001$ , Tamhane post-hoc test,  $\alpha = 0.05$ , outlier ( $2.06 \text{ mM d}^{-1}$ ) removed from analysis for the third oxidative half cycle). Similarly, the maximum Fe(III) reduction rates increased significantly throughout the experiment (one-way ANOVA,  $F = 2912.535$ ,  $df = 2, 5$ ,  $P < 0.001$ , Tamhane post-hoc test,  $\alpha = 0.05$ , outlier ( $1.27 \text{ mM d}^{-1}$ ) removed from analysis for the second reductive half cycle).

Having found a statistically significant influence of the number of microbial Fe cycles on the maximum Fe(II) oxidation and Fe(III) reduction rates, we further wanted to know if different Si concentrations would have a similar effect. Therefore, we compared maximum rates of all three setups (no Si, low Si and high Si) during the first, second and third microbial Fe cycle.

For the first oxidative half cycle no statistically significant difference was found (one-way ANOVA,  $F = 6.778$ ,  $df = 2, 6$ ,  $P = 0.029$ , Tamhane post-hoc with  $\alpha = 0.05$  showed no difference between Si concentrations). Conversely, differing Si concentrations had a significant effect during microbial Fe(III) reduction: the setup with high Si had the lowest maximum Fe(III) reduction rate and the low Si setup the highest (one-way ANOVA,  $F = 31.737$ ,  $df = 2, 6$ ,  $P = 0.001$ , Tukey HSD post-hoc test,  $\alpha = 0.05$ ).

A similar effect of Si on the maximum rate was observed for the second oxidative half cycle where all three Si concentrations differed significantly: the setup without Si showed the highest maximum Fe(II) oxidation rate and the low Si setup showed the lowest maximum Fe(II) oxidation rate (one-way ANOVA,  $F = 155.453$ ,  $df = 2, 6$ ,  $P < 0.001$ , Tukey HSD post-hoc test,  $\alpha = 0.05$ ). During the second reductive half cycle the maximum Fe(III) reduction rate of the high Si setup was significantly higher than for the setup without or with low Si (one-way ANOVA,  $F = 12.196$ ,  $df = 2, 6$ ,  $P = 0.008$ , Tamhane post-hoc test,  $\alpha = 0.05$ ).

For the last Fe redox cycle both the maximum Fe(II) oxidation (one-way ANOVA,  $F = 175.862$ ,  $df = 2, 6$ ,  $P < 0.001$ , Tukey HSD post-hoc test,  $\alpha = 0.05$ ) and the maximum Fe(III) reduction rate (one-way ANOVA,  $F = 778.150$ ,  $df = 2, 6$ ,  $P < 0.001$ , Tukey HSD post-hoc test,  $\alpha = 0.05$ ) of the high Si setup were significantly higher than for the no and low Si setups.

## 5. SUPPLEMENTARY TEXT S5: LIGHT AND FLUORESCENT MICROSCOPY SECOND MICROBIAL FE CYCLE

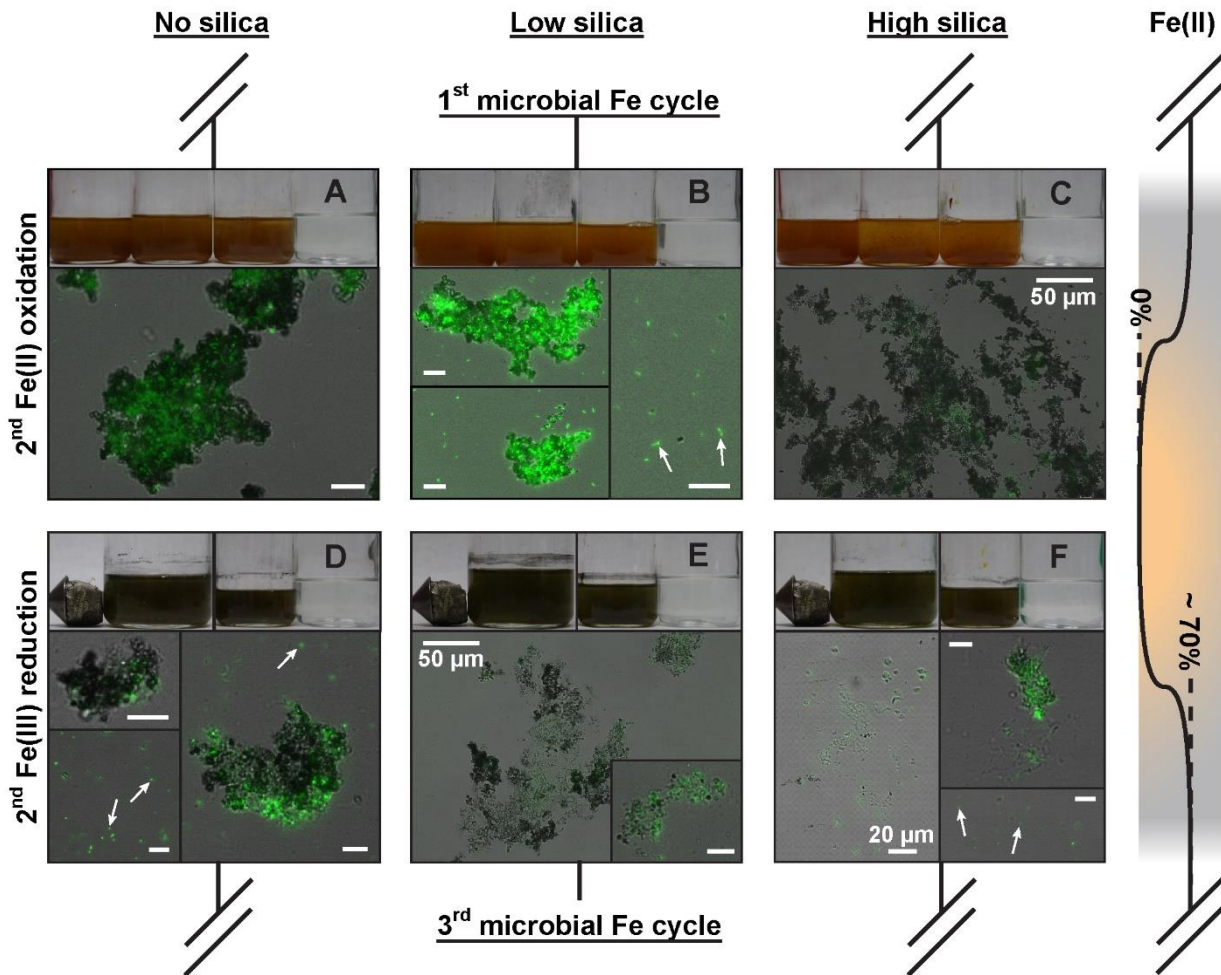


Fig. S2. Overlay of fluorescent and light microscopy images showing cells (green) and mineral particles (dark) over the course of the second microbial Fe cycle. The different panels show the oxidative half cycle (odd row number) and the reducing half cycle (even number) for Si-free (first column), low Si (second column) and high Si (last column) setups. Orange colors mark oxidizing conditions, grey colors reducing conditions. The magnet in panels D, E and F was placed next to the bottles in order to test for the presence of magnetic minerals like magnetite. Unless stated otherwise all scale bars are 10  $\mu\text{m}$ .



## 6. SUPPLEMENTARY TEXT S6: SCANNING ELECTRON MICROSCOPY (SEM) SECOND MICROBIAL FE CYCLE

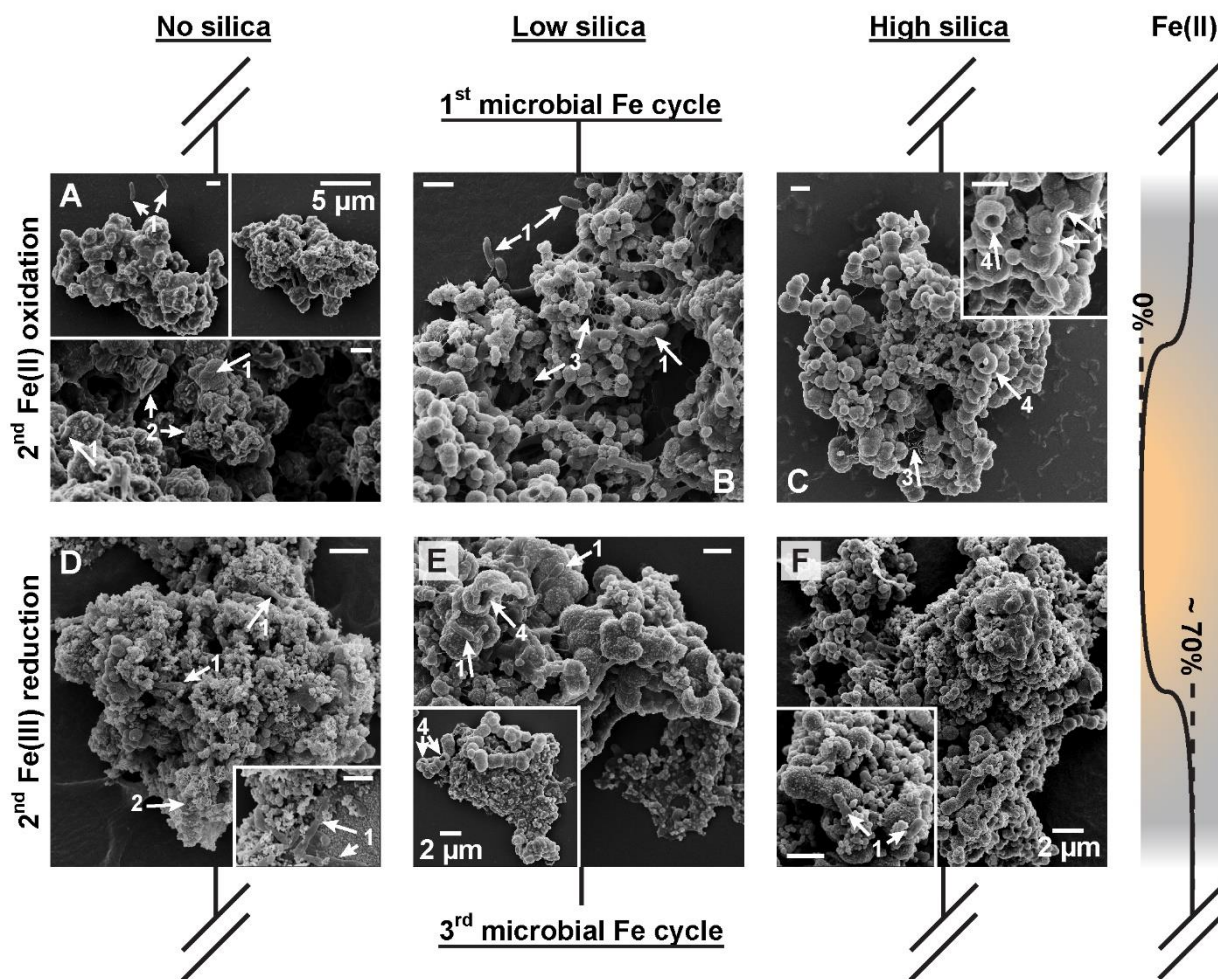
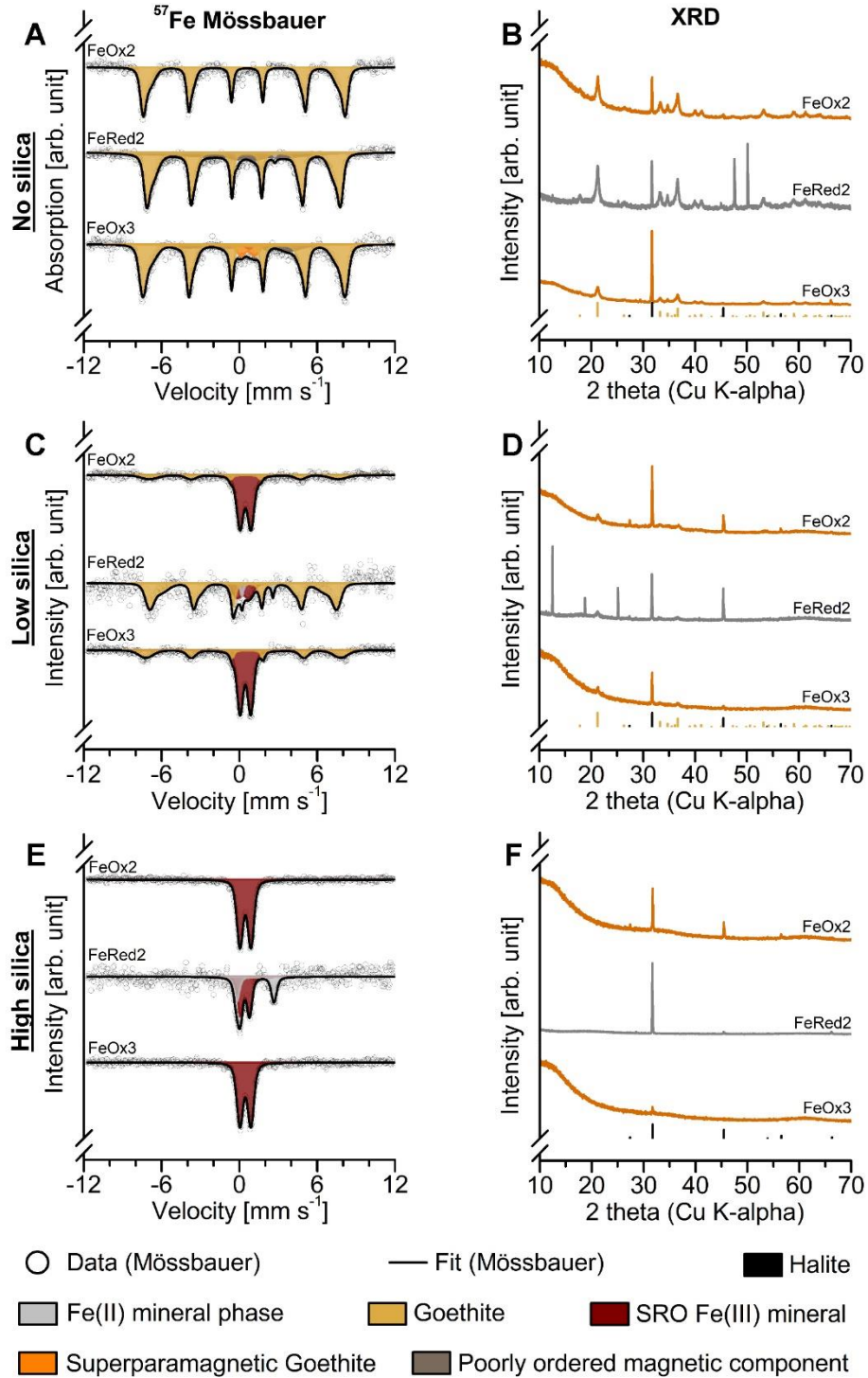


Fig. S3. SEM micrographs of cell-mineral aggregates formed during the second microbial Fe cycle. The different panels show the oxidative half cycle (odd row number) and the reducing half cycle (even row number) for Si-free (first column), low Si (second column) and high Si (last column) setups. Orange colors mark oxidizing conditions, grey colors reducing conditions. Arrows labelled with number 1 indicate cells, arrows labelled with number 2 higher crystalline parts of the cell-minerals aggregates, arrows labelled with number 3 remains of putative exopolysaccharides and arrows labelled with number 4 hollow mineral spheres. Unless stated otherwise all scale bars are 1 μm.

## 7. SUPPLEMENTARY TEXT S7: MINERALOGICAL ANALYSES OF SECOND MICROBIAL FE CYCLE AND THIRD OXIDATIVE HALF CYCLE; DEVELOPMENT OF MOESSBAUER HYPERFINE PARAMETERS OVER TIME



---

← Fig. S4.  $^{57}\text{Fe}$  Moessbauer spectra and X-ray diffractograms of mineral products taken at the of the oxidative and reductive half cycles. Results are complementary to mineralogical data shown in the main text. Panels A and B show the no Si setup, C and D the low Si setup and E and F the high Si setup. Orange colors in the X-ray diffractograms mark mineral products of oxidative half cycles. Grey colors mark mineral products of the reductive half cycles.

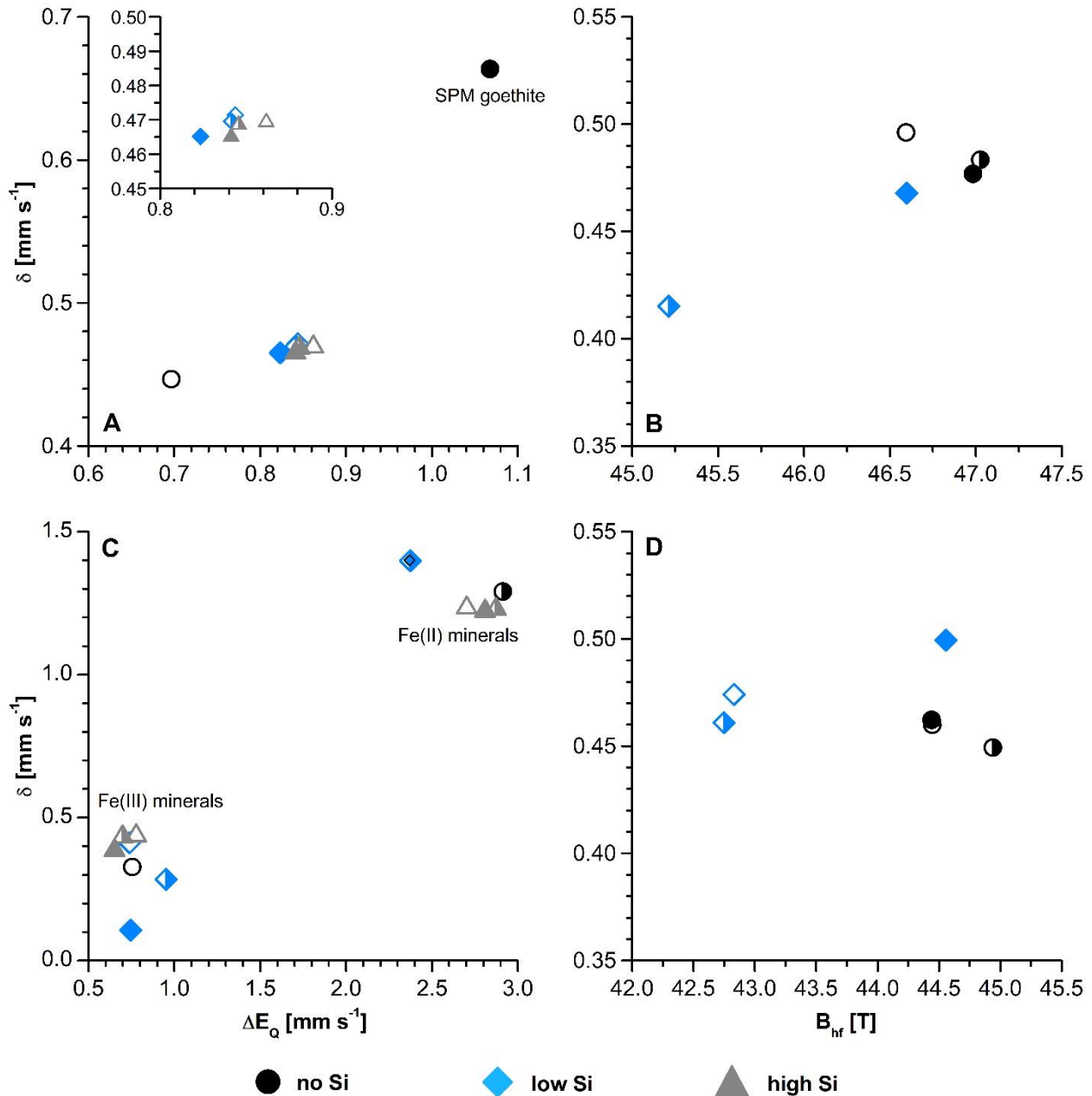


Fig. S5. Moessbauer spectroscopic analysis of Fe(III) (oxyhydr)oxides and Fe(II) minerals formed during microbial Fe cycling. (A) shows the isomer shift ( $\delta$ ) relative to the quadrupole splitting ( $\Delta E_Q$ ) of paramagnetic mineral phases (such as short-range ordered Fe(III) (oxyhydr)oxides) formed during oxidative half cycle. Inset shows the hyperfine parameters of minerals formed in the presence of either low or high concentrations at a smaller scale. (B) shows the center shift relative to the mean magnetic hyperfine field ( $B_{hf}$ ) for magnetically ordered (highly crystalline) Fe(III) (oxyhydr)oxides formed during oxidative half cycle. (C) shows the center shift relative to the quadrupole splitting for paramagnetic Fe(III) (oxyhydr)oxides and Fe(II) minerals formed during reductive half cycles. Note the separation between Fe(III) (low  $\Delta E_Q$ ) and Fe(II) (high  $\Delta E_Q$ ) mineral phases. (D) shows the center shift relative to the mean magnetic hyperfine field for magnetically ordered Fe(III) (oxyhydr)oxides formed during reductive half cycles. Black circles mark minerals formed in the absence of Si. Blue diamonds mark minerals formed in the presence of low concentrations of Si. Grey triangles mark minerals formed in the presence of high concentrations of Si. Open symbols: minerals formed during the first microbial Fe cycle; half-filled symbols: minerals formed during the second microbial Fe cycle; closed symbols: minerals formed during the third microbial Fe cycle.  $^{57}\text{Fe}$  Moessbauer data for minerals formed during oxidative half cycle was acquired at 77 K. Data for minerals formed during reductive half cycles was acquired at 140 K.

## **8. SUPPLEMENTARY TEXT S8: CALCULATIONS OF CELL-Fe(III) MINERAL AGGREGATE SETTLING VELOCITY AND WATER COLUMN RESIDENCE TIME**

Calculations of the cell-Fe(III) mineral aggregate settling velocity and water column residence time will be made available on <http://pangaea.de>.

### **REFERENCES**

Schad M., Halama M., Bishop B., Konhauser K. O. and Kappler A. (2019) Temperature fluctuations in the Archean ocean as trigger for varve-like deposition of iron and silica minerals in banded iron formations. *Geochim. Cosmochim. Acta* **265**, 386-412.



## General conclusions and outlook

Banded Iron Formations (BIFs) are frequently used to reconstruct the environment on the Archean to Paleoproterozoic Earth. Major deposits were formed during the Neoproterozoic and early Paleoproterozoic, a period in time just before Earth witnessed the first significant oxygenation of the atmosphere-ocean system, the Great Oxidation Event (GOE, e.g. Lyons et al., 2014). BIFs can inform about this critical turning point in Earth's history and the environmental changes during the time leading up to it, provided not only individual environmental factors and biological and abiotic mechanisms controlling their deposition are understood but also their mutual interactions (see e.g. Bekker et al., 2014; Konhauser et al., 2017; Schad et al., 2019, for reviews).

The goal of this PhD thesis was to better constrain how a continuum of factors and mechanisms including: (1) the geochemistry (i.e. nutrient availability) and physical properties (e.g. temperature) of the early ocean, (2) microbial processes (e.g. anoxygenic photoautotrophic Fe(II) oxidation and microbial Fe(III) reduction), and, (3) diagenetic and low-grade metamorphic processes taking place during the formation and transformation of primary Fe(III) mineral precipitates, would have influenced the genesis of BIFs. Specifically, the interdependence and interplay of these factors and mechanisms was the focus of this thesis. To this end we focused on laboratory studies, including simulated low-grade metamorphism and microbial (co-)cultivation experiments, which allowed to specifically manipulate and control individual factors and mechanisms. Furthermore, we extrapolated our results to BIF depositional environments and compared our findings with existing models for BIF genesis developed based on the analysis of the BIF rock record to validate our findings.

## 1. INFLUENCE OF LOW-GRADE METAMORPHISM ON NUTRIENT CYCLING

In **chapter 1** we quantified the influence of low-grade metamorphism (170°C, 1.2 kbar) on the post-depositional remobilization of phosphate ( $\text{PO}_4^{3-}$ ) from primary Fe(III) (oxyhydr)oxides. We showed that the metamorphic mineral transformation pathway was driven by the organic carbon ( $\text{C}_{\text{org}}$ ) reactivity. In the absence of  $\text{C}_{\text{org}}$  or in the presence of complex  $\text{C}_{\text{org}}$ , hematite was the main metamorphic Fe mineral product. Conversely, in the presence of highly reactive glucose as biomass proxy, magnetite and vivianite were formed. Although low-grade metamorphism as a function of  $\text{C}_{\text{org}}$  reactivity had a profound impact on the metamorphic mineral transformation, its influence on  $\text{PO}_4^{3-}$  remobilization was minor and a maximum <10 mol.%  $\text{PO}_4^{3-}$  was remobilized. In a comparable study, Robbins et al. (2015) found similarly low metamorphic remobilization of Zn and Ni. These results thus collectively emphasize that BIFs record ancient seawater composition with high fidelity. Furthermore, the low extent of  $\text{PO}_4^{3-}$  remobilization during simulated low-grade metamorphism supports a  $\text{PO}_4^{3-}$ -poor Archean to early Paleoproterozoic ocean (e.g. Hao et al., 2020b; Jones et al., 2015). This low  $\text{PO}_4^{3-}$ -bioavailability would have limited early net primary production to fractions of the modern level, thus slowing the aerial expansion of early cyanobacteria down and limiting their ability to oxygenate the atmosphere and surface ocean (e.g. Hao et al., 2020b; Laakso and Schrag, 2018; Reinhard et al., 2017). Consequently, the role of early cyanobacteria in the deposition of major BIFs might have been equally limited. Instead,  $\text{PO}_4^{3-}$ -limiting conditions would have favored anoxygenic photoautotrophic Fe(II)-oxidizing bacteria (photoferrotrophs; Jones et al., 2015), whose metabolic activity would have resulted in the deposition of BIFs. Only with the increase in (oxidative) continental weathering towards the Neoproterozoic-Paleoproterozoic boundary and the resulting increase in  $\text{PO}_4^{3-}$  fluxes to the ocean would the importance of early cyanobacteria for the deposition of BIFs have increased (e.g. Hao et al., 2020a; Hao et al., 2020b; Kendall et al., 2015; Konhauser et al., 2011).

## 2. CONSEQUENCES OF TEMPERATURE CYCLING FOR THE ORIGIN OF THE BANDING IN BIFS

Having established the likelihood of photoferrotrophy as major driver for the deposition of BIFs during the Archean eon and probably also during the early Paleoproterozoic in **chapter 1**,



we next examined how temperature would have influenced the metabolic activity of photoferrotrophs during the deposition of BIFs (**chapter 2**). Temperature is an important environmental factor modulating the activity of microbes and the abiotic precipitation of minerals in modern environments. Posth et al. (2008) suggested that temperature fluctuations in the Precambrian ocean could have acted as unifying trigger for the alternating deposition of Fe- and Si-rich layers in BIFs, thus explaining their characteristic banding. We verified this model in a series of experiments conducted under conditions representative for an Archean ocean (high Fe and Si), including: a continuous growth experiment (>160 days), experiments determining the influence of temperature on Fe(II) oxidation by our model photoferrotroph (*Rhodovulum iodosum*), and experiments examining abiotic Si precipitation kinetics. Our results suggest that *R. iodosum* was metabolically active during warm periods (26°C), resulting in the precipitation of primary cell-Fe(III) mineral aggregates while most of the dissolved Si stayed in solution. During cold periods (5°C) the activity of *R. iodosum* was muted and instead Si was precipitated abiotically. Although the alternating deposition of Fe- and Si-rich layers was driven by temperature fluctuations, it was the co-precipitation of C<sub>org</sub> with primary Fe(III) (oxyhydr)oxides which ultimately caused the separation between Fe and Si. C<sub>org</sub> either occupied functional surface groups necessary for Si sorption or caused changes in the characteristics of the primary Fe(III) (oxyhydr)oxides leading to the electrostatic repulsion of Si. Extrapolation of our experimental data onto the ca. 2.6-2.4 Ga Hamersley Basin, Western Australia, suggests that temperature fluctuations explain the characteristic lamination of BIFs on the microband level (millimeter to sub-millimeter scale; Trendall, 2002; Trendall and Blockley, 1970). However, higher levels of banding such as meso- (up to several centimeter thickness) and macrobands (meter to several meter thickness) require mechanisms that influence microbial activity and abiotic Si precipitation on longer timescales. Such mechanisms include but are not limited to (1) fluctuations in hydrothermal activity resulting in variations of bioavailable Fe(II) (e.g. Bekker et al., 2014), (2) rising or falling sea-levels, (3) prolonged subaerial volcanism suppressing microbial Fe(II) oxidation, (4) glacials and interglacials, favoring either abiotic Si precipitation or microbial Fe(II) oxidation and (5) Milankovitch forcing, leading to climate oscillations at timescales of hundreds of thousands to millions of years (Lantink et al., 2019).

### 3. INFLUENCE OF MICROBIAL FE CYCLING ON THE COMPOSITION OF PRIMARY BIF SEDIMENTS

Based on the results of **chapter 2**, the objective of **chapter 3** was to determine how primary cell-Fe(III) mineral aggregates would have been modified by microbial Fe(III) reduction while settling through the water column. Specifically, we wanted to examine the effect of repeated and dynamic microbial Fe redox cycling on the primary BIF mineral identity and the formation and properties of secondary minerals. A study by Konhauser et al. (2005) suggested that under ideal conditions as much as 70% of the initially formed Fe(III) could have been reduced and cycled back into the water column. However, it remains unresolved how and to which extent photoferrotrophy and microbial Fe(III) reduction would have interacted during microbial Fe cycling in the water column. Therefore, we co-cultivated the marine photoferrotroph *Chlorobium* sp. N1 with a marine Fe(III)-reducing enrichment culture under conditions relevant for an Archean to early Paleoproterozoic ocean. Our results suggest that photoferrotrophy and microbial Fe(III) reduction formed a highly dynamic microbial Fe redox cycle. Microbial Fe(II) oxidation resulted in the formation of cell-Fe(III) mineral-Si aggregates, while microbial Fe(III) reduction caused the reductive dissolution of these aggregates with concomitant release of Si and C<sub>org</sub>. Mineralogical analysis suggest the formation of goethite and/or short-range ordered (SRO) Fe(III) minerals such as ferrihydrite during Fe(II) oxidation, where increasing Si concentrations favored the formation of SRO Fe(III) minerals. During microbial Fe(III) reduction the Fe(III) minerals were partially reduced, resulting in the formation of dissolved Fe(II) (Fe<sup>2+</sup>) and a Fe(II) mineral phase consisting of siderite and/or an Fe(II)-silicate. The extent of Fe(II) mineral formation increased with increasing Si concentration. Independent of the Si concentration no magnetite formation was observed. The formation of magnetite was likely precluded by the high dynamicity of our experimental system, the combined inhibitory effect of co-precipitated C<sub>org</sub> and Si and the complexation of Fe<sup>2+</sup> by C<sub>org</sub> during Fe(III) reduction. Collectively, these results suggest that water column Fe cycling in the Archean to early Paleoproterozoic ocean was highly dynamic and resulted in the co-deposition of a ferrihydrite-Si composite and a mixed Fe(II) mineral phase. Magnetite, however, was likely formed during the later occurring sediment diagenesis, probably facilitated by the release of Si and C<sub>org</sub> from cell-mineral aggregates in the water column and the longer timescale of sediment diagenesis. This also confirms previous studies which suggested that ferrihydrite (hematite) and siderite as well as Fe(II)-silicates were

either formed in the water column or are of early diagenetic origin (e.g. Beukes and Gutzmer, 2008; Heimann et al., 2010; Kaufman et al., 1990; Muhling and Rasmussen, 2020; Pecoits et al., 2009; Sun et al., 2015), whereas magnetite was formed later during the paragenetic sequence (e.g. Beukes and Gutzmer, 2008) and references therein; Pecoits et al., 2009).

#### **4. CYCLES WITHIN CYCLES – INFLUENCE OF NUTRIENT, TEMPERATURE AND MICROBIAL FE CYCLING ON THE GENESIS OF BIFS**

Collectively, the results of this PhD study highlight the complexity underlying the genesis of Neoproterozoic to early Paleoproterozoic BIFs, showing that they are the product of the interplay and interdependence between environmental factors (e.g., nutrient availability, temperature), microbial processes (photoferrotrophy, microbial Fe(III) reduction) and low-grade metamorphism. Furthermore, the results of this thesis have several important implications for some of the key aspects concerning BIF genesis and some of their key characteristics:

##### **(1) The fidelity with which BIFs record ancient seawater composition.**

The results in **chapter 1**, in communion with a similar study by Robbins et al. (2015), suggest that low-grade metamorphism (170°C, 1.2 kbar) had limited influence on the post-depositional mobility of nutrients like  $\text{PO}_4^{3-}$  and biologically important trace elements like Ni and Zn. Therefore, BIFs record ancient seawater composition with high fidelity, which makes them well-suited for paleo-environmental reconstructions.

##### **(2) The mechanism responsible for the initial deposition of BIFs.**

The results in **chapter 1** support a  $\text{PO}_4^{3-}$ -poor Archean to early Paleoproterozoic ocean (Hao et al., 2020b; Jones et al., 2015). Even when considering the remobilization of up to 10% of the initially immobilized  $\text{PO}_4^{3-}$ , seawater  $\text{PO}_4^{3-}$  concentrations would not have exceeded 0.61  $\mu\text{M}$ . These low  $\text{PO}_4^{3-}$  concentrations would have favored the metabolic activity of photoferrotrophs over early cyanobacteria, due to their lower nutrient requirements (Jones et al., 2015). Consequently, Fe(II) oxidation by photoferrotrophs resulting in the formation of poorly soluble Fe(III) (oxyhydr)oxides was likely the main mechanism for the formation of primary Fe-bearing BIF minerals. Even increased (oxidative) weathering towards the Neoproterozoic/Paleoproterozoic boundary and resulting higher  $\text{PO}_4^{3-}$  fluxes to the ocean would not necessarily have resulted in a

waning importance of photoferrotrophy for the deposition of BIFs. Photoferrotrophs are well adapted to low-light conditions and even when forced deeper into the water column, they would still have been able to oxidize sufficient quantities of  $\text{Fe}^{2+}$  to explain the deposition of BIFs (Kappler et al., 2005). Only when the oxygenation of the ocean exceeded depths of ~100 m photoferrotrophy would have become insignificant for the deposition of BIFs.

### **(3) The nature and composition of primary BIF sediments.**

Fe(II) oxidation by photoferrotrophs in **chapter 2 and 3** resulted in the formation of cell-Fe(III) mineral aggregates. The mineralogy consisted of a mixture of SRO Fe(III) minerals (e.g. ferrihydrite) and goethite at Si concentrations approaching the lower limit of putative seawater Si concentrations (0.67 mM, saturation with respect to cristobalite; Maliva et al., 2005; Siever, 1992). At Si concentrations approaching the upper limit of putative seawater Si concentrations during Archean to early Paleoproterozoic (2.2 mM, saturation with respect to amorphous silica), only SRO Fe(III) minerals were formed. This is consistent with previous studies which suggested Fe(III) (oxyhydr)oxides as precursor minerals in BIFs (Ahn and Buseck, 1990; Beukes and Gutzmer, 2008; Pecoits et al., 2009; Sun et al., 2015) Additionally, the co-deposition of Si with the cell-Fe(III) mineral aggregates formed in our experiments, especially at high Si concentrations, also supports a Si-bearing ferrihydrite as primary BIF mineral phase (Alibert, 2016; Fischer and Knoll, 2009).

The results presented in **chapter 3** further suggest that the primary cell-Fe(III) mineral aggregates formed by photoferrotrophs would have provided a viable substrate for microbial Fe(III) reduction, thus enabling microbial Fe cycling already in the water column. Individual cell-Fe mineral aggregates could have been cycled up to 6 times before being deposited on the seafloor, making microbial Fe cycling an important process during the formation of primary BIF sediments. Microbial Fe cycling and accompanying mineral transformations would have caused the release of Si and  $\text{C}_{\text{org}}$  from cell-Fe mineral aggregates and the formation of a mixed Fe(II) mineral phase, comprising of siderite and/or Fe(II)-silicates. Therefore, the primary BIF sediments likely consisted of a mixture of a ferrihydrite-Si composite and Fe(II) minerals. While siderite and Fe(II)-silicate do not necessarily represent primary seawater precipitates as advocated by previous studies (see e.g. Beukes et al., 1990; Kaufman et al., 1990; Klein and Beukes, 1989

for siderite, Johnson et al., 2018; Muhling and Rasmussen, 2020 for Fe(II)-silicates), they might have been an important constituent of the primary BIF sediments.

#### **(4) The characteristic lamination of BIFs.**

The results of the study conducted in **chapter 2** suggest that the alternating deposition of Fe- and Si-rich layers on the millimeter to sub-millimeter scale (microbands) represents a primary sedimentary feature and is the result of biannual temperature cycles. These microbands could thus also be considered to be chemical varves, where the combination of one Fe-rich and one Si-rich band equals one year of precipitation (Trendall, 2002). However, given the high affinity of Si to adsorb onto Fe(III) (oxyhydr)oxides (e.g. Davis et al., 2002; Sigg and Stumm, 1981; Swedlund and Webster, 1999) a mechanism for its deposition separate from Fe(III) (oxyhydr)oxides is required. In this regard our results further suggest that  $C_{org}$  which was co-precipitated with the Fe(III) (oxyhydr)oxides (partially) prevented the adsorption of Si.

However, our results obtained in **chapter 3** indicate that the efficiency with which  $C_{org}$  prevents Si adsorption is dependent on the Si concentration. Less Si was adsorbed to Fe(III) (oxyhydr)oxides at lower Si concentrations, suggesting that the separation between Fe- and Si-rich bands would have been particularly pronounced at lower seawater Si concentrations. Additionally, we found that the reductive dissolution of the Fe(III) (oxyhydr)oxides during microbial Fe(III) reduction caused the release of Si back into solution, a process which has previously been inferred to explain the development of the characteristic banding of BIFs during sediment diagenesis (e.g. Fischer and Knoll, 2009; Hashizume et al., 2016; Nealson and Myers, 1990). In contrast to these previous studies, we argue that the release of Si from primary Fe(III) (oxyhydr)oxides already in the water column would have re-enforced the  $C_{org}$ -driven separation between Fe- and Si-rich bands and severely limited their co-precipitation. That said, we cannot exclude further remobilization of Si as a consequence of microbial Fe(III) reduction during sediment diagenesis.

#### **(5) The low $C_{org}$ content of BIFs.**

One of the long-standing paradoxes of BIF genesis is, that despite their apparent biogeneity, with <0.5 wt.% (Gole and Klein, 1981)  $C_{org}$  is conspicuously absent from the rock record. There are several potential explanations for this phenomenon including the degradation of  $C_{org}$  during microbial Fe(III) reduction, fermentation or methanogenesis (e.g. Konhauser et al.,

2005), release of  $C_{org}$  from primary ferrihydrite during the transformation to hematite (Jelavić et al., 2020) or the decomposition of  $C_{org}$  during low-grade metamorphic processes (e.g. Halama et al., 2016; Köhler et al., 2013; Posth et al., 2013). Our results in **chapter 3** suggest that depending on the Si concentration, the initial association of  $C_{org}$  with Fe(III) (oxyhydr)oxides might already have been limited. At lower Si concentrations  $C_{org}$  would have restricted the co-precipitation of Si (see point 4), while the reverse would have occurred at high Si concentrations. Furthermore, our experimental results suggest that some  $C_{org}$  would have been released from cell-Fe mineral aggregates during microbial Fe cycling in the water column, thus limiting the extent to which Fe minerals and  $C_{org}$  were co-deposited in primary BIF sediments. Our results, therefore, offer a potential explanation for the low  $C_{org}$  content in BIFs.

## 5. THE WAY FORWARD – OUTLOOK AND FUTURE EXPERIMENTS

This PhD thesis highlighted the complex interplay and interdependence of environmental factors, microbial activity and abiotic sediment diagenesis and low-grade metamorphism. This created an equally complex product consisting of Fe minerals, Si and  $C_{org}$ . Paradoxically, the latter is virtually absent from the BIF rock record; despite being identified as a key factor for BIF genesis in the work presented here.  $C_{org}$  determined the mineral transformation pathway in our low-grade metamorphism experiments, it was identified as ultimately causing the separation between Fe- and Si-rich bands in BIFs. Together with Si,  $C_{org}$  controlled the Fe mineral (trans)formations during microbial Fe cycling. Recent studies by Konhauser et al. (2018) and Bishop et al. (2019) further add to the intricacy revolving around  $C_{org}$  during BIF genesis. These studies suggest that nutrients and trace elements assimilated by phytoplankton or adsorbed onto cell surfaces rather than the primary mineralogy explain the trace elements stoichiometry of BIFs. Therefore, the way forward must undoubtedly be to better understand the fate of  $C_{org}$  during the genesis of BIFs while considering its association with Si and Fe minerals.

The goal of future experiments should be to better understand the composition of the primary precipitate formed. Our results indicate that the co-precipitation of Si and  $C_{org}$  is dependent on the Si concentration, where at lower Si concentrations more  $C_{org}$  is co-precipitated with Fe(III) minerals and at higher Si concentrations more Si than  $C_{org}$  is co-precipitated with the Fe(III) minerals. Performing experiments with defined concentrations of Fe(III), Si and  $C_{org}$

would help to determine to which extent they are co-precipitated given specific (aqueous) ratios. In addition to  $C_{\text{org}}$  and Si concentrations, the Fe concentration should be varied as well. Due to experimental restrictions, laboratory experiments meant to simulate Precambrian ocean conditions are often performed at elevated concentrations of Fe. For example the microbial cultivation experiments conducted in this PhD thesis were performed at Fe(II) concentrations of ~5 mM, which is approximately one order of magnitude higher than the maximum concentrations assumed for the early ocean (0.03-0.5 mM; Holland, 1973; Morris, 1993). Consequently, this shifts the composition of the precipitate from being Si-dominated (which would have been the case in the early ocean) to being Fe-dominated. This has potentially important implications for the extent of  $C_{\text{org}}$ -Fe mineral co-precipitation, the affinity of nutrients and trace elements to sorb onto this primary precipitate as well as its reactivity during (microbial) transformation. Constraining the extent of  $C_{\text{org}}$ -Fe(III) mineral co-precipitation in dependence of the Si concentration will not only allow us to draw conclusions on the extent to which both contributed to the trace element stoichiometry of BIFs but also on the further transformation of the Fe minerals and  $C_{\text{org}}$  themselves. For example processes like microbial Fe(III) reduction are critically dependent on the availability of  $C_{\text{org}}$  and the reactivity of the primary mineral precipitate since on one hand, it determines if such reactions can take place, and on the other, also controls reaction kinetics and the extent of these reactions.

The role and fate of  $C_{\text{org}}$  during the genesis of BIFs remains especially unexplored. Past experimental studies looked into  $C_{\text{org}}$ -Fe(III) mineral associations in primary cell-Fe(III) mineral aggregates formed either by photoferrotrophs (e.g. Posth et al., 2010; Wu et al., 2014) or cyanobacteria (Swanner et al., 2015), the reactivity of these aggregates and microbial biomass towards trace elements (e.g. Bishop et al., 2019; Eickhoff et al., 2014; Martinez et al., 2016) or the trace element stoichiometry of the microbial biomass (e.g. Konhauser et al., 2018). However, these studies seldom extended beyond the stage of primary precipitate formation. Changes in  $C_{\text{org}}$  composition and reactivity (e.g. major and trace element, carbohydrate, lipid, and protein content, functional groups, aromaticity vs. aliphaticity, electron exchange capacity, etc.) as well as availability/abundance have rarely been considered in the context of BIF genesis. Considering the importance role of  $C_{\text{org}}$  as substrate for processes such as microbial Fe(III) reduction, as redox partner during low-grade metamorphic mineral transformations and potential carrier of the trace element composition preserved in BIFs, deciphering its fate during BIF genesis should be a high

priority. Along the paragenetic sequence of BIFs, the availability and reactivity of  $C_{org}$  is expected to decrease considerably, resulting in it being virtually absent from the rock record nowadays. Experimentally assessing changes in the composition, reactivity, and availability/abundance of  $C_{org}$  and products of its decomposition following processes like fermentation and methanogenesis, microbial Fe(III) reduction, diagenetic heating and low-grade metamorphism could allow us to draw conclusions on the feasibility and extent of downstream reactions or mineral transformations at a given point in the paragenetic sequence. Additionally, experimentally determining changes in the  $C_{org}$  (trace) element composition, i.e. the loss or enrichment of certain (trace) elements along the paragenetic sequence would also allow us to assess the suitability of  $C_{org}$  as carrier of the BIF trace element stoichiometry or the use of trace element patterns as biosignatures.

A potential key process in the transformation/degradation of  $C_{org}$  during BIF genesis is fermentation. Fermentation connects the initial formation of  $C_{org}$  during primary production with the subsequent microbial Fe(III) reduction and other microbial metabolisms such as methanogenesis by breaking complex  $C_{org}$  down and providing substrates such as volatile fatty acids. In our microbial Fe cycling experiments in **chapter 3** we “artificially” provided  $C_{org}$  degradation products by adding volatile fatty acids (i.e. lactate) in order to facilitate microbial Fe(III) reduction. However, it remains unknown if the biomass produced by photoferrotrophs would actually be accessible to fermenting bacteria, thus coupling primary production by photoferrotrophs to microbial Fe(III) reduction. Preliminary results of experiments conducted with a marine fermenting isolate (*Crassaminicella profunda*, Lakhali et al., 2015) suggest that  $C_{org}$  provided in the form of cell-Fe(III) minerals formed by photoferrotrophs is not available to this strain. However, other experiments where freeze-dried biomass of *Shewanella oneidensis* MR-1 was used as  $C_{org}$  substrate, an organic-rich marine sediment (see Laufer et al., 2016) was used as inoculum and microbial respiration was inhibited by the addition of Na-azide showed a strong increase in dissolved organic carbon over time and the formation of fermentation products such as acetate and  $H_2$ . This suggests that a microbial consortium is necessary for the fermentation of microbial biomass in order to form low molecular weight organic compounds that can potentially be used by Fe(III)-reducing bacteria. Another potentially problematic point is the formation of cell-Fe(III) mineral aggregates by photoferrotrophs where the  $C_{org}$  is tightly associated with Fe(III) minerals. Previous work suggested that Fe(III) minerals can protect associated  $C_{org}$  against



degradation (e.g. Lalonde et al., 2012), which could potentially limit the efficiency of  $C_{org}$  fermentation. Furthermore, the potential importance of fermentation is also linked to the uncertainty regarding the composition of the primary precipitate: Depending on the extent to which  $C_{org}$  is associated primary Fe(III) (oxyhydr)oxides it is possible that the amount compounds like volatile fatty acids formed during fermentation would be too low to fuel downstream processes such as methanogenesis, microbial Fe(III) reduction or low-grade metamorphism, with potentially important implications for the further transformation of primary BIF sediments.

Other research questions are connected to the feasibility and/or extent of microbial Fe(III) reduction. For example, the origin of magnetite in BIFs is still unresolved. Both water column Fe cycling (**chapter 3**) and low-grade metamorphism (e.g. Halama et al., 2016) do not explain the presence of magnetite in BIFs. However, results by Han et al. (2020) suggest that longer experimental timescales (>30 days), result in the formation of magnetite but remains to be tested under conditions representative for the early ocean. Alternatively, magnetite could have been formed either through the reaction of primary Fe(III) (oxyhydr)oxides with hot Fe(II)-rich hydrothermal fluids (Li et al., 2017) or through thermal decomposition of siderite (Rasmussen and Muhling, 2018), a process whose relevance for the least altered BIFs has yet to be confirmed experimentally. Additionally, even though the results of this PhD thesis (**chapter 1**) and a previous study (Robbins et al., 2015) suggest that low-grade metamorphism has only little influence on the post-depositional mobility of nutrients ( $PO_4^{3-}$ ) and trace elements (Ni, Zn), it remains unresolved how microbial Fe cycling and/or microbial Fe(III) reduction and related mineral and  $C_{org}$  transformations influence the fidelity with which BIFs record the ancient seawater composition.

Finally, the aerial expansion of early cyanobacteria and the resulting oxygenation leading up to and during the GOE (Lyons et al., 2014) would have profoundly influenced the availability of nutrients and resulted in the emergence of new terminal electron acceptors (e.g.  $O_2$  or nitrate; Schad et al., 2019), thus significantly increasing the variety of potential microbial metabolisms. Therefore, in order to (1) better understand the marine microbial Fe cycle leading up to and following the GOE, (2) determine its importance for the genesis of (early) Paleoproterozoic BIFs and (3) determine its influence on and connection to nutrient and trace element cycling as well as other biogeochemical cycles, other microbial processes should be considered in future microbial

Fe cycling experiments. These should include but are not limited to production of O<sub>2</sub> by cyanobacteria and the resulting chemical oxidation of Fe(II) (e.g. Cloud, 1973; Cloud, 1968), Fe(II) oxidation by microaerophilic Fe(II)-oxidizers (e.g. Chan et al., 2016) and or Fe(II) oxidation by nitrate-reducing Fe(II)-oxidizers (e.g. Straub et al., 1996).

Although our knowledge on the co-evolution of the inanimate world and microbial life during the Precambrian and our understanding of the processes underlying the genesis of BIFs as tool to reconstruct the environment of that time have advanced significantly, much remains to be learned. This vast conundrum is best tackled taking an interdisciplinary approach and answering some of the above discussed questions might prove to be a valuable first step.

## REFERENCES

- Ahn J. H. and Buseck P. R. (1990) Hematite nanospheres of possible colloidal origin from a Precambrian banded iron formation. *Science* **250**, 111-113.
- Alibert C. (2016) Rare earth elements in Hamersley BIF minerals. *Geochim. Cosmochim. Acta* **184**, 311-328.
- Bekker A., Planavsky N., Rasmussen B., Krapez B., Hofmann A., Slack J., Rouxel O. and Konhauser K. O. (2014) Iron formations: Their origins and implications for ancient seawater chemistry. In *Treatise on Geochemistry, second ed. Vol. 9* (eds. H. D. Holland and K. K. Turekian). Elsevier, Netherlands. pp. 561-628.
- Beukes N. J. and Gutzmer J. (2008) Origin and paleoenvironmental significance of major iron formations at the Archean-Paleoproterozoic boundary. *Rev. Econ. Geol.* **15**, 5-47.
- Beukes N. J., Klein C., Kaufman A. J. and Hayes J. (1990) Carbonate petrography, kerogen distribution, and carbon and oxygen isotope variations in an early Proterozoic transition from limestone to iron-formation deposition, Transvaal Supergroup, South Africa. *Econ. Geol.* **85**, 663-690.
- Bishop B. A., Flynn S. L., Warchola T. J., Alam M. S., Robbins L. J., Liu Y., Owtrim G. W., Alessi D. S. and Konhauser K. O. (2019) Adsorption of biologically critical trace elements to the marine cyanobacterium *Synechococcus* sp. PCC 7002: Implications for marine trace metal cycling. *Chem. Geol.* **525**, 28-36.
- Chan C. S., Emerson D. and Luther III G. W. (2016) The role of microaerophilic Fe-oxidizing micro-organisms in producing banded iron formations. *Geobiology* **14**, 509-528.
- Cloud P. E. (1973) Paleocological significance of the banded iron-formation. *Econ. Geol.* **68**, 1135-1143.
- Cloud P. E. (1968) Atmospheric and Hydrospheric Evolution on the Primitive Earth Both secular accretion and biological and geochemical processes have affected Earth's volatile envelope. *Science* **160**, 729-736.

- Davis C. C., Chen H.-W. and Edwards M. (2002) Modeling silica sorption to iron hydroxide. *Environ. Sci. Technol.* **36**, 582-587.
- Eickhoff M., Obst M., Schröder C., Hitchcock A. P., Tyliczszak T., Martinez R. E., Robbins L. J., Konhauser K. O. and Kappler A. (2014) Nickel partitioning in biogenic and abiogenic ferrihydrite: the influence of silica and implications for ancient environments. *Geochim. Cosmochim. Acta* **140**, 65-79.
- Fischer W. W. and Knoll A. H. (2009) An iron shuttle for deepwater silica in Late Archean and early Paleoproterozoic iron formation. *Geol. Soc. Am. Bull.* **121**, 222-235.
- Gole M. J. and Klein C. (1981) Banded iron-formations through much of Precambrian time. *J. Geol.* **89**, 169-183.
- Halama M., Swanner E. D., Konhauser K. O. and Kappler A. (2016) Evaluation of siderite and magnetite formation in BIFs by pressure-temperature experiments of Fe(III) minerals and microbial biomass. *Earth Planet. Sci. Lett.* **450**, 243-253.
- Han X., Tomaszewski E. J., Sorwat J., Pan Y., Kappler A. and Byrne J. M. (2020) Effect of Microbial Biomass and Humic Acids on Abiotic and Biotic Magnetite Formation. *Environ. Sci. Technol.* **54**, 4121-4130.
- Hao J., Knoll A. H., Huang F., Hazen R. M. and Daniel I. (2020a) Cycling phosphorus on the Archean Earth: Part I. Continental weathering and riverine transport of phosphorus. *Geochim. Cosmochim. Acta* **273**, 70-84.
- Hao J., Knoll A. H., Huang F., Schieber J., Hazen R. M. and Daniel I. (2020b) Cycling phosphorus on the Archean Earth: Part II. Phosphorus limitation on primary production in Archean ecosystems. *Geochim. Cosmochim. Acta* **280**, 360-377.
- Hashizume K., Pinti D., Orberger B., Cloquet C., Jayananda M. and Soyama H. (2016) A biological switch at the ocean surface as a cause of laminations in a Precambrian iron formation. *Earth Planet. Sci. Lett.* **446**, 27-36.
- Heimann A., Johnson C. M., Beard B. L., Valley J. W., Roden E. E., Spicuzza M. J. and Beukes N. J. (2010) Fe, C, and O isotope compositions of banded iron formation carbonates demonstrate a major role for dissimilatory iron reduction in ~2.5 Ga marine environments. *Earth Planet. Sci. Lett.* **294**, 8-18.
- Holland H. D. (1973) The oceans; a possible source of iron in iron-formations. *Econ. Geol.* **68**, 1169-1172.
- Jelavić S., Mitchell A. and Sand K. (2020) Fate of organic compounds during transformation of ferrihydrite in iron formations. *Geochem. Perspect. Lett.* **15**, 25-29.
- Johnson J. E., Muhling J. R., Cosmidis J., Rasmussen B. and Templeton A. S. (2018) Low-Fe(III) Greenalite Was a Primary Mineral From Neoproterozoic Oceans. *Geophys. Res. Lett.* **45**, 3182-3192.
- Jones C., Nomosatryo S., Crowe S. A., Bjerrum C. J. and Canfield D. E. (2015) Iron oxides, divalent cations, silica, and the early earth phosphorus crisis. *Geology* **43**, 135-138.
- Kappler A., Pasquero C., Konhauser K. O. and Newman D. K. (2005) Deposition of banded iron formations by anoxygenic phototrophic Fe(II)-oxidizing bacteria. *Geology* **33**, 865-868.

- Kaufman A. J., Hayes J. and Klein C. (1990) Primary and diagenetic controls of isotopic compositions of iron-formation carbonates. *Geochim. Cosmochim. Acta* **54**, 3461-3473.
- Kendall B., Creaser R. A., Reinhard C. T., Lyons T. W. and Anbar A. D. (2015) Transient episodes of mild environmental oxygenation and oxidative continental weathering during the late Archean. *Sci. Adv.* **1**, e1500777.
- Klein C. and Beukes N. J. (1989) Geochemistry and sedimentology of a facies transition from limestone to iron-formation deposition in the early Proterozoic Transvaal Supergroup, South Africa. *Econ. Geol.* **84**, 1733-1774.
- Köhler I., Konhauser K. O., Papineau D., Bekker A. and Kappler A. (2013) Biological carbon precursor to diagenetic siderite with spherical structures in iron formations. *Nat. Commun.* **4**, 1741.
- Konhauser K. O., Newman D. K. and Kappler A. (2005) The potential significance of microbial Fe(III) reduction during deposition of Precambrian banded iron formations. *Geobiology* **3**, 167-177.
- Konhauser K. O., Planavsky N. J., Hardisty D. S., Robbins L. J., Warchola T. J., Haugaard R., Lalonde S. V., Partin C. A., Oonk P. B. H., Tsikos H., Lyons T. W., Bekker A. and Johnson C. M. (2017) Iron formations: A global record of Neoproterozoic to Palaeoproterozoic environmental history. *Earth Sci. Rev.* **172**, 140-177.
- Konhauser K. O., Lalonde S. V., Planavsky N. J., Pecoits E., Lyons T. W., Mojzsis S. J., Rouxel O. J., Barley M. E., Rosière C., Fralick P. W., Kump L. R. and Bekker A. (2011) Aerobic bacterial pyrite oxidation and acid rock drainage during the Great Oxidation Event. *Nature* **478**, 369-373.
- Konhauser K. O., Robbins L. J., Alessi D. S., Flynn S. L., Gingras M. K., Martinez R. E., Kappler A., Swanner E. D., Li Y.-L., Crowe S. A., Planavsky N. J., Reinhard C. T. and Lalonde S. V. (2018) Phytoplankton contributions to the trace-element composition of Precambrian banded iron formations. *Geol. Soc. Am. Bull.* **130**, 941-951.
- Laakso T. A. and Schrag D. P. (2018) Limitations on limitation. *Global Biogeochem. Cycles* **32**, 486-496.
- Lakhal R., Pradel N., Postec A., Ollivier B., Cayol J.-L., Godfroy A., Fardeau M.-L. and Gales G. (2015) *Crassaminicella profunda* gen. nov., sp. nov., an anaerobic marine bacterium isolated from deep-sea sediments. *Int. J. Syst. Evol. Microbiol.* **65**, 3097-3102.
- Lalonde K., Mucci A., Ouellet A. and Gélinas Y. (2012) Preservation of organic matter in sediments promoted by iron. *Nature* **483**, 198-200.
- Lantink M. L., Davies J. H., Mason P. R., Schaltegger U. and Hilgen F. J. (2019) Climate control on banded iron formations linked to orbital eccentricity. *Nat. Geosci.* **12**, 369.
- Laufer K., Nordhoff M., Røy H., Schmidt C., Behrens S., Jørgensen B. B. and Kappler A. (2016) Coexistence of microaerophilic, nitrate-reducing, and phototrophic Fe(II) oxidizers and Fe(III) reducers in coastal marine sediment. *Appl. Environ. Microbiol.* **82**, 1433-1447.
- Li Y.-L., Konhauser K. O. and Zhai M. (2017) The formation of magnetite in the early Archean oceans. *Earth Planet. Sci. Lett.* **466**, 103-114.

- Lyons T. W., Reinhard C. T. and Planavsky N. J. (2014) The rise of oxygen in Earth's early ocean and atmosphere. *Nature* **506**, 307-315.
- Maliva R. G., Knoll A. H. and Simonson B. M. (2005) Secular change in the Precambrian silica cycle: insights from chert petrology. *Geol. Soc. Am. Bull.* **117**, 835-845.
- Martinez R. E., Konhauser K. O., Paunova N., Wu W., Alessi D. S. and Kappler A. (2016) Surface reactivity of the anaerobic phototrophic Fe(II)-oxidizing bacterium *Rhodovulum iodolum*: Implications for trace metal budgets in ancient oceans and banded iron formations. *Chem. Geol.* **442**, 113-120.
- Morris R. C. (1993) Genetic modelling for banded iron-formation of the Hamersley Group, Pilbara Craton, Western Australia. *Precambrian Res.* **60**, 243-286.
- Muhling J. R. and Rasmussen B. (2020) Widespread deposition of greenalite to form Banded Iron Formations before the Great Oxidation Event. *Precambrian Res.* **339**, 105619.
- Nealson K. H. and Myers C. R. (1990) Iron reduction by bacteria: a potential role in the genesis of banded iron formations. *Am. J. Sci.* **290**, 35-45.
- Pecoits E., Gingras M. K., Barley M. E., Kappler A., Posth N. R. and Konhauser K. O. (2009) Petrography and geochemistry of the Dales Gorge banded iron formation: Paragenetic sequence, source and implications for palaeo-ocean chemistry. *Precambrian Res.* **172**, 163-187.
- Posth N. R., Hegler F., Konhauser K. O. and Kappler A. (2008) Alternating Si and Fe deposition caused by temperature fluctuations in Precambrian oceans. *Nat. Geosci.* **1**, 703-708.
- Posth N. R., Huelin S., Konhauser K. O. and Kappler A. (2010) Size, density and composition of cell-mineral aggregates formed during anoxygenic phototrophic Fe(II) oxidation: Impact on modern and ancient environments. *Geochim. Cosmochim. Acta* **74**, 3476-3493.
- Posth N. R., Köhler I., Swanner E. D., Schröder C., Wellmann E., Binder B., Konhauser K. O., Neumann U., Berthold C., Nowak M. and Kappler A. (2013) Simulating Precambrian banded iron formation diagenesis. *Chem. Geol.* **362**, 66-73.
- Rasmussen B. and Muhling J. R. (2018) Making magnetite late again: evidence for widespread magnetite growth by thermal decomposition of siderite in Hamersley banded iron formations. *Precambrian Res.* **306**, 64-93.
- Reinhard C. T., Planavsky N. J., Gill B. C., Ozaki K., Robbins L. J., Lyons T. W., Fischer W. W., Wang C., Cole D. B. and Konhauser K. O. (2017) Evolution of the global phosphorus cycle. *Nature* **541**, 386.
- Robbins L. J., Swanner E. D., Lalonde S. V., Eickhoff M., Paranich M. L., Reinhard C. T., Peacock C. L., Kappler A. and Konhauser K. O. (2015) Limited Zn and Ni mobility during simulated iron formation diagenesis. *Chem. Geol.* **402**, 30-39.
- Schad M., Konhauser K. O., Sánchez-Baracaldo P., Kappler A. and Bryce C. (2019) How did the evolution of oxygenic photosynthesis influence the temporal and spatial development of the microbial iron cycle on ancient Earth? *Free Radic. Biol. Med.* **140**, 154-166.
- Siever R. (1992) The silica cycle in the Precambrian. *Geochim. Cosmochim. Acta* **56**, 3265-3272.
- Sigg L. and Stumm W. (1981) The interaction of anions and weak acids with the hydrous goethite ( $\alpha$ -FeOOH) surface. *Colloids Surf.* **2**, 101-117.

- Straub K. L., Benz M., Schink B. and Widdel F. (1996) Anaerobic, nitrate-dependent microbial oxidation of ferrous iron. *Appl. Environ. Microbiol.* **62**, 1458-1460.
- Sun S., Konhauser K. O., Kappler A. and Li Y.-L. (2015) Primary hematite in Neoproterozoic to Paleoproterozoic oceans. *Geol. Soc. Am. Bull.* **127**, 850-861.
- Swanner E. D., Wu W., Hao L., Wüstner M. L., Obst M., Moran D. M., McIlvin M. R., Saito M. A. and Kappler A. (2015) Physiology, Fe(II) oxidation, and Fe mineral formation by a marine planktonic cyanobacterium grown under ferruginous conditions. *Front. Earth Sci.* **3**, 60.
- Swedlund P. J. and Webster J. G. (1999) Adsorption and polymerisation of silicic acid on ferrihydrite, and its effect on arsenic adsorption. *Water Res.* **33**, 3413-3422.
- Trendall, A. F. (2002) The significance of iron-formation in the Precambrian stratigraphic record. *Precambrian Sedimentary Environments: a Modern Approach to Depositional Systems*, *Spec. Publ. Internat. Assoc. Sedimentol.* **33**, 33-66.
- Trendall A. F. and Blockley J. B. (1970) The iron formations of the Hamersley Group, Western Australia, with special reference to the associated crocidolite. *Western Austr. Geol. Surv., Bull.*, **119**, 353 pp.
- Wu W., Swanner E. D., Hao L., Zeitvogel F., Obst M., Pan Y. and Kappler A. (2014) Characterization of the physiology and cell–mineral interactions of the marine anoxygenic phototrophic Fe(II) oxidizer *Rhodovulum iodolum* – implications for Precambrian Fe(II) oxidation. *FEMS Microbiol. Ecol.* **88**, 503-515.

## Acknowledgments

First of all, I would like to thank my two supervisors, Prof. Andreas Kappler and Prof. Kurt O. Konhauser, for all their advice, help, effort and motivation over the past almost 4 years. Especially for giving me the freedom to do things my own way and pursue my own interests. Special thanks to Prof. Andreas Kappler who gave me the opportunity to stay in his group following my M. Sc. thesis, which sent me on a journey around the world, allowing me to establish many contacts in- and outside the academic world. Special thanks also to Prof. Kurt O. Konhauser for helping to keep the different projects on track by pointing out alternative courses of action and infusing them with the necessary background knowledge on BIF geochemistry and geology. Thanks to him also for staying patient even though I was not always the best at keeping him involved and up to speed.

Secondly, I would like to thank Prof. James Nebelsick who agreed, short notice and without hesitation, to be the second examiner for my PhD thesis.

Special thanks to Dr. Tina Gauger, supervisor of my Bachelor thesis, who sparked my interest in in Geomicrobiology and early Earth.

Additionally, I would like to thank Dr. James M. Byrne, Dr. Katharine Thompson, Dr. Allison Enright and Timm Bayer for revising and providing feedback for individual parts of my thesis.

Furthermore, I'd like to thank Dr. James M. Byrne for introducing me into the fascinating world of Moessbauer spectroscopy, electron microscopy and Synchrotron facilities, which fundamentally influenced and shaped my research interest.

Next, I would like to thank Dr. Casey Bryce for looking out for me during my first conference the "1<sup>st</sup> Geobiology Society Conference" in Banff, Canada, back in 2017, and for all of her help and advice over the years.

## Acknowledgments

---

A big “thank you” also to Ellen Röhm, Lars Grimm and Franziska Schädler for their technical support and guidance during the past years and for finding solutions to countless problems.

Thanks also to the (past) “Early Earth/BIF” team, Dr. Maximilian Halama, Dr. Wenfang Wu, Dr. Aleksandra Mloszewska, Dr. Elif Koeksoy, Dr. Viola Warter, Dr. Xiaohua Han, Dr. Markus Maisch and Kai Simmak for many fruitful discussions and valuable feedback.

Additionally, I would like to thank the Moessbauer team (past and current members), Dr. James M. Byrne, Dr. Prachi Joshi, Dr. Zhe Zhou, Dr. Viola Warter, Dr. Markus Maisch, Julian Sorwat and Timm Bayer for their help over the past years.

Thank you also to everybody involved in the ESRF beamtime in March 2018: Dr. James M. Byrne, Dr. Catherine McCammon, Dr. Elisabeth Tomaszewski and Dr. Valerio Cerantola. Whisky tasted never better than the glass we had together at 2.30 h in the morning, when we finally got our measurements to run.

Special thanks go to my current and past office members Dr. Jing He, Dr. Wenfang Wu, Dr. Julia Otte, Dr. Zhe Zhou, Dr. Xiaohua Han, Dr. Dandan Chen, Dr. Louisa Notini, Edgardo Valenzuela, Monique Patzner, Franziska Schädler, Verena Nikeleit, Lars Grimm, Sören Drabesch and Lydia Olson. Thanks for pep and fun talks, discussions, feedback, shared beers, pastries, and chocolate.

A very honorable mention also to all the past and current coffee machines of the Geomicrobiology group, who provided me with an unlimited supply of black, revitalizing gold.

Thank you also to all present and past Geomicrobiology group members I did not mentioned so far for a thoroughly enjoyable time in Tübingen. Thank you for all the fun nights out, the BBQs, your help and support. It means the world to me.

Further thanks go to the various students of Prof. Sean Crowe’s and Prof. Kurt O. Konhauser’s groups whom I linked up with at different conferences and had many fun nights out.

Thank you also to all the students in Prof. Harald Thorwarth’s group at the University of Rottenburg (a. N.), who made two extensive measurement campaigns in fall 2019 so much more enjoyable.



Thanks also to all the people who I met over the last years (and I might have forgotten to mention), who played their individual roles in this PhD endeavour.

Someone who probably played a somewhat underrated but very important role over the last months is Viktoria Krause, my official in charge at the employment exchange in Tübingen. Thanks to her I had the time and freedom to write my thesis up relatively undisturbed.

Finally, I would like to thank my parents, my sisters, extended family (Chinese and German) and my friends at home. Thank you for your unrelenting support, your motivation and for staying in touch with me despite me burying myself in my work, keeping me linked to the world outside of science and keeping me down to Earth.

Last but not least, the biggest thanks go to my partner Yuge Bai, for her unrelenting support and positivity, her unconditional love, for dragging me up from my lowest lows and sharing my greatest joys. Thank you for enduring all of my frustrations and tempers. Thank you for always being there when I needed you and for lighting up my days. I could not have done it without you! 我爱你!



---

## Curriculum Vitae

### Personal data

---

<b>Name</b>	Manuel Alexander Schad
<b>Current address</b>	Salzwasenweg 12 72074 Tuebingen Germany
<b>E-mail</b>	manuel.schad@uni-tuebingen.de
<b>Data and place of birth</b>	April 7 <sup>th</sup> , 1991, Stuttgart, Germany
<b>Citizenship</b>	German

### Academic education

---

Since 02/2017	<b>Ph.D. in Geoecology</b> , Eberhard Karls University Tuebingen, Germany
Thesis title	<i>Cycles within cycles - The significance of temperature cycling, microbial Fe cycling and low-grade metamorphic nutrient immobilization for the genesis of banded iron formations</i> Geomicrobiology group, Center for Applied Geosciences, Eberhard Karls University Tuebingen
Supervisors	Prof. Dr. Andreas Kappler, Prof. Dr. Kurt O. Konhauser
10/2013 – 09/2016	<b>M.Sc. in Geoecology</b> , Eberhard Karls University Tuebingen, Germany
Thesis title	<i>Layering processes in Banded Iron Formations: Deposition mechanisms, sedimentation and diagenesis</i> Geomicrobiology group, Center for Applied Geosciences, Eberhard Karls University Tuebingen
Supervisors	Prof. Dr. Andreas Kappler, Dr. Maximilian Halama

10/2010 – 10/2013	<b>B.Sc. in Geoecology</b> , Eberhard Karls Universität Tuebingen, Germany
Thesis title	<i>Effect of UV radiation on Acidovorax sp. strain BoFeNI – Quantification of oxidative protein damage</i>
	Geomicrobiology group, Center for Applied Geosciences, Eberhard Karls University Tuebingen
Supervisors	Prof. Dr. Andreas Kappler, Dr. Tina Gauger

---

### Conference contributions and workshops

---

12/2019	“The fundamental nature of Earth’s earliest oceans – status quo and future perspectives” Workshop, Göttingen, Germany <b>Talk</b> – “Remobilization of phosphorous during diagenetic and metamorphic transformation of precursor minerals of Banded Iron Formations”
08/2019	Goldschmidt conference, Barcelona, Spain <b>Talk</b> – “Influence of microbial Fe cycling on the formation of primary BIF sediments”
09/2017	GeoBremen, Bremen, Germany <b>Talk</b> – “Temperature fluctuations in the Precambrian ocean could have caused alternating deposition of Fe-rich and Si-rich layers in Banded Iron Formations”
06/2017	1 <sup>st</sup> Geobiology Society Conference, Banff, Canada <b>Poster</b> – “Temperature fluctuations in the Precambrian ocean could have caused alternating deposition of Fe-rich and Si-rich layers in Banded Iron Formations”

**Teaching and supervising experience**

---

- Winter term 2019      **Lecture – “Statistics in Geo- and Environmental Sciences”**  
Geomicrobiology group, Eberhard Karls University Tuebingen
- Winter term 2017,  
2018 and 2019      **Lab course – “Spectroscopic and Microscopic Analysis in the Environment”**  
Geomicrobiology group, Eberhard Karls University Tuebingen
- 09/2017      **Field excursion – “Geomicrobiology and Biogeochemistry of High Alpine Fe-rich Cold-Water Springs”**  
Geomicrobiology group, Eberhard Karls University Tuebingen

**Other training and practical experience**

---

- 10/2016 – 12/2016      2-month research internship at the University of Alberta, Canada,  
group of Prof. Dr. K.O. Konhauser
- 08/2016      10-day excursion Barberton Greenstone Belt, South Africa, DFG  
Schwerpunktprogramm SPP 1833 – “Building a Habitable Earth”
- 09/2016 – 12/2016      Research assistant, Geomicrobiology group, University of Tuebingen
- 11/2014 – 03/2015      Research assistant, Geomicrobiology group, University of Tuebingen

## Publication record

---

### In preparation:

**Schad M.**, Halama M., Robbins L. J., Warchola T. J., Tejada J., Kirchhof R., Lalonde S.V., Swanner E. D., Planavsky N. J., Thorwarth H., Mansor M., Konhauser K. O., Kappler A. Phosphate remobilization from banded iron formations depends on metamorphic mineral transformations. For submission to *GSA Bulletin*.

**Schad M.**, Byrne J. M., ThomasArrigo L. K., Kretzschmar R., Konhauser K. O., Kappler A. Microbial Fe cycling in a simulated Precambrian ocean environment: Implications for secondary mineral (trans)formation and deposition during BIF genesis. For submission to *Geochimica et Cosmochimica Acta*.

Nikeleit V., Melage A., Bianchini G., Sauter L., Buessecker S., Gotterbarm S., **Schad M.**, Sánchez-Baracaldo P., Kappler A., Bryce C. Inhibition of phototrophic metabolisms by nitric oxide in ferruginous environments. In preparation.

### Published:

**Schad M.**, Halama M., Bishop B., Konhauser K. O., Kappler A. (2019). Temperature fluctuations in the Archean ocean as trigger for varve-like deposition of iron and silica minerals in Banded Iron Formations. *Geochimica et Cosmochimica Acta*, **265**, 386-412.

**Schad M.**, Konhauser K. O., Sánchez-Baracaldo P., Kappler A., & Bryce C. (2019). How did the evolution of oxygenic photosynthesis influence the temporal and spatial development of the microbial iron cycle on ancient Earth?. *Free Radical Biology and Medicine*, **140**, 154-166.

Bryce C., Blackwell N., Schmidt C., Otte J., Huang Y.-M., Kleindienst S., Tomaszewski E., **Schad M.**, Warter V., Peng C., Byrne J. M., Kappler A. (2018). Microbial anaerobic Fe(II) oxidation – Ecology, mechanisms and environmental implications. *Environmental Microbiology*, **20**, 3462-3483.